UNIVERSITY OF OVIEDO

DEPARTMENT OF ELECTRICAL, ELECTRONICS, COMPUTERS AND SYSTEMS ENGINEERING

Ph.D. PROGRAM ON ENERGY AND PROCESS CONTROL

Ph.D. THESIS

RESEARCH ON POWER SUPPLIES FOR OLED LAMPS BASED ON SWITCHED CAPACITOR CONVERTERS

BY

GILBERTO MARTÍNEZ

JULY 2018

DIRECTOR: JOSÉ MARCOS ALONSO ÁLVAREZ
CO-DIRECTOR: RENÉ OSORIO SÁNCHEZ

UNIVERSIDAD DE OVIEDO

DEPARTAMENTO DE INGENIERÍA ELÉCTRICA, ELECTRÓNICA, COMPUTADORES Y SISTEMAS

PROGRAMA DE DOCTORADO EN ENERGÍA Y CONTROL DE PROCESOS

TESIS DOCTORAL

INVESTIGACIÓN EN SISTEMAS DE ALIMENTACIÓN PARA LÁMPARAS OLED BASADOS EN CONVERTIDORES DE CAPACIDADES CONMUTADAS

POR

GILBERTO MARTÍNEZ

JULIO 2018

DIRECTOR: JOSÉ MARCOS ALONSO ÁLVAREZ

CO-DIRECTOR: RENÉ OSORIO SÁNCHEZ

INDEX OF CONTENT

INDEX OF FIGURES

ABSTRACT

Chapter 2 presents an analysis of the OLED technique, since more compact, small and flat organic-lighting-emitting-diode (OLED) drivers are arising to enable new design possibilities such as avant-garde interior floor and table lamps, mirror and ceiling lamps, ablaze tiles and partition wall lighting applications. Thus, OLED drivers arise as the best option, owing to their compactness, size and flatness. OLED lamps allow lighting designers and architects to develop their ideas down to the smallest detail owing to their easy integration and customization. Since their slimness is just few millimeters thin, OLEDs can be integrated into many different areas, and allow light sources to be designed in a variety of shapes and sizes. An important advantage of the OLEDs against inorganic lighting-emitting diodes (LEDs), it is the way they emit light; OLEDs are surface light sources, whilst LEDs are point sources. Thereby, the light generated by OLEDs has a naturally soft and comfortable diffuse characteristic and it is glare-free.

OLED lamps consist of a large semiconductor area sandwiched between two electrodes, where the organic materials are built-in. In this way, an electrical field is generated among the organic layers, which produce the capacitive behavior. Owing to this, OLED lamps have a different dynamic behavior compared to LEDs.

Chapter 3 presents the different OLED photo-electrical-thermal (PET) models, which represents the OLED structure and their photo-electrical-thermal behavior by means of an equivalent PET model, or by a simple equivalent electrical circuit that combines resistors and a capacitor. In these models, the ohmic losses are generated from the contact resistances of the organic layers, bulk conduction within the organic layers and electrode resistance.

Chapter 4 presents the analysis of different switched-capacitor (SC) converters topologies, to drive OLED lamps, because of their great advantages as to high power density and owing to the fact that they are light, small and cheaper in comparison with other solutions as linear power supplies and conventional DC-DC converters, owing to the fact that they do not use any large energy storage components. Resonant SC converters show high efficiency and low EMI noise, because they employ a small resonant inductor, which is connected in series with a switched

capacitor in order to resonate at a frequency higher than the switching frequency, thus allowing them to attain zero-current-switching (ZCS). Resonant SC converters consist of diodes, switches, and capacitors. As aforementioned, these converters do not use any large inductor, which leads to a high power density of the converter, making them suitable for OLED lamp driving. Some resonant SC converter applications are for instance, portable and any low-profile electronic equipment, such as notebook computers, tablets and portable digital assistants.

Therefore, a review of resonant SC converters for OLED lamp driving is carried out in chapter 4 of this work, in which the unidirectional resonant switched-capacitor (URSC) step-up converter arise as the best option for driving OLED lamps, based on the performance comparative results among the different resonant SC converters presented in the state of the art. The benefits of using the URSC step-up converter instead of conventional non-resonant and resonant SC converters, fractional-voltage-conversion-ratio (FVCR) resonant SC converters, dual-phase (DP) converters, step-down half bridge resonant SC converter with isolation transformer, and the step-down SC converter with coupling inductors are: high output voltage regulation, low output voltage and current ripples, high efficiency, no efficiency dependency on conversion ratio, low EMI noise, and high power density.

In chapter 5, an analysis and design of a URSC step-up converter for OLED lamp driving is carried out. The URSC is designed to operate in closed loop with constant current variable inductor (VI) control technique. Owing to the fact that the OLED power of the resonant SC converter is regulated by its resonant frequency, which is controlled by the resonant tank integrated by the $L_r - C_r$ network, a control parameter that regulates the output power of the resonant SC converter is needed. Hence, the VI control technique is proposed to regulate the output power of the resonant SC, which reduces the complexity of the control loop and circuitry, and increases the power density of the OLED driver because it is operated by a simple constant current source to meet the operating point of the VI. In this way, it is possible to achieve more compact OLED drivers.

A proposed SPICE-based electrical-magnetic model and the analysis and design of the VI used in this work as well as its application to an LED driver are presented in chapter 5. Also, some additional works in the literature about VI study and application are illustrated.

In chapter 5, the URSC step-up converter is analyzed and designed for driving a 21.8 W OLED lamps array. The resonant inductor is designed to operate at a resonant frequency above the switching frequency for any OLED power. Under this condition, a good dynamic behavior against input voltage or luminous flux variations is obtained.

Simulation and experimental results of a URSC step-up converter design example for a 21.8 W OLED lamps array supplied from 48Vdc are presented in chapter 6, in which a maximum energy efficiency η of 92.97% is obtained. The simulation and experimental results of the VI inductor and the URSC converter are in a good agreement one another.

NOMENCLATURE

AHB	Asymmetrical half bridge
BB	Buck-boost
BOM	Bill of materials
CIE	Comission Internationale de L'Eclairage
CRI	Color rendering index
DALI	Digital addressable lighting interface
DCM	Discontinous conduction mode
DMX	Digital multiplexing communication protocol
DP	Dual-phase
DSI	Digital serial interface
EMI	Electromagnetic interference
FVCR	Fractional-voltage-conversion-ratio
FWHM	Full width at the half maximum of the multi-SPD $[m^3]$
HB	Half-bridge
HBZ	Half bridge zeta
LED	Lighting-emitting diode
MCB	Multi-configurable bidirectional
OLED	Organic-lighting-emitting diode
PET	Photo-electrical-thermal
PFC	Power factor correction
PI	Proportional-integral

PWL	Piecewise linear
PWM	Pulse-width-modulation
RSC	Resonant switched-capacitor
SC	Switched-capacitor
SMPS	Switched mode power supply
SPD	Spectral power distribution
SPET	scale-photometrical-electrical-thermal
SSL	Solid state lighting
TEM	Theoretical equivalent model
URSC	Unidirectional resonant switched-capacitor
VI	Variable inductor
VPWL	Voltage-control piecewise linear
ZAHB	Zeta asymmetrical half bridge
ZCS	Zero-current-switching
ZVS	Zero-voltage-switching
$\boldsymbol{A_m}$	Cross section area of the variable reluctance $[m^2]$
$\boldsymbol{A_{OLED}, S}$	Surface area of the OLED $[mm^2]$
$\boldsymbol{A_0}$	Cross section area of the constant reluctance $[m^2]$
$\boldsymbol{A_w}$	Cross section area of the magnetic core $[m^2]$
$\boldsymbol{B, B_w}$	Magnetic flux density $[T]$
$\boldsymbol{C_d}$	Diffusion capacitor of the equivalent electrical OLED model $[F]$
$\boldsymbol{C_{in}}$	Input capacitor $[F]$
$\boldsymbol{C_{iss}}$	Input capacitance of transistors Q_1 and Q_2 $[F]$

$\boldsymbol{C_{GS}}$	Gate-source capacitance of transistors Q_1 and Q_2 $[F]$
$\boldsymbol{C_g}$	Geometric capacitor of the equivalent electrical OLED model $[F]$
$\boldsymbol{C_{glass}}$	Glass heat capacity of the OLED material $[J/kg°C]$
$\boldsymbol{C_{jc}}$	Junction to case thermal capacitance $[J/°C]$
$\boldsymbol{C_{hs}}$	Heatsink thermal capacitance $[J/°C]$
$\boldsymbol{C_O}$	Output filter capacitor $[F]$
$\boldsymbol{C_r}$	Resonant capacitor $[F]$
$\boldsymbol{C_S}$	Switched capacitor $[F]$
$\boldsymbol{C_{\theta C}}$	Thermal capacitance of the OLED $[J/°C]$
$\boldsymbol{d}$	Thickness of the active layer of the OLED $[mm]$
$\boldsymbol{E}$	Luminous efficacy $[lm/W]$
$\boldsymbol{E_0}$	Rated luminous efficacy $[lm/W]$
$\boldsymbol{f_m}$	Resonant frequency of a sine wave of 540° $[Hz]$
$\boldsymbol{f_n}$	Resonant frequency of a sine wave of 360° $[Hz]$
$\boldsymbol{f_S}$	Switching frequency $[Hz]$
$\boldsymbol{F_{dc}, F_p, \mathcal{F}_w}$	Magnetomotive forces of the VI $[A]$
$\boldsymbol{I_B}$	Average balance current during the operation interval t_3-t_5 $[A]$
$\boldsymbol{I_{B2}}$	Average balance current during the operation interval t_4-t_5 $[A]$
$\boldsymbol{I_D, I_d}$	LED current in steady state $[A]$
$\boldsymbol{I_{Davg\_Q1}, I_{Davg\_Q2}}$	Average drain current of MOSFETs Q_1 and Q_2 $[A]$
$\boldsymbol{I_{Davg\_D1}, I_{Davg\_D2}}$	Average diode current of diodes D_1 and D_2 $[A]$
$\boldsymbol{I_{Dp\_Q1}, I_{Dp\_Q2}}$	Maximum drain current of MOSFETs Q_1 and Q_2 $[A]$
$\boldsymbol{I_{Dp\_D1}, I_{Dp\_D2}}$	Maximum diode current of diodes D_1 and D_2 $[A]$

I_{dc}	Auxiliary winding DC bias current $[A]$
I_f	Forward current of the OLED $[A]$
I_{fo}	Reference forward current $[A]$
I_{in}	Input current $[A]$
I_K	OLED knee current $[A]$
I_L	Luminous intensity of the OLED $[cd]$
iL_O	Output inductor current $[A]$
iL_r	Resonant inductor current $[A]$
I_M	OLED maximum current $[A]$
I_{OLED}	DC OLED current $[A]$
I_p	Primary winding bias current $[A]$
I_Q	OLED rated current $[A]$
I_{rms1}	RMS current of the charge operation stage $[A]$
I_{rms2}	RMS current of the discharge operation stage $[A]$
I_{rms3}, I_{rms4}	RMS currents of the balance operation stage $[A]$
I_S	Reverse bias saturation current of the LED $[A]$
$I_{sat}(T_a)$	Saturation current of the OLED at the operating ambient temperature $[A]$
i_w	Current of the winding $[A]$
k_{air}	Convective heat transfer coefficient $[W/m°C]$
k_e	Relative rate of luminous efficacy reduction constant due to temperature rise
k_{glass}	Thermal conductivity coefficient of the OLED material $[W/m°C]$
$k_{peak,m}$	Temperature coefficient of the peak wavelength
k_h	LED power loss constant

$\boldsymbol{k_I}$	Rate of the luminous flux variation constant as a function of forward current
$\boldsymbol{k_{jc}}$	Junction to case thermal coefficient $[°C/W^2]$
$\boldsymbol{k_{Rs}}$	Resistance drop rate $[\Omega/°C]$
$\boldsymbol{k_T}$	Negative rate of the luminous flux variation
$\boldsymbol{k_v}$	Voltage drop rate $[mV/°C]$
$\boldsymbol{k_{\Delta\lambda,m}}$	Temperature coefficient of the FWHM of the multi-SPD
$\boldsymbol{k_1, k_3}$	Brauer's coefficients of the magnetic material $Am^{-1}T^{-1}$
$\boldsymbol{k_2}$	Brauer's coefficient of the magnetic material T^{-2}
$\boldsymbol{L_c}$	Critical size of the OLED area $[m]$
$\boldsymbol{L_e}$	Stray inductance of the connection wire of the OLED $[H]$
$\boldsymbol{l_m}$	Magnetic path length of the variable reluctance $[m]$
$\boldsymbol{L_O}$	Output inductor $[H]$
$\boldsymbol{l_0}$	Magnetic path length of the constant reluctance $[m]$
$\boldsymbol{L_r}$	Resonant inductor $[H]$
$\boldsymbol{n}$	Ideality factor of the LED
$\boldsymbol{n(T_a)}$	Ideality factor of the OLED at the operating ambient temperature
$\boldsymbol{N_{dc1}, N_{dc2}}$	Auxiliary windings of the VI
$\boldsymbol{N_p}$	Main winding of the VI
$\boldsymbol{N_u}$	Nusselt number
$\boldsymbol{N_w}$	Number of turns of the winding
$\boldsymbol{p}$	OLED perimeter $[m]$
$\boldsymbol{P_{cond\_Q1}, P_{cond\_Q2}}$	Power conduction losses of transistors Q_1 and Q_2 $[W]$
$\boldsymbol{P_{core}}$	Core loss of the resonant inductor $[W]$

$\boldsymbol{P_{Cr\_Lr}}$	Power dissipation across the capacitor C_r and inductor L_r $[W]$
$\boldsymbol{P_D, P_d}$	LED power in steady state $[W]$
$\boldsymbol{P_{D1}, P_{D2}}$	Power diode losses $[W]$
$\boldsymbol{P_{D\_Q2}}$	Power losses of the diode of transistor Q_2 $[W]$
$\boldsymbol{P_{el}, P_{OLED}}$	**O**LED power $[W]$
$\boldsymbol{P_{fres}}$	Power loss of the feedback resistor $[W]$
$\boldsymbol{P_{gate}}$	Gate power losses of transistors Q_1 and Q_2 $[W]$
$\boldsymbol{P_h}$	**O**LED power converted to heat $[W]$
$\boldsymbol{P_{heat}}$	LED power converted to heat $[W]$
$\boldsymbol{P_{loss}}$	Total power loss of the URSC converter $[W]$
$\boldsymbol{P_{opt}, P_{opt,m}}$	Optical power of the OLED $[W]$
$\boldsymbol{P_v}$	Relative core loss of the magnetic $[W/m^3]$
$\boldsymbol{Q_{OLED}}$	OLED electrical charge $[C]$
$\boldsymbol{q}$	Elementary charge of the LED $[C]$
$\boldsymbol{R_{bi}}$	Bias resistor of the equivalent electrical OLED model $[\Omega]$
$\boldsymbol{R_{Cr}}$	Stray resistance across the passive component C_r $[\Omega]$
$\boldsymbol{R_D}$	Equivalent resistance of the LED in steady state $[\Omega]$
$\boldsymbol{R_{DSon}}$	Drain-source on-resistance of MOSFETs Q_1 and Q_2 $[\Omega]$
$\boldsymbol{R_e}$	Series electrode resistance of the equivalent electrical OLED model $[\Omega]$
$\boldsymbol{R_f}$	Feedback resistor $[\Omega]$
$\boldsymbol{R_{hs}}$	Heatsink thermal resistance $[°C/W]$
$\boldsymbol{R_{jc}}$	Junction to case thermal resistance $[°C/W]$
$\boldsymbol{R_{jco}}$	Rated junction to case thermal resistance $[°C/W]$

$\boldsymbol{R_{LC}}$	Total stray resistance across the passive components C_r and L_r [Ω]
$\boldsymbol{R_{Lr}}$	Stray resistance across the passive component L_r [Ω]
$\boldsymbol{R_{OLED}}$	Equivalent static OLED resistance [Ω]
$\boldsymbol{R_p}$	Leakage resistance of the equivalent electrical OLED model [Ω]
$\boldsymbol{R_s}$	Dynamic series resistance of the equivalent electrical OLED model [Ω]
$\boldsymbol{R_{S1}}$	Series resistance of the switch of two positions [Ω]
$\boldsymbol{R_\theta}$	Material thermal resistance of the OLED $[°C/W]$
$\boldsymbol{R_{\theta Ca}}$	Thermal case to ambient resistance of the OLED $[°C/W]$
$\boldsymbol{R_{\theta conv}}$	Thermal convection resistance of the OLED $[°C/W]$
$\boldsymbol{R_{\theta jc}}$	Thermal conduction resistance of the OLED $[°C/W]$
$\boldsymbol{R_{\theta rad}}$	Thermal radiation resistance of the OLED $[°C/W]$
$\boldsymbol{\Re_c, \Re_l, \Re_r, \Re_m}$	Variable reluctances of the VI $[A/Wb]$
$\boldsymbol{\Re_g, \Re_O}$	Constant reluctance of the VI $[A/Wb]$
$\boldsymbol{R_\gamma}$	Dynamic resistance [Ω]
$\boldsymbol{T_a}$	Ambient temperature $[°C]$
$\boldsymbol{T_C}$	Case temperature of the OLED $[°C]$
$\boldsymbol{t_{glass}}$	Thickness of the glass substrate of the OLED material $[\mu m]$
$\boldsymbol{T_O}$	Rated temperature $[°C]$
$\boldsymbol{T_j}$	Junction temperature of the LED $[°C]$
$\boldsymbol{T_1}$	Characteristic temperature of the OLED $[°C]$
$\boldsymbol{T_{hs}}$	Heatsink temperature $[°C]$
$\boldsymbol{U}$	Luminance uniformity
$\boldsymbol{V_{bi}}$	Bias voltage source of the equivalent electrical OLED model $[V]$

$\boldsymbol{V_{DC}}$	DC voltage supply $[V]$
$\boldsymbol{V_{cg}}$	Voltage of the **g**eometric capacitor of the electrical OLED model $[V]$
$\boldsymbol{V_{Cr}}$	Resonant capacitor voltage $[V]$
$\boldsymbol{V_{D,} V_d}$	LED voltage in steady state $[V]$
$\boldsymbol{V_{DS\_Q1}, V_{DS\_Q2}}$	Drain-source voltage of MOSFETs Q_1 and Q_2 $[V]$
$\boldsymbol{V_e}$	Effective volume of the magnetic core $[m^3]$
$\boldsymbol{V_f}$	Forward voltage of the OLED $[V]$
$\boldsymbol{V_{fb}}$	Feedback voltage $[V]$
$\boldsymbol{V_{GS}}$	Gate-source voltage of transistors Q_1 and Q_2 $[V]$
$\boldsymbol{V_K}$	OLED knee voltage $[V]$
$\boldsymbol{V_{in}}$	Input voltaje $[V]$
$\boldsymbol{V_M}$	OLED maximum voltage $[V]$
$\boldsymbol{V_{OLED}}$	DC OLED voltage $[V]$
$\boldsymbol{v_{OLED}}$	Volume of the OLED $[m^3]$
$\boldsymbol{V_Q}$	OLED rated voltage $[V]$
$\boldsymbol{V_{R\_D1}, V_{R\_D2}}$	Reverse voltage of diodes D_1 and D_2 $[V]$
$\boldsymbol{V_{refA}, V_{refB}, V_{I_{OLED}}}$	Reference voltage A and B and OLED current reference $[V]$
$\boldsymbol{V_{rs}}$	Voltage across the dynamic series resistance of the OLED $[V]$
$\boldsymbol{V_t, V_O}$	Threshold voltage of the equivalent electrical OLED model $[V]$
$\boldsymbol{V_T}$	Thermal voltage of the diode $[V]$
$\boldsymbol{V_T(T_a)}$	Threshold voltage of the OLED at the operating ambient temperature $[V]$
$\boldsymbol{v_w}$	Voltage of the winding $[V]$
$\boldsymbol{V_\gamma}$	Threshold voltage $[V]$

$\boldsymbol{Z_n}$	Equivalent resonant tank impedance $[\Omega]$
$\Delta \boldsymbol{I_{OLED}}$	Ripple current of the OLED $[A]$
$\Delta \boldsymbol{V_{OLED}}$	Ripple voltage of the OLED $[V]$
$\boldsymbol{\mathcal{E}}$	OLED surface emissivity
$\boldsymbol{\mathcal{E}_0}$	Permitivity of free space $[F/m]$
$\boldsymbol{\mathcal{E}_r}$	Relative permitivity of the active layer of the OLED $[F/m]$
$\boldsymbol{\mu_0}$	Permeability of the free space $[H/m]$
$\boldsymbol{\nu}$	Fringing factor
$\boldsymbol{\eta}$	Energy efficiency $[\%]$
$\boldsymbol{\sigma}$	Steffen-Boltzmann constant $[W/m^2{}^\circ C^4]$
$\emptyset_{\boldsymbol{dc}}$	DC flux bias $[Wb]$
$\boldsymbol{\phi_o}$	Nominal luminous flux $[lm]$
$\boldsymbol{\phi_v}, \boldsymbol{\phi}$	Luminous flux $[lm]$
$\emptyset_{\boldsymbol{w}}$	Magnetic flux $[Wb]$
$\boldsymbol{\lambda}$	Temperature coefficient $[V/^\circ C]$
$\boldsymbol{\Delta\lambda_m}$	Full width at the half maximum of the multi-SPD $[m^3]$
$\boldsymbol{\Delta\lambda_{m,r}}$	Reference Full width at the half maximum of the multi-SPD $[m^3]$
$\boldsymbol{\lambda_{peak}}, \boldsymbol{\lambda_{peak,m}}$	Peak wavelength of the OLED $[m^3]$
$\boldsymbol{\lambda_{peak,m,r}}$	Reference peak wavelength of the OLED $[m^3]$
$\boldsymbol{\rho_{glass}}$	Glass density of the OLED material $[kg/m^3]$

PUBLICATIONS

1 Gilberto Martínez, J. Marcos Alonso and R. Osorio, “Analysis and Design of a Unidirectional Resonant Switched Capacitor Step-up Converter for OLED Lamp Driving Based on Variable Inductor,” *IEEE Journal of Emerging and Selected Topics in Power Elect., Accepted for future publication.*

2 Gilberto Martínez, J. Marcos Alonso and R. Osorio, “Analysis and Design of a Unidirectional Resonant Switched Capacitor Step-up Converter for OLED Lamp Driving Based on Variable Inductor,” *IEEE Ind. Appl. Society Conference*, Oct . 2017, pp. 1-8.

3 Gilberto Martínez and J. Marcos Alonso, “A Review on Switched Capacitor Converters with High Power Density for OLED Lamp Driving,” *IEEE Ind. Appl. Society Conference*, Oct. 2015, pp. 1-8.

4 J. M. Alonso, G. Martínez, M. Perdigão, M. Cosetin, R. N. do Prado; “A Systematic Approach to Modelling Complex Magnetic Devices using SPICE: Application to Variable Inductors,” IEEE Trans. on Power Electronics, Vol. 31, pp. 7735-7746, May. 2016.

5 J. M. Alonso, G. Martínez, M. Perdigão, M. Cosetin, R. N. do Prado; “Modeling Magnetics Devices Using Spice: Application to Variable Inductors,” *IEEE Applied Power Electronics Conference and Exposition APEC Conference*, Mar. 2016, pp. 1115-1122.

6 J. M. Alonso, M. S. Perdigão, M. A. Dalla Costa, G. Martínez and R. Osorio, “Analysis and Experiments on a Single-Inductor Half-Bridge LED Driver with Magnetic Control,” *IEEE Trans. on Power Electronics*, vol. 32, pp. 9179-9190, Jan. 2017.

7 J. M. Alonso, M. S. Perdigão, M. A. Dalla Costa, G. Martínez and R. Osorio, “Analysis and Design of a Novel Variable-Inductor-Based LED Driver for DC Lighting Grids,” *IEEE Ind. Appl. Society Conference*, Oct. 2016, pp. 1-8.

8 R. Osorio, J. M. Alonso, S. E. Pinto, G. Martínez, N. Vázquez, M. Ponce-Silva and A. J. Martínez, “Simplified electrical modelling of power LEDs for DC-DC converter analysis and simulation”, Int. J. Circ. Theor. Appl., April, 2017.

ACHIEVEMENTS

An important achievement obtained as a result of the development of this research work is the following:

- First prize paper award from the IAS Industrial Lighting and Display Committee at the 2017 IEEE IAS Conference.

1. Introduction

As an introduction of this dissertation, the background of lighting applications that relates to the interest of the development of this research work, framework, objectives and structure of this dissertation are presented.

1.1. Background

Lighting has been a very important technology in the world, since the invention of incandescent bulbs and fluorescent tubes till the solid-state lighting technology. In regards to energy consumption around the world, lighting represents an important amount, and consumes over 20% of the energy supplied for the energy generation systems in the world. Therefore, more efficient light sources are needed nowadays, in order to reduce the global carbon footprint due to energy generation. In addition, it is important to ensure a high color quality light source because it has a positive psychological impact on people's daily life. Also, it is extremely important the use of light sources that require minimal harmful materials during their production. Fortunately, OLED technology fulfilled both requirements. On the other hand, OLED technology offers innovative designs as to shape, size, flatness, thinness, and bendable form factor.

Nowadays, more efficient and high power density OLED drivers are needed in order to achieve a less energy consumption and high power density lamp-driver integration. Due to the fact that linear power supplies are low power density and low efficiency, DC-DC converters that meet high power density and high efficiency are investigated. Some high-efficiency LED drivers, such as buck-boost (BB) and an LED power supply based on a synchronous buck converter are reported in [1]-[2]. The BB converter processes only a part of the LED power owing to the fact that the LED power is supplied by two sources, the DC input voltage source and the BB converter output [1]. The synchronous buck converter drives a split LED string; the first LED string is driven by the buck converter and the second LED string is placed in series with the input voltage source [2]. These works obtain a good efficiency, around 92-93%, at maximum LED power, but they present a low power density due to the use of bulky and heavy switching inductors, input and output filter capacitors. These LED drivers show high output ripple current, which can reduce the OLED's life span and could cause eye-visible luminous flux variations.

A fly-back converter operating as a current regulator between the DC voltage source and the LED is presented in [3]; the converter returns a part of the energy from the output filter capacitor to the DC link input capacitor, which lowers the power conversion losses because only a small part of the LED power is processed by the fly-back converter [3]. An integrated half bridge zeta (HBZ) asymmetrical half bridge (AHB) converter is presented in [4], which obtains high efficiency on an entire output voltage range at constant low output current. In this way, it achieves high efficiency either at high output voltage or low output voltage as reported in [4]. A half bridge (HB) LC series resonant converter based on high power HB-LED driver is proposed in [5]. It operates under zero-voltage-switching (ZVS), and drives the LED load by means of two sources; the input DC bus source supplies the cut-in voltage and the second source regulates the forward current, which leads to obtain high efficiency because not all the LED power is processed by the HB-LC series resonant converter. A high input-voltage-ripple-rejection zeta asymmetrical half bridge (ZAHB), which overcomes the performance drawbacks of the AHB such as limited duty cycle range, non-linear DC gain and not fully cancellation of the low frequency ripple, is reported in [6].

Even though, the converters reported in [1]-[6] show high peak efficiencies in the range of 92-96%, regrettably, they show very low power density compared to the SC converters due to the total number of components, bulky and heavy inductors and switching transformers, DC link and output filter capacitors. Therefore, they do not allow the designers to attain a compact, flat and small OLED driver + OLED lamp system. Moreover, it is important to mention the drawbacks of using electrolytic capacitors to reduce the output voltage and current ripples, which lower the lifetime of the driver, and on the other hand, the use of coupling transformers, which are difficult to design and more expensive to manufacture. Hence, it is clear that LED drivers reported in the state of the art are not the best option for driving OLED lamps, or integrating OLED driver + OLED lamp system, due to the fact that they are bulky and larger, which makes their use difficult in this lighting application.

Other type of converters used to drive OLED lamps are SC converters, which consist of diodes, switches, and capacitors. These converters do not use any large inductor, and switched capacitors are small [7]-[9], which enables them to provide a high power density. Thereby, SC converters are very attractive for lighting OLED applications. In regards to the energy efficiency, SC converters can achieve it by inserting a pretty small inductor in series with the resonant capacitor and working under ZCS. In this way, this dissertation focuses on the study of the OLED technology and SC converters for driving OLED lamps.

1.2. Framework

The research developed in this dissertation is framed under the lighting research field. The research work is focused on studying more efficient power supplies for driving OLED lamps and they also achieve high power density for the best OLED driver + OLED lamp integration. The study of more efficient technologies applied in the lighting field is researched by the lighting field research group of the electrical and electronics engineering department of the University of Oviedo. This research frames the following areas of investigation in lighting:

- OLED photo-electrical-thermal (PET) modeling.
- SC converters.
- Variable inductor (VI) control strategy.

The research work developed in this dissertation is framed under the project "Research for the energy efficiency improvement in intelligent cities: lighting, integration in urban furniture and adaptation to the environment" with the reference: ENE2013-41491-R. Project completion: October 31st, 2017.

1.3. Objectives

Study of SC converters for the application in the optimization of OLED lighting systems with special emphasis to study resonant SC converters for the application in the output power regulation stage of the OLED lighting system as well as studying control techniques that can be applied to the power supply system for OLED lamps. During the development of this dissertation, the electrical performance of the different resonant SC converters reported in the state of the art will be experimented in order to confirm their advantages and disadvantages. Besides, it is an objective of this dissertation to study the different OLED lamp shapes as well as their photometric, electrical and thermal parameters.

1.4. Structure of the document

This dissertation is structured as follows: In Chapter 2, the basic structure and the principle of operation of the OLED and the different OLED structures to obtain white light are addressed. Besides, this chapter tackles the photometric, electrical and thermal operating conditions of the OLED. Chapter 3 presents a review of the state of the art of PET OLED models, because it is important to know the electrical, photometric and thermal behavior of the OLED lamp before carrying out any electrical design of OLED drivers, prototyping, and fixtures development. In Chapter 4, a review of the state of the art about non-resonant and resonant SC converters is carried out. A summary and comparison of the electrical performance of the different resonant SC converters is presented at the end of the chapter. The unidirectional resonant switched-capacitor (URSC) converter shows the best performance compared to the other SC converters investigated, because it presents advantages as high efficiency and high power density. In Chapter 5, the analysis and design of the URSC converter is carried out. In Chapter 6, the URSC converter performance is analyzed by means of electrical simulations and an *ad hoc* laboratory prototype. Conclusions, achievements, contributions and future works of this dissertation are presented in Chapter 7. In Attachments section, all publications carried out during the development of this dissertation are included.

2. OLED fundamentals

The OLED (organic lighting-emitting diode) lamp technology is studied in this work. First of all, a revision of the state of technology of the OLED is carried out. In this revision, the OLED fundamentals as architecture design, principle of operation, white light generation techniques, driving and supply considerations are explained. At the end of this section, a comparison of electrical and photometric parameters among OLED lamps is presented.

The first part of this chapter explains the basic structure and the principle of operation of the OLED. Afterwards, an energy conversion efficiency comparison of the OLED against lighting-emitting diode (LED) and a color rendering index (CRI) comparison of the different light sources are fulfilled. Besides, the different OLED structures to obtain white light and a CRI comparative obtained among them are presented.

The second part of the chapter tackles the photometric parameters of the OLED, the equivalent electrical circuit, and the operation considerations and operation reliability of the OLED. Moreover, OLED static and dynamic thermal models of the OLED are briefly described.

In the last part of the chapter, the definition and the description of the OLED lamp are presented. In addition, some lighting applications of the OLED lamp as well as a brief comparative among the different OLED lamps are shown.

2.1. Basic structure of the OLED

The OLED consists of an electro-luminescent layer that is formed by a thin film of organic components that react to a determined electrical stimulation, which makes them generating and emitting light by themselves. This thin film of organic components consists of three thin organic layers: an electrons transport layer, a holes transport layer and an emission layer. On the other hand, the thin film of organic components is allocated between two fine layers that are anode and cathode as shown in Fig. 2.1 [10]-[13]. In general, these layers are built of molecules or polymers that conduct electricity. Its conductivity levels are found between the insulator and conductor. Therefore, they are known as organic semiconductors. The choice of the organic materials and its structure of the layers determine the performance characteristics of the OLED as they are: emitted color, lifespan, and energy efficiency.

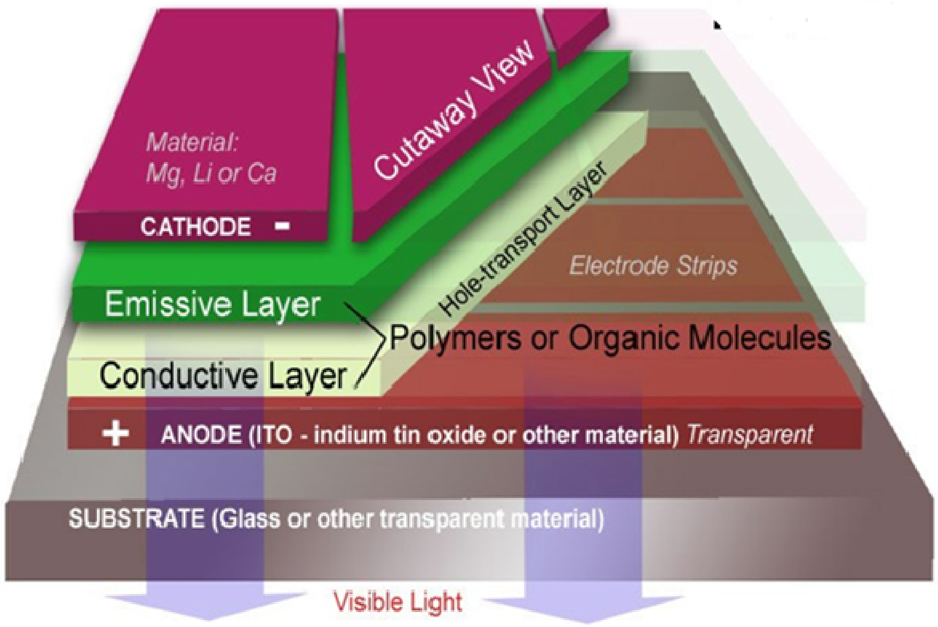

Fig. 2.1. Basic structure of the OLED.

2.2. Operation principle of the OLED

The OLED is voltage biased as shown in Fig. 2.1, which causes an electron flow from cathode to anode. Thereby, the cathode provides electrons to the electrons transport layer and the anode subtracts them from the holes transport layer. Promptly, the electrons transport layer begins to bias negatively because of electrons excess whilst the holes transport layer is biased with holes because of lack of electrons. The electrostatic forces attract electrons and holes one another, and they recombine each other. This happens closer to the electrons transport layer, because in the organic semiconductors, the holes move faster than the electrons. This is different in the inorganic semiconductors. The recombination phenomena is the fact where an atom traps an electron. This electron moves from a higher energy layer to a lower energy layer, which releases energy equal to the difference between initial and final energies in a way of photon. The recombination phenomena causes a radiation emission at a frequency that is in the visible region and it is visible as a light spot of a determined color [10]. When a dc current is applied to the OLED, it behaves as a LED and its characteristic curve of V-I is described as an exponential curve.

2.3. Comparative of the energy conversion of OLED versus LED

A comparative of efficiencies of energy conversion of the OLED versus LED is shown in Fig. 2.2. It is observed that OLED efficiency is higher than LED efficiency in the range of the visible spectrum more sensible to the human eye [14][15]. These efficiencies are obtained at a luminance of $1000\ cd/m^2$. The gray curve represents the response curve to the photopic sensitiveness of the human eye.

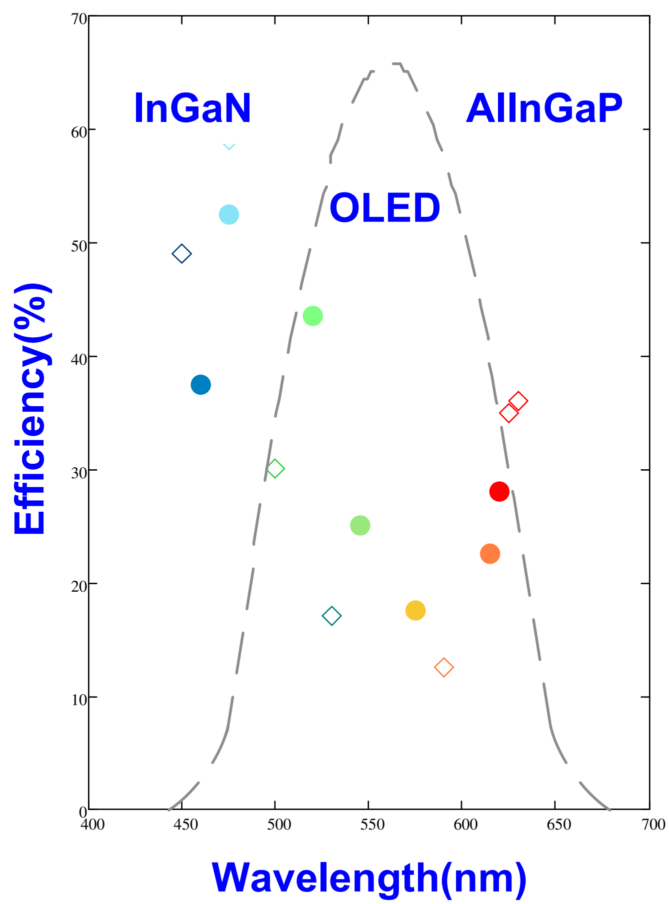

Fig. 2.2. Efficiencies: a) OLED (circles) and b) LED (rhombus).

2.4. CRI Comparative of the different light sources

The CRI of the spectrum produced by the fluorescent tube has a value lower than 80, thereby it is considered as poor light source. Also, the CRI of the blue LED that uses In-Ga-N material technology in combination with phosphor is lower than 80, so that it is not qualified as an adequate light source. However, the CRI of the OLED can be higher than 80 by combining three or more organic materials in the emission layer. The different CRI values are illustrated with respect to the different light emission source spectrum in Fig. 2.3.

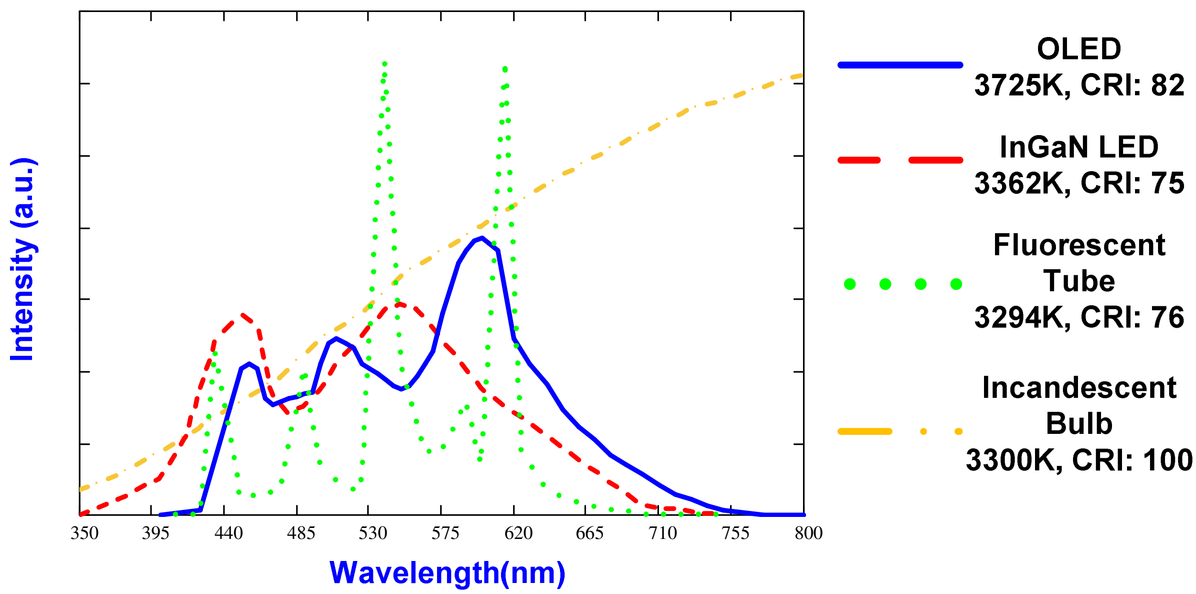

Fig. 2.3. Light emission spectrums: a) incandescent bulb, b) fluorescent bulb, c) LED and d) OLED.

2.5. Type of OLED structure for white light

2.5.1. Single emission layer OLED

This approach uses three phosphorescent materials (red, green and blue) in a single emission layer [14]. The light emission spectrum fulfilled and its building are shown in Fig.2.4. Also, the parameters obtained are the following: a) chromaticity coordinates CIE (Comission Internationale de L'Eclairage): 0.38/0.45, CRI: 78, efficiency: 6.7% and luminous efficacy: 11.11 lm/W. The data are obtained based on a current density of 10 mA/cm^2 and a luminance of 1000 cd/m^2.

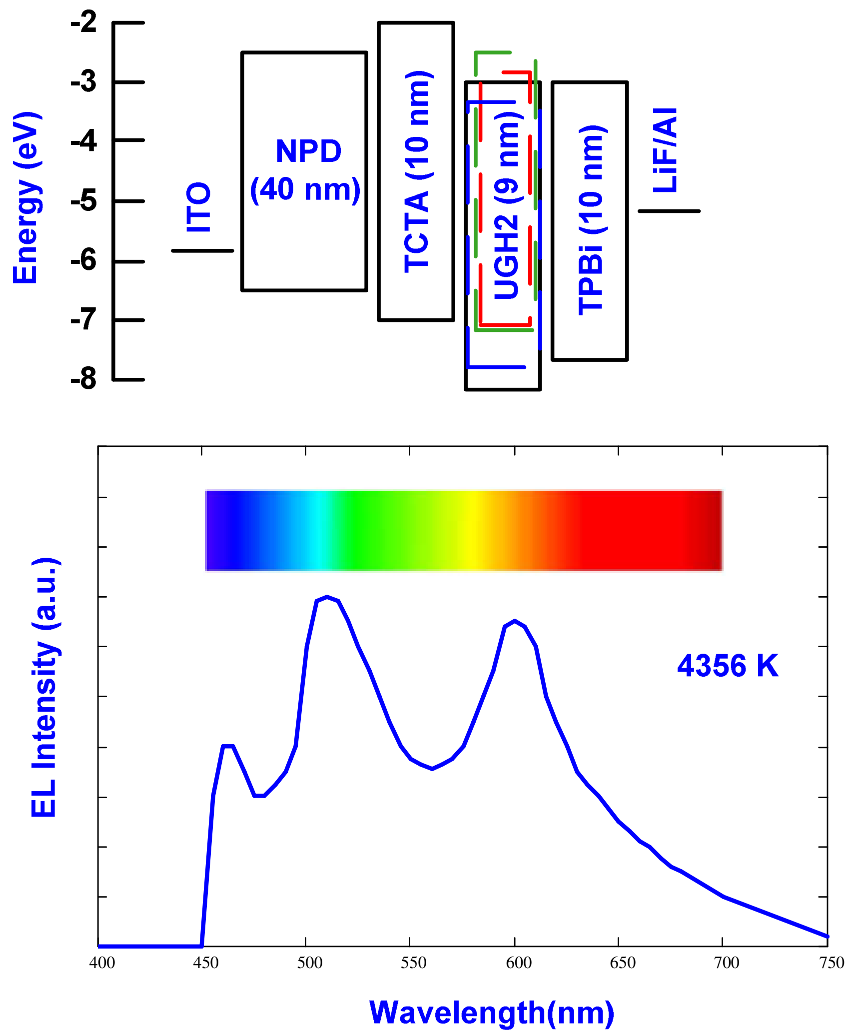

Fig. 2.4. Light emission spectrum and structure of single emission layer OLED.

2.5.2. Fluorophores-Phosphors OLED

It consists of a blue fluorescent material, a green phosphorescent material and a red phosphorescent material in the emission layer, which is internally integrated by several layers to avoid the energy transfer from the fluorescent material to the phosphorescent materials [14]. The light spectrum and its structure are illustrated in Fig.2.5. The parameters obtained are the following: a) chromaticity coordinates CIE (Comission Internationale de L'Eclairage): 0.39/0.40, CRI: 85, efficiency: 18.4% and luminous efficacy: 23.8 lm/W. The data are obtained based on a current density of 10 mA/cm^2 and a luminance of 500 cd/m^2.

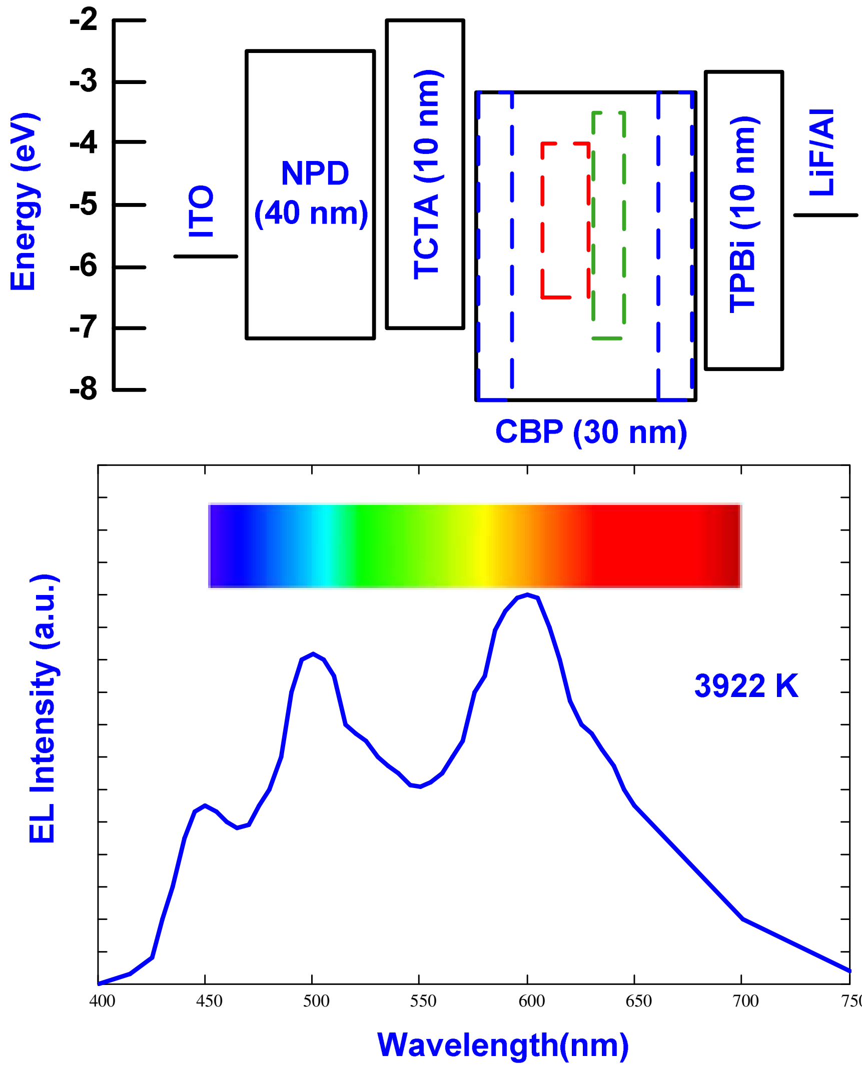

Fig. 2.5. Light emission spectrum and structure of fluorophores-phosphors (FP) OLED.

2.5.3. Tandem (Stack up) OLED

This method consists of an interlayer of charge injection and a dopant electrons transport layer between 2, 3 or more units of OLED as shown in Fig. 2.6 [14]. The visible light spectrum of the 3 OLED units stacked up is also shown in Fig. 2.6. The current density is $10\ mA/cm^2$ and the luminance is $1000\ cd/m^2$, both are used in order to obtain the following parameters: chromaticity coordinates CIE: $0.35/0.44$, CRI: 66, luminous efficacy: $11\ lm/W$ and efficiency: 27%.

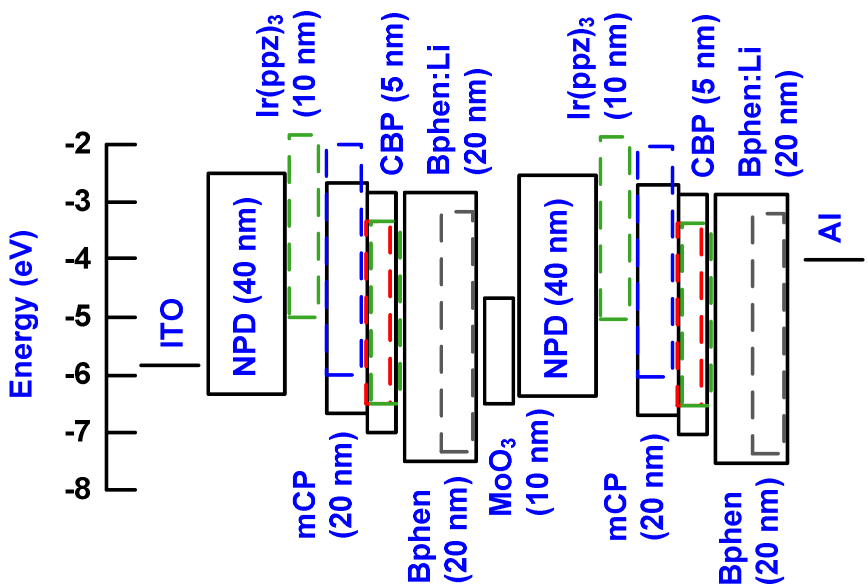

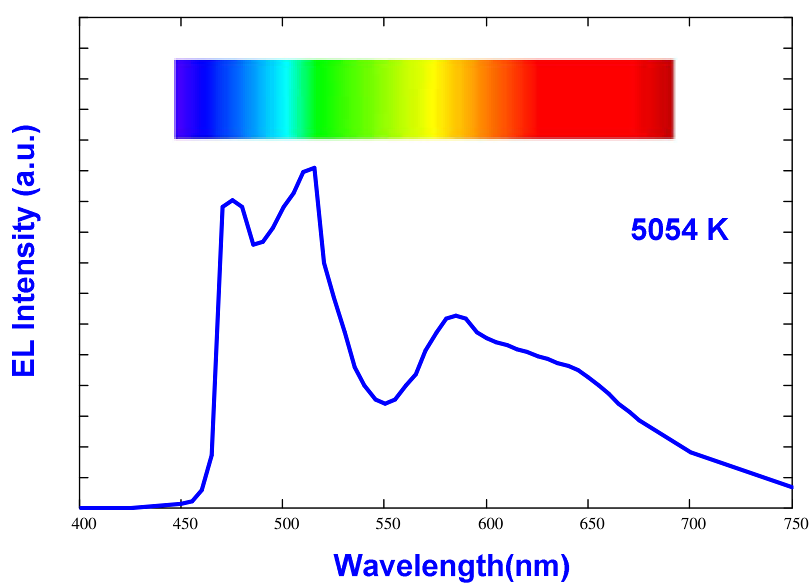

Fig. 2.6. Light emission spectrum and structure of Tandem OLED.

2.5.4. Multiple emission layer OLED

It consists of three separated dopant phosphor emission layer as shown in Fig. 2.7 [14]. In order to achieve the desired light spectrum, thick and concentration of doping of the phosphor materials should be adjusted. Additionally, two emission layers or non-doping host are used to avoid the blue phosphor energy transfer towards the green and red phosphors. The light spectrum of the multiple emission layer OLED is shown in Fig. 2.7. Which is generated at a luminance of $1000\ cd/m^2$. The chromaticity coordinates CIE: $0.44/0.46$, CRI: 80, efficiency: 14.4% and a luminous efficacy: 33 lm/W are obtained.

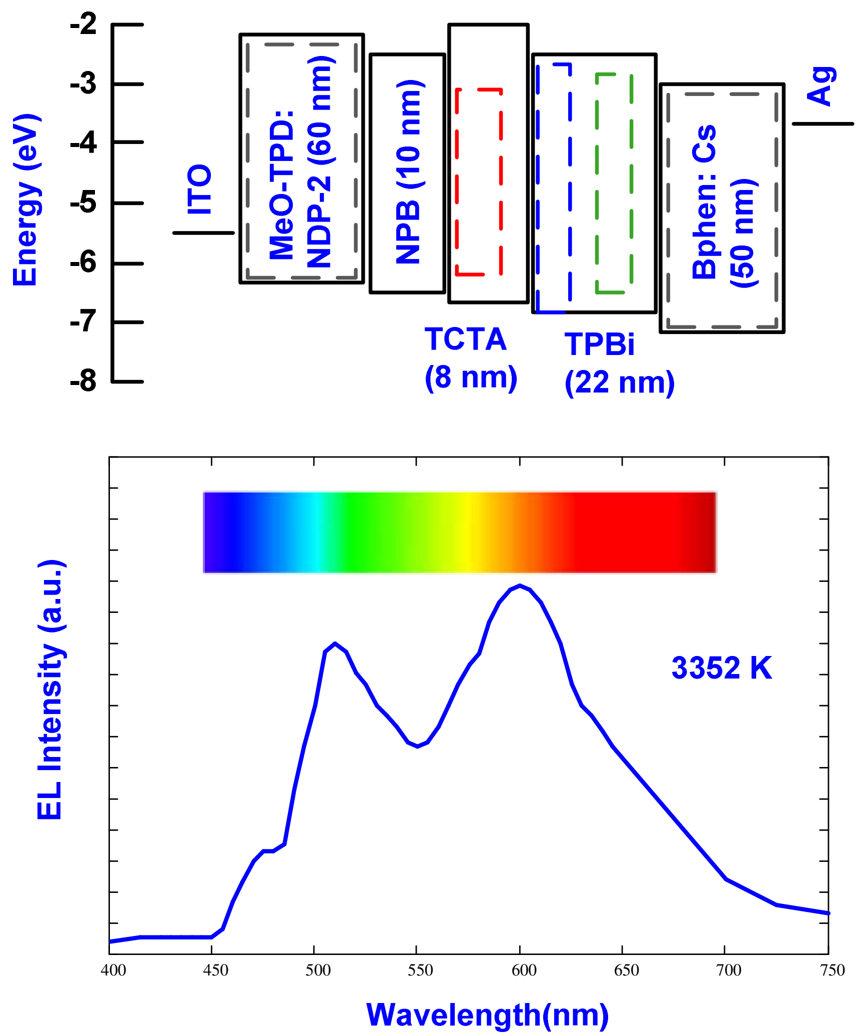

Fig. 2.7. Light emission spectrum and structure of multiple emission layer OLED.

2.5.5. Cascade-emission layer OLED

This approach uses an emission layer and a transport layer [14]. The emission layer is internally integrated by four phosphor materials. The light spectrum of the cascade-emission layer OLED is shown in Fig. 2.8. This is generated at a luminance of $1000\ cd/m^2$. The chromaticity coordinates CIE: $0.37/0.48$, CRI: 72, efficiency: 19.2% and a luminous efficacy: $28.1\ lm/W$.

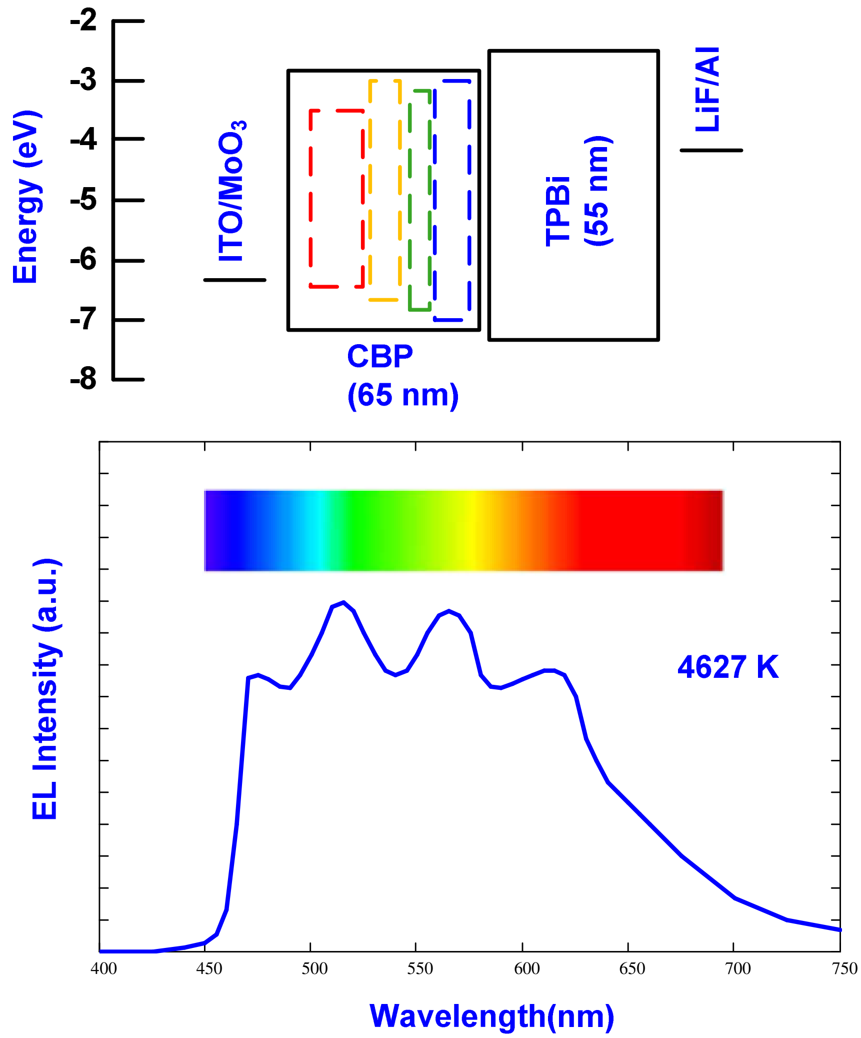

Fig. 2.8. Light emission spectrum and structure of cascade-emission layer OLED.

2.5.6. Cascade-emission layer with exciton conversion OLED

This approach manages the basis of the cascade-emission layer with the inclusion of the green phosphor material, which is integrated between the red and yellow emisors inside of the emission layer as illustrated in Fig. 2.9 [14]. The light spectrum is also shown in Fig. 2.9. This is generated at a luminance of $5000\ cd/m^2$. Then, the chromaticity coordinates CIE are: $0.44/0.45$, CRI: 85, efficiency: 23.3% and luminous efficacy: $31\ lm/W$.

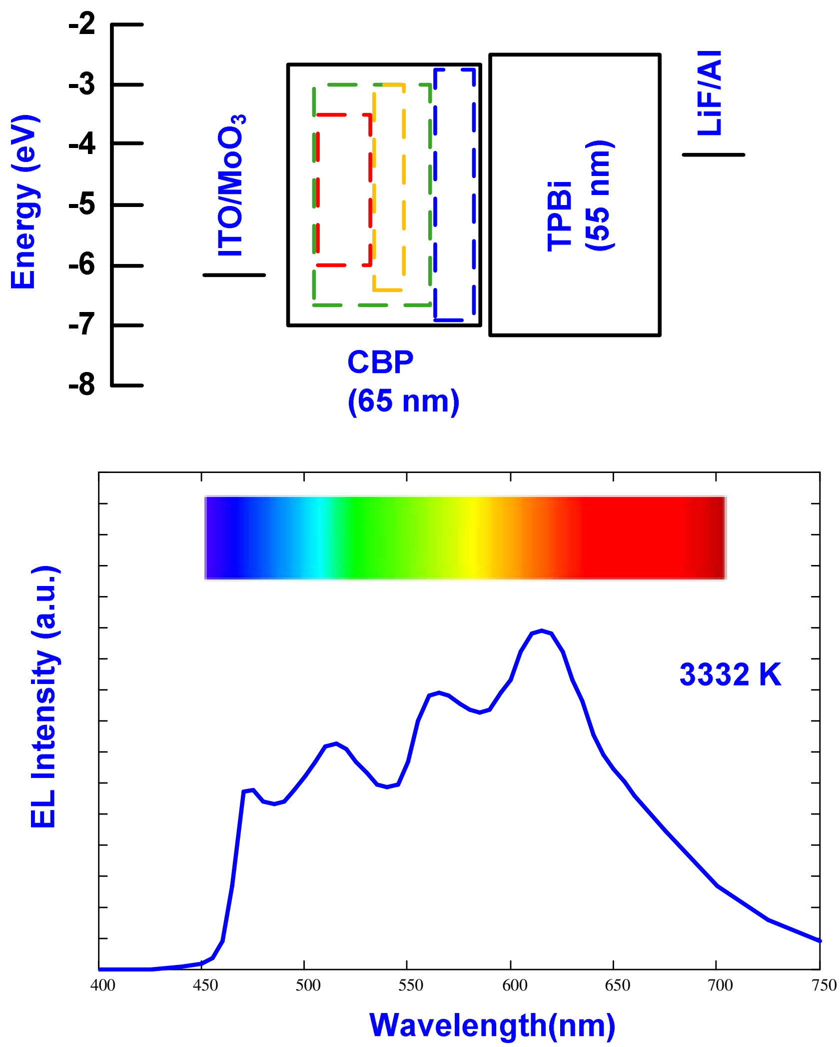

Fig. 2.9. Light emission spectrum and structure of cascade-emission layer with exciton conversion OLED.

2.6. CRI Comparative of the different white light structures

The different CRI values in regards to the efficiency of the single emission layer, FP, tandem and multiple emission layer OLED structures to generate white light are shown in Fig. 2.10 [14]. The results shown are based on a luminance of 1000 cd/m^2. The quadrants A-D denotes the limits of the CRI: 80 and efficiency: 20%, which indicate an acceptable light quality factor and a good efficiency of the white light structure OLED.

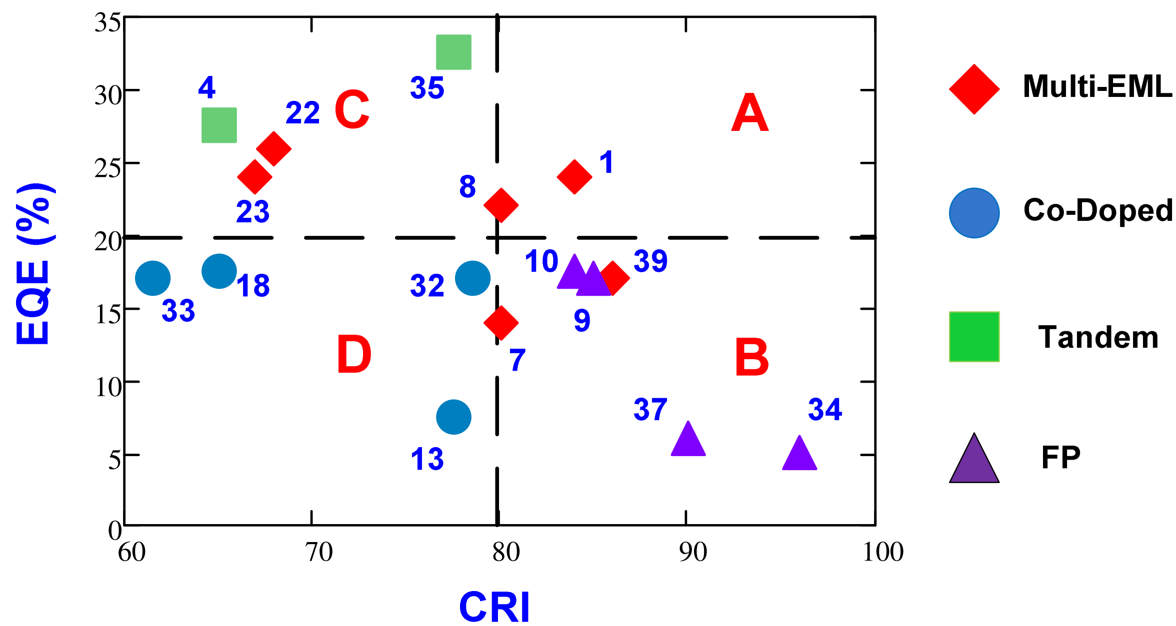

Fig. 2.10. CRI comparative: a) single emission layer (circles), b) FP (triangles), c) tandem (squares) and d) multiple emission layer (rhombus).

2.7. Photometric parameters

2.7.1. Luminous flux

The luminous flux is the total amount of light produced by the light source. The luminous flux is measured in lumens (lm) [16].

2.7.2. Luminous intensity

The luminous intensity is the amount of light projected over a specific direction. The luminous intensity is measured in candles (cd) [16].

2.7.3. Illuminance

The illuminance is the amount of light that arrives to a surface. The illuminance is measured in luxes (lux) [16].

2.7.4. Luminance

The luminance is the amount of light that is perceived by the human eye from a lighted surface. The luminance is measured in candles by square meter (cd/m^2) [16].

The luminous flux, luminous intensity, illuminance and luminance photometric parameters scheme is illustrated in Fig. 2.11.

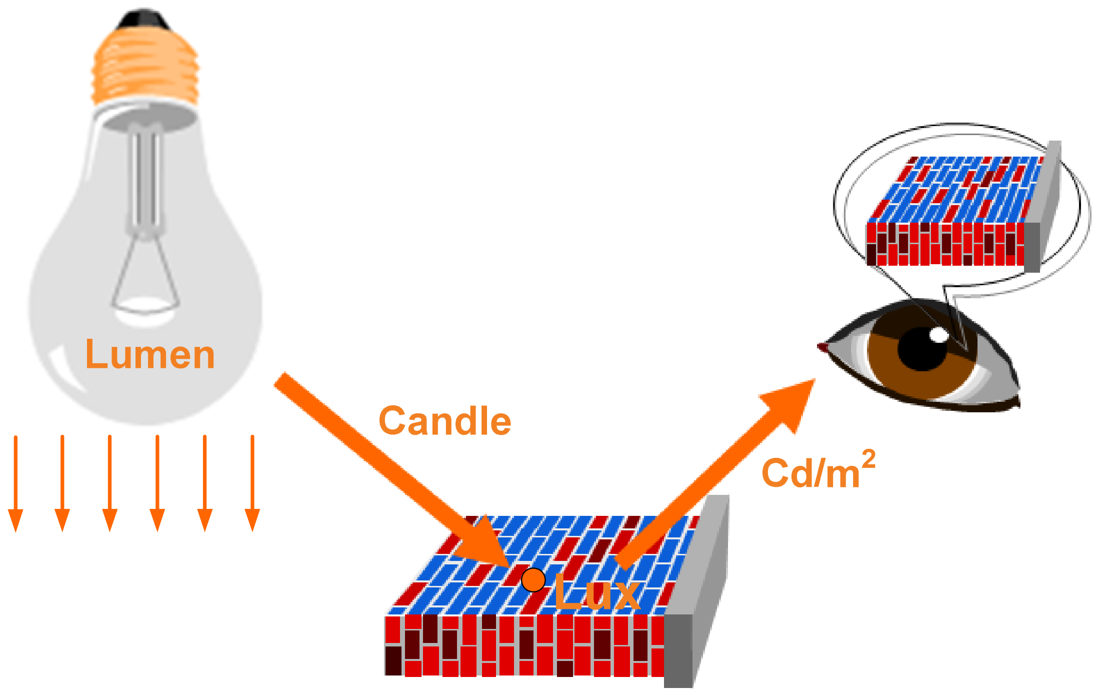

Fig. 2.11. Photometric parameters illustration.

2.8. Equivalent electrical circuit of the OLED

The equivalent electrical circuit of the OLED is illustrated in Fig. 2.12. The OLED can be operated by the same topologies used for driving the conventional LED, and by considering the behavior of the circuit of the Fig. 2.12 [17]. This is because of the OLED supplied by a dc current behaves very similar to the conventional LED. Therefore, the characteristic V-I of the OLED describes an exponential or parabolic behavior.

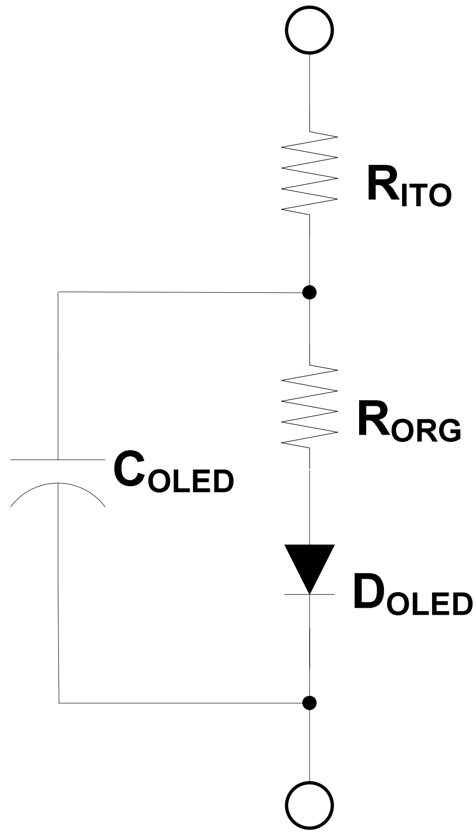

Fig. 2.12. Equivalent electrical circuit of the OLED.

2.9. Operation considerations of the OLED

The OLED and LED operated by an electronic driver is quite similar. In most of the applications, LED drivers can also be used for driving OLEDs. However, some basic rules and characteristics of the OLED must be considered [18][19]. The OLED must be operated by an electronic driver that supplies a direct current (dc) constant current and not a dc constant voltage. This is in order to drive a dc constant current through it and avoid having variations of luminous flux. The reason is that the luminous flux delivered by the OLED is proportional to its operating dc current, but not proportional to its operating dc voltage.

2.9.1. Operation modes of the OLED

Constant current operation mode

In this operation mode, the luminous flux of the OLED is more stable under current, temperature and tolerance variations. The characteristic current-luminance curve is shown in Fig. 2.13. It is observed that the curve presents small changes of luminance when current changes.

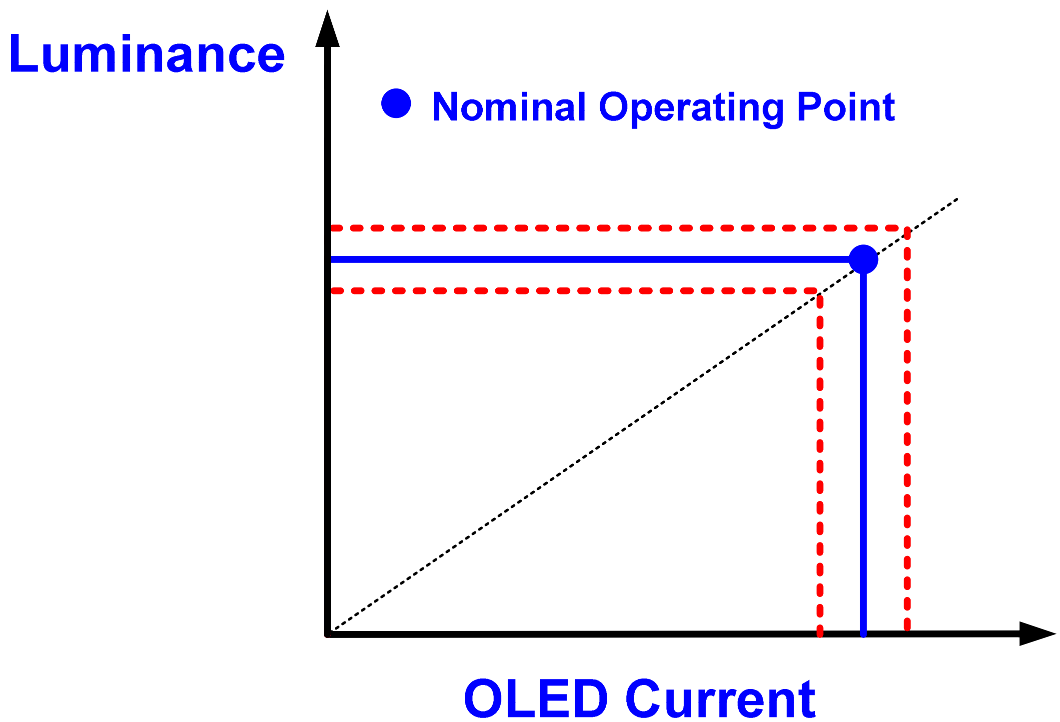

Fig. 2.13. Current-luminance curve of the constant current operation mode.

Then, constant current operation mode will drive a constant dc current through the OLED throughout its lifespan, even though its forward voltage will be increased, due to the increased of its static resistance. In addition, OLED lifetime will be longer than when it is driven by constant voltage.

Constant voltage operation mode

In this operation mode, the OLED is driven by constant dc voltage, the luminous flux through the OLED experiments significant variations under small voltage variations, temperature and manufacturing tolerance, as illustrated in Fig. 2.14. The characteristic voltage-luminance curve shows that under small voltage variations, the luminance is quite changed.

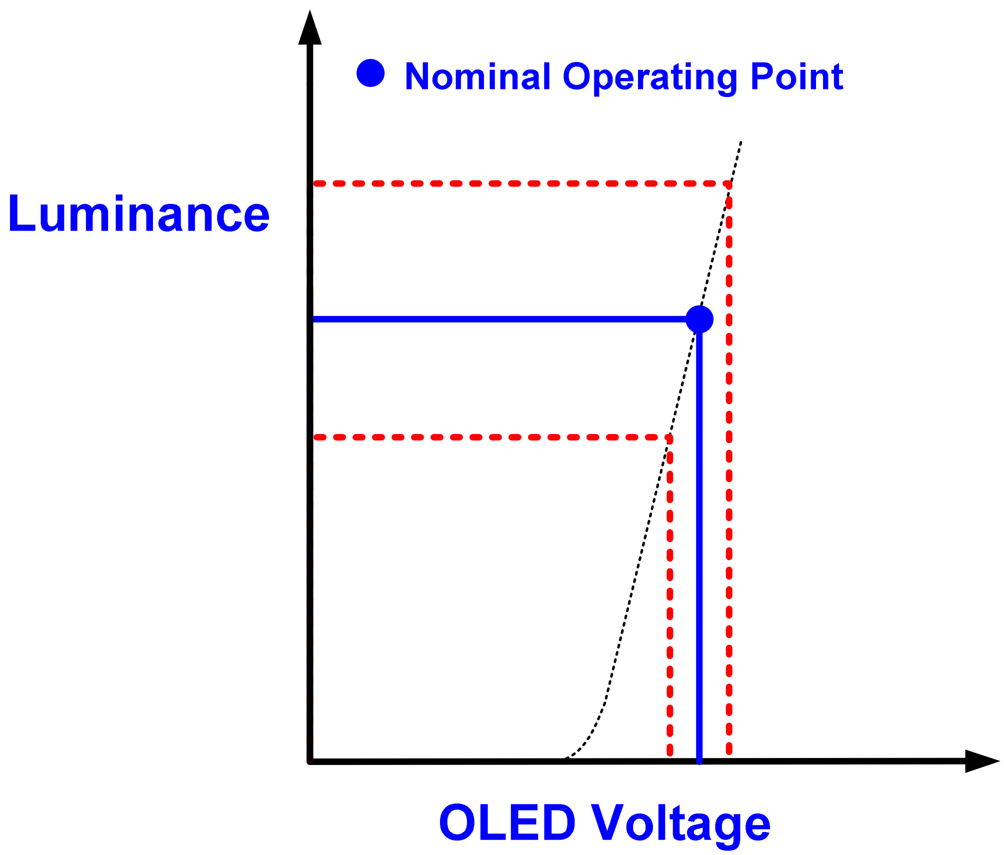

Fig. 2.14. Voltage-luminance curve of the constant voltage operation mode.

Moreover, the static resistance of the OLED increases in a more significant way, due to the type of operation mode. Then, the increased of static resistance decreases the operation current, and the luminous flux consequently. Even worse, it decreases the lifetime of the OLED. The tolerance changes of the OLED from one to another affect more in this operation mode. Therefore, the electronic drivers that supply constant dc voltage must be designed to compensate the OLED voltage changes in a more accurate way. Regrettably, it is not possible in the most of the electronic drivers.

Limit current operation mode

In this operation mode, a constant dc voltage drives the OLED along with a series resistance. This is a quite inaccurate control technique, which lowers the luminous flux and lifetime of the OLED as well as energy efficiency is lowered due to thermal issues.

2.9.2. Dimming operation of the OLED

The dimming of the OLED must be driven by a dc amplitude and not by the duty cycle of the PWM as well as ensuring that the ripple current over the dc current is small.

To ensure the maximum possible lifetime of the OLED, the OLED nominal current must be obtained from the datasheet in order to be set on the electronic driver. Exceeding the maximum dc current of the OLED, will lower its lifetime. Thereby, setting the nominal dc current by means of a PWM-based that exceeds the maximum dc current of the OLED, that is, the average dc current equals to the nominal dc current of the OLED, will lower the lifetime of the OLED significantly. Due to these drawbacks, this technique is not adequate to drive the OLED.

The electronic drivers for LEDs or OLEDs are designed to have a low ac current ripple of low or high frequency over the nominal dc current. It can be in a sinusoidal or triangular shape. A high ripple current lowers the lifetime of the OLED. So that, it must be limited to a maximum of ±15% of the nominal dc current of the OLED.

A great difference between the OLED and LED is the internal stray capacitance. The capacitance of the OLED is quite high, which can cause current and voltage spikes when the OLED is switched on and switched off or in other words, due to the rise and fall flanks of the

PWM signal. Due to this inconvenience, the electronic driver must be adequately designed to obtain voltage spikes lower than 5% of the nominal voltage and current spikes lower than 15% of the nominal current.

DC current amplitude dimming operation

As was mentioned previously, the dimming OLED must be driven by a dc current amplitude as shown in Fig. 2.15. This technique increase the lifetime of the OLED, but it can cause color variations on white OLEDs.

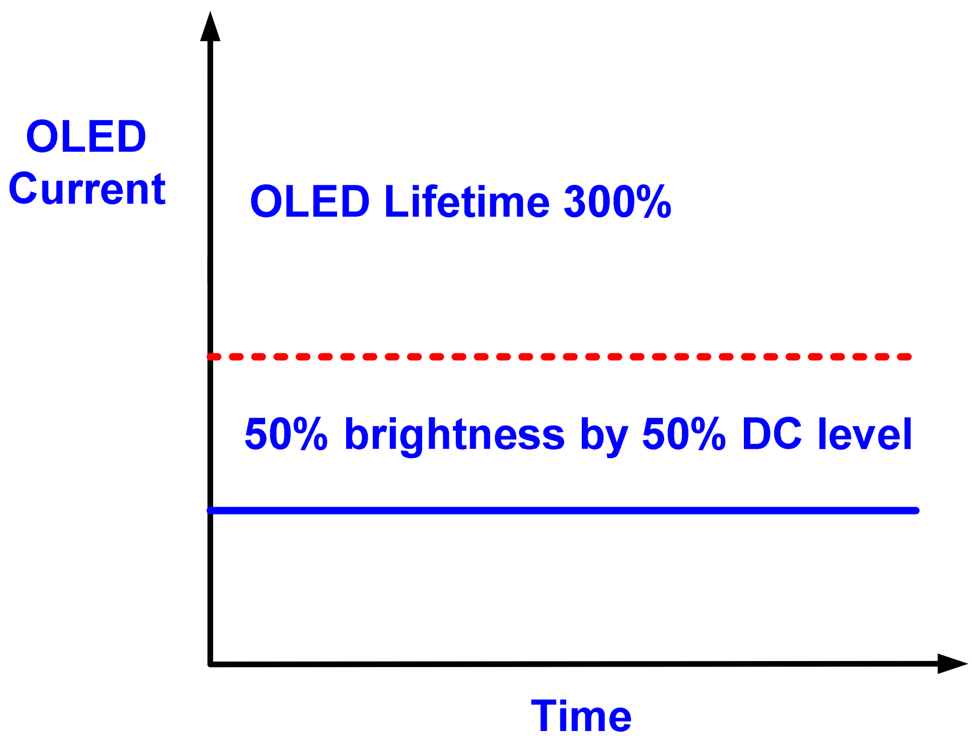

Fig. 2.15. DC current amplitude dimming operation curve.

PWM dimming operation

The PWM-based dimming technique is illustrated in Fig. 2.16, which lowers the OLED current by obtaining the average current of the PWM signal. However, the lifetime is lowered, even though it is not as worse as that operated over 100% of the nominal dc current. But, it is not as good as that operated by the dc current amplitude. On the other hand, PWM-based dimming technique has the advantage of achieving color OLED stability. Hence, the PWM-based dimming technique can be used as long as the maximum dc current OLED is not exceeded, which means that the maximum peak current and voltage at transitions from turn-off to turn-on and vice versa are not exceeded in accordance with the specifications of OLED datasheet.

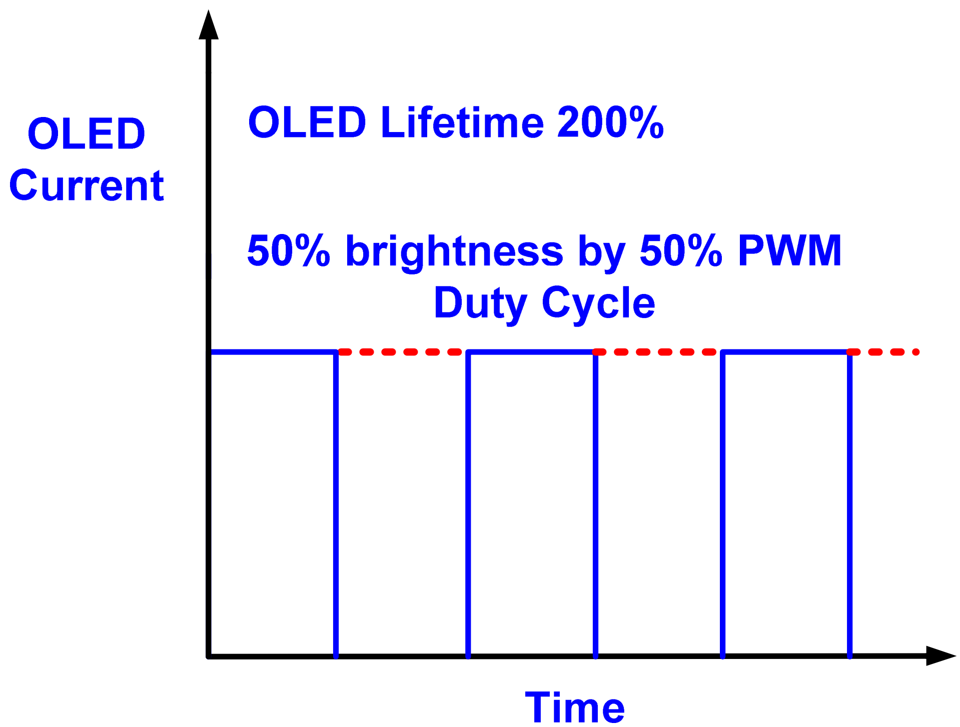

Fig. 2.16. PWM dimming operation curve.

Logaritmic dimming operation

The dimming of an OLED based on a logarithmic curve that provides a resolution of 8 bits is recommended, owing to the OLED current is stepped up from zero to the maximum OLED current at a ratio of 255 steps. This sort of dimming technique avoid the luminous flux changes being visible in the low luminance levels region, as shown in Fig. 2.17. On the other hand, when a lineal dimming is used, a resolution at least of 10-12 bits must be ensured.

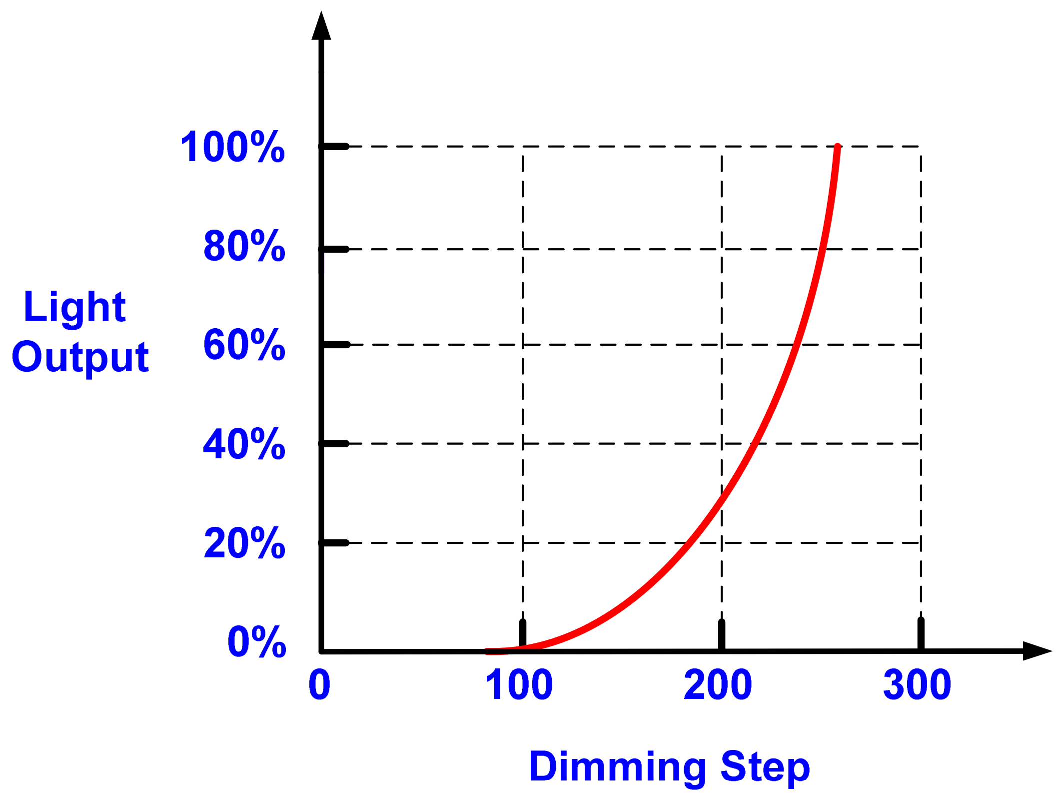

Fig. 2.17. Logarithmic dimming operation curve.

The most common low-voltage dimming interfaces are 1-10V, DSI, DALI, DMX and PWM [19]. Nonetheless, these interfaces are not recommended to dim OLEDs, due to the fact that they are based on PWM, which lowers the OLED lifespan. In addition, they are not as accurate as pursued. In order to optimize the lifetime and have a more accurate luminous flux, the electronic driver must be designed to have no more than ±5% output current variation.

2.9.3. Forward voltage variations of the OLED

The forward voltage of the OLED is lower when any of the following conditions is presented in accordance with the specifications:

- ✓ Lower tolerance of the forward voltage.
- ✓ Low dc bias current.
- ✓ Higher operating temperature of the OLED.

On the contrary, the forward voltage of the OLED is higher when any of the following conditions is presented in accordance with the specifications:

- ✓ Higher tolerance of the forward voltage.
- ✓ High dc bias current.
- ✓ Lower operating temperature of the OLED.
- ✓ End-of-life of the OLED.

Due to the forward voltage variations, the electronic driver must have a strict output voltage variation range, thus compensating the forward voltage variations over and lower the nominal forward voltage in order to achieve constant current through the OLED.

OLEDs must be connected in series when there have been several OLEDs to operate in the luminary. Moreover, OLEDs must be operated by an electronic driver that supplies constant current. On the other hand, modular electronic drivers can be used to operate single OLEDs. When the OLEDs are connected in series, the total maximum forward voltage of the chain is equivalent to the maximum forward voltage of the OLED by the number of OLEDs in series and vice versa, the total minimum forward voltage of the chain is equivalent to the minimum forward voltage of the OLED by the number of OLEDs in series. Then, the electronic driver must be designed to operate in under voltage detection when the total forward voltage of the OLEDs is under the minimum in accordance with the specification. On the contrary, the electronic driver must operate in over voltage detection when the total forward voltage of the OLEDs is over the maximum in accordance with the specification.

2.9.4. Short-circuit protection of the OLED

OLEDs can be electrically damaged by mechanical stress or incorrect lamp connection. The short-circuit failure mode behavior of the OLED is different to the LED, because of the OLED has a small resistance through it known as deviation resistance. Then, as the heating of the deviation resistance increases, thermal issues on the OLED are increased. Thus, the OLED must be operated by constant current due to the deviation resistance causes a voltage drop across it, but not a zero voltage. Then, the electronic driver must be able to regulate at the OLED nominal current in this failure mode or stepped into over current protection [19].

2.10. OLED Thermal model

The main heat transfer mechanism in organic or inorganic LEDs is heat conduction, because the heat is transferred from junction to ambient using a heatsink, creating a thermal path of the OLED from junction to ambient, and can be modeled with a thermal equivalent circuit. For instance, some thermal models of LEDs take the thermal resistances of all materials involved in the LED construction into consideration [20]. On the other hand, other LED thermal models take compact models into account to predict static and dynamic behavior [21][22]. In addition to the thermal models aforementioned, a simplified static model and dynamic models are found in [23]-[25].

The thermal model under steady state conditions is shown in Fig. 2.18 [26]. The R_{jc} is the LED junction to case thermal resistance, the R_{hs} is the heatsink thermal resistance, and the heatsink temperature T_{hs}. In practice, a heatsink compound is used between the LED and the heatsink to ensure a good thermal dissipation. The thermal resistances R_{jc} and R_{hs} present an opposition to the heat flow and depend on the thermal conductivity and thickness of their materials. The thermal resistance of the thermal conductor is relatively small in comparison with the LED junction to case thermal resistance R_{jc} so that it is neglected from the LED system analysis.

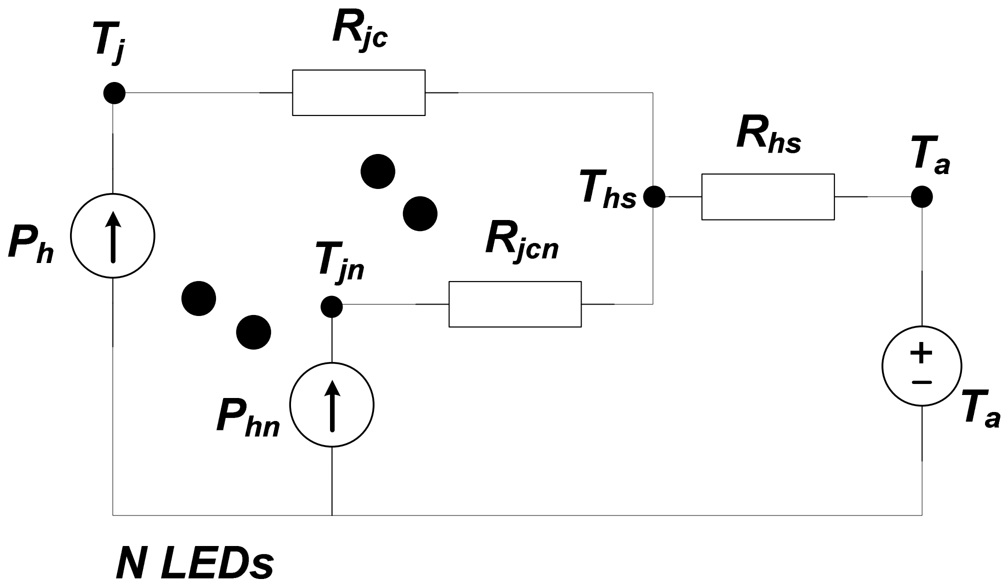

Fig. 2.18. Steady state thermal equivalent circuit of the LED system.

The equivalent dynamic thermal model circuit of the LED is illustrated in Fig. 2.19 [26]. This thermal model includes the junction to case thermal capacitance C_{jc} and the heatsink thermal capacitance C_{hs}. Both capacitances represent the amount of heat that is stored by the LED and the heatsink, which depend on the volume and density of their materials.

However, some effects are not considered in these models, as they are heat transfer by convection and radiation, phosphor conversion losses, and the three-dimensional (3-D) effects. So that, these models should be used carefully in the organic or inorganic LED thermal design.

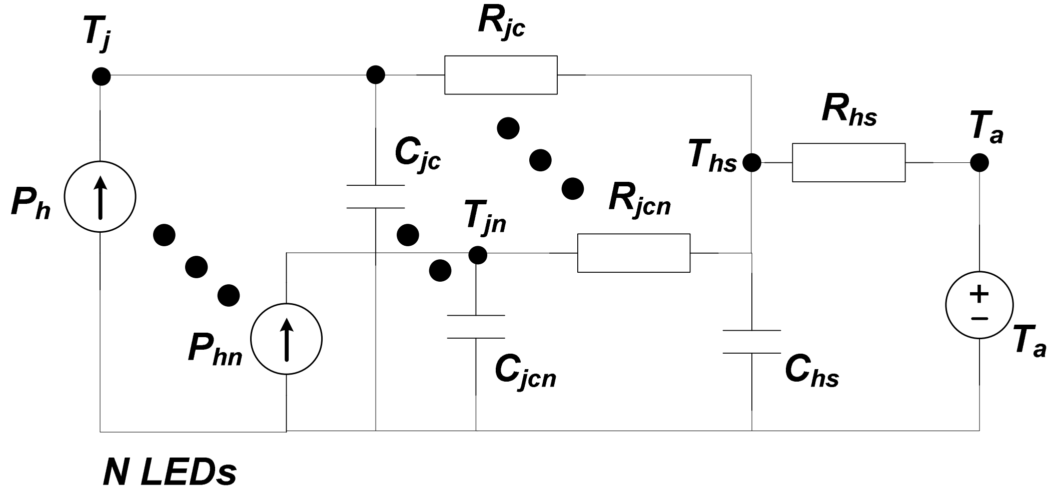

Fig. 2.19. Equivalent dynamic thermal model circuit of the LED system.

2.11. OLED operation reliability

The OLED lamps must be operated under certain conditions of operating temperature to fulfill a reliable operation throughout the targeted timeframe. Therefore, the reliability requirements of the OLED lamp have to be reviewed in the datasheet before a lighting system is designed [27]. Apart from the likelihood of abrupt failures based on L0C10, the luminous flux maintenance of the OLED lamp under operation is also affected. For instance, the Phillips Brite FL300 is designed for L70B50 lifetime at 10,000 hrs at an organic layer temperature of 50°C. This temperature is reached when the OLED lamp is operated at a rated current at room temperature, and can be affected by a change of its power dissipation, its thermal dissipation, and the ambient temperature. The OLED lamp lifetime under different operating luminous flux and organic layer temperatures conditions and placed in vertical position, is illustrated in Fig. 2.20. Note that L0C10 stands for the point in time at which 10% of the initial population fails due to abrupt failures. Hence, it is shown in Fig. 2.20 that an increase in the organic layer temperature of the OLED at a given luminous flux and OLED current will decrease the OLED lifetime. On the other hand, reducing the OLED current, will increase the OLED lifetime and decreasing the organic layer temperature of the OLED, will also improve the OLED lifetime.

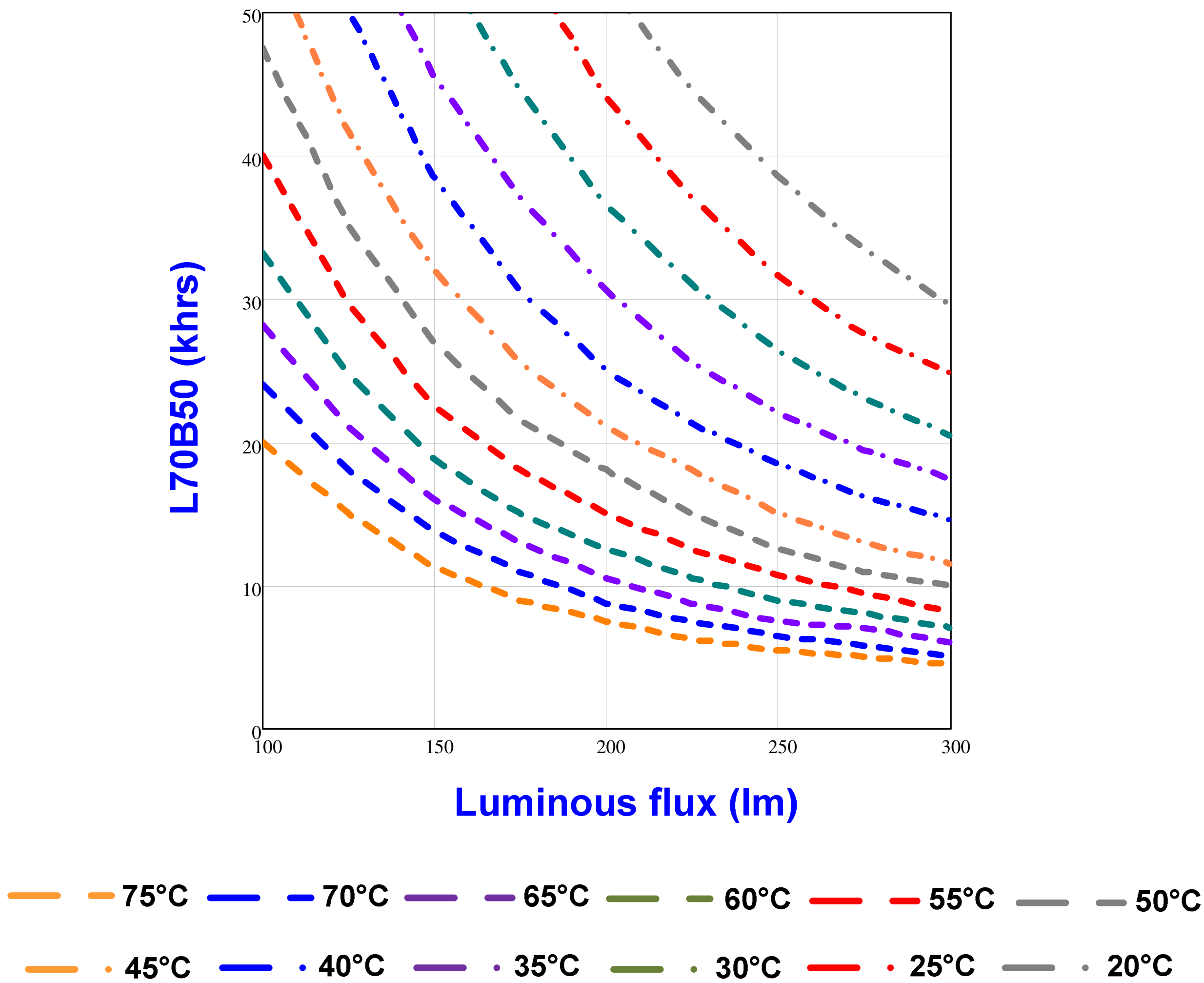

Fig. 2.20. OLED lifetime curves under different operating conditions.

The OLED organic layer temperature is ambient temperature dependent as aforementioned. This temperature dependency is shown in Fig. 2.21 under two different operating OLED currents as they are 0.135 A and 0.368 A, and placed in vertical position. The organic layer temperature of the OLED depends on its placement orientation, air movement on it, and its type of mounting structure. Therefore, an increase in the ambient temperature will cause an increase in the OLED organic layer temperature.

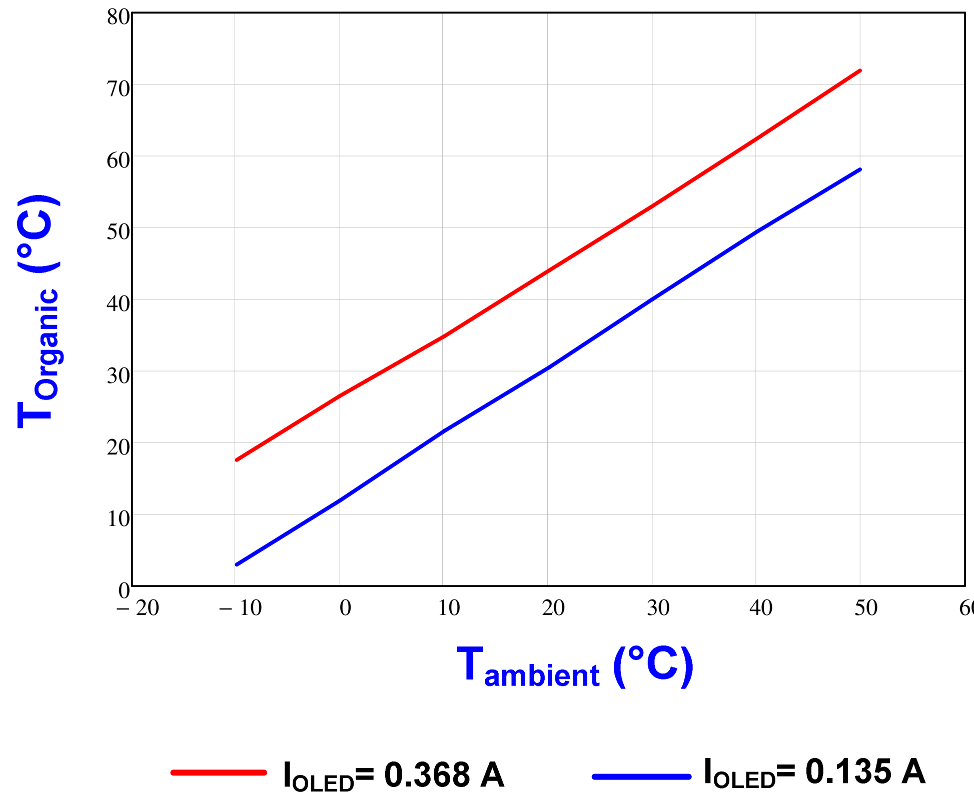

Fig. 2.21. OLED organic layer temperature curves under different ambient temperatures.

Cooling efficiency is dependent on the quality of the thermal coupling between the OLED lamp and the mounting component, which is usually made of aluminum. This fact is true if the mounting component is intended to function as a heat sink. Thus, the thermal contact between the OLED and the mounting component should be optimized in order to improve the temperature of the OLED.

The organic layer temperatures of the OLED lamp mounted under different materials and operating at different luminous flux and at room temperature are shown in Fig. 2.22. The type of mounting materials used are wood and aluminum metal. The wood plate dimensions are: 16 mm thickness and an area of 160 cm^2. On the other hand, the aluminum plate dimensions are: 1.5 mm thickness and an area of 160 cm^2. As it is expected and shown in Fig. 2.22, an aluminum metal plate happens to be the best mounting material because it conducts the heat in a more efficient mode.

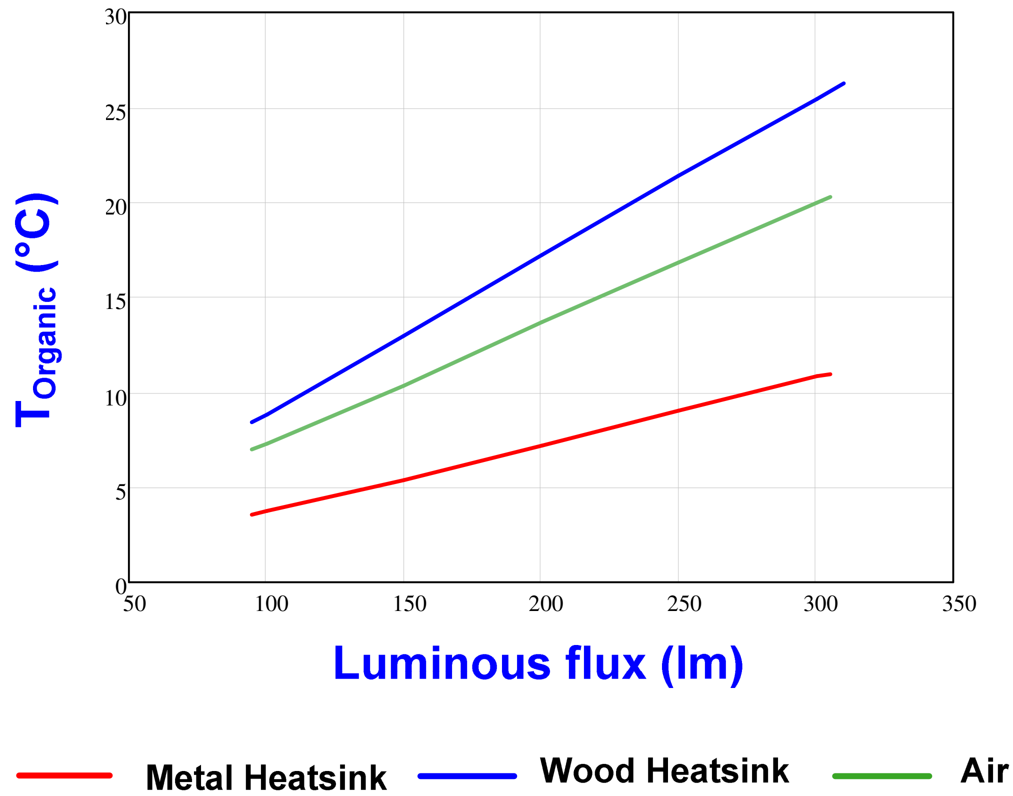

Fig. 2.22. OLED organic layer temperature curves under different luminous flux.

OLED lamp aging

During the OLED lamp lifetime the OLED voltage increases, which causes an increase of its power dissipation and its organic layer temperature under constant OLED current driving. Note that this fact is even worse at the end of life of the OLED lamp. Therefore, it must be taken into consideration when the thermal design of the lighting system is carried out.

2.12. Definition of the OLED lamp

The OLED lamp is a soft and diffuse light source of superficial area so that it is a light source of great extent and free dazzle compared to the conventional light sources such as the incandescent, the halogen and the LED, which are all spot light sources.

2.13. Description of the OLED lamp

The OLED lamp has a thin structure of light weight, flexible and clear finishes. Hence, the OLED is not just a light source, but also, it is a very attractive and predominant element in the avant-garde interior design area, leading to the interiors, buildings, museums, offices, stores and public room decoration.

2.14. Lighting applications of the OLED

The OLED can be used in different lighting applications such as ablaze tiles and partition wall, so that it is possible to light walls and floors [28]-[29]. In addition, the OLED can be used as mirror owing to its clear material layers, except the cathode, which is made of metal, usually aluminum. Therefore, the OLED will be a mirror when it is off and a light source of superficial area when it is on. A ceiling lamps design based on OLEDs are shown in Fig. 2.23.

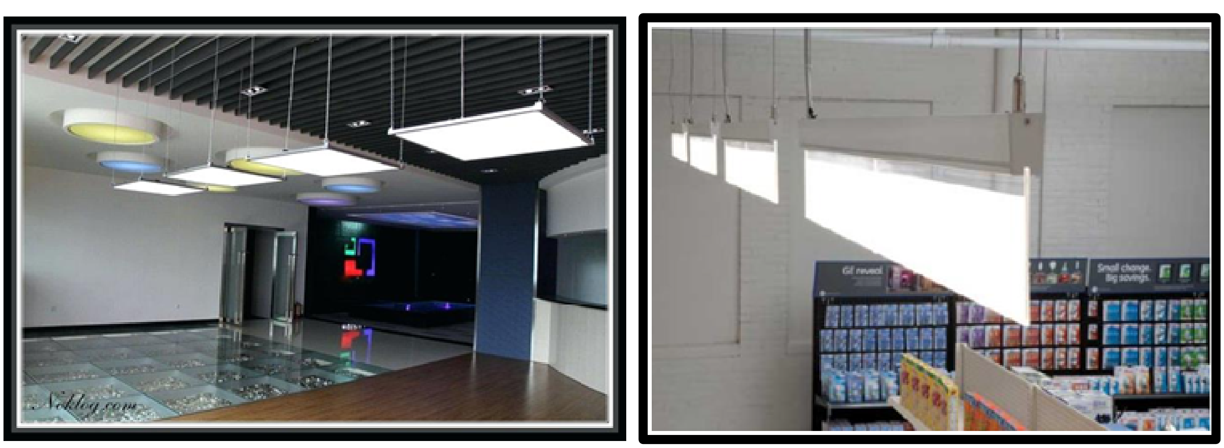

Fig. 2.23. OLED lamp of ceiling.

Nonetheless, there are other types of lamps design based on OLEDs such as avant-garde interior lamps to be placed on tables as shown in Fig. 2.24, or floor lamps as illustrated in Fig. 2.25 [29].

Fig. 2.24. OLED lamp of table.

Fig. 2.25. OLED lamp of floor.

The mirror lamp design is illustrated in Fig. 2.26. Even though, it can also be used on windows. Thereby, it will be a simple window during the day and a light source during the night [29]. This is possible owing to its clear finishes, that is, the cathode must be made of a clear material.

Fig. 2.26. OLED lamp of mirror type.

2.15. Comparative of the commercial OLED lamps

The different electrical, photometrical and thermal parameters of the commercial OLED lamps are illustrated in Table 2.1. The OLED suppliers are: LG, Osram and Philips [30]-[37]. Commercial OLED shapes such as octagonal, rectangular, square, and flexible rectangular are shown in Fig. 2.27.

Fig. 2.27. Commercial OLED lamp shapes.

Table. 2.1. Electrical-photometrical-thermal comparative of the commercial OLED lamps.

Supplier	Description	Voltage (V)	Current (A)	Power (W)	Luminance (cd/m^2)	Luminous Efficacy (lm/W)	Luminous Flux (lm)	CCT (K)	CRI	L70 (hrs)	Max. Amb. Temp. (°C)
Osram	Orbeos CDW-030	6	0.117	0.7	2000	40	-	3400	80	10,000	40
Osram	Orbeos RDW-046	6	0.1	0.6	2000	40	-	3400	80	10,000	40
Osram	Orbeos SDW-058	6	0.283	1.7	2000	40	-	3400	80	10,000	40
Phillips	Brite FL300	20	0.368	7.4	8300	40-50	300	3000-4000	80	10,000	40
LG	N6SD30	8.5	1.7	14.5	-	60	850	3000	90	40,000	40
LG	N6SB40	6	0.060	0.4	3000	55	20	4000	90	30,000	40
LG	N6SB30	8.5	0.040	0.3	3000	60	20	3000	90	40,000	40
LG	N6SA40	6	0.230	1.4	3000	55	75	4000	90	30,000	40
LG	N6SA35	6	0.230	1.4	-	55	75	3500	90	30,000	40
LG	N6SA30	8.5	0.150	1.3	3000	60	75	3000	90	40,000	40
LG	N8SA30	8.5	0.120	1	-	80	75	3000	>80	50,000	40
LG	N6SC40	6	0.480	2.9	3000	50	150	4000	90	30,000	40
LG	N6SC30	8.5	0.3	2.6	3000	60	150	3000	90	40,000	40
LG	N6BA40	6	0.230	1.4	3000	55	75	4000	90	30,000	40
LG	N6BA30	8.5	0.150	1.3	3000	60	75	3000	90	40,000	40
LG	N6BB40	6	0.8	4.8	3000	50	250	4000	90	30,000	40
LG	N6BB30	8.5	0.5	4.3	3000	60	250	3000	90	40,000	40
LG	F6BA40	6	0.230	1.4	3000	55	75	4000	90	30,000	40
LG	F6BA30	8.5	0.150	1.3	-	60	75	3000	90	40,000	40
LG	N6OA40	6	0.230	1.4	3000	55	75	4000	90	30,000	40
LG	N6OA30	8.5	0.150	1.3	3000	60	75	3000	90	40,000	40

2.16. Conclusions

The OLED lamp presents the advantage of being a superficial area light source in comparison with the inorganic LED, which is a spot light source. Then, it means that the illuminance level delivered by the OLED lamp over a surface must be better.

In addition, the OLED lamp presents the advantages of the shape, light weight, small thickness and size, which allows for an integration with the electronic driver, which must have as high power density as possible in order to have a lighting system integration of small size for interior applications for instance.

The Philips Brite FL300 OLED lamp is chosen as the OLED lamp in this research work.

3. OLED photo-electrical-thermal modeling

OLED lamps consist of a large semiconductor area sandwiched between two electrodes, where the organic materials are built-in as discussed in chapter 2. Because of this, an electrical field is generated between the organic layers, which makes the OLED lamp to have a significant capacitive behavior. Therefore, OLED lamps are different in electrical behavior when it is compared to other light sources like LEDs. However, the static characteristics of the OLED are similar to those of the LED. From an electrical point of view, the OLED structure can be defined as an equivalent circuit that combines resistances and a capacitor.

The OLED lamp used as a load in a switched mode power supply (SMPS) has a pretty specific electrical behavior, which must be studied before connecting it to the SMPS. The electrical analysis consists of the static and dynamic characteristics.

Since OLED photometric, electrical and thermal behavioral characteristics are one another dependent, it is necessary to study a PET (photo-electrical-thermal) model of OLED that represents a more complete behavior of the OLED lamp due to the three electrical, thermal and photometrical variables involved.

Then, this chapter presents a state of the art review about OLED electrical models, PET basic design theory and PET OLED models, which are needed in order to understand the basic theory of PET before addressing the PET OLED models, which are complex models.

3.1. OLED modeling

The equivalent electrical circuit model of OLED is used as a static and dynamic load for designing and simulating OLED drivers. From an electrical point of view, the OLED structure can be defined as an equivalent circuit that combines resistors and a capacitor. The ohmic losses are generated from the contact resistances of the organic layers, bulk conduction within the organic layers and electrode resistance. The capacitive behavior comes from the stacked structure of the organic layers of the OLED.

3.1.1. OLED electrical equivalent device for driver topology design

The literature mentions different types of OLED electrical equivalent models, which must be as simple as possible and provide good electrical and radiative properties of the OLED [38]-[44]. Also, it must be easy-built with resistors, capacitors and diodes and offers a good accuracy.

A large signal OLED model is shown in Fig. 3.1 [45]. The circuit consists of a series resistance R_e, which represents the electrode resistance, a capacitor that represents the electrical field formed among the organic layers, the leakage resistance R_p generated due to the charge injection into the OLED structure when the diode is off and the threshold voltage V_t, simple diode D and the dynamic series resistance R_s. The simplicity of this OLED model is the main revenue, but a drawback is that there is a small current flowing through R_p at very low polarization voltages, that is, when OLED is off. However, if the OLED is turned off, the voltage decreases slowly in time due to the time constant formed by R_p and C [46].

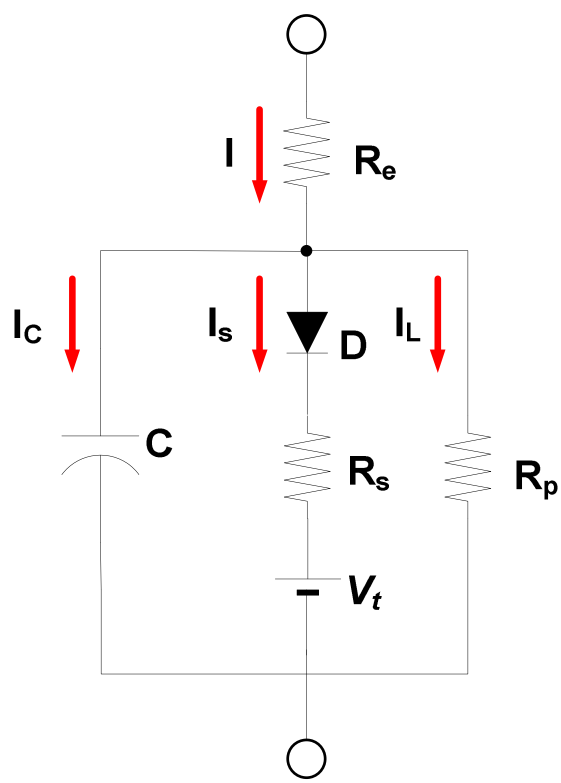

Fig. 3.1. OLED equivalent electrical model.

The OLED model shown in Fig. 3.1 has the benefits of being a large signal model and has two electrical time constants formed by R_e and C when the diode is on and R_p and C when the diode is off. The first time constant is typically measured in microseconds and the second one is measured in milliseconds close to a second. Other disadvantages of the OLED model are the accuracy and the temperature dependence of the parameters.

Nevertheless, the operating temperature of the OLED is much lower than that of the inorganic LED. For instance, the operating temperature of the OLED is about 40°C, whilst the junction temperature of the LED is above 100°C. In addition, the temperature variations of the operating OLED are defined between room temperature and 50°C, where degradations start, which reduces the influence of the temperature on the OLED. For instance, a ±10°C temperature variation at about 40°C, leads to a voltage variation of ±2.5% and ±5% [47]. In [38], it is shown that the luminance versus DC bias current curve is not quite dependent on temperature. Therefore, temperature effects are excluded from this study.

Model Parameters identification

The model parameter identification is achieved by static regime and impedance analysis measurements. The static part consists of measuring the voltage across the OLED and the current through it in order to determine the threshold voltage V_t and the dynamic series resistance R_s. Moreover, the leakage resistance R_p is obtained by measuring the points of the V-I semi logarithmic scale curve below the threshold voltage as illustrated in Fig. 3.2.

In the static regime, it is considered that the current flowing through the leakage resistance R_p is negligible in comparison with the current flowing through the dynamic resistance R_s, and that capacitor C is an open circuit. A curve fitting procedure is applied to the $V_{rs}(I)$ static curve in order to know the non-linear relationship between the current through the OLED and the voltage across R_s.

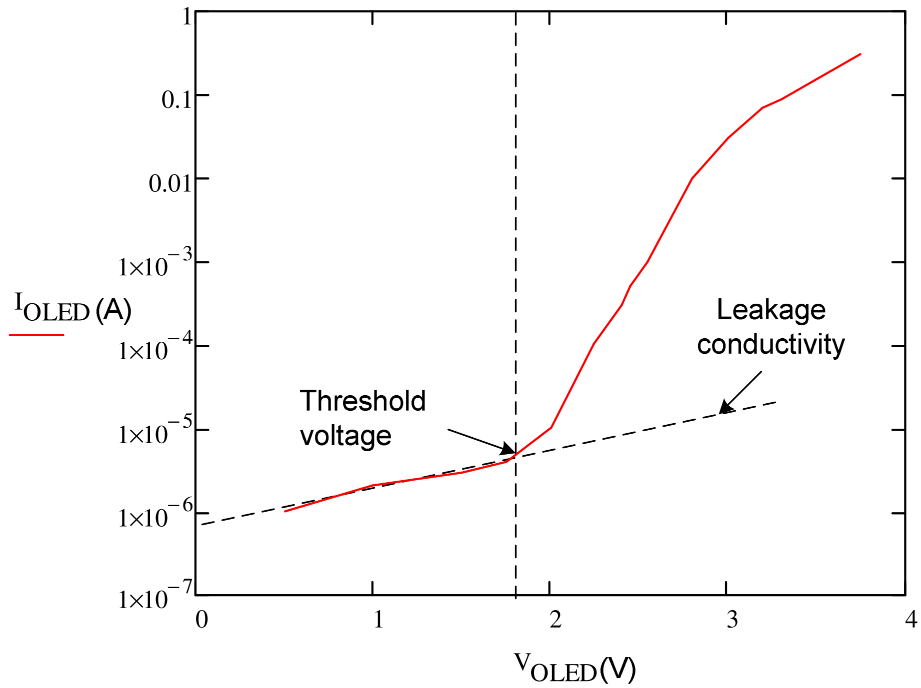

Fig. 3.2. Static curve of the OLED in semi logarithmic scale.

The impedance measurements are made by using an impedance analyzer type Solartron Modulab MTS. An ac voltage is coupled to the bias voltage applied to the OLED. Therefore, if the maximum value of this bias voltage is lower than the threshold voltage of the OLED, the OLED is off. From Fig. 3.3 impedance measurements of an OLED Orbeos CDW-031 with a bias voltage of 20mV and an ac voltage amplitude of 10mV, it is possible to know the values of R_e and C.

For instance, the phase curve is -90° at very low frequencies, which represents a pure capacitive behavior of the OLED, and then the phase crosses zero, which represents a pure resistive behavior of the OLED. Hence, on one hand, the value of the capacitor C is calculated when the phase curve is at -90°, and on the other hand, the electrode resistor R_e is calculated when the phase curve is at 0°. But, as the leakage resistor R_p value is pretty high, it is determined at very low frequency, which is not possible to measure it with the impedance analyzer used.

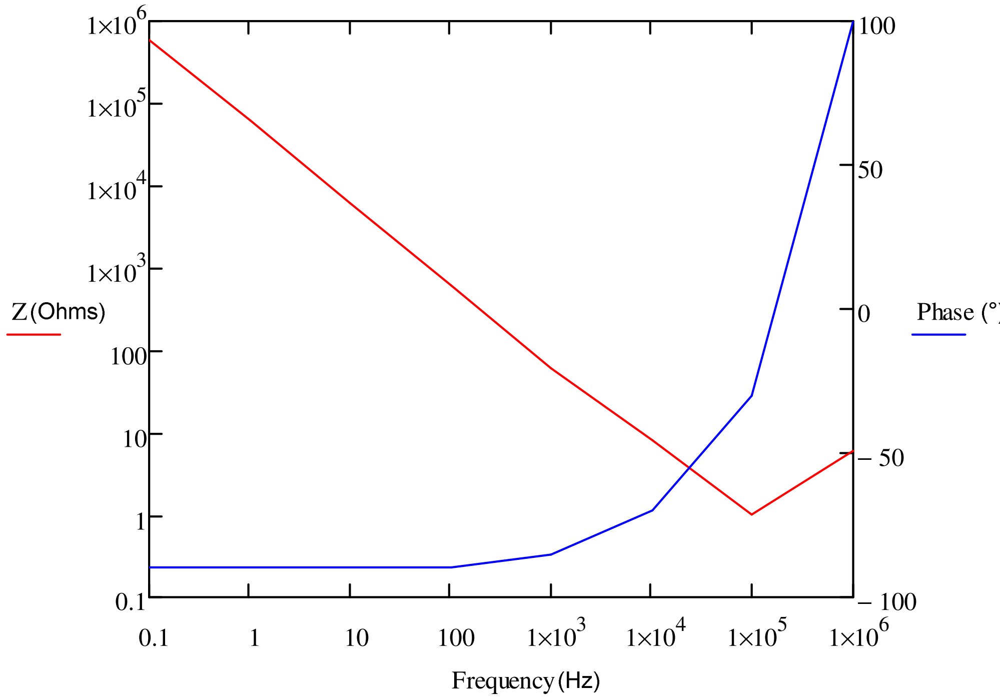

Fig. 3.3. OLED impedance and phase at 20mV bias voltage.

The values of the capacitor C and the electrode resistor R_e at different bias voltages below the threshold voltage are illustrated in Table 3.1. The values of the capacitor C and the electrode resistor R_e behave constant under the different bias voltages. Hence, the capacitance only depends on the geometric capacity as shown below.

$$C = \frac{\mathcal{E}_0 \mathcal{E}_r S}{d} \tag{3.1}$$

Where $\mathcal{E}_0$ is the permittivity of free space, $\mathcal{E}_r$ is the relative permittivity of the active layer, S is the surface area of the OLED and d is the thickness of the active layer.

Table 3.1. Capacitor C and electrode resistor R_e values at different bias voltages.

Bias voltage (mV)	**Capacitor C (μF)**	**Electrode resistor R_e (Ω)**
20	2.94	1.35
500	2.95	1.35
1000	3	1.4
1500	2.93	1.36

On the other hand, when the bias voltage is higher than the threshold voltage of the OLED, the OLED is on and the values of the capacitor C, the electrode resistor R_e and the dynamic series resistance R_s at different bias voltages above the threshold voltage are shown in Table 3.2.

The electrode resistance R_e behaves constant in value owing to the fact that it represents the contact resistance of the electrode and the capacitor C value is not constant anymore, as it is increased by more than two times in comparison with the value when the OLED is off at about 1.8V threshold voltage. In addition, for instance, the impedance measurements of the OLED Orbeos CDW-031 with a bias voltage of 4V and an ac voltage amplitude of 10mV are shown in Fig. 3.4.

Table 3.2. Capacitor C and resistors R_e and R_s values at different bias voltages.

Bias voltage (V)	**Capacitor C (μF)**	**Electrode resistor R_e (Ω)**	**Dynamic series resistor R_s (Ω)**
2	4	1.38	36k
2.5	6.9	1.35	544
3	4.3	1.4	3.5
3.5	1.9	1.35	1.48
4	0.98	1.35	1.22

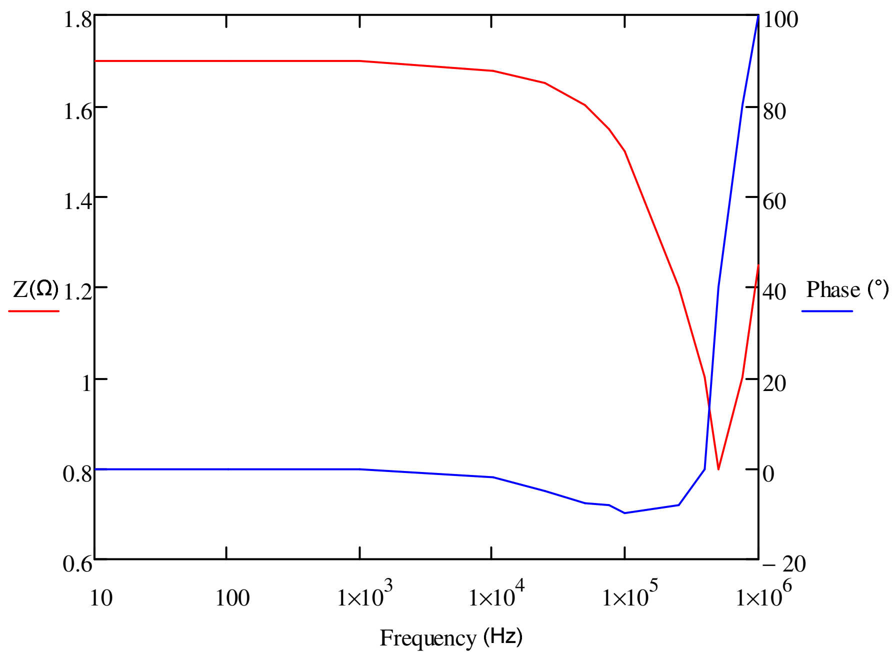

Fig. 3.4. OLED impedance and phase at 4V bias voltage.

The capacitance C is proposed to be constant at about 4.5 μF for the sake of simplicity after some analysis in the dynamic regime not reported in this work. This leads to a limiting factor of the OLED model accuracy. From a dynamic point of view, owing to the fact that this capacitor is voltage dependent, the time constant formed by R_e and C is also voltage dependent. Then, for instance, if the OLED is switched on and off periodically, the time constant is under or over estimated depending on the bias voltage. The parameters of the OLED model are shown in Table 3.3.

Table 3.3. OLED model parameters.

R_e (Ω)	R_p (kΩ)	C (μF)	V_t (V)	R_s (Ω)
1.35	750	4.5	1.8	0.27

OLED Model accuracy

A pulsed current source with variable duty cycle, current and frequency was used to drive the OLED Orbeos CDW-031, and validate the accuracy of the OLED model under a dynamic change. The OLED voltage deviation between simulations and experimental results presented is 50 mV, equivalent to an error of 1.5%. On the other hand, there is no delay in response time between the simulated normalized current and the experimental normalized light output. Moreover, the OLED model is less accurate at frequencies lower than 1 kHz.

3.1.2. OLED equivalent circuit model with temperature coefficient and intrinsic capacitor

There are two types of OLED models, which are predictive OLED model [48] and impedance-spectroscopy-based OLED model [49]. The predictive OLED models provide consistent results with the device physics for a very good accuracy. But, this model requires many data input as geometry, device structure and the physical properties of the materials, which are difficult to find in the supplier's OLED specifications [50]. The impedance-spectroscopy-based OLED model requires a small signal model at different operating points to define a non-linear large signal model with a large domain of validity. The OLED model parameters are voltage dependent [49]. Other OLED models consider only the static behavior [51][52]. In addition, there are other OLED models that consider the dynamic behavior, but it is assumed that the OLED capacitance is not voltage dependent [53]-[56]. The OLED models that consider the capacitance variation and the dynamics of the OLED, do not take into consideration the temperature effects on the static behavior.

A simple method to characterize OLED lamps is proposed in [50], in which the architecture and the physics materials are not known. This approach takes into account the effects of the temperature and the voltage-dependent capacitor value.

The OLED equivalent circuit is illustrated in Fig. 3.5. The circuit consists of an inductor L_e and a resistor R_e, which represent the the stray inductance and resistance of the wire, a diode D_{OLED} and a capacitor C_{OLED}.

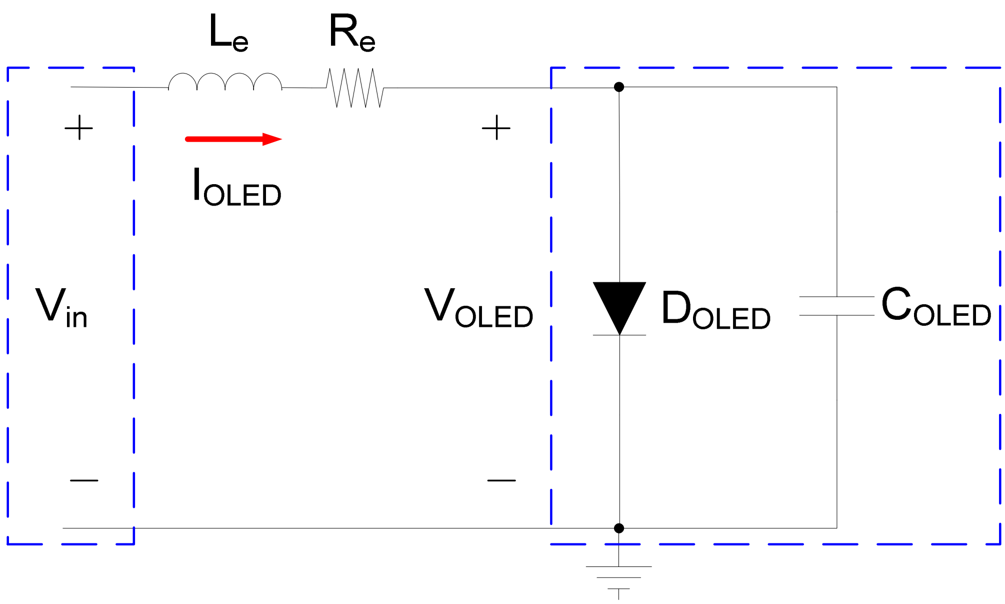

Fig. 3.5. OLED equivalent electrical circuit.

Four-parameter Taylor-series-based OLED model

In organic materials, the current is limited by the bulk material, that is, by space-charge-limited current properties or by contacts, that is, by injection-limited current. According to the device architecture, the physical properties, and the operating conditions, one of the two current limiting types is dominant. The transition between these two mechanisms is not straightforward and requires the combination of injection models and transport models to obtain an accurate V-I characteristic on a broad operating range [57].

The approached proposed is to approximate the V-I characteristic of the OLED with a behavioral model that considers the OLED current obeys the Shockley diode expression. This approach does not consider the device physics. Then, it is possible to further simplify the

Shockley diode expression by using the Taylor series [53]-[56]. The V-I characteristic curve and the OLED equivalent model are obtained [58][59].

$$I_{OLED}(T_a) = I_{sat}(T_a) \sum_{j=0}^{\infty} \frac{\left(\frac{V_{OLED(20°C)}+(T_a-20°C)\lambda - r_s I_{OLED}(T_a)}{n(T_a)V_T(T_a)}\right)^j}{j!} \tag{3.2}$$

Where:

$$r_s = \frac{V_M - V_Q}{I_M - I_Q} \tag{3.3}$$

$$n(T_a) = \frac{V_K - V_M - r_s(I_K - I_M)}{V_T(T_a)\ln\left(\frac{I_K}{I_M}\right)} \tag{3.4}$$

$$I_{sat}(T_a) = \frac{I_K}{e^{\left(\frac{V_{K(20°C)}+(T_a-20°C)\lambda - r_s I_K}{n(T_a)V_T(T_a)}\right)}} \tag{3.5}$$

$$\lambda = \frac{V_{Q(40°C)} - V_{Q(20°C)}}{(T_a - 20°C)} \tag{3.6}$$

Where: r_s is the dynamic series resistance of the OLED, V_M and I_M are the OLED maximum voltage and current, V_Q and I_Q are the OLED rated voltage and current, V_K and I_K are the OLED knee voltage and current, $V_T(T_a)$ is the threshold voltage of the OLED at the operating ambient temperature, T_a is the operating ambient temperature, λ is the temperature coefficient, $I_{sat}(T_a)$ is the saturation current of the OLED at the operating ambient temperature, and $n(T_a)$ is the ideality factor of the OLED at the operating ambient temperature. The experimental parameters as the maximum operating point (V_M, I_M), the rated operating point (V_Q, I_Q) and the knee point (V_K, I_K) of the Orbeos CDW-031 are listed in Table 3.4 [60]. The OLED parameters are obtained at 25°C ambient temperature. The error percentage of deviation between the calculated OLED current in accordance with (3.2) and the experimental OLED current is shown in Fig. 3.6. The highest error percentage deviation is lower than 2% found from 10°C to 40°C ambient temperatures.

Table 3.4. Electrical parameters of the Taylor series model at 25°C.

Knee point (V_K, I_K) (V, mA)	**Rated operating point (V_Q, I_Q) (V, mA)**	**Maximum operating point (V_M, I_M) (V, mA)**	**Dynamic resistance $r_s(\Omega)$**	**Ideality factor $n(T_a)$**	**R. Saturation current $I_{sat}(T_a)$(A)**	**Temp. coefficient $\lambda(V/°C)$**
(2.89,12)	(3.4,121)	(3.87,318)	2.376	3.047	$8.458\ x\ 10^{-19}$	-7.45

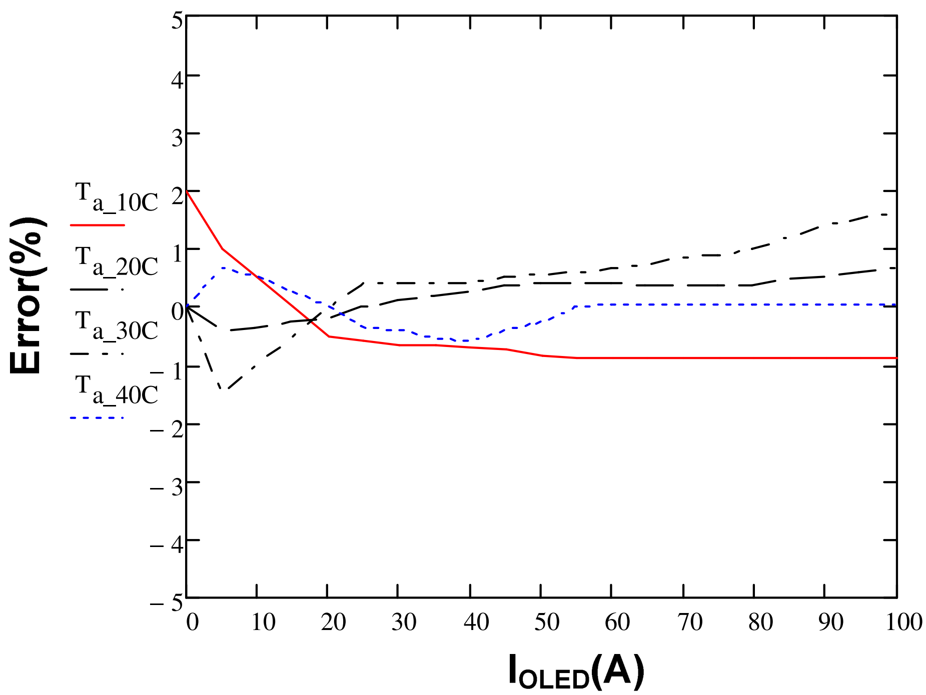

Fig. 3.6. Error percentage deviation between calculated and experimental OLED current.

VPWL and PWL based OLED equivalent models

The equivalent OLED electrical model that is integrated by the VPWL (voltage-controlled piecewise linear) and PWL (piecewise linear) models is shown in Fig. 3.7. The OLED model takes into consideration the temperature effects from 10°C to 40°C. From the circuit shown in Fig. 3.7, the transient and ac frequency response simulations can be tackled.

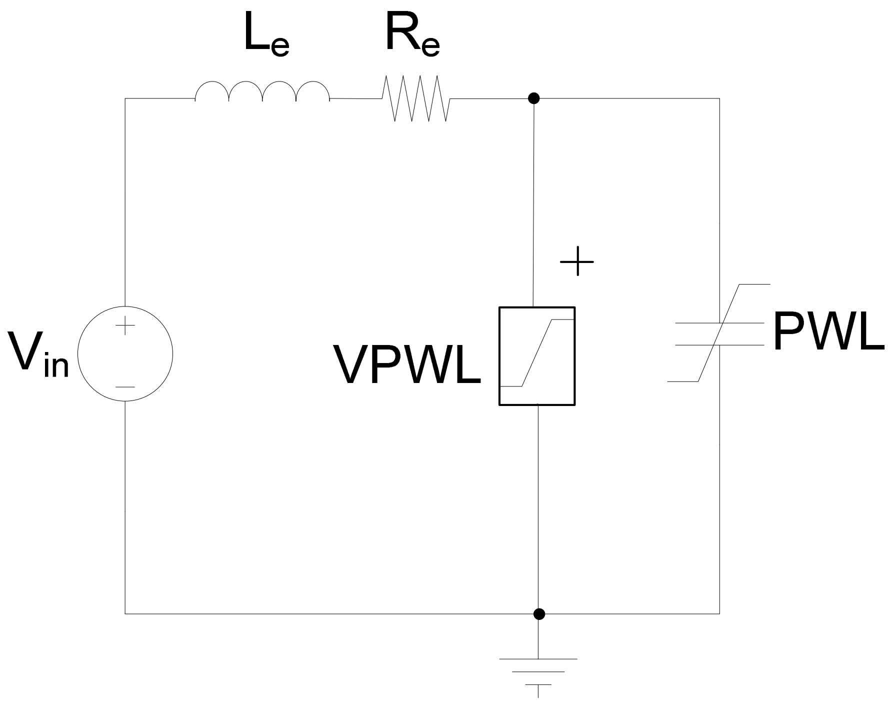

Fig. 3.7. VPWL and PWL-based equivalent OLED electrical model.

The OLED capacitance is voltage-frequency-temperature dependent [39], [61]-[64]. The OLED equivalent capacitance is obtained between two relaxation frequencies, in which the capacitance is constant. The OLED presents a pseudo-inductive charge relaxation effect at the lower frequency. An experimental constant capacitance between a 1 Hz - 100 kHz frequency range and a constant capacitance under small temperature variations from 25°C ± 15°C are obtained. Then, the temperature effect over the capacitance can be neglected. The equivalent capacitance of the OLED Orbeos CDW-031 as a function of the OLED voltage curve is illustrated in Fig. 3.8. And then, the capacitor charge in function of the OLED voltage can be calculated from (3.7).

$$Q_{OLED} = \int C_{OLED} dV_{OLED} \tag{3.7}$$

Where: Q_{OLED} is the OLED electrical charge and V_{OLED} is the OLED voltage.

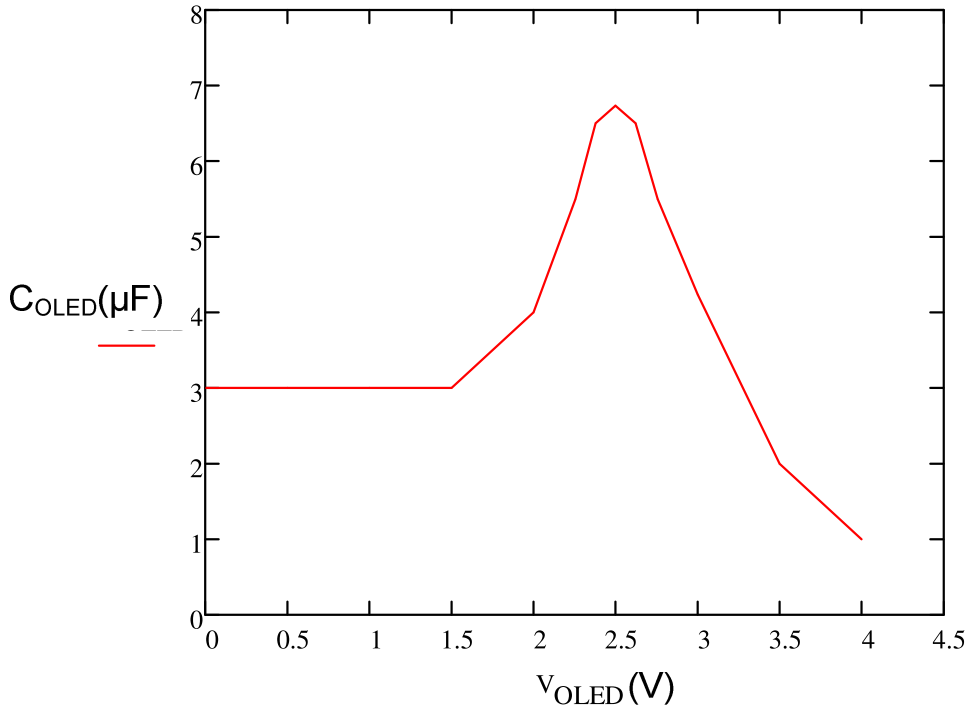

Fig. 3.8. Experimental equivalent capacitance of the OLED.

A frequency response simulation based on the circuit shown in Fig. 3.7 and the experimental impedance measurements are an important analysis carried out in this work. In which, input impedance amplitude and phase of the OLED model and OLED lamp are measured. The OLED voltage is varied from 20mV to 3.5V in steps of 0.5V. The simulation and experimental results reported presented a pretty good accuracy among them. However, a small discrepancy between simulation and experimental results at an OLED voltage of 3V is presented. It is solved by increasing the data points of the V-I static curve of the OLED between the knee point and the rated point from 5 to 30 points. This issue is presented due to the fact that this operating point of the OLED is within the nonlinear region of the V-I static curve of the OLED, and it is right at the common end point of two piecewise segments, leading to a jumping problem for the operating point during operation and to a convergence problem. In order to avoid this jumping problem for the operating point, more data points are required within the nonlinear region to make sure that the operating point is working along its corresponding piecewise segment.

The OLED transient behavior cannot be represented by a model with a fixed capacitance [45]. Hence, it is needed to carry out a transient simulation based on the circuit shown in Fig. 3.9. In addition, the OLED must be studied experimentally under the electrical conditions set up in the transient simulation in order to validate the simulation results experimentally.

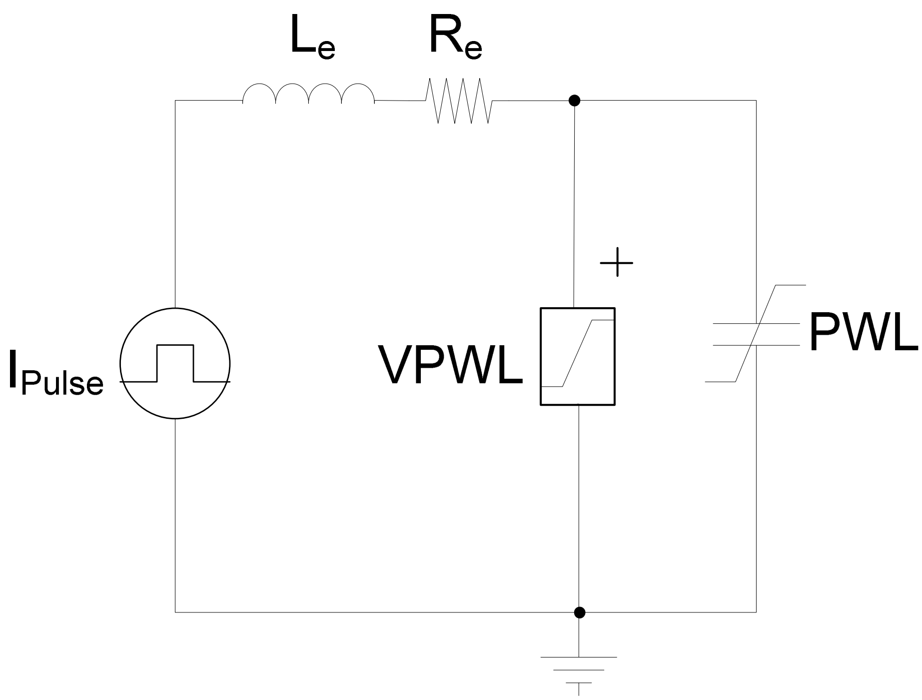

Fig. 3.9. Transient VPWL and PWL-based equivalent electrical circuit.

The good agreement between transient simulation and experimental results reported in this work represent a good dynamic behavior of the OLED model. Owing to the high capacitance of the OLED lamp, the high frequency signals are attenuated. Therefore, only the dc component of the signals is seen by the OLED. Based on this, it is only necessary to predict the V-I static characteristic of the OLED at this operating point. However, this is not the case at lower operating frequencies.

3.1.3. Modeling and characterization of OLEDs including capacitance effect

The proposed TEM (theoretical equivalent model) is shown in Fig. 3.10 [65]. This model consists of the electrode resistance R_e, the leakage resistance R_p, the geometric capacitor C_g, diodes D_1, D_2 and D_3, voltage source V_{bi} and threshold voltage source V_o, resistance R_{bi} and dynamic series resistance R_s.

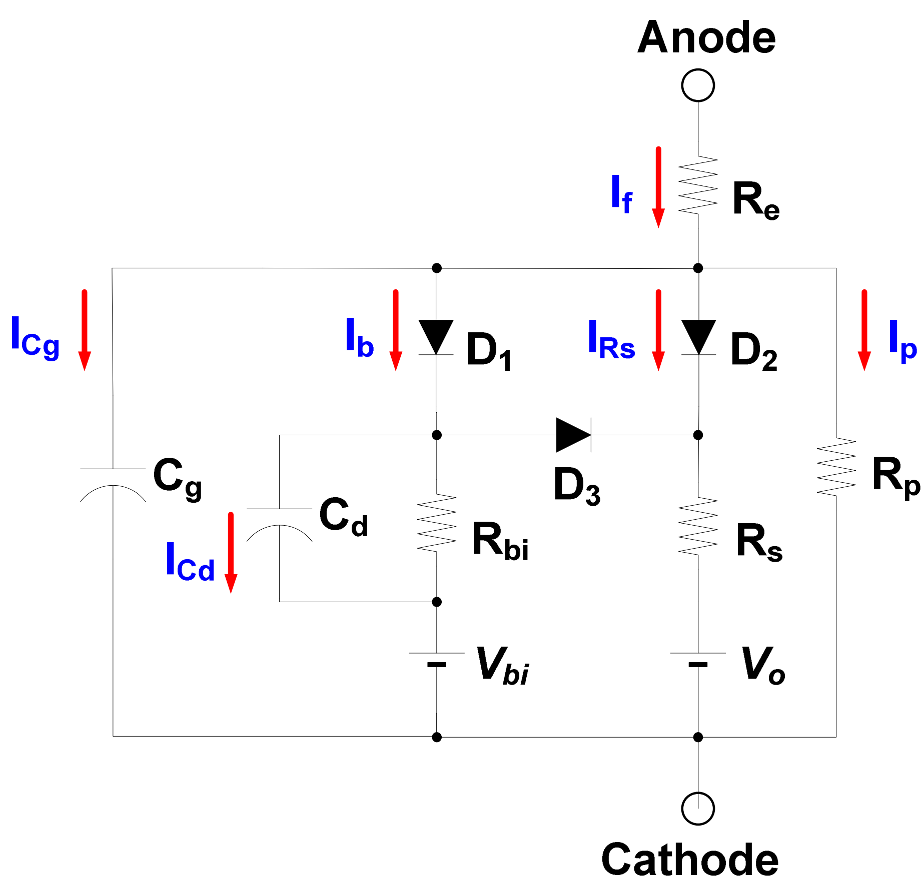

Fig. 3.10. OLED TEM circuit.

The leakage current flow through R_p is significant when diodes D_1 and D_2 are off. Resistances R_e and R_p affect the device operation in region 1, which is shown in Fig. 3.11. The forward voltage of the OLED is lower than the voltage V_{bi} and the forward current is very small. Hence, the OLED has an ohmic behavior. In region 2, the forward voltage of the OLED is higher than the voltage V_{bi} and the charge injection into the OLED starts, owing to the fact that capacitor C_d starts charging and then, a small forward current flows through resistances R_{bi} and R_e. Since R_p is much greater than R_{bi} and R_e, it is considered as an open circuit. In region 3, the threshold voltage of the OLED is reached and the forward current of the OLED initiates conducting in a significant way. Diode D_3 provides a path of discharge to the two capacitances as they are the geometric capacitance C_g and the diffusion capacitance C_d. The geometric capacitance is equivalent to the form factor of the OLED, which is the ratio between the OLED area and the thickness of the organic materials of the OLED.

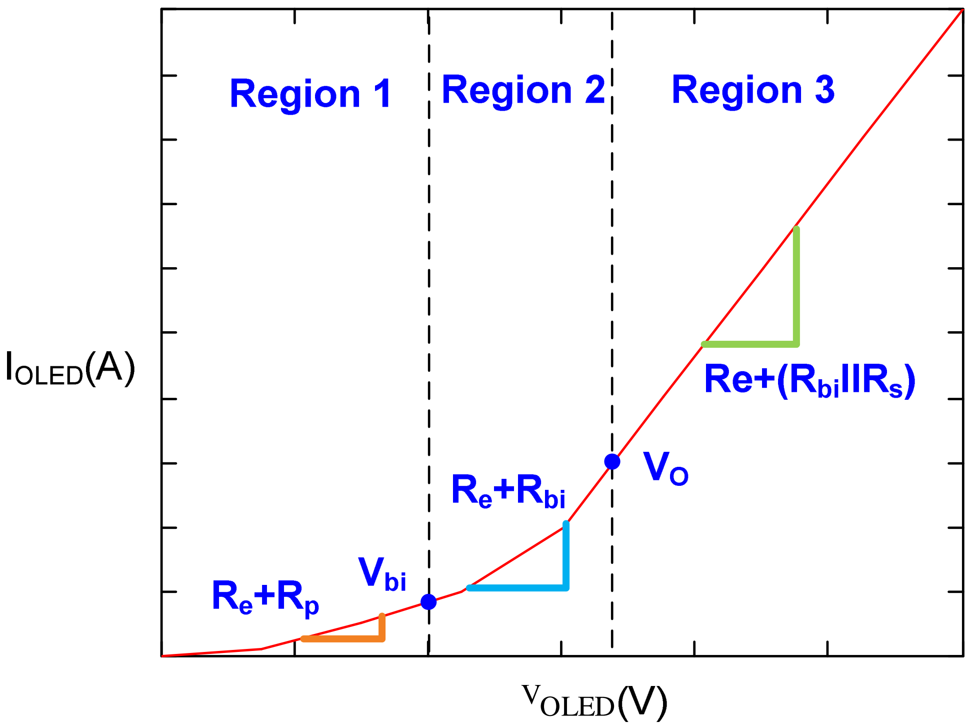

Fig. 3.11. OLED static V-I curve.

The OLED is fully depleted at very low forward voltage and the capacitance is independent of the voltage. Therefore, the capacitance of the OLED is equivalent to the C_g capacitance and only depends on the dielectric properties, device area and thickness of the OLED. The OLED capacitance remains constant till the charge injection from the electrode starts, which is indicated by V_{bi}. This carrier injection increases due to the effect of the C_d capacitance. When the forward voltage is much higher than the threshold voltage of the OLED, a significant radiative recombination occurs in the emission layer of the OLED causing the reduction of the amount of charge, which decreases the capacitance of the OLED [39], [66]-[67].

Characterization and parameter identification

The procedure to obtain the resistor R_e is based on Fig. 3.12(a). The voltage E must be lower than the voltage V_{bi} in order to limit the peak current. First, S_1 is at position a and the OLED capacitor is charged up to voltage E. Later, S_1 is at position b and the OLED is short-circuited. The current is only limited by the resistors R_e and R_{s1}. The charge stored in the capacitor causes a peak current through the external path, which helps find the resistor value of R_e.

$$R_e = \left(\frac{V_f}{I_{pk}}\right) - R_{s1} \tag{3.8}$$

The V-I static curve of the OLED is obtained by means of the circuit shown in Fig. 3.12(b), which consists of a constant current source and a ramp voltage source. The inflexion point of the V-I static curve is taken jointly with a photo sensor to determine the point when the OLED light emission occurs. The resistances R_{bi}, R_s and R_p are obtained by using a linear regression method to the curve illustrated in Fig. 3.11. The leakage resistance R_p is found from the inverse slope of the V-I curve in region 1. The temperature rise causes an increase in the OLED conductivity, which lowers its electrical resistance. Also, the energy required for the recombination phenomena is lower, so that a lower forward voltage is required to drive the OLED [45], [47], [66]-[67], [68]-[72].

The determination of the diffusion capacitance C_d has been obtained by different methods, but they use sophisticated equipment. For instance, they obtain the capacitance by including admittance spectroscopy [49], [73], static discharge [74], and large-signal measuring [75]. Therefore, an approach that combines the V-I static characteristic and the transient OLED voltage characteristic during the charge stage is proposed in order to obtain the diffusion capacitance C_d. The circuit used to obtain the capacitance C_d is shown in Fig. 3.12(c).

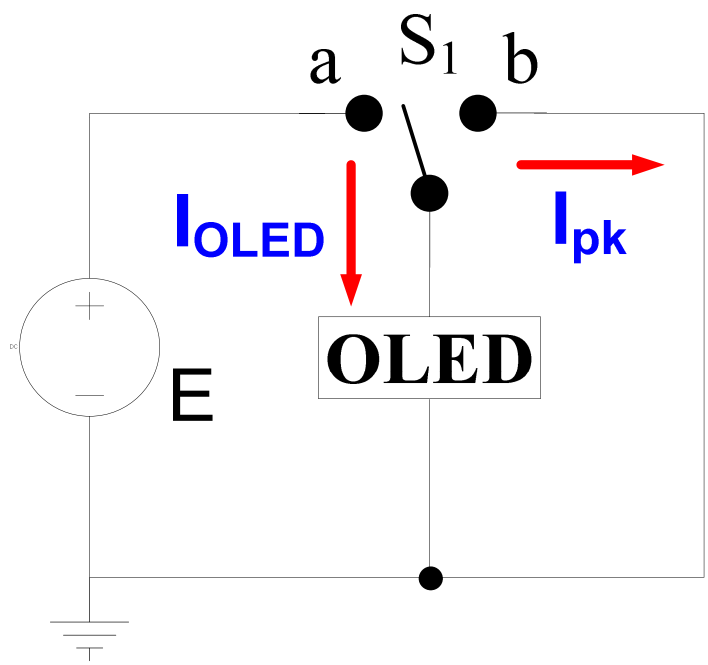

a)

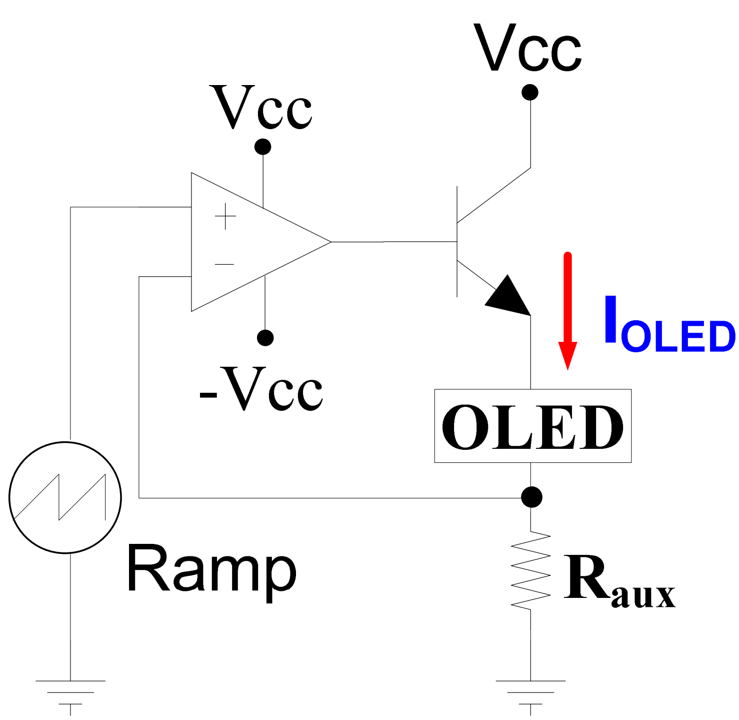

b)

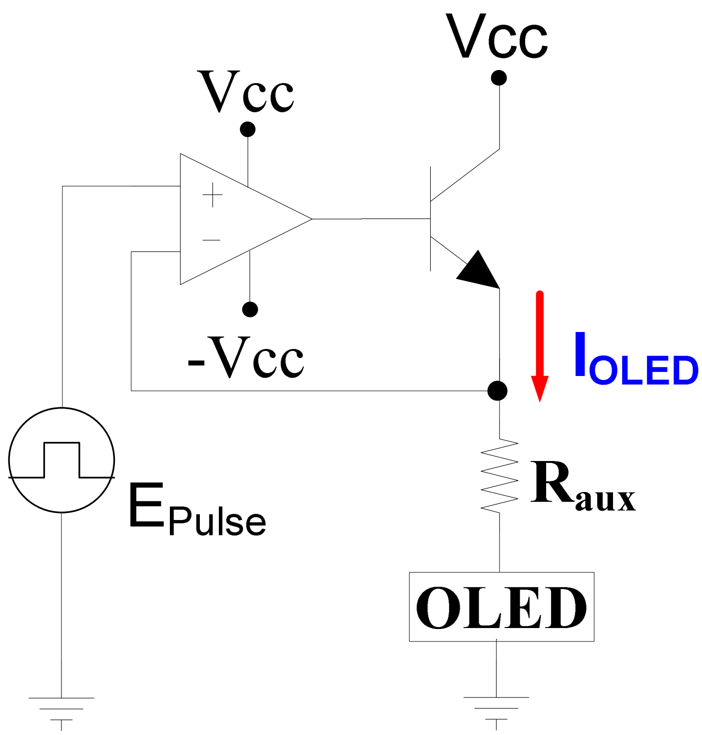

c)

Fig. 3.12. OLED parameters identification circuits: a) R_e, b) R_p, R_s, R_{bi}, V_o, and V_{bi} and c) C_g and C_d.

The voltage amplitude of the step E_{step} must be slightly higher than the rated OLED voltage to avoid getting current spikes. An extra resistor R_{aux} is used to limit the forward current. The curve of the diffusion capacitance obtained is illustrated in Fig. 3.13.

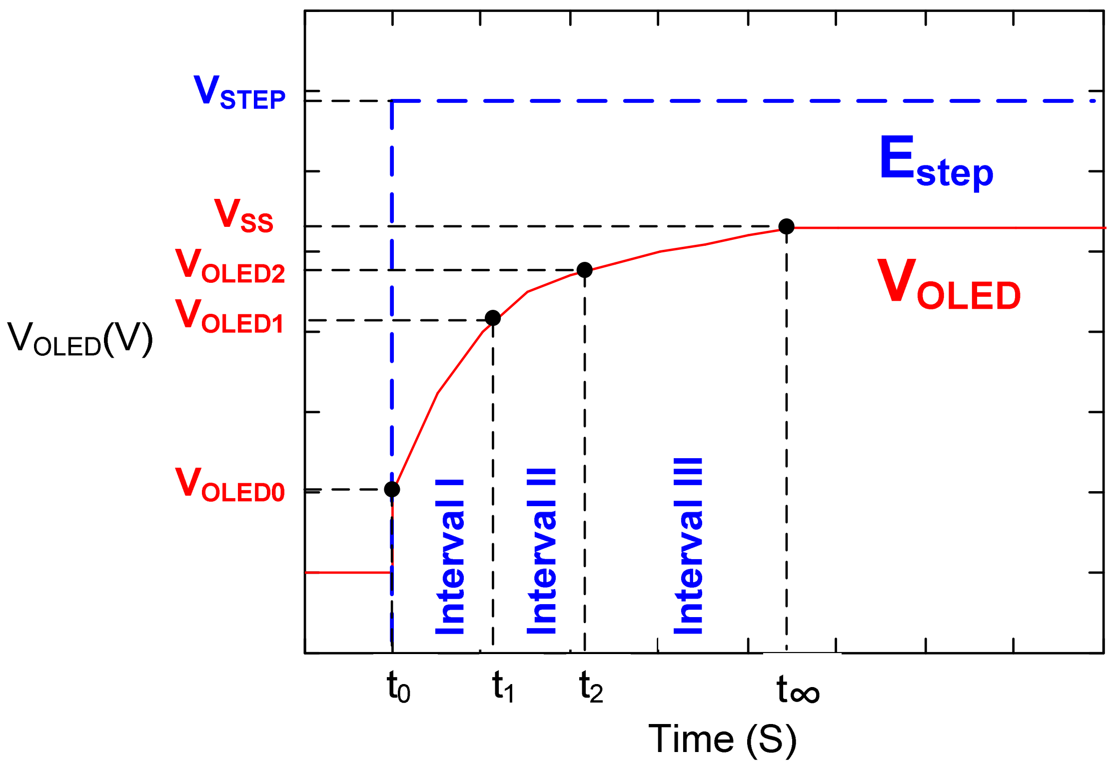

Fig. 3.13. Diffusion capacitance identification curve: step voltage (blue) and OLED voltage (red).

In interval I ($t_o - t_1$), the step voltage E_{step} is applied at t_0, which causes that the forward voltage increases instantaneously, due to the current flow through R_e and C_g. Thereby, the time constant is defined by the equivalent resistance $R_e + R_{aux}$ and C_g.

In interval II ($t_1 - t_2$), the voltage V_{cg} reached V_{bi} and C_d starts charging. The time constant is lower, owing to the equivalent capacitance $C_g + C_d$ and the parallel resistance $(R_e + R_{aux})\|(R_{bi})$.

In interval III ($t_2 - t_\infty$), the voltage V_{cg} is higher than V_o and the current starts flowing through R_s. The time constant is changed, owing to the equivalent capacitance $C_g + C_d$ and the parallel resistance $(R_e + R_{aux})\|(R_{bi})\|(R_s)$.

Since the equations are known, the capacitances can be calculated by using a mathematical method to approximate the theoretical response of the experimental response. The least square method is applied jointly with an algorithm for error minimization MinErr in Mathcad. This procedure determines the best fit line to data and returns the parameters of the model that come closest to satisfy the equations of the model as they are C_g and C_d.

A transient simulation and experimental results of transient comparison was carried out to validate the accuracy of the OLED model RMW-046. The results showed a discrepancy of 290 mV equivalent to 8.5% error. The OLED model is more accurate for frequencies of 1 kHz and 10 kHz than 100 kHz and the model is less accurate at frequencies lower than 1 kHz.

3.1.4. Simplified electrical modelling of power LEDs for DC-DC converter analysis and simulation

A power LED model based on electrical variables and the equivalent resistance concept that is addressed in discharge lamp modeling and that is suitable to carry out fast simulations of the LED converter system [76]. This model obtains acceptable simulation results of LED-dc-dc converter system simulations with a feasible parameter extraction process. The LED parameters are obtained by taking pretty straightforward measurements of voltage and current by means of multimeter and scope. So far, there are some models proposed in the literature [59], [77]-[87]. But, they are difficult to obtain due to temperature effect and optical considerations. So that, a simplified electrical nonlinear dynamic model to simulate LED-converter systems is proposed.

The model proposed is extrapolated from the model of a discharge lamp [88][89]. In which, the equivalent resistance and the constant time of the lamp is considered. This model just considers electrical variables owing to optical variables are used to meet suitable illumination. In other words, the optical variables do not present any effect over the electrical performance of the LED. On the other hand, the temperature variable is indirectly considered in the LED due to the power is directly affected by the temperature as in the discharge lamp [88][89].

Power LED behavior and modeling

Stationary-state behavior

Power LEDs present a steady-state voltage-current characteristic, in which each point of the curve is measured when they are reached steady state, similarly to the conventional diode as shown in Fig. 3.14.

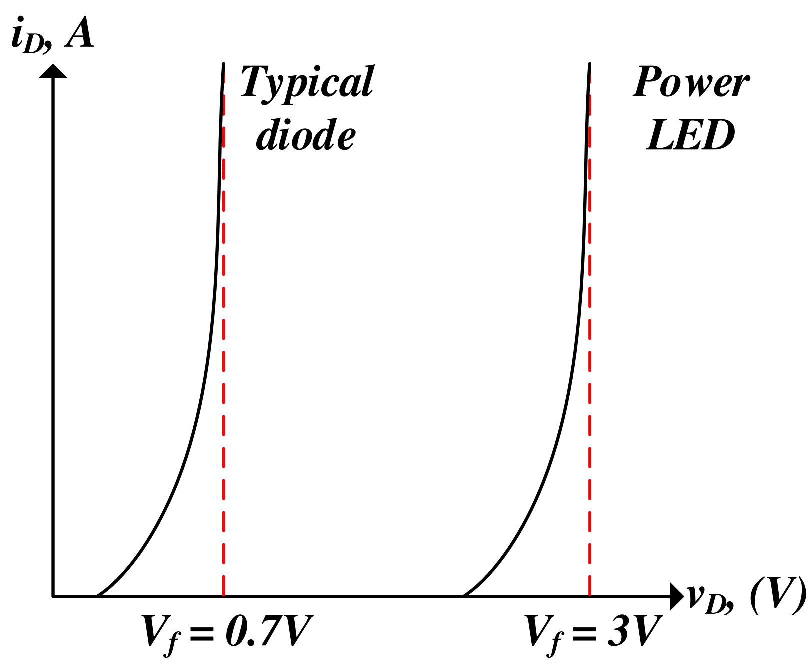

Fig. 3.14. Steady state curve of the LED and conventional diode.

The Shockley diode expression (3.9) is used to model the diode behavior, and it is used to model the power LED behavior in this work. From (3.9), it is observed that the LED current I_D is junction temperature T_j and LED voltage V_D dependent. The junction temperature T_j is in function of the LED power P_D (3.10). The LED voltage is in function of the LED power P_D and the equivalent resistance R_D of the LED (3.11). Then, the LED current I_D can be expressed as a function of the LED power P_D and the equivalent resistance R_D of the LED (3.12).

$$I_D = I_S\left(e^{\frac{qV_D}{nkT_j}} - 1\right) \tag{3.9}$$

$$T_j = f_2(P_D) \tag{3.10}$$

$$V_D = f_3(P_D, R_D) = \sqrt{P_D R_D} \tag{3.11}$$

$$I_D = f_4(P_D) = \sqrt{\frac{P_D}{R_D}} \tag{3.12}$$

Power LEDs present a different equivalent resistance R_D at each operating point, and it is in function of the LED current I_D and the LED voltage V_D. Hence, by combining (3.9), (3.10), (3.11), and (3.12), the equivalent resistance R_D is in function of the LED power P_D (3.13). The graphical representation of the equivalent resistance R_D is illustrated in Fig. 3.15. Due to this fact, it is pretty difficult to solve (3.13) in a closed form, the expression given by equation (3.14) is proposed owing to the fact that the behavioral of the equivalent resistance of the discharge lamp in [89] is quite similar to the LED power equivalent resistance R_D, as illustrated in Fig. 3.15.

$$R_D = f_4(P_D) \tag{3.13}$$

$$R_D = f_4(P_D) = B_1 {P_D}^{B_2} + B_3 \tag{3.14}$$

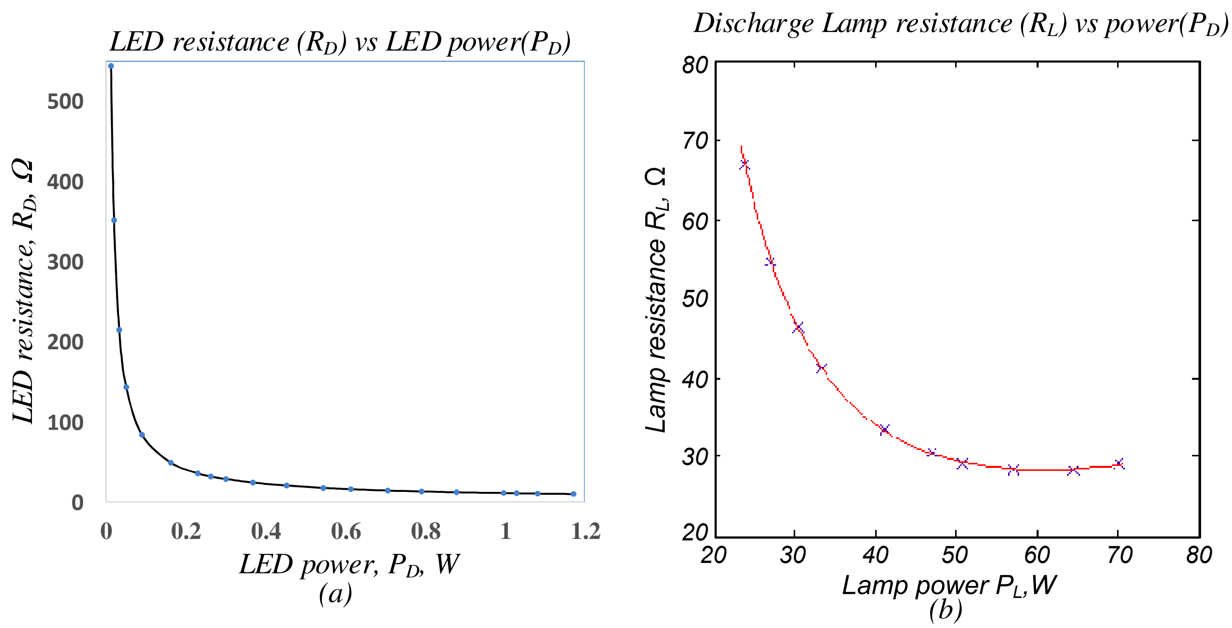

Fig. 3.15. Equivalent resistance curve: a) R_D vs LED power P_D and b) R_L vs HID power P_L under steady state.

Dynamic behavior

The time constant of LEDs is similar in behavior to that time constant of discharge lamps. The dynamic electrical model is presented in [88]-[89]. The time constant is related to the dynamic behavior of the LED, and represents the dynamic response of the LED when the current is time-dependent. The LED time constant depends on the LED voltage response, and can be obtained from the LED voltage by applying a current step to the LED [88][89]. The power LEDs present a very fast dynamic response, which leads to a quite small time constant in the order of nano-seconds.

The transient response test circuit shown in Fig. 3.16 is used to demonstrate the behavior illustrated in Fig. 3.17(a) and Fig. 3.17(b). But, the rise time of the current step applied to the LED is not short enough to observe the constant time in the LED voltage with precision. So that, an approximation of the constant time of the LED is measured in the test. In order to improve the dynamic behavior of the circuit under test, a Mosfet PSMN1R2-25YL with low on-resistance and low parasitic capacitances and good switching behavior is used to get an approximation of the time constant of the LED. The time constant is considered as the time needed to meet 100% LED voltage at the point of 100 % LED current. Thereby, the time constant obtained is 17 ns as illustrated in Fig. 3.17(b).

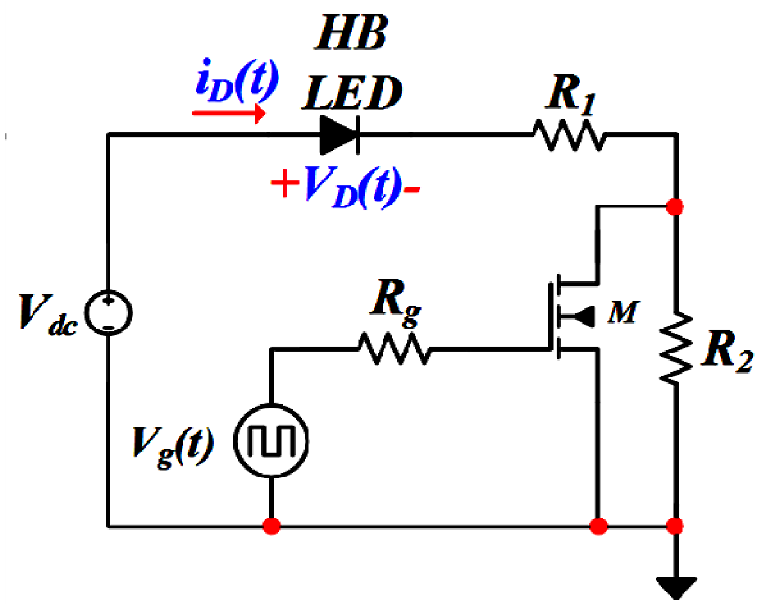

Fig. 3.16. Transient response circuit test.

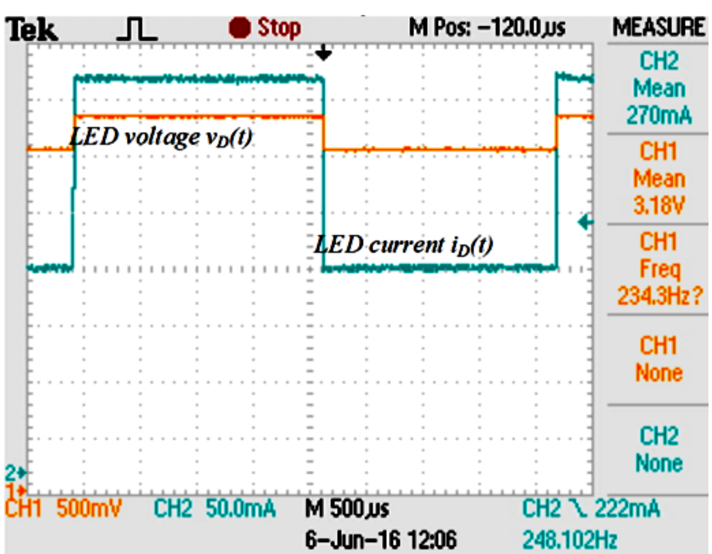

a)

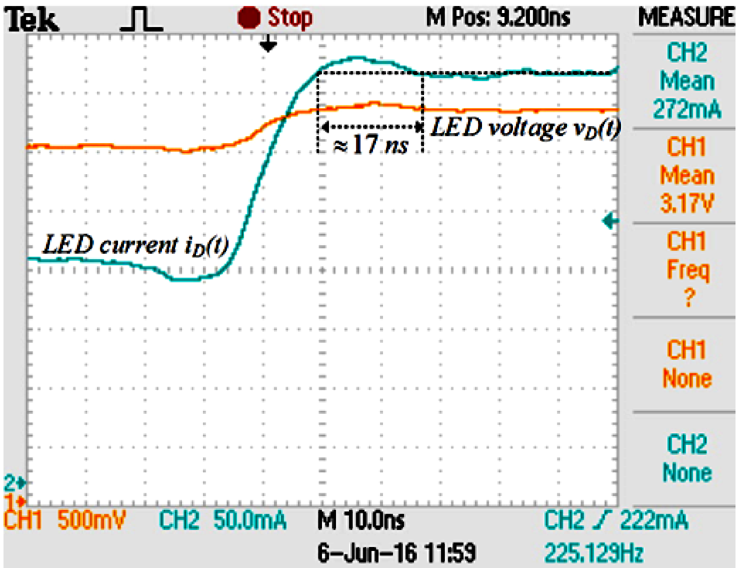

b)

Fig. 3.17. Transient response of the LED LMT-P12Y-77-N: a) voltage response under current step and b) voltage response zoom in.

LED modeling

The equivalent resistance R_D of the LED can then be expressed in function of the LED power P_D (3.15).

$$R_D(t) = f(P_{Dx}(t)) = B_1 P_{Dx}(t)^{B_2} + B_3 \tag{3.15}$$

Where P_{Dx} is the LED power variable and the time constant of the LED is modeled by a RC network as shown in Fig. 3.18.

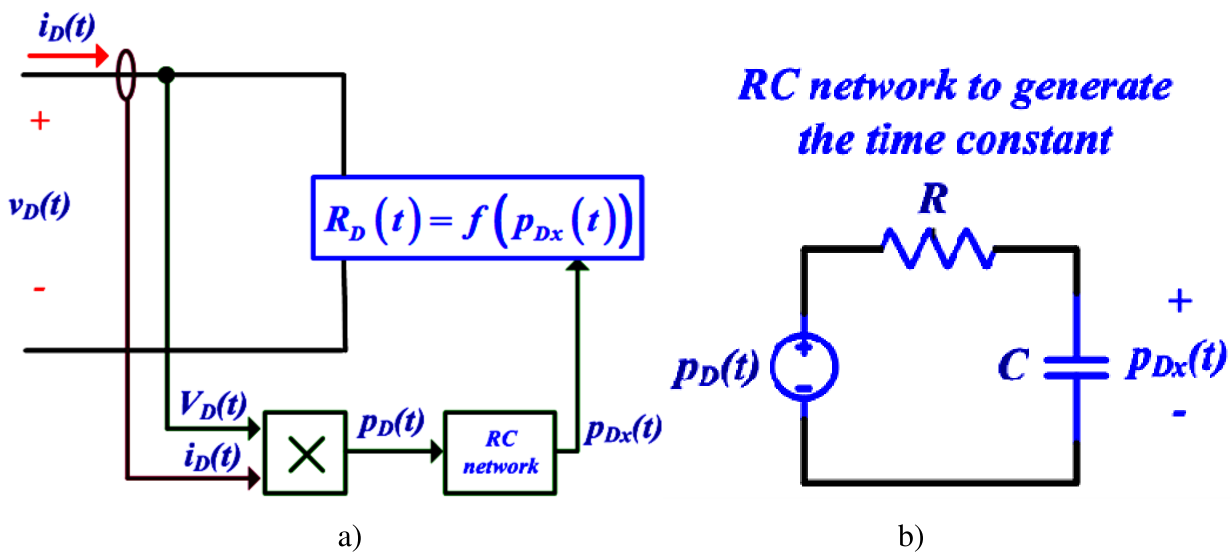

Fig. 3.18. LED model proposed: a) block diagram and b) RC network diagram.

Evaluation of the LED parameters

The schematic used to obtain the steady state LED parameters in accordance with (3.16) is shown in Fig. 3.19.

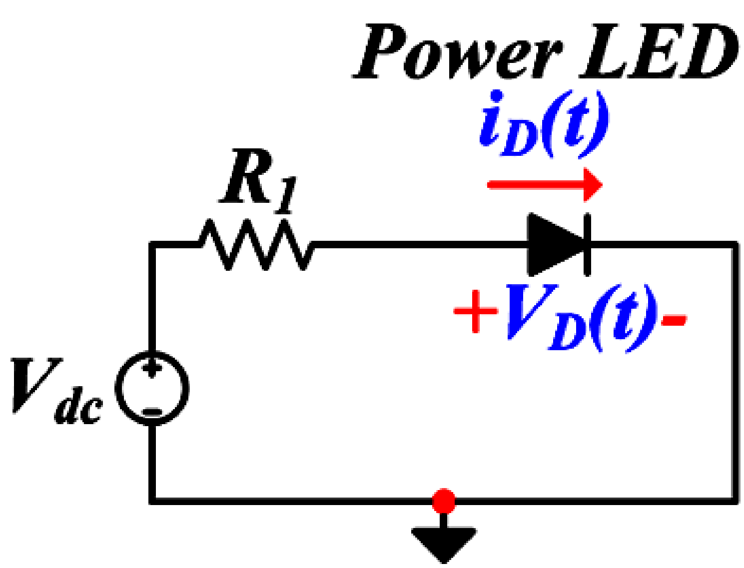

Fig. 3.19. Steady state test circuit.

At stationary state, (3.15) is converted into (3.16):

$$R_D = f(P_{Dx}) = B_1 {P_{Dx}}^{B_2} + B_3 \tag{3.16}$$

The variables B_1, B_2 and B_3 from (3.16) can be found by applying a curve fitting method to experimental data of Fig. 3.20(a). Then, the theoretical results from (2.16) are also shown in Fig. 3.20(a). The relative error between experimental and theoretical results is 1.13%. The V-I experimental and theoretical results curve is illustrated in Fig. 3.20(b). In which, it is shown that (3.16) reproduces the threshold voltage of the LED from the exponential term ${P_{Dx}}^{B_2}$.

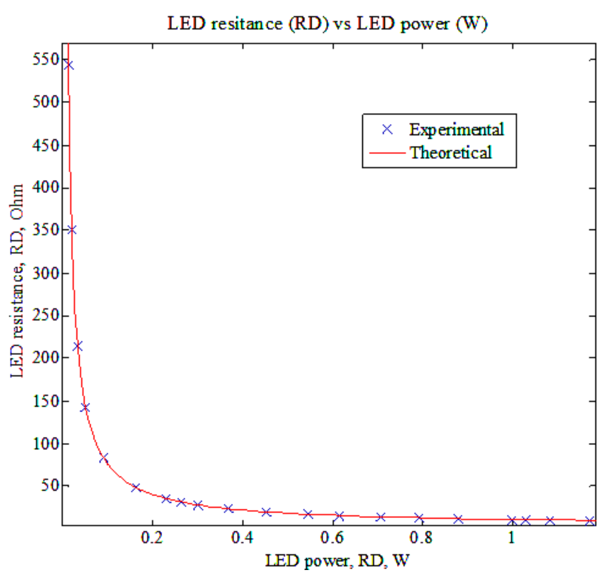

a)

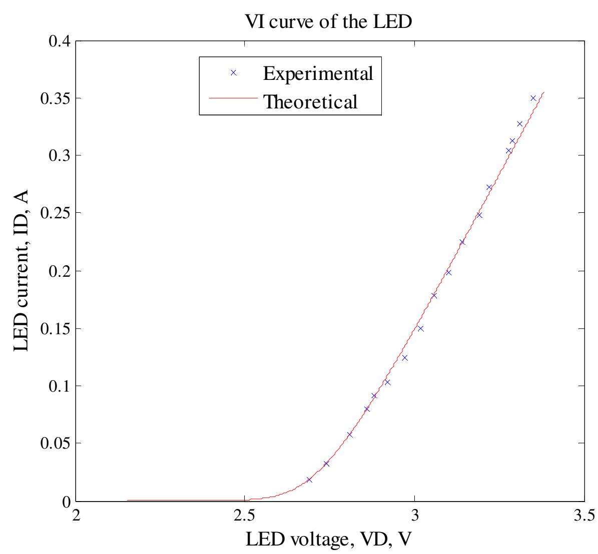

b)

Fig. 3.20. Steady state curves: a) P_D vs R_D, and b) V_D vs I_D.

The Simulink-based circuit of the power LED model is shown in Fig. 3.21 based on the technique used in [88][89]. In which, $V_D(t)1$ and $P_D(t)1$ are voltage-controlled sources, $V_D(t)$ and $V_D(t)2$ are voltage sensors, $I_D(t)$ is a current sensor, $P_D(t)$ and $i_D(t) * R_D(t)$ are multipliers, $R_D(t)$ is a function block, R_i is a resistor, C_i is a capacitor and the saturation block or resistance limiter, which is set from 0.1 to 10kΩ in order to avoid getting unwanted unmodeled operation points in the simulation.

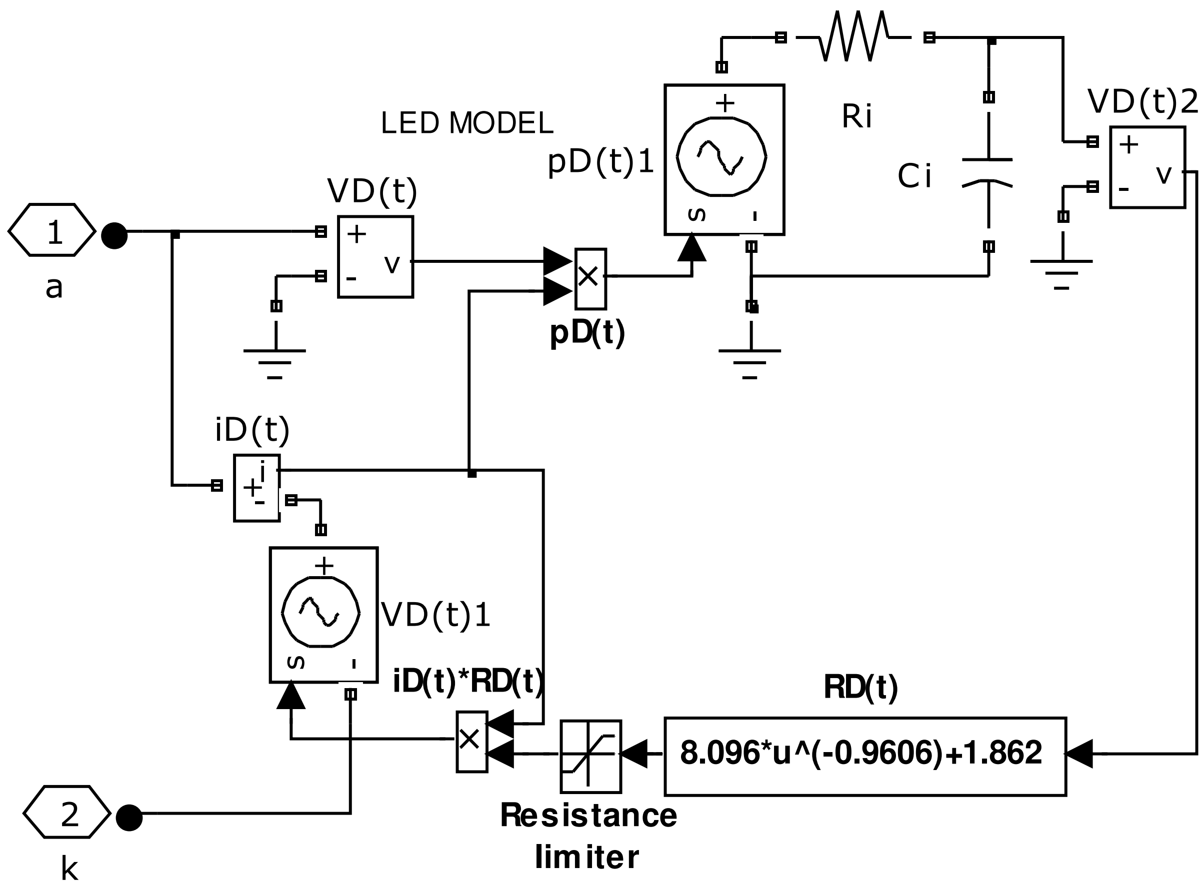

Fig. 3.21. Simulink-based circuit of the LED model.

The theoretical and experimental results of the LED under a transient operation presented a good agreement regarding the LED dynamic behavior.

3.1.5. A general PET theory for LED systems

The photometrical, electrical and thermal features of the LED systems are dependent one another. Then, it is possible to optimize the design of LED systems by considering these three factors together. A general theory that ties the photometrical, electrical and thermal parameters of the LED system is presented [90]. Thermal design is a critical and indispensable consideration of the circuit design, due to the fact that it affects the peak luminous output of the LED system.

A disadvantage of LED technology is that the luminous flux decreases as the LED junction temperature increases [91]-[93]. Then, the maximum luminous light output of the LED occurs at an operating power lower than the rated LED power [94]. It is pointed out that the quantum efficiency and the junction thermal resistance of the LED are the two limiting factors in LED technology [95]. The luminous efficacy of LEDs typically decreases from about 0.2 % to 1 % per Celsius degree temperature rise [94, 96]. Some LED technology research works reports the relationship of LED efficacy degradation and the junction temperature of the LED [91, 92, 93, 96, 97]. Due to the LED aging effect, the LED luminous efficacy degradation is higher, and the LED light output can drop up to a further 45% [98]. The LED thermal problem is tackled in [99][100]. The luminous efficacy drop due to thermal problem and which results in the luminous output reduction of the LED is addressed in [101].

The photometrical parameters such as luminous flux and luminous efficacy, the electrical parameters such as electrical power, LED current and voltage, and the thermal parameters such as junction and heatsink temperature and the thermal resistance are tied together. The luminous output and thermal relationship is studied in [96][97]. The non-linear thermal behavior of the junction to case thermal resistance of the LED with respect to the electrical power consumption is found in [102]. The junction to case thermal resistance of the LED could be affected by mounting and cooling methods, the size and orientation of the heatsink. Thus, the analysis of the junction thermal resistance and thermal management are studied in [102]-[108]. Some techniques to control the luminous output of LED systems are proposed in [109][110]. An LED model is proposed to model the thermal junction resistance and the light output in [111]. But, the model fits for the LED itself, and not for the LED system, which includes the thermal design of the heatsink and the electrical power control.

This work proposed a general theory that ties the photometrical, electrical and thermal parameters of the LED system. It is based on a thermal model of the LED and heatsink. The model meets the optimal operating point at maximum luminous output and provides the design parameters to obtain an optimal thermal design.

General photo-electro-thermal theory

The total luminous flux ϕ_v of a LED system, which consists of N number of LEDs is in accordance with (3.17).

$$\phi_v = NEP_d \tag{3.17}$$

Where: E is the luminous efficacy and P_d is the real LED power.

The luminous efficacy E of the LED decreases as the LED junction temperature increases.

$$E = E_0\left[1 + k_e\left(T_j - T_o\right)\right] \tag{3.18}$$

Where: E_0 is the rated efficacy at a rated temperature T_o, k_e is the relative rate of efficacy reduction due to the temperature rise.

The LED electrical power is defined as $P_d = V_d I_d$. But, a part of the LED electrical power is dissipated as heat. Then:

$$P_{heat} = k_h P_d = k_h V_d I_d \tag{3.19}$$

Where: V_d is the LED voltage, I_d is the LED current and k_h is a constant lower than 1 and it stands for the LED power that turns into heat. The measurement approach to obtain k_h is found in [112].

The thermal model under steady state conditions is shown in Fig. 3.22. The R_{jc} is the LED junction to case thermal resistance, the R_{hs} is the heatsink thermal resistance and the heatsink temperature T_{hs}. In practice, a heatsink compound is used between the LED and the heatsink to ensure a good thermal dissipation. The thermal resistance of the thermal conductor is relatively small in comparison with the LED junction to case thermal resistance R_{jc} so that it is neglected from the LED system analysis.

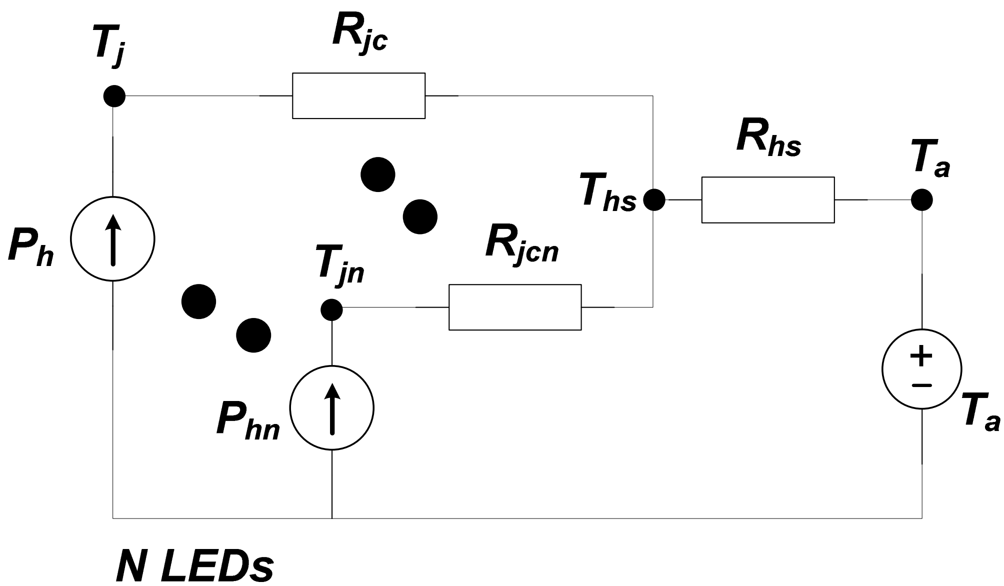

Fig. 3.22. Steady state thermal equivalent circuit of the LED system.

The steady state heatsink temperature is shown below:

$$T_{hs} = T_a + R_{hs}(N k_h P_d) \tag{3.20}$$

Then, the LED junction temperature is illustrated in (3.21).

$$T_j = T_a + \left(R_{jc} + N R_{hs}\right) k_h P_d \tag{3.21}$$

Hence, the total luminous flux can be expressed as follows:

$$\phi_v = N E_0 \left\{ [1 + k_e (T_a - T_o)] P_d + k_e k_h \left(R_{jc} + N R_{hs}\right) {P_d}^2 \right\} \tag{3.22}$$

From (3.22), the luminous flux ϕ_v is related to the electrical power P_d of the LED, the thermal resistance of the heatsink R_{hs} and the junction to case thermal resistance R_{jc}. Then, the photometrical, electrical, and thermal parameters of the LED system are integrated.

Owing to the fact that k_e is negative and lower than unity, (3.22) is in the form of $\phi_v = \alpha_1 P_d - \alpha_2 {P_d}^2$ where α_1 and α_2 are positive coefficients. Then, as P_d increases near zero, the luminous flux ϕ_v increases linearly owing to the second term $\alpha_2 {P_d}^2$ is negligible at P_d small. Then, as P_d increases, the second negative term will lower the luminous flux ϕ_v in a significant way. The luminous flux will drop faster after reaching its maximum point of luminous flux due to P_d and R_{jc} increases. Then, the parabola of the luminous flux is not symmetrical and the maximum point can be obtained from $\frac{d\phi_v}{dP_d} = 0$. In [102], it is shown that k_h will be reduced slightly under dimming conditions. In addition, the degradation of LED efficacy with junction temperature rise is assumed to be linear, thereby k_e is assumed to be constant [94].

By differentiating (3.22) with respect to P_d and by assuming that k_e, k_h and R_{jc} are constant, and then isolating for the LED power at which the luminous flux is maximum, (3.23) is obtained.

$$P_d = -\frac{[1 + k_e(T_a - T_o)]}{2k_e k_h \left(R_{jc} + NR_{hs}\right)} \qquad (3.23)$$

The LED power P_d at which the luminous flux is maximum could be lower if $\left(R_{jc} + NR_{hs}\right)$ is increased. So that, it is possible that P_d could be presented at a lower power level instead of the rated power of the LED. Then, it is possible that the LED power P_d could be at a higher level if a larger heatsink with a lower thermal resistance R_{hs} is used.

The effects of the junction to case thermal resistance R_{jc} of the LED are related to (3.22), because of R_{jc} increases as the P_d increases, leading to a reduction of the luminous flux ϕ_v. It is noticeable when P_d exceeds the rated LED power, which results in a slightly asymmetric parabolic luminous flux function. The general theory is able to manipulate the nonlinear junction to case thermal resistance R_{jc}. R_{jc} is a complex and nonlinear function of the LED heat dissipation P_{heat} and the thermal design of the mounting structure. Then, a theoretical simplified linear function is shown:

$$R_{jc} = R_{jco}(1 + k_{jc}P_d) \tag{3.24}$$

Where R_{jco} is the rated junction to case thermal resistance at 25°C and k_{jc} is a positive coefficient. Hence, by combining (3.22) and (3.24), the luminous flux expression that takes into consideration the temperature-dependent R_{jc} is illustrated below.

$$\phi_v = NE_0\{[1 + k_e(T_a - T_o)]P_d + k_e k_h(R_{jco} + NR_{hs})P_d{}^2 + [k_e k_h k_{jc} R_{jco}]P_d{}^3\} \tag{3.25}$$

Optimal design procedure of LED systems

The luminous flux and luminous efficacy of the OLED obtained at any operating conditions can be analyzed against the theoretical R_{hs}=0°C/W by using Fig. 3.23 as follows [113]. As the cooling effect increases, that is, the R_{hs} is decreased, P_d increases, that is, from A to D points. A large positive slope of $\frac{d\phi_v}{dP_d}$ stands for that a small increase of P_d leads to a large increase of ϕ_v. Then, the initial linear part of the $\frac{d\phi_v}{dP_d}$ curve presents a good efficacy. On the other hand, as P_d moves to around the LED rated power, the slope is zero or small. So that, a large increase of P_d leads to a small increase of ϕ_v. The LED power must not exceed the LED rated power in order to not reduce the LED lifespan. Hence, the intersection points of the curves against the LED rated power indicates how the luminous flux is upgraded. If the thermal design allows, the LED system should be designed in such a way that the maximum ϕ_v is reached at a higher LED power than the LED rated power and the intersection point of ϕ_v-P_d curve against the LED rated power achieves a value between 80% or 96% of the maximum ϕ_v. At this point, the LED rated power must be chosen as the LED operating power.

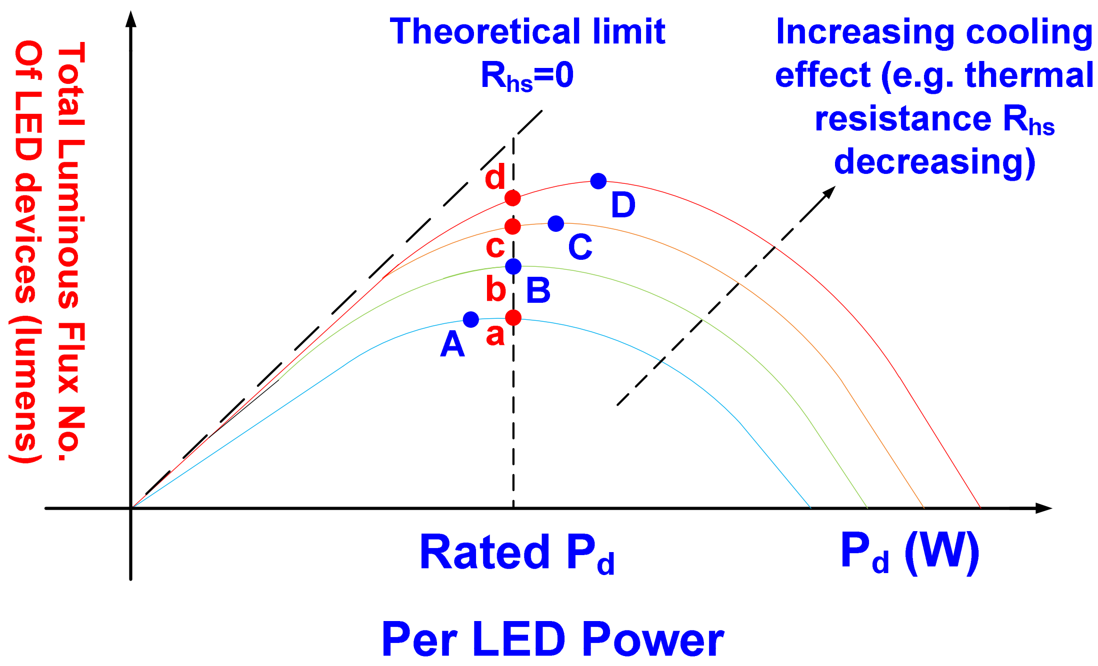

Fig. 3.23. Impact of cooling effects on the luminous flux.

3.1.6. Characterization, modeling and analysis of OLEDs with different structures

OLEDs of different structures can be characterized and modeled by using the PET theory and the SPD (spectral power distribution) modeling [114]. The operating temperature variation of the OLED leads to a non-uniform depreciation of its light output, which increases the luminance non-uniformity over time and degrades the lifespan of the OLED. The optical measurement technique in order to determine the spatial temperature distribution in the organic layers of the OLED is studied in [115]. Based on the electrical-thermal interaction of the OLED modeling, an accurate prediction of the operating characteristics of the OLED can be achieved [68]. The framework of the PET theory and SPD modeling describes the photometrical, electrical, thermal, and chromatic characteristics of the OLED system. The framework-based OLED model can be used to evaluate and optimize the OLED system [90][116].

Characterization and PET modeling of the OLED

An Orbeos CMW-031 is characterized and modeled. It is important to mention that the organic layers must be protected from the air due to they are sensible to moisture and oxygen. The optical measurement is performed under steady state thermal and electrical conditions with the help of a PMS-50 spectro-photocolorimeter and an integrating sphere at 20°C ambient temperature. The voltage changes of the OLED during the heating period are captured by a transient thermal tester (T3ster).

On the other hand, the temperature-dependent optical power and the wall-plug efficiency of the OLED are measured by the TeraLED system. In the case of the voltage-temperature sensitivity calibration, a current of 0.005A is set in the temperature-controlled oven at different ambient temperatures and under pulsed-current source of a small duty cycle. The junction temperature of the OLED is obtained by the voltage response curve and the voltage-temperature sensitivity calibration. Then, the luminance and temperature distribution of the OLED under different current magnitudes are captured by the LUMICAM 1300 imaging photometer-colorimeter and LWIR camera. The experimental measurements are performed under the setup illustrated in Fig. 3.24.

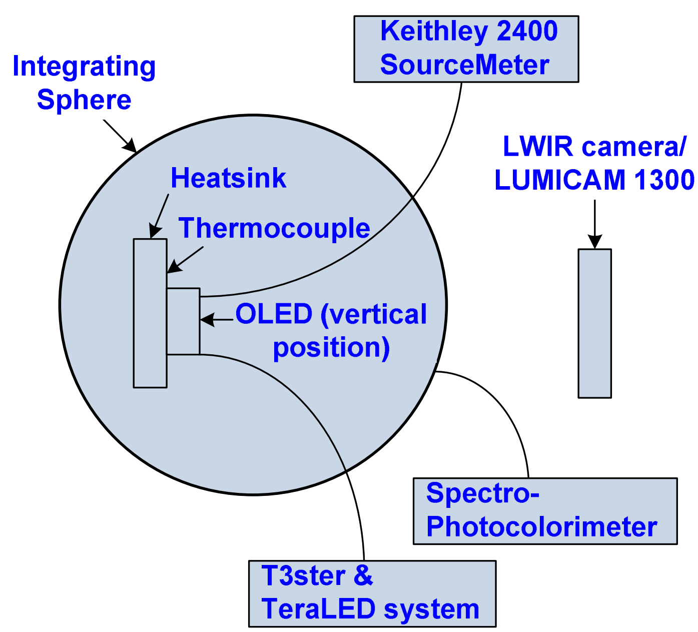

Fig. 3.24. Experimental measurement setup of the OLED.

Rate of reduction of luminous efficacy with junction temperature of the OLED

The luminous intensity I_L of OLEDs is given by (3.26), which is described as the amount of light power dependent of the junction temperature [117].

$$I_L = I_{L|25°C} exp \frac{-(T_j - 25°C)}{T_1} \tag{3.26}$$

Where T_1 and T_j are the characteristic and junction temperatures of the OLED respectively. A high characteristic temperature leads to a less temperature-dependent luminous flux. Thus, the luminous efficacy E is:

$$E = E_{|25°C} exp \frac{-(T_j - 25°C)}{T_1} \tag{3.27}$$

The luminous flux ϕ_v is:

$$\phi_v = P_d E \tag{3.28}$$

Where P_d is the electrical power.

The temperature coefficient k_e is the reverse of the characteristic temperature as illustrated below [112]:

$$k_e = -\frac{1}{T_1} \tag{3.29}$$

As a remark, the OLEDs usually obtained lower luminous efficacy in comparison with the LEDs, but OLEDs of large surface area can perform under more stable luminous efficacy because k_e is smaller. Thus, a small k_e can reduce the dependency of the characteristic temperature from the junction temperature. Therefore, the OLED is less sensitive than the LED under operating temperature changes.

Heat dissipation coefficient

The input electrical power of the OLED is not completely turned into light due to a generated internal heat in the chip [118][119]. Hence, the input electrical power of the OLED is converted into optical power and heat dissipation power. Thereby, the heat dissipation coefficient k_h stands for the LED power that is dissipated as heat. The wall-plug efficiency of the OLED is decreased linearly as the junction temperature increases and the wall-plug efficiency of the OLED is decreased in a parabolic manner as the electrical power increases. Then, k_h is a two-dimensional function of electrical power and temperature.

$$k_h = 1 - \frac{P_{opt}}{P_d} = 1 - \frac{(\sigma T_{hs} + \tau)\left(\chi {P_d}^2 + \delta P_d + \gamma\right)}{\mu} \tag{3.30}$$

Where P_{opt} is the optical power, T_{hs} is the heatsink temperature and σ, τ, χ, δ, γ and μ are constant coefficients, which are dependent on the thermal-optical-electrical characteristics of the OLED. The measured heat dissipation coefficients of the OLEDs LTS-10015 and CMW-031 and LEDs GW5BWF15L00 and XREWHTL1-0000-00C01 are illustrated in Table 3.5. As observed, the variation range of k_h is narrower in OLEDs than LEDs and the heat dissipation coefficients are higher in OLEDs than in LEDs.

Table 3.5. Heat dissipation coefficients comparison.

Heat dissipation coefficient	**OLED LTS-10015**	**OLED CMW-031**	**LED GW5BWF15L00**	**LED XREWHTL1-0000-00C01**
k_h	0.905-0.937	0.959-0.987	0.72-0.86	0.67-0.84

Thermal resistance

The OLED produces over the 90% of its power as a heat. The convection and radiation thermal resistances are quite dependent on the outer area of the OLED surface. Due to low thermal conductivity of the organic materials, it is necessary a substrate to upgrade the heat transfer of the OLED. In OLEDs, there are two heat dissipation paths. One is downward through the organic layers and the substrate and the other is upward through the encapsulant and package surface. So that, the junction to case thermal resistance R_{jc_OLED} of the OLED is expressed as follows [120]:

$$R_{jc\_OLED} = \frac{\left(T_j - T_a\right)}{\left(P_d - P_{opt}\right)} \tag{3.31}$$

The measured thermal resistances of the OLEDs LTS-10015 and CMW-031 and LEDs GW5BWF15L00 and XREWHTL1-0000-00C01 are shown in Table 3.6. In addition, the measured thermal resistances of the OLEDs LTS-10015 and CMW-031 are shown in Fig. 3.25(a) and Fig. 3.25(b) respectively. On one hand, the thermal resistance of the metal substrate of the LTS-10015 is 0.34°C/W, which is the 58% of the total thermal resistance of the OLED. On the other hand, the thermal resistance of the glass substrate of the CMW-031 is 2.6°C/W, which is the 81% of the total thermal resistance of the OLED.

Table 3.6. Thermal resistance comparison.

Thermal resistance	**OLED LTS-10015**	**OLED CMW-031**	**LED GW5BWF15L00**	**LED XREWHTL1-0000-00C01**
R_{jc}	0.59°C/W	3.1°C/W	6°C/W	12°C/W

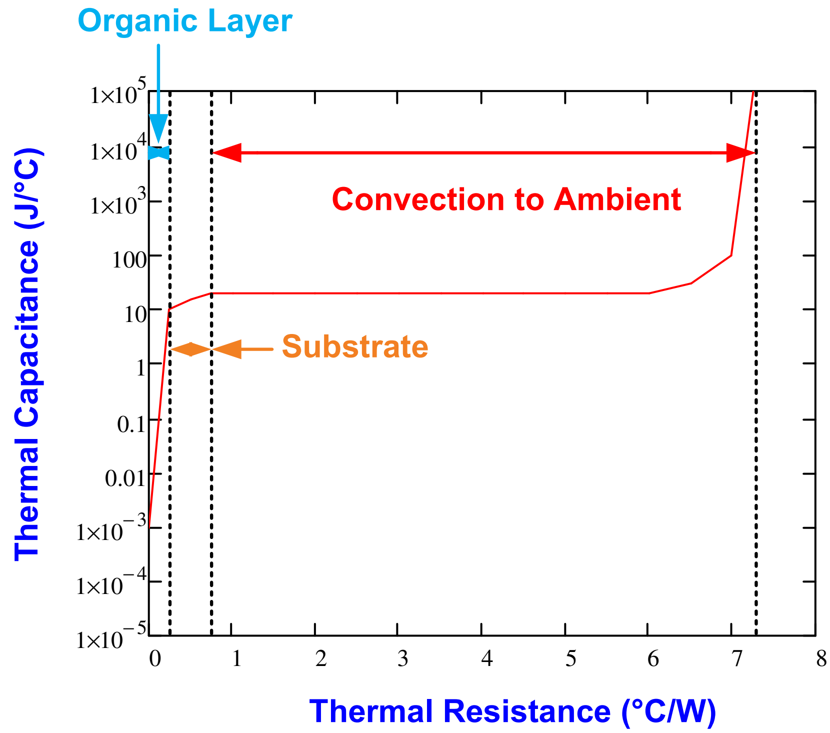

a)

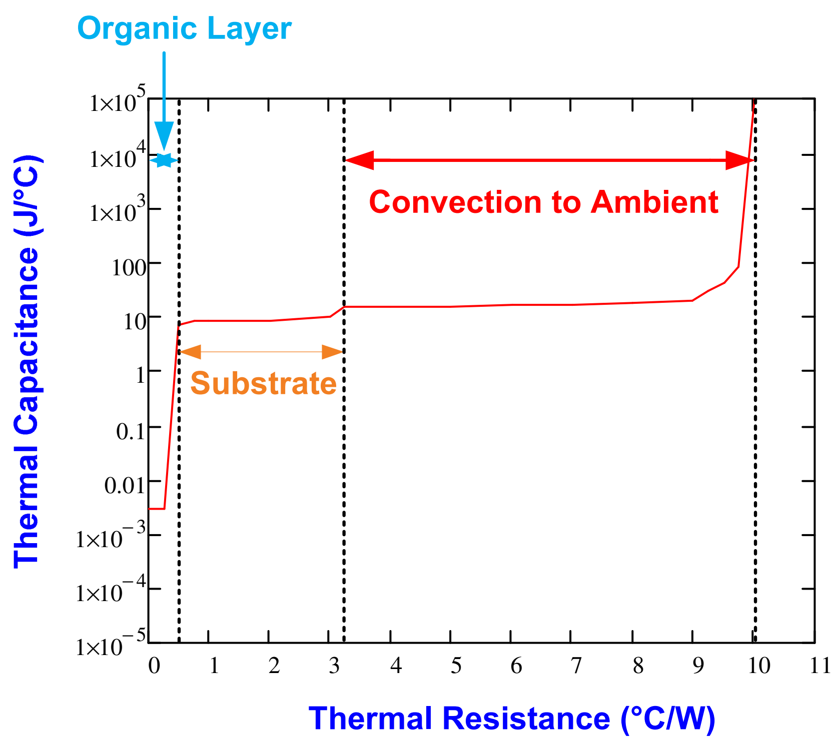

b)

Fig. 3.25. Experimental OLED thermal resistance R_{jc}: a) LTS-10015 and b) CMW-031.

Luminous flux

The total luminous flux can be calculated as the asymmetric convex parabolic curve $\phi_v = \alpha_1 P_d - \alpha_2 {P_d}^2 - \alpha_3 {P_d}^3$, where α_1, α_2 and α_3 are positive coefficients and P_d is the OLED power. Owing to the operating range of the OLED lies on the left side from the peak of this parabolic curve and α_3 is much smaller than α_1 and α_2 and affects on the right side from the peak of the parabolic curve, $\alpha_3 {P_d}^3$ can be neglected.

$$\phi_v = NE_0\{[1 + k_e(T_a - T_o)]P_d + k_e k_h(R_{jc} + NR_{hs}){P_d}^2\} \tag{3.32}$$

The measured and calculated total luminous flux under different electrical powers of the OLEDs LTS-10015 and CMW-031 presented a maximum error of 12.8%. Owing to R_{jc} and k_e of the OLEDs are small in value, the luminous flux and OLED power relationship tends to be more linear than that of the LED.

Spectral power distribution

The chromatic aspects of OLEDs can be explained by using the SPD (spectral power distribution). The SPD of the OLED is achieved based on a multi-SPD model presented in [121]. The peak wavelength λ_{peak} and the full width at the half maximum (FWHM) $\Delta\lambda$ of the multi-SPD under temperature effects are shown below:

$$\lambda_{peak,m}(T_j) = k_{peak,m}(T_j - T_o) + \lambda_{peak,m,r} \tag{3.33}$$

$$\Delta\lambda_m(T_j) = k_{\Delta\lambda,m}(T_j - T_o) + \Delta\lambda_{m,r} \tag{3.34}$$

Where $\lambda_{peak,m}$ is the peak wavelength, $k_{peak,m}$ is the temperature coefficient of the peak wavelength, $\lambda_{peak,m,r}$ is the reference peak wavelength, $\Delta\lambda_m$ is the FWHM, $k_{\Delta\lambda,m}$ is the temperature coefficient of the FWHM and $\Delta\lambda_{m,r}$ is the reference FWHM of the multi-SPD. T_o is the reference ambient temperature. Moreover, the optical power $P_{opt,m}$ is defined by (3.35), which is temperature and electrical power dependent.

$$P_{opt,m}(T_j, P_d) = (\alpha_m T_j + \beta_m)(\chi_m P_d + \gamma_m) \tag{3.35}$$

Where α_m, β_m, χ_m and γ_m are the temperature and electrical power coefficients of the optical power of the muti-SPD.

The calculated and measured values of the CCT (correlated color temperature) of the OLEDs LTS-10015 and CMW-031 obtained in this work presented an absolute error of less than 100 K. So that, the results confirms the accuracy of the methodology of the multi-SPD model to obtain the OLED color characteristics.

Luminance distribution and uniformity

The luminance of the OLED depends on the voltage drop across the organic materials and it can be inhomogeneous due to the conductivity of the electrode material and the size of the pixel [122]. The luminance uniformity U of the OLED can be calculated by (3.36) and (3.37):

$$U = 1 - \frac{\sum_{m=1}^{n} L_1 exp\left(\frac{mD}{n(aI^2+bI+c)}\right) - nL_1}{\sum_{m=1}^{n} L_1 exp\left(\frac{mD}{n(aI^2+bI+c)}\right)} \; if \; D \geq D_s \tag{3.36}$$

$$U = 1 - \frac{\sum_{m=1}^{n} L_1 exp\left(\frac{mD}{n(aI^2+bI+c)}\right) - nL_1 exp\left(\frac{D}{D_s}\right)}{\sum_{m=1}^{n} L_1 exp\left(\frac{mD}{n(aI^2+bI+c)}\right)} \; if \; D < D_s \tag{3.37}$$

Where L_1 is the initial luminance and n is the division number across the target length D, D_s is the current spreading length and a, b and c are constants obtained from the current spreading length curve by applying a curve-fitting method to it.

The calculated and experimental luminance distributions of the OLEDs LTS-10015 and CMW-031 are reported in this work, where the luminance intensities of both OLEDs are increased as the injection current increases, but the luminance uniformities are lowered as the as the current increases. The LTS-10015 OLED achieves a better luminous uniformity than the CMW-031 because of a larger current spreading length.

3.1.7. Scale-photo-electro-thermal model for OLEDs

A good understanding of the scale, photometrical, electrical, and thermal domains of the OLEDs leads to carry out a good design of the lighting design system. The model proposed is based on an equivalent electrical circuit that link together the electrical, photometrical and thermal domains of the OLED and it is easy to be implemented in a computer-based simulator [123]. The results will show how the scale factor influences on the heat transfer mechanism and the temperature on the electrical ad photometrical performance respectively.

OLED scale-photo-electro-thermal model

The proposed SPET (scale-photometrical-electrical-thermal) model for OLEDs is shown in Fig. 3.26, which consists of voltage and current dependent sources and passive elements. The OLED SPET model interactions are physically explained by the cause and effect principle in [124], which the cause is the electrical domain and the effect is the photometrical domain, but the scale-thermal domain makes an opposition to the effect. The electrical model illustrated in Fig. 3.26(a) is formed by the dynamic series resistor R_s, the electrode resistance R_e, the leakage resistance R_p, the capacitor C, the ideal diode D and the threshold voltage V_o. In steady state, on one hand, when the forward voltage is lower than V_o, the current flows through the electrode resistance R_e and the leakage resistance R_p. On the other hand, when the forward voltage is higher than V_o, the current flows through the electrode resistance R_e and the series resistance R_s. The characterization methodology of the electrical model is not tackled in this section, owing to it is performed in section 3.1.3.

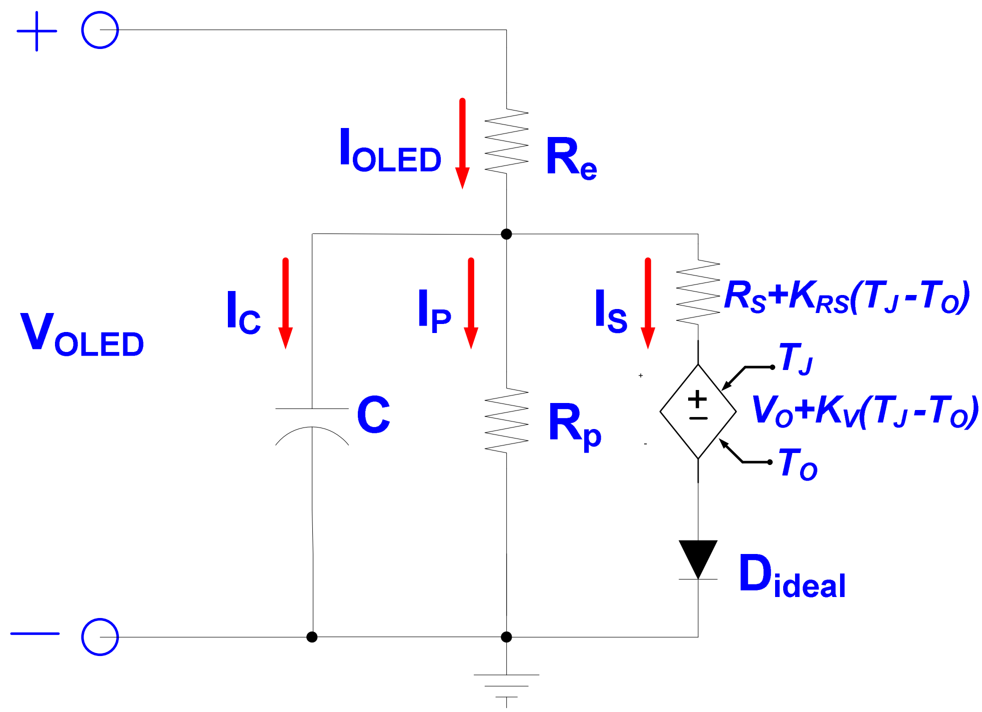

+
IOLED
Re
VOLED
IC
IP
IS
RS+KRS(TJ-TO)
TJ
VO+KV(TJ-TO)
TO
C
Rp
Dideal
—

a)

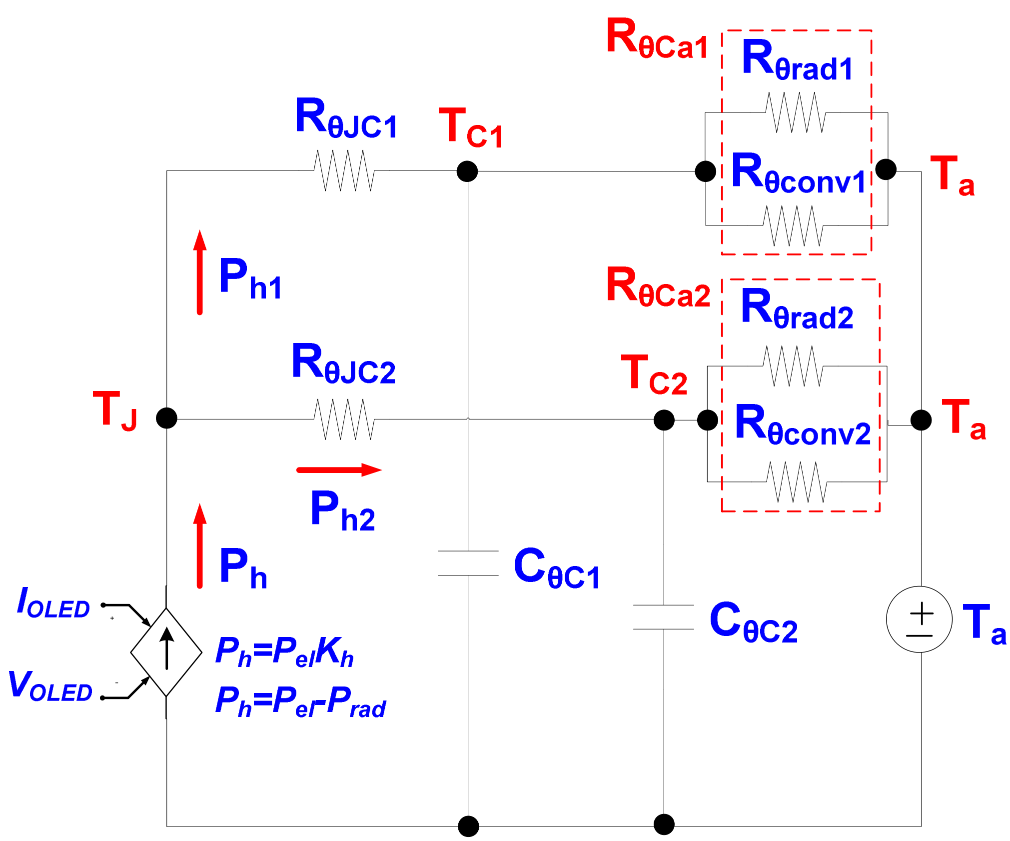

RθCa1
Rθrad1
RθJC1
TC1
Rθconv1
Ta
Ph1
RθCa2
Rθrad2
RθJC2
TC2
TJ
Rθconv2
Ta
Ph2
Ph
CθC1
IOLED
CθC2
Ta
Ph=PelKh
VOLED
Ph=Pel-Prad

b)

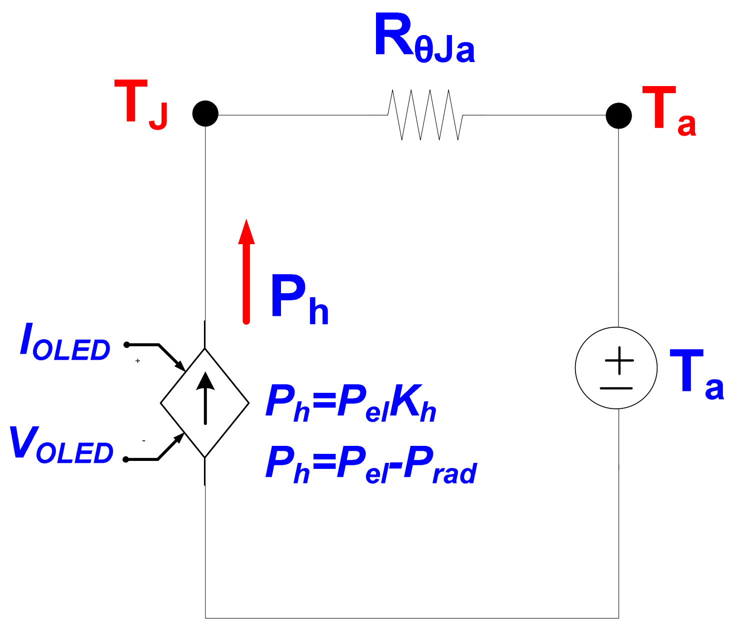

c)

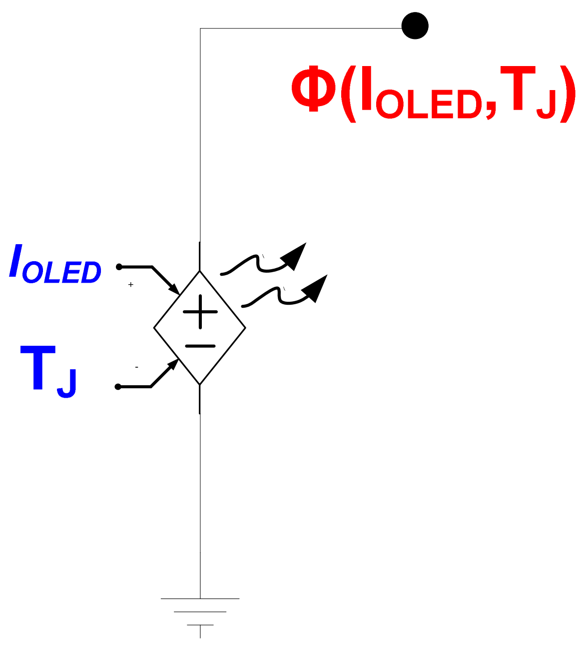

d)

Fig. 3.26. OLED SPET model: a) electrical model and b) scale-thermal model, c) equivalent scale-thermal model and d) photometrical model.

Scale-thermal characterization

The heating process in OLEDs is due to the joule effect and non-radiative recombination. The OLED operating temperature depends on its self-heating due to the power dissipation turned into heat. The power density of the OLEDs is much lower than that of the LED. Thereby, a large area reduces the power density, but improves the thermal exchange from the OLED to the ambient by means of convection and radiation. The purpose of scale-thermal characterization is to investigate the thermal radiation, convection and conduction in OLEDs. A simplified thermal structure of the OLED is illustrated in Fig. 3.27. R_{θ} resistances are the OLED material thermal resistances, $R_{\theta jc}$ is the OLED thermal conduction resistance, $R_{\theta rad}$ is the OLED thermal radiation resistance and $R_{\theta conv}$ is the OLED thermal convection resistance. Then, the OLED thermal radiation resistance, $R_{\theta rad}$ is calculated [125].

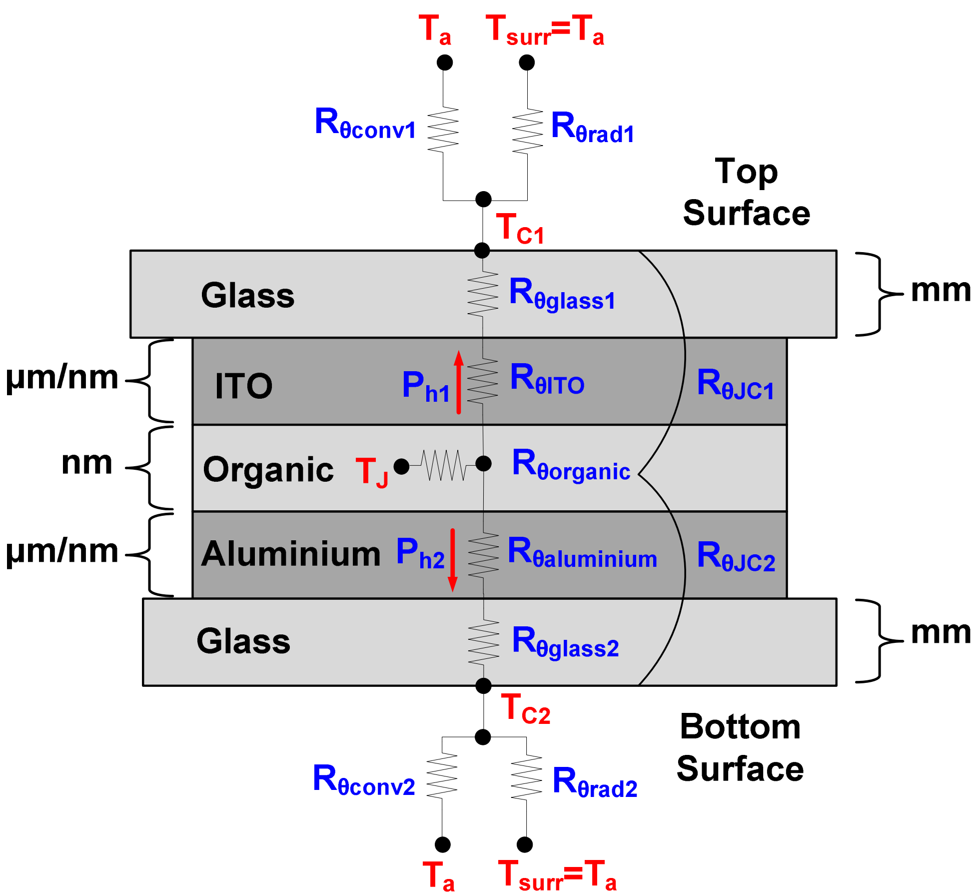

Fig. 3.27. OLED thermal scheme.

$$R_{\theta rad} = \frac{1}{4\varepsilon\sigma {T_a}^3 A_{OLED}} \tag{3.38}$$

Where ε is the OLED surface emissivity, σ is the Steffen-Boltzmann constant, T_a is the ambient temperature and A_{OLED} is the total area of the OLED surface. The heat transfer by natural convection, that is, no forced air is used as those fans is reported in the literature, but assuming a uniform temperature along the OLED panel [125][126]. So that, the OLED thermal convection resistance $R_{\theta conv}$ is calculated as shown below.

$$R_{\theta conv} = \frac{L_c}{k_{air} N_u A_{OLED}} \tag{3.39}$$

Where L_c is the critical size, which is in function of the OLED orientation, k_{air} is the convective heat transfer coefficient and N_u is the Nusselt number. Note, when the OLED is vertical oriented, L_c is equal to the OLED height. On the other hand, when it is horizontal oriented, $L_c = A_{OLED}/p$ where p is the OLED perimeter.

As it is shown in Fig. 3.27, there are 2 thermal dissipation paths, where heat power P_{h1} flows to the lighting surface (ITO side) and P_{h2} flows to the back surface (aluminium side). The heat transfer coefficient by conduction h_{cond} is directly dependent on the thermal conductivity $k_{material}$ and thickness $t_{material}$ of each material used in the thermal dissipation path [127][128]. The thickness of the organic layers and electrodes is lower than that of the glass substrate t_{glass} so that the thermal resistances of the electrodes are neglected. Then, the junction to case thermal resistances $R_{\theta jc1}$ and $R_{\theta jc2}$ are determined.

$$R_{\theta jc\_i} = \frac{t_{glass}}{k_{glass} A_{OLED}} \tag{3.40}$$

Where i is the sub-index that denotes the OLED thermal dissipation path: 1 to the lighting surface and 2 to the back surface. The case to ambient thermal resistance $R_{\theta ca}$ is as shown in

(3.41). The $R_{\theta rad}$ is much higher than $R_{\theta conv}$ in OLEDs, which leads to a thermal exchange mechanism mostly by convection.

$$R_{\theta ca\_i} = \frac{R_{\theta conv\_i} R_{\theta rad\_i}}{R_{\theta conv\_i} + R_{\theta rad\_i}} \tag{3.41}$$

By applying Thévenin analysis to the circuit illustrated in Fig. 3.27(b), the equivalent scale-thermal model that consists of a junction to ambient thermal resistance $R_{\theta ja}$ is found, as shown in (3.42).

$$R_{\theta ja} = \frac{\left(R_{\theta jc1} + R_{\theta ca1}\right)\left(R_{\theta jc2} + R_{\theta ca2}\right)}{\left(R_{\theta jc1} + R_{\theta ca1}\right) + \left(R_{\theta jc2} + R_{\theta ca2}\right)} \tag{3.42}$$

The junction temperature T_j, which considers both thermal dissipation paths and OLED orientations is illustrated.

$$T_j = T_a + R_{\theta ja} P_h \tag{3.43}$$

In this way, the heat flow P_h to each side of the OLED by considering steady state thermal behavior is given.

$$P_{h\_i} = \frac{R_{\theta ja\_(3-i)}}{R_{\theta ja1} + R_{\theta ja2}} P_h \tag{3.44}$$

The case temperature T_c of each side of the OLED is calculated by:

$$T_{c\_i} = T_a + R_{\theta ca\_i} P_{h\_i} \tag{3.45}$$

In addition, the thermal capacitance $c_{\theta c}$ must be taken into consideration, because of it represents the OLED capacity of storage heat.

$$c_{\theta c\_i} = c_{glass}\rho_{glass}v_{OLED} \tag{3.46}$$

Where c_{glass} is the glass heat capacity, ρ_{glass} is the glass density and v_{OLED} is the volume of the OLED considering the OLED as a pure glass plate.

Electro-thermal characterization

The electrical properties of OLEDs have a strong dependency on thermal properties. Hence, the two most significant effects on temperature rise are the voltage drop and series resistance reduction [47], [126], [129]. The voltage drop effect occurs due to the energy gap reduction. Then, a lower forward voltage is needed to drive the OLED when temperature increases owing to the energy required for the electron-hole recombination is lower. The rate of voltage drop as a function of temperature rise is denoted by k_v, which is a negative coefficient and measured in $V/°C$. The series resistance reduction occurs due to the electrical conductivity increase of organic materials [71]. So that, a series resistance lowers as the temperature rises due to the hopping process is accelerated [47]. The rate of series resistance drop is given by k_{Rs}, which is a negative coefficient and measured in $\Omega/°C$. The forward voltage as a function of the thermal parameters is calculated.

$$V_f(I_f, T_a) = \frac{V_o + k_v(T_a - T_o) + I_f[R_e + R_s + k_{Rs}(T_a - T_o)]}{1 - I_f\left[\left(k_v k_h R_{\theta ja}\right) - \left(I_f k_{Rs} k_h R_{\theta ja}\right)\right]} \tag{3.47}$$

Where T_o is the reference junction temperature, I_f is the forward current and k_h is the power heat coefficient.

Scale-photo-electro-thermal characterization

The scale factor is directly related with temperature rise in OLEDs in the SSL (solid state lighting). Therefore, the electrical and thermal interaction in the OLED will result in a photometrical performance of the SSL system. The luminous flux ϕ is junction temperature T_j and forward current I_f dependent and behaves in a quasi-linear form. Hence, the luminous flux ϕ can be calculated by (3.48).

$$\phi(I_f, T_j) = \phi_o\{[1 + k_I(I_f - I_{fo})][1 + k_T(T_j - T_o)]\} \tag{3.48}$$

Where k_I is the rate of the luminous flux variation as a function of forward current, k_T is the negative rate of the luminous flux variation as a function of temperature rise, I_{fo} is the reference forward current and ϕ_o is the nominal luminous flux. Thereby, the SPET integration is achieved in (3.49).

$$\phi(I_f, T_a) = \phi_o\left\{[1 + k_I(I_f - I_{fo})]\left[1 + k_T\left(T_a - T_o + I_f R_{\theta ja} k_h\left(\frac{V_o + k_v(T_a - T_o) + I_f[R_e + R_s + k_{Rs}(T_a - T_o)]}{1 - I_f\left[\left(k_v k_h R_{\theta ja}\right) - \left(I_f k_{Rs} k_h R_{\theta ja}\right)\right]}\right)\right)\right]\right\} \tag{3.49}$$

An OLED Osram orbeos RMW-046 is used to obtain the SPET model parameters reported in this work. The light measurements are achieved by using an integrating sphere at different controlled temperatures at steady state. The electrical performance is obtained by applying a current ramp on the OLED and measuring the OLED voltage under different temperatures. The experimental results are in a good agreement with the calculation results owing to the maximum error in the linear region is 3.34% and in the non-linear region is 13.56%. The calculated and experimental results of the case temperature T_c for vertical and horizontal orientation of the OLED presented a maximum error is 5.63%. As a remark, there is a difference in temperature between horizontal and vertical OLED position. Then, when it is at the horizontal position, the temperature is 6.5°C higher in comparison with the vertical position and at a rated OLED operating current.

The calculated and experimental photometrical results under different forward currents showed that when the OLED is operated at the rated OLED current, the luminous flux ϕ and luminous efficacy intersect one another, which indicates an optimal operating point. This operating point represents a balance system, because of the maximum luminous flux ϕ and luminous efficacy are obtained. The maximum error of luminous flux ϕ and luminous efficacy between calculated and experimental results are 7.05% and 6.8% respectively. In regards to temperature effect on the OLED voltage, it is illustrated in this work that the voltage drop lowers, as the temperature increases. The maximum error between calculated and experimental results of the OLED voltage under temperature exposition is -2.1%.

3.2. FL300 Phillips Lumiblade OLED lamp

The FL300 Phillips Lumiblade OLED lamp is shown in Fig. 3.28. The nominal electrical parameters of the OLED lamp are the following: V_{OLED}= 19.73 V, R_{OLED}= 53.66 Ω, P_{OLED}= 7.26 W and I_{OLED}= 368 mA [31]. The operating DC OLED current I_{OLED} and voltage V_{OLED} curve of the FL300 Phillips Lumiblade OLED lamp under ambient temperature condition is illustrated in Fig. 3.29.

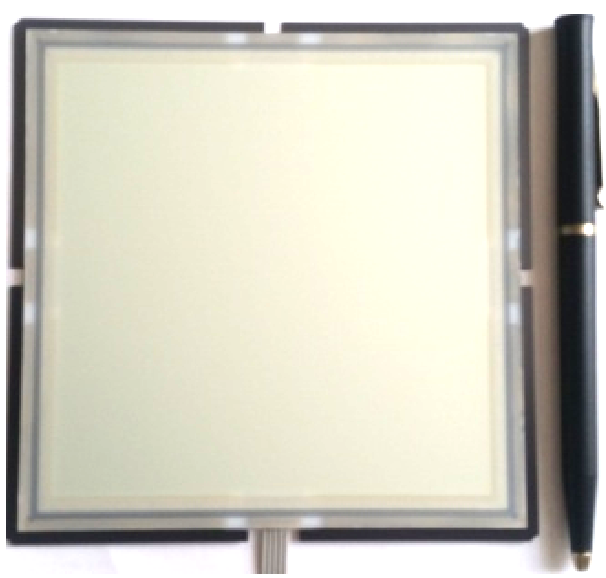

Fig. 3.28. FL300 Phillips Lumiblade OLED lamp.

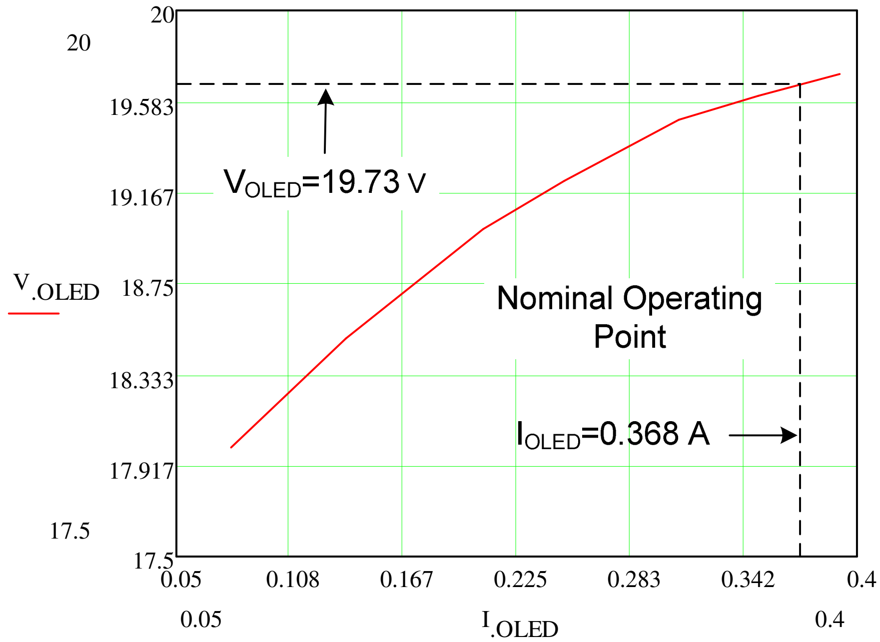

Fig. 3.29. Operating DC I_{OLED} and V_{OLED} curve.

3.3. Analysis and design of the OLED modeling for a FL300 Phillips OLED lamp

A FL300 Phillips OLED lamp is modeled based on the simplified electrical modeling of power LEDs for DC-DC converter analysis and simulation design theory [76], [31]. Because this modeling methodology is simple, sophisticated lab equipment is not required.

The equivalent resistance R_{OLED} of the OLED is expressed in function of the LED power P_{OLED} (3.50) [76].

$$R_{OLED} = f(P_{OLEDx}) = B_1 {P_{OLEDx}}^{B_2} + B_3 \tag{3.50}$$

Steady state experimental analysis of the OLED

The electrical parameters of the OLED under steady state regime are obtained based on Fig. 3.30. The experimental procedure consists of the following steps:

1. Operate the OLED at the nominal operating point during 10 min.
2. Measure the OLED voltage V_{OLED} and OLED current I_{OLED}.
3. Calculate OLED powers P_{OLED} and OLED static DC resistances R_{OLED} for different operating points.

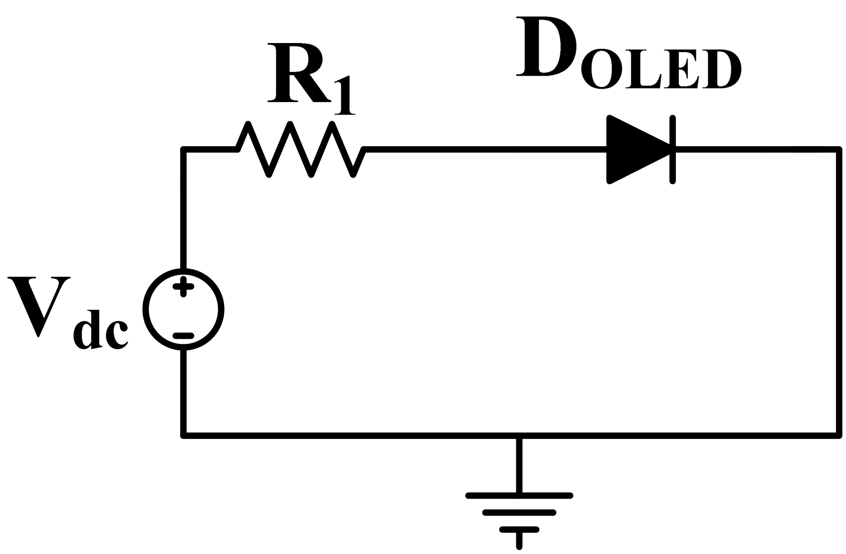

Fig. 3.30. Steady state test circuit.

The nominal parameters of the circuit illustrated in Fig. 3.30 are as follows: V_{DC}= 26.1 V, V_{OLED}= 20.6 V, R_1=15.1 Ω, P_{OLED}= 7.58 W, I_{OLED}= 368 mA [31]. The experimental results under steady state conditions are shown in Table 3.7. The constant unitless values B_1= 322, B_2= -0.8931 and B_3= 2.831 in order to calculate (3.50) are obtained by applying a curve fitting method (non-linear least squares) over the P_{OLED} and R_{OLED} data in Table 3.7. The calculation methodology is achieved by using the curve fitting toolbox of Matlab.

Table 3.7. Steady state experimental measurements.

Sample	V_{OLED} **(V)**	I_{OLED} **(A)**	P_{OLED} **(W)**	R_{OLED} **(Ω)**
1	20.8	0.39	8.112	53.333
2	20.6	0.368	7.5808	55.978
3	20.4	0.335	6.834	60.895
4	20.3	0.305	6.1915	66.557
5	20	0.271	5.42	73.800
6	19.8	0.239	4.7322	82.845
7	19.6	0.208	4.0768	94.231
8	19.4	0.183	3.5502	106.011
9	19.1	0.15	2.865	127.333
10	18.9	0.122	2.3058	154.918
11	18.6	0.091	1.6926	204.396
12	18.2	0.062	1.1284	293.548
13	17.4	0.031	0.5394	561.290

Hence, the calculated and experimental results of the OLED power P_{OLED} and the OLED static resistance R_{OLED} are illustrated in Fig. 3.31(a). As it is shown, the experimental results are in a good agreement with the calculated results. The maximum relative error between calculated and experimental results is 1.6 %. The OLED power P_{OLED} range is from 0.5394 W to 8.112 W and the OLED static resistance range is from 53.33 Ω to 561.29 Ω.

On the other hand, the calculated and experimental results of the OLED voltage V_{OLED} and the OLED current I_{OLED} are shown in Fig. 3.31(b). The OLED voltage V_{OLED} range is from 17.4 V to 20.8 V and the OLED current range is from 0.031 A to 0.39 A.

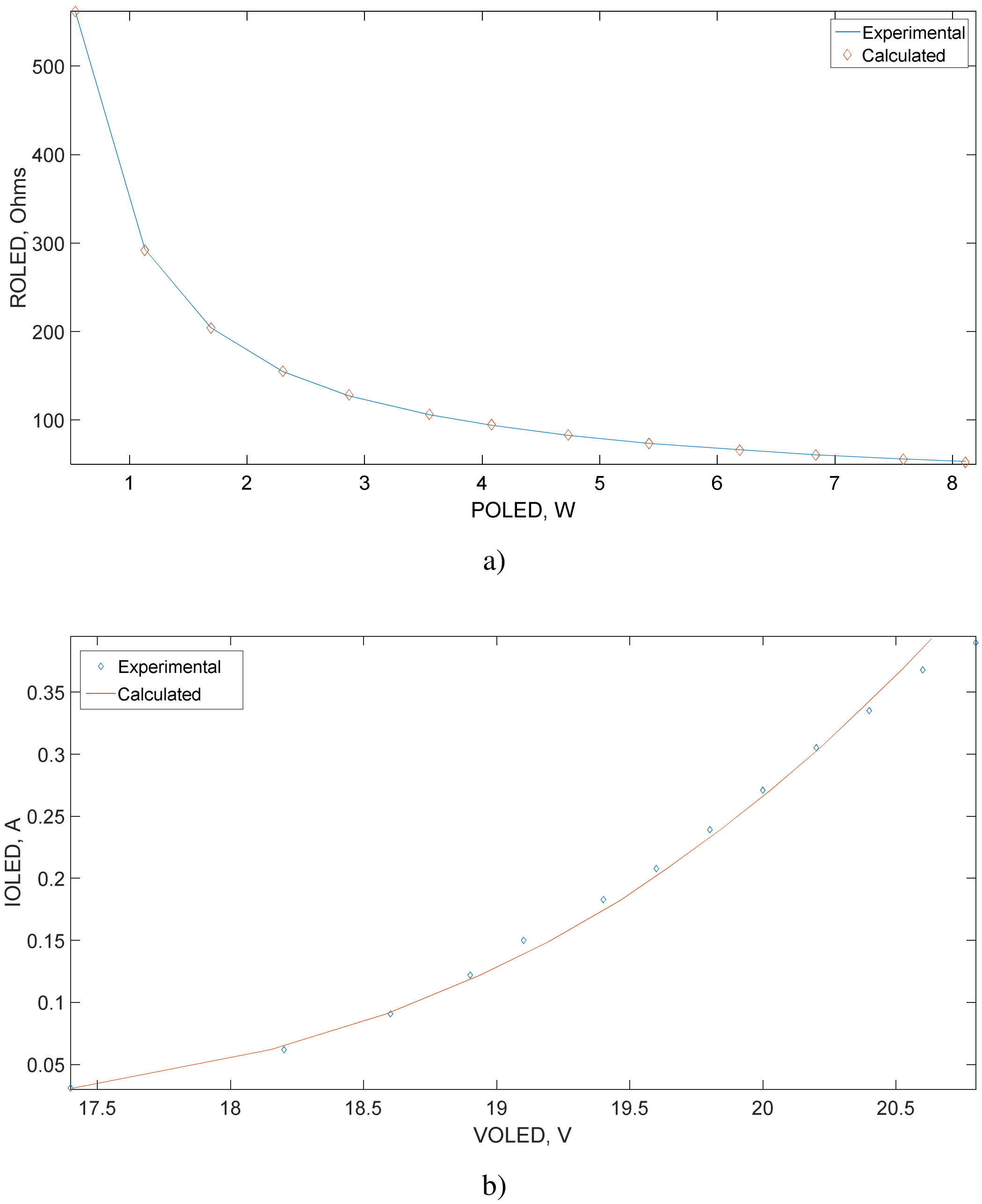

Fig. 3.31. Steady state calculated and experimental results: a) P_{OLED} vs R_{OLED} and b) V_{OLED} vs I_{OLED}. (1W/div), (100 Ω/div), (0.5V/div) and (50mA/div).

Dynamic state experimental analysis of the OLED

The time constant of the OLED can be considered as to that of the discharge lamps, which is addressed in [88][89] and to that of the LED power in [76]. As it was stated in [76], the time constant shows the dynamic response of the OLED and it is measured from the OLED voltage V_{OLED} under an OLED current I_{OLED} step-up. The circuit illustrated in Fig. 3.32 is used to obtain the dynamic response of the OLED under an OLED current I_{OLED} step-up. The parameters of the circuit shown in Fig. 3.32 are the following: V_{DC}= 26V, R_1= 14.9 Ω, R_2= 75 Ω and a N-channel Mosfet PSMN1R2-25YL Q_1 is used to step up and step down the OLED current I_{OLED}.

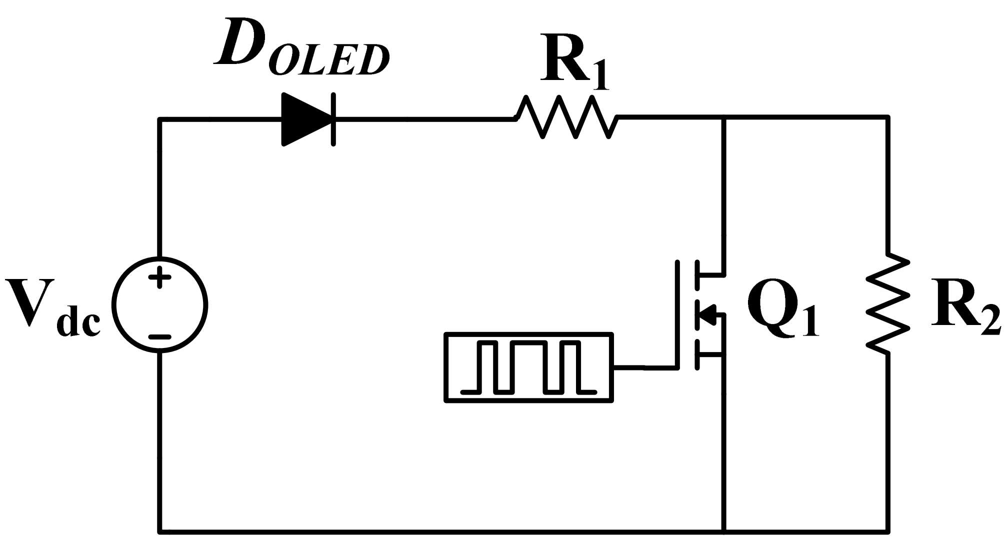

Fig. 3.32. Dynamic state test circuit under an OLED current step-up.

The experimental results of the OLED dynamic response under an OLED current I_{OLED} step-up condition are shown in Fig. 3.33. The time constant is calculated from the initial point when the OLED current I_{OLED} has reached 100% to the final point when the OLED voltage V_{OLED} has reached 63.2% of its final value. This is performing under an OLED current I_{OLED} step-up from 76 mA to 327 mA condition. The time constant obtained is 4.25µs as shown in Fig. 3.33.

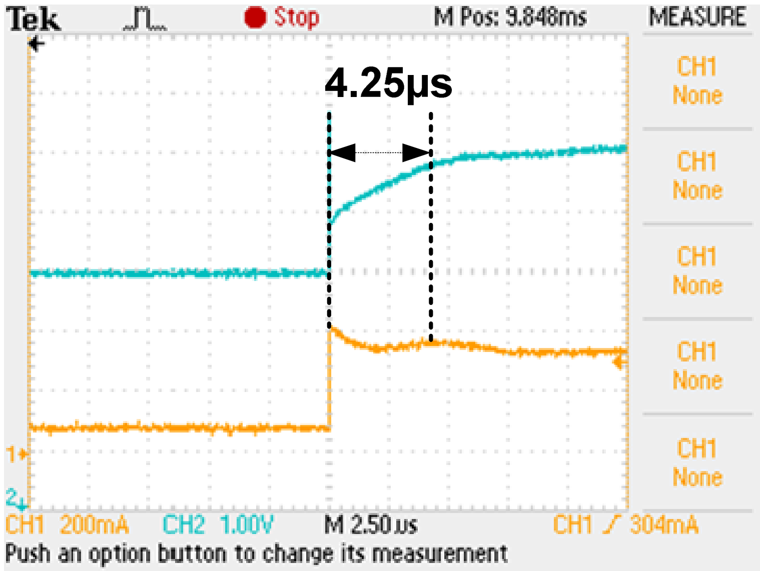

Fig. 3.33. Dynamic response of the OLED under an OLED current step-up. V_{OLED} (1V/div) and I_{OLED} (200 mA/div). (2.5μs).

The circuit shown in Fig. 3.34 is used to obtain the dynamic response of the OLED under an OLED current I_{OLED} switched-off. The parameters of the test circuit are the following: V_{DC}= 21 V, R_1= 14.9 Ω and an N-channel Mosfet PSMN1R2-25YL Q_1. The dynamic response of the OLED under an OLED current I_{OLED} switched-off condition from 121 mA to 0 mA is shown in Fig. 3.35. The time constant obtained is 300μs as shown in Fig. 3.35.

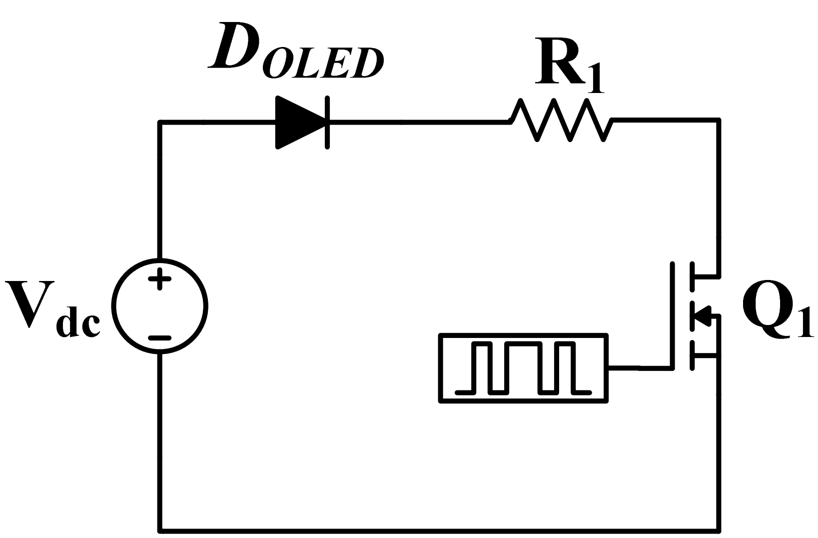

Fig. 3.34. Dynamic state test circuit under an OLED current step-down.

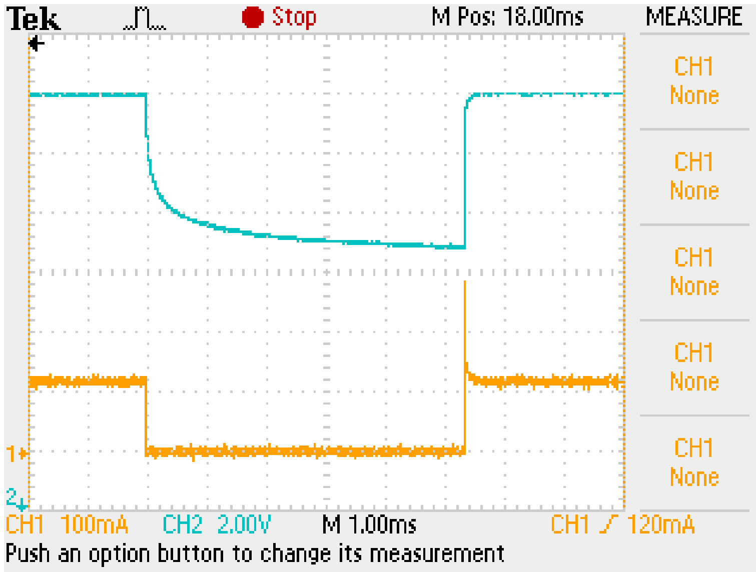

Fig. 3.35. Dynamic response of the OLED under an OLED current switched-off. V_{OLED} (2V/div) and I_{OLED} (100 mA/div). (1ms).

Simulation of the OLED modeling

The Simulink-based OLED model transient simulation circuit is shown in Fig. 3.36. The transient simulation is intended to obtain the dynamic response behavior of the OLED model. The Simulink simulation circuit of the OLED model is based on the technique used in [88][89]. In which, $V_D(t)1$ and $P_D(t)1$ are voltage-controlled sources, $V_D(t)$ and $V_D(t)2$ are voltage sensors, $I_D(t)$ is a current sensor, $P_D(t)$ and $i_D(t) * R_D(t)$ are multipliers, $R_D(t)$ is a function block, R_i is a resistor, C_i is a capacitor that integrate the time constant and the saturation block or resistance limiter, which is set from 0.1 to 10 kΩ. R_{i1} and R_{i2} are limit current resistors, an N-channel Mosfet and the equivalent OLED capacitor C_{i1}, which is assumed in value by means of the heuristic approach. The parameters of the circuit are the following: V_{DC}= 25.2 V, R_1= 14.9 Ω, R_2= 75 Ω and C_{i1}=6μF. The time constant effect is implemented by R_i=1Ω and C_i=4.25μF. The simulation results are shown in Fig. 3.37, which are obtained by applying an OLED current I_{OLED} step-up from 76 mA to 327 mA.

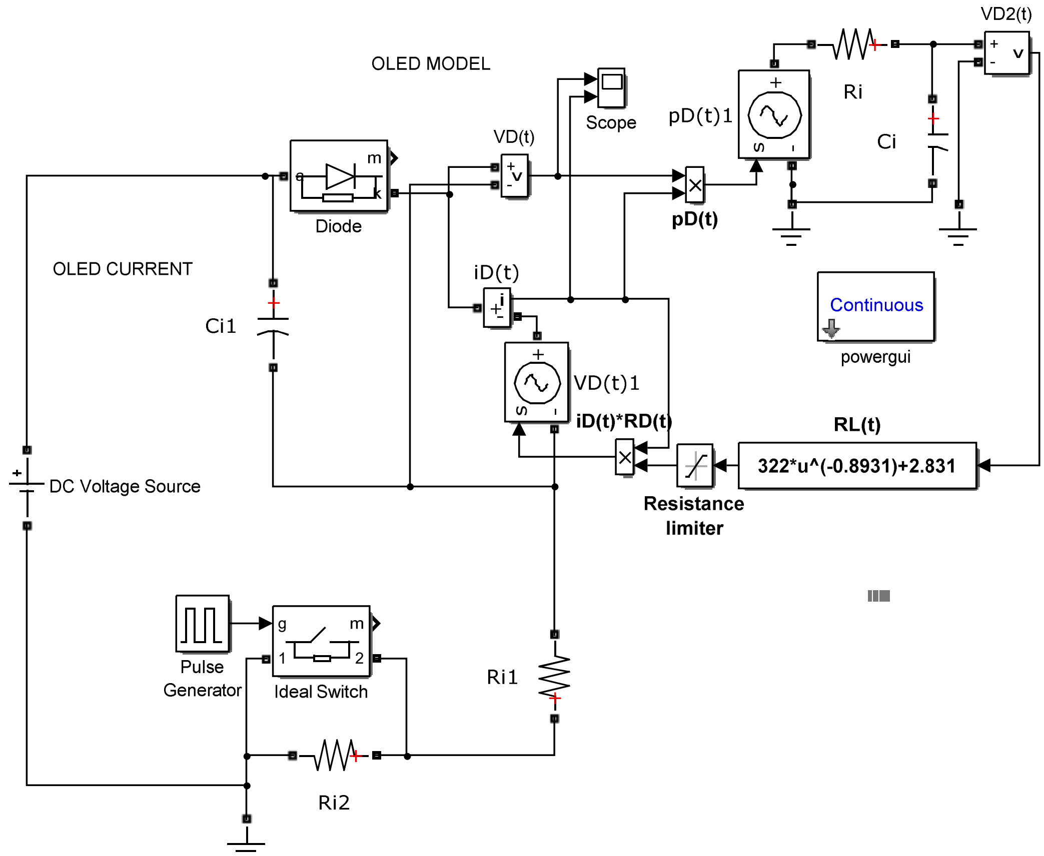

Fig. 3.36. Simulink-based transient simulation circuit.

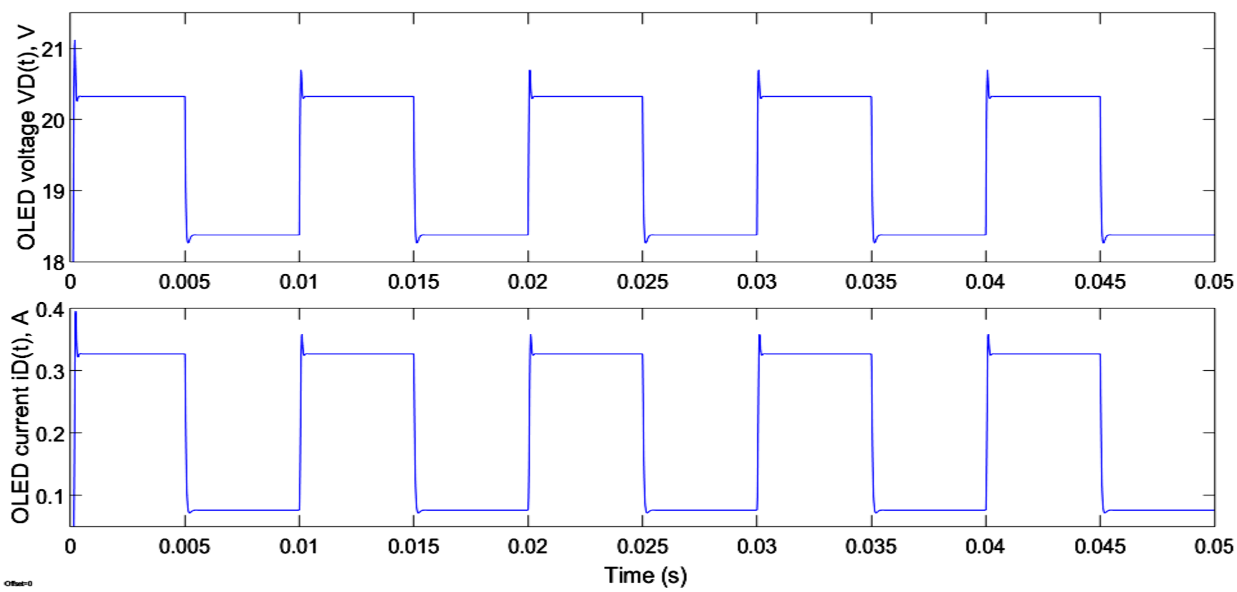

Fig. 3.37. Transient simulation of the OLED model under an OLED current step-up. (0.5V/div), (100 mA/div) and (5 ms/div).

A transient simulation result is illustrated in Fig. 3.38, in which the resistor R_{i2} is removed from the Simulink-based OLED model circuit shown in Fig. 3.36 in order to perform an OLED current I_{OLED} switched-off from 121 mA to 0 mA at input voltage V_{DC}= 21 V.

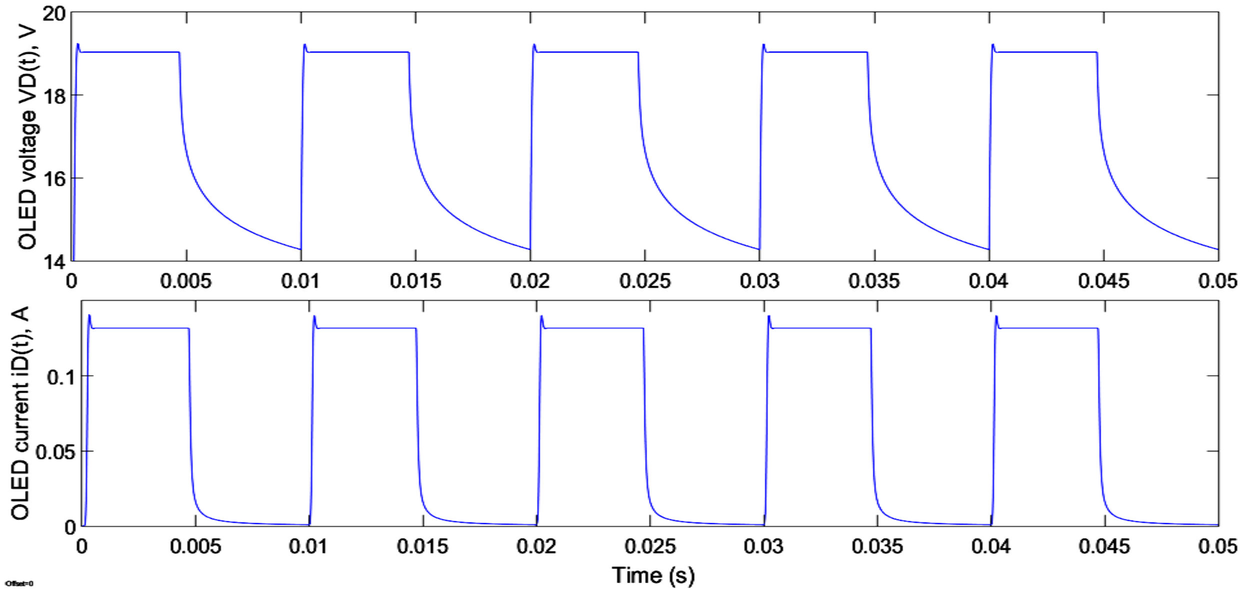

Fig. 3.38. Transient simulation of the OLED model under an OLED current switched-off. (1 V/div), (50 mA/div) and (5 ms/div).

As it is shown, the OLED capacitance behavior is well noted when the OLED current I_{OLED} is switched-off, and the OLED voltage V_{OLED} is discharging. But, there are some small inaccuracies between the simulation and experimental results; the maximum OLED voltage difference in percentage is 1.6% between simulation and experimental results.

3.4. Conclusions

A review of the art state of the OLED models was tackled. The OLED models review shows the different works proposed related to electrical, PET and SPET OLED models. The simplified electrical modeling of power LEDs for DC-DC converter analysis and simulation is one of the simplest approaches reported in order to find the electrical OLED model because sophisticated equipment is not needed to achieve the modeling. Therefore, it represents a good option to study the equivalent electrical OLED model of the FL300 Phillips Lumiblade OLED lamp. This theory relies on the fact that the electrical power of the OLED obtained considers the thermal effect due to the OLED power is affected by its junction temperature.

Thereby, the equivalent electrical OLED model of the FL300 Phillips Lumiblade OLED lamp was obtained by means of the simplified electrical modeling of power LEDs for DC-DC converter analysis and simulation approach. The calculated and experimental steady state and dynamic state results of the OLED equivalent electrical model obtained show a good accuracy. The maximum relative error presented between calculated and experimental results of the OLED power P_{OLED} and the OLED static resistance R_{OLED} is 1.6 %.

4. Switched capacitor converters

Nowadays, it is very important to develop high power density OLED drivers in order to achieve an adequate lamp-driver integration, owing to the slim shape and size of the lamp. Then, OLED lamp driver suppliers must make interior designers' and architects' life easier by obtaining small and lightweight drivers. Therefore, it is important to make a review of the different power supplies in the state of the art in order to find the best option in performance, cost, and size, as well as other advantages, to operate OLED lamps. One way to drive OLED lamps is by means of linear power supplies because of their ease of design, low electromagnetic interference (EMI) noise and low output voltage ripple. Nevertheless, these power supplies have the disadvantages of low efficiency, bulky and heavy structure because of the large energy storage components that are required.

On the other hand, conventional switched DC-DC converters have the benefit of high efficiency in comparison with linear power supplies. Also, they are easy to design and very mature in terms of good performance. However, these converters have the drawbacks of high EMI noise, high output voltage ripple, bulky and heavy structure due to the use of large magnetics and capacitors, since their size is dependent on the switching frequency. Thus, one way to reduce the components size of the DC-DC converter is by increasing the switching frequency. But, increasing the switching frequency affects efficiency so that soft-switching circuits are used in which the size of the components are large, making DC-DC converters bulky.

Other type of converters used to drive OLED lamps are switched capacitor (SC) converters, which consist of diodes, switches, and capacitors. These converters do not use any large inductor, and they are small. This leads to a high power density of the converter, making it very attractive for the aforementioned lighting OLED applications, which require high-power-density converters. Some applications are for instance, portable and any low-profile electronic equipment, such as notebook computers, tablets and portable digital assistants.

This dissertation focuses on analyzing different SC converters topologies in order to highlight their advantages and disadvantages, in terms of efficiency, voltage conversation ratio, EMI noise, power density, output voltage ripple and power level. This work discards the use of linear power supplies and conventional DC-DC converters due to more expensive bill of materials (BOM) cost, low power density and low efficiency inconveniences.

This chapter is organized in the following form; firstly, non-resonant SC converters are presented in which the different topologies and their principle of operation are explained. Thereafter, resonant SC converters are introduced in which a brief description of this type of converters is explained. On the other hand, the circuit structure and the principle of operation of the different resonant SC converters are explained and shown as follows: conventional resonant switched-capacitor (RSC) converters, fractional-voltage-conversion-ratio RSC converters, dual-phase RSC converters, multi-configurable bidirectional RSC converter, step-down half bridge RSC converter with isolation transformer, and step-down SC converter with coupling inductors. Afterwards, a summary and comparison of the electrical performance of the different resonant SC converters is presented in order to select the best resonant SC converter in performance as a proposed topology to design an OLED driver.

4.1. Non-resonant SC converters

The family of non-resonant SC converters consists of step-up, step-down and inverter converters (Fig. 4.1), which achieve different voltage conversion ratios. This type of converters do not use any magnetic component owing to the fact that the switched capacitor is charged and discharged to the input voltage and output voltage during switching operation modes. Each of these converters has two diodes, D_1 and D_2, two switches, Q_1 and Q_2, one switched capacitor, C_1, and one output filter capacitor, C_O. The switches, Q_1 and Q_2 are operated at 50% duty cycle in a complementary way by a pulse width modulation (PWM) technique, which requires a dead-time interval. Fig. 3.1(a) shows the step-up converter, which has a voltage conversion ratio of 2. In Fig. 4.1(b) the step-down converter with a voltage conversion ratio of 1/2 is shown. Finally, Fig. 4.1(c) illustrates the inverter converter, whose voltage conversion ratio is -1 [7]-[9][130][131].

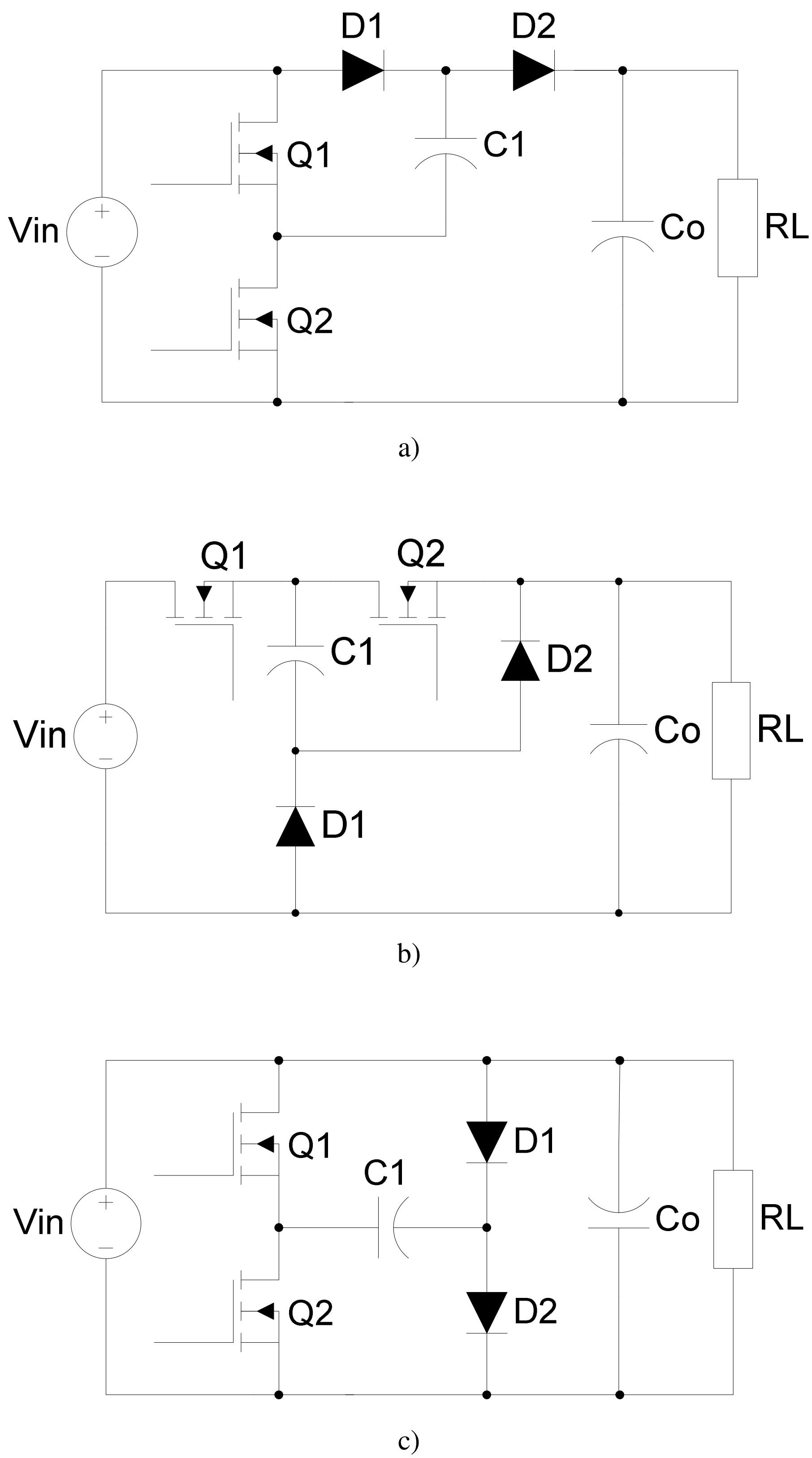

Fig. 4.1. Non-resonant SC converters: a) step-up, b) step-down and c) inverter.

As an example of operation, the non-resonant SC step-up converter shown in Fig. 4.1(a) consists of charge and discharge operation modes. In charge operation mode shown in Fig. 4.2, Q_2 is switched-on while Q_1 is off, the switched capacitor, C_1, is charged to the input voltage V_{in}, through D_1, which is forward biased. In this operation mode, C_O is discharged to the load.

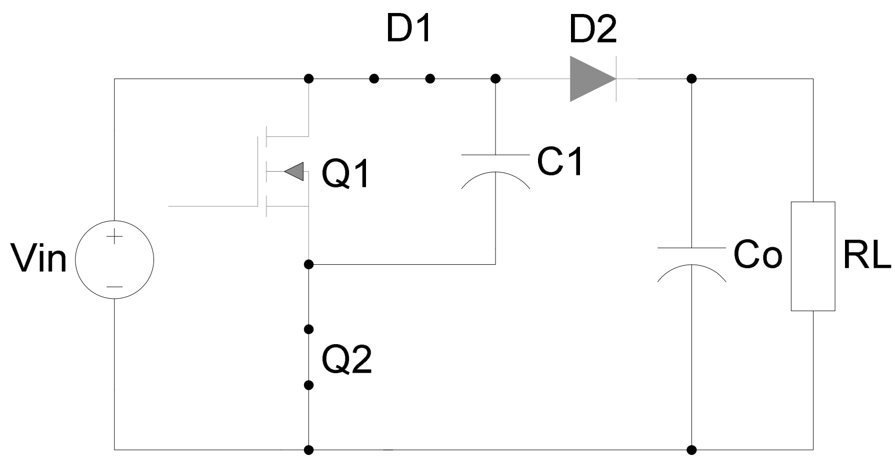

Fig. 4.2. Non-resonant SC step-up converter charge operation mode.

In discharge operation mode as illustrated in Fig. 4.3, Q_1 is switched-on and Q_2 is switched-off while the switched capacitor, C_1 is discharged to the load, charging C_O, through D_2 that is forward biased.

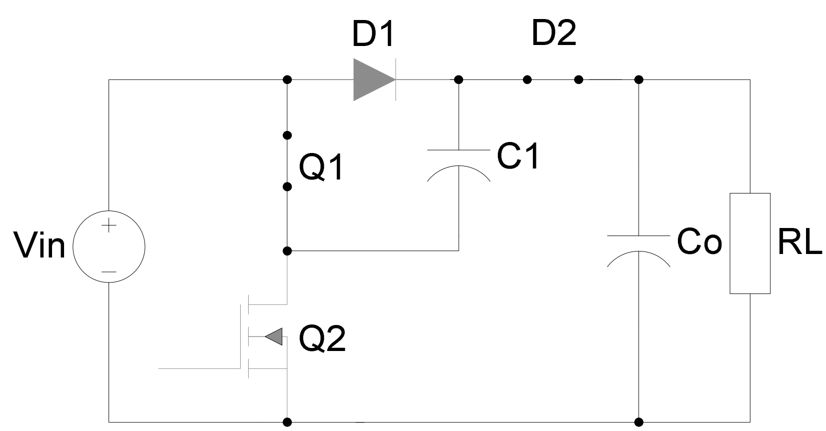

Fig. 4.3. Non-resonant SC step-up converter discharge operation mode.

Fig. 4.4 illustrates the switching waveforms of the transistors, Q_1 and Q_2, during both charge and discharge operation modes of the step-up non-resonant SC converter.

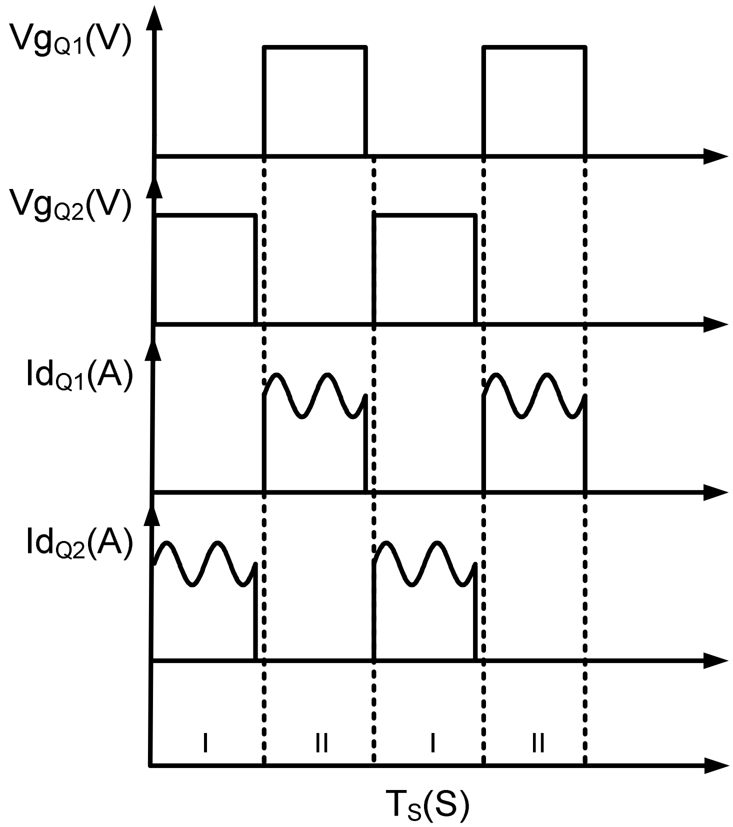

Fig. 4.4. Switching waveforms of the step-up non-resonant SC converter: (I) charge and (II) discharge operation modes.

4.2. Resonant SC converters

Resonant SC converters use a small resonant inductor in series with the switched capacitor in order to operate under zero current switching (ZCS), which reduces switching losses and EMI noise and improves voltage conversion ratio, efficiency and output voltage regulation. In addition, they can be operated at higher switching frequencies because of ZCS operation, which leads to a higher power density of the converter. In order to operate under ZCS, the resonance frequency has to be greater than the switching frequency.

4.2.1. Conventional RSC converters

Non-resonant SC converters are converted into conventional RSC converters by inserting a small resonant inductor L_r in series with the switched capacitor in order to operate under ZCS. This family consists of step-up, step-down and inverter converters, as shown in Fig. 4.5(a)-(c). Voltage conversion ratios are 2, 1/2 and -1 as those non-resonant SC converters [132]-[138].

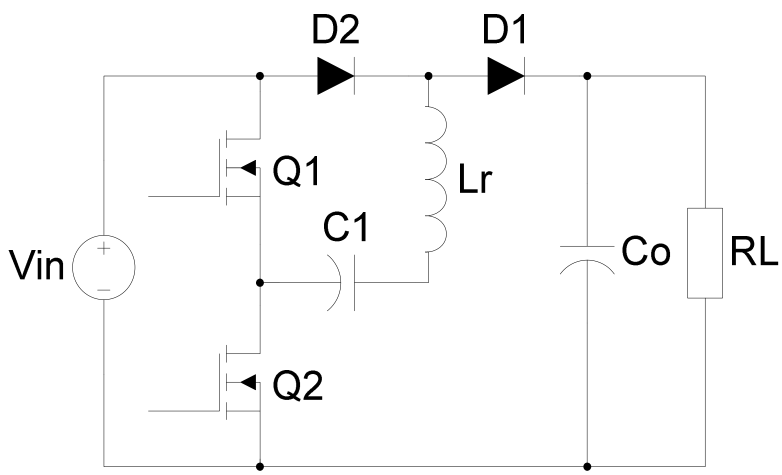

a)

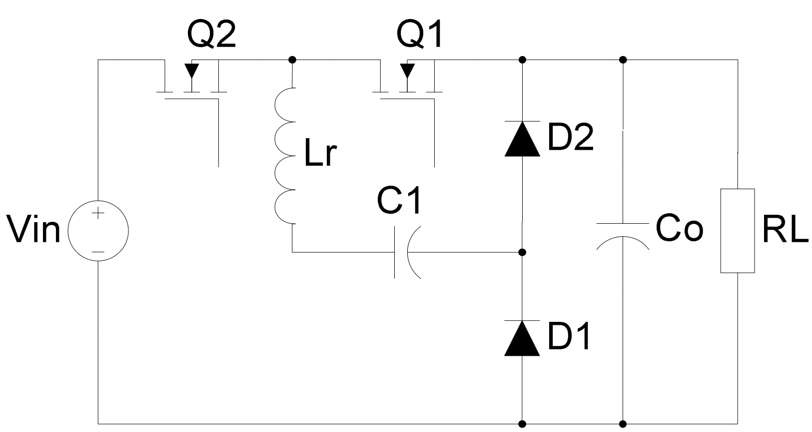

b)

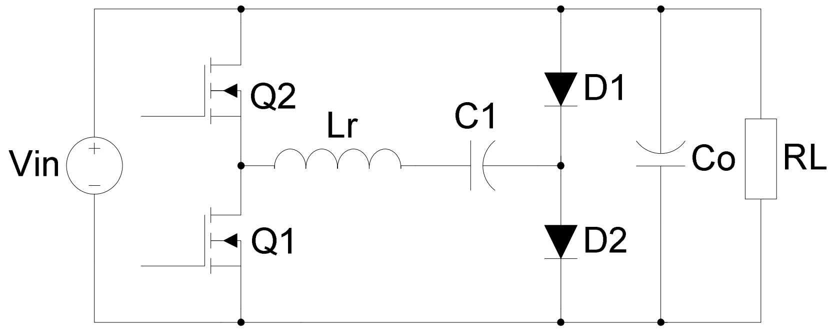

c)

Fig. 4.5. Conventional RSC converters: a) step-up, b) step-down and c) inverter.

As an example of operation, the RSC step-up converter shown in Fig. 4.5(a) consists of four operation modes as are charge, off, discharge and off. This last operation mode enters after charge and discharge operation modes. The switches, Q_1 and Q_2 are operated at 50% duty cycle in a complementary way with a small dead-time, just like non-resonant step-up converter. In the charge operation mode, as shown in Fig. 4.6, Q_2 is switched on under ZCS operation while Q_1 is off, since the switched capacitor C_1 and the resonant inductor L_r enter into resonance at a frequency higher than the operation frequency, which is a condition to operate in ZCS. In this operation mode, C_1 is charged to the input voltage, V_{in}, through D_2, and C_O is discharged to the load.

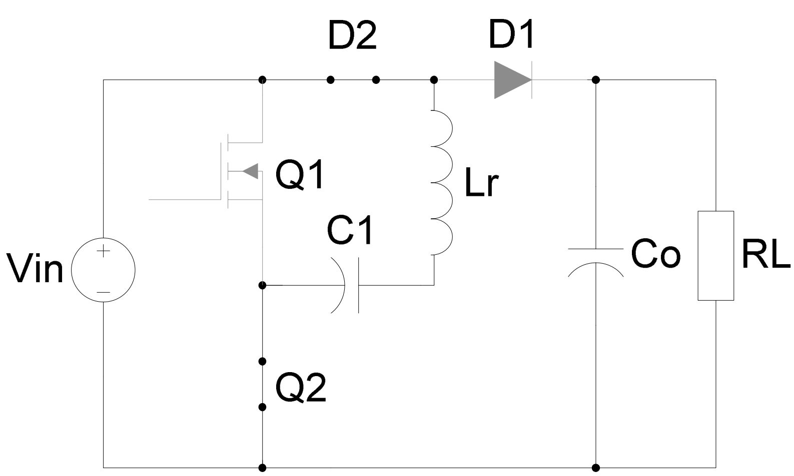

Fig. 4.6. RSC step-up converter charge operation mode.

In the off operation mode, as illustrated in Fig. 4.7, the current through the switched capacitor C_1 and the resonant inductor L_r are zero while Q_2 is switched-off under ZCS operation. Also, the output filter capacitor, C_O is still discharging to the load. D_1 and D_2 are reverse biased.

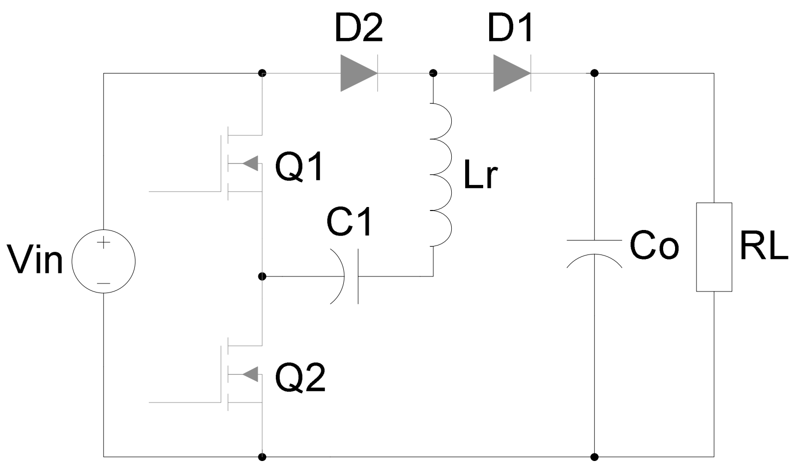

Fig. 4.7. RSC step-up converter off operation mode.

In the discharge operation mode, as shown in Fig. 4.8, Q_1 is switched on under ZCS operation while Q_2 is off. The switched capacitor C_1 is discharged to the load, charging the output filer capacitor, C_O, through D_1 that is forward biased.

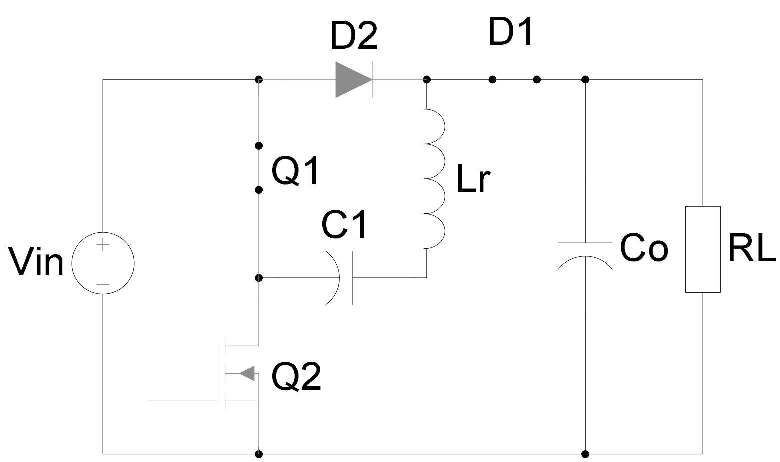

Fig. 4.8. RSC step-up converter discharge operation mode.

The fourth and last operation mode is shown in Fig. 4.9. This operation mode is equal to off operation mode. The current through the switched capacitor C_1 and the resonant inductor, L_r are zero, while Q_1 and Q_2 are off and D_1 and D_2 are reverse biased.

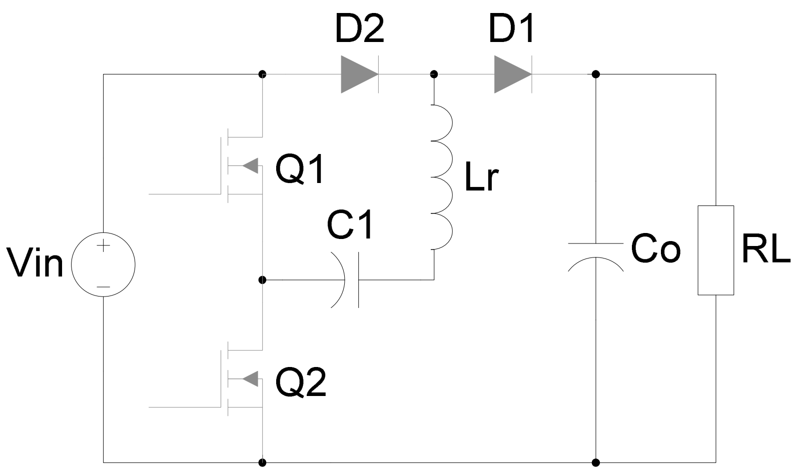

Fig. 4.9. RSC step-up converter off operation mode.

Fig. 4.10 shows the switching waveforms of transistors Q_1 and Q_2 under ZCS operation as well as resonant current, i_{L_r}, through L_r during the four operation modes of the conventional RSC converter.

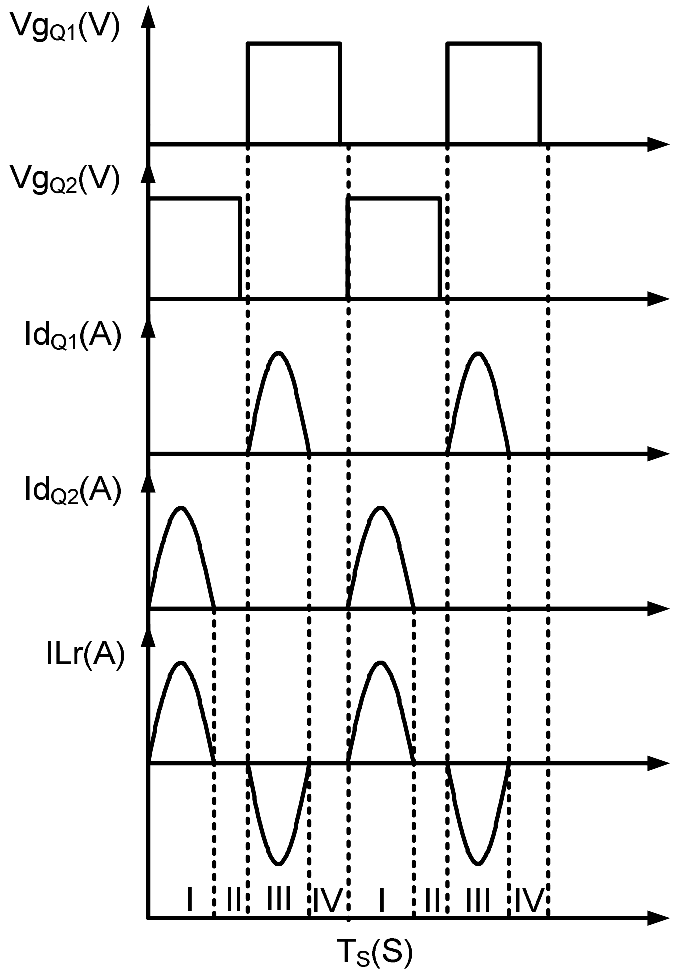

Fig. 4.10. Switching waveforms of the conventional step-up RSC converter: (I) charge, (II) off, (III) discharge and (IV) off operation modes.

4.2.2. Fractional-voltage-conversion-ratio RSC converters

The fractional-voltage-conversion-ratio (FVCR) RSC converters are proposed as a solution to achieve output voltage ratios greater or lower than those output voltage ratios of the conventional RSC converters [139]-[141]. FVRC RSC converter family consists of step-up, step-down and inverter converters with voltage conversion ratio of 3, 1/3 and -0.5, respectively, as illustrated in Fig. 4.11. Then, these converters are designed for voltage conversion ratios greater or lower by inserting extra cells of diodes, D_3, D_4 and D_5, and switched capacitors, C_2 and C_3. Also, operation under ZCS is achieved by using a small resonant inductor in series with switched capacitors. Fig. 4.11(a)-(c) shows step-up, step-down and inverter converters with voltage conversion ratios of 3, 1/3 and -0.5, respectively.

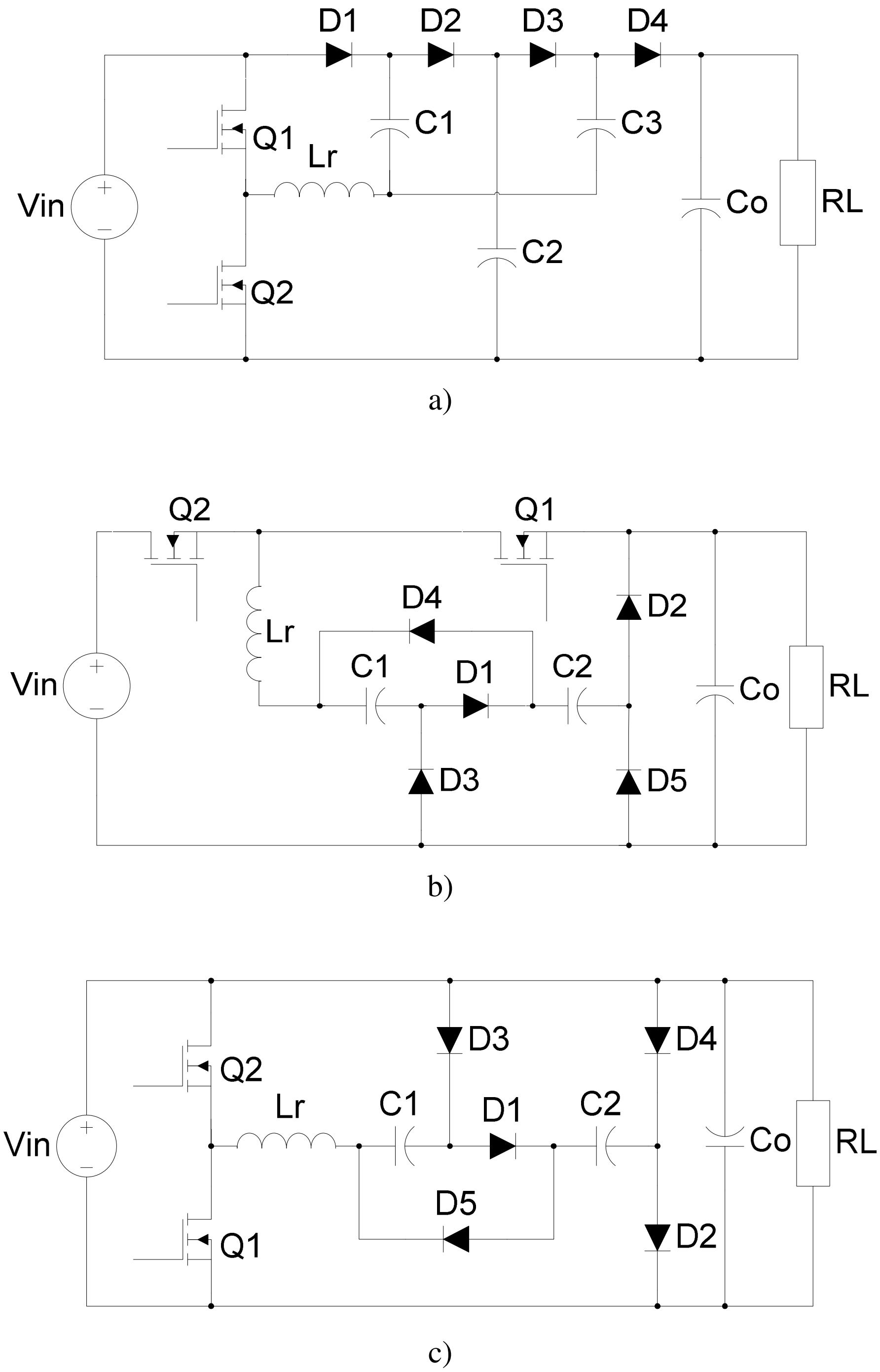

Fig. 4.11. FVCR RSC converters: a) step-up, b) step-down and c) inverter.

The FVCR RSC step-up converter illustrated in Fig. 4.11(a) consists of four operation modes as those in conventional RSC converters, which are charge, off, discharge and off. This step-up converter obtains a voltage conversion ratio of 3, which is possible by inserting diodes D_3 and D_4, and switched capacitors, C_2 and C_3. It is important to mention that C_2 is greater in value than C_1 and C_3. In the charge operation mode shown in Fig. 4.12, Q_2 is turned on and Q_1 is off, C_1 is charged to the input voltage V_{in} through D_1 that is forward biased, while C_3 is charged to the voltage across C_2 through D_3, which is forward biased. D_2 and D_4 are reverse biased. Thereby, C_1 and C_3 are in series with the resonant inductor L_r. In this operation mode, the output filter capacitor, C_O is discharging to the load.

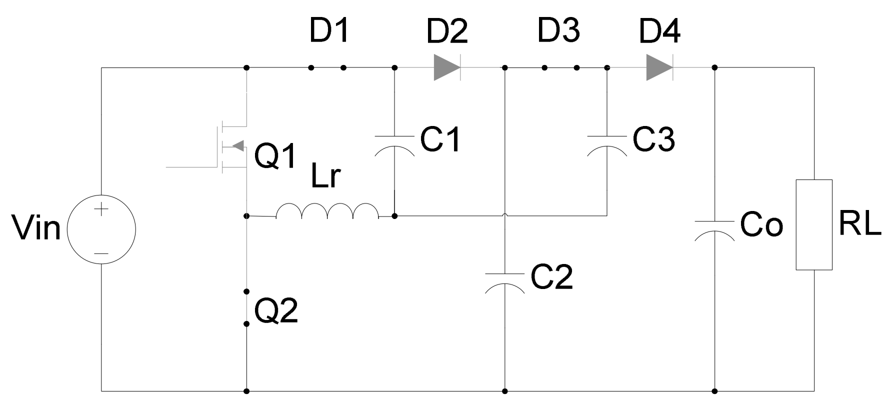

Fig. 4.12. FVCR RSC step-up converter charge operation mode.

In the off operation mode, as illustrated in Fig. 4.13, the current through the switched capacitors C_1 and C_3 and the resonant inductor L_r are zero while Q_2 is turned off under ZCS operation. D_1, D_2, D_3 and D_4 are reverse biased. The output filter capacitor C_O is still discharging to the load.

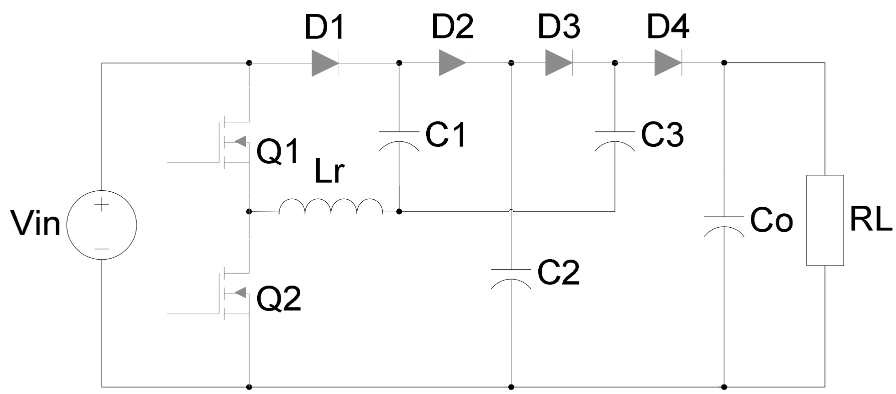

Fig. 4.13. FVCR RSC step-up converter off operation mode.

In the discharge operation mode shown in Fig. 4.14, when Q_1 is turned on and Q_2 is turned off, C_1 is discharged to C_2 through D_2 that is forward biased, while C_3 is discharged to the output filter capacitor C_O through D_4 that is forward biased. The output voltage conversion ratio of 3 is obtained owing to the fact that the input voltage V_{in} is in series with the voltage of C_3 that is equal to twice the input voltage V_{in}. D_1 and D_3 are reverse biased.

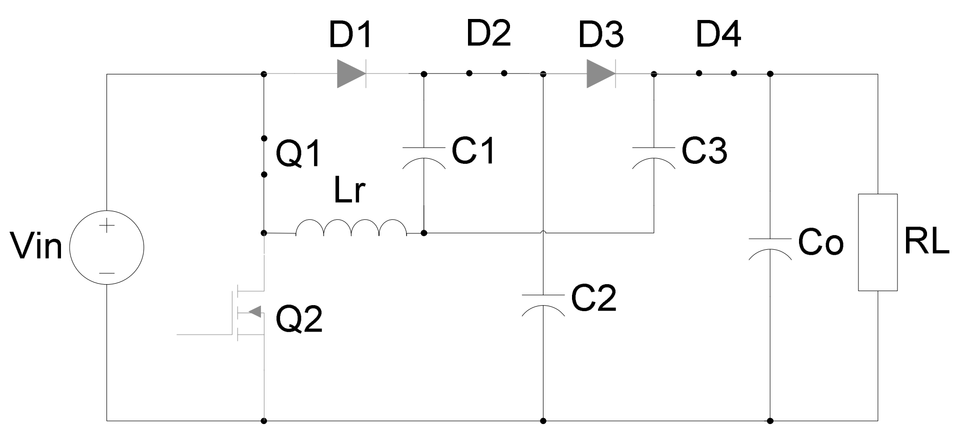

Fig. 4.14. FVCR RSC step-up converter discharge operation mode.

The last operation mode is equal to off operation mode, as illustrated in Fig. 4.15. The current through the switched capacitors C_1 and C_3 and the resonant inductor L_r are zero. Transistor Q_1 is switched-off under ZCS condition, Q_2 is off and D_1, D_2, D_3 and D_4 are reverse biased, while the output filter capacitor C_O keeps discharging to the load.

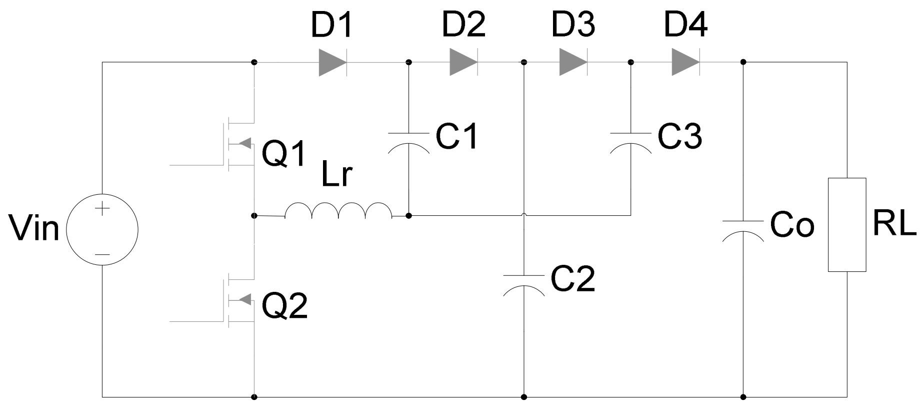

Fig. 4.15. FVCR RSC step-up converter off operation mode.

The switching waveforms of transistors Q_1 and Q_2 and resonant current, iL_r, through L_r are equal to those of the conventional RSC step-up converter, as shown in Fig. 4.10.

4.2.3. Dual-phase RSC converters

The dual-phase (DP) RSC converters family are built from the combination of two conventional RSC converters family as shown in Fig. 4.16(a)-(e). This family consists of step-up, step-down, inverter, summation and subtraction converters with voltage conversion ratios of 2, 0.5, -1, $V_{in1} + V_{in2}$ and $V_{in2} - V_{in1}$, respectively [142].

These dual-phase converters are intended to achieve a more stable output voltage and lower output voltage ripple in comparison with RSC conventional converters. The only difference in components with respect to conventional RSC converters is the addition of a second switched capacitor, C_2. This type of converters provides an output voltage ripple that is half to those of conventional RSC converters.

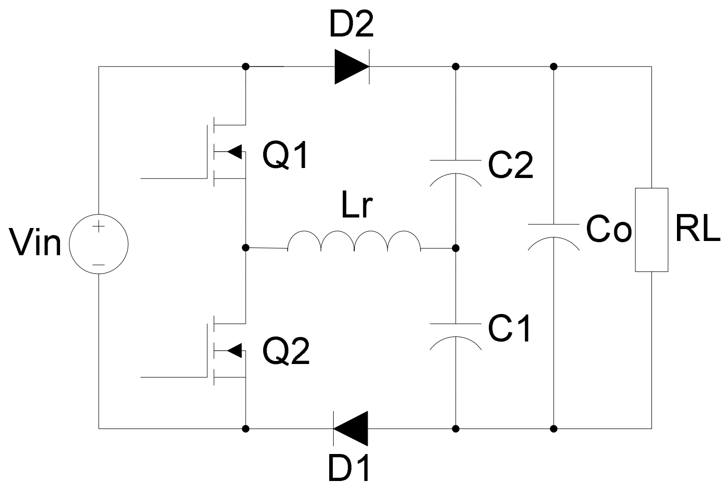
D2
Q1
C2
Lr
Vin
Co
RL
C1
Q2
D1

a)

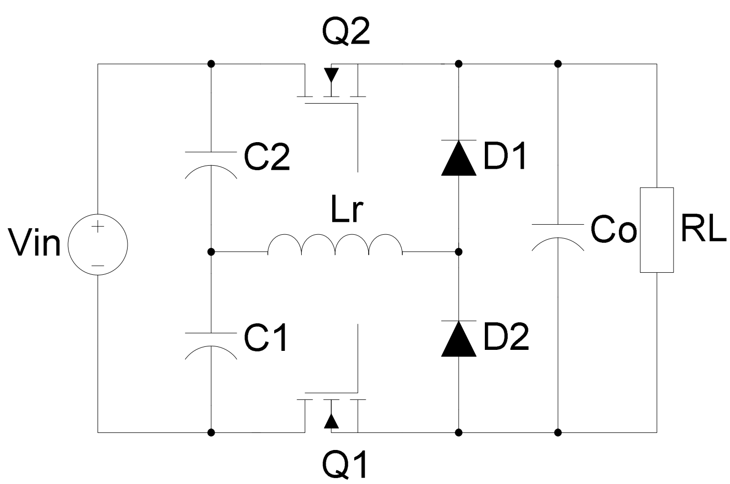
Q2
C2
D1
Lr
Vin
Co
RL
C1
D2
Q1

b)

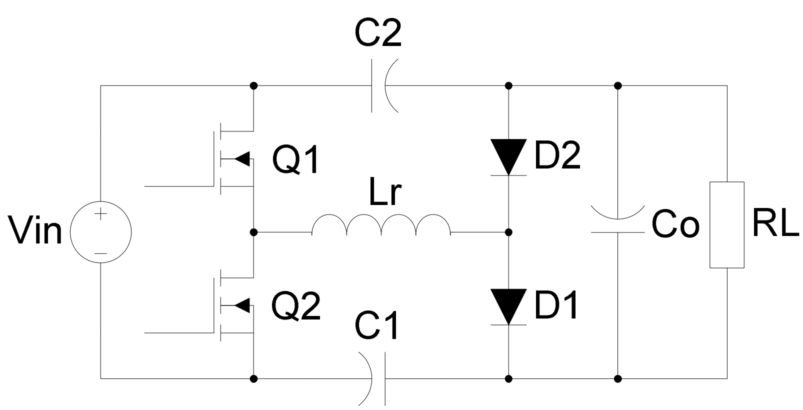
C2
Q1
D2
Lr
Vin
Co
RL
Q2
D1
C1

c)

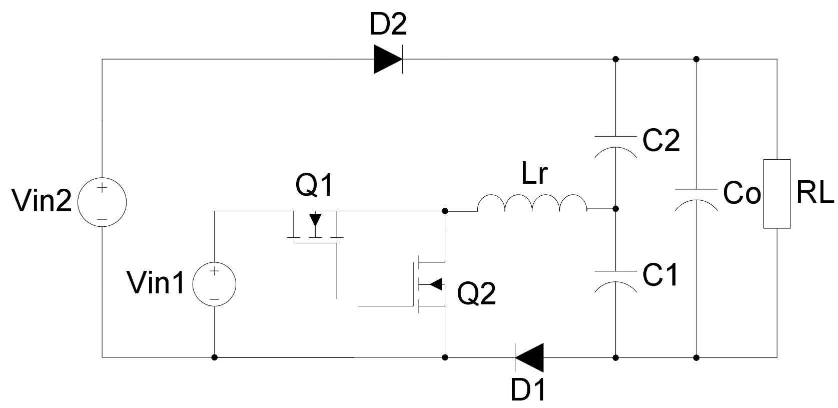

d)

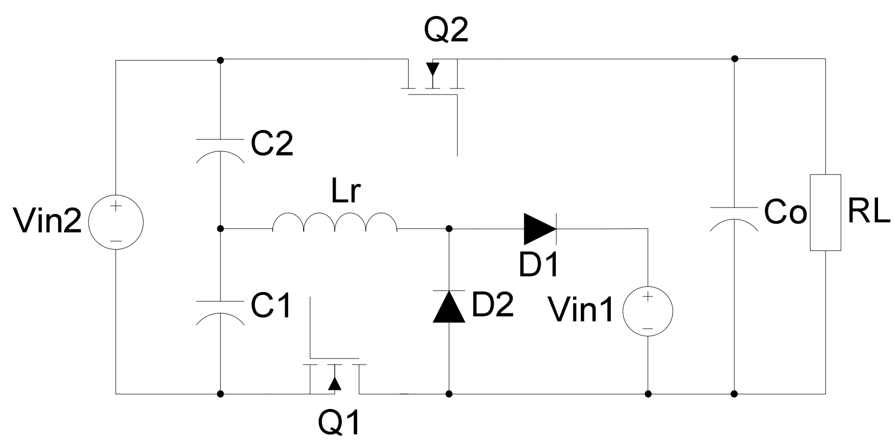

e)

Fig. 4.16. Dual-phase RSC converters: a) step-up, b) step-down, c) inverter, d) summation and e) subtraction.

The DP RSC step-up converter shown in Fig. 4.16(a) consists of four operation modes as that of the conventional RSC step-up converter. These are charge, off, discharge and off. In the charge operation mode, as shown in Fig. 4.17, transistor Q_1 is turned-on under ZCS while Q_2 is off. Then, C_1 is charged to the input voltage, V_{in}, through D_1 that is forward biased, while C_2 is discharged to the output filter capacitor C_O. C_1 is in series with the resonant inductor L_r. The output filter capacitor C_O is discharged to the load.

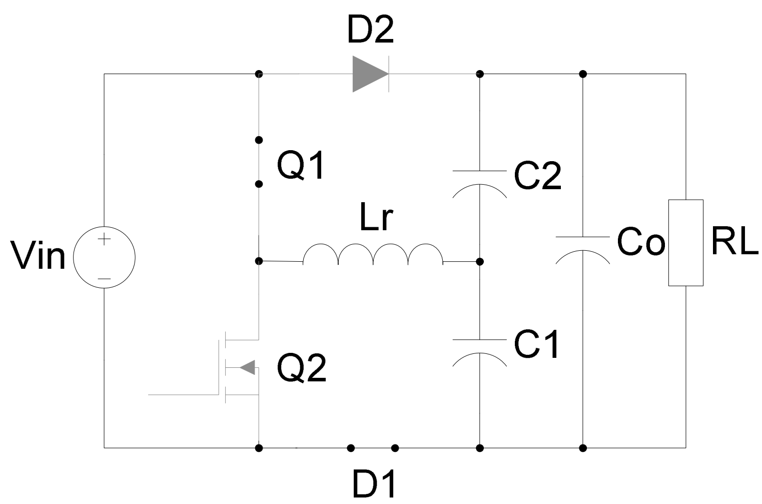

Fig. 4.17. DP RSC step-up converter charge operation mode.

In the off operation mode, as illustrated in Fig. 4.18, the current through the switched capacitor C_1 and C_2 and the resonant inductor L_r are zero owing to the fact that D_1 and D_2 are reverse biased. Transistor Q_1 is turned off under ZCS operation and the output filter capacitor C_O keeps discharging to the load.

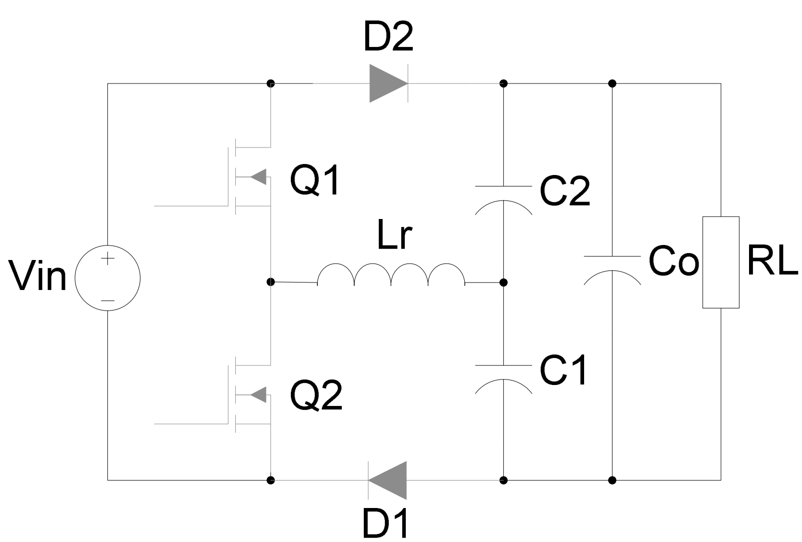

Fig. 4.18. DP RSC step-up converter off operation mode.

In the discharge operation mode, as shown in Fig. 4.19, Q_2 is turned on under ZCS operation, while Q_1 is off. C_2 is charged to the input voltage V_{in} through D_2, which is forward biased, while C_1 is discharged to the output filter capacitor C_O, through the forward biased diode D_2.

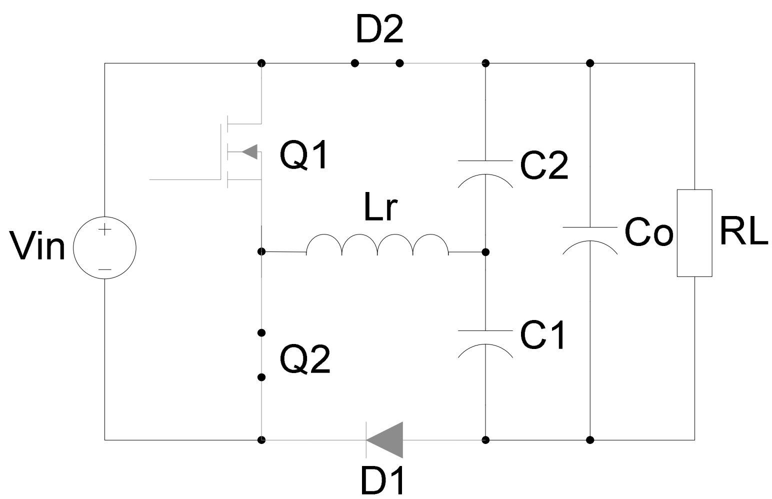

Fig. 4.19. DP RSC step-up converter discharge operation mode.

The fourth operation mode is equal to the off operation mode, as illustrated in Fig. 4.20.

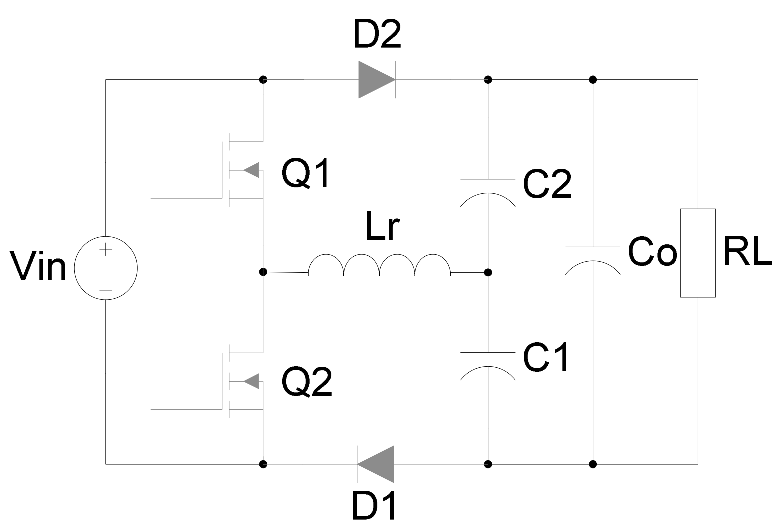

Fig. 4.20. DP RSC step-up converter off operation mode.

The switching waveforms of transistors Q_1 and Q_2 and resonant current, iL_r, through L_r are equal to that of the conventional RSC step-up converter, as shown in Fig. 4.10. However, it is important to take into consideration that the operation sequence of Q_1 and Q_2 is opposite to that of the conventional RSC step-up converter.

4.2.4. Multi-configurable bidirectional RSC converter

A multi-configurable bidirectional (MCB) RSC converter is shown in Fig. 4.21. This converter is built based on the principles of the conventional RSC converters, and can be configured into different types of operation modes by considering uni-directional power flowing [143][144]. Table 4.1 shows the possible switch configurations for 7 different unidirectional conversion modes, in which switches can be short-circuited, disconnected or replaced by a diode. This converter consists of three switching states, which are charge, discharge and balance. This last third state is included in order to balance the remaining energy of the switched capacitor, which improves the switching behavior of the transistors. The addition of this third state is the main difference with respect to those conventional RSC converters of two states.

The efficiency of the MCB RSC converter is kept constant under different voltage conversion ratios, which can be upper or lower than unity, as well as being wide and continuous. In this converter the efficiency does not depend on voltage conversion ratio, as it is the case in conventional RSC converters. Thus, efficiency just depends on conduction losses. In conventional RSC converters it is difficult to achieve a desired output voltage, because the resultant charge energy balance into the switched capacitor is not zero after charge and discharge switching periods, that is, the remaining energy on the switched capacitor avoids converging to the desired voltage. On the contrary, MCB RSC converters make an energy balance on the switched capacitor after charge and discharge switching states by means of an additional switch, Q_5 or Q_6, which is used to create a trajectory for the resonant current of the switched capacitor C_1 when its charge is balanced to its initial charge state by reversing its polarity. Output filter capacitor and load can be connected at any output terminals, but considering power flowing direction based on transistors operation sequence.

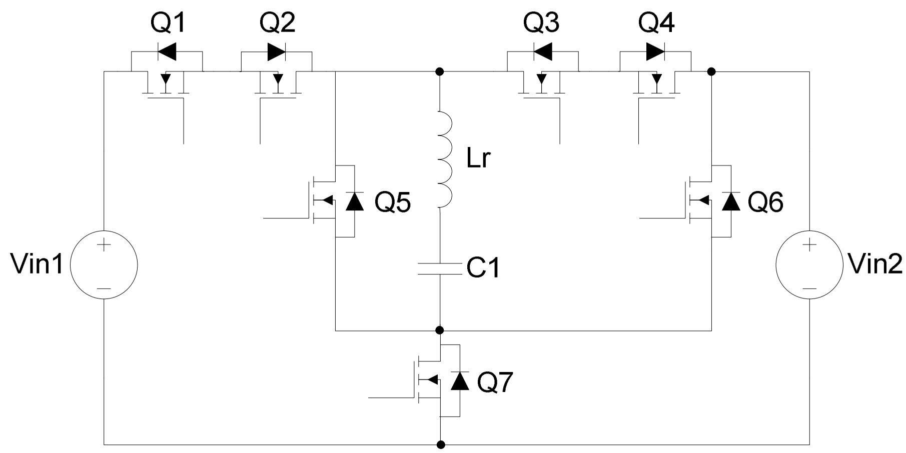

Fig. 4.21. Bidirectional MCB-RSC converter.

Table. 4.1. Switch mapping for uni-directional derivatives in the MCB-RSC Converter[1].

Converter Function	Q1	Q2	Q3	Q4	Q5	Q6	Q7
Step up-down	1	D	2	2	3	O	S
Step up	1	D	S	D	3	O	S
Step down	1	D	2	D	D	O	S
Doubler step up-down	S	3	S	D	3	O	1
Doubler step down	S	D	S	D	3	O	1
Divider step up-down	1	S	2	S	O	3	2
Divider step down	1	S	2	S	O	D	2

1. Number and letter characters in the table represent the following: S - MOSFET is short-circuited; O - MOSFET is disconnected; D – just a diode is needed; numbers represent the switching states into which MOSFET are active.

The uni-directional RSC step-up converter configuration is shown in Fig. 4.22. It consists of 3 operation modes, which are charge, discharge and balance, and it is integrated by two switches, Q_1 and Q_5, two diodes, D_1 and D_2, placed instead of Q_2 and Q_4, switched capacitor, C_1, resonant inductor, L_r and output filter capacitor, C_O. When a load resistor in parallel with an output filter capacitor is connected to one of the output terminals, the unidirectional step-up RSC converter behaves as a current source, by which the output voltage just depends on the load resistor.

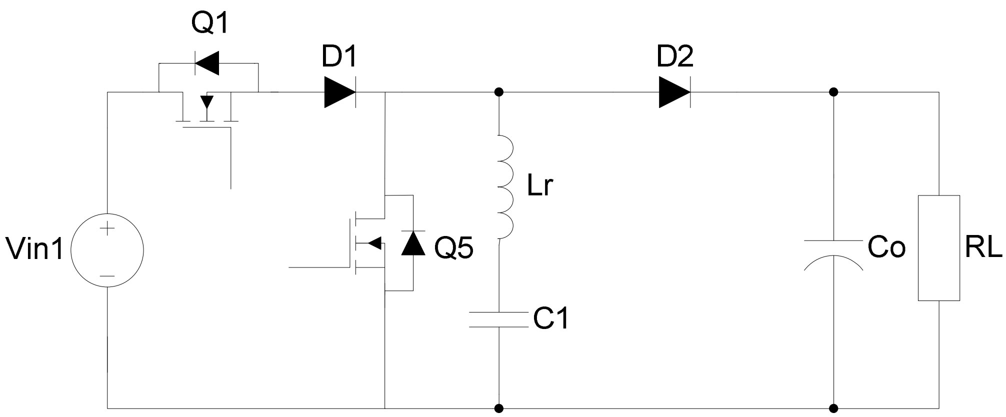

Fig. 4.22. Uni-directional step up RSC converter.

In the charge operation mode, as illustrated in Fig. 4.23, Q_1 is turned on under ZCS and D_1 is forward biased so that C_r is charged to the input voltage, V_{in}. In this stage, Q_5 is off and D_2 is reverse biased. Transistor Q_1 is turned on under ZCS operation. Then, the resonant inductor L_r and the switched capacitor C_r integrate the resonant circuit. The output filter capacitor, C_O, is discharged to the load.

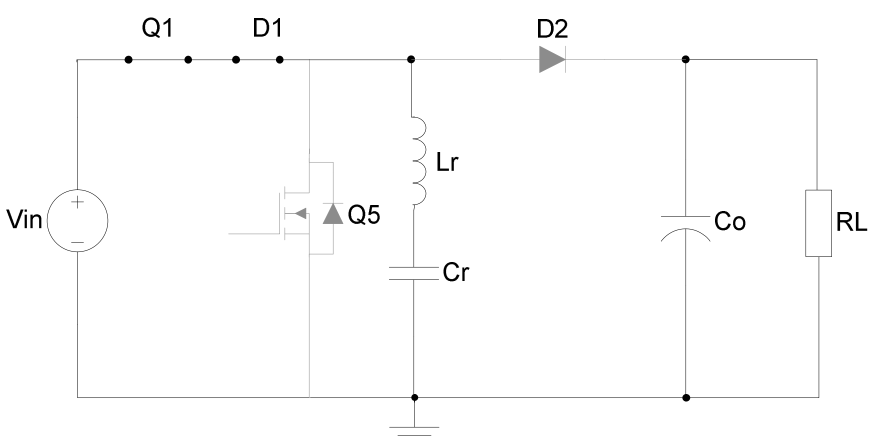

Fig. 4.23. Uni-directional step up RSC converter charge operation mode.

The discharge operation mode circuit is shown in Fig. 4.24. The switched capacitor C_r is discharged to the output through the forward biased D_2 and the resonant inductor, L_r, while Q_1, Q_5 and D_1 are off.

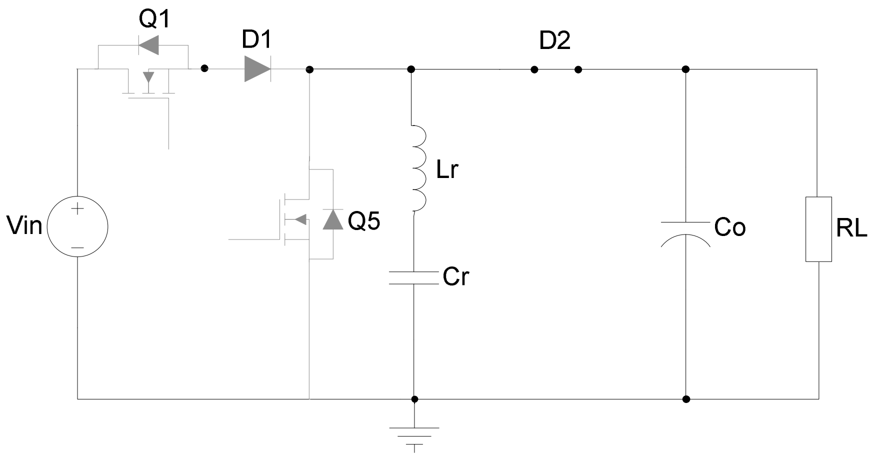

Fig. 4.24. Uni-directional step up RSC converter discharge operation mode.

The balance operation mode is illustrated in Fig. 4.25. When Q_5 is turned on, the resonant tank is short-circuited to balance the energy stored in the switched capacitor C_r. Transistor Q_1 is off and diodes D_1 and D_2 are reverse biased. The output filter capacitor,C_O, keeps discharging to the load.

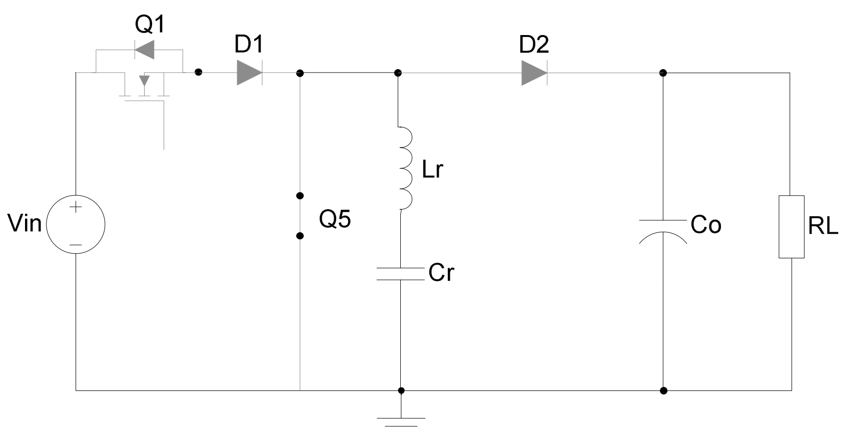

Fig. 4.25. Uni-directional step up RSC converter balance operation mode.

The switching waveforms of transistors Q_1 and Q_5, the resonant current, iL_r, through L_r and the switched capacitor voltage across C_r are shown in Fig. 4.26.

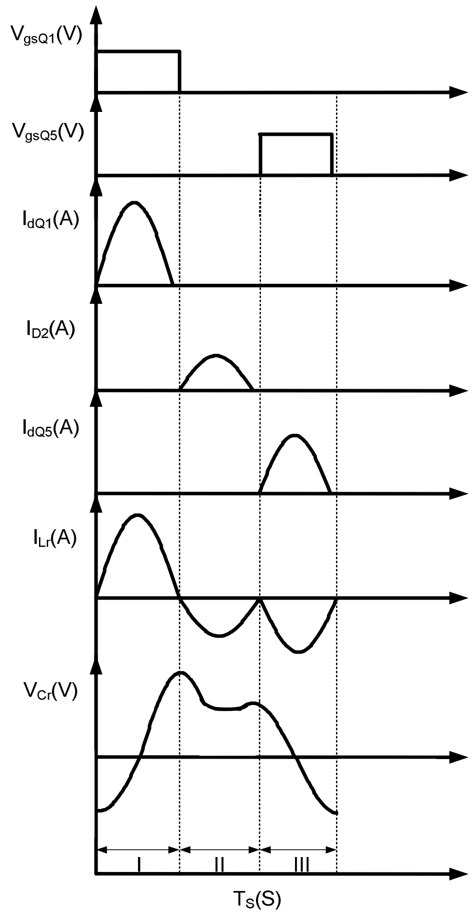

Fig. 4.26. Switching waveforms of the unidirectional step-up RSC converter: (I) charge, (II) discharge and (III) balance operation modes.

4.2.5. Step-down half bridge RSC converter with isolation transformer

A step-down half bridge RSC converter with isolation transformer is described in this section. It consists of two switches Q_1 and Q_2, four diodes, D_1, D_2, D_3 and D_4, two capacitors, C_{in1} and C_{in2}, for removing dc current in the transformer, T_1, and which must be greater in value than the switched capacitor, C_S, a switched capacitor, C_S, an output inductor, L_O, an output filter capacitor, C_O, and an isolation transformer T_1, as shown in Fig. 4.27. The output current is controlled by the switched capacitor, C_S, and it is connected in series with a small output inductor L_O, which operates in discontinuous conduction mode (DCM) in order to achieve ZCS in the transistors and improve efficiency. Then, the switched capacitor C_S and the output inductor L_O integrate the resonant circuit. The magnetizing inductance of the isolation transformer helps reducing switching losses due to ZVS operation in the transistors, which increases efficiency. The output voltage ripple is very low because of the large output filter capacitor [145]-[147].

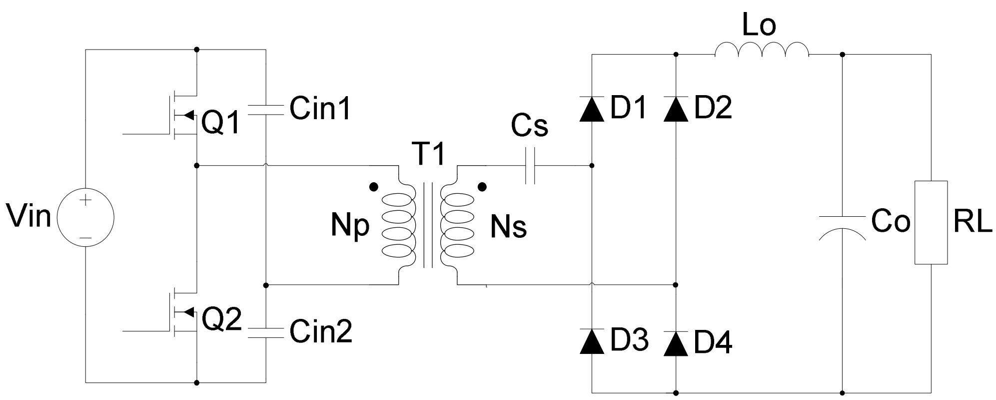

Fig. 4.27. A step-down half bridge RSC converter with isolation transformer.

The step-down half bridge RSC converter with isolation transformer consists of 5 operation modes in a half switching cycle. In the first operation mode, as shown in Fig. 4.28, Q_1 is turned on while Q_2 is off, and C_S is charged until the current through L_O reaches zero. In this stage, D_1 and D_4 are forward biased. Transistor Q_1 is turned on under ZCS operation.

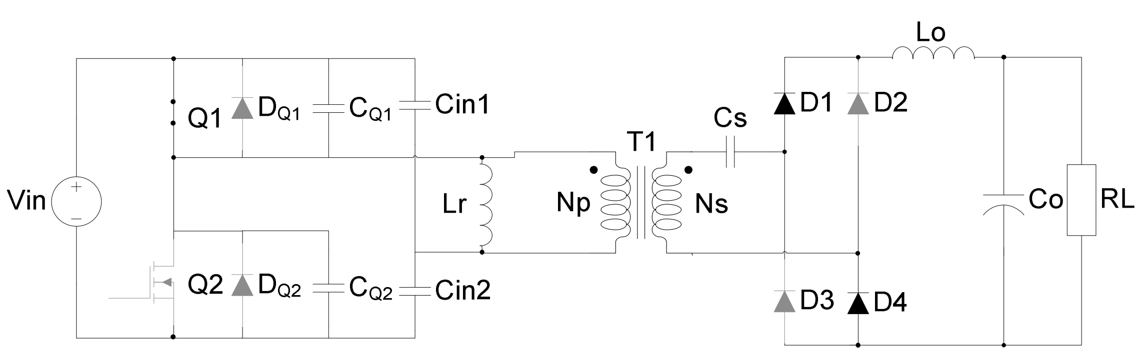

Fig. 4.28. A step-down half bridge RSC converter first operation mode.

In the second operation mode, as illustrated in Fig. 4.29, C_S is fully charged and Q_1 is still on, while D_1 and D_4 are reverse biased. The current through the output inductor L_O is zero. The output filter capacitor C_O is discharged to the load.

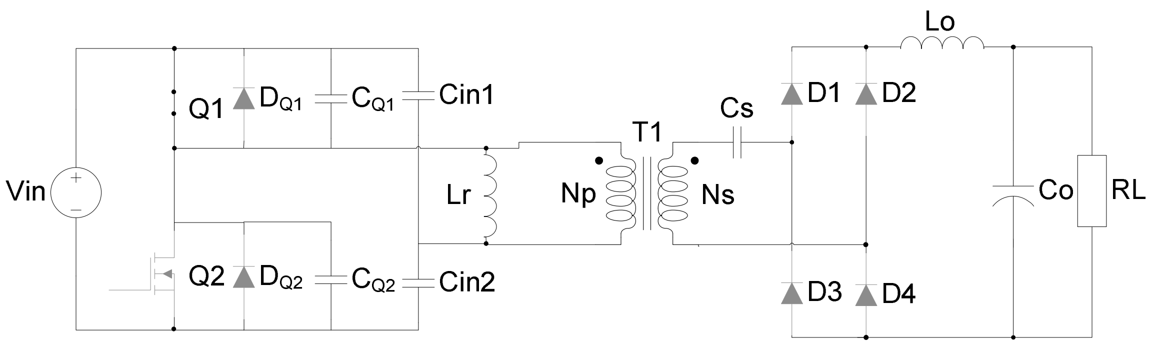

Fig. 4.29. A step-down half bridge RSC converter second operation mode.

In the third operation mode, which is shown in Fig. 4.30, Q_1 is turned off under ZVS and the switched capacitor C_S is fully charged, while the output filter capacitor C_O is still discharging to the load.

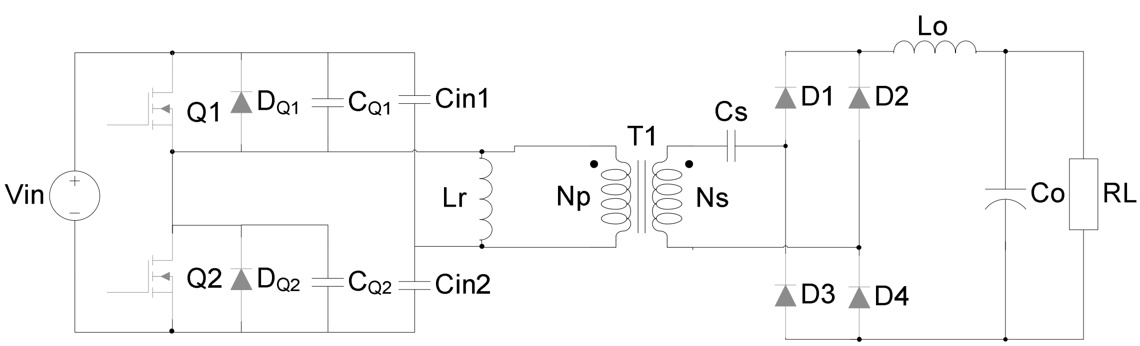

Fig. 4.30. A step-down half bridge RSC converter third operation mode.

The fourth operation mode is illustrated in Fig. 4.31. The switched capacitor C_S is discharged to the output inductor L_O. Transistors Q_1 and Q_2 are off and D_2 and D_3 are forward biased. This operation mode ends when the voltage across C_{Q2} is zero and the voltage across C_{Q1} is the equal to the input voltage V_{in}.

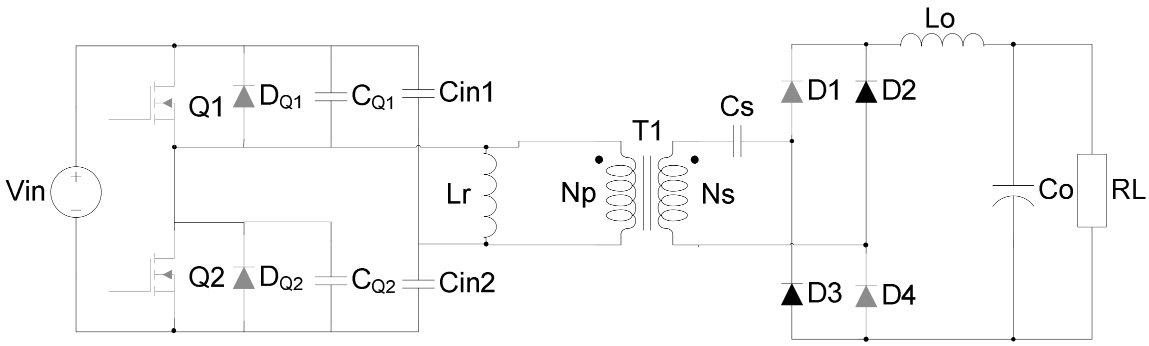

Fig. 4.31. A step-down half bridge RSC converter fourth operation mode.

The fifth operation mode is shown in Fig. 4.32. The voltage across the capacitor C_{Q2} is zero and D_{Q2} is forward biased. Transistors Q_1 and Q_2 are off and D_2 and D_3 are forward biased. In this operation mode, the inductor L_r is demagnetized and the operation mode ends when the inductor is fully demagnetized.

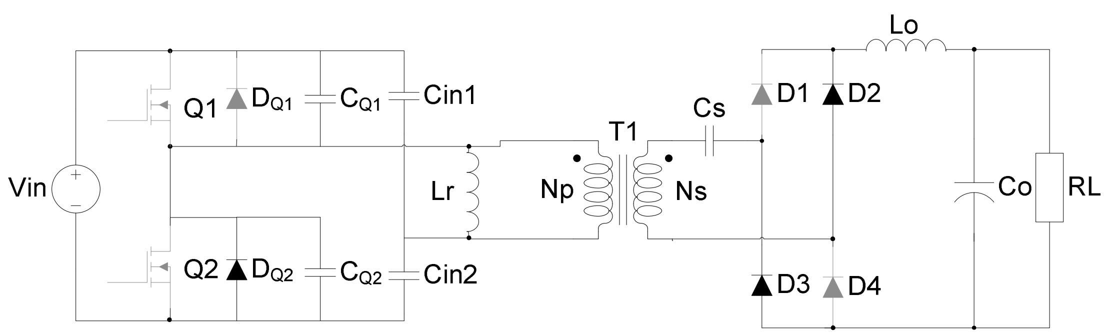

Fig. 4.32. A step-down half bridge RSC converter fifth operation mode.

In Fig. 4.33 the switching waveforms of the step-down half bridge are presented. Transistors Q_1 and Q_2 gate signals, the resonant current, iL_O, the secondary current through the transformer T_1 and the switched capacitor voltage across C_S waveforms are shown in Fig. 4.33.

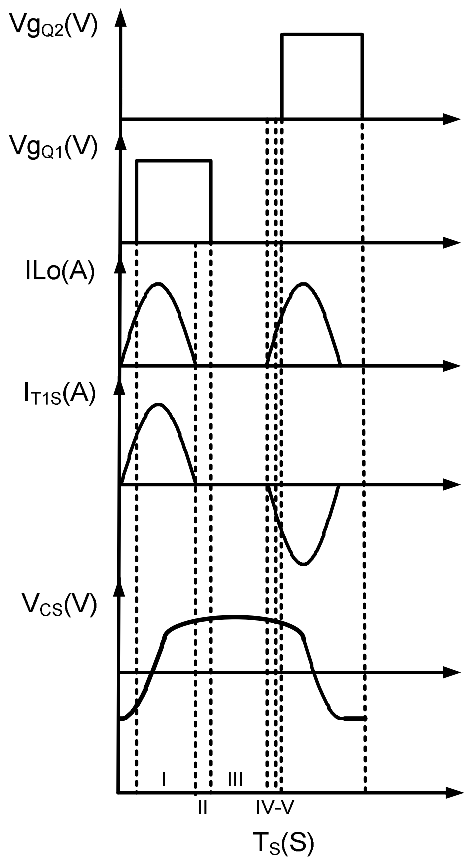

Fig. 4.33. Step-down half bridge RSC converter switching waveforms.

4.2.6. Step-down SC converter with coupling inductors

Step-down SC converter with coupling inductors are based on the conventional step-down SC converter, which includes two switches, Q_1 and Q_2, three diodes, D_1, D_2 and D_3, one switched capacitor, C_1, three coupling inductors, L_1, L_2 and L_3 and one output filter capacitor, C_O, as shown in Fig. 4.34 [148]. Coupling inductors L_1, L_2 and L_3, work in DCM operation based on Flyback transformer operation principles, in order to solve issues of switching losses and reduce peak current magnitudes on transistors, which leads to high power factor correction (PFC) in off-line applications, high efficiency and low EMI noise, as well as providing wide voltage conversion ratio. Output voltage ripple is also low for the same reasons as those in previously presented RSC converters with low output voltage ripple.

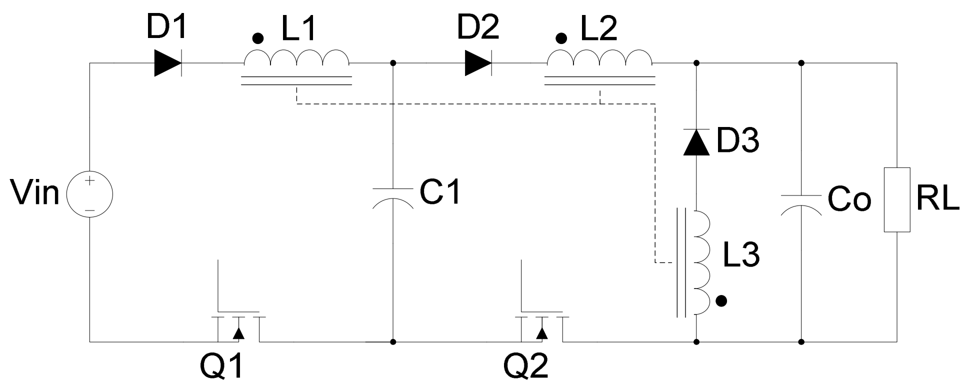

Fig. 4.34. Step-down RSC converter with coupling inductors.

In this converter, the average output power is limited by the capacitance of C_1, when considering constant input voltage, V_{in}, and switching frequency, f_S. Also, the output power keeps constant at different low output voltage values so that different load conditions can be applied without affecting output power. In addition, output voltage depends only on load parameters. Inductor L_3 works in DCM and delivers current to the load when the currents in L_1 and L_2, reach zero.

However, even though the step-down SC converter with coupling inductors works in DCM operation, efficiency is lower than all aforementioned RSC converters, except for conventional SC converters. Another drawback is the high dependency of output power on the input voltage.

4.3. Summary and comparison

SC converters present disadvantages of poor voltage conversion ratio and output voltage regulation as well as low efficiency and high EMI noise due to switching losses, which are caused by switched capacitor charge and discharge oscillatory currents, since these are only limited by the internal resistances of the devices.

The efficiency and the voltage conversion ratio of conventional RSC converters depend on the load conditions, being both lower as the load decreases, which is an important drawback of this type of SC converters.

FVCR RSC converters present the advantages of wide, fractional and quite constant voltage conversion ratio and constant efficiency, because the output voltage just varies a 10% when the output power varies a 400%. Also, the energy efficiency of the converter is quite constant at a different output power, except at very low output power. Therefore, the voltage conversion ratio and energy efficiency of the converter still depends on the load, even though the dependency is pretty small. In addition, lower output voltage ripple is provided in comparison with conventional RSC converters. Nevertheless, the power density of the converter is lower due to the extra components required.

DP RSC converters provide an output voltage more stable than conventional RSC converters because the output voltage ripple is half to those of conventional RSC converters. Their efficiency is high and constant under different load conditions, except at very light load. The output voltage ripple is quite low, similar to fractional RSC converters. However, it uses a second switched capacitor, which makes it more expensive and with lower power density.

MCB RSC converters present high and constant efficiency under different voltage conversion ratios. Another advantage against conventional RSC, FVCR RSC and DP RSC converters is that efficiency does not depend on voltage conversion ratio. Also, MCB RSC converters present the advantage of balance stage, which helps improve switching stress on the transistors. This is because the resultant charge energy balance into the switched capacitor is zero after charge and discharge switching periods. For instance in the conventional RSC converters, the resultant charge energy balance into the switched capacitor is not zero after charge and discharge switching periods. This way, the remaining energy on the switched capacitor avoids converging to the desired output voltage.

The step-down half-bridge RSC converter with isolation transformer presents the disadvantages of high output voltage ripple, efficiency dependency on voltage conversion ratio and low power density due to the fact that it breaks the nature of this type of SC and RSC converters that do not use or use small inductors or magnetics.

The step-down SC converter with coupling inductors presents very low efficiency and also, breaks the nature of this type of SC and RSC converters that do not use or use small inductors or magnetics. Another drawback is the high dependency of output power on the input voltage.

Table 4.2 shows a comparison of all SC converters performance, in terms of output voltage regulation, output voltage ripple, efficiency, efficiency dependency on conversion ratio, EMI noise and isolation and PFC capability. As can be seen, multi-configurable bidirectional RSC converters present the best performance compared to the other SC converters.

Table. 4.2. SC converters performance comparison

Type of SC converter	High output voltage regulation	Low output voltage ripple	High efficiency	No efficiency dependency on voltage conversion ratio	Low EMI noise	High power density	Isolation	PFC capability
Non-resonant SC	–	–	–	–	–	+	–	–
Conventional RSC	–	–	–	–	+	+	–	–
FVCR RSC	+	+	+	–	+	–	–	–
DP RSC	+	+	+	–	+	+	–	–
MCB RSC	+	+	+	+	+	+	–	–
Step-down HB RSC with isolation transformer	–	–	+	–	+	–	+	–
Step-down SC with coupling inductors	+	+	–	+	–	–	–	+

4.4. Conclusions

A comparison study of SC converter topologies have been carried out, showing that the MCB RSC converter arises as the most convenient topology for OLED lamp driving, in terms of efficiency, EMI noise, output voltage regulation, no efficiency dependency of the voltage conversion ratio, low output voltage ripple and high power density.

Based on the comparison results, this work will focus on the study of the MCB RSC converters. As first approach, the unidirectional RSC step-up converter will be tackled in order to drive OLED lamps.

5. Analysis and design of the URSC step-up converter

As discussed in the previous chapter, the URSC step-up converter is the best option to drive OLED lamps because it provides high output voltage regulation, low output voltage and current ripples, high efficiency, no efficiency dependency on conversion ratio, low EMI noise, and high power density [149]. Therefore, a detail explanation of operation and an analysis and design calculation of the URSC step-up converter are presented in this chapter. It is important to mention that the URSC step-up converter was studied to work in a different mode of operation, that is, switching and resonant frequencies ratio much lower than the unity as proposed in [143][144][150]. Under this condition, a good dynamic behavior against input voltage or luminous flux variations is obtained. Also, the piecewise linear modeling of the OLED lamp and the variable inductor (VI) parameters are analyzed.

5.1. Operation of the URSC step-up converter

The operation of the URSC step-up converter shown in Fig. 5.1 is explained in the following. The converter has four operation modes: charge, discharge, off and balance.

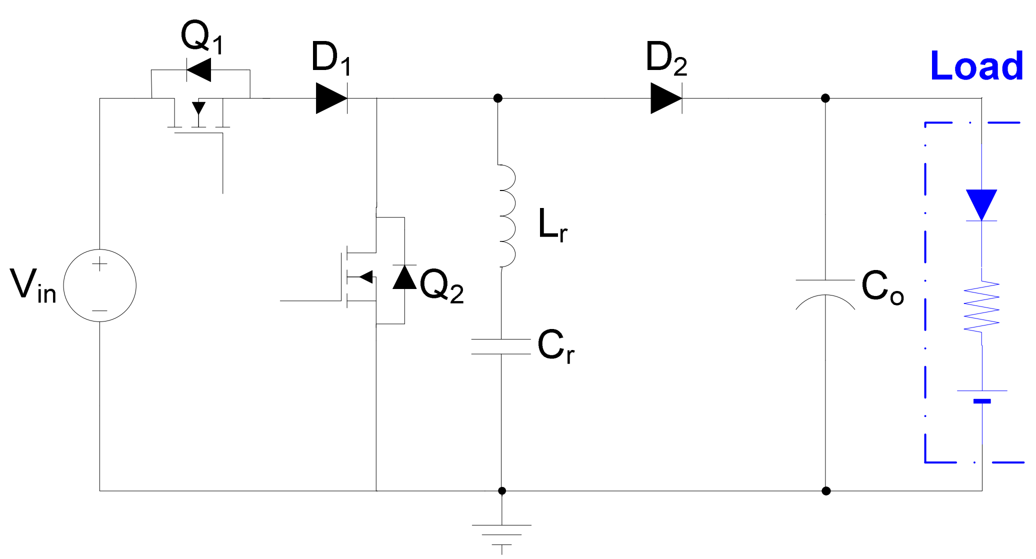

Fig. 5.1. URSC step-up converter.

5.1.1. Charge operation stage: t_0-t_1

Fig. 5.2 shows the equivalent circuit for charge operation stage. As can be seen, transistor Q_1, and diode D_1, are on, while transistor Q_2, and diode D_2 are off. The resonant capacitor C_r, is charged through, Q_1 and D_1, while the output filter capacitor C_O, is discharged to the load.

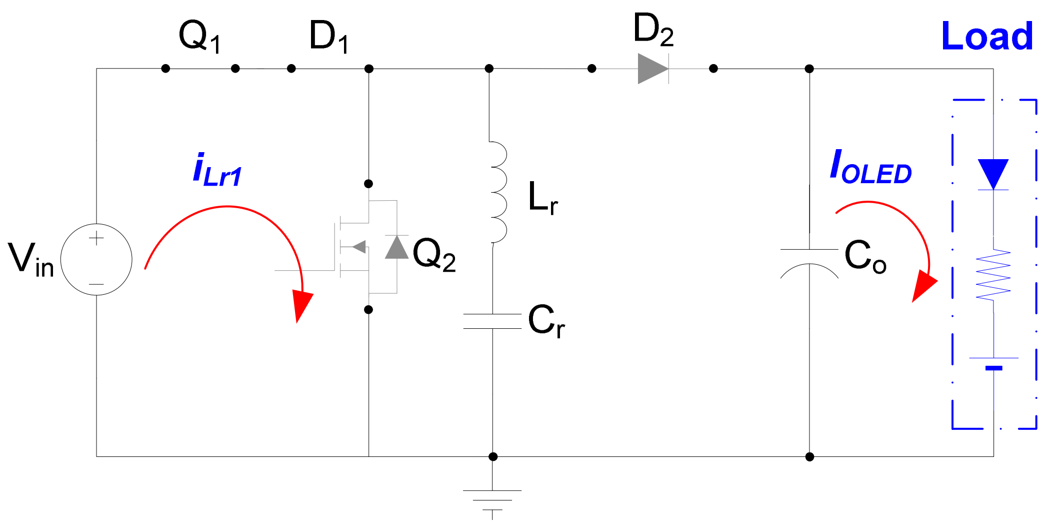

Fig. 5.2. Stage t_0-t_1.

It is important to mention that the resonant current i_{Lr} at the beginning of this stage is not zero due to the conduction period of the freewheeling diode of Q_2 in the balance stage.

5.1.2. Discharge operation stage: t_1-t_2

Fig. 5.3 illustrates the discharge operation stage, where transistors Q_1 and Q_2, and diode D_1 are off, while diode D_2, is on. The resonant capacitor C_r, is discharged through D_2, and the output filter capacitor C_O, is charged.

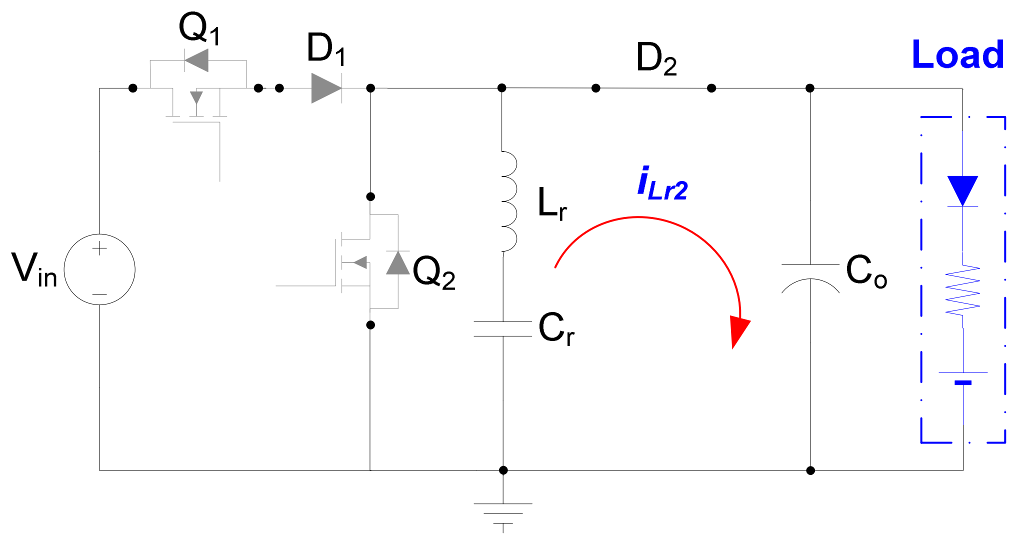

Fig. 5.3. Stage t_1-t_2.

5.1.3. *Off operation stage: t_2-t_3*

In this operation stage, transistors Q_1 and Q_2, and diodes D_1 and D_2, are off. The resonant inductor current i_{Lr} through $L_r - C_r$, is zero. Fig. 5.4 shows the off operation stage equivalent circuit.

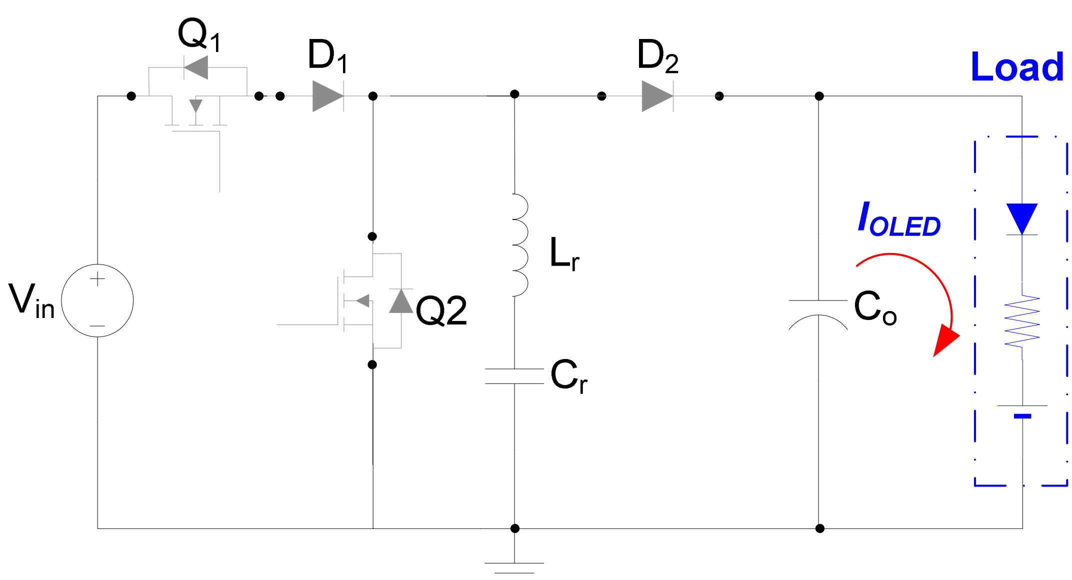

Fig. 5.4. Stage t_2-t_3.

5.1.4. Balance operation stage: t_3-t_5

The balance operation stage circuit is shown in Fig. 5.5. In which during t_3-t_4, transistor Q_1, and diodes D_1 and D_2, are off, while transistor Q_2 is on and the output filter capacitor C_O, keeps discharging to the load. The resonant tank, $L_r - C_r$, is shortcircuited in order to balance the energy stored in C_r, so that the same charge level as that at instant t_0 is attained for the next charge operation state. At the end of this stage during t_4-t_5, the current is flowing through Q_2 with reverse polarity. Thereby, transistors Q_1 and diodes D_1 and D_2, are off, while the resonant capacitor C_r is charged.

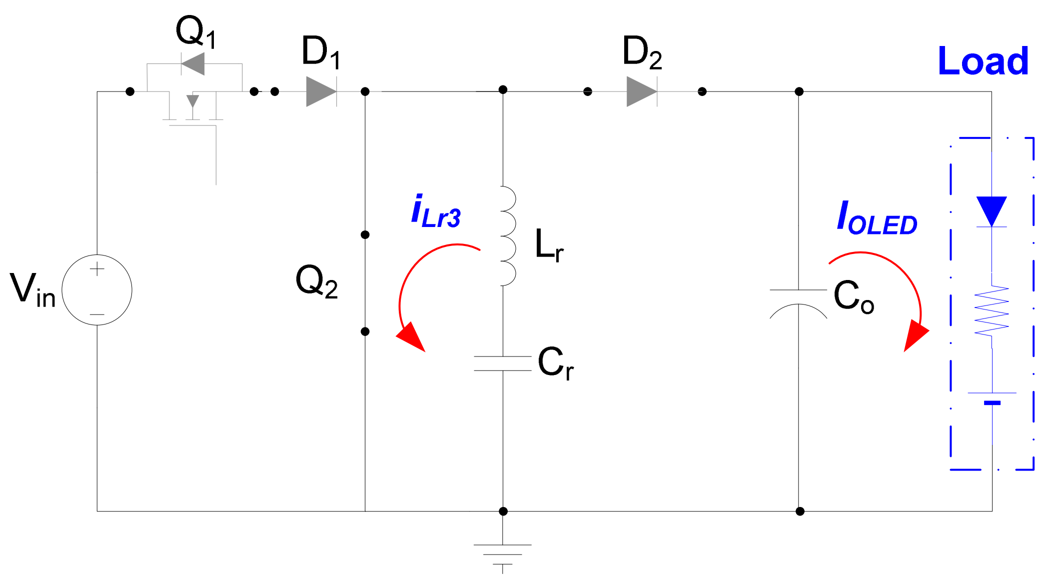

Fig. 5.5. Stage t_3-t_5.

The waveforms corresponding to each operation state of the URSC step-up converter are shown in the Fig. 5.6.

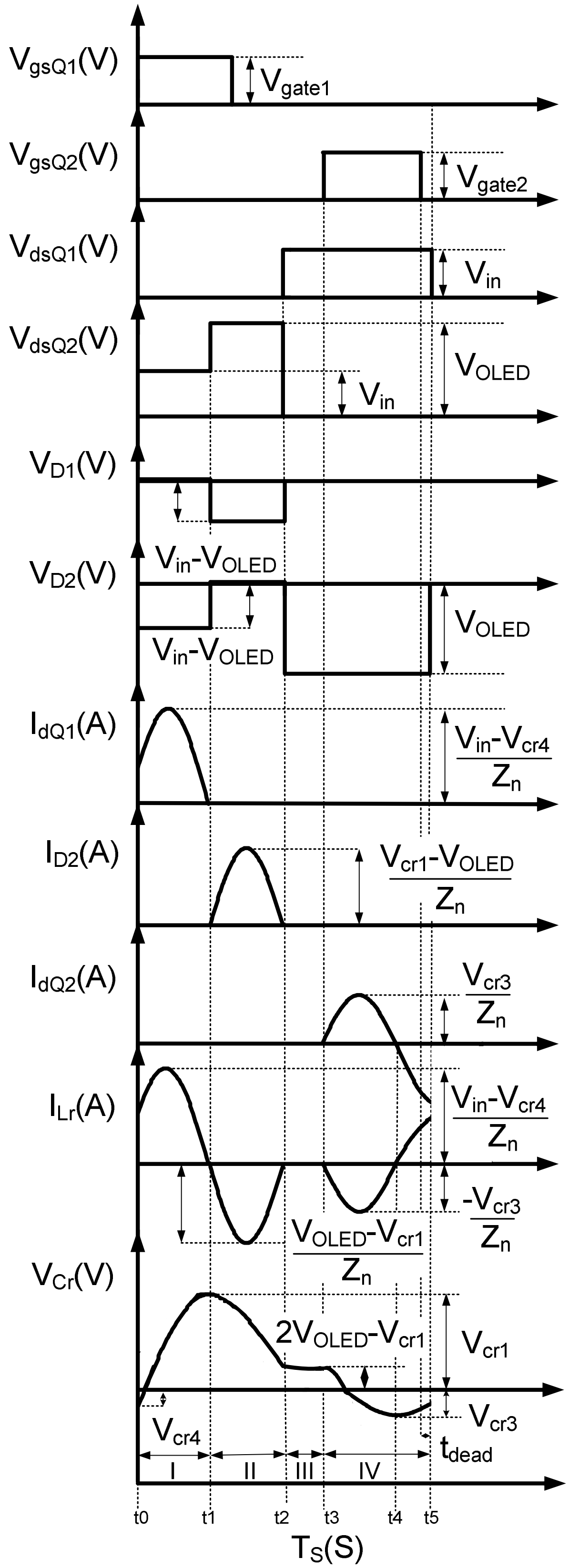

Fig. 5.6. Main waveforms of the RSC step-up converter during one switching period.

5.2. Analysis and design of the step-up converter

The theoretical analysis of the URSC step-up converter shown in Fig. 5.1 is carried out based on the methodology used in [143][144][150]. First, by analyzing the charge operation stage circuit shown in Fig. 5.2, the expressions (5.1) and (5.2) are obtained.

$$\frac{di_{Lr}}{dt} = \frac{V_{in} - V_{Cr}}{L_r} \tag{5.1}$$

$$\frac{dV_{Cr}}{dt} = \frac{i_{Lr}}{C_r} \tag{5.2}$$

Now, from (5.1) and (5.2) and after some manipulation, V_{Cr} is obtained in (5.3). Then, by substituting (5.3) into (5.2), and isolating and solving for i_{Lr}, (5.4) is obtained, which is the expression of the resonant inductor current i_{Lr}.

$$V_{Cr} = V_{in} - (V_{in} - V_{Cr}(0)) \cos \omega t \tag{5.3}$$

$$i_{Lr} = \frac{V_{in} - V_{Cr}(0)}{Z_n} \sin \omega t \tag{5.4}$$

Where V_{in} is the DC input voltage and Z_n is the equivalent resonant tank impedance as shown in (5.5).

$$Z_n = \sqrt{\frac{L_r}{C_r}} \tag{5.5}$$

Similarly, the circuits shown from Fig. 5.3 to Fig. 5.5 can be analyzed in order to obtain the expressions for V_{Lr} and I_{Cr}, which lead to the form of (5.3) and (5.4), where V_{in} takes the values of the DC OLED voltage V_{OLED} and 0, respectively. Based on the afore-mentioned procedure, (5.6) and (5.7) are found for the maximum V_{Cr} values at the end of discharge and t_3-t_4 balance operation stages by considering $\omega t = \pi$.

$$V_{Cr2} = 2V_{OLED} - V_{cr1} \tag{5.6}$$

$$V_{Cr3} = -V_{cr2} \tag{5.7}$$

Where V_{Cr1}, V_{Cr2} and V_{Cr3} are the capacitor C_r voltages at t_1, t_2 and t_4, respectively.

In addition, (5.4), (5.8), (5.9) and (5.10) show the obtained expressions for the resonant inductor current i_{Lr} for discharge and t_3-t_4 and t_4-t_5 balance operation stages:

$$i_{Lr} = \frac{V_{OLED} - V_{cr1}}{Z_n} \sin \omega t \quad when \quad t_1 < t < t_2 \tag{5.8}$$

$$i_{Lr} = \frac{-V_{cr2}}{Z_n} \sin \omega t \quad when \quad t_3 < t < t_4 \tag{5.9}$$

$$i_{Lr} = \frac{-V_{cr3}}{Z_n} \sin \omega t \quad when \quad t_4 < t < t_5 \tag{5.10}$$

The resonant frequency f_n is known as follows:

$$f_n = \frac{1}{2\pi\sqrt{L_r C_r}} \tag{5.11}$$

In this analysis, the resonant frequency f_m expression is used [2]-[4]:

$$f_m = \frac{1}{3\pi\sqrt{L_r C_r}} \tag{5.12}$$

The URSC step-up converter must operate under the condition shown in (5.13).

$$f_m > f_s \tag{5.13}$$

The time duration of $t_4 - t_5$ for the balance stage is obtained in (5.14) by considering that t_3-t_4 time interval duration is π and that t_3-t_5 time interval duration is one third of the inverse of the switching frequency f_s. Then, it is as follows:

$$t_4 - t_5 = \frac{\frac{1}{3f_s} - \pi\sqrt{L_r C_r}}{\sqrt{L_r C_r}} \tag{5.14}$$

In order to find the average balance current I_B during the t_3-t_4 and t_4-t_5 time intervals, which both integrate the total conduction time of the balance stage, the average balance currents from (5.9) and (5.10) are calculated to find their sum as shown in (5.15).

$$\langle I_B \rangle = -2V_{cr2} f_s C_r - V_{cr2} f_s C_r \left(\cos\left(\frac{\frac{1}{3f_s} - \pi\sqrt{L_r C_r}}{\sqrt{L_r C_r}} \right) - 1 \right) \tag{5.15}$$

The average OLED voltage V_{OLED} is defined from the OLED parameters as shown in (5.16).

$$V_{OLED} = I_{OLED} R_\gamma + V_\gamma \tag{5.16}$$

Then, in order to find the average input current I_{in}, the input/output energy balance is used, which involves the energy efficiency η, the input voltage V_{in}, the input current I_{in} and the OLED voltage V_{OLED} and OLED current I_{OLED}. The result is shown in (5.17).

$$I_{in} = \frac{I_{OLED}\left(I_{OLED} R_\gamma + V_\gamma\right)}{V_{in}\eta} \tag{5.17}$$

Also, by involving (5.18) and knowing that the average resonant inductor current in one complete cycle is zero, then (5.19) is obtained.

$$\langle i_{D2} \rangle = -I_{OLED} \tag{5.18}$$

$$I_{in} - I_{OLED} + I_B = 0 \tag{5.19}$$

Then, by substituting (5.15) and (5.17) in (5.19) and isolating for V_{cr2}, (5.20) is obtained.

$$V_{Cr2} = -\frac{I_{OLED} - \frac{I_{OLED}(I_{OLED}R_\gamma + V_\gamma)}{V_{in}\eta}}{2C_r f_s + C_r f_s \left(\cos\left(\frac{\frac{1}{3f_s} - \pi\sqrt{L_r C_r}}{\sqrt{L_r C_r}}\right) - 1\right)} \tag{5.20}$$

By inserting (5.6) in (5.20) and isolating for V_{cr1}, the capacitor C_r voltage level V_{cr1} is obtained as shown in (5.21).

$$V_{Cr1} = 2(I_{OLED}R_\gamma + V_\gamma) + \frac{I_{OLED} - \frac{I_{OLED}(I_{OLED}R_\gamma + V_\gamma)}{V_{in}\eta}}{2C_r f_s + C_r f_s \left(\cos\left(\frac{\frac{1}{3f_s} - \pi\sqrt{L_r C_r}}{\sqrt{L_r C_r}}\right) - 1\right)} \tag{5.21}$$

5.2.1. Resonant inductor calculation

The resonant inductor L_r is obtained by calculating the average of i_{Lr} from (5.8) and making it equal to (5.18) and then isolating for L_r, thereby the resonant inductor L_r is shown in (5.22).

$$L_r = \frac{\left(\frac{1}{3f_s}\right)^2}{C_r\left(\pi + 2\sin^{-1}\left(\frac{\sqrt{2C_r f_s V_\gamma + 2C_r f_s R_\gamma I_{OLED} - \frac{I_{OLED}(I_{OLED}R_\gamma + V_\gamma)}{V_{in}\eta}}}{\sqrt{2C_r f_s V_\gamma - I_{OLED} + 2C_r f_s R_\gamma I_{OLED}}}\right)\right)^2} \tag{5.22}$$

5.2.2. OLED current calculation

From (5.22), OLED current I_{OLED} is isolated, then (5.23) is obtained.

$$I_{OLED} = \frac{b\left(V_{in}\eta - V_{in}\eta R_\gamma c\right) + V_{in}\eta R_\gamma c - V_\gamma}{2R_\gamma} + \frac{\sqrt{\begin{array}{c} b^2\left({V_{in}}^2\eta^2{R_\gamma}^2c^2 - 2{V_{in}}^2\eta^2 R_\gamma c + {V_{in}}^2\eta^2\right) + \\ b\left(-2{V_{in}}^2\eta^2{R_\gamma}^2c^2 + 2{V_{in}}^2\eta^2 R_\gamma c - 2V_{in}\eta R_\gamma c V_\gamma - 2V_{in}\eta V_\gamma\right) \\ +{V_{in}}^2\eta^2{R_\gamma}^2c^2 + 2V_{in}\eta R_\gamma c V_\gamma + {V_\gamma}^2 \end{array}}}{2R_\gamma} \tag{5.23}$$

Where b and c are variables used to simplify the expression (5.23):

$$b = \left(\sin\left(\frac{\frac{1}{3f_s} - \pi\sqrt{L_rC_r}}{2\sqrt{L_rC_r}}\right)\right)^2 \tag{5.24}$$

$$c = 2C_rf_s \tag{5.25}$$

5.2.3. Output filter capacitor calculation

An important parameter to keep in mind in OLED drivers development is the dynamic resistance R_γ, which must be taken into consideration to properly select the output capacitance value, needed to achieve the desired OLED ripple current ΔI_{OLED} and ripple voltage ΔV_{OLED}. Therefore, it is possible to find an expression that relates the output filter capacitor C_o and the output voltage ripple ΔV_{OLED} in (5.26), to obtain the output capacitor value [143][144][150].

$$C_o = \frac{I_{OLED}}{\Delta V_{OLED}}\left(\frac{1}{f_s} - \frac{1}{3f_n}\right) \tag{5.26}$$

5.3. Design calculation of the URSC step-up converter

The design calculation of the URSC step-up converter for driving an OLED load is carried out in this section [143][144][150][151]. The OLED lamp load is formed by three FL300 OLED lamps in series array [31]. The operating DC OLED current I_{OLED} and voltage V_{OLED} values curve of the single FL300 OLED lamp at ambient temperature is illustrated in Fig. 5.7.

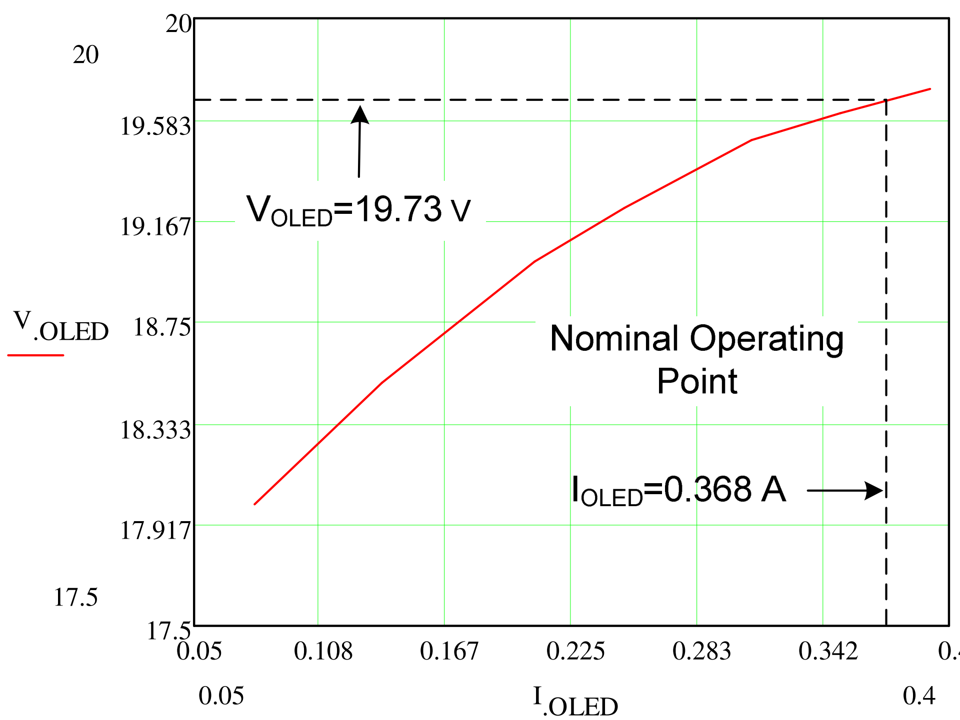

Fig. 5.7. Operating DC I_{OLED} and V_{OLED} values curve.

The nominal DC OLED current I_{OLED} and voltage V_{OLED} of the OLED load that consists of three FL300 OLED lamps in series array and the proposed input design parameters of the URSC step-up converter are shown in Table 5.1.

Table 5.1. Input design parameters of the URSC step-up converter.

Input voltage V_{in} (V)	**DC OLED voltage** V_{OLED} (V)	**Nominal OLED current** I_{OLED} (A)	**Nominal OLED power** P_{OLED} (W)	**Equivalent OLED resistance** R_{OLED} (Ω)	**voltage ripple** ΔV_{OLED} (%)	**current ripple** ΔI_{OLED} (%)	**Switch. freq.** f_S (kHz)	**Energy efficiency** η (%)
48	59.2	0.368	21.8	161	0.5	6.6	100	92.97

In addition to the input design parameters of the URSC step-up converter, it is necessary to know the dynamic resistance R_γ and the threshold voltage V_γ of the FL300 OLED load piecewise linear model. Then, the dynamic resistance R_γ and the threshold voltage V_γ of the single FL300 OLED lamp are calculated by means of the squares minimum linear regression approach [151].

The number of samples n_O in regards to the DC OLED voltage V_{OLED} and current I_{OLED} values shown in Fig. 5.7, is $n_O = 7$ in this calculation. The different DC OLED voltage V_{OLED} and current I_{OLED} values of the single FL300 OLED lamp are illustrated in Table 5.2.

Table 5.2. FL300 OLED lamp V_{OLED} and I_{OLED} values.

DC OLED voltage V_{OLED} (V)	**OLED current** I_{OLED} (A)
18	0.0783
18.5	0.1373
19	0.2082
19.22	0.25
19.5	0.3090
19.61	0.35
19.71	0.392

Owing to the DC OLED voltage V_{OLED} and current I_{OLED} values of the single FL300 OLED lamp are known, the threshold voltage V_γ of the single FL300 OLED lamp can be calculated from (5.27).

$$V_\gamma = \frac{\left[\sum I_{OLED}(I_{OLED}V_{OLED}) - \sum V_{OLED} \sum {I_{OLED}}^2\right]}{(\sum I_{OLED})^2 - n_O \sum {I_{OLED}}^2} \tag{5.27}$$

Then, from (5.27), the threshold voltage obtained is $V_\gamma = 17.737\,V$. On the other hand, the dynamic resistance R_γ is calculated as shown in (5.28).

$$R_\gamma = \frac{[n_O(I_{OLED}V_{OLED}) - \sum V_{OLED} \sum I_{OLED}]}{n_O\left(\sum {I_{OLED}}^2\right) - (\sum I_{OLED})^2} \tag{5.28}$$

The dynamic resistance calculated from (5.28) is $R_\gamma = 5.437\,\Omega$. Therefore, the equivalent dynamic resistance R_γ and the threshold voltage V_γ calculated for three FL300 OLED lamps in series are $R_\gamma = 16.312\,\Omega$ and $V_\gamma = 53.212\,V$, respectively. The equivalent DC OLED voltage V_{OLED} of the three FL300 OLED lamps in series array is expressed in function of the total dynamic resistance R_γ, the threshold voltage V_γ and the DC OLED current I_{OLED} in (5.29). And then, it is outlined in Fig. 5.8.

$$V_{OLED} = R_\gamma I_{OLED} + V_\gamma \tag{5.29}$$

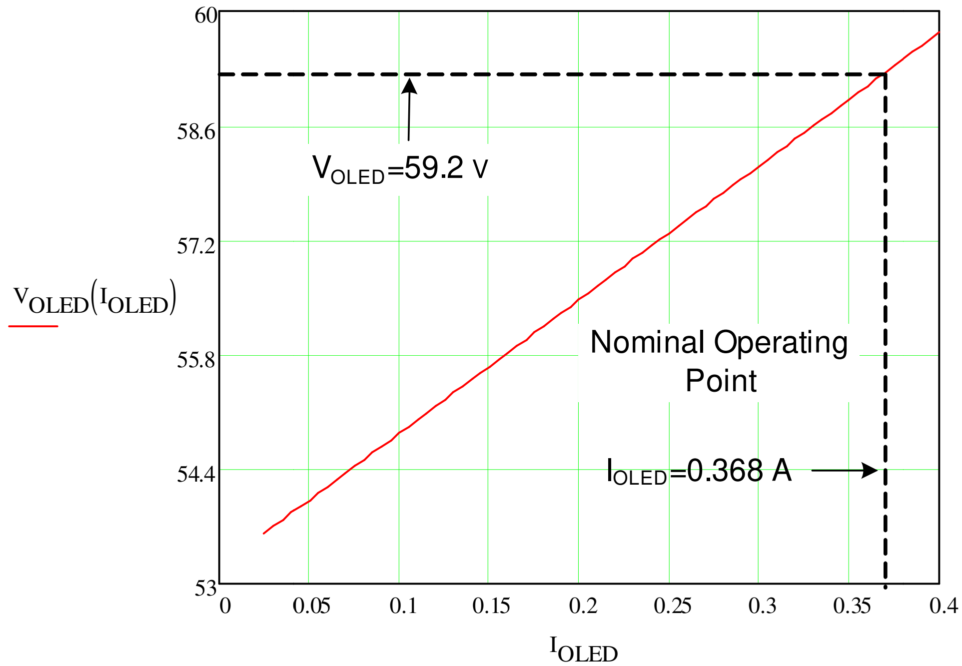

Fig. 5.8. Piecewise linear model DC V_{OLED}.

The equivalent DC OLED resistance at nominal power R_{OLED} is obtained by dividing V_{OLED} between I_{OLED}. Therefore, $R_{OLED} = 161\ \Omega$. The FL300 OLED lamp is illustrated in Fig. 5.9.

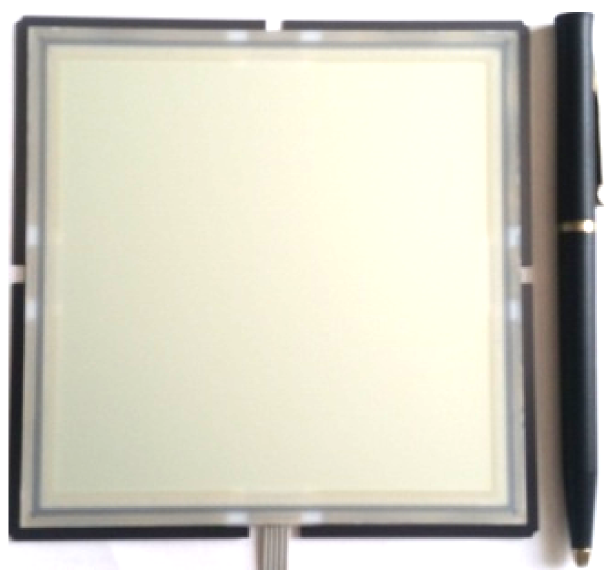

Fig. 5.9. FL300 OLED lamp.

Since all input design parameters are described, the capacitor voltage V_{cr2} from (5.20) can be calculated. The proposed capacitor value is $C_r = 46.2\ nF$, in order to find the capacitor voltage V_{Cr2}, which is $V_{Cr2} = 19.39\ V$. On the other hand, the capacitor voltage V_{Cr1} is calculated from (4.21) as $V_{Cr1} = 99.02\ V$.

The resonant inductor L_r is obtained from (5.22) as $L_r = 12.64\ \mu H$ and then, the tank impedance is calculated from (5.5) as $Z_n = 16.54\ \Omega$. The resonant frequency f_m is then calculated from (5.12) as $f_m = 138.9$ kHz.

The output filter capacitor C_o is obtained from (5.26) as $C_o = 10$μ. A summary of the calculated voltages, currents and component values of the URSC step-up converter is shown in Table 5.3.

Table 5.3. Design calculation summary of the URSC step-up converter.

Resonant capacitor C_r (nF)	**Resonant inductor** L_r (μH)	**Output filter capacitor** C_o (μF)	**Tank impedance** Z_n (Ω)	**Resonant frequency** f_m (kHz)	**OLED threshold voltage** V_γ (V)	**OLED dynamic resistance** R_γ (Ω)
46.2	12.64	10	16.54	138.9	53.212	16.312

5.4. Dimensioning of power semiconductors of the URSC step-up converter

In this section, the dimensioning of the switching diodes and transistors of the URSC step-up converter is tackled owing to the fact that it is important to know the diodes' and transistors' maximum electrical operating ratings demanded by the URSC step-up converter in order to ensure a good performance of the converter by operating them in a safe operation region. Based on this fact, the appropriate selection of diodes' and transistors' can be carried out. Therefore, operating these devices within the data-sheets limits assures safe and reliable operation of the converter. Note that a thermal analysis of the devices such as the case temperature, or junction temperature is not addressed in this work.

Transistor Q_1 calculation

The maximum drain current I_{Dp_Q1} circulating through the transistor Q_1 during the interval t_0-t_1 in the charge operation stage must be calculated as illustrated in (5.31), in order to know the maximum operating drain current of transistor Q_1. Owing to V_{cr4} is needed to calculate (5.31), V_{cr4} is obtained based on (5.3). Hence, V_{cr4} is shown in (5.30).

$$V_{Cr4} = 0 - (0 - V_{Cr3}) \cos\left(\frac{\frac{1}{3f_s} - \pi\sqrt{L_r C_r}}{\sqrt{L_r C_r}}\right) \tag{5.30}$$

$$I_{Dp\_Q1} = \frac{V_{in} - V_{cr4}}{Z_n} \tag{5.31}$$

From section 5.3 and Table 5.3, V_{cr1}= 99.02 V, V_{in}= 48 V and Z_n= 16.54 Ω are obtained. In this way, V_{cr4}= -6.63V and I_{Dp_Q1}= 3.3 A.

The average drain current I_{Davg_Q1} through the transistor Q_1 during the interval t_0-t_1 is calculated as shown in (5.32).

$$I_{Davg\_Q1} = \frac{I_{OLED}\left(I_{OLED} R_\gamma + V_\gamma\right)}{V_{in}\eta} \tag{5.32}$$

From Table 5.1 and Table 5.3, R_γ= 16.312 Ω, V_γ= 53.212 V and I_{OLED}=0.368 A are obtained. The average drain current calculation is I_{Davg_Q1}= 0.488 A.

On the other hand, the maximum operating drain-source voltage of Q_1 V_{DS_Q1} demanded by the URSC converter is V_{in}, as illustrated in Fig. 5.6. Hence, V_{DS_Q1}= 48 V.

Diode D₁ calculation

In this calculation section, it is not necessary to calculate maximum and average diode D_1 currents, because they are the same as those calculated average and maximum transistor Q_1 drain currents, owing to the fact that D_1 and Q_1 operate at the same time in charge operation stage as shown in Fig. 5.2. Therefore, I_{Dp_D1}= 3.3 A and I_{Davg_D1}= 0.488 A. In regards to the maximum reverse operating voltage of D_1 in the URSC converter, it is V_{R_D1}= $V_{in} - V_{OLED}$= 11.2 V as illustrated in Fig. 5.6.

Diode D_2 calculation

The maximum diode current I_{Dp_D2}, which circulates through the diode D_2 during the interval t_1-t_2 in the discharge operation stage is calculated as follows:

$$I_{Dp\_D2} = \frac{V_{cr1} - V_{OLED}}{Z_n} \tag{5.33}$$

Likewise, V_{OLED}= 59.2 V and V_{cr1}= 99.02 V are obtained from Table 5.1 and section 5.3 respectively, in order to calculate (5.33). The calculation result is I_{Dp_D2}= 2.4 A. The average diode current I_{Davg_D2} is calculated from (5.23), so that, I_{Davg_D2}=0.368 A.

On the other hand, the maximum reverse operating voltage of D_2 is V_{R_D2}= V_{OLED}= 59.2 V as depicted in Fig. 5.6.

Transistor Q_2 calculation

The maximum drain current I_{Dp_Q2} circulating through the transistor Q_2 during the interval t_3-t_4 in the balance operation stage is calculated by using (5.34). Note that V_{cr3}=V_{cr2} in terms of capacitor voltage magnitude, as mentioned in section 5.2.

$$I_{Dp\_Q2} = \frac{V_{cr3}}{Z_n} \tag{5.34}$$

Then, from section 5.3, V_{cr2}=19.39 V. Based on this, the calculation result is I_{Dp_Q2}= 1.2 A.

The average drain current I_{Davg_Q2} through the transistor Q_2 during the interval t_3-t_4 is calculated based on (5.15). However, (5.15) is simplified, owing to the fact that just the maximum drain current of the transistor Q_2 in the interval t_3-t_4 of the interval t_3-t_5 of the balance operation stage is investigated. Hence, I_{Davg_Q2} is calculated as the following:

$$I_{Davg\_Q2} = 2V_{cr2}f_sC_r \tag{5.35}$$

From Table 5.1 and Table 5.3, C_r= 46.2 nF and f_s= 100 kHz are obtained. So that, the calculation result is I_{Davg_Q2}= 0.18 A.

Regarding the maximum operating drain-source voltage of Q_2 V_{DS_Q2} in the URSC converter, it is V_{DS_Q2}= V_{OLED} as shown in Fig. 5.6. Thereby, V_{DS_Q2}= 59.2 V.

A summary of the calculation results of the maximum and average currents of transistors Q_1 and Q_2 and diodes D_1 and D_2 is shown in Table 5.4.

Table 5.4. Summary of maximum and average currents of Q_1 and Q_2 and D_1 and D_2.

Max drain current I_{Dp_Q1} $(\boldsymbol{A})$	**Average drain current** I_{Davg_Q1} $(\boldsymbol{A})$	**Max drain current** I_{Dp_Q2} $(\boldsymbol{A})$	**Average drain current** I_{Davg_Q2} $(\boldsymbol{A})$	**Max diode current** I_{Dp_D1} $(\boldsymbol{A})$	**Average diode current** I_{Davg_D1} $(\boldsymbol{A})$	**Max diode current** I_{Dp_D2} $(\boldsymbol{A})$	**Average diode current** I_{Davg_D2} $(\boldsymbol{A})$
3.3	0.488	1.2	0.18	3.3	0.488	2.4	0.368

Likewise, a summary of the calculation results of the maximum drain and reverse voltages of transistors Q_1 and Q_2 and diodes D_1 and D_2 is illustrated in Table 5.5.

Table 5.5. Calculation summary of maximum drain voltages of $Q_1$and Q_2 and reverse voltages of D_1 and D_2.

Drain-source voltage V_{DS_Q1} $(\boldsymbol{V})$	**Drain-source voltage** V_{DS_Q2} $(\boldsymbol{V})$	**Reverse voltage** V_{R_D1} $(\boldsymbol{V})$	**Reverse voltage** V_{R_D2} $(\boldsymbol{V})$
48	59.2	11.2	59.2

Since the maximum ratings of current and voltage of the transistors Q_1 and Q_2 and switching diodes D_1 and D_2 have been calculated, Q_1 and Q_2 and D_1 and D_2 can be selected. In addition, it is important to take into consideration two important parameters of transistor and diode components, as they are on-resistance R_{DSon} in the transistor and forward voltage V_f in the switching diode, due to these two factors affect the energy efficiency of the URSC converter, based on the fact that this converter is considered to have only conduction losses, according to the principle of operation under ZCS. Also note that in order to increase the power density of the URSC converter, a surface mounted device (SMD) transistor and a SMD diode are proposed to be used.

Based on the aforementioned information about maximum current and voltage ratings and some important parameters of power components to consider, the parameters of the proposed and available transistor and switching diode used in the URSC converter are shown in Table 5.6 and Table 5.7.

Table 5.6. Electrical parameters of the SMD transistor BUK7613-100E.

Drain current I_D $(\boldsymbol{A})$	**Drain-source voltage** V_{DS} $(\boldsymbol{V})$	**On-Resistance** R_{DSon} $(\boldsymbol{m\Omega})$	**Input capacitance** C_{iss} $(\boldsymbol{nF})$	**Saturation current** I_s $(\boldsymbol{pA})$	**Ideality factor** n
72	100	13	3.3	0.6766	1

Table 5.7. Electrical parameters of the SMD Schottky diode MBR20100CT.

Reverse voltage V_R $(\boldsymbol{V})$	**Average forward current** $I_{f(AV)}$ $(\boldsymbol{A})$	**Peak forward current** $I_{f(Peak)}$ $(\boldsymbol{A})$	**Forward voltage** V_f $(\boldsymbol{V})$	**Saturation current** I_{s1} $(\boldsymbol{\mu A})$	**Ideality factor** n
100	10	20	0.77	10	1.5

Note that information in regards to the reverse recovery time of the Schottky diode MBR20100CT is not available from the suppliers' datasheet.

5.5. Energy efficiency analysis

The energy efficiency η parameter of the URSC converter can be obtained by calculating the RMS current of each individual operation stage of the URSC converter. In this way, it is necessary to calculate the RMS current value of each individual operation stage as they are charge, discharge and balance from (5.8), (5.9), (5.10) and (5.31).

However, beforehand, it is needed to calculate the average of the maximum input current of the interval t_0-t_1 by using (5.31). Afterwards, isolate for θ, which is the magnitude in radians of the angle θ involved to calculate I_{rms1} of the charge stage. In this way, the expression obtained for θ is as follows:

$$\theta = \cos^{-1}\left(\frac{I_{in}}{f_s C_r\left(V_{in} + V_{cr2}\cos\left(\frac{\frac{1}{3f_s}-\pi\sqrt{L_r C_r}}{\sqrt{L_r C_r}}\right)\right)} - 1\right) \tag{5.36}$$

In the following, the RMS current of the charge operation stage is shown. It is clear that I_{rms1} is calculated in the angular frequency interval duration from θ to π. Therefore, I_{rms1} is obtained by calculating (5.31) as shown below in (5.37).

$$I_{rms1} = g\sqrt{\frac{f_s C_r}{Z_n}.\left(\frac{\pi}{2} + \frac{\sin\left(2\cos^{-1}\left(\frac{I_{in}}{f_s C_r g} - 1\right)\right)}{4} - \frac{\cos^{-1}\left(\frac{I_{in}}{f_s C_r g} - 1\right)}{2}\right)} \tag{5.37}$$

Where g is a variable used to simplify the expression (5.37):

$$g = \left(V_{in} + V_{cr2}\cos\left(\frac{\frac{1}{3f_s} - \pi\sqrt{L_r C_r}}{\sqrt{L_r C_r}}\right)\right) \tag{5.38}$$

On the other hand, the RMS current of the discharge operation stage is calculated by using (5.8). Thereby, I_{rms2} is obtained in (5.39).

$$I_{rms2} = \sqrt{\frac{f_s C_r}{Z_n}.\frac{\pi}{2}.}\,(V_{OLED} - V_{cr1}) \tag{5.39}$$

In (5.40) and (5.41), I_{rms3} and I_{rms4} are obtained from (5.9) and (5.10), respectively. I_{rms3} and I_{rms4} are the equivalent RMS current of the balance operation stage. Note that I_{rms3} and I_{rms4} sum the RMS current of the balance operation stage during the intervals of operation t_3-t_4 and t_4-t_5 of the transistor Q_2 in order to calculate the power losses dissipated across the R_{DSon}.

$$I_{rms3} = \sqrt{\frac{f_s C_r}{Z_n} . \frac{\pi}{2} . (V_{cr2})} \tag{5.40}$$

$$I_{rms4} = \sqrt{\frac{f_s C_r {V_{cr2}}^2}{Z_n} . \left(\frac{\pi}{2} + \frac{\sin\left(2\left(\frac{\frac{1}{3f_s} - \pi\sqrt{L_r C_r}}{\sqrt{L_r C_r}}\right)\right)}{4} - \frac{\frac{1}{3f_s} - \pi\sqrt{L_r C_r}}{2\sqrt{L_r C_r}} \right)} \tag{5.41}$$

An additional expression to define the average input current I_{in} is needed in order to continue this calculation. So that, rearranging (5.19), (5.42) is obtained.

$$I_{in} = I_{OLED} + 2C_r V_{cr2} f_s + C_r V_{cr2} f_s \left(\cos\left(\frac{\frac{1}{3f_s} - \pi\sqrt{L_r C_r}}{\sqrt{L_r C_r}} \right) - 1 \right) \tag{5.42}$$

Transistor Q_1 and Q_2 power dissipation

The transistor power dissipation calculation is carried out by considering power conduction and switching power losses as well known. However, in this calculation switching conduction losses are neglected based on the fact that this URSC converter works under ZCS condition. In this way, the power dissipation calculation of the transistors Q_1 and Q_2 will just take into consideration, conduction losses and gate power losses due to the fact that it is necessary to control de switching speeds of the transistors, which improves the switching behavior, even though, it causes a slight power loss.

Therefore, the power conduction losses of the transistor Q_1 and Q_2 and any other device that has a parasitic resistance involved through the current flow path are calculated based on (5.43).

$$P_{cond} = {I_{rms}}^2 R \tag{5.43}$$

Then, the power conduction losses of the transistor Q_1 and Q_2 are expressed in the following.

$$P_{cond\_Q1} = g^2 \frac{f_s C_r R_{DSon}}{Z_n} . \left(\frac{\pi}{2} + \frac{\sin\left(2\cos^{-1}\left(\frac{I_{in}}{f_s C_r g} - 1\right)\right)}{4} - \frac{\cos^{-1}\left(\frac{I_{in}}{f_s C_r g} - 1\right)}{2} \right) \tag{5.44}$$

$$P_{cond\_Q2} = {V_{cr2}}^2 R_{DSon} \frac{f_s C_r}{Z_n} . \left(\pi + \frac{\sin\left(2\left(\frac{\frac{1}{3f_s} - \pi\sqrt{L_r C_r}}{\sqrt{L_r C_r}}\right)\right)}{4} - \frac{\frac{1}{3f_s} - \pi\sqrt{L_r C_r}}{2\sqrt{L_r C_r}} \right) \tag{5.45}$$

On the other hand, the gate power losses of the transistor Q_1 and Q_2 are expressed as the following [152].

$$P_{gate} = {V_{GS}}^2 f_s . (C_{iss} + C_{GS}) \tag{5.46}$$

Diode D_1 and D_2 power dissipation

The Schottky diode equation shown in (5.47) is used to calculate the forward voltage V_f of the diodes D_1 and D_2 at a certain forward current of operation owing to the fact that it offers a better accuracy to obtain the forward voltage than using the threshold voltage of the diode [76]. Note, it is considered to operate the diodes at ambient temperature condition.

$$V_f = nV_T \ln\left(\frac{I_f}{I_s} + 1\right) \tag{5.47}$$

Where: V_T is the thermal voltage, n is the diode ideality factor or emission coefficient, I_f is the forward current of operation and I_s is the saturation current.

In this way, the power diode losses of the diodes D_1 and D_2 are calculated in (5.48) and (5.49).

$$P_{D1} = I_{in} nV_T \ln\left(\frac{I_{in}}{I_s} + 1\right) \tag{5.48}$$

$$P_{D2} = I_{OLED} nV_T \ln\left(\frac{I_{OLED}}{I_s} + 1\right) \tag{5.49}$$

Passive components power dissipation

The power dissipation across the capacitor C_r and inductor L_r, which are connected in series, are calculated based on the expression (5.50), because the RMS current that flows through C_r and L_r are equal in each operation stage, as they are charge, discharge and balance. Note that the power losses of the C_o capacitor are neglected in this analysis, due to the fact that it is assumed that the output current is constant and the voltage ripple is neglected as worked in [143][144].

$$P_{Cr\_Lr} = I_{rms1}^2 R_{LC} + I_{rms2}^2 R_{LC} + I_{rms3}^2 R_{LC} + I_{rms4}^2 R_{LC} \tag{5.50}$$

Thus, by substituting (5.37), (5.39), (5.40) and (5.41) into the expression (5.50), which lays down that the sum up of each operation state power losses across the passive components C_r and L_r, yields the total power dissipation; which is denoted by the square RMS current values: I_{rms1}, I_{rms2}, I_{rms3} and I_{rms4} times total stray resistance R_{LC} across the passive components C_r and L_r as shown in (5.51).

$$P_{Cr\_Lr} = R_{LC}\left(g^2 \frac{f_s C_r}{Z_n} . \left(\frac{\pi}{2} + \frac{\sin\left(2\cos^{-1}\left(\frac{I_{in}}{f_s C_r g} - 1\right)\right)}{4} - \frac{\cos^{-1}\left(\frac{I_{in}}{f_s C_r g} - 1\right)}{2} \right) \right.$$
$$+ \frac{f_s C_r}{Z_n} . \frac{\pi}{2} (V_{OLED} - V_{cr1})^2 + \frac{f_s C_r}{Z_n} . \frac{\pi}{2} (V_{cr2})^2 \qquad (5.51)$$
$$\left. + \frac{f_s C_r {V_{cr2}}^2}{Z_n} . \left(\frac{\pi}{2} + \frac{\sin\left(2\left(\frac{\frac{1}{3f_s} - \pi\sqrt{L_r C_r}}{\sqrt{L_r C_r}}\right)\right)}{4} - \frac{\frac{1}{3f_s} - \pi\sqrt{L_r C_r}}{2\sqrt{L_r C_r}} \right) \right)$$

Where R_{LC} is:

$$R_{LC} = R_{Lr} + R_{Cr} \qquad (5.52)$$

Another important aspect to take into consideration in this analysis, is the magnetic losses of the inductor L_r. Then, it is necessary to use an expression that calculates the core losses, which is in function of the magnetic flux density and switching frequency at the operating point as needed. In this way, the Steinmetz equation is proposed to calculate the core losses P_{core} of L_r. The Steinmetz expression is illustrated in (5.53) [153].

$$P_{core} = aB^b {f_s}^c \qquad (5.53)$$

Where: a, b and c are the Steinmetz coefficients, B is the magnetic flux density and f_s is the switching frequency.

Concerning the Steinmetz a, b and c coefficients, they are obtained from the expression (5.53) by means of the curve fitting toolbox in Matlab and by entering the suppliers' information regarding effective volume V_e, relative core losses P_v, magnetic flux density B, core loss P_{core} and switching frequency f_s as shown in Table 5.8 and Table 5.9. A calculation comparison between the P_{core} obtained from the suppliers' datasheet and the P_{core} obtained from the Steinmetz expression are illustrated in Fig. 5.10. As it is shown, a good matching is obtained between both calculation results.

Table 5.8. N87 EFD25 material datasheet information.

Effective volume V_e $(\boldsymbol{mm^3})$	**Relative core losses** P_v $(\boldsymbol{W/mm^3})$	**Flux density** B $(\boldsymbol{T})$	**Core losses** P_{core} $(\boldsymbol{mW})$
3310	4.35x10e^{-6}	0.025	14.4
-	7 x10e^{-6}	0.03	23.2
-	15 x10e^{-6}	0.04	49.7
-	25 x10e^{-6}	0.05	82.8
-	37.5 x10e^{-6}	0.06	124
-	55 x10e^{-6}	0.07	182
-	75 x10e^{-6}	0.08	248
-	100 x10e^{-6}	0.09	331
-	135 x10e^{-6}	100	447
-	200 x10e^{-6}	125	662
-	300 x10e^{-6}	150	993
-	450 x10e^{-6}	175	1490
-	600 x10e^{-6}	200	1990

Table 5.9. Steinmetz coefficients.

a	$\boldsymbol{b}$	$\boldsymbol{c}$
1.866	2.211	0.3136

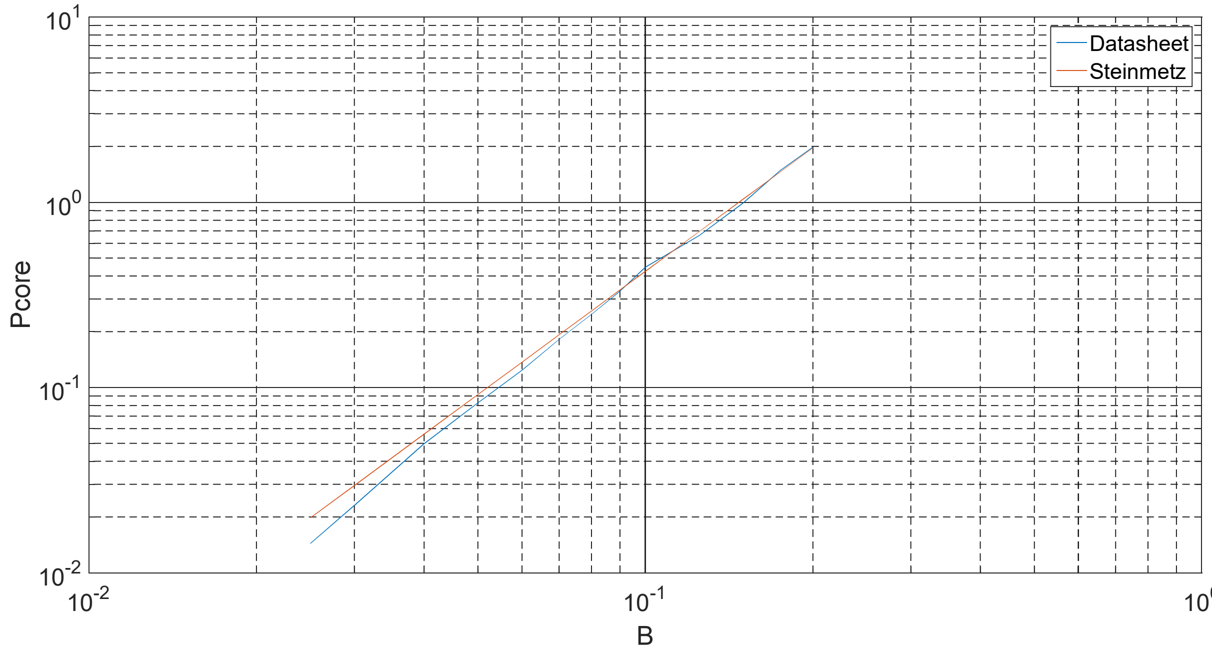

Fig. 5.10. P_{core} under different B operating points and constant f_s.

In addition, the power losses caused by the feedback resistor involved in the closed loop system of the URSC converter are included in this calculation. A basic expression that calculates the power in the resistor is shown in (5.54).

$$P_{fres} = {I_{OLED}}^2 R_f \tag{5.54}$$

In this point, the total power loss P_{loss} defined by the sum of all the power dissipations calculated in each active or passive component that integrate the URSC converter is shown in (5.55).

$$P_{loss} = P_{cond\_Q1} + P_{cond\_Q2} + P_{gate} + P_{D1} + P_{D2} + P_{Cr\_Lr} + P_{core} + P_{fres} \tag{5.55}$$

Also, the OLED power P_{OLED} is expressed in (5.56).

$$P_{OLED} = I_{OLED}\left(I_{OLED} R_\gamma + V_\gamma\right) \tag{5.56}$$

As last step, substitute (5.44) to (5.46), (5.48), (5.49), (5.51), (5.53) and (5.54) into (5.55). And then, since (5.55) is already solved, substitute (5.55) and (5.56) into (5.57), which is the expression that calculates the electrical energy efficiency η. In this way, the electrical energy efficiency η expression is illustrated in (5.58).

$$\eta = \frac{P_{OLED}}{P_{OLED} + P_{loss}} \tag{5.57}$$

$$\eta = \frac{I_{OLED}\left(I_{OLED}R_{\gamma} + V_{\gamma}\right)}{\begin{gathered} I_{OLED}\left(I_{OLED}R_{\gamma} + V_{\gamma}\right) + g^{2}\frac{f_s C_r R_{DSon}}{Z_n}.\left(\frac{\pi}{2} + \frac{\sin\left(2\cos^{-1}\left(\frac{I_{in}}{f_s C_r g}-1\right)\right)}{4} - \frac{\cos^{-1}\left(\frac{I_{in}}{f_s C_r g}-1\right)}{2}\right) + \\ {V_{cr2}}^{2}R_{DSon}\frac{f_s C_r}{Z_n}.\left(\pi + \frac{\sin\left(2\left(\frac{\frac{1}{3f_s}-\pi\sqrt{L_r C_r}}{\sqrt{L_r C_r}}\right)\right)}{4} - \frac{\frac{1}{3f_s}-\pi\sqrt{L_r C_r}}{2\sqrt{L_r C_r}}\right) + 2{V_{GS}}^{2}f_s.\left(C_{iss}+C_{GS}\right) + \\ I_{in}nV_T\ln\left(\frac{I_{in}}{I_s}+1\right) + I_{OLED}nV_T\ln\left(\frac{I_{OLED}}{I_s}+1\right) + \\ R_{LC}\left(\begin{gathered} g^{2}\frac{f_s C_r}{Z_n}.\left(\frac{\pi}{2} + \frac{\sin\left(2\cos^{-1}\left(\frac{I_{in}}{f_s C_r g}-1\right)\right)}{4} - \frac{\cos^{-1}\left(\frac{I_{in}}{f_s C_r g}-1\right)}{2}\right) + \frac{f_s C_r}{Z_n}.\frac{\pi}{2}\left(V_{OLED}-V_{cr1}\right)^{2} \\ + \frac{f_s C_r}{Z_n}.\frac{\pi}{2}\left(V_{cr2}\right)^{2} + \frac{f_s C_r {V_{cr2}}^{2}}{Z_n}.\left(\frac{\pi}{2} + \frac{\sin\left(2\left(\frac{\frac{1}{3f_s}-\pi\sqrt{L_r C_r}}{\sqrt{L_r C_r}}\right)\right)}{4} - \frac{\frac{1}{3f_s}-\pi\sqrt{L_r C_r}}{2\sqrt{L_r C_r}}\right) \end{gathered}\right) + \\ aB^{b}{f_s}^{c} + {I_{OLED}}^{2}R_f \end{gathered}} \tag{5.58}$$

Where:

$$I_{in} = I_{OLED} + 2C_r V_{cr2} f_s + C_r V_{cr2} f_s\left(\cos\left(\frac{\frac{1}{3f_s} - \pi\sqrt{L_r C_r}}{\sqrt{L_r C_r}}\right) - 1\right) \tag{5.59}$$

$$g = \left(V_{in} + V_{cr2} \cos\left(\frac{\frac{1}{3f_s} - \pi\sqrt{L_r C_r}}{\sqrt{L_r C_r}} \right) \right) \tag{5.60}$$

Recalling the input and calculated design parameters shown in Table 5.1, Table 5.3 and section 5.3 and section 5.4 for solving (5.58) as well as entering the following parameters: $V_T = 26\,mV$, $C_{GS} = 10\,nF$, $R_f = 1\Omega$, $B = 0.095\,T$ and $V_{GS} = 11.82\,V$, the electrical energy efficiency η obtained for the nominal I_{OLED} of the URSC converter, is $\eta = 93.4$.

5.6. Variable inductor (VI)

In this work, the variable inductor (VI) control technique is employed to drive the OLED current I_{OLED} of the URSC step-up converter. The VI structure is presented in Fig. 5.11. The VI operation is as follows: a DC current bias I_{dc} is injected through the auxiliary windings N_{dc1} and N_{dc2}, which are connected with reverse polarity in order to cancel the AC voltage component generated across them. The DC flux bias $\emptyset_{dc}$ circulating through the outer arms of the magnetic core generated by the injected DC current bias I_{dc} biased the operating point of the magnetic material in the $B - H$ curve, working very close to the saturation knee. This DC flux bias $\emptyset_{dc}$ modifies the variable reluctances of the material, which makes a change in the main winding N_p inductance [154][155]. Some literature about VI basics, simulation models and applications are presented in [156]-[180].

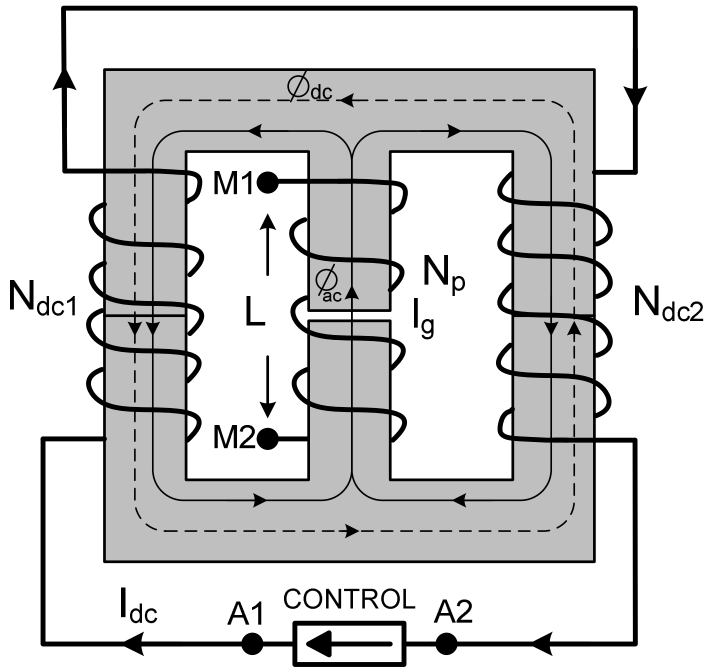

Fig. 5.11. Variable inductor structure.

The VI reluctance model is shown in Fig. 5.12. It consists of the variable reluctances $\Re_c, \Re_l$ and $\Re_r$, the constant reluctance $\Re_g$ and the magnetomotive forces F_{dc} and F_p. The variable reluctances magnitudes $\Re_c, \Re_l$ and $\Re_r$ depend on the operating point of the magnetic material that is settled by the injected DC current bias to the auxiliary windings. $\Re_c, \Re_l$ and $\Re_r$ are in function of the magnetic permeability μ of the magnetic material. The constant reluctance magnitude $\Re_g$ is depending on the central air gap of the magnetic structure and the magnetomotive forces F_{dc} and F_p magnitudes depend on the number of turns of the windings N_{dc} and N_p and the current magnitudes I_{dc} and I_p, respectively. The variable reluctances $\Re_c, \Re_l$ and $\Re_r$ model the non-linear behavior of the magnetic material.

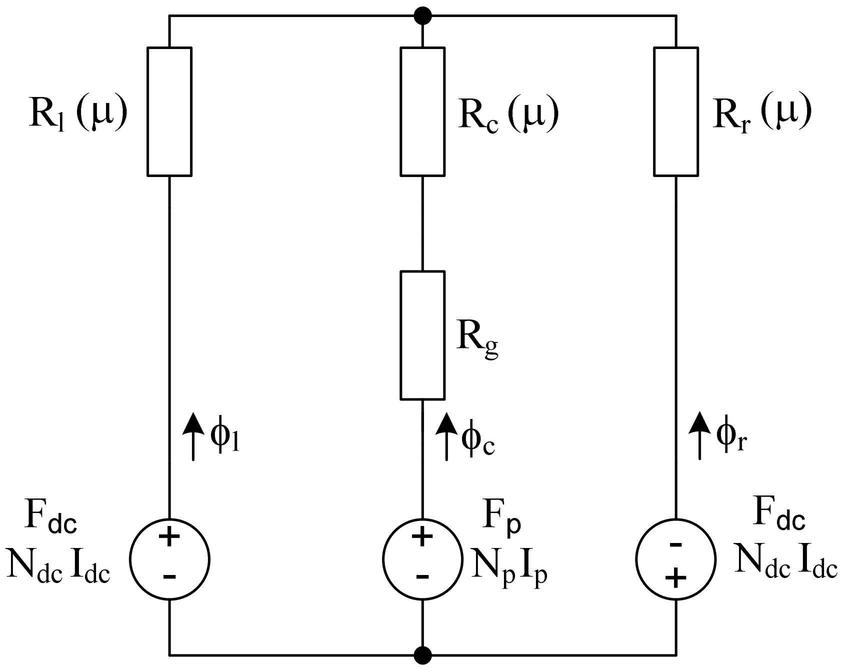

Fig. 5.12. VI equivalent reluctance model.

5.6.1. Constant reluctance model

The constant reluctance $\mathfrak{R}_0$ models the behavior of the non-ferromagnetic section of the magnetic structure, namely, the air gap of the magnetic core and it is represented by a resistance. The constant reluctance is calculated as shown in (5.61).

$$\mathfrak{R}_0 = \frac{l_0}{\mu_0 A_0 \nu} \tag{5.61}$$

Where, l_0 is the magnetic path length and A_0 is the cross section area of the constant reluctance $\mathfrak{R}_0$, which is on the central arm of the magnetic core. μ_0 is the permeability of the free space and ν is the fringing factor, which takes into consideration the phenomenon in which the magnetic flux flowing in a magnetic core spreads out into the surrounding medium as in the vicinity of the air gap.

5.6.2. Variable reluctance model

As it was already discussed, the variable reluctance $\Re_m$ models the non-linear behavior of the magnetic material used. Then, the variable reluctance $\Re_m$ is calculated from (5.62).

$$\Re_m(\mu) = \frac{l_m}{\mu(B)A_m} \tag{5.62}$$

Where, l_m is the magnetic path length and A_m is the cross section area of the variable reluctance $\Re_m$, which is on the outer arms of the magnetic core. $\mu(B)$ is the magnetic permeability of the material and it is in function of the magnetic flux density of the material. This is so because the variable reluctance $\Re_m$ is in function of the magnetic permeability $\mu(B)$ and it depends of the operation point inside the $B - H$ curve. In [154][155] it was proposed to use Brauer's expression to model $B - H$ curve. This model relates the magnetic field intensity H and the magnetic flux density B as shown in (5.63).

$$H(B) = \left(k_1 e^{k_2 B^2} + k_3\right)B \tag{5.63}$$

Where, k_1, k_2 and k_3 are the Brauer's coefficients of the magnetic material.

On the other hand, the differential magnetic permeability $\mu(B)$ is found by calculating (5.64).

$$\mu(B) = \frac{dB}{dH} \tag{5.64}$$

Therefore, from (5.63) and (5.64), (5.65) is shown below:

$$\mu(B) = \left[k_1(1 + 2k_2B^2)e^{k_2B^2} + k_3\right]^{-1} \tag{5.65}$$

The Brauer's coefficients k_1, k_2 and k_3 shown in Table 4.10 are obtained from the TDK-EPCOS N87 material datasheet [181]. The coefficients are recommended for $25°C$ ambient temperature.

Table 5.10. Brauer's coefficients for N87 material at $25°C$.

Coefficient	Value
k_1	$0.062\ Am^{-1}T^{-1}$
k_2	$42.995\ T^{-2}$
k_3	$302.904\ Am^{-1}T^{-1}$

5.6.3. Winding model

The winding model is represented by expressions (5.66) and (5.67), which define the electrical and magnetic interaction of the magnetic structure.

$$\mathcal{F}_w(t) = N_w \cdot i_w(t) \tag{5.66}$$

$$v_w(t) = N_w \cdot \frac{d\emptyset_w(t)}{dt} = N_w A_w \frac{dB_w(t)}{dt} \tag{5.67}$$

Where, $\mathcal{F}_w$ is the magnetomotive force, N_w is the number of turns of the winding, i_w is the current of the winding, v_w is the voltage of the winding, $\emptyset_w$ is the magnetic flux, A_w is the cross section area of the magnetic core and B_w is the magnetic flux density.

5.6.4. VI model elements

The variable reluctance model is illustrated in Fig. 5.13. It consists of a behavioral voltage source E_m that emulates the resistive behavior of the variable reluctance under certain magnetic flux $\emptyset_R$ flow. The behavioral current source G_{mb} represents the magnetic flux density magnitude, which is converted into voltage across the parallel resistor at node B_m. The behavioral current source G_{mu} represents the magnetic permeability magnitude of the material, and then it is converted into voltage across the parallel resistor at node U_m.

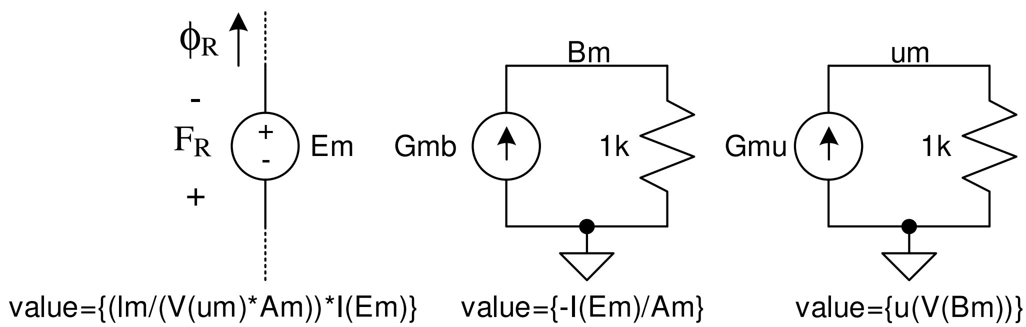

Fig. 5.13. Variable reluctance model.

The winding model is shown in fig. 5.14. It consists of the magnetic and electrical parts. The electrical part is integrated by a voltage dependent voltage source EV_w, whose dependency in voltage magnitude comes from the magnetic flux $\emptyset_w$ flowing through the winding N_w, owing to the fact that the number of turns N of the winding is constant. The behavioral voltage source EF_w represents the magnetomotive force in the magnetic part and the behavioral current source GV_w represents the magnetic flux density magnitude. The $1m\Omega$ resistor is used to avoid convergence issues.

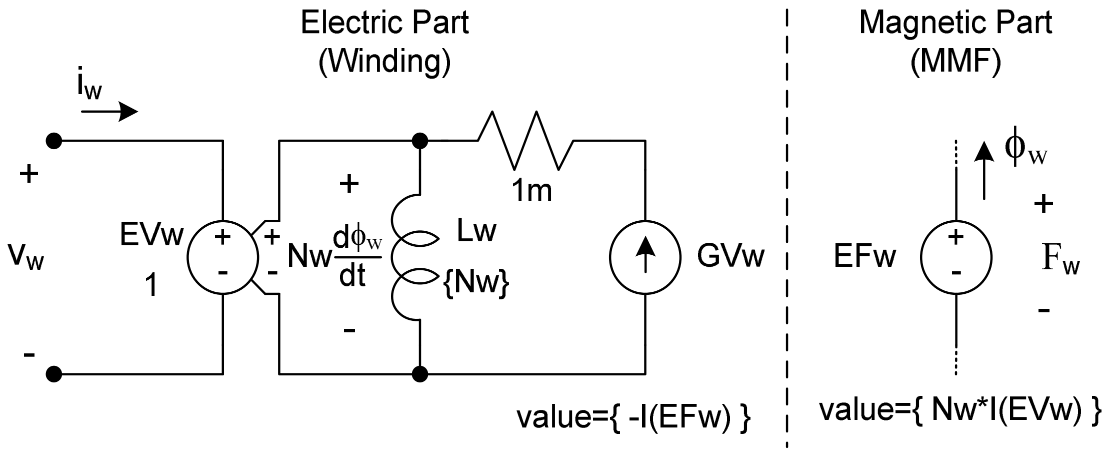

Fig. 5.14. Winding model.

5.7. Conclusions

The analysis and design of the URSC step-up converter for driving an OLED lamp load of three FL300 OLED lamps has been addressed in this chapter. In addition, of the study of the URSC step-up converter, the objective of finding an expression that relates the variable inductance and the OLED lamp current I_{OLED} is achieved. In this way, the OLED lamp current I_{OLED} can be controlled and dimmed by the VI, while the URSC step-up converter is controlled by means of the switching frequency.

6. Simulation and experimental analysis

Since the analysis and design of the URSC converter was carried out in the chapter 5 [143][144][150], now the simulation and experimental study of the URSC step-up converter OLED driver can be tackled. The LTspice software simulator is used to achieve the open and closed loop URSC step-up converter simulations for driving an OLED load under the VI control technique [182]. Moreover, the VI model proposed for this OLED driver is simulated. Also, the small signal characteristics of the VI inductor built are studied by making several experimental measurements using a laboratory test circuit [183]-[185].

6.1. Design of the laboratory prototype

A laboratory prototype for validating the performance of the URSC step-up OLED driver based on VI technique for OLED lamps is implemented as shown in Fig. 6.1. The OLED driver is integrated by the URSC converter + VI, the operational subtractor based on LM358A op-amp, theLM358B proportional-integral (PI) controller, the constant current source LM358C+PBSS4540Z and the PWM driver based on PIC12HV615.

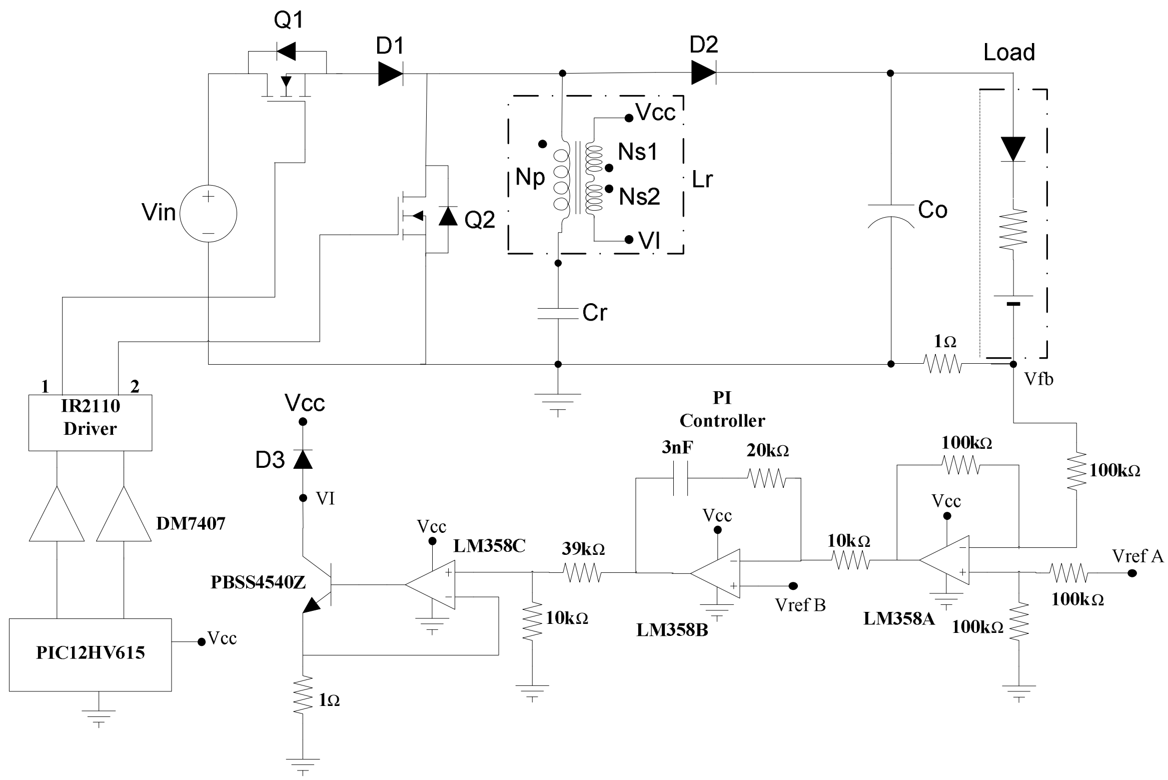

Fig. 6.1. Schematic diagram of laboratory prototype.

In Table 6.1, the list of materials for the laboratory prototype implementation is included according to the component values calculations in Chapter 5 [181][186]-[192].

Table 6.1. Components list of the laboratory prototype.

Reference	Description
Q_1, Q_2	BUK7613-100E FET Transistors
D_1, D_2	MBR20100CT Schottky Diodes
C_r C_{r1}, C_{r2}, C_{r3}, C_{r4}, C_{r5} C_{r6}	$C_{r1} \| C_{r2} \| C_{r3} \| C_{r4} \| C_{r5} + C_{r6}$ PHE450RD5100J10nF, 650V Capacitor 15nF J 1000V 378 MKP Capacitor
L_r	EFD 25/13/9 Inductor Np=11T, 66x0.08mm Ns1=Ns2=63T, 35AWG GAP=0.57 mm
C_o	ECQE2106KFB10uF, 250V Capacitor

A brief performance explanation of the closed loop URSC step-up OLED driver prototype based on VI shown in Fig. 6.2 is presented in the following.

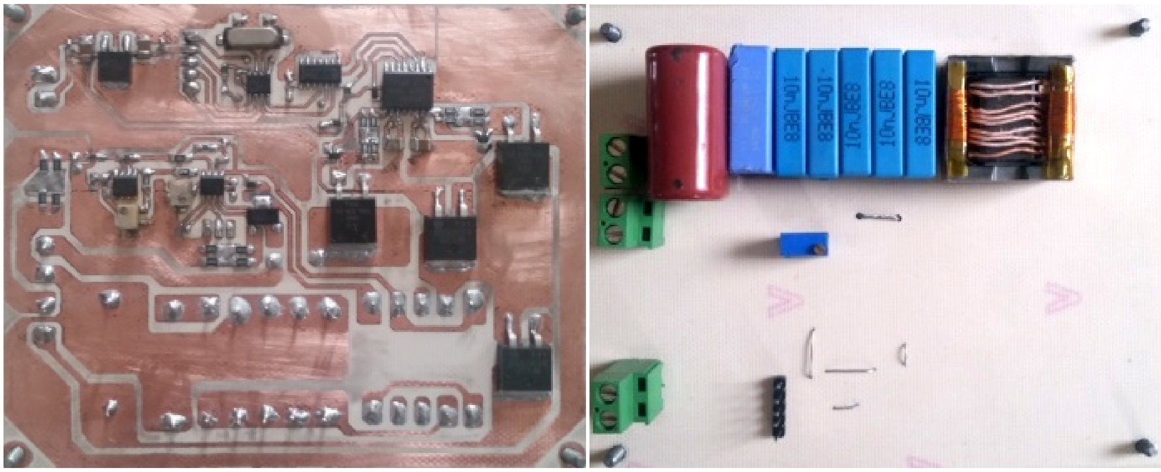

Fig. 6.2. URSC laboratory prototype.

The control operation of the URSC step-up OLED driver is achieved as follows: the microcontroller PIC12HV615 generates the 5V PWM signals for transistors Q_1 and Q_2 at a switching frequency f_S of 100 kHz, with an on time of one third of the switching period, and they both are out of phase for 180 degrees according to the principle of operation of the URSC step-up OLED driver. Open collector DM7407 buffers take charge of supplying 12V PWM signals to the high-low side driver IR2110 driver, which is in charge of commanding transistors Q_1 and Q_2.

The operational subtractor based on LM358A op-amp senses, through the negative input terminal, the average OLED current I_{OLED} from a 1Ω resistor placed in series with the load, in order to subtract the feedback voltage V_{fb} from the reference voltage V_{refA}, which is equal to $V_{refB} + V_{I_{OLED}}$, because V_{fb} is never equivalent to V_{refB} as needed by the error amplifier LM358B to bias the VI and obtain the desired OLED current I_{OLED}. Then, the subtractor output $V_{refA} - V_{fb}$ adequate its output voltage to follow V_{refB} reference voltage value to that DC bias current that finds the resonant inductor value L_r for fulfilling the average OLED current I_{OLED}.

The voltage V_{refB} is the equivalent in DC bias current and the voltage $V_{I_{OLED}}$ is the equivalent in OLED current I_{OLED}.

In order to compensate average OLED current I_{OLED} changes from input voltage variations or load steps down and up, a PI controller defined as in (6.1) is proposed [193].

$$G_C(s) = k_c \frac{1 + s/2\pi f_z}{s} \tag{6.1}$$

Nonetheless, a modeling of the system to attain a frequency response analysis of the URSC step-up converter in cascade with PI controller is not tackled in this work; it will be undertaken in a future work.

The resulting voltage from the operational LM358A subtractor is then compared to the voltage reference V_{refB} to set the average OLED current I_{OLED}. Then, LM358B PI controller compensates the error voltage between the resulting voltage of the subtractor and V_{refB}. The output signal of the controller is then applied to the constant current source LM358C + PBSS4540Z to supply an adequate control bias current to the VI.

Then, it is clear that OLED current I_{OLED} is well regulated against input voltage V_{in} and DC OLED voltage V_{OLED} variations under the following operation conditions of the VI: (a) L_r is decreased in value when $V_{fb} > V_{I_{OLED}}$, that is, when I_{OLED} is increased and (b) L_r is increased in value when $V_{fb} < V_{I_{OLED}}$, that is, when I_{OLED} is decreased, owing to the two subtractions in the closed loop control shown in Fig. 6.1, that is $V_{refA} - V_{fb} = \left(V_{refB} + V_{I_{OLED}}\right) - V_{fb}$ and $\left(V_{refB} + V_{I_{OLED}} - V_{fb}\right) - V_{refB} = V_{I_{OLED}} - V_{fb}$.

6.2. VI model simulation

The schematic of the electrical-magnetic VI model is illustrated in Fig. 6.3 in order to implement the VI model simulation under the design conditions optimized for the URSC step-up converter operation control before integrating the VI model + URSC step-up converter system. It consists of the non-linear reluctors ui, uc and ur, the air gap ug, the linear reluctor uk and the windings $U1, U2$ and $U3$. The VI design parameters are calculated and found in the Attachments of this dissertation [183]-[185].

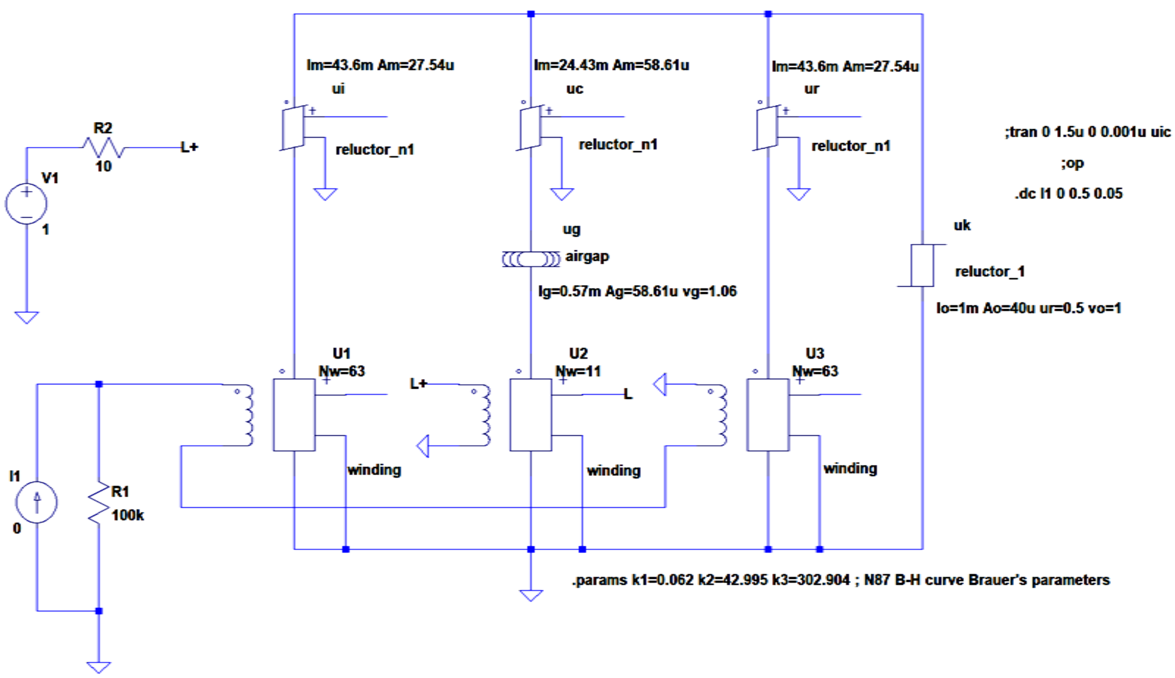

Fig. 6.3. Schematic of the magnetic-electrical VI model.

The Spice symbols, the electrical equivalent circuits and the Spice models of the electrical-magnetic VI circuit are described in Table 6.2. The expressions that define the airgap ug, linear reluctor uk, non-linear reluctors ui, uc and ur and windings $U1$, $U2$ and $U3$ are defined in Chapter 5.

Table 6.2. Spice symbols and models of the electrical-magnetic model of VI.

LTspice Symbol	Equivalent Circuit	Spice Model
Air Gap 	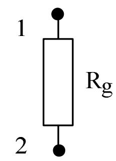	;AIRGAP .subcktairgap 1 2 ; vg, fringing factor ; lg, length ; Ag, area .param pi=3.1415926 .param u0=4*pi*1e-7 Rg 1 2 {lg/(u0*Ag*vg)} .ends airgap
Linear Reluctor 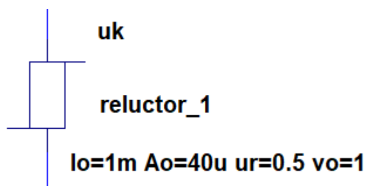	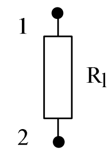	; LINEAR RELUCTOR .subckt reluctor_1 1 2 ; vo, fringing factor ; ur, relative permeability ; lo, length ; Ao, area .param pi=3.1415926 .param u0=4*pi*1e-7 Rr1 1 2 {lo/(ur*u0*Ao*vo)} .ends reluctor_1
Non-linear Reluctor 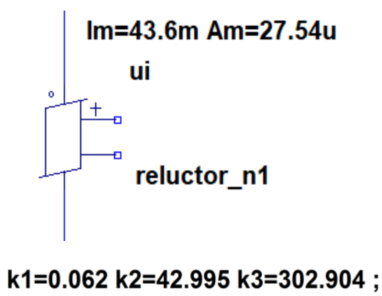	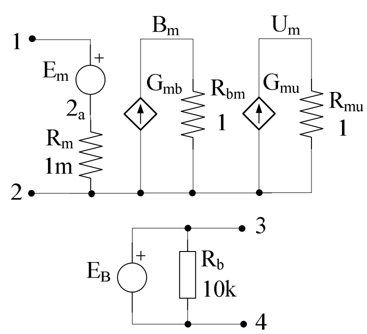	;NON-LINEAR RELUCTOR .subckt reluctor_n1 1 2 3 4 ; 2, positive mmf pin ; 1, negative mmf pin ; 3, 4, B output ; lm, length, Am, area ; k1, k2, k3, material ; coefficients according to ; Brauer's approximation .funcud(B) {1/(k1* +(1+2*k2*B*B)*exp(k2*B*B)+k3)} ;differential permeability Em 1 2a +value={(lm/(V(um,2)*Am))*I(Em)} Rm 2a 2 1m; small resistance to ; avoid voltage loop Gmb 2 Bm value={I(Em)/Am} Rbm Bm 2 1 Gmu 2 um value={ud(V(Bm,2))} Rmu um 2 1 ; B Output EB 3 4 value={V(Bm,2)} RB 3 4 10k .ends reluctor_n1
Winding 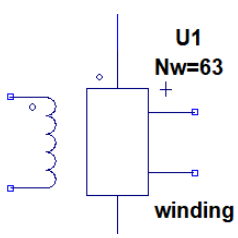	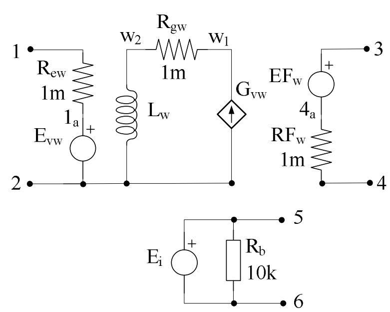	;WINDING .subckt winding 1 2 3 4 5 6 ; 1,2 electric pins ; 3,4 magnetic pins ; 5,6 inductance value pins ; Nw, number of turns ; magnetic part EFw 3 4a value={Nw*I(EVw)} RFw 4a 4 1m ;small resistance to ;avoid voltage loop ;electric part GVw 2 w1 value={-I(EFw)} Rgw w1 w2 1m Lw w2 2 {Nw} EVw 1a 2 value={V(w2,2)} Rew 1 1a 1m ;to avoid voltage loop ;inductance calculation Ei 5 6 value={-Nw*I(EFw)/I(EVw)} Ri 5 6 10k .ends winding

The simulation results of the VI model proposed for the URSC step-up converter are shown in Fig. 6.4. The inductance value of L_r vs DC bias current curve of the VI is shown. As can be observed, the DC bias current is set to run from 0 mA to 500 mA and the VI value ranges from 5.8 μH to 15.78 μH. The operation nominal inductance value is 12.64 μH as calculated in Chapter 5.

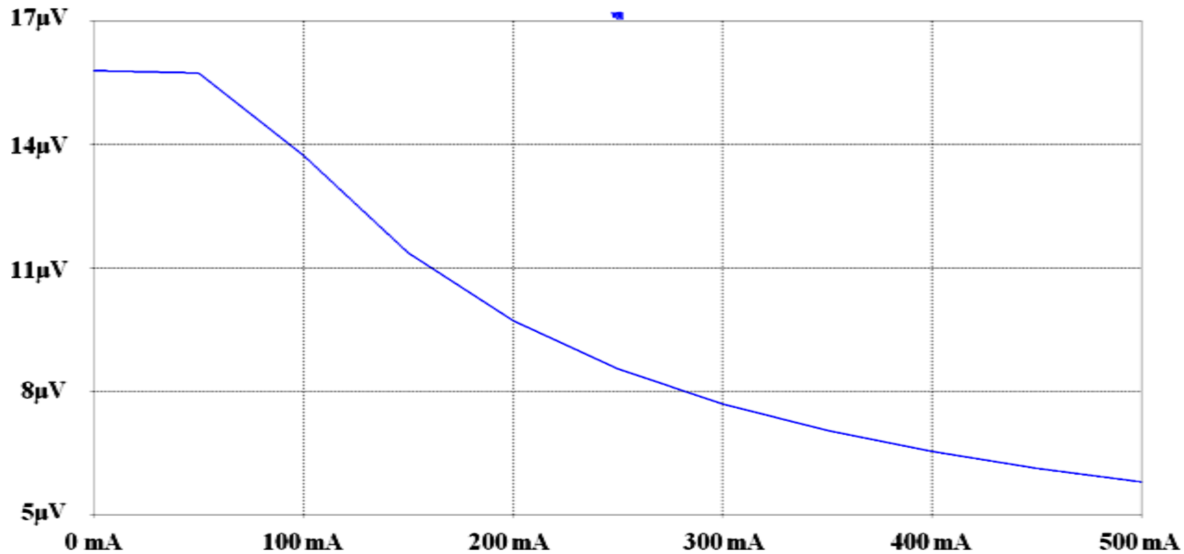

Fig. 6.4. Inductance vs DC bias current curve of the VI inductor simulation (3 μV/div and 100 mA/div).

6.3. URSC step-up converter + VI model Simulation

The schematic of the URSC step-up converter closed loop + VI model for driving an OLED load consists of three sections, which are the URSC step-up converter, the VI electrical-magnetic model and the constant current source + PI controller as shown in Fig. 6.5.

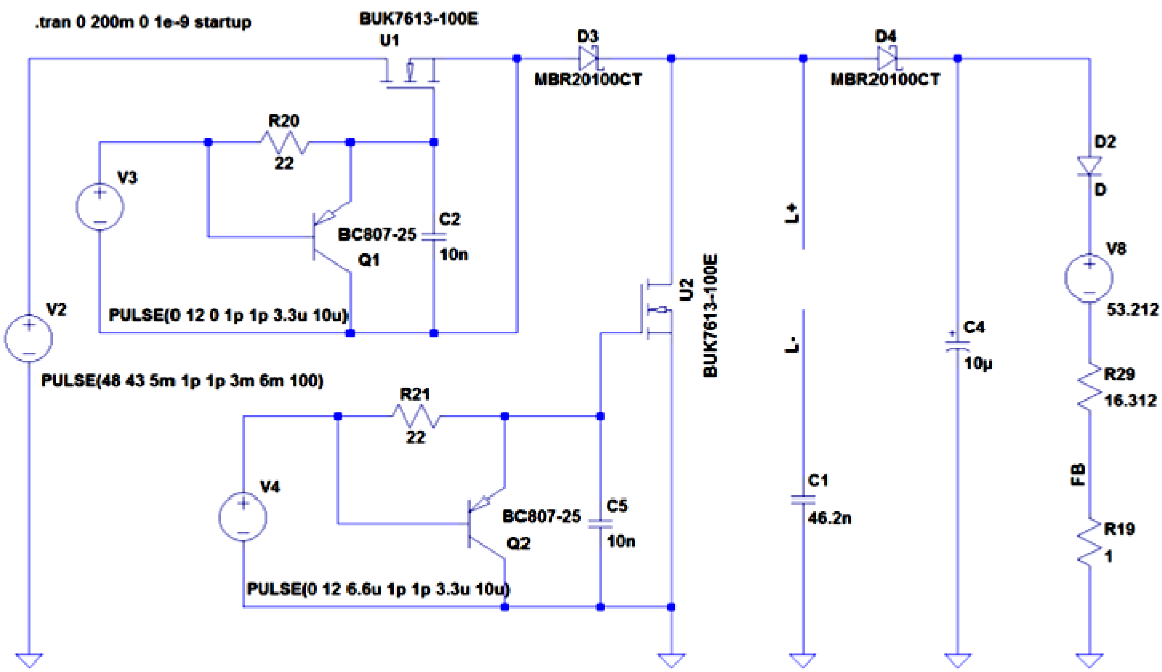
.tran 0 200m 0 1e-9 startup
BUK7613-100E
U1
D3
MBR20100CT
D4
MBR20100CT
R20
22
V3
BC807-25
Q1
C2
10n
D2
D
V8
53.212
V2
PULSE(0 12 0 1p 1p 3.3u 10u)
U2
BUK7613-100E
L+
L-
C4
10µ
PULSE(48 43 5m 1p 1p 3m 6m 100)
R21
22
R29
16.312
FB
C1
46.2n
V4
BC807-25
Q2
C5
10n
R19
1
PULSE(0 12 6.6u 1p 1p 3.3u 10u)

a)

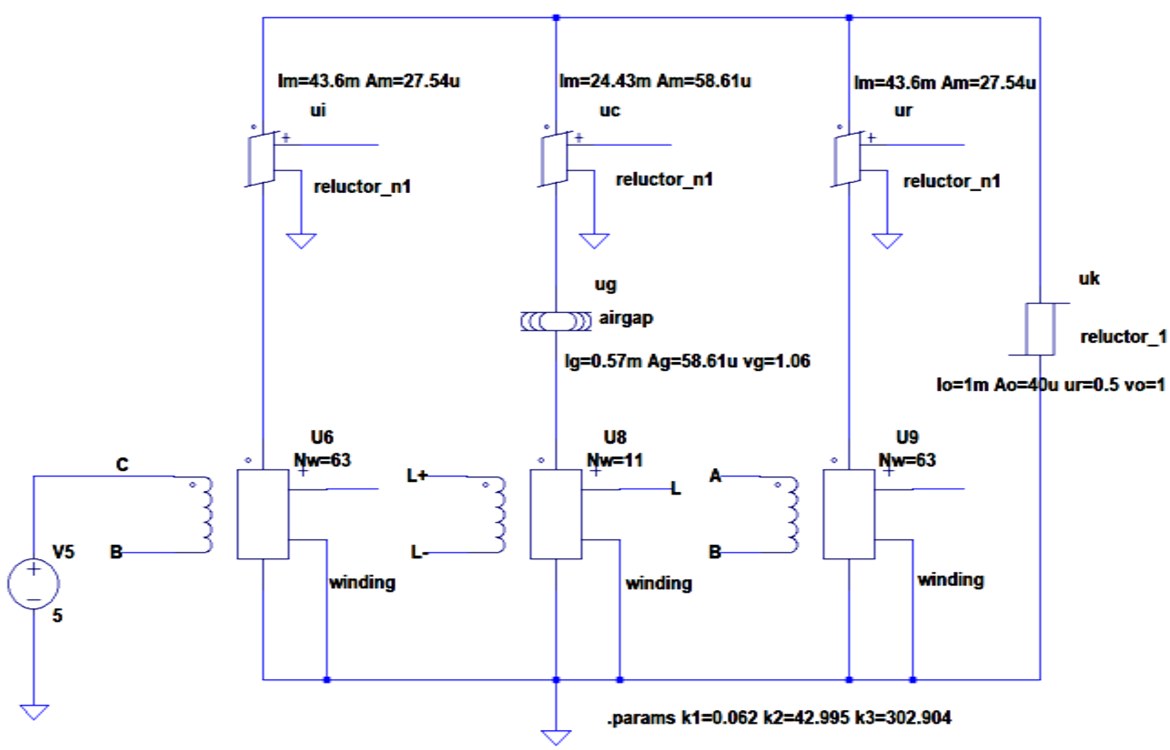
lm=43.6m Am=27.54u
ui
reluctor_n1
lm=24.43m Am=58.61u
uc
reluctor_n1
lm=43.6m Am=27.54u
ur
reluctor_n1
ug
airgap
lg=0.57m Ag=58.61u vg=1.06
uk
reluctor_1
lo=1m Ao=40u ur=0.5 vo=1
U6
Nw=63
U8
Nw=11
U9
Nw=63
C
B
V5
5
L+
L-
L
A
B
winding
winding
winding
.params k1=0.062 k2=42.995 k3=302.904

b)

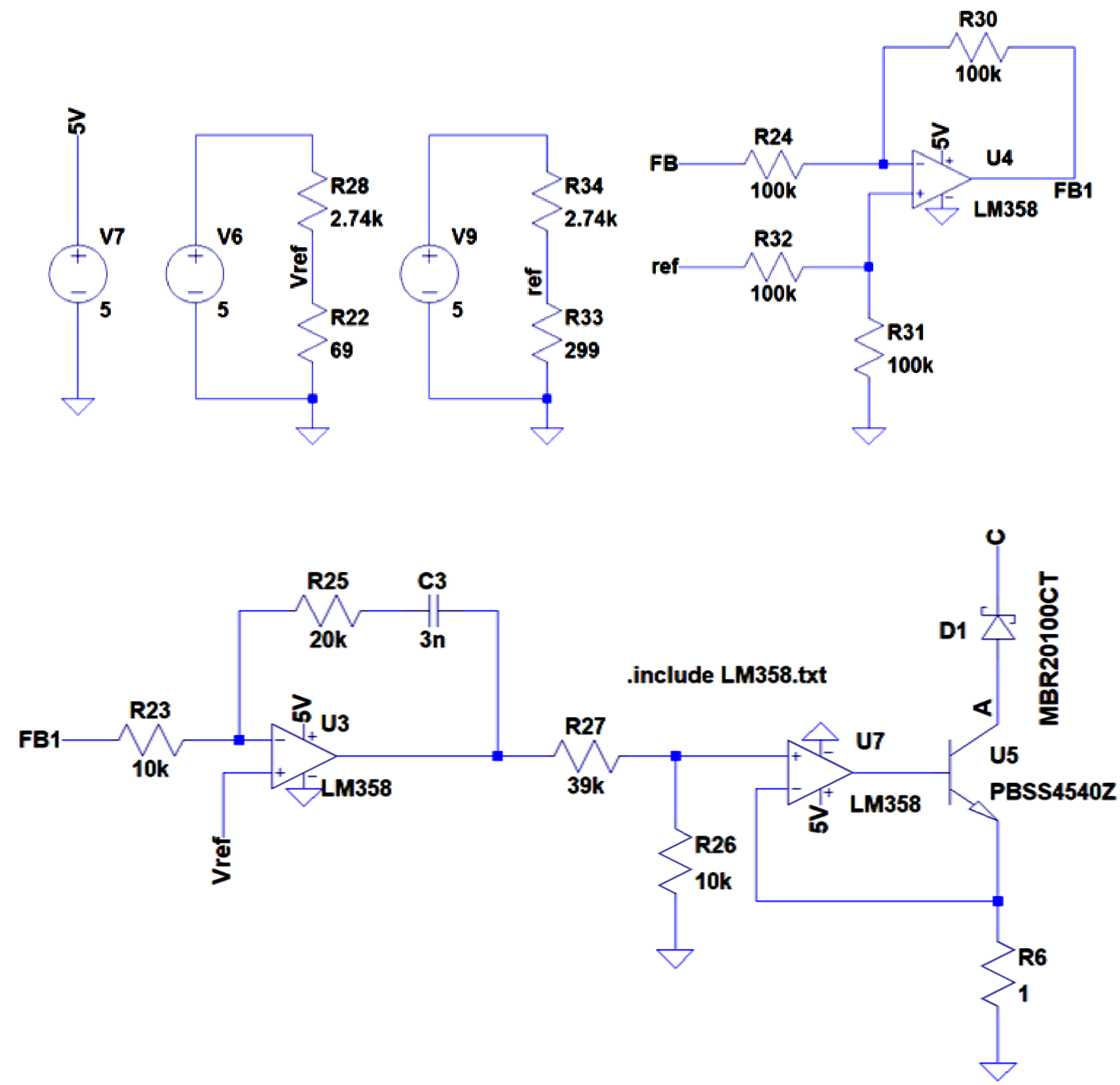

c)

Fig. 6.5. URSC step-up converter closed loop: a) URSC step-up converter, b) electrical-magnetic VI model and c) constant current source + PI controller.

Fig. 6.6 illustrates the resonant current I_{Lr} and voltage V_{Cr}. Fig. 6.7 shows the nominal DC OLED voltage V_{OLED} and OLED current I_{OLED} of the URSC step-up converter.

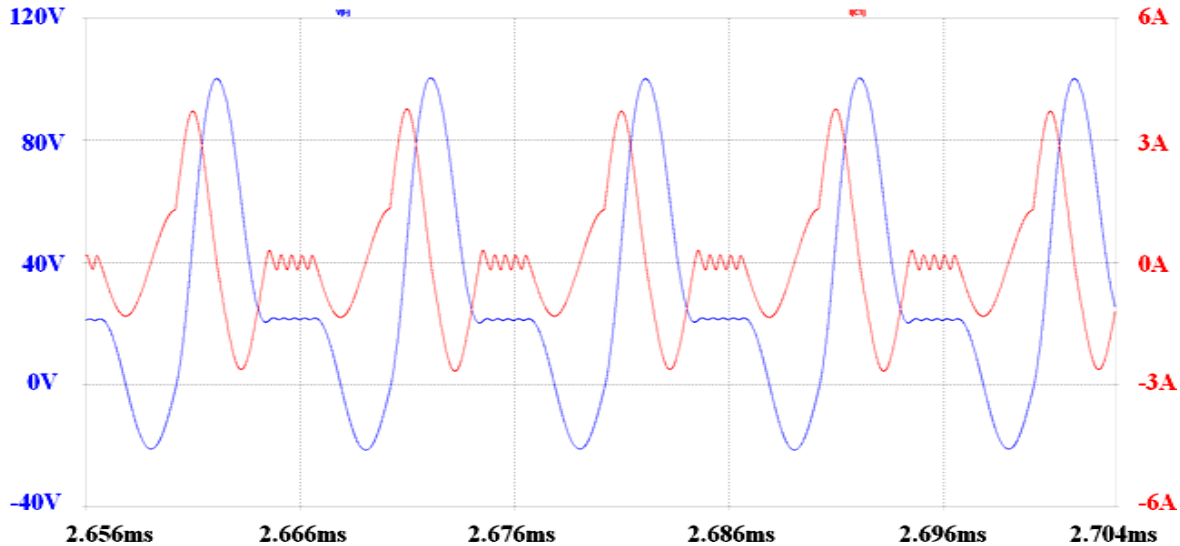

Fig. 6.6. Resonant tank waveforms: Blue: resonant capacitor voltage V_{Cr} and Red: resonant inductor current i_{Lr}. (40V/div, 3A/div and 10µs/div).

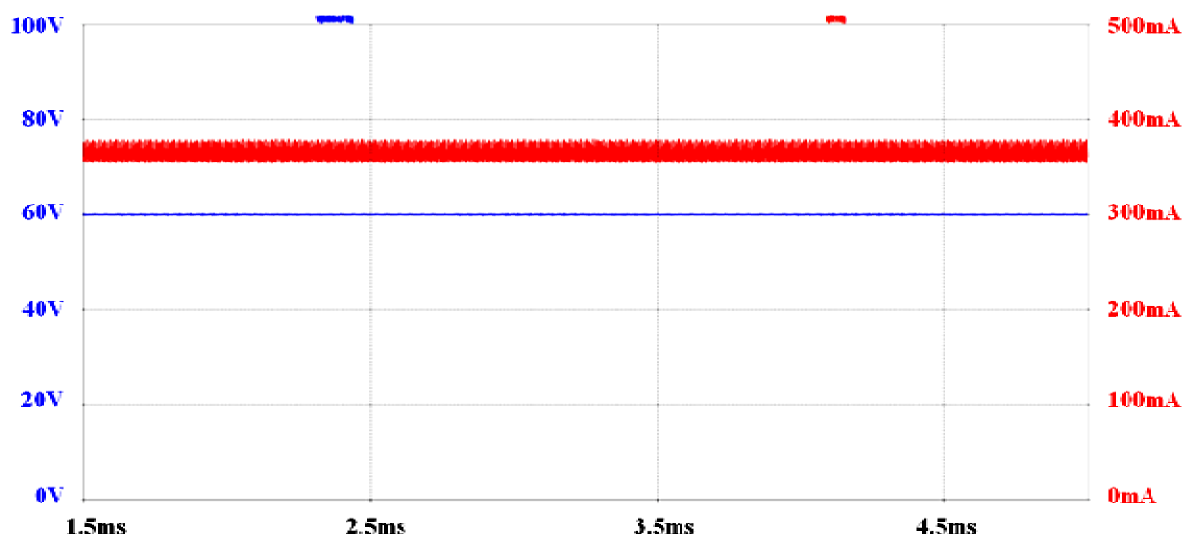

Fig. 6.7. Steady state load waveforms: Blue: DC OLED voltage V_{OLED} and Red: OLED current I_{OLED}. (20 V/div, 100 mA/div and 1ms/div).

Fig. 6.8 shows the dynamic response of the URSC step-up converter in closed loop under input voltage V_{in} step-down and up from 48V to 43V respectively. As shown, good dynamic behavior is achieved owing to the fact that the OLED current I_{OLED} is well regulated to 368mA.

The stabilization time of the OLED current I_{OLED} after a step-down input voltage is applied is about 1 ms.

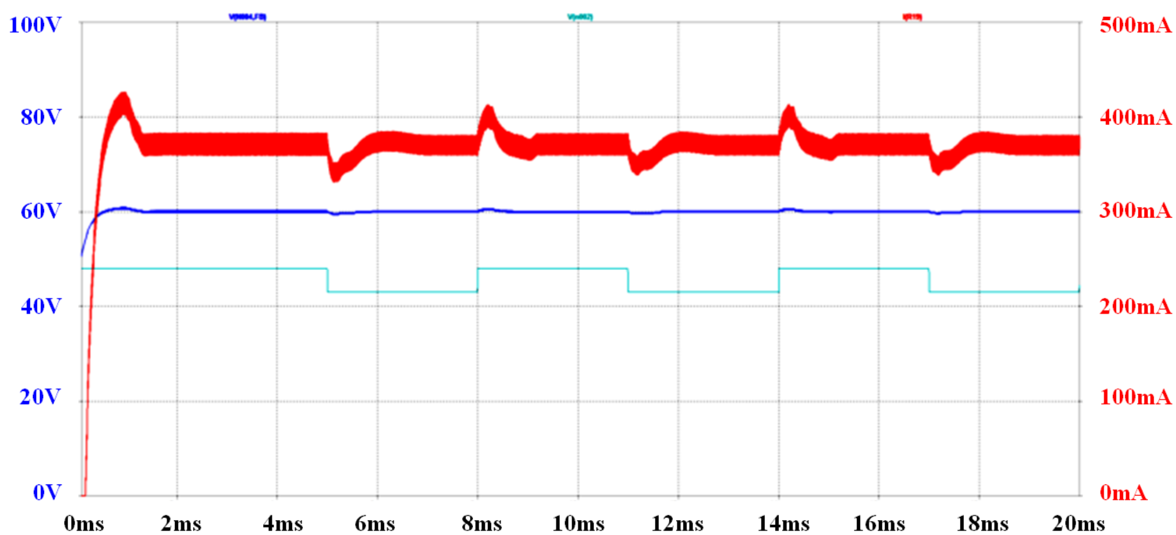

Fig. 6.8. Transient response waveforms: Blue: DC OLED voltage V_{OLED} 20V/div, Red: OLED current I_{OLED} 100mA/div and Green: input voltage V_{in} 20V/div. (2ms/div).

6.4. Experimental Results

The variable inductor built for the laboratory prototype of the URSC is shown in Fig. 6.9. The small-signal characteristics are used to know the dynamic response and stability of the system. The small-signal characteristic of the VI is simply the variation of the AC winding inductance of the main winding $U2$ in function of the DC bias current supplied to the auxiliary windings $U1$ and $U3$ connected one another with inverse polarity. Therefore, the values of the AC winding inductance $U2$ are obtained in accordance with the circuit of Fig. 6.10. As shown, a power supply and LCR Meter are used in order to bias the auxiliary windings and measure the AC main winding inductance, where the LCR meter supplies the AC main winding with 1Vrms at 100 kHz, whilst the DC bias current through the auxiliary windings is swept from 0 mA to 500 mA.

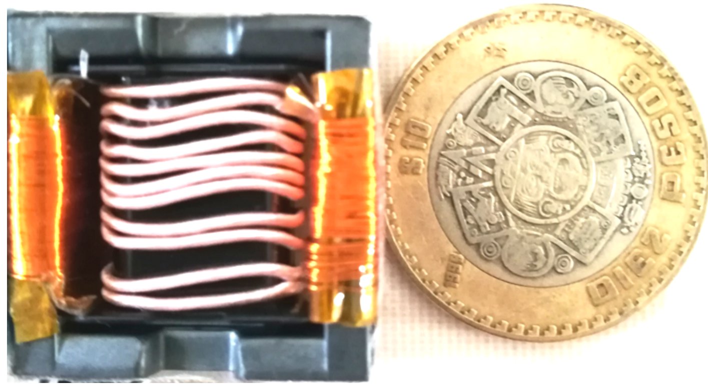

Fig. 6.9. Variable inductor for the laboratory prototype.

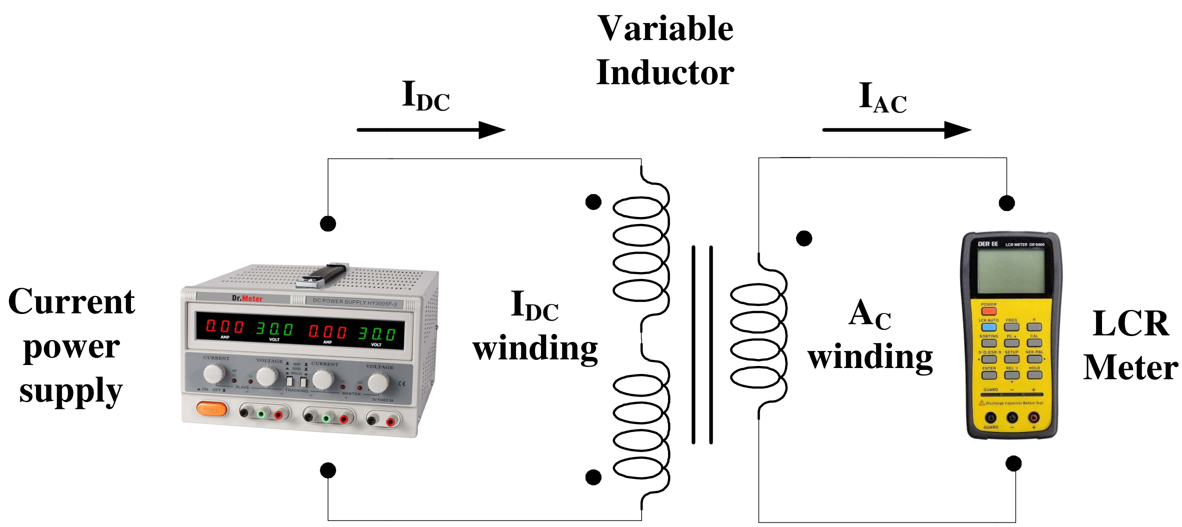

Fig. 6.10. Small-signal measurement circuit of the VI.

The inductance value of L_r vs DC bias current curve of the VI is shown in Fig. 6.11. As can be observed, it finds a very good agreement between simulation and experimental curve of the VI inductor.

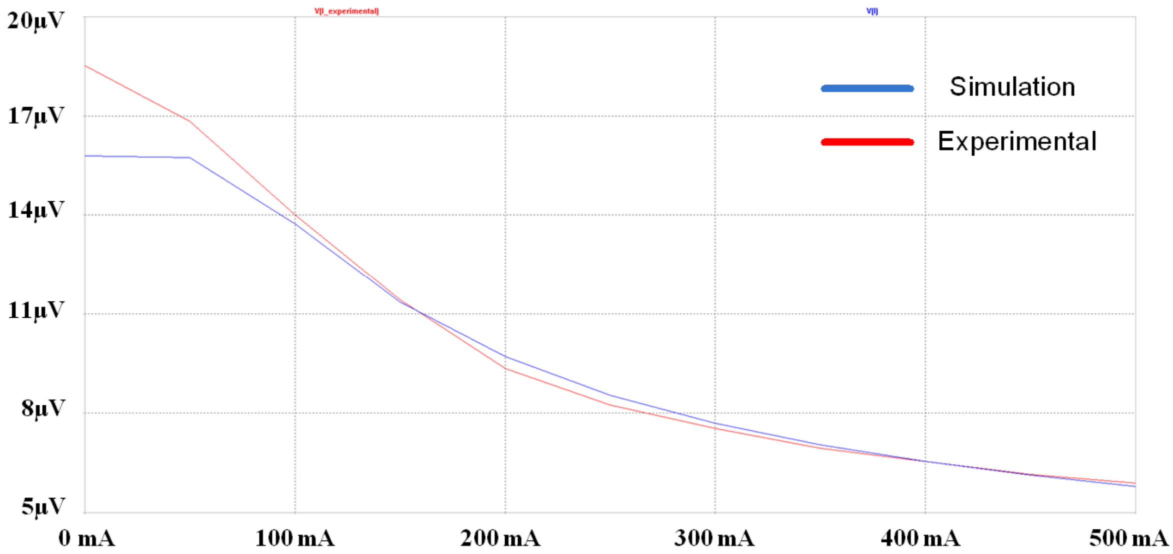

Fig. 6.11. Inductance vs DC bias current curve of the VI inductor: a) simulation (Blue) and b) experimental (Red). (3 µV/div and 100 mA/div).

Fig. 6.12 illustrates the behavior of the DC OLED voltage V_{OLED} and OLED current I_{OLED} in steady state. As it can be seen, DC OLED voltage V_{OLED} and OLED current I_{OLED} stabilize at about 59.2 V and 368 mA.

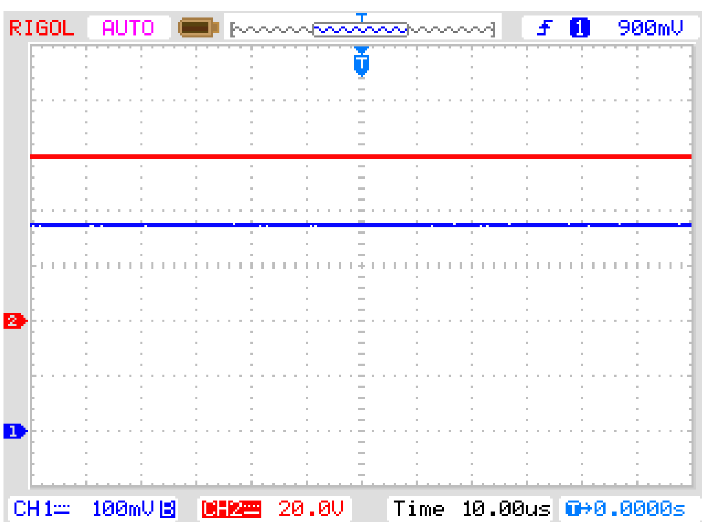

Fig. 6.12. Steady state load waveforms: Red: DC OLED voltage V_{OLED} 20V/div and Blue: OLED current I_{OLED} 100mA/div.

Fig. 6.13 shows the switching waveforms on Q_1, which do not show overlapping between both signals. Fig. 6.14 shows the resonant current I_{Lr} and the resonant voltage V_{Cr} of the URSC converter.

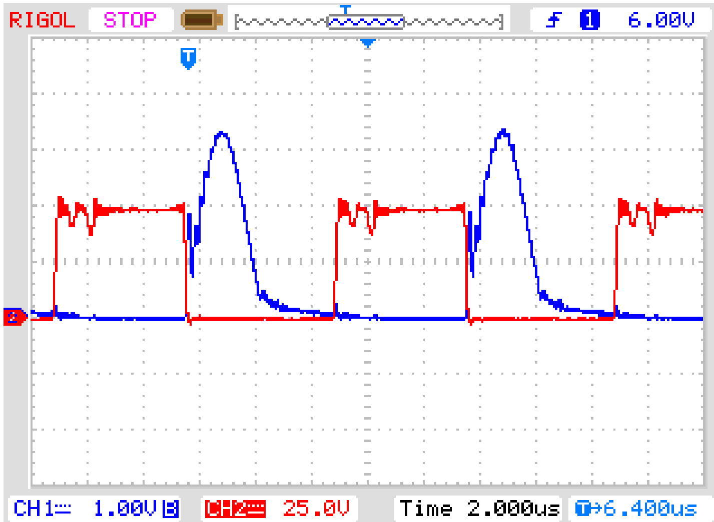

Fig. 6.13. Switching waveforms of Q_1: Red: drain-source voltage 20V/div and (Blue) drain current 1A/div.

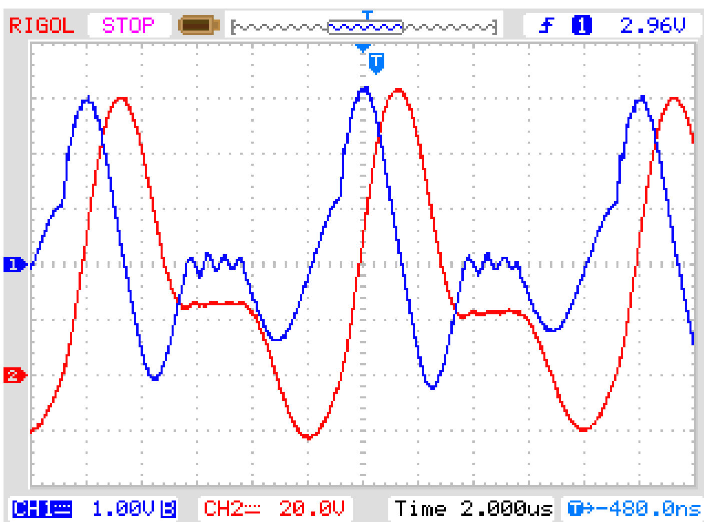

Fig. 6.14. Resonant tank waveforms: Red: resonant capacitor voltage V_{Cr} 20V/div and Blue: resonant inductor current i_{Lr} 1A/div.

Fig. 6.15 shows the dynamic response of the URSC converter in closed loop under a DC OLED voltage V_{OLED} decrease of 4V from 59.2V nominal by short-circuiting 5 1N4001 rectifier diodes from a 75 in series rectifier diodes dummy load.

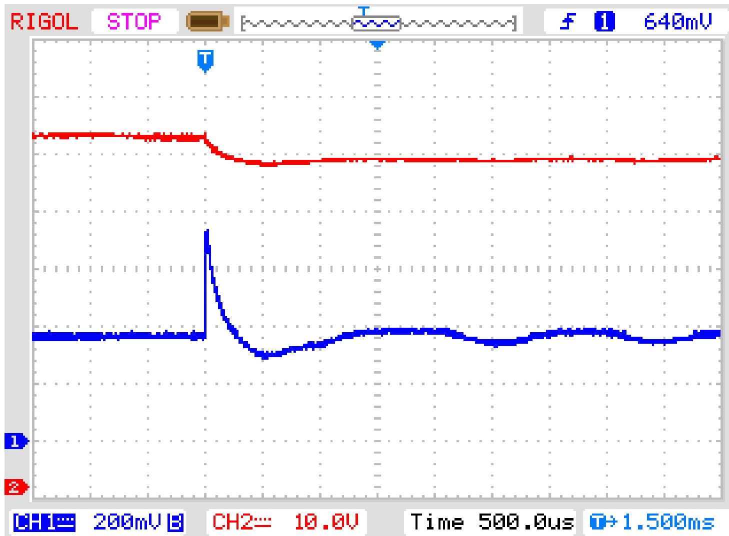

Fig. 6.15. Transient response waveforms: Red: DC OLED voltage V_{OLED} 10V/div and Blue: OLED current I_{OLED} 200mA/div.

Fig. 6.16 represents the experimental average OLED current I_{OLED} of the URSC converter at constant reference voltage V_{refB} under different input voltage V_{in} in open loop. The average OLED current I_{OLED} is dimmed from 0 mA to 445 mA by keeping constant V_{refB} at 127 mV and sweeping the input voltage from 0 V to 53 V.

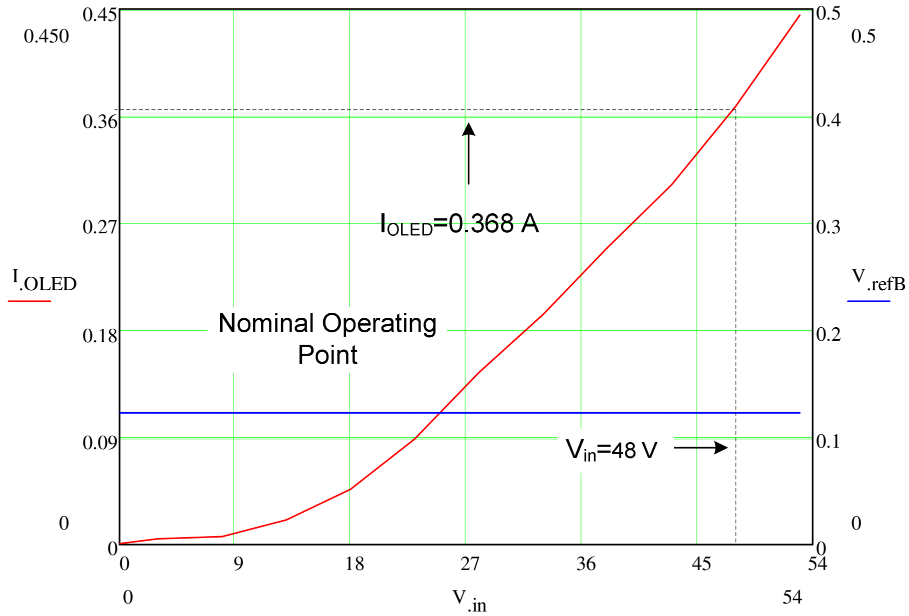

Fig. 6.16. I_{OLED} vs V_{in} in open loop.

The experimental average OLED current I_{OLED} under different resonant inductor L_r values and reference voltage V_{refB} values at constant input voltage V_{in} in open loop is shown in Fig. 6.17 and Fig. 6.18, respectively. The average OLED current I_{OLED} is dimmed from 135 mA to 390 mA by keeping constant the input voltage V_{in} at 48 V and sweeping the reference voltage V_{refB} from 105 mV to 270 mV.

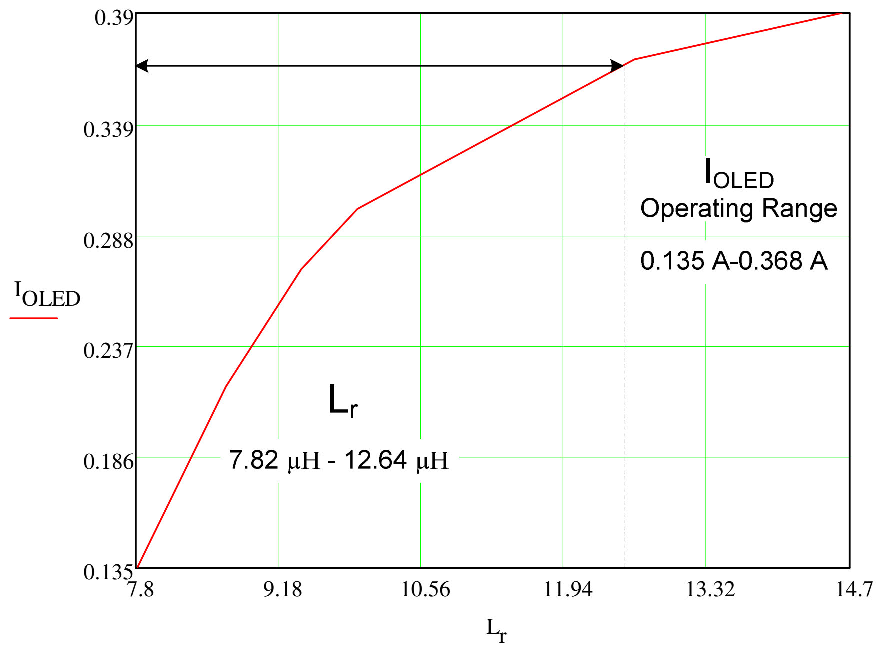

Fig. 6.17. I_{OLED} vs L_r in open loop.

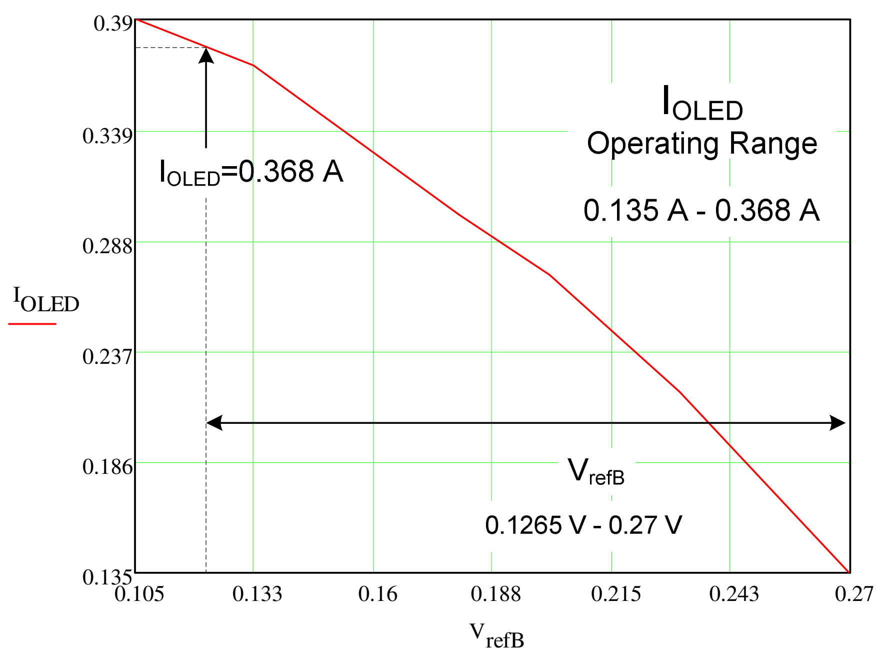

Fig. 6.18. I_{OLED} vs V_{ref} in open loop.

Fig. 6.19 depicts the experimental electrical efficiencies η under different average OLED power P_{OLED}. This is dimmed from 7.6 W to 23 W by keeping constant the input voltage V_{in} at 48 V and sweeping the reference voltage V_{refB} from 105 mV to 270 mV. The electrical efficiency η measured at nominal P_{OLED} is 92.97%.

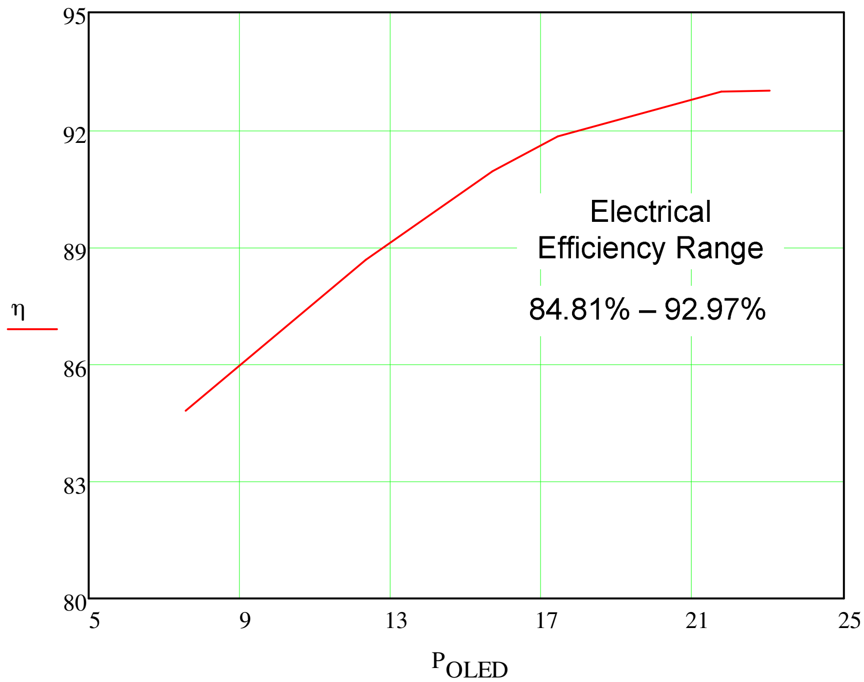

Fig. 6.19. Electrical efficiency η vs P_{OLED} in open loop.

6.5. Conclusions

In this chapter, the URSC step-up converter + VI inductor has been simulated by using the VI model based on the electrical-magnetic model in its simplest way. Owing to, this methodology reduces the complexity of the SPICE-based simulation circuit of the VI magnetic + electrical model, which is based on the VI reluctance model, in which the fundamental magnetic elements used are airgap, linear reluctor, non reluctor, and winding. The VI model simulation and experimental results present a very good agreement one another.

The VI control technique provides a very good output current regulation and dynamic response to the URSC step-up converter by means of resonant frequency control.

However, it is needed to improve the switching behavior of the URSC step-up converter by operating the switching frequency equal to the resonant frequency by means of implementing additional hardware that can achieve this operating condition. This could improve even more the efficiency of the converter.

7. Conclusions, contributions and future works

In this section, the conclusions obtained during the development of this investigation and contributions of this dissertation are presented. Besides, achievements of this dissertation and future works identified are listed.

7.1. Conclusions

A revision of the state of technology of the OLED has been carried out in order to study the OLED technology and understand the OLED fundamentals, as they are the architecture design, principle of operation, driving, supply and operating considerations such as electrical, photometric and thermal, as well as the different shapes and types of OLED lamps. This allows us to operate OLED lamps in a safe region and design OLED systems in a more efficient way.

A review of the art state of the OLED models has been carried out, which presents the different investigations related to electrical, PET and SPET OLED models. The simplified electrical modeling of power LEDs for DC-DC converter analysis and simulation arises as the simplest approach reported in the state of the art. Its great advantage is that it does not need any sophisticated equipment for the OLED modeling development. In this way, it presents the best option to obtain the equivalent electrical OLED model of the FL300 Phillips Lumiblade OLED lamp. Thereby, the equivalent electrical OLED model of the OLED lamp was obtained by using this approach. The calculated and experimental steady state and dynamic state results of the OLED equivalent electrical model presented a 1.6% maximum relative error between calculated and experimental results of the OLED power P_{OLED} and the OLED static resistance R_{OLED} at steady state and OLED current I_{OLED} and OLED DC voltage V_{OLED} at dynamic state.

A review of the state of the art of SC converters has been carried out, making emphasis on the resonant SC converters, which are used for regulating the output power of the OLED lamp. Among the different SC converter topologies, resonant converters stand out because they provide low EMI noise and high efficiency. Moreover, resonant SC converters provide compactness, simplicity, low cost and the possibility of integration OLED driver + OLED lamp. A comparison of resonant SC converters topologies presented in the state of the art has been carried out, where the URSC converter arises as the best option for OLED driving and OLED driver + OLED lamp integration.

The URSC converter has been analyzed and designed, obtaining an output power control function of the resonant SC converter as a function of the VI control parameter, L_r, which is the control technique proposed to regulate the output power owing to the fact that the OLED power of the resonant SC converter is regulated by its resonant frequency; resonant frequency is controlled by the resonant tank integrated by the $L_r - C_r$ network. In this way, the VI control technique reduces the complexity of the control loop and circuitry, which increases the power density of the OLED driver because it is operated by a simple constant current source to meet the operating point of the VI. This fact leads to a more efficient OLED driver + OLED lamp integration, because it is possible to achieve high power density OLED drivers.

The URSC converter has been tested in an *ad hoc* laboratory prototype, whose experimental results obtained presented a good behavior to drive OLED lamps because it provides a high efficiency, high output voltage regulation and high output voltage conversion ratio, low output voltage and current ripples, no efficiency dependency on conversion ratio and low EMI noise. The VI control technique showed a very good output current regulation and dynamic response to the URSC step-up converter.

7.2. Contributions

The contributions of this research work are the following:

- Review and comparison of the different OLED lamps existing in the market in regards to electrical, photometrical and thermal aspects.
- Review of the state of the art of the OLED PET models.

- Equivalent electrical modeling of the FL300 Phillips Lumiblade OLED lamp.
- Review of the state of the art of SC converters for OLED lamp driving.
- A comparative analysis among the different resonant SC converters was performed. This analysis determined that the most adequate resonant SC converter for OLED lamp driving and OLED driver + OLED lamp integration system is the URSC converter.
- Analysis and design of the URSC converter + VI closed loop OLED lamp driver.
- Simulation model of the closed loop URSC converter + VI for OLED lamp driving.
- Theoretical analysis of the power dissipation of the closed loop URSC converter + VI OLED lamp driver.
- Experimental verification of the URSC converter + VI closed loop OLED lamp driver.
- An *ad hoc* laboratory prototype implementation for the URSC + VI closed loop OLED lamp driver.

7.3. Future Works

Continuing the research work developed in this dissertation, the following future work research lines are proposed:

- Study other control strategies for the output power regulation of the closed loop URSC converter + VI OLED lamp system. For instance, variable capacitor (VC) control technique can be a good option owing to the fact that the output power control function of the resonant SC converter can be in function of the VC control parameter, C_r, because the OLED power of the resonant SC converter is regulated by its resonant frequency, which is controlled by the resonant tank integrated by the $L_r - C_r$ network. However, a control circuitry for the VC operation is necessary, in order to set the operating point of the VC.
- Analyze other resonant SC converters for OLED lamp driving.
- Design and study the URSC converter for operating at higher switching frequencies in order to achieve more compact OLED drivers.

- Analyze dimming techniques for the closed loop URSC converter + VI OLED lamp system.
- Study and development of modeling techniques of SC converters, which can be applied to the URSC converter, so that the frequency response of the closed loop URSC converter + VI OLED lamp system can be analyzed for different design conditions and cases.
- Study of digital control techniques, which can be applied to the closed loop URSC converter + VI OLED lamp system, in order to increase the power density of the OLED driver. A digital control approach provides even more design simplicity of the closed loop URSC + VI OLED lamp system as well as hardware implementation and OLED driver manufacturing.

References

[1] Y. J. Chen, W. C. Yang, C. S. Moo and Y. C. Hsieh, "A High Efficiency Driver for High-Brightness White LED Lamp," *IEEE TENCON*, Nov. 2010, pp. 2313-2317.

[2] A. Pollock, H. Pollock and C. Pollock, "High Efficiency LED Power Supply," *IEEE Journal of Emerging and Selected Topics in Power Elect.*, vol. 3, pp. 617-623, Sept. 2015.

[3] W. C. Yang, Y. J. Chen and C. S. Moo, "An Efficient Driver for Dimmable LED Lighting," *IEEE Conf. on Industrial Elect. and Appl.*, Jun. 2011, pp. 2331-2336.

[4] J. L. Baek, J. K. Kim, J. B. Lee, H. S. Youn and G. W. Moon, "Integrated Asymmetrical Half-bridge Zeta Converter for DC/DC Stage of LED Driver with Wide Output Voltage Range and Low Output Current," *IEEE Trans. on Industrial Elect.*, vol. 62, pp. 7489-7498, Dec. 2015.

[5] S. Madhumita and T. M. Binvy, "LC Series Resonant Converter Based High Power HB LED Lamp Driver with ZVS," *IEEE INDICON*, Dec. 2016, pp. 1-6.

[6] M. Arias, I. Castro, D. G. Lamar, A. Vázquez and J. Sebastián, "Optimized Design of a High Input-Voltage-Ripple-Rejection Converter for LED Lighting," *IEEE Trans. on Power Elect.*, vol. 33, pp. 5192-5205, Jun. 2018.

[7] O. C. Mak, Y. C. Wong, and A. Ioinovici, "Step-up DC power supply based on a switched-capacitor circuit," *IEEE Trans. Ind. Electron.*, vol. 42, pp. 90–97, Feb. 1995.

[8] J. Liu, Z. Chen, and Z. Du, "A new design of power supplies for pocket computer systems," *IEEE Trans. Ind. Electron.*, vol. 45, pp. 228–235, Apr. 1998.

[9] Bengtsson, "A switch in methods," *New Electronics,* Aug1997, pp. 40-41.

[10] https://en.wikipedia.org/wiki/OLED.

[11] Optoelectronics Industry Development Association, “Organic Light Emitting Diodes for General Illumination Update 2002, An OIDA Technology Roadmap”, Department of Energy Office of Building Technology, State and Community Programs, pp. 1-78, Aug 2002.

[12] OSRAM. Introduction to OLED Technology 2012 [Online] Available: http://www.osram-oled.com.

[13] M.O. Wendling, “The OLED Opportunity”, Osram, London 2012.

[14] Yi-Lu Chang and Zheng-Hong Lu, “White Organic Light-Emitting Diodes for Solid-State Lighting”, Journal of Display Technology, vol. 9, no. 6, pp. 459-468, June 2013.

[15] Sheryl Nathan, Noel Shammas and Steve Grainger, “The future of high-power conventional semiconductor based light emitting diodes (LEDs) against organic light emitting diodes (OLEDs),” UPEC, pp. 697–700, 2007.

[16] IRIS Lighting systems. Cooper lighting: how to read photometrics [Online]. Available: http://www.scribd.com.

[17] Falk Wieland, Henry Gueldner and Olaf Ruediger Hild, “Renewable Energy and Lightings-logically or artificially”, Institute of electrical Engineering, Technische Universitaet Dresden, Germany.

[18] OSRAM. Orbeos OLED application guide 2011 [Online] Available: http://www.osram-oled.com.

[19] Osram. User guideline for operation of OLEDs with electronic driver systems 2014 [Online]. Available: http://www.osram-oled.com.

[20] G. Farkas, S. Haque, F. Wall, P. S. Martin, A. Poppe, Q. van Voorst Vader, and G. Bognar, “Electric and thermal transient effects in high power optical devices,” in *Proc. 20th Annu. IEEE Semiconductor Thermal Measurement and Management Symp.*, 2004, pp. 168–176.

[21] P. Baureis, “Compact modeling of electrical, thermal and optical LED behavior,” in *Proc. 35th European Solid-State Device Research Conf.*, 2005, pp. 145–148.

[22] Y. Lianqiao, H. Jianzheng, and S. Moo Whan, “Dynamic thermal analysis of high-power LEDs at pulse conditions,” *IEEE Electron Device Lett.*, vol. 29, no. 8, pp. 863–866, Aug. 2008.

[23] S. Y. Hui and Y. X. Qin, “A general photo-electro-thermal theory for light emitting diode (LED) systems,” *IEEE Trans. Power Electron.*, vol. 24, no. 8, pp. 1967–1976, Aug. 2009.

[24] Y. X. Qin, D. Y. Lin, H. S. H. Chung, W. Yan, and S. Y. R. Hui, “Dynamic control of a light-emitting diode system based on the general photo-electro-thermal theory,” in *Proc. IEEE Energy Conversion Cong, and Expo., ECCE 2009*, pp. 2815–2820.

[25] T. Xuehui and S. Y. R. Hui, “Dynamic photo-electro-thermal theory for light-emitting diode systems,” *IEEE Trans. Ind. Electron.*, vol. 59, no. 4, pp. 1751–1759, Apr. 2012.

[26] V. C. Bender, T. B. Marchesan, and J. M. Alonso, “Solid state lighting: A concise review of the state of the art on LED and OLED modeling,” *IEEE Ind. Electron. Magazine*, vol. 9, no. 2, pp. 6–16, Jun. 2015.

[27] Philips Lumiblade. Design-in guide. 2014 [Online]. Available: http://www.lumiblade.com.

[28] C. Branas, F. J. Azcondo, and J. M. Alonso, “Solid state lighting: A system review,” *IEEE Ind. Electron. Magazine*, vol. 7, no. 4, pp. 6–14, Dec. 2013.

[29] Philips Lumiblade. The world of OLED lighting. 2014 [Online]. Available: http://www.lumiblade.com.

[30] Philips Lumiblade. OLED Compendium for Journalists [Online]. Available: http://www.lumiblade.com.

[31] Lumiblade OLED Panel. Brite FL300. Product sheet. 2014 [Online]. Available: http://www.lumiblade.com.

[32] Lumiblade OLEDs. Product catalog OLED panels 2012 [Online]. Available: http://www.lumiblade.com.

[33] Osram. Orbeos CDW-030 OLED. Information sheet 2014 [Online] Available: http://www.osram-oled.com.

[34] Osram. Orbeos RDW-046 OLED. Information sheet 2014 [Online] Available: http://www.osram-oled.com.

[35] Osram. Orbeos SDW-058 OLED. Information sheet 2014 [Online] Available: http://www.osram-oled.com.

[36] LG Chem. OLED light panel user guide v1.0 [Online] Available: http://www.lgoledlight.com.

[37] LG Chem. OLED light panel brochure 2014 [Online] Available: http://www.lgoledlight.com.

[38] J. Drechsel, M. Pfeiffer, X. Zhou, A. Nollau, and K. Leo, "Organic Mip-diodes by p-doping of amorphous wide-gap semiconductors: CV and impedance spectroscopy," *Synthetic Metals*, vol. 127, no. 1–3, pp. 201–205, Mar. 2002.

[39] S. Nowy, W. Ren, A. Elschner, W. Lövenich, and W. Brütting, "Impedance spectroscopy as a probe for the degradation of organic light emitting diodes," *J. Appl. Phys.*, vol. 107, no. 5, pp. 054501-1–054501-9, Mar. 2010.

[40] H. Park, H. Kim, S. K. Dhungel, and J. Yi, "Impedance spectroscopy analysis of organic light-emitting diodes fabricated on plasma-treated indium-tin-oxide surfaces," *J. Korean Phys. Soc.*, vol. 51, no. 3, pp. 1011–1015, Sep. 2007.

[41] J. Ahn, D. Chung, and J. Lee, "Equivalent-circuit analysis of organic light emitting diodes by using the frequency-dependent response of an ITO/Alq3/Al device," *J. Korean Phys. Soc.*, vol. 46, no. 2, pp. 546–550, Feb. 2005.

[42] W. N. Cheung, P. J. Edwards, and G. N. French, "Determination of LED equivalent circuits using network analyzer measurements," in *Proc. Optoelectron. Microelectron. Mater. Dev.*, 1998, pp. 232–235.

[43] R. L. Lin and Y. F. Chen, "Equivalent circuit model of light-emitting diode for system analyses of lighting drivers," in *Conf. Rec. IEEE IAS Annu. Meeting*, 2009, pp. 1–5.

[44] J. Jacobs, D. Hente, and E. Waffenschmidt, "Drivers for OLEDs," in Conf. Rec. IEEE IAS Annu. Meeting, 2007, pp. 1147–1152.

[45] D. Buso, S. Bhosle, Y. Liu, M. Ternisien, C. Renaud and Y. Chen, "OLED electrical equivalent device for driver topology design," IEEE Trans. Ind. Appl., vol. 50, no. 2, pp. 1459–1468, Mar./Apr. 2014.

[46] C. Pinot, “Modélisation électrique des diodes électroluminescentes organiques multicouches dopées. Application à De Nouvelles Architectures,” Ph.D. dissertation, Ecole Polytechnique, Palaiseau, France, 2008.

[47] Poppe, L. Pohl, E. Kollár, Z. Kohári, H. Lifka, and C. Tanase, “Methodology for thermal and electrical characterization of large area OLEDs,” in *Proc. 25th Annu. IEEE SEMI-THERM*, 2009, pp. 38–44.

[48] P. Kordt*et al.*, “Modeling of organic light emitting diodes: From molecular to device properties,” *Adv. Funct. Mater.*, vol. 25, no. 13, pp. 1955–1971, Apr. 2015.

[49] M.-N. Tsai, T. C. Chang, P.-T. Liu, C.-W. Ko, C.-J. Chen, and K.-M. Lo, “Short-diode like diffusion capacitance of organic light emission devices,” *Thin Solid Films*, vol. 498, nos. 1–2, pp. 244–248, Mar. 2006.

[50] R.-L. Lin, J.-Y. Tsai, D. Buso and G. Zissis, “OLED equivalent circuit model with temperature coefficient and intrinsic capacitor,” *IEEE Trans. Ind. Appl.*, vol. 52, no. 1, pp. 493–501, Jan./Feb. 2016.

[51] Y. Li, J. W. Lee, B. S. Lee, C. S. Lu, and W. H. Chen, “A novel SPICE compatible current model for OLED circuit simulation,” in *Proc. NSTI Nanotechnol. Conf. Trade Show*, Anaheim, CA, USA, May 2005, vol. 3, pp. 103.

[52] Haldi, A. Sharma, W. J. Potscavage, Jr., and B. Kippelen, “Equivalent circuit model for organic single-layer diodes,” *J. Appl. Phys.*, vol. 104, no. 6, pp. 1–6, Sep. 2008.

[53] L.-m. Yan and H. Wang, “Research on the models of OLED-on-silicon pixel circuits,” in *Proc. Int. Symp. High Density Packag. Micro syst. Integr.*, Jun. 2007, pp. 1–4.

[54] D. Shin, Y. Kim, N. Chang, and M. Pedram, “Dynamic voltage scaling of OLED displays,” in *Proc. DAC*, Jun. 2011, pp. 53–58.

[55] B. Zhao *et al.*, “A new OLED SPICE model for pixel circuit simulation in OLED-on-silicon micro display design,” *J. Semicond.*, vol. 33, no. 7, Jul. 2012, Art. ID. 075007.

[56] J. Kowal, D. Hente, and D. U. Sauer, “Model parameterization of nonlinear devices using impedance spectroscopy,” *IEEE Trans. Instrum. Meas.*, vol. 58, no. 7, pp. 2343–2350, Jul. 2009.

[57] P. López Varo, J. A. Jiménez Tejada, J. A. López Villanueva, and M. J. Deen, “Space-charge and injection limited current in organic diodes: a unified model,” *Organic Electron.*, vol. 15, no. 10, pp. 2526–2535, Oct. 2014.

[58] R.-L. Lin, Y.-C. Chang, and C.-C. Lee, “Optimal design of LED array for single-loop CCM buck-boost LED Driver,” *IEEE Trans Ind. Appl.*, vol. 49, no. 2, pp. 761–768, Mar./Apr. 2013.

[59] R.-L. Lin, J.-Y. Tsai, J. Marcos Alonso, and D. Gacio, “Four-parameter Taylor series based light-emitting-diode model,” in *Conf. Rec. IEEE IAS Annu. Meeting*, Vancouver, BC, Canada, Oct. 5–9, 2014, pp. 1–6.

[60] ORBEOS CDW-031 Datasheet. [Online]. Available: http://uk.rs-online.com/web/p/oled-lighting/6925330/

[61] F. A. Castro *et al.*, “Crossover from capacitive to pseudo inductive charge relaxation in organic/polymeric light-emitting diodes,” *Appl. Phys. Lett.*, vol. 87, no. 1, Jul. 2005, Art. ID. 013505.

[62] S. H. Kim *et al.*, “Impedance spectroscopy of single and double layer polymer light-emitting diode,” *J. Appl. Phys.*, vol. 87, no. 2, pp. 882–888, May 2000.

[63] G. Nenna*et al.*, “Insights into thermal degradation of organic light emitting diodes induced by glass transition through impedance spectroscopy,” *J. Appl. Phys.*, vol. 105, no. 12, Jun. 2009, Art. ID. 123 511.

[64] S. Nowy, “Understanding losses in OLEDs: Optical device simulation and electrical characterization using impedance spectroscopy,” Ph.D. dissertation, Inst. Phys., Univ. Augsburg, Augsburg, Germany, 2010.

[65] V. C. Bender, N. D. Barth, F. B. Mendes, R. A. Pinto, J. M. Alonso and T. B. Marchesan, “Modeling and characterization of organic light-emitting diodes including capacitance effect,” *IEEE Trans. Electron Devices*, vol. 62, no. 10, pp. 3314–3321, Oct. 2015.

[66] V. Shrotriya and Y. Yang, “Capacitance–voltage characterization of polymer light-emitting diodes,” *J. Appl. Phys.*, vol. 97, no. 5, p. 054504, Feb. 2005.

[67] H. Campbell, D. L. Smith, and J. P. Ferraris, “Electrical impedance measurements of polymer light-emitting diodes,” *Appl. Phys. Lett.*, vol. 66, no. 22, pp. 3030–3032, May 1995.

[68] Z. Kohári, E. Kollár, L. Pohl, and A. Poppe, “Nonlinear electro-thermal modeling and field-simulation of OLEDs for lighting applications II: Luminosity and failure analysis,” *Microelectron. J.*, vol. 44, no. 11, pp. 1011–1018, Nov. 2013.

[69] N. Li, X. Gao, B. Ding, X. Sun, X. Ding, and X. Hou, “Determination of capacitance-voltage characteristics of organic semiconductor devices by combined current-voltage and voltage decay measurements,” *Sci. China Technol. Sci.*, vol. 54, no. 4, pp. 826–829, Apr. 2011.

[70] Y. S. Lee, J.-H. Park, and J. S. Choi, “Frequency-dependent electrical properties of organic light-emitting diodes,” *J. Korean Phys. Soc.*, vol. 42, no. 2, pp. 294–297, Feb. 2003.

[71] P. Schwamb, T. C. G. Reusch, and C. J. Brabec, “Passive cooling of large-area organic light-emitting diodes,” *Organic Electron.*, vol. 14, no. 8, pp. 1939–1945, Aug. 2013.

[72] H. Pang, L. Michalski, M. S. Weaver, R. Ma, and J. J. Brown, “Thermal behavior and indirect life test of large-area OLED lighting panels,” *J. Solid State Lighting*, vol. 1, no. 1, p. 7, May 2014.

[73] J. Bisquert, G. Garcia-Belmonte, Á. Pitarch, and H. J. Bolink, “Negative capacitance caused by electron injection through interfacial states in organic light-emitting diodes,” *Chem. Phys. Lett.*, vol. 422, nos. 1–3, pp. 184–191, Apr. 2006.

[74] W. Brütting, H. Riel, T. Beierlein, and W. Riess, “Influence of trapped and interfacial charges in organic multilayer light-emitting devices,” *J. Appl. Phys.*, vol. 89, no. 3, pp. 1704–1712, Feb. 2001.

[75] E. Pinotti, A. Sassella, A. Borghesi, and R. Paolesse, “Characterization of organic semiconductors by a large-signal capacitance-voltage method at high and low frequencies,” *Synth. Met.*, vol. 138, no. 1, pp. 15–19, Jun. 2003.

[76] R. Osorio, J. M. Alonso, S. E. Pinto, G. Martínez, N. Vázquez, M. Ponce-Silva and A. J. Martínez, “Simplified electrical modelling of power LEDs for DC-DC converter analysis and simulation”, Int. J. Circ. Theor. Appl., April, 2017.

[77] Park J, Lee CC. An electrical model with junction temperature for light-emitting diodes and the impact on conversion efficiency. IEEE Electron Device Letters 2005; 26(5): 308–310.

[78] Baureis P. Compact modeling of electrical, thermal and optical LED behavior. IEEE Solid-State Device Research Conference, ESSDERC 2005; 145–148.

[79] Marcuse D, Kaminow I. Computer model of a super luminescent LED with lateral confinement. IEEE Journal of Quantum Electronics 1981; 17(7): 1234–1244.

[80] Gacio D, Alonso JM, Garcia J, Perdigao MS, Saraiva E, Bisogno FE. Effects of the junction temperature on the dynamic resistance of white LEDs. IEEE Transactions on Industry Applications 2013; 49(2): 750–760.

[81] Farkas G, Vader QV, Poppe A, Bognar G. Thermal investigation of high power Optical Devices by transient testing. IEEE Transactions on Components and Packaging Technologies 2005; 28(1): 45–50.

[82] Poppe A, Lasance CJM. On the standardization of thermal characterization of LEDs. 25th Annual IEEE Semiconductor Thermal Measurement and Management Symposium (SEMI-THERM), San Jose, CA, 2009; 151–158.

[83] Poppe A. Multi-domain compact modeling of LEDs: an overview of models and experimental data. Microelectronics Journal 2015; 46(12, Part A): 1138–1151.

[84] Lasance CJM, Poppe A. Challenges in LED thermal characterisation. 10th International Conference on Thermal, Mechanical and Multi-Physics simulation and Experiments in Microelectronics and Microsystems (EuroSimE), Delft, 2009; 1–11.

[85] Górecki K. Modelling mutual thermal interactions between power LEDs in SPICE. Microelectronics Reliability 2015; 55(2): 389–395.

[86] Almeida PS, Bender VC, Braga HAC, Dalla Costa MA, Marchesan TB, Alonso JM. Static and dynamic photo-electro-thermal modeling of LED lamps including low-frequency current ripple effects. IEEE Transactions on Power Electronics 2015; 30(7): 3841–3851.

[87] Bender VC, Marchesan TB, Alonso JM. Solid-state lighting: a concise review of the state of the art on LED and OLED modeling. IEEE Industrial Electronics Magazine 2015; 9(2): 6–16.

[88] Osorio R, Pinto S, Vázquez N, Martínez G, Ponce M, Padilla A, Prado J. Stationary state error reduction on the electrical modelling of high pressure sodium lamps. IET Electric Power Applications 2011; 5(4): 350–358.

[89] Osorio R, Vázquez N, Hernández C, Rodríguez E, Pinto SE, Juárez M. Electric dynamic modeling of HID lamps for electronic ballast design. IEEE Transactions on Industrial Electronics 2010; 57(5): 1655–1662.

[90] S. Y. R. Hui and Y. X. Qin, “A general photo-electro-thermal theory for light emitting diode (LED) systems”, IEEE Transactions on Power Electronics, vol. 24, no. 8, pp. 554-562, Aug. 2009.

[91] J. M. Zhou, W. Yan, “Experimental investigation on the performance characteristics of white LEDs used in illumination application”, in Proc. PESC’07, Jun. 2007, Orlando USA. pp. 1436-1440.

[92] J. H. Cheng, C. K. Liu, Y. L. Chao, R. M. Tain, “Cooling performance of silicon-based thermoelectric device on high power LED”, 24th International Conference on Thermo electrics, Jun. 2005, Clemson USA. pp. 53-56.

[93] T. Zahner, “Thermal management and thermal resistance of high power LEDs”, 13th International Workshop on Thermal Investigation of ICs and Systems, THERMINIC’07, Sep. 2007, Budapest Hungary. pp. 195-195.

[94] Luxeon Power Light Source, Data Sheet DS51.

[95] S. Buso, G. Spiazzi, M. Meneghini, G. Meneghesso, "Performance degradation of high-brightness light emitting diodes under DC and pulsed bias", IEEE Transactions on Device and Materials Reliability, vol. 8, no. 2, pp. 312-322, Jun 2008.

[96] J. Garcia, D. G. Lamar, M. A. Costa, J. M. Alonso, M. R. Secades, "An estimator of luminous flux for enhanced control of high brightness LEDs", in Proc. IEEE PESC'08, Jun. 2008, Rhodes Greece. pp. 1852-1856.

[97] Biber, Cathy, "LED light emission as a function of thermal conditions", IEEE Semiconductor Thermal Measurement and Management Symposium, March. 2008, San Jose USA. pp. 180-184.

[98] L. Trevisanello, M. Meneghini, G. Mura, M. Vanzi, M. Pavesi, G. Meneghesso, E. Zanoni, "Accelerated life test of high brightness light emitting diodes", IEEE Transactions on Device and Materials Reliability, vol. 8, no. 2, pp. 304-311, Jun. 2008.

[99] J. Bielecki, A. S. Jwania, E. Khatib, T. Poorman, "Thermal considerations for LED components in an automotive lamp", Twenty Third Annual IEEE Semiconductor Thermal Measurement and Management Symposium, 2007. SEMI-THERM'07, Mar. 2007, San Jose USA. pp. 37-43.

[100] J. F. Van, D. Michele. M. Colgan, "White LED sources for vehicle forward lighting", Proceedings of SPIE 2002, vol. 4776, pp. 195-205.

[101] J. Petroski, "Thermal Challenges facing new generation LEDs for lighting applications", Proceedings of SPIE 2003, vol. 4776, pp. 215-222.

[102] J. Lalith, Y. M. Gu, N. Nadarajah, "Characterization of thermal resistance coefficient of high-power LEDs", Sixth International Conference on Solid State Lighting, Aug. 2006, San Diego USA. pp. 63370-63377.

[103] L. Yuan, S. Liu, M. X. Chen, X. B. Luo, “Thermal analysis of high power LED array packaging with micro channel cooler”, 7th International Conference on Electronic Packaging Technology, 2006. ICEPT '06, Aug. 2006, Shanghai China. pp. 1-5.

[104] J. Petroski, “Spacing of high-brightness LEDs on metal substrate PCB's for proper thermal performance”, The Ninth Intersociety Conference on Thermal and Thermo mechanical Phenomena in Electronic Systems, 2004. ITHERM'04, Jun. 2004, Las Vegas USA. pp. 507-514.

[105] Z. L. Ma, X. R. Zheng, W. J. Liu, X. W. Lin, W. L. Deng, “Fast thermal resistance measurement of high brightness LED”, 6th International Conference on Electronic Packaging Technology, 2005, ICEPT’05, Aug. 2005, Shenzhen China. pp. 614-616.

[106] B. Siegal, “Practical considerations in high power LED junction temperature measurements”, 31st International Conference on Electronics Manufacturing and Technology, IEMT’06, Nov. 2006. Kuala Lumpur Malaysia. pp. 62-66.

[107] M. Arik, C. Becker, S. Weaver, J. Petroski, “Thermal management of LEDs: package to system,” Proc. of SPIE 2004, vol. 5187, pp. 64-75.

[108] Q. Cheng, “Thermal management of high-power white LED package”, 8th International Conference on Electronic Packaging Technology, 2007, ICEPT’07, Aug. 2007, Shanghai China. pp. 1-5.

[109] B. Ackermann, V. Schulz, C. Martiny, A. Hilgers, X. Zhu, “Control of LEDs”, in Proc. IEEE IAS’06, Oct. 2006, Tampa Florida USA. pp. 2608-2615.

[110] M. Nishikawa, Y. Ishizuka, H. Matsuo, K. Shigematsu, “An LED drive circuit with constant-output-current control and constant-luminance control”, Telecommunications Energy Conference, 2006, INTELEC'06, Sep. 2006, Rhode island USA. pp. 1-6.

[111] P. Baureis, “Compact modeling of electrical, thermal and optical LED behavior”, Proceedings of 35th European Solid-State Device Research Conference, 2005, Sep. 2005, Grenoble France. pp. 145-148.

[112] Y.X. Qin, D.Y. Lin and S.Y.R. Hui, “A Simple method for comparative study on the thermal performance of light emitting diodes (LED) and fluorescent lamps”, to appear in IEEE APEC 2009 and the IEEE Transactions on Power Electronics.

[113] S.Y.R. Hui, “Light maximization design method for light-emitting-diode systems”, patent pending.

[114] H.T. Chen, W.C.H Choy and S.Y.R. Hui, “Characterization, modeling, and analysis of organic light-emitting diodes with different structures”, IEEE Transactions on Power Electronics, vol. 31, no. 1, pp. 581-592, Jan 2016.

[115] J. Buytaert, J. Bleumers, A. Steen, and P. Hanselaer, “Optical determination of the junction temperature of OLEDs,” *Org. Electron.*, vol. 14, no. 11, pp. 2770–2776, Nov. 2013.

[116] S.Y. R. Hui, H. T. Chen, and X. H. Tao, “An extended photo-electro-thermal theory for LED systems—A tutorial from device characteristic to system design for general lighting [invited paper],” *IEEE Trans. Power Electron.*, vol. 27, no. 1, pp. 4571–4583, Nov. 2012.

[117] E. F. Schubert, *Light-Emitting Diodes*, 2nd ed. Cambridge, U. K.: Cambridge Univ. Press, 2006.

[118] M. Furno, T. C. Rosenow, M. C. Gather, B. Lussem, and K. Leo, “Analysis of the external and internal quantum efficiency of multi-emitter, white organic light emitting diodes,” *Appl. Phys. Lett.*, vol. 101, no. 14, pp. 143304-1–143304-4, Oct. 2012.

[119] Cester, D. Bari, J. Framarin, N. Wrachien, G. Meneghesso, S. Xia, V. Adamovich, and J. J. Brown, “Thermal and electrical stress effects of electrical and optical characteristics of Alq3/NPD OLED,” *Microelectron. Reliab.*, vol. 50, no. 9–11, pp. 1866–1870, Nov. 2010.

[120] H. T. Chen, X. H. Tao, and S. Y. R. Hui, “Estimation of optical power and heat dissipation coefficient for the photo-electro-thermal theory for LED systems,” *IEEE Trans. Power. Electron.*, vol. 27, no. 4, pp. 2176–2183, Apr. 2012.

[121] H. T. Chen and S. Y. R. Hui, “Dynamic prediction of correlated color temperature and color rendering index of phosphor-coated white light-emitting diodes,” *IEEE Trans. Ind. Electron.*, vol. 61, no. 2, pp. 784–797, Feb. 2014.

[122] K. Neyts, M. Marescaux, A. U. Nieto, A. Elschner, W. Lovenich, K. Fehse, Q. Huang, K. Walzer, and K. Leo, “Inhomogeneous luminance in organic light emitting diode related to electrode resistivity,” *J. Appl. Phys.*, vol. 100, no. 11, pp. 114513-1–114513-4, Dec. 2006.

[123] V. C. Bender, N. D. Barth, R. A. Pinto, J. M. Alonso and T. B. Marchesan, “Scale-photo-electro-thermal model for organic light-emitting diodes,” *IET Optoelectronics*, vol. 10, no. 3, pp. 100–110, 2016.

[124] Bohm, D.: ‘Causality and chance in modern physics’ (Routledge & Kegan Paul, 1957).

[125] Sturm, J.C., Wilson, W., Iodice, M.: ‘Thermal effects and scaling in organic light-emitting flat-panel displays’, IEEE J. Sel. Top. Quantum Electron., 1998, 4, (1), pp. 75–82.

[126] Çengel, Y.A.: ‘Heat & mass transfer: a practical approach’ (McGraw-Hill Education, 2009).

[127] Qi, X., Forrest, S.R.: ‘Thermal analysis of high intensity organic light-emitting diodes based on a transmission matrix approach’, J. Appl. Phys., 2011, 110, (12), p. 124516.

[128] Bergemann, K.J., Krasny, R., Forrest, S.R.: ‘Thermal properties of organic light-emitting diodes’, Org. Electron., 2012, 13, (9), pp. 1565–1568.

[129] Pohl, L., Kollár, E., Poppe, A., et al.: ‘Nonlinear electro-thermal modeling and field-simulation of OLEDs for lighting applications I: Algorithmic fundamentals’, Microelectron. J., 2012, 43, (9), pp. 624–632.

[130] Sam Ben-Yaakov, Switched Capacitors Converters, 2009.

[131] S. S. Ang and A. R. Oliva, Power-Switching Converters, *London: Taylor and francis group*, 1957, Chap. 8.

[132] K. W. E. Cheng and P. D. Evans, “Unified theory of extended-period quasi-resonant converters*,” IEE Proceedings-Electric Power Applications*, vol. 147, pp. 119-130, March 2000.

[133] K. W. E. Cheng and P. D. Evans, “Parallel-mode extended period quasi-resonant converter,” *IEEE Proc. Inst. Elect. Eng.*, vol. 138, pp. 243–251, Sept. 1991.

[134] Dongyuan Qiu, Bo Zhang and Chunfang Zheng, “Duty Ratio Control of Resonant Switched Capacitor DC-DC Converter,” Proceedings of the Eighth International Conference on Electrical Machines and Systems, Sept. 2005, pp. 1138-1141.

[135] K. W. E. Cheng, “New generation of switched capacitor converters,” *in Proc. IEEE PESC’98*, May 1998, pp. 1529-1535.

[136] K. Kuwabara and E. Hiyachika, "Switched-capacitor DC-DC converters," 10th International Telecommunications Energy Conference INTELEC '88, Nov 1988, pp. 213-218.

[137] K. W. E. Cheng, "Zero-current switching switched-capacitor converters," *IEEE Proc.-Electr. Power Appl.,* Vol. 148, pp. 403-409, Sept. 2001.

[138] Y. P. B. Yeung, K. W. E. Cheng, D. Sutanto and S. L. Ho, "Zero-current switching switched-capacitor quasi-resonant step-down converter," *IEEE Proc.-Electr. Power Appl.,* Vol. 149, pp. 111-121, March 2002.

[139] Y. P. B. Yeung, K. W. E. Cheng, S. L. Ho, K. K. Law, and D. Sutanto, "Unified Analysis of Switch Capacitor Resonant Converters," *IEEE Transactions on Industrial Electronics*, vol. 51, pp. 864-873, Aug. 2004.

[140] Y. P. B. Yeung, K. W. E. Cheng and D. Sutanto, "Multiple and Fractional Voltage Conversion Ratios for Switched-Capacitor Resonant Converters," *IEEE* PESC. 2001 32nd Annual, Jun 2001, pp. 1289-1294.

[141] Y. P. B. Yeung, K. W. E. Cheng, S. L. Ho, K. K. Law, and D. Sutanto, "Design and Analysis of Switched-Capacitor-Based Step-Up Resonant Converters," *IEEE Transactions on Circuits and Systems*, vol. 52, pp. 943-948, May. 2005.

[142] Y. Ye, K. W. E. Cheng, J. Liu, and C. Xu, "A Family of Dual-Phase-Combined Zero-Current Switching Switched-Capacitor Converters," *IEEE Transactions on Power Electronics*, vol. 29, pp. 4209-4218, Aug. 2014.

[143] A. Cervera, M. Evzelman, M. M. Peretz, and S. Ben-Yaakov, "A High Efficiency Resonant Switched Capacitor Converter with Continuous Conversion Ratio," *IEEE Energy Conversion Congress and Exposition*, Sept. 2013, pp. 4969-4976.

[144] A. Cervera, M. Evzelman, M. M. Peretz, and S. Ben-Yaakov, “A High Efficiency Resonant Switched Capacitor Converter with Continuous Conversion Ratio,” *IEEE Transactions on Power Electronics*, vol. 30, pp. 1373-1382, March 2015.

[145] E. E. dos Santos Fo, F. L. M. Antunes, P. H. A. Miranda and E. M. Sá, “A LED Driver with Switched Capacitor,” Group of Energy Processing and Control - GPEC, Fortaleza, CE, Brazil.

[146] E. E. dos Santos Fo, P. H. A. Miranda, E. M. Sá, F. L. M. Antunes, “A LED Driver with Switched Capacitor,” *IEEE Transactions on Industry Applications*, vol. 50, pp. 3046-3053, Sept./Oct 2014.

[147] P. H. A. Miranda, E. M. Sá, A. V. L. de Oliveira, E. E. dos Santos Fo, F. L. M. Antunes, “A Switched-Capacitor Driver for Power LEDs,” *IEEE XI Brazilian Power Electronics Conference*, Sept. 2011, pp. 918-923.

[148] O. Tetervenoks, “Sensorless Converter for Low-Power LED Lamp with Improved Power Factor,” *IEEE 2014 Electric Power Quality and Supply Reliability Conference (PQ)*, June 2014, pp. 285-290.

[149] Gilberto Martínez and J. Marcos Alonso, “A Review on Switched Capacitor Converters with High Power Density for OLED Lamp Driving,” *IEEE Ind. Appl. Society Conference*, pp. 1-8, Oct. 2015.

[150] Gilberto Martínez, J. Marcos Alonso and R. Osorio, “Analysis and Design of a Unidirectional Resonant Switched Capacitor Step-up Converter for OLED Lamp Driving Based on Variable Inductor,” *IEEE Ind. Appl. Society Conference*, pp. 1-8, Oct. 2017.

[151] http://mathworld.wolfram.com/LeastSquaresFitting.html.

[152] RHOM Semiconductor, Application Note AEK59-D1-0065-2, pp.1-3.

[153] R. Ridley, “Magnetics core loss”, APEC Industry session on magnetic, 23 Mar. 2016.

[154] J. M. Alonso, G. Martínez, M. Perdigão, M. Cosetin, R. N. do Prado; “Modeling Magnetics Devices Using Spice: Application to Variable Inductors,” *IEEE Applied Power Electronics Conference and Exposition APEC Conference*, pp. 1115-1122, Mar. 2016.

[155] J. M. Alonso, G. Martínez, M. Perdigão, M. Cosetin, R. N. do Prado; “A Systematic Approach to Modelling Complex Magnetic Devices using SPICE: Application to Variable Inductors,” IEEE Trans. on Power Electronics, Vol. 31, Nº 11, pp. 1-12, Nov. 2016.

[156] Kislovski, A. S., “Quasi-linear controllable inductor,” Proc. of the IEEE, Vol. 75, No. 2, Feb. 1987, pp. 267-269.

[157] Kislovski, A. S., “Linear variable inductor in dc current sensors utilized in telecom solar battery chargers,” Proc. on International Telecom. Energy Conf., 1989, pp. 1-3.

[158] Kislovski, A. S., “Linear variable inductor (LVI) in single-phase off-line telecom rectifiers,” Proc. of IEEE Int. Telecom. Energ. Conf. (INTELEC), 1995, pp. 93-98.

[159] Birx, Daniel L., and Louis L. Reginato; "Saturable inductor and transformer structures for magnetic pulse compression." U.S. Patent No. 4,928,020. 22 May 1990.

[160] Medini, D., Ben-Yaakov S., "A current-controlled variable-inductor for high frequency resonant power circuits," Applied Power Electronics Conference and Exposition, pp. 219-225, vol. 1, 13-17 Feb. 1994.

[161] Wölfle, Werner Hugo, and William Gerard Hurley, "Quasi-active power factor correction with a variable inductive filter: theory, design and practice," Power Electronics, IEEE Transactions on 18.1 (2003): 248-255.

[162] Alonso, J. M.; Dalla Costa, M. A.; Cardesín, J.; Garcia, J.; “Magnetic dimming of electronic ballasts”, Electronic Letters, vol. 41, nº 12, June 2005.

[163] Perdigão, M. S.; Alonso, J. M.; Vaquero, D. G.; Saraiva, E. S.; "Magnetically Controlled Electronic Ballasts With Isolated Output: The Variable Transformer Solution," Industrial Electronics, IEEE Transactions on , vol. 58, no. 9, pp. 4117-4129, Sept. 2011.

[164] Hamill, D. C.; "Gyrator-capacitor modeling: a better way of understanding magnetic components," Applied Power Electronics Conference and Exposition, vol. 1, pp. 326-332, 1994.

[165] Rozanov, E.; Ben-Yaakov, S.; “Analysis of current-controlled inductors by new SPICE behavioral model,” HAIT Journal of Sc. and Eng. B, Vol. 2, Iss. 3-4, pp. 558-570, 2005.

[166] Ngo, K. D. T.; "Subcircuit modeling of magnetic cores with hysteresis in PSpice," Aerospace and Electronic Systems, IEEE Transactions on , vol. 38, no. 4, pp. 1425-1434, Oct. 2002.

[167] Perdigao, M. S.; Alonso, J. M.; Dalla Costa, M. A.; Saraiva, E. S.; "A variable inductor MATLAB/Simulink behavioral model for application in magnetically-controlled electronic ballasts," Power Electronics, Electrical Drives, Automation and Motion, International Symposium on, pp. 349-354, 11-13 June 2008.

[168] Perdigao, M. S.; “Research and Development on New Control Techniques for Electronic Ballasts based on Magnetic Regulators,” Ph. D. dissertation, University of Coimbra, 2011.

[169] “Tutorial on How to Define the Saturable Core Element.” PSIM Software. Powersim Inc. July 2006.

[170] Alonso, J. M.; Dalla Costa, M. A.; Rico-Secades, M.; Cardesín, J.; Garcia, J.; “Investigation of a New Control Strategy for Electronic Ballasts Based on Variable Inductor”, IEEE Trans. on Industrial Electronics, Vol. 55, Nº 1, pp. 3-10, January 2008.

[171] Alonso, J. M.; Perdigao, M. S.; Gacio, D.; Campa, L.; Saraiva, E. S.; "Magnetic control of DC-DC resonant converters provides constant frequency operation," Electronics Letters, vol. 46, no. 6, pp. 440-442, March 18, 2010.

[172] Alonso, J. M.; Perdigão, M. S.; Vaquero, D. G.; Calleja, A. J.; Saraiva, E. S.; "Analysis, Design, and Experimentation on Constant-Frequency DC-DC Resonant Converters With Magnetic Control," Power Electronics, IEEE Transactions on , vol. 27, no. 3, pp. 1369-1382, March 2012.

[173] Perdigao, M. S.; Alonso, J. M.; Dalla Costa, M. A.; Saraiva, E. S.; "Comparative Analysis and Experiments of Resonant Tanks for Magnetically Controlled Electronic Ballasts," Industrial Electronics, IEEE Transactions on, vol. 55, no. 9, pp. 3201-3211, Sept. 2008.

[174] Perdigao, M. S.; Trovao, J. P. F.; Alonso, J. M.; Saraiva, E. S.; "Large-Signal Characterization of Power Inductors in EV Bidirectional DC–DC Converters Focused on Core Size Optimization," Industrial Electronics, IEEE Transactions on, vol. 62, no. 5, pp. 3042-3051, May 2015.

[175] Perdigao, M. S.; Alonso, J. M.; Saraiva, E. S.; "Magnetically-controlled dimming technique with isolated output," Electronics Letters, vol. 45, no. 14, pp. 756-758, July 2009.

[176] Perdigao, M. S.; Alonso, J. M.; Dalla Costa, M. A.; Saraiva, E. S.; "Using Magnetic Regulators for the Optimization of Universal Ballasts," Power Electronics, IEEE Transactions on, vol. 23, no. 6, pp. 3126-3134, Nov. 2008.

[177] Perdigao, M. S.; Menke, M.; Seidel, A. R.; Pinto, R. A.; Alonso, J. M.; "A review on variable inductors and variable transformers: Applications to lighting drivers," IEEE Trans. on Industry Applications, Jan. 2016.

[178] Pinto, R. A.; Alonso, J. M.; Perdigao, M. S.; da Silva, M. F.; do Prado, R. N., "A new technique to equalize branch currents in multiarray LED lamps based on variable inductor," Industry Applications Society Annual Meeting, IEEE, pp. 1-9, 5-9 Oct. 2014.

[179] Brauer, John R.; "Simple equations for the magnetization and reluctivity curves of steel," Magnetics, IEEE Transactions on, vol. 11, no. 1, pp. 81,81, Jan 1975.

[180] Hülsmann, T.; “Nonlinear Material Curve Modeling and Sensitivity Analysis for MQS-Problems,” Master Thesis, Faculty of Electrical, Information and Media Engineering, Bergische Universitat Wuppertal, 2012.

[181] “Ferrite Cores and Accessories”, Datasheet, EPCOS, September 2006.

[182] “LTspice IV. Getting Started Guide,” Linear Technology, 2011.

[183] J. M. Alonso, G. Martínez, M. Perdigão, M. Cosetin, R. N. do Prado; “Modeling Magnetics Devices Using Spice: Application to Variable Inductors,” *IEEE Applied Power Electronics Conference and Exposition APEC Conference*, pp. 1115-1122, Mar. 2016.

[184] J. M. Alonso, G. Martínez, M. Perdigão, M. Cosetin, R. N. do Prado; “A Systematic Approach to Modelling Complex Magnetic Devices using SPICE: Application to Variable Inductors,” IEEE Trans. on Power Electronics, Vol. 31, Nº 11, pp. 1-12, Nov. 2016.

[185] J. Marcos Alonso, Marina S. Perdigão, Guirguis Zaki Abdelmessih, Marco A. Dalla Costa, and Yijie Wang, “SPICE Modeling of Variable Inductors and Its Application to Single Inductor LED Driver Design,” IEEE Trans. on Industrial Electronics, Vol. 64, Nº 7, pp. 5894-5903, Jul 2017.

[186] “BUK7613-100EN-channel TrenchMOS standard level FET”, Product Datasheet, NXP, Oct. 2012.

[187] “MBRB20H100CTG Switch Mode Power Rectifier 100V 20A”, Datasheet, Semiconductor Components Industries, Jan 2015.

[188] “PHE450 Series Double Metallized Polypropylene Film”, Datasheet, KEMET Electronics Corporation, May 2015.

[189] “AC and pulse metallized polypropylene film capacitors”, Product Specification, Philips Components, Oct. 1996.

[190] “Metallized Polyester Film Capacitor”, Product Specification, Panasonic, Sept. 2017.

[191] “High Side and Low Side Driver IR2110”, Datasheet, International Rectifier, Mar. 2005.

[192] “PIC12F615/HV6158-Pin Flash-Based 8-BitCMOS Microcontrollers”, Datasheet, Microchip Technology, 2006.

[193] Katsuhiko Ogata, Ingenieria de Control Moderna, 3rd. ed., México: Prentice Hall, 1998, Chap. 5.

Attachments

In this attachments section, the VI magnetic design calculation of the closed loop URSC converter + VI OLED lamp driver and documents of papers published, which are listed in the publications section of this dissertation are included. These documents are separated PDF files in the same folder of this dissertation document.

This article has been accepted for publication in a future issue of this journal, but has not been fully edited. Content may change prior to final publication. Citation information: DOI 10.1109/JESTPE.2018.2827324, IEEE Journal of Emerging and Selected Topics in Power Electronics

Analysis and Design of a Unidirectional Resonant Switched Capacitor Step-up Converter for OLED Lamp Driving Based on Variable Inductor

Gilberto Martínez, José Marcos Alonso, *Senior Member, IEEE,* and René Osorio

***Abstract*-This paper presents an analysis and design of a unidirectional resonant switched capacitor (URSC) step-up converter for OLED lamp driving. The URSC converter includes a very small inductor in series with the switched capacitor to improve the switching behavior. Also, the URSC converter presents the advantages of high power density, higher efficiency compared to other SC converters, low output voltage and current ripples and low EMI noise, which make it adequate for driving OLED lamps. URSC is designed to operate in closed loop with constant current VI control technique. By working the resonant inductor as a VI, the OLED current can be regulated and dimmed because of resonant frequency change. Simulation and experimental results of the VI inductor, which are in a good agreement, and the results of a URSC step-up converter design example for a 21.8 W OLED lamps array supplied from 48Vdc are presented, where a maximum 92.97% efficiency is obtained.**

***Index Terms*- Organic-Lighting-Emitting-Diode (OLED), Switched-Capacitor (SC), Resonant Switched-Capacitor (RSC), Variable Inductor (VI), Closed-Loop Operation.**

I. INTRODUCTION

In [1], a review of SC converters for OLED lamp driving was presented, where the URSC step-up converter was proposed as the best option for driving OLED lamps, based on the performance comparative results among the different SC converters under study [2]-[14], and relying on the collected experimental results of the URSC step-up converter. The benefits of using the URSC step-up converter instead of conventional non-resonant and resonant SC converters, fractional-voltage-conversion-ratio RSC converters, dual-phase converters, step-down half bridge RSC converter with isolation transformer, and step-down SC converter with coupling inductors are: high output voltage regulation, low output voltage and current ripples, high efficiency, no efficiency dependency on conversion ratio, low EMI noise, and high power density [1].

The objectives of this work are to use an RSC converter that meets high efficiency and high power density and that can supply and regulate the OLED lamp power, to study an output power control method of the RSC converter, to analyze the RSC converter in order to obtain an output power control function of the RSC as a function of the control parameter and to achieve an *ad-hoc* laboratory prototype in order to experimentally confirm a good agreement with the control function of the RSC converter.

The OLED power of the RSC converter is regulated by its resonant frequency, which is controlled by the resonant tank integrated by the $L_r - C_r$ network [15]. Based on this fact, a control parameter that regulates the output power of the RSC converter is needed. Hence, the VI control technique is proposed to regulate the output power of the RSC, which reduces the complexity of the control loop and circuitry, and increases the power density of the OLED driver because it is operated by a simple constant current source to meet the operating point of the VI. In this way, it is possible to achieve more compact OLED drivers. A proposed SPICE-based electrical-magnetic model and the analysis and design of the VI used in this work as well as its application to an LED driver are presented in [16]-[18]. Also, some additional works in the literature about VI study and application are illustrated in [19]-[20]. However, due to lack of space, the analysis and design of the VI will be omitted in this work.

Nowadays, more compact, small and flat OLED drivers are arising to enable new design possibilities such as avant-garde interior floor and table lamps, mirror and ceiling lamps, ablaze tiles and partition wall lighting applications; however, LED drivers are bulky and larger, which makes their use difficult in the aforementioned lighting applications. Thus, the main difference between OLED drivers and LED drivers relies on their compactness, size and flatness [21]-[22]. The OLED can be operated by the same topologies used for driving the conventional LED; this is because the OLED supplied by a dc current behaves very similarly to the conventional LED. Therefore, the V-I characteristic of the OLED shows an exponential behavior [22]-[23].

Some high efficiency LED drivers, such as buck-boost (BB) and an LED power supply based on a synchronous buck converter are reported in [24]-[25]. The BB converter processes only a part of the LED power owing to the fact that the LED power is supplied by two sources, the DC input voltage source and the BB converter output [24]. The

2168-6777 (c) 2018 IEEE. Personal use is permitted, but republication/redistribution requires IEEE permission. See http://www.ieee.org/publications_standards/publications/rights/index.html for more information.

This article has been accepted for publication in a future issue of this journal, but has not been fully edited. Content may change prior to final publication. Citation information: DOI 10.1109/JESTPE.2018.2827324, IEEE Journal of Emerging and Selected Topics in Power Electronics

synchronous buck converter drives a split LED string; the first LED string is driven by the buck converter and the second LED string is placed in series with the input voltage source [25]. These works obtain a good efficiency, around 92-93%, at maximum LED power, but they present a low power density due to the use of bulky and heavy switching inductors, input and output filter capacitors. These LED drivers show high output ripple current, which can reduce the OLED's life span and could cause eye-visible luminous flux variations. A fly-back converter functioning as a current regulator between the DC voltage source and the LED is presented in [26]; the converter returns a part of the energy from the output filter capacitor to the DC link input capacitor, which lowers the power conversion losses because only a small part of the LED power is processed by the fly-back converter [26]. An integrated half bridge zeta (HBZ) asymmetrical half bridge (AHB) converter is presented in [27], which obtains high efficiency on an entire output voltage range at constant low output current. In this way, it achieves high efficiency either at high output voltage or low output voltage as reported in [27]. A HB-LC series resonant converter based on high power HB-LED driver is proposed in [28]. It operates under ZVS, and drives the LED load by means of two sources; the input DC bus source supplies the cut-in voltage and the second source regulates the forward current, which leads to obtain high efficiency because not all the LED power is processed by the HB-LC series resonant converter. A high input-voltage-ripple-rejection ZAHB (zeta asymmetrical half bridge), which overcomes the performance drawbacks of the AHB such as limited duty cycle range, non-linear DC gain and not fully cancellation of the low frequency ripple, is reported in [29]. Even though, the converters reported in [24]-[29] show high peak efficiencies in the range of 92-96%, regrettably, they show very low power density compared to the SC converters due to the total number of components, bulky and heavy inductors and switching transformers, DC link and output filter capacitors. Therefore, they do not allow the designers to attain a compact, flat and small OLED driver + OLED lamp system. Moreover, it is important to mention the drawbacks of using electrolytic capacitors to reduce the output voltage and current ripples, which lower the lifetime of the driver, and on the other hand, the use of coupling transformers, which are difficult to design and more expensive to manufacture.

In this work, the URSC step-up converter is analyzed and designed for driving a 21.8 W OLED lamps array [15]. The resonant inductor is designed to operate at a resonant frequency above the switching frequency for any OLED power. Under this condition, a good dynamic behavior against input voltage or luminous flux variations is obtained.

In section II, the operation of the URSC step-up converter is presented. In section III, the analysis and design of the URSC step-up converter is carried out. Section IV illustrates the design of a laboratory prototype. Simulations and experimental results are shown in sections V and VI. Conclusions are presented in section VII.

II. Operation of The Unidirectional Resonant Switched Capacitor Step-Up Converter

Fig. 1 shows the URSC step-up converter, which consists of two switches, Q_1 and Q_2, two diodes, D_1 and D_2, a resonant capacitor, C_r, a resonant inductor, L_r, and an output filter capacitor, C_O. The converter has four operation modes, namely, charge, discharge, off and balance, where this last stage balances the remaining charge into the resonant capacitor before the beginning of the next switching period, in order to further improve the switching behavior of the converter. In addition, the URSC step-up converter behaves as a current source; therefore, the output voltage amplitude depends on the OLED dc equivalent resistance. In the following, the different operation intervals of the URSC step-up converter are presented. Figs. 2 to 5 illustrate the equivalent circuit in each time interval. Fig. 6 shows the main waveforms of the converter operation.

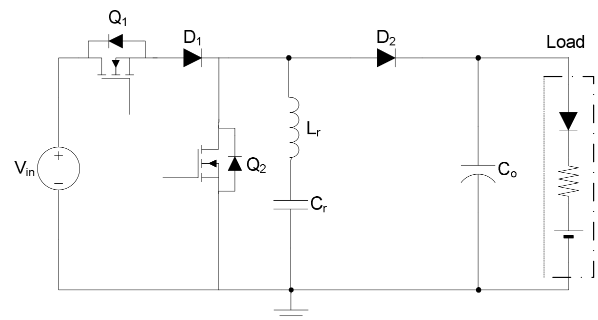

Fig. 1. URSC step-up converter.

A. Charge Operation Stage: $t_0<t_1$

Fig. 2 shows the equivalent circuit for charge operation stage. As can be seen, transistor Q_1, and diode D_1, are on, while transistor Q_2, and diode, D_2 are off. The resonant capacitor C_r, is charged through, Q_1 and D_1, while the output filter capacitor C_O, is discharged to the load. It is important to mention that the resonant current I_{Lr} at the beginning of this stage is not zero due to the conduction period of the freewheeling diode of Q_2 in the balance stage.

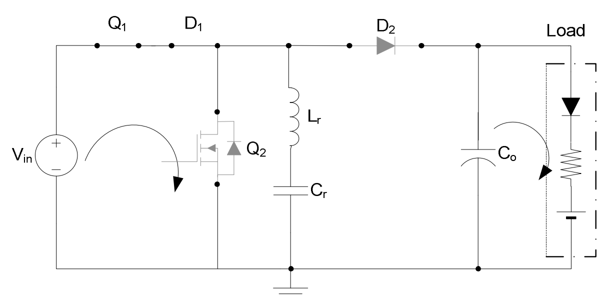

Fig. 2. Stage $t_0<t_1$.

B. Discharge Operation Stage: $t_1<t_2$

Fig. 3 illustrates the discharge operation stage, where transistors Q_1 and Q_2, and diode D_1 are off, while diode D_2, is

2168-6777 (c) 2018 IEEE. Personal use is permitted, but republication/redistribution requires IEEE permission. See http://www.ieee.org/publications_standards/publications/rights/index.html for more information.

This article has been accepted for publication in a future issue of this journal, but has not been fully edited. Content may change prior to final publication. Citation information: DOI 10.1109/JESTPE.2018.2827324, IEEE Journal of Emerging and Selected Topics in Power Electronics

on. The resonant capacitor C_r, is discharged through D_2, and the output filter capacitor C_O, is charged.

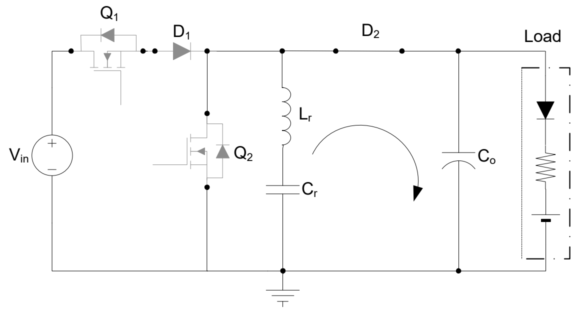

Fig. 3. Stage $t_1<t_2$.

C. Off Operation Stage: $t_2<t_3$

In this operation stage, transistors Q_1 and Q_2, and diodes D_1 and D_2, are off. The resonant inductor current i_{Lr} through $L_r - C_r$, is zero. Fig. 4 shows the off operation stage equivalent circuit.

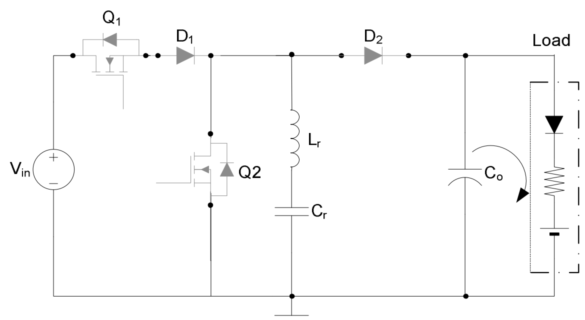

Fig. 4. Stage $t_2<t_3$.

D. Balance Operation Stage: $t_3<t_5$

The balance operation stage circuit is shown in Fig. 5. In which during $t_3<t_4$, transistor Q_1, and diodes D_1 and D_2, are off, while transistor Q_2 is on and the output filter capacitor C_O, keeps discharging to the load. The resonant tank, $L_r - C_r$, is shortcircuited in order to balance the energy stored in C_r, so that the same charge level as that at instant t_0 is attained for the next charge operation state. At the end of this stage during $t_4<t_5$, the current is flowing through the body diode of Q_2, thereby, transistors Q_1 and Q_2, and diodes D_1 and D_2, are off, while the resonant capacitor C_r is charged.

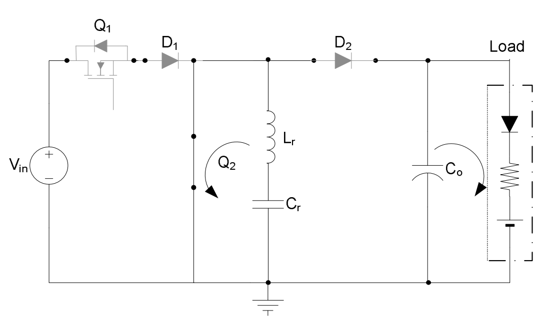

Fig. 5. Stage $t_3<t_5$.

The waveforms corresponding to each operation state are shown in the Fig. 6.

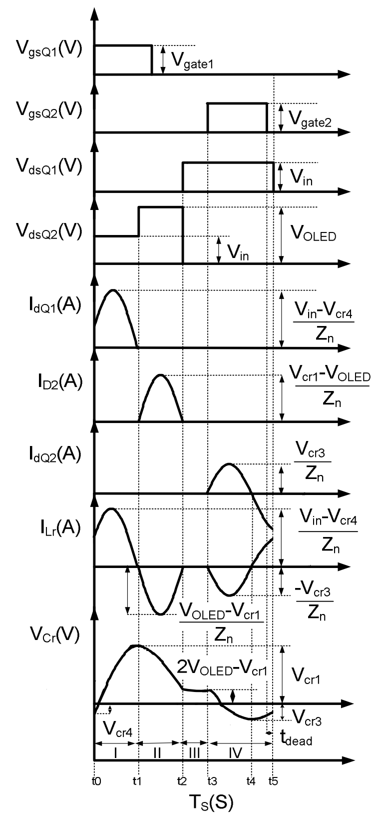

Fig. 6. Main waveforms of the RSC step-up converter during one switching period.

III. Analysis and Design of the URSC Step-Up Converter

In this section, the analysis and design of the URSC step-up converter is carried out based on the methodology used in [11][12]. First, by analyzing the charge operation stage circuit shown in Fig. 2, the expressions (1) and (2) are obtained.

$$\frac{di_{Lr}}{dt} = \frac{V_{in} - V_{Cr}}{L_r} \tag{1}$$

$$\frac{dV_{Cr}}{dt} = \frac{i_{Lr}}{C_r} \tag{2}$$

Now, from (1) and (2) and after some manipulation, V_{Cr} is obtained in (3). And then by substituting (3) into (2), and isolating and solving for i_{Lr}, (4) is obtained, which is the expression of the resonant inductor current i_{Lr}.

$$V_{Cr} = V_{in} - (V_{in} - V_{Cr}(0)) \cos \omega t \tag{3}$$

$$i_{Lr} = \frac{V_{in} - V_{Cr}(0)}{Z_n} \sin \omega t \tag{4}$$

Where V_{in} is the DC input voltage and Z_n is the equivalent resonant tank impedance:

2168-6777 (c) 2018 IEEE. Personal use is permitted, but republication/redistribution requires IEEE permission. See http://www.ieee.org/publications_standards/publications/rights/index.html for more information.

This article has been accepted for publication in a future issue of this journal, but has not been fully edited. Content may change prior to final publication. Citation information: DOI 10.1109/JESTPE.2018.2827324, IEEE Journal of Emerging and Selected Topics in Power Electronics

$$Z_n = \sqrt{\frac{L_r}{C_r}} \tag{5}$$

Similarly, the circuits shown from Fig. 3 to Fig. 5 can be analyzed in order to obtain the expressions for V_{Lr} and I_{Cr}, which lead to the form of (3) and (4), where V_{in} takes the values of the DC OLED voltage V_{OLED} and 0, respectively. Based on the afore-mentioned procedure, (6) and (7) are found for the maximum V_{Cr} values at the end of discharge and t_3-t_4 balance operation stages by considering $\omega t = \pi$.

$$V_{Cr2} = 2V_{OLED} - V_{cr1} \tag{6}$$

$$V_{Cr3} = -V_{cr2} \tag{7}$$

Where V_{Cr1}, V_{Cr2} and V_{Cr3} are the capacitor C_r voltages at t_1, t_2 and t_4, respectively.

In addition, (4), (8), (9) and (10) show the obtained expressions for the resonant inductor current i_{Lr} for discharge and t_3-t_4 and t_4-t_5 balance operation stages:

$$i_{Lr} = \frac{V_{OLED} - V_{cr1}}{Z_n} \sin \omega t \quad when \qquad t_1 < t < t_2 \tag{8}$$

$$i_{Lr} = \frac{-V_{cr2}}{Z_n} \sin \omega t \qquad when \qquad t_3 < t < t_4 \tag{9}$$

$$i_{Lr} = \frac{-V_{cr3}}{Z_n} \sin \omega t \qquad when \qquad t_4 < t < t_5 \tag{10}$$

The resonant frequency f_n is known as follows:

$$f_n = \frac{1}{2\pi\sqrt{L_r C_r}} \tag{11}$$

In this analysis, the resonant frequency f_m expression is used [11][12]:

$$f_m = \frac{1}{3\pi\sqrt{L_r C_r}} \tag{12}$$

The URSC step-up converter operates under the following condition:

$$f_m > f_s \tag{13}$$

The time duration of $t_4 - t_5$ for the balance stage is obtained by considering that $t_3<t_4$ time interval duration is π and that $t_3<t_5$ time interval duration is one third of the inverse of the switching frequency. Then, it is as follows:

$$t_4 - t_5 = \frac{\frac{1}{3f_s} - \pi\sqrt{L_r C_r}}{\sqrt{L_r C_r}} \tag{14}$$

The next step is to find the average balance current I_B during the $t_3<t_4$ and $t_4<t_5$ time intervals, which both integrate the total conduction time of the balance stage. Thus, the total average balance current is the sum of the calculated average balance currents from (9) and (10) as shown in (15).

$$\langle I_B \rangle = -2V_{cr2} f_s C_r - V_{cr2} f_s C_r \left(\cos\left(\frac{\frac{1}{3f_s} - \pi\sqrt{L_r C_r}}{\sqrt{L_r C_r}} \right) - 1 \right) \tag{15}$$

The average OLED voltage V_{OLED} is defined from the OLED parameters as shown in (16).

$$V_{OLED} = I_{OLED} R_\gamma + V_\gamma \tag{16}$$

Then, in order to find the average input current I_{in}, the input output energy balance is used, which involves the energy efficiency η, the input voltage V_{in}, the input current I_{in} and the OLED voltage V_{OLED} and OLED current I_{OLED}. The result is shown in (17).

$$I_{in} = \frac{I_{OLED}\left(I_{OLED} R_\gamma + V_\gamma\right)}{V_{in}\eta} \tag{17}$$

Also, by involving (18) and knowing that the average resonant inductor current in one complete cycle is zero, then (19) is obtained.

$$\langle i_{D2} \rangle = -I_{OLED} \tag{18}$$

$$I_{in} - I_{OLED} + I_B = 0 \tag{19}$$

Then, by substituting (15) and (17) in (19) and isolating for V_{cr2}, (20) is obtained.

$$V_{Cr2} = -\frac{I_{OLED} - \frac{I_{OLED}\left(I_{OLED} R_\gamma + V_\gamma\right)}{V_{in}\eta}}{2C_r f_s + C_r f_s \left(\cos\left(\frac{\frac{1}{3f_s} - \pi\sqrt{L_r C_r}}{\sqrt{L_r C_r}} \right) - 1 \right)} \tag{20}$$

By inserting (6) in (20) and isolating for V_{cr1}, the capacitor C_r voltage level V_{cr1} is obtained as shown in (21).

$$V_{Cr1} = 2\left(I_{OLED} R_\gamma + V_\gamma\right) + \frac{I_{OLED} - \frac{I_{OLED}\left(I_{OLED} R_\gamma + V_\gamma\right)}{V_{in}\eta}}{2C_r f_s + C_r f_s \left(\cos\left(\frac{\frac{1}{3f_s} - \pi\sqrt{L_r C_r}}{\sqrt{L_r C_r}} \right) - 1 \right)} \tag{21}$$

The resonant inductor L_r is obtained by calculating the average of i_{Lr} from (8) and making it equal to (18) and then isolating for L_r, thereby the resonant inductor L_r is shown in (22).

$$L_r = \frac{\left(\frac{1}{3f_s}\right)^2}{C_r \left(\pi + 2\sin^{-1}\left(\frac{\sqrt{2C_r f_s V_\gamma + 2C_r f_s R_\gamma I_{OLED} - \frac{I_{OLED}\left(I_{OLED} R_\gamma + V_\gamma\right)}{V_{in}\eta}}}{\sqrt{2C_r f_s V_\gamma - I_{OLED} + 2C_r f_s R_\gamma I_{OLED}}} \right) \right)^2} \tag{22}$$

2168-6777 (c) 2018 IEEE. Personal use is permitted, but republication/redistribution requires IEEE permission. See http://www.ieee.org/publications_standards/publications/rights/index.html for more information.

This article has been accepted for publication in a future issue of this journal, but has not been fully edited. Content may change prior to final publication. Citation information: DOI 10.1109/JESTPE.2018.2827324, IEEE Journal of Emerging and Selected Topics in Power Electronics

From (22), OLED current I_{OLED} is isolated, then (23) is obtained.

$$I_{OLED} = \frac{b(V_{in}\eta - V_{in}\eta R_\gamma c) + V_{in}\eta R_\gamma c - V_\gamma}{2R_\gamma} + \frac{\sqrt{\begin{array}{c} b^2(V_{in}^2\eta^2 R_\gamma^2 c^2 - 2V_{in}^2\eta^2 R_\gamma c + V_{in}^2\eta^2) + \\ b(-2V_{in}^2\eta^2 R_\gamma^2 c^2 + 2V_{in}^2\eta^2 R_\gamma c - 2V_{in}\eta R_\gamma c V_\gamma - 2V_{in}\eta V_\gamma) \\ + V_{in}^2\eta^2 R_\gamma^2 c^2 + 2V_{in}\eta R_\gamma c V_\gamma + V_\gamma^2 \end{array}}}{2R_\gamma} \quad (23)$$

Where b and c are variables used to simplify the expression (23):

$$b = \left(\sin\left(\frac{\frac{1}{3f_s} - \pi\sqrt{L_r C_r}}{2\sqrt{L_r C_r}}\right)\right)^2 \quad (24)$$

$$c = 2C_r f_s \quad (25)$$

An important parameter to keep in mind in OLED drivers development is the dynamic resistance R_γ, which must be taken into consideration to properly select the output capacitance value, needed to achieve the desired OLED ripple current ΔI_{OLED} and OLED ripple voltage ΔV_{OLED}. Therefore, it is possible to find an expression that relates the output filter capacitor C_o and the output voltage ripple ΔV_{OLED} in (26), to obtain the output capacitor value [11][12].

$$C_o = \frac{I_{OLED}}{\Delta V_{OLED}}\left(\frac{1}{f_s} - \frac{1}{3f_n}\right) \quad (26)$$

IV. Design of the Laboratory Prototype

A laboratory prototype for validating the performance of the closed loop unidirectional RSC step-up OLED driver based on VI technique for OLED lamps has been developed as shown in Fig. 7.

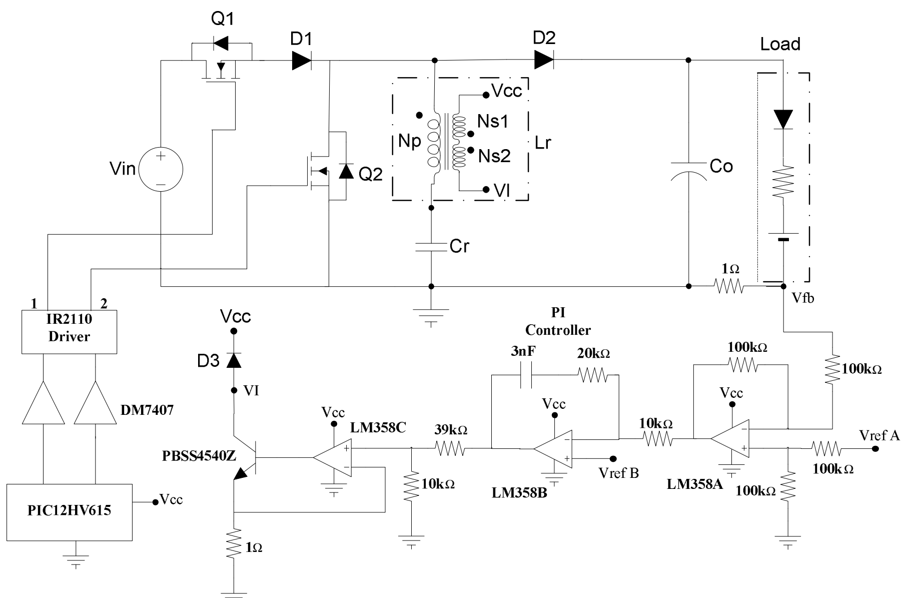

Fig. 7. Schematic diagram of laboratory prototype.

The load is formed by three FL300 OLED lamps in series array, where its nominal DC OLED voltage is 59.2V and nominal OLED current is 368mA for a nominal OLED power of 21.8W [30]. The FL300 OLED lamp is shown in Fig. 8. The calculated model parameters of the OLED's array at room temperature are: $V_\gamma = 53.21\,V$ and $R_\gamma = 16.31\,\Omega$. The equivalent OLED resistance at nominal power is $R_{OLED} = 161\,\Omega$. The selected OLED current ripple is $\Delta I_{OLED} = 6.6\%$. Some additional specifications of the laboratory prototype are the following: V_{in}=48 V; f_S=100 kHz; t_{dead}=100ns; η=92.97%. Since the input design parameters were already described, the design calculation can be addressed. To find the capacitor C_r voltage V_{cr2} from (20), $C_r = 46.2\,nF$ is proposed, therefore, $V_{Cr2} = 19.39\,V$ is calculated. Now, as from (21), the capacitor C_r voltage V_{Cr1} can be calculated as $V_{Cr1} = 99.02\,V$. Then, the resonant inductor L_r is obtained from (22) as $L_r = 12.64\,\mu H$. The tank impedance is extracted from (5) as $Z_n = 16.54\Omega$. The resonant frequency f_m is then calculated from (12) as f_m = 138.9 kHz. From (26), the output filter capacitor is $C_o = 10\mu$ by selecting the OLED voltage ripple as ΔV_{OLED} = 0.5%.

2168-6777 (c) 2018 IEEE. Personal use is permitted, but republication/redistribution requires IEEE permission. See http://www.ieee.org/publications_standards/publications/rights/index.html for more information.

This article has been accepted for publication in a future issue of this journal, but has not been fully edited. Content may change prior to final publication. Citation information: DOI 10.1109/JESTPE.2018.2827324, IEEE Journal of Emerging and Selected Topics in Power Electronics

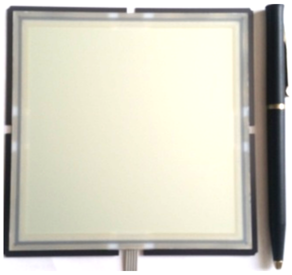

Fig. 8. FL300 OLED lamp.

In Table I, the list of materials for the laboratory prototype implementation is included according to the component values calculations from Section III.

TABLE I. COMPONENTS LIST OF THE LABORATORY PROTOTYPE.

Reference	Description
Q_1, Q_2	BUK7613-100E FET Transistors
D_1, D_2	MBR20100CT Schottky Diodes
C_r $C_{r1}, C_{r2}, C_{r3}, C_{r4}, C_{r5}$ C_{r6}	$C_{r1}\|\|C_{r2}\|\|C_{r3}\|\|C_{r4}\|\|C_{r5}+C_{r6}$ PHE450RD5100J10nF, 650V Capacitor 15nF J 1000V 378 MKP Capacitor
L_r	EFD 25/13/9 Inductor Np=9T, 66x0.08mm Ns1=Ns2=53T, 35AWG GAP=0.35 mm
C_o	ECQE2106KFB10uF, 250V Capacitor

The variable inductor built for the laboratory prototype of the URSC is shown in Fig. 9.

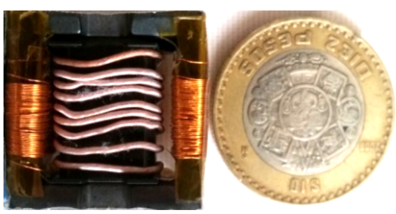

Fig. 9. Variable inductor for the laboratory prototype.

A brief performance explanation of the closed loop URSC step-up OLED driver prototype based on VI shown in Fig. 10 is presented in the following.

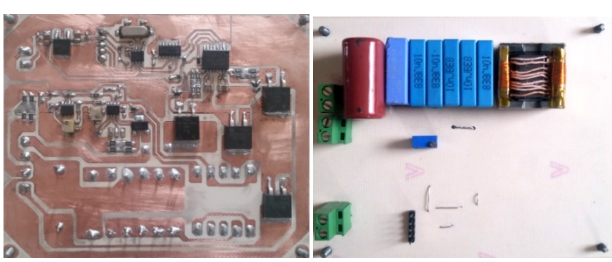

Fig. 10. URSC laboratory prototype.

The control operation of the URSC step-up OLED driver is achieved as follows: the microcontroller PIC12HV615 generates the 5V PWM signals for transistors Q_1 and Q_2 at a switching frequency f_S of 100 kHz, with an On-time of one third of the switching period, and they both are out of phase for 180 degrees according to the principle operation of the URSC step-up OLED driver. Open collector DM7407 buffers just take charge of supply 12V PWM signals to the high-low side driver IR2110 driver, which is in charge of commanding transistors Q_1 and Q_2.

The VI L_r control operation is as follows: a reference DC current bias I_{ref} is injected through the auxiliary windings N_{s1} and N_{s2}, which are connected one another with reverse polarity in order to cancel the AC voltage component generated across them. The injected I_{ref} causes a DC flux bias $\emptyset_{dc}$ that circulates mainly through the variable reluctances $\Re_m$ of the outer arms of the magnetic core due to the higher reluctance $\Re_o$ of the center arm, which is air gapped; this flux biases the operating point of the magnetic material in the $B-H$ curve, producing a change of the main winding N_p inductance. The variable reluctance value depends on the operating point of the magnetic material that is settled by means of the injected I_{ref} and is a function of the magnetic permeability μ of the magnetic material [16]-[17].

The control loop of the OLED driver is shown in Fig. 7 and performs as the following: the OLED current I_{OLED} is fed back through the 1Ω sensing resistor and the LM358A amplifier to the control input of the LM358B error amplifier. The output voltage of the LM358B is adapted by the LM358C to drive the constant current source in order to meet the operating point of the VI and to produce regulation at the output current of the URSC converter. The feedback voltage V_{fb} is compared to a reference voltage V_{refA}, because V_{fb} must be equivalent to V_{refB} to meet the operating point of the VI and I_{OLED}; where $V_{refA} = V_{refB} + V_{I_{OLED}}$. Hence, $V_{refA} - V_{fb}$ is equivalent to V_{refB} reference voltage, which is equivalent to that DC bias current that finds the resonant inductor value L_r for fulfilling the average I_{OLED}. $V_{I_{OLED}}$ is the equivalent to I_{OLED}. To compensate average OLED current I_{OLED} changes from input voltage variations or load steps down and up, a PI controller defined as in (27) is proposed. Nonetheless, a complete modeling analysis of the URSC converter + VI is out of the scope of this work due to lack of space.

$$G_C(s) = k_c \frac{1 + s/2\pi f_z}{s} \tag{27}$$

The control output voltage of the LM358B error amplifier is increased as I_{OLED} increases, whilst L_r is decreased because V_{fb} is greater than $V_{I_{OLED}}$. On the other hand, the control output voltage of the LM358B is decreased as I_{OLED} decreases while L_r is decreased because V_{fb} is lower than $V_{I_{OLED}}$. The control laws $V_{fb} > V_{I_{OLED}}$ and $V_{fb} < V_{I_{OLED}}$ are based on the fact that $V_{refA} - V_{fb} = \left(V_{refB} + V_{I_{OLED}}\right) - V_{fb}$ and $\left(V_{refB} + V_{I_{OLED}} - V_{fb}\right) - V_{refB} = V_{I_{OLED}} - V_{fb}$.

2168-6777 (c) 2018 IEEE. Personal use is permitted, but republication/redistribution requires IEEE permission. See http://www.ieee.org/publications_standards/publications/rights/index.html for more information.

This article has been accepted for publication in a future issue of this journal, but has not been fully edited. Content may change prior to final publication. Citation information: DOI 10.1109/JESTPE.2018.2827324, IEEE Journal of Emerging and Selected Topics in Power Electronics

V. SIMULATIONS RESULTS

Fig. 11 illustrates the circuit schematic of the URSC with the VI electrical-magnetic model in closed loop for simulating the unidirectional RSC step-up converter. The VI model is proposed in [16]-[17].

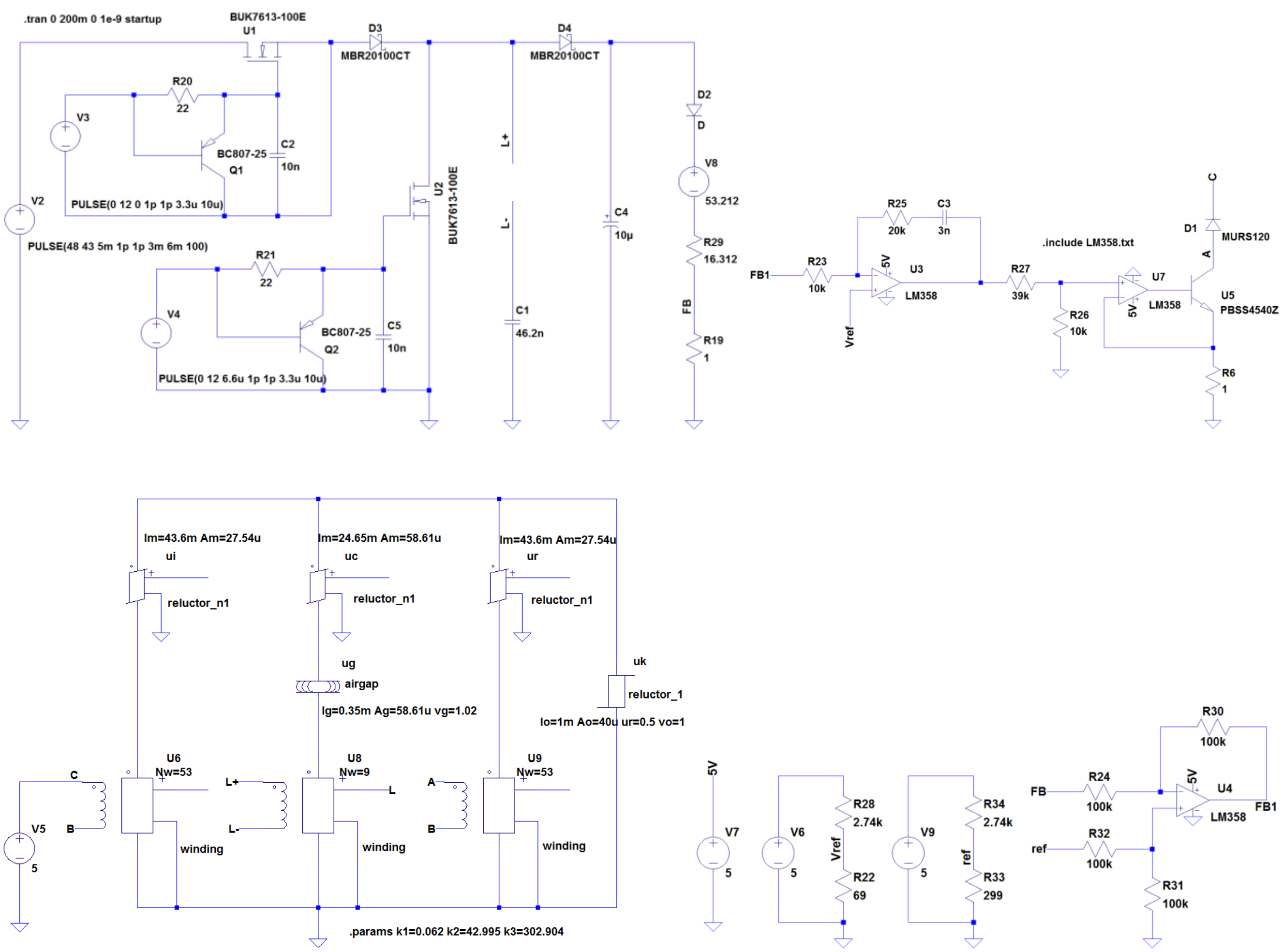

Fig. 11. URSC and VI model in closed loop.

The inductance value of L_r vs DC bias current curve of the VI is shown in Fig. 12. As can be observed, it finds a very good agreement between simulation and experimental curve of the VI inductor.

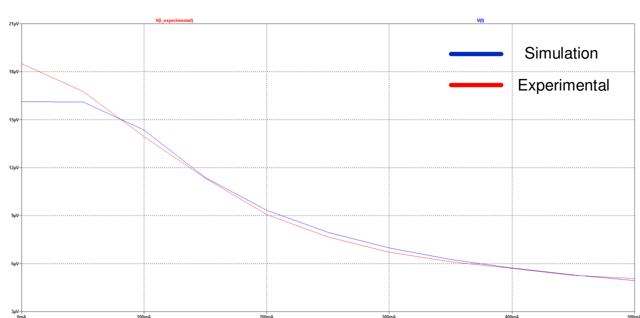

Fig. 12. Inductance vs DC bias current curve of the VI inductor: a) Simulation (Blue) and b) Experimental (Red). (3 µV/div and 100 mA/div).

Fig. 13 illustrates the resonant current I_{Lr} and the resonant voltage V_{Cr}.

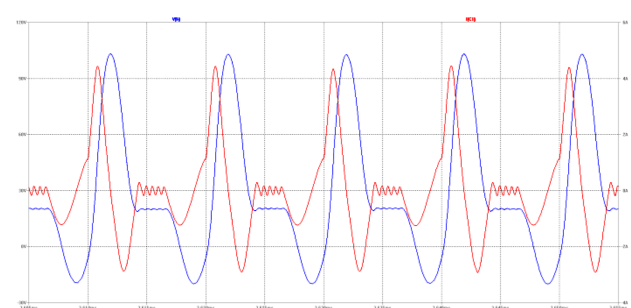

Fig. 13. Resonant tank waveforms: Blue: resonant capacitor voltage V_{Cr} and Red: resonant inductor current i_{Lr}. (30V/div, 2A/div and 5µs/div).

Fig. 14 shows the nominal DC OLED voltage V_{OLED} and OLED current I_{OLED} of the URSC step-up converter.

2168-6777 (c) 2018 IEEE. Personal use is permitted, but republication/redistribution requires IEEE permission. See http://www.ieee.org/publications_standards/publications/rights/index.html for more information.

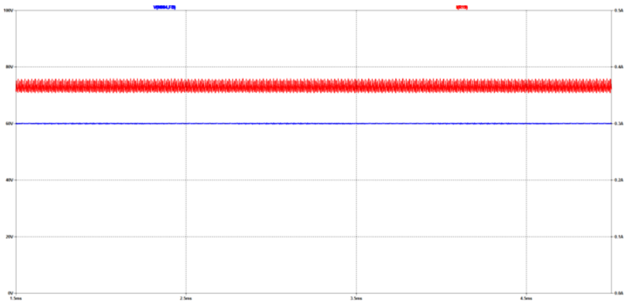

Fig. 14. Steady state load waveforms: Blue: DC OLED voltage V_{OLED} and Red: OLED current I_{OLED}. (20 V/div, 100 mA/div and 1ms/div).

Fig. 15 shows the dynamic response of the URSC step-up converter in closed loop under input voltage V_{in} step-up and down from 48V to 43V respectively. As shown, good dynamic behavior is achieved owing to the fact that the OLED current I_{OLED} is well regulated to 368mA. The stabilization time of the OLED current I_{OLED} after a step-down input voltage is applied is about 1 ms.

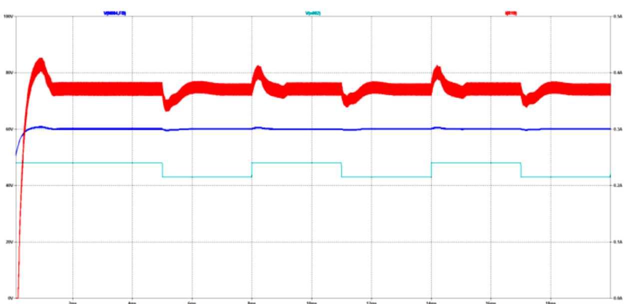

Fig. 15. Input voltage step-down transient response waveforms: Blue: DC OLED voltage V_{OLED} 20V/div, Red: OLED current I_{OLED} 100mA/div and Green: input voltage V_{in} 20V/div. (2ms/div).

VI. EXPERIMENTAL RESULTS

Fig. 16 illustrates the behavior of the DC OLED voltage V_{OLED} and OLED current I_{OLED} in steady state. As it can be seen, DC OLED voltage V_{OLED} and OLED current I_{OLED} stabilize at about 59.2 V and 368 mA.

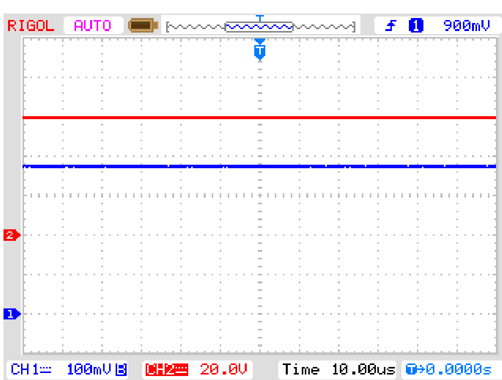

Fig. 16. Transient response waveforms: Red: DC OLED voltage V_{OLED} 20V/div and Blue: OLED current I_{OLED} 200mA/div.

Fig. 17 shows the switching waveforms on Q_1, which do not show overlapping between both signals.

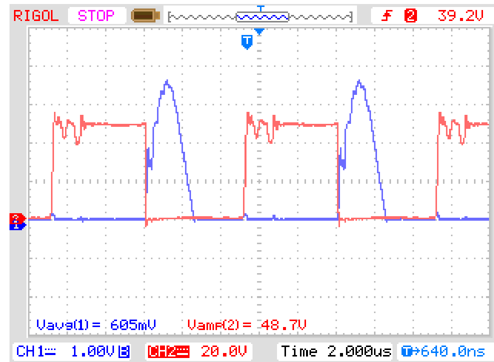

Fig. 17. Switching waveforms of Q_1: Red: drain-source voltage 20V/div and (Blue) drain current 1A/div.

Fig. 18 shows the resonant current I_{Lr} and the resonant voltage V_{Cr} of the URSC converter.

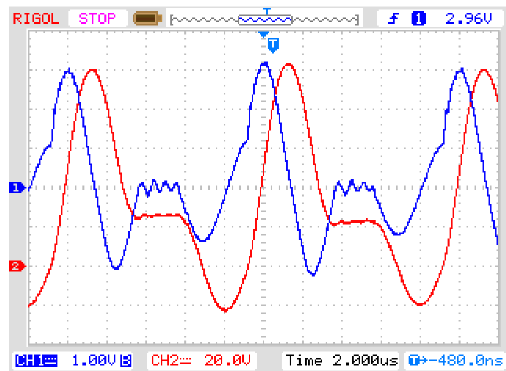

Fig. 18. Resonant tank waveforms: Red: resonant capacitor voltage V_{Cr} 20V/div and Blue: resonant inductor current i_{Lr} 1A/div.

Fig. 19 shows the dynamic response of the URSC converter in closed loop under a DC OLED voltage V_{OLED} decrease of 4V from 59.2V nominal by short-circuiting 5 1N4001 rectifier diodes from a 75 in series rectifier diodes dummy load.

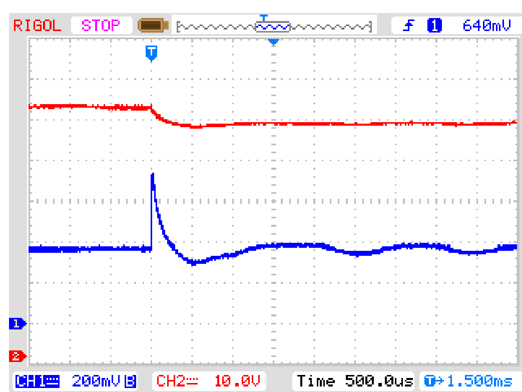

Fig. 19. Transient response waveforms: Red: DC OLED voltage V_{OLED} 10V/div and Blue: OLED current I_{OLED} 200mA/div.

2168-6777 (c) 2018 IEEE. Personal use is permitted, but republication/redistribution requires IEEE permission. See http://www.ieee.org/publications_standards/publications/rights/index.html for more information.

This article has been accepted for publication in a future issue of this journal, but has not been fully edited. Content may change prior to final publication. Citation information: DOI 10.1109/JESTPE.2018.2827324, IEEE Journal of Emerging and Selected Topics in Power Electronics

Fig. 20 represents the experimental average OLED current I_{OLED} of the URSC converter at constant reference voltage V_{refB} under different input voltage V_{in} in open loop. The average OLED current I_{OLED} is dimmed from 0 mA to 445 mA by keeping constant V_{refB} at 122.5 mV and sweeping the input voltage from 0 V to 53 V.

The experimental average OLED current I_{OLED} under different resonant inductor L_r values and reference voltage V_{refB} values at constant input voltage V_{in} in open loop is shown in Fig. 21 and Fig. 22, respectively. The average OLED current I_{OLED} is dimmed from 135 mA to 405 mA by keeping constant the input voltage V_{in} at 48 V and sweeping the reference voltage V_{refB} from 73.3 mV to 196 mV.

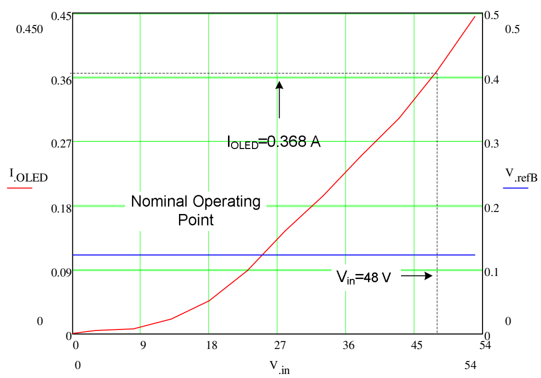

Fig. 20. I_{OLED} vs V_{in} in open loop.

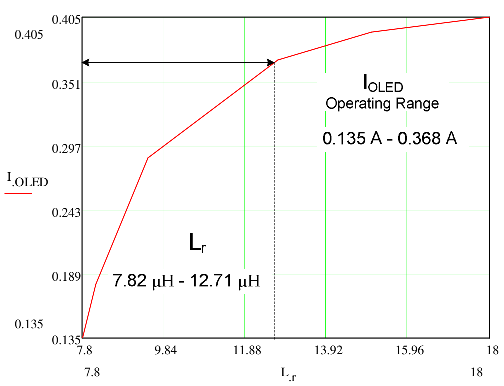

Fig. 21. I_{OLED} vs L_r in open loop.

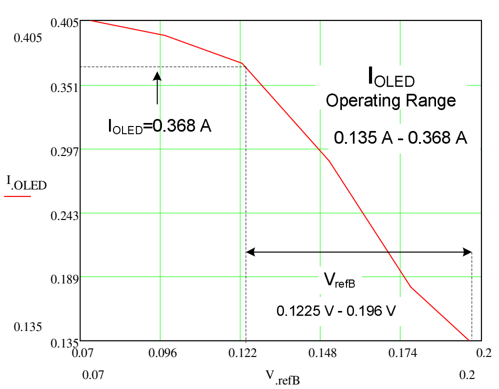

Fig. 22. I_{OLED} vs V_{ref} in open loop.

Fig. 23 depicts the experimental electrical efficiencies η under different average OLED power P_{OLED}. This is dimmed from 7.91 W to 25.08 W by keeping constant the input voltage V_{in} at 48 V and sweeping the reference voltage V_{refB} from 73.3 mV to 196 mV. The electrical efficiency η measured at nominal P_{OLED} is 92.97%.

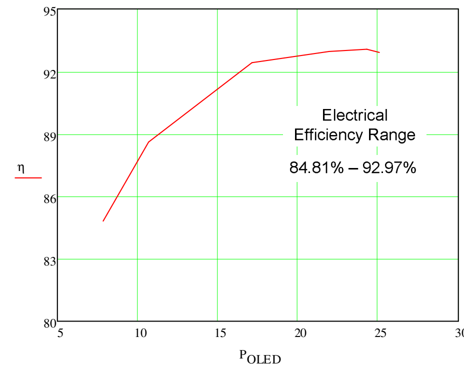

Fig. 23. Electrical efficiency η vs P_{OLED} in open loop.

VII. CONCLUSIONS

URSC step-up converter finds a very good behavior to drive OLED lamps because it provides a very good efficiency, VI control loop simplicity, high power density and low cost. The VI control technique provides a very good output current regulation and dynamic response to the URSC step-up converter by means of resonant frequency control. This paper has been focused on designing and analyzing experimentally the URSC step-up converter.

REFERENCES

[1] G. Martínez and J. M. Alonso, "A Review on Switched Capacitor Converters with High Power Density for OLED Lamp Driving," *IEEE Ind. Appl. Society Conference*, Oct. 2015, pp. 1-8.

[2] K. W. E. Cheng and P. D. Evans, "Parallel-Mode Extended Period Quasi-Resonant Converter," *IEEE Proc. Inst. Elect. Eng.*, vol. 138, pp. 243–251, Sept. 1991.

[3] K. W. E. Cheng and P. D. Evans, "Unified Theory of Extended-Period Quasi-Resonant Converters," *IEEE Proceedings-Electric Power Applications*, vol. 147, pp. 119-130, March 2000.

[4] O. C. Mak, Y. C. Wong, and A. Ioinovici, "Step-up DC Power Supply Based on a Switched-Capacitor Circuit," *IEEE Trans. Ind. Electron.*, vol. 42, pp. 90–97, Feb. 1995.

[5] J. Liu, Z. Chen, and Z. Du, "A New Design of Power Supplies for Pocket Computer Systems," *IEEE Trans. Ind. Electron.*, vol. 45, pp. 228–235, Apr. 1998.

[6] H. Bengtsson, "A Switch in Methods," *New Electronics*, pp. 40-41, Aug. 1997.

[7] S. S. Ang and A. R. Oliva, Power-Switching Converters, *London: Taylor and francis group*, 1957, Chap. 8.

[8] K. W. E. Cheng, "New Generation of Switched Capacitor Converters," *in Proc. IEEE PESC'98*, May 1998, pp. 1529-1535.

[9] Y. P. B. Yeung, K. W. E. Cheng, S. L. Ho, K. K. Law, and D. Sutanto, "Unified Analysis of Switch Capacitor Resonant Converters," *IEEE Transactions on Industrial Electronics*, vol. 51, pp. 864-873, Aug. 2004.

[10] Y. Ye, K. W. E. Cheng, J. Liu, and C. Xu, "A Family of Dual-Phase-Combined Zero-Current Switching Switched-Capacitor Converters," *IEEE Transactions on Power Electronics*, vol. 29, pp. 4209-4218, Aug. 2014.

2168-6777 (c) 2018 IEEE. Personal use is permitted, but republication/redistribution requires IEEE permission. See http://www.ieee.org/publications_standards/publications/rights/index.html for more information.

[11] A. Cervera, M. Evzelman, M. M. Peretz, and S. Ben-Yaakov, "A High Efficiency Resonant Switched Capacitor Converter with Continuous Conversion Ratio," *IEEE Energy Conversion Congress and Exposition*, Sept. 2013, pp. 4969-4976.

[12] A. Cervera, M. Evzelman, M. M. Peretz, and S. Ben-Yaakov, "A High Efficiency Resonant Switched Capacitor Converter with Continuous Conversion Ratio," *IEEE Transactions on Power Electronics*, vol. 30, pp. 1373-1382, March 2015.

[13] P. H. A. Miranda, E. M. Sá.A. V. L. de Oliveira, E. E. dos Santos Fo, F. L. M. Antunes, "A Switched-Capacitor Driver for Power LEDs," *IEEE XI Brazilian Power Electronics Conference*, Sept. 2011, 918-923.

[14] O. Tetervenoks, "Sensorless Converter for Low-Power LED Lamp with Improved Power Factor," *IEEE 2014 Electric Power Quality and Supply Reliability Conference (PQ)*, June 2014, pp. 285-290.

[15] G. Martínez, J. M. Alonso and R. O. Sánchez, "Analysis and Design of a Unidirectional Resonant Switched Capacitor Step-up Converter for OLED Lamp Driving Based on Variable Inductor," *IEEE Ind. Appl. Society Conference*, Oct. 2017, pp. 1-8.

[16] J. M. Alonso, G. Martínez, M. Perdigão, M. Cosetin, R. N. do Prado; "A Systematic Approach to Modelling Complex Magnetic Devices Using SPICE: Application to Variable Inductors," *IEEE Trans. on Power Electronics*, vol. 31, pp. 7735-7746, May. 2016.

[17] J. M. Alonso, M. S. Perdigão, G. Z. Abdelmessih, M. A. Dalla Costa, and Y. Wang, "SPICE Modeling of Variable Inductors and Its Application to Single Inductor LED Driver Design," *IEEE Trans. on Industrial Electronics*, vol. 64, pp. 5894-5903, July 2017.

[18] J. M. Alonso, M. S. Perdigão, M. A. Dalla Costa, G. Martínez and R. Osorio, "Analysis and Experiments on a Single-Inductor Half-Bridge LED Driver with Magnetic Control," *IEEE Trans. on Power Electronics*, vol. 32, pp. 9179-9190, Jan. 2017.

[19] S. B. Yaakov and M. M. Peretz, "A Self-Adjusting Sinusoidal Power Source Suitable for Driving Capacitive Loads," *IEEE Trans. on Power Electronics*, vol. 21, pp. 890-898, Jul. 2006.

[20] S. B. Yaakov and M. M. Peretz, "Modeling and Behavioral SPICE Simulation of a Self-Adjusting Current-Fed Push-Pull Parallel Resonant Inverter (SA-CFPPRI)," *IEEE Annual Power Electronics Specialists Conference*, Jun. 2004, pp. 61-67.

[21] Lumiblade OLED Driver-Low Voltage. Product sheet. 2018.

[22] Lumiblade OLEDs. Product Catalog Sheet. 2012.

[23] J. Jacobs, D. Hente and E. Waffenschmidt, "Drivers for OLEDs," *IEEE Ind. Appl. Society Conference*, Sept. 2007, pp. 1147-1152.

[24] Y. J. Chen, W. C. Yang, C. S. Moo and Y. C. Hsieh, "A High Efficiency Driver for High-Brightness White LED Lamp," *IEEE TENCON*, Nov. 2010, pp. 2313-2317.

[25] A. Pollock, H. Pollock and C. Pollock, "High Efficiency LED Power Supply," *IEEE Journal of Emerging and Selected Topics in Power Elect.*, vol. 3, pp. 617-623, Sept. 2015.

[26] W. C. Yang, Y. J. Chen and C. S. Moo, "An Efficient Driver for Dimmable LED Lighting," *IEEE Conf. on Industrial Elect. and Appl.*, Jun. 2011, pp. 2331-2336.

[27] J. L. Baek, J. K. Kim, J. B. Lee, H. S. Youn and G. W. Moon, "Integrated Asymmetrical Half-bridge Zeta Converter for DC/DC Stage of LED Driver with Wide Output Voltage Range and Low Output Current," *IEEE Trans. on Industrial Elect.*, vol. 62, pp. 7489-7498, Dec. 2015.

[28] S. Madhumita and T. M. Binvy, "LC Series Resonant Converter Based High Power HB LED Lamp Driver with ZVS," *IEEE INDICON*, Dec. 2016, pp. 1-6.

[29] M. Arias, I. Castro, D. G. Lamar, A. Vázquez and J. Sebastián, "Optimized Design of a High Input-Voltage-Ripple-Rejection Converter for LED Lighting," *IEEE Trans. on Power Elect.*, vol. 33, pp. 5192-5205, Jun. 2018.

[30] Lumiblade OLED Panel. Brite FL300. Product Sheet. 2014.

2168-6777 (c) 2018 IEEE. Personal use is permitted, but republication/redistribution requires IEEE permission. See http://www.ieee.org/publications_standards/publications/rights/index.html for more information.

Analysis and Design of a Unidirectional Resonant Switched Capacitor Step-up Converter for OLED Lamp Driving Based on Variable Inductor

Gilberto Martínez[1], J. Marcos Alonso[1] and R. Osorio Sánchez[2]

(1) University of Oviedo, Electrical & Electronics Eng. Dept., 33204-Gijón, Asturias, Spain
(2) University of Guadalajara, Electronics Eng. Dept., 46600-Ameca, Jalisco, México.
gilbertomar9@hotmail.com; marcos@uniovi.es; reneosorios@yahoo.com

***Abstract*-This paper presents an analysis and design of a unidirectional resonant switched capacitor (URSC) step-up converter for OLED lamp driving. The URSC converter includes a very small inductor in series with the switched capacitor to improve the switching behavior. Also, the URSC converter presents the advantages of high power density, higher efficiency compared to other SC converters, low output voltage and current ripples and low EMI noise, which make it adequate for driving OLED lamps. URSC is designed to operate in closed loop with constant current VI control technique. By working the resonant inductor as a VI, the OLED current can be regulated and dimmed because of resonant frequency change. Simulation and experimental results of the VI inductor, which are in a good agreement, and the results of a URSC step-up converter design example for a 21.8 W OLED lamps array supplied from 48Vdc are presented, where a maximum 91.5% efficiency is obtained.**

***Index Terms*- Organic-Lighting-Emitting-Diode (OLED), Switched-Capacitor (SC), Resonant Switched-Capacitor (RSC), Variable Inductor (VI), Closed-Loop Operation.**

I. INTRODUCTION

In [1], a review of SC converters for OLED lamp driving was presented, where the URSC step-up converter was proposed as the best option for driving OLED lamps, based on the performance comparative results among the different SC converters under study [2]-[14], and relying on the collected experimental results of the URSC step-up converter. The benefits of using the URSC step-up converter instead of conventional non-resonant and resonant SC converters, fractional-voltage-conversion-ratio RSC converters, dual-phase converters, step-down half bridge RSC converter with isolation transformer, and step-down SC converter with coupling inductors are: high output voltage regulation, low output voltage and current ripples, high efficiency, no efficiency dependency on conversion ratio, low EMI noise, and high power density [1].

In this work, the URSC step-up converter is analyzed and designed for driving a 21.8 W OLED lamps array. The resonant inductor is designed to operate at a resonant frequency above the switching frequency for any OLED power. Under this condition, a good dynamic behavior against input voltage or luminous flux variations is obtained.

In section II, the operation of the URSC step-up converter is presented. In section III, the analysis and design of the URSC step-up converter is carried out. Section IV illustrates the design of a laboratory prototype. Simulations and experimental results are shown in sections V and VI. Conclusions are presented in section VII.

II. OPERATION OF THE UNIDIRECTIONAL RESONANT SWITCHED CAPACITOR STEP-UP CONVERTER

Fig. 1 shows the URSC step-up converter, which consists of two switches, Q_1 and Q_2, two diodes, D_1 and D_2, a resonant capacitor, C_r, a resonant inductor, L_r, and an output filter capacitor, C_O. The converter has four operation modes, namely, charge, discharge, off and balance, where this last stage balances the remaining charge into the resonant capacitor before the beginning of the next switching period, in order to further improve the switching behavior of the converter. In addition, the URSC step-up converter behaves as a current source; therefore, the output voltage amplitude depends on the OLED dc equivalent resistance. In the following, the different operation intervals of the URSC step-up converter are presented. Figs. 2 to 5 illustrate the equivalent circuit in each time interval. Fig. 6 shows the main waveforms of the converter operation.

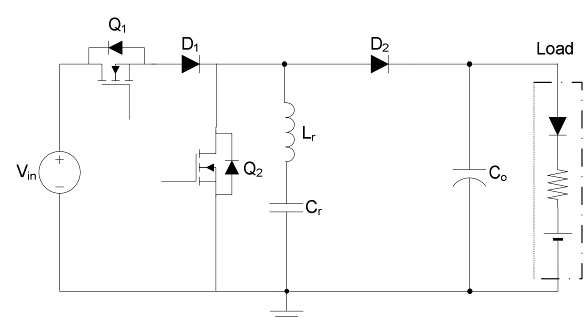

Fig. 1. URSC step-up converter.

A. *Charge Operation Stage: $t_0<t_1$*

Fig. 2 shows the equivalent circuit for charge operation stage. As can be seen, transistor Q_1, and diode D_1, are on, while transistor Q_2, and diode, D_2 are off. The resonant capacitor C_r, is charged through, Q_1 and D_1, while the output filter capacitor C_O, is discharged to the load. It is important to

978-1-5090-4894-6/17/$31.00 © 2017 IEEE

mention that the resonant current I_{Lr} at the beginning of this stage is not zero due to the conduction period of the freewheeling diode of Q_2 in the balance stage.

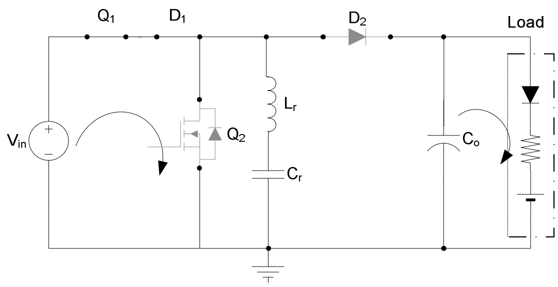

Fig. 2. Stage $t_0<t_1$.

B. *Discharge Operation Stage: $t_1<t_2$*

Fig. 3 illustrates the discharge operation stage, where transistors Q_1 and Q_2, and diode D_1 are off, while diode D_2, is on. The resonant capacitor C_r, is discharged through D_2, and the output filter capacitor C_O, is charged.

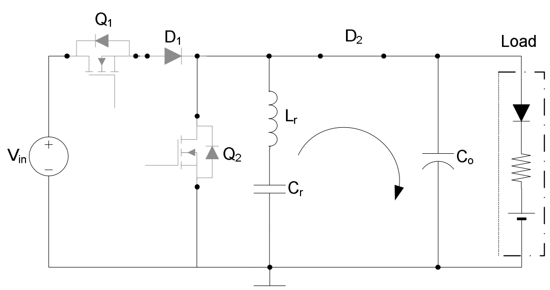

Fig. 3. Stage $t_1<t_2$.

C. *Off Operation Stage: $t_2<t_3$*

In this operation stage, transistors Q_1 and Q_2, and diodes D_1 and D_2, are off. The resonant inductor current i_{Lr} through $L_r - C_r$, is zero. Fig. 4 shows the off operation stage equivalent circuit.

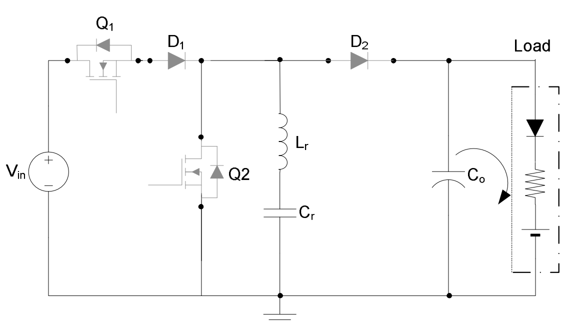

Fig. 4. Stage $t_2<t_3$.

D. *Balance Operation Stage: $t_3<t_5$*

The balance operation stage circuit is shown in Fig. 5. In which during $t_3<t_4$, transistor Q_1, and diodes D_1 and D_2, are off, while transistor Q_2 is on and the output filter capacitor C_O, keeps discharging to the load.The resonant tank, $L_r - C_r$, is shortcircuited in order to balance the energy stored in C_r, so that the same charge level as that at instant t_0 is attained for the next charge operation state. At the end of this stage during $t_4<t_5$, the current is flowing through the body diode of Q_2, thereby, transistors Q_1 and Q_2, and diodes D_1 and D_2, are off, while the resonant capacitor C_r is charged.

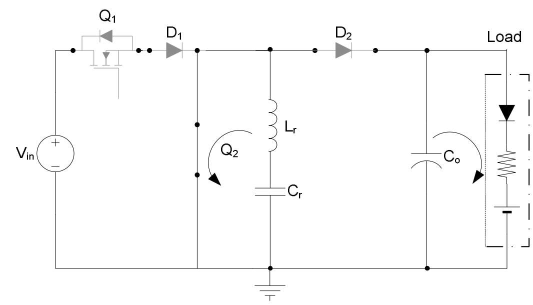

Fig. 5. Stage $t_3<t_5$.

The waveforms corresponding to each operation state are shown in the Fig. 6.

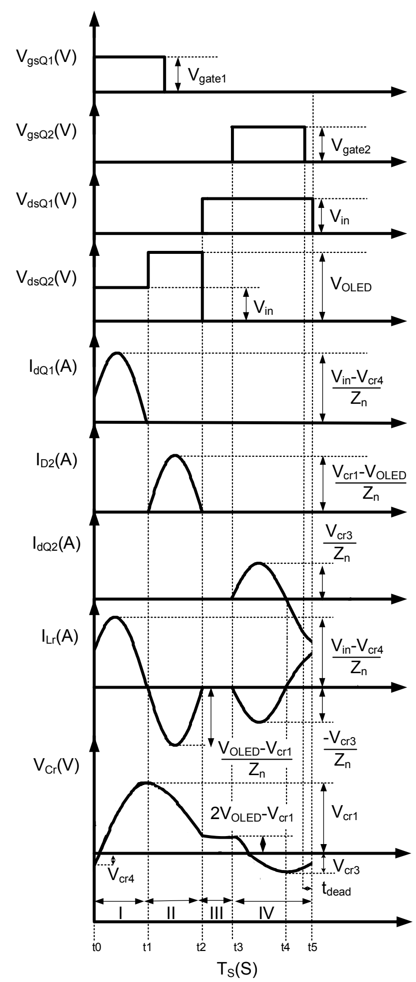

Fig. 6. Main waveforms of the RSC Step-up converter during one switching period.

III. Analysis and Design of the URSC Step-Up Converter

In this section, the analysis and design of the URSC step-up converter is carried out based on the methodology used in [11][12]. First, by analyzing the charge operation stage circuit shown in Fig. 2, the expressions (1) and (2) are obtained.

$$\frac{di_{Lr}}{dt} = \frac{V_{in}-V_{Cr}}{L_r} \tag{1}$$

$$\frac{dV_{Cr}}{dt} = \frac{i_{Lr}}{C_r} \tag{2}$$

Now, from (1) and (2) and after some manipulation, V_{Cr} is obtained in (3). And then by substituting (3) into (2), and isolating and solving for i_{Lr}, (4) is obtained, which is the expression of the resonant inductor current i_{Lr}.

$$V_{Cr} = V_{in} - (V_{in} - V_{Cr}(0))\cos\omega t \tag{3}$$

$$i_{Lr} = \frac{V_{in}-V_{Cr}(0)}{Z_n}\sin\omega t \tag{4}$$

Where V_{in} is the DC input voltage and Z_n is the equivalent resonant tank impedance:

$$Z_n = \sqrt{\frac{L_r}{C_r}} \tag{5}$$

Similarly, the circuits shown from Fig. 3 to Fig. 5 can be analyzed in order to obtain the expressions for V_{Lr} and I_{Cr}, which lead to the form of (3) and (4), where V_{in} takes the values of the DC OLED voltage V_{OLED} and 0, respectively. Based on the afore-mentioned procedure, (6) and (7) are found for the maximum V_{Cr} values at the end of discharge and t_3-t_4 balance operation stages by considering $\omega t = \pi$.

$$V_{Cr2} = 2V_{OLED} - V_{cr1} \tag{6}$$

$$V_{Cr3} = -V_{cr2} \tag{7}$$

Where V_{Cr1}, V_{Cr2} and V_{Cr3} are the capacitor C_r voltages at t_1, t_2 and t_4, respectively.

In addition, (4), (8), (9) and (10) show the obtained expressions for the resonant inductor current i_{Lr} for discharge and t_3-t_4 and t_4-t_5 balance operation stages:

$$i_{Lr} = \frac{V_{OLED}-V_{cr1}}{Z_n}\sin\omega t \quad when \quad t_1 < t < t_2 \tag{8}$$

$$i_{Lr} = \frac{-V_{cr2}}{Z_n}\sin\omega t \quad when \quad t_3 < t < t_4 \tag{9}$$

$$i_{Lr} = \frac{-V_{cr3}}{Z_n}\sin\omega t \quad when \quad t_4 < t < t_5 \tag{10}$$

The resonant frequency f_n is expressed as follows:

$$f_n = \frac{1}{3\pi\sqrt{L_r C_r}} \tag{11}$$

The URSC step-up converter operates under the following condition:

$$f_n > f_s \tag{12}$$

The time duration of $t_4 - t_5$ for the balance stage is obtained by considering that $t_3<t_4$ time interval duration is π and that $t_3<t_5$ time interval duration is one third of the inverse of the switching frequency f_s plus the dead time t_{dead}. Then, it is as follows:

$$t_4 - t_5 = \frac{t_{dead}+\frac{1}{3f_s}-\pi\sqrt{L_r C_r}}{\sqrt{L_r C_r}} \tag{13}$$

The next step is to find the average balance current I_B during the $t_3<t_4$ and $t_4<t_5$ time intervals, which both integrate the total conduction time of the balance stage. Thus, the total average balance current is the sum of the calculated average balance currents from (9) and (10) as shown in (14).

$$\langle I_B\rangle = -2V_{cr2}f_s C_r - V_{cr2}f_s C_r\left(\cos\left(\frac{t_{dead}+\frac{1}{3f_s}-\pi\sqrt{L_r C_r}}{\sqrt{L_r C_r}}\right)-1\right) \tag{14}$$

The average OLED voltage V_{OLED} is defined from the LED parameters as shown in (15).

$$V_{OLED} = I_{OLED}R_\gamma + V_\gamma \tag{15}$$

Then, in order to find the average input current I_{in}, the input output energy balance is used, which involves the energy efficiency η, the input voltage V_{in}, the input current I_{in} and the OLED voltage V_{OLED} and OLED current I_{OLED}. The result is shown in (16).

$$I_{in} = \frac{I_{OLED}(I_{OLED}R_\gamma+V_\gamma)}{V_{in}\eta} \tag{16}$$

Also, by involving (17) and knowing that the average resonant inductor current in one complete cycle is zero, then (18) is obtained.

$$\langle i_{D2}\rangle = -I_{OLED} \tag{17}$$

$$I_{in} - I_{OLED} + I_B = 0 \tag{18}$$

Then, by substituting (14) and (16) in (18) and isolating for V_{cr2}, (19) is obtained.

$$V_{Cr2} = -\frac{I_{OLED} - \frac{I_{OLED}(I_{OLED}R_\gamma + V_\gamma)}{V_{in}\eta}}{2C_r f_s + C_r f_s\left(\cos\left(\frac{t_{dead} + \frac{1}{3f_s} - \pi\sqrt{L_r C_r}}{\sqrt{L_r C_r}}\right) - 1\right)} \quad (19)$$

By inserting (6) in (19) and isolating for V_{cr1}, the capacitor C_r voltage level V_{cr1} is obtained as shown in (20).

$$V_{Cr1} = 2(I_{OLED}R_\gamma + V_\gamma) + \frac{I_{OLED} - \frac{I_{OLED}(I_{OLED}R_\gamma + V_\gamma)}{V_{in}\eta}}{2C_r f_s + C_r f_s\left(\cos\left(\frac{t_{dead} + \frac{1}{3f_s} - \pi\sqrt{L_r C_r}}{\sqrt{L_r C_r}}\right) - 1\right)} \quad (20)$$

The resonant inductor L_r is obtained by calculating the average of i_{Lr} from (8) and making it equal to (17) and then isolating for L_r, thereby the resonant inductor L_r is shown in (21).

$$L_r = \frac{\left(t_{dead} + \frac{1}{3f_s}\right)^2}{C_r\left(\pi + 2\sin^{-1}\left(\frac{\sqrt{2C_r f_s V_\gamma + 2C_r f_s R_\gamma I_{OLED} - \frac{I_{OLED}(I_{OLED}R_\gamma + V_\gamma)}{V_{in}\eta}}}{\sqrt{2C_r f_s V_\gamma - I_{OLED} + 2C_r f_s R_\gamma I_{OLED}}}\right)\right)^2} \quad (21)$$

From (21), OLED current I_{OLED} is isolated, then (22) is obtained.

$$I_{OLED} = \frac{b(V_{in}\eta - V_{in}\eta R_\gamma c) + V_{in}\eta R_\gamma c - V_\gamma}{2R_\gamma} + \frac{\sqrt{\begin{array}{c} b^2(V_{in}^2\eta^2 R_\gamma^2 c^2 - 2V_{in}^2\eta^2 R_\gamma c + V_{in}^2\eta^2) + \\ b(-2V_{in}^2\eta^2 R_\gamma^2 c^2 + 2V_{in}^2\eta^2 R_\gamma c - 2V_{in}\eta R_\gamma c V_\gamma - 2V_{in}\eta V_\gamma) \\ + V_{in}^2\eta^2 R_\gamma^2 c^2 + 2V_{in}\eta R_\gamma c V_\gamma + V_\gamma^2 \end{array}}}{2R_\gamma} \quad (22)$$

Where b and c are variables used to simplify the expression (22):

$$b = \left(\sin\left(\frac{t_{dead} + \frac{1}{3f_s} - \pi\sqrt{L_r C_r}}{2\sqrt{L_r C_r}}\right)\right)^2 \quad (23)$$

$$c = 2C_r f_s \quad (24)$$

An important parameter to keep in mind in OLED drivers development is the dynamic resistance R_γ, which must be taken into consideration to properly select the output capacitance value, needed to achieve the desired OLED ripple current ΔI_{OLED} and OLED ripple voltage ΔV_{OLED}. Therefore, it is possible to find an expression that relates the output filter capacitor C_o and the output voltage ripple ΔV_{OLED} in (25), to obtain the output capacitor value [11][12].

$$C_o = \frac{I_{OLED}}{\Delta V_{OLED}}\left(\frac{1}{f_s} - \frac{1}{3f_n}\right) \quad (25)$$

IV. Design of the Laboratory Prototype

A laboratory prototype for validating the performance of the closed loop unidirectional RSC step-up OLED driver based on VI technique for OLED lamps has been developed as shown in Fig. 7.

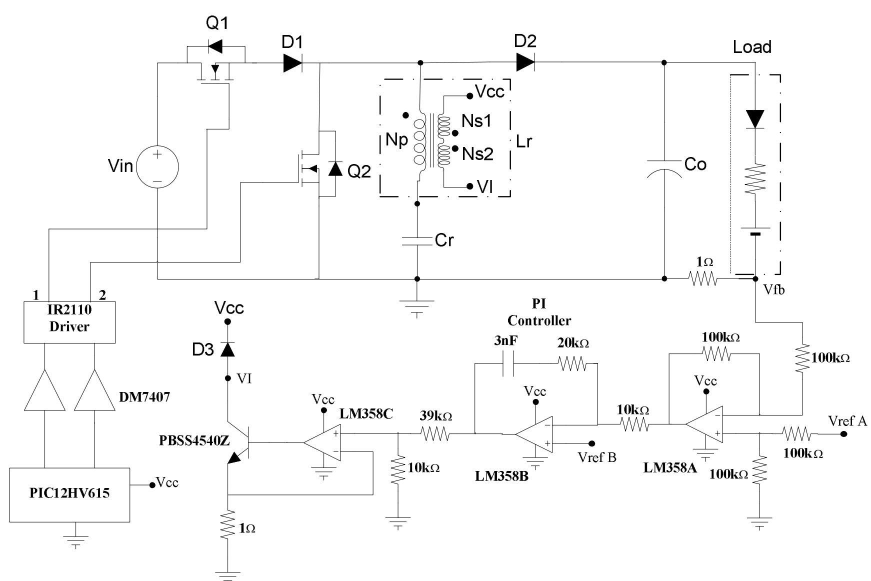

Fig. 7. Schematic diagram of laboratory prototype.

978-1-5090-4894-6/17/$31.00 © 2017 IEEE

The load is formed by three FL300 OLED lamps in series array, where its nominal DC OLED voltage is 59.2V and nominal OLED current is 368mA for a nominal OLED power of 21.8W [15]. The FL300 OLED lamp is shown in Fig. 8. The calculated model parameters of the OLED's array at room temperature are: $V_\gamma = 53.21\,V$ and $R_\gamma = 16.31\,\Omega$. The equivalent OLED resistance at nominal power is $R_{OLED} = 161\,\Omega$. The selected OLED current ripple is $\Delta I_{OLED} = 6.6\%$. Some additional specifications of the laboratory prototype are the following: V_{in}=48 V; f_S=100 kHz; t_{dead}=100ns; η=91.5%. Since the input design parameters were already described, the design calculation can be addressed. To find the capacitor C_r voltage V_{cr2} from (19), $C_r = 46.2\,nF$ is proposed, therefore, $V_{Cr2} = 19.39\,V$ is calculated. Now, as from (20), the capacitor C_r voltage V_{Cr1} can be calculated as $V_{Cr1} = 99.02\,V$. Then, the resonant inductor L_r is obtained from (21) as $L_r = 13.63\,\mu H$. The tank impedance is extracted from (5) as $Z_n = 17.18\Omega$. The resonant frequency f_n is then calculated from (11) as $f_n = 133.7$ kHz. From (25), the output filter capacitor is $C_o = 10\mu$ by selecting the OLED voltage ripple as $\Delta V_{OLED} = 0.5\%$.

Fig. 8. FL300 OLED lamp.

In Table I, the list of materials for the laboratory prototype implementation is included according to the component values calculations from Section III.

TABLE I. COMPONENTS LIST OF THE LABORATORY PROTOTYPE.

Reference	Description
Q_1, Q_2	BUK7613-100E FET Transistors
D_1, D_2	MBR20100CT Schottky Diodes
C_r C_{r1}, C_{r2}, C_{r3}, C_{r4}, C_{r5} C_{r6}	$C_{r1}\|\|C_{r2}\|\|C_{r3}\|\|C_{r4}\|\|C_{r5}+C_{r6}$ PHE450RD5100J10nF, 650V Capacitor 15nF J 1000V 378 MKP Capacitor
L_r	EFD 25/13/9 Inductor Np=9T, 66x0.08mm Ns1=Ns2=53T, 35AWG GAP=0.35 mm
C_o	ECQE2106KFB10uF, 250V Capacitor

The variable inductor built for the laboratory prototype of the URSC is shown in Fig. 9.

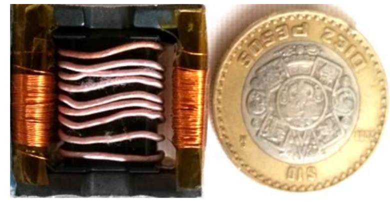

Fig. 9. Variable inductor for the laboratory prototype.

A brief performance explanation of the closed loop URSC step-up OLED driver prototype based on VI shown in Fig. 10 is presented in the following.

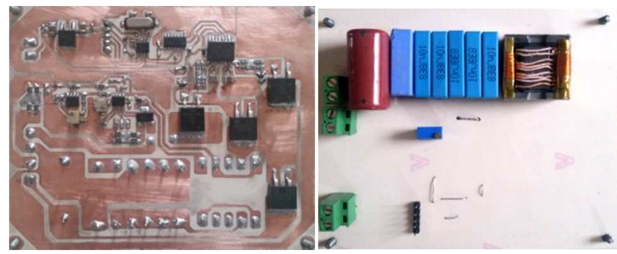

Fig. 10. URSC laboratory prototype.

The control operation of the URSC step-up OLED driver is achieved as follows: the microcontroller PIC12HV615 generates the 5V PWM signals for transistors Q_1 and Q_2 at a switching frequency f_S of 100 kHz, with an On-time of one third of the switching period, and they both are out of phase for 180 degrees according to the principle operation of the URSC step-up OLED driver. Open collector DM7407 buffers just take charge of supply 12V PWM signals to the high-low side driver IR2110 driver, which is in charge of commanding transistors Q_1 and Q_2.

The operational subtractor based on LM358A op-amp senses through the negative input terminal the average OLED current I_{OLED} from a1Ω resistor placed in series with the load in order to subtract the feedback voltage V_{fb} from the reference voltage V_{refA}, which is equal to $V_{refB} + V_{fb}$, owing to V_{fb} is never equivalent to V_{refB} as needed by the error amplifier LM358B to bias the VI and obtain the desired OLED current I_{OLED}. Then, the subtractor $V_{refA} - V_{fb}$ adequate its output voltage to follow V_{refB} reference voltage value to that DC bias current that finds the resonant inductor value L_r for fulfilling the average OLED current I_{OLED}. The voltage V_{refB} is the equivalent in DC bias current.

To compensate average OLED current I_{OLED} changes from input voltage variations or load steps down and up, a PI controller defined as in (26) is proposed.

$$G_C(s) = k_c \frac{1+s/2\pi f_z}{s} \tag{26}$$

Nonetheless, a modeling of the system to attain a frequency response analysis of the URSC step-up converter in cascade with PI controller is not tackled in this work; it will be undertaken in a future work.

The resulting voltage from the operational LM358A subtractor is then compared to the voltage reference V_{refB} to set the average OLED current I_{OLED}. Then, PI LM358B controller to compensate the error voltage between the resulting voltage of the subtractor and V_{refB}. The output signal of the controller is then applied to the constant current source LM358C+PBSS4540Z to supply an adequate control bias current to the VI.

V. SIMULATIONS RESULTS

Fig. 11 illustrates the circuit schematic of the URSC with the VI electrical-magnetic model in closed loop for simulating the unidirectional RSC step-up converter. The VI model is proposed in [16].

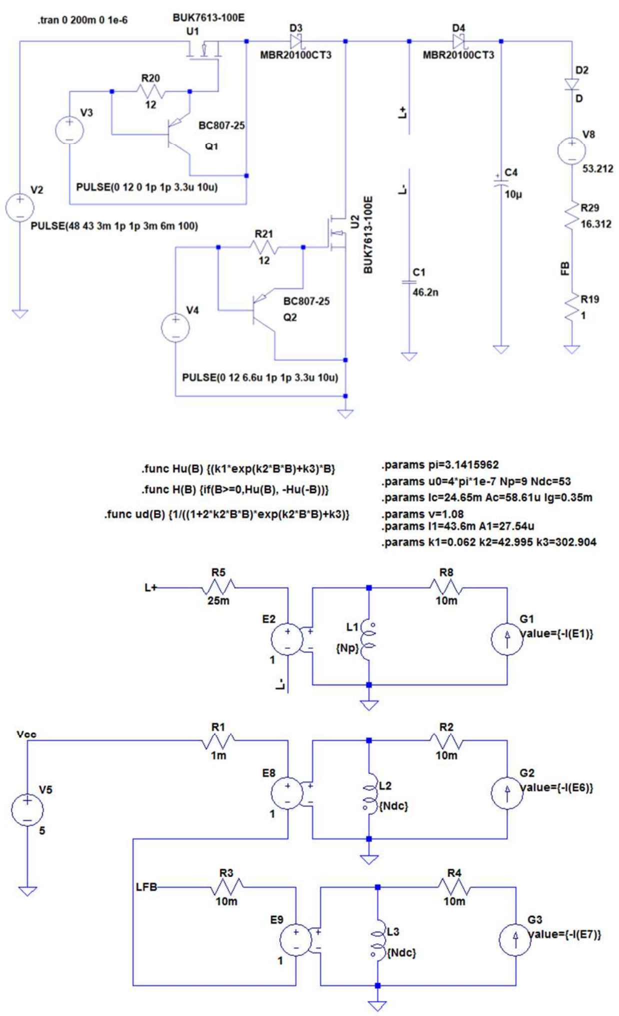

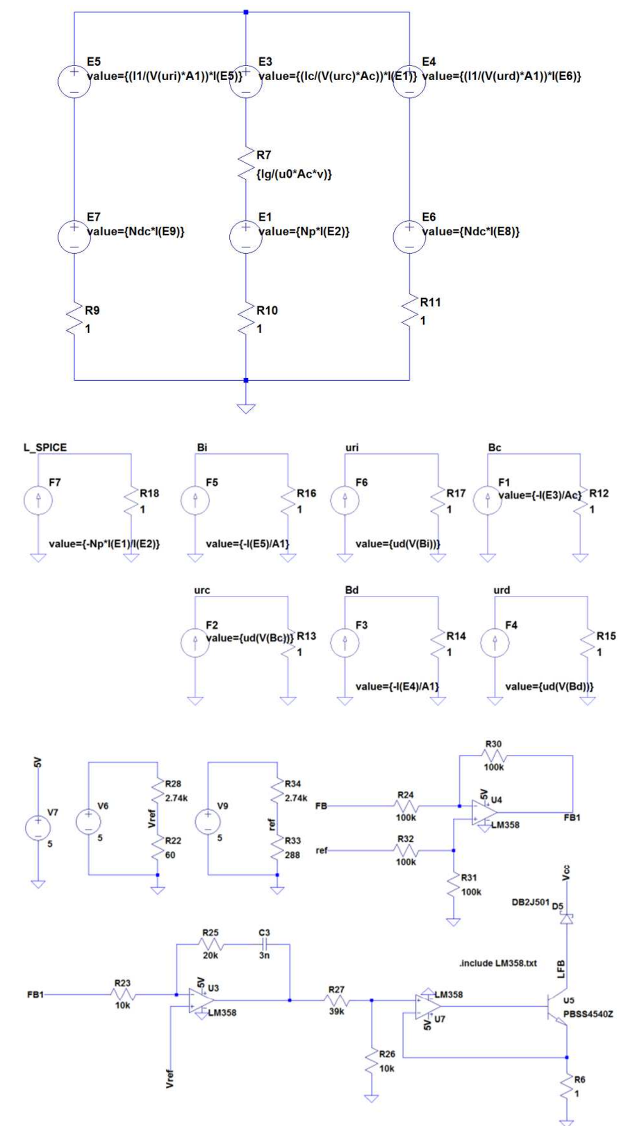

Fig. 11. URSC and VI model in closed loop.

The inductance value of L_r vs DC bias current curve of the VI is shown in Fig. 12. As can be observed, it finds a very good agreement between simulation and experimental curve of the VI inductor.

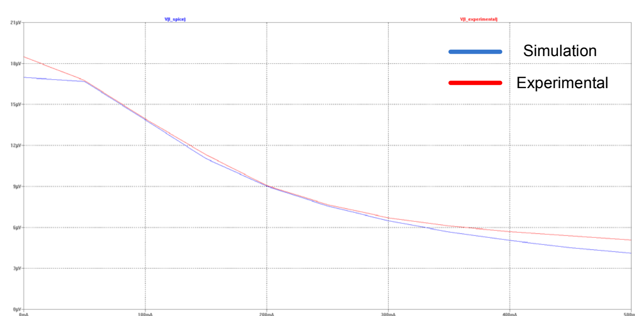

Fig. 12. Inductance vs DC bias current curve of the VI inductor: a) Simulation(Blue) and b) Experimental (Red). (3 µV/div and 100 mA/div).

Fig. 13 illustrates the resonant current I_{Lr} and the resonant voltage V_{Cr}. Fig. 14 shows the nominal DC OLED voltage V_{OLED} and OLED current I_{OLED} of the URSC step-up converter.

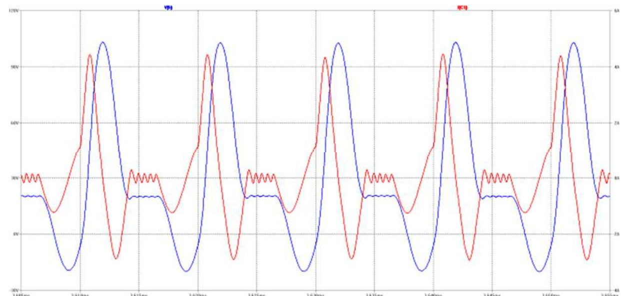

Fig. 13. Resonant tank waveforms: Blue: resonant capacitor voltage V_{Cr} and Red: resonant inductor current i_{Lr}. (30V/div, 2A/div and 5µs/div).

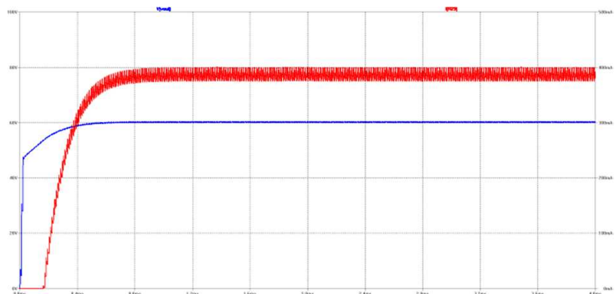

Fig. 14. Steady state load waveforms: Blue: DC OLED voltage V_{OLED} and Red: OLED current I_{OLED}. (20 V/div, 100 mA/div and 400µs/div).

Fig. 15 shows the dynamic response of the URSC step-up converter in closed loop under input voltage V_{in} step-up and down from 48V to 43V respectively. As shown, good dynamic behavior is achieved owing to the fact that the OLED current I_{OLED} is well regulated to 368mA. The stabilization time of the OLED current I_{OLED} after a step-down input voltage is applied is about 1 ms.

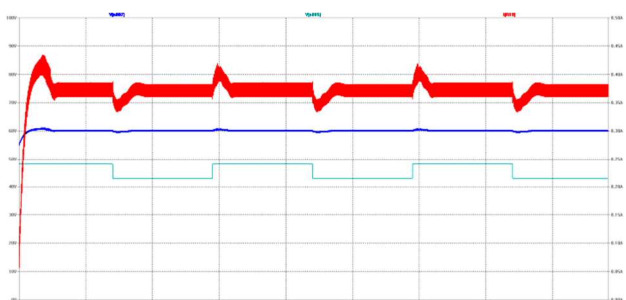

Fig. 15. Input voltage step-down transient response waveforms: Blue: DC OLED voltage V_{OLED} 10V/div, Red: OLED current I_{OLED} 50mA/div and Green: input voltage V_{in} 10V/div. (2ms/div).

VI. EXPERIMENTAL RESULTS

Fig. 16 illustrates the behavior of the DC OLED voltage V_{OLED} and OLED current I_{OLED} when OLED driver is turned on. The input voltage transient step is from 0 V to 48 V. As it can be seen, DC OLED voltage V_{OLED} and OLED current I_{OLED} stabilize at about 59.2 V and 368 mA.

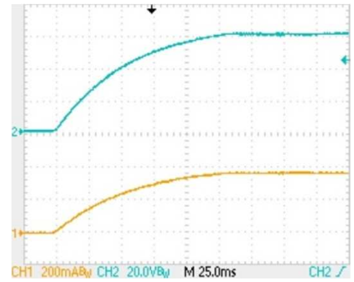

Fig. 16. Transient response waveforms: Green: DC OLED voltage V_{OLED} 20V/div and Orange: OLED current I_{OLED} 200mA/div.

Fig. 17 shows the switching waveforms on Q_1, which do not show overlapping between both signals.

Fig. 17. Switching waveforms of Q_1: Red: drain-source voltage 20V/div and (Blue) drain current 1A/div.

Fig. 18 shows the resonant current I_{Lr} and the resonant voltage V_{Cr} of the URSC converter. Fig. 19 shows the dynamic response of the URSC converter in closed loop under a DC OLED voltage V_{OLED} decrease of 4V from 59.2V nominal by short-circuiting 5 1N4001 rectifier diodes from a 75 in series rectifier diodes dummy load.

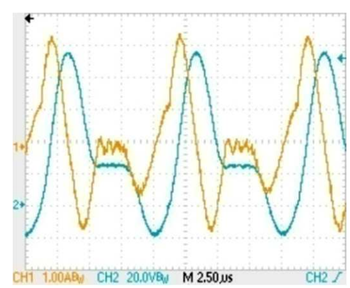

Fig. 18. Resonant tank waveforms: Green: resonant capacitor voltage V_{Cr} 20V/div and Orange: resonant inductor current i_{Lr} 1A/div.

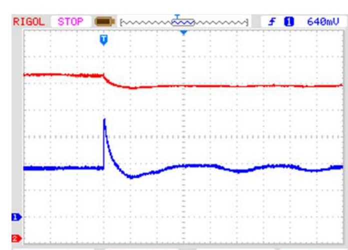

Fig. 19. Transient response waveforms: Red: DC OLED voltage V_{OLED} 10V/div and Blue: OLED current I_{OLED} 200mA/div.

Fig. 20 represents the experimental average OLED current I_{OLED} of the URSC converter at constant reference voltage V_{refB} under different input voltage V_{in} in open loop. The average OLED current I_{OLED} is dimmed from 0 mA to 445 mA by keeping constant V_{refB} at 107 mV and sweeping the input voltage from 0 V to 53 V.

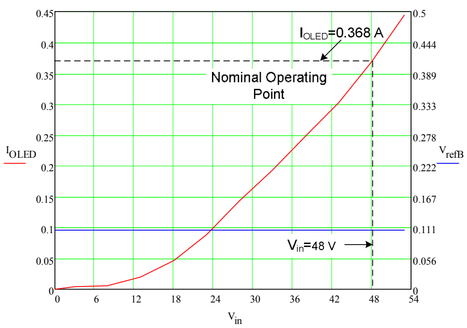

Fig. 20. I_{OLED} vs V_{in} in open loop.

The experimental average OLED current I_{OLED} under different voltage V_{refB} at constant input voltage V_{in} in open loop is shown in Fig. 21. The average OLED current I_{OLED} is dimmed from 31 mA to 430 mA by keeping constant the input voltage V_{in} at 48 V and sweeping the reference voltage V_{refB} from 0 mV to 248 mV.

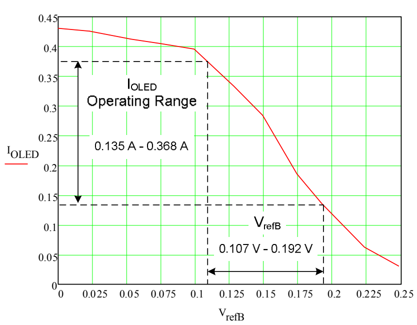

Fig. 21. I_{OLED} vs V_{ref} in open loop.

Fig. 22 depicts the experimental electrical efficiencies η under different average OLED power P_{OLED}. This is dimmed from 23.42 W to 8.14 W by keeping constant the input voltage V_{in} at 48 V and sweeping the reference voltage V_{refB} from 99 mV to 192 mV. The electrical efficiency η measured at nominal P_{OLED} is 91.5%.

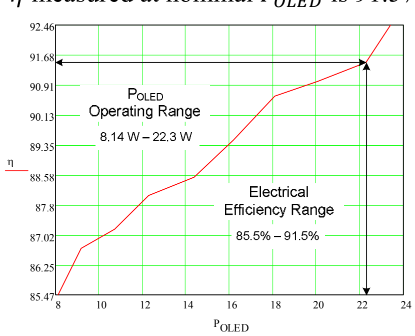

Fig. 22. Electrical efficiency η vs P_{OLED} in open loop.

VII. CONCLUSIONS

URSC step-up converter finds a very good behavior to drive OLED lamps because it provides a very good efficiency, VI control loop simplicity, high power density and low cost. The VI control technique provides a very good output current regulation and dynamic response to the URSC step-up converter by means of resonant frequency control. This paper has been focused on designing and analyzing experimentally the URSC step-up converter.

REFERENCES

[1] Gilberto Martinez and J. Marcos Alonso, "A Review on Switched Capacitor Converters with High Power Density for OLED Lamp Driving," *IEEE Ind. Appl. Society Conference*, pp. 1-8, Oct. 2015.

[2] Cheng and P. D. Evans, "Parallel-mode extended period quasiresonant converter," *Proc. Inst. Elect. Eng.*, pt. B, vol. 138, no. 5, pp. 243–251, Sept. 1991.

[3] K. W. E. Cheng and P. D. Evans, "Unified theory of extended-period quasiresonant converters," *IEE Proceedings-Electric Power Applications*, vol. 147, no 2, pp. 119-130, 2000.

[4] O. C. Mak, Y. C. Wong, and A. Ioinovici, "Step-up DC power supply based on a switched-capacitor circuit," *IEEE Trans. Ind. Electron.*, vol. 42, pp. 90–97, Feb. 1995.

[5] J. Liu, Z. Chen, and Z. Du, "A new design of power supplies for pocket computer systems," *IEEE Trans. Ind. Electron.*, vol. 45, pp. 228–235, Apr. 1998.

[6] Bengtsson, "A switch in methods," *New Electronics,* Aug1997, pp. 40-41.

[7] Simon S. Ang and Alejandro R. Oliva, Power-Switching Converters, 2nd ed., 1957, p. 341-371.

[8] K. W. E. Cheng, "New generation of switched capacitor converters," *in Proc. IEEE PESC'98*, pp. 1529-1535.

[9] Y. P. Benny Yeung, K. W. E. Cheng, S. L. Ho, K. K. Law, and Danny Sutanto, "Unified Analysis of Switch Capacitor Resonant Converters," *IEEE Transactions on Industrial Electronics*, vol. 51, no.4, pp. 864-873, Aug. 2004.

[10] Yuanmao Ye, Ka Wai Eric Cheng, Junfeng Liu, and Cuidong Xu, "A Family of Dual-Phase-Combined Zero-Current Switching Switched-Capacitor Converters," *IEEE Transactions on Power Electronics*, vol. 29, no.8, pp. 4209-4218, Aug. 2014.

[11] Alon Cervera, Michael Evzelman, Mor Mordechai Peretz, and Shmuel (Sam) Ben-Yaakov, "A High Efficiency Resonant Switched Capacitor Converter with Continuous Conversion Ratio," University of Negev, Beer-Sheva, Israel, pp. 4969-4976, 2013.

[12] Alon Cervera, Michael Evzelman, Mor Mordechai Peretz, and Shmuel (Sam) Ben-Yaakov, "A High Efficiency Resonant Switched Capacitor Converter with Continuous Conversion Ratio," *IEEE Transactions on Power Electronics*, vol. 30, no.3, pp. 1373-1382, March 2015.

[13] Pedro H. A. Miranda, Edison M.Sá Jr., Antonio V. L. de Oliveira, Esio E. dos Santos F, Fernando L. M. Antunes, "A Switched-Capacitor Driver for Power LEDs," Federal Education Inst. of Science and Technology of Ceará, CE Brasil, pp. 918-923, 2011.

[14] Olegs Tetervenoks, "Sensorless Converter for Low-Power LED Lamp with Improved Power Factor," IEE Eng. Inst., Technical University of Riga, Riga, Latvia, pp. 285-290, 2014.

[15] Lumiblade OLED Panel. Brite FL300. Product sheet. 2014.

[16] J. M. Alonso, G. Martínez, M. Perdigão, M. Cosetin, R. N. do Prado; "A Systematic Approach to Modelling Complex Magnetic Devices using SPICE: Application to Variable Inductors," IEEE Trans. on Power Electronics, Vol. 31, Nº 11, pp. 1-12, Nov. 2016.

A Review on Switched Capacitor Converters with High Power Density for OLED Lamp Driving

Gilberto Martínez[1, 2] and J. Marcos Alonso[2]

(1) Continental Automotive R&D; ID HMI Hardware Development Dept., 45601-GDL, Jalisco, México
(2) University of Oviedo, Electrical & Electronics Eng. Dept., 33204-Gijón, Asturias, Spain
gilberto.martinez@continental-corporation.com; marcos@uniovi.es

***Abstract*- This paper presents a review of high-power-density non-resonant and resonant switched-capacitor (SC) converters topologies for driving organic-lighting-emitting-diode (OLEDs) lamps. These converters are light, small and cheaper in comparison with the linear power supplies and conventional DC-DC converters owing to the avoidance of large magnetic components. Resonant SC (RSC) converters show high efficiency and low EMI noise because they employ a small resonant inductor, which is connected in series with a switched capacitor in order to resonate at a frequency higher than switching frequency, thus allowing them to attain zero-current-switching (ZCS). The bidirectional step-up RSC converter has been identified as one of the best candidates to be used as an OLED driver. Simulation and experimental results from a laboratory prototype designed to supply a 60V 25W OLED lamp from a dc 30 V voltage source are presented.**

***Index Terms*- Electromagnetic Interference (EMI), Organic-Lighting-Emitting-Diodes (OLEDs), Power Factor Correction (PFC), Resonant-Switched-Capacitor (RSC), Switched-Capacitor (SC), Zero-Current-Switching (ZCS).**

I. INTRODUCTION

Nowadays, OLED lamps allow lighting designers and architects to develop their ideas down to the smallest detail owing to their easy integration and customization. Since their slimness is just few millimeters thin, OLEDs can be integrated into many different areas, and allow light sources to be designed in a variety of shapes and sizes [1]. These can be used on luminous walls and ceilings, windows that shine brightly with daylight even when it is dark, mirrors and indoors lamps [1][2]. The greatest difference between OLEDs and inorganic LEDs lies in the way they emit light. OLEDs are surface light sources, not point sources. The light generated by OLEDs has a naturally soft and comfortable diffuse characteristic and is glare-free.

One way to drive OLED lamps is by means of linear power supplies because of their ease of design, low EMI noise and low output voltage ripple. Nevertheless, these power supplies have the disadvantages of low efficiency, bulky and heavy because of the large energy storage components that are required.

This work has been supported in part by the Spanish government under research grant ENE2013-41491-R.

On the other hand, conventional switched DC-DC converters have the benefit of high efficiency in comparison with linear power supplies. Also, they are easy to design and very mature in terms of good performance. However, these converters have the drawbacks of high EMI noise, high output voltage ripple, bulky and heavy due to use of large magnetics and capacitors, since their size is dependent on the switching frequency. One way to reduce the components size of the DC-DC converter is by increasing the switching frequency. But, increasing the switching frequency affects efficiency so that soft-switching circuits are used, in which the size of the components are large, making DC-DC converters bulky [3][4].

Other type of converters used to drive OLED lamps are SC converters, which consist of diodes, switches, and capacitors. These converters do not use any large inductor, and switched capacitors are small [5]-[7]. This leads to a high power density of the converter, making it very attractive for the aforementioned lighting OLED applications, which require high-power-density converters. Examples are portable and any low-profile electronic equipment applications, such as notebook computers, tablets and portable digital assistants.

Due to low power density inconvenience of linear power and conventional switched DC-DC converters, this work focuses on analyzing different SC converters topologies in order to highlight their advantages and disadvantages, in terms of efficiency, voltage conversation ratio, EMI noise, power density, output voltage ripple and power level.

II. NON-RESONANT SC CONVERTERS

The family of non-resonant SC converters consists of step-up, step-down and inverter converters. Each of these converters has two diodes, D_1 and D_2, two switches, Q_1 and Q_2, one switched capacitor, C_1, and one output filter capacitor, C_O. Fig. 1a shows the step-up converter, which has a voltage conversion ratio of 2. In Fig. 1b the step-down converter with a voltage conversion ratio of 1/2 is shown. Finally, Fig. 1c illustrates the inverter converter, whose voltage conversion ratio is -1 [8].

For instance, non-resonant SC step-up converter consists of charge and discharge operation modes, in which the switches, Q_1 and Q_2 are operated at 50% duty cycle in a complementary way by PWM technique, and require of a dead-time.

In charge operation mode, Q_2 is switched-on while Q_1 is off, the switched capacitor, C_1, is charged to the voltage source V_{in}, through D_1. In this operation mode, C_O is discharged to the load.

In discharge operation mode, Q_1 is switched-on and Q_2 is switched-off while the switched capacitor, C_1 is discharged to the load, charging C_O, through D_2.

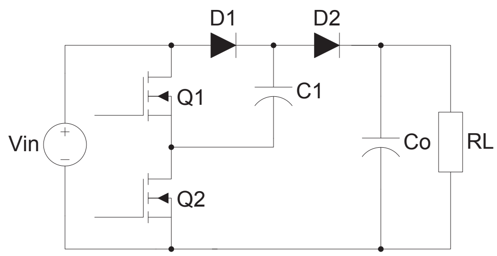

(a)

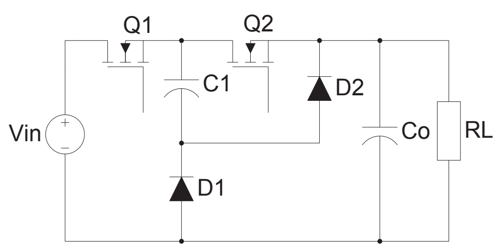

(b)

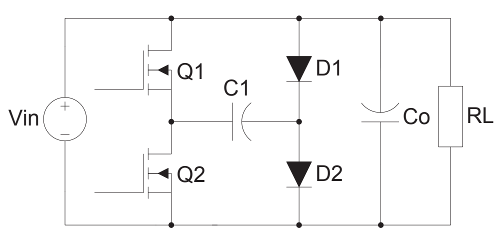

(c)

Fig. 1. Non-resonant SC converters: (a) Step-up, (b) Step-down and (c) Inverter.

Fig. 2 illustrates the switching waveforms of the transistors, Q_1 and Q_2, during both charge and discharge operation modes.

These converters present disadvantages of poor voltage conversion ratio and output voltage regulation as well as low efficiency and high EMI noise due to switching losses, which are caused by switched capacitor charge and discharge oscillatory currents, since these are only limited by the internal resistances of the devices.

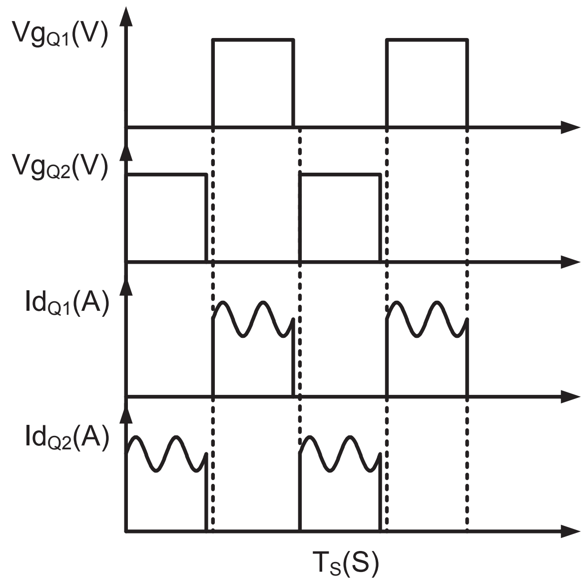

Fig. 2. Switching waveforms of the step-up non-resonant SC converter.

III. Resonant SC Converters

Due to the disadvantages of conventional SC converters, resonant SC converters were introduced [9]-[14]. These converters use a small resonant inductor in series with the switched capacitor in order to operate under ZCS, which reduces switching losses and EMI noise and improves voltage conversion ratio, efficiency and output voltage regulation. In addition, they can be operated at higher switching frequencies because of ZCS operation, which leads to higher power density of the converter. In order to operate under ZCS, the resonance frequency has to be greater than the switching frequency.

A. *Conventional RSC Converters*

Conventional non-resonant SC converters are transformed into RSC converters by inserting a small resonant inductor L_r in series with the switched capacitor in order to operate under ZCS [9]. This family consists of step-up, step-down and inverter converters, as shown in Fig. 3(a)-(c). Voltage conversion ratios are the same to those conventional non-resonant SC converters.

For instance, RSC step-up converter consists of four operation modes, and it is shown in Fig. 3a. The switches, Q_1 and Q_2 are operated at 50% duty cycle in a complementary way with a small dead-time, just like non-resonant step-up converter.

On the other hand, in the first operation mode, Q_2 is switched on under ZCS operation while Q_1 is off, since the switched capacitor, C_1 and the resonant inductor, L_r enter into resonance at a frequency higher than the operation frequency, which is a condition to operate into ZCS. In this operation mode, C_1 is charged to the voltage source, V_{in}, through D_2, and C_O is discharged to the load.

In the second operation mode, the current through the switched capacitor, C_1 and the resonant inductor, L_r are zero while Q_2 is switched-off under ZCS operation. Also, the output filter capacitor, C_O is still discharging to the load.

In the third operation mode, Q_1 is switched on under ZCS operation while Q_2 is off, the switched capacitor, C_1 is discharged to the load, charging C_O, through D_1.

In the fourth and last operation mode, the current through the switched capacitor, C_1 and the resonant inductor, L_r are zero as the second operation mode, while Q_1 is switched off under ZCS operation, and the output filter capacitor C_O is discharged to the load.

Fig. 4 shows the switching waveforms of the transistors Q_1 and Q_2 under ZCS operation as well as resonant current, iL_r, through L_r during the four operation modes.

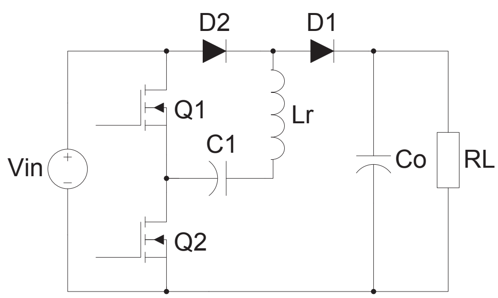

(a)

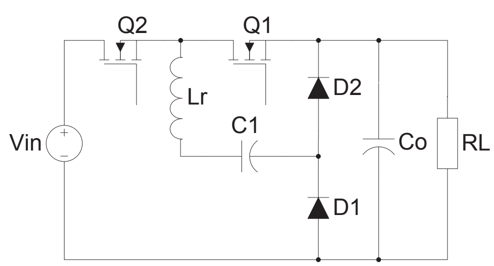

(b)

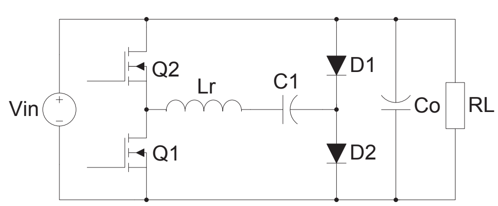

(c)

Fig. 3. Resonant SC converters: (a) Step-up, (b) Step-down and (c) Inverter.

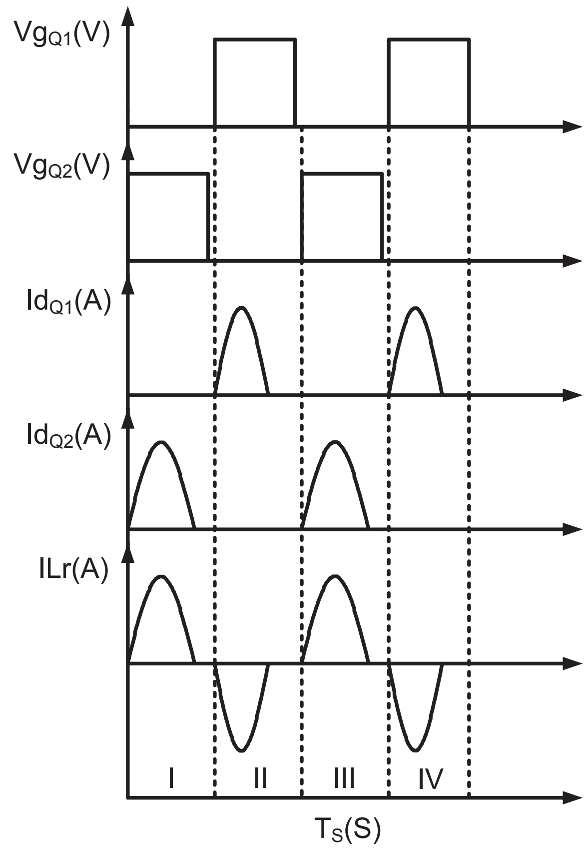

Fig. 4. Switching waveforms of the step-up RSC converter.

However, the efficiency and the voltage conversion ratio of conventional RSC converters depend on the load conditions, being both lower as the load decreases, which is an important drawback of this type of SC converters.

B. *Fractional-Voltage-Conversion-Ratio RSC Converters*

The fractional-voltage-conversion-ratio (FVCR) RSC converter family consists of step-up, step-down and inverter converters with voltage conversion ratio of 3, 1/3 and -0.5, respectively, as illustrated in Fig. 5 [10]. These converters are designed for voltage conversion ratios greater than those of the aforementioned conventional RSC converters by inserting extra cells of diodes, D_3, D_4 and D_5, and switched capacitors, C_2 and C_3. Also, operation under ZCS is achieved by using a small resonant inductor in series with switched capacitors. Fig. 5(a)-(c) shows step-up, step-down and inverter converters with voltage conversion ratios of 3, 1/3 and -0.5, respectively.

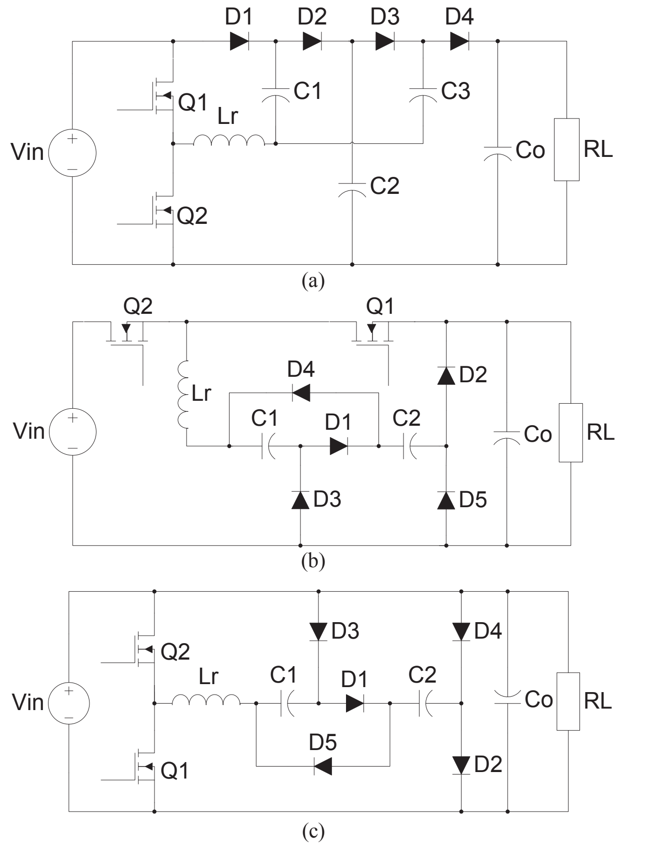

Fig. 5. Fractional RSC converters: (a) Step-up, (b) Step-down and (c) Inverter.

These converters present the advantages of wide, fractional and quite constant voltage conversion ratio and constant efficiency because the highest the voltage ratio from input to output is, the smallest variation effect on the efficiency and voltage conversion ratio dependency on the load are. In addition, lower output voltage ripple is provided in comparison with conventional RSC converters. Nevertheless, the power density of the converter is lower due to the extra components required.

C. *Dual-Phase RSC Converters*

The dual-phase (DP) converter family is shown in Fig. 6(a)-(c). This family consists of step-up, step-down and inverter converters with voltage conversion ratios of 2, 0.5 and -1, respectively [11]. These dual-phase converters are based on conventional RSC converters with an additional switched capacitor, C_2, added to the circuit. Also, this type of converters provides an output voltage more stable because the output voltage ripple is half to those of conventional RSC converters. Their efficiency is quite high and constant under different load conditions, except at very light load, in which case it decreases rapidly. The output voltage ripple is quite low, similar to fractional RSC converters, but the size of the output filter capacitor for dual-phase RSC converters is smaller than fractional RSC converters, which improves the power density of the converter.

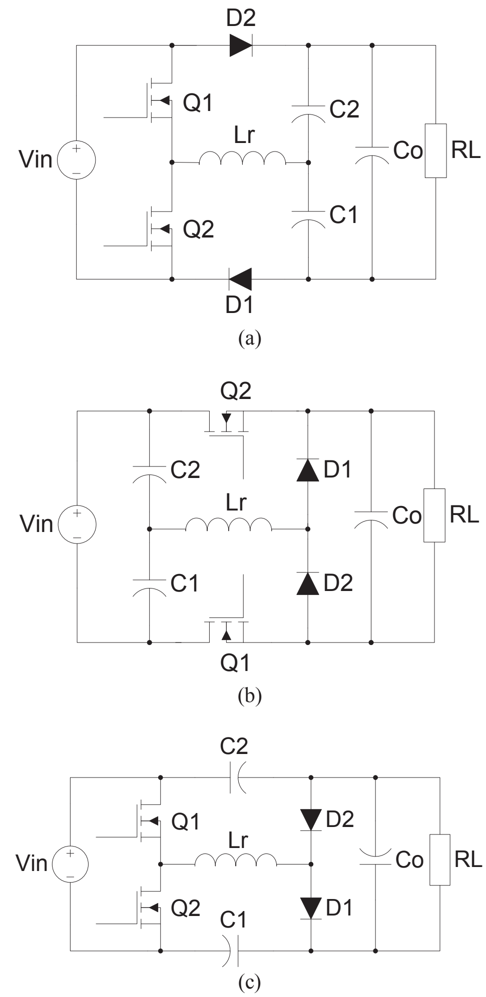

Fig. 6. Dual-phase RSC converters: (a) Step-up, (b) Step-down and (c) Inverter.

D. *Multi-Configurable Bidirectional RSC Converter*

A multi-configurable bidirectional (MCB) RSC converter is shown in Fig. 7 [12]. This converter is built based on the principles of the conventional RSC converters, and can be configured into different types of operation modes by considering uni-directional power flowing. Table I shows the possible switch configurations for 7 different unidirectional conversion modes, in which switches can be short-circuited, disconnected or replaced by a diode.

This converter consists of three switching states, which are charge, discharge and balance. This last third state is included in order to balance the remaining energy of the switched capacitor, which is the main difference with respect to those conventional RSC converters.

978-1-4799-8374-0/15/$31.00 © 2015 IEEE

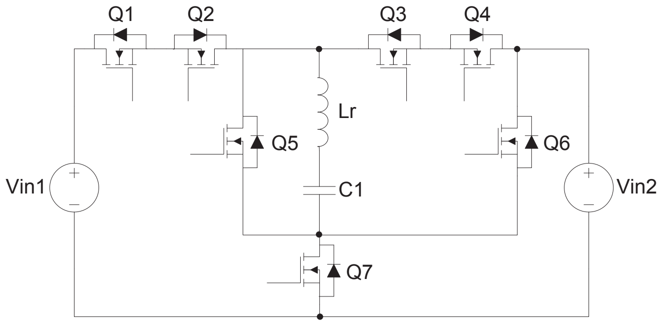

Fig. 7. Bidirectional MCB-RSC converter.

TABLE. I. SWITCH MAPPING FOR UNI-DIRECTIONAL DERIVATIVES IN THE MCB-RSC CONVERTER[1].

Converter Function	Q1	Q2	Q3	Q4	Q5	Q6	Q7
Step up-down	1	D	2	2	3	O	S
Step up	1	D	S	D	3	O	S
Step down	1	D	2	D	D	O	S
Doubler step up-down	S	3	S	D	3	O	1
Doubler step down	S	D	S	D	3	O	1
Divider step up-down	1	S	2	S	O	3	2
Divider step down	1	S	2	S	O	D	2

1. Numbers and letters characters in the table represent the following: S - MOSFET is short-circuited; O - MOSFET is disconnected; D – just a diode is needed; numbers represent the switching states into which MOSFET are active.

For instance, the basic uni-directional step-up converter configuration is shown in Fig. 8. It consists of two switches, Q_1 and Q_5, two diodes, D_1 and D_2, placed instead of Q_2 and Q_4, switched capacitor, C_2, resonant inductor, L_r and output filter capacitor, C_O. When a load resistor in paralleled with an output filter capacitor is connected to one of the output terminals, the unidirectional step-up RSC converter behaves a current sourcing, by which the output voltage just depends on the load resistor.

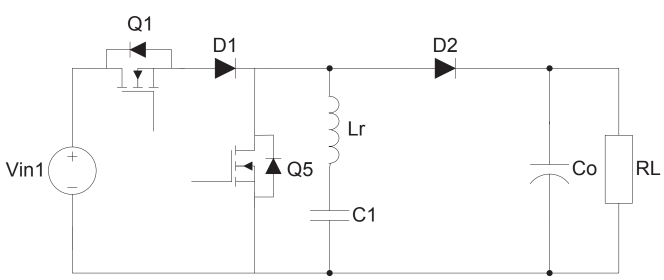

Fig. 8. Uni-directional step up RSC converter.

Its efficiency is kept constant under different voltage conversion ratios, which can be upper or lower than unity as well as being wide and continuous. Efficiency does not depend on voltage conversion ratio, as conventional RSC converters do. Then, efficiency just depends on conduction losses, which is an advantage with respect to those conventional, fractional and dual-phase RSC converters, in which efficiency depends on voltage conversion ratio. In conventional RSC converters it is difficult to achieve a desired output voltage because the resultant charge energy balance into the switched capacitor is not zero after charge and discharge switching periods, that is, the remaining energy on the switched capacitor avoids converging to the desired voltage. On the contrary, multi-configurable bidirectional RSC converter make an energy balance on the switched capacitor after charge and discharge switching states by means of an additional switch, *Q5* or *Q6*, which is used to create a trajectory for the resonant current on the switched capacitor when its charge is balanced to its initial charge state by reversing its polarity. In addition, output voltage regulation can be made by applying timing delays between switching states, i.e, changing operation frequency effectively. This feature is an advantage over conventional, fractional and dual-phase RSC converters. Output filter capacitor and load can be connected at any output terminals, but considering power flowing direction based on transistors operation sequence.

E. *Step-Down Half Bridge RSC Converter with Isolation Transformer*

A step-down half bridge RSC converter with isolation transformer is described [13]. It consists of two switches Q_1 and Q_2, four diodes, D_1, D_2, D_3 and D_4, 2 capacitors, C_{in2} and C_{in1}, for removing current continues on the transformer, T_1, a switched capacitor, C_S, a resonant inductor, L_O and an output filter capacitor, C_O, as shown in Fig. 9. Output current is controlled by switched capacitor, *Cs*, and it is connected in series with a small resonant inductor *Lo,* which operates in DCM in order to achieve ZCS on transistors and improve efficiency. The magnetizing inductance of the isolation transformer helps reducing switching losses due to ZVS operation in transistors, which increases efficiency. Nevertheless, efficiency is still lower than fractional, dual-phase and bidirectional RSC converters efficiency. Also, this step-down half-bridge RSC converter with isolation transformer has the disadvantages of high output voltage ripple in comparison with aforementioned RSC converters, efficiency dependency on voltage conversion ratio and low power density.

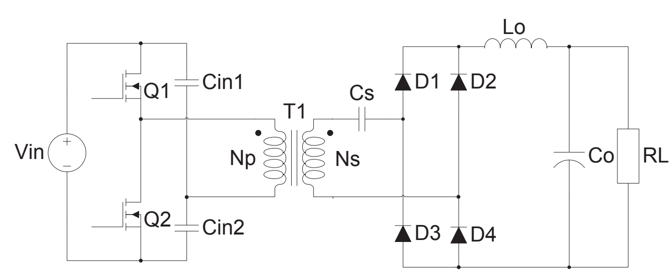

Fig. 9. A step-down half bridge RSC converter with isolation transformer.

F. *Step-Down SC Converter with Coupling Inductors*

Step-down SC converter with coupling inductors are based on conventional step-down SC converter, which includes two switches, Q_1 and Q_2, three diodes, D_1, D_2 and D_3, one switched capacitor, C_1, three coupling inductors, L_1, L_2 and L_3 and one output filter capacitor, C_O, as shown in Fig. 10 [14]. Coupling inductors L_1, L_2 and L_3, work in DCM operation based on Flyback transformer operation principles, in order to solve issues of switching losses and reduce peak current magnitudes on transistors, which leads to high PF in off-line applications, high efficiency and low EMI noise, as well as providing wide voltage conversion ratio. Output voltage ripple is also low, for the same reasons as in previously presented RSC converters with low output voltage ripple.

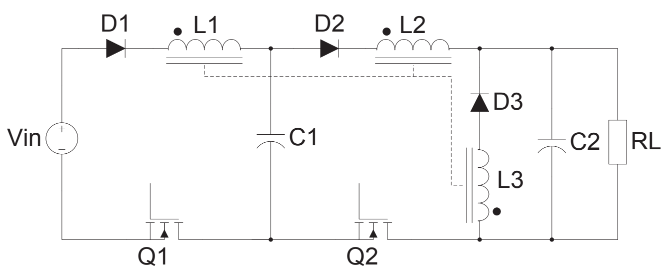

Fig. 10. Step-down RSC converter with coupling inductors.

In this converter, the average output power is limited by the capacitance value of C_1, when considering constant input voltage, V_{in} and switching frequency, f_S. Also, the output power keeps constant at different low output voltage values so that different load conditions can be applied without affecting output power. In addition, output voltage depends only on load parameters. Inductor L_3 works in DCM and delivers current to the load when current on L_1 and L_2, reach zero.

However, even though the step-down SC converter with coupling inductors works in DCM operation, efficiency is lower than all aforementioned RSC converters, except for conventional SC converters. Another drawback is the high dependency of output power on the input voltage.

IV. SUMMARY AND COMPARISON

Table II shows a comparison of all SC converters performance, in terms of output voltage regulation, output voltage ripple, efficiency, efficiency dependency on conversion ratio, EMI noise and isolation and PFC capability. As can be seen, multi-configurable bidirectional RSC converter present the best performance compared to the other SC converters.

TABLE II. SC CONVERTERS PERFORMANCE COMPARISON.

Type of SC converter	High output voltage regulation	Low output voltage ripple	High efficiency	No efficiency dependency on conversion ratio	Low EMI noise	High power density	Isolation	PFC capability
Non-resonant SC	–	–	–	–	–	+	–	–
Conventional RSC	–	–	–	–	+	+	–	–
Fractional voltage conversion ratio RSC	+	+	+	–	+	–	–	–
Dual-phase RSC	+	+	+	–	+	+	–	–
Multi-configurable bidirectional RSC	+	+	+	+	+	+	–	–
Step-down half-bridge RSC with isolation transformer	–	–	+	–	+	–	+	–
Step-down SC with coupling inductors	+	+	–	+	–	–	–	+

V. SIMULATION RESULTS

As shown in previous section, the bidirectional step-up RSC converter presents the best performance in terms of the different characteristics considered. Therefore, this converter is proposed as one of the best options to be employed as OLED drivers. In order to test this converter, a real application has been considered in Fig. 11 with the following specifications: V_{in}=30 V; f_S=217 kHz; f_n=225 kHz; L_r=5.8 µH; C_1=38.19 nF; C_O=10 µF and the series parasitic resistances: R_{Lr}=41mΩ, R_{C1}=200mΩ and R_{Co}=41mΩ. The OLED lamp consists of three Philips OLED lamps type Brite FL300 connected in series [15]. Its equivalent series voltage is 20 V and the equivalent series resistance is 54.34 Ω. The nominal OLED current is 0.368 A. The DC equivalent resistance $R_o = 163\ \Omega$ is obtained by dividing the output voltage V_O and the nominal output current I_O. The proposed application uses BUK7613-100E FET transistors for U_1 and U_2, QBC807 BJTs transistors for Q_1 and Q_2, MBRB20H100CTT4G fast recovery diodes for D_1 and D_2 and a 300ns deadtime between U_1 and U_2.

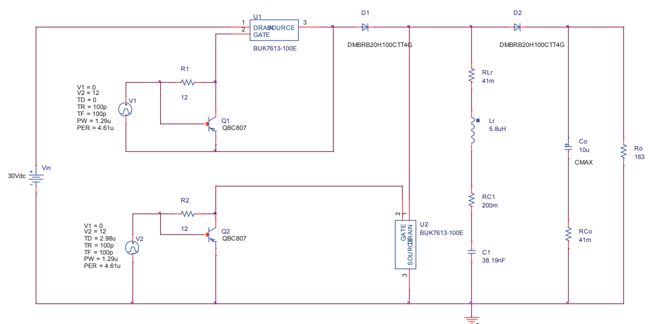

Fig. 11. Prototype of the OLED driver based on RSC converter.

Simulation results can be seen in Fig. 12. Note that three switching states on both the current of the resonant inductor L_r and the voltage across the switched capacitor C_1 are visualized in Fig. 12(a). In Fig. 12(b), the output voltage on the capacitor C_O and the output current I_O are shown. It can be seen in Fig. 12(a) that after the third switching state (charge balance) occurs, the voltage on the switched capacitor C_1 is adjusted to the initial point voltage magnitude, which helps reducing switching losses on the RSC converter. In Fig. 12(b), it is observed that output voltage V_O and output current I_O are quite well regulated.

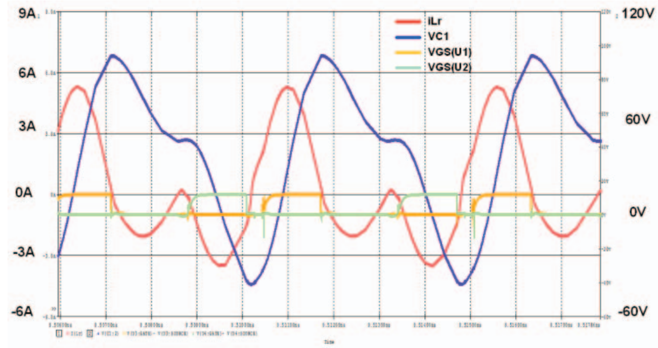

(a)

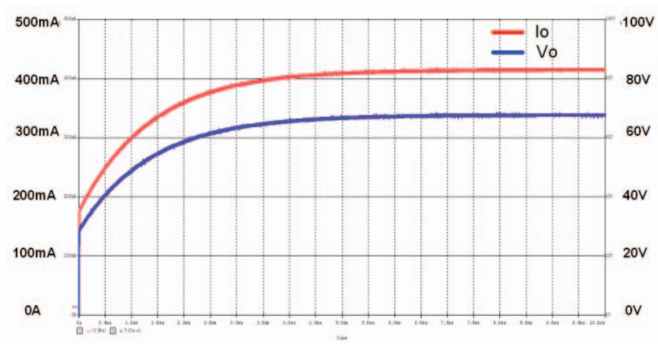

(b)

Fig. 12. Simulation results of bidirectional step-up RSC converter: (a) iL_r and V_{C1} and (b) V_O and i_O.

VI. EXPERIMENTAL RESULTS

A prototype was built for the bidirectional RSC step-up converter based on the parameters of section V. The efficiency achieved by this prototype was 88%, which is really good for the RSC converters family. Fig. 13 depicts the waveforms of voltage across capacitor C_1 and current through inductor L_r, respectively.

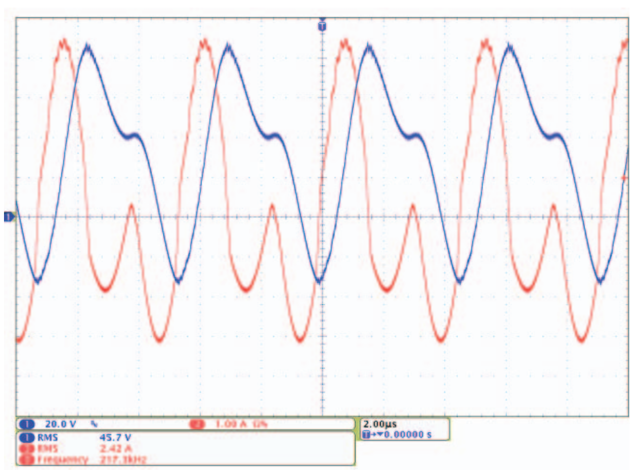

Fig. 13. Capacitor voltage V_{C1} and Inductor current iL_r. 20 V/div, 1 A/div, 2 µs/div.

978-1-4799-8374-0/15/$31.00 © 2015 IEEE

As can be seen, the bidirectional RSC step-up converter is operating according to the expected behavior since the resonant voltage and current across C_1 and L_r pass through the three modes of operation: charge, discharge and balance. Also, ZCS is achieved working at a natural frequency of 225 kHz, which ensures ZCS beginning with $f_n > f_S$.

Fig. 14 shows the waveforms of output voltage and output current of the bidirectional RSC step-up converter. As can be seen, the bidirectional RSC step-up converter is supplying 65 V output voltage and 392 mA output current, which gives an output power equal to 25.5 W. The demanded input power is 29 W at an input voltage of 30 V, with an average input current of 951 mA. The output voltage conversion ratio is equal to 2.16 times the input voltage.

IV. Conclusions

SC converters appear as a very good option to drive OLED lamps because they provide compactness, simplicity, low cost and the possibility of integration. Therefore, this paper has been focused on reviewing the different non-resonant and resonant topologies of SC converters that can be used as OLED drivers, highlighting their features and possibilities. Among the different SC converter topologies, resonant converters stand out owing to their capability of providing soft switching and, therefore, low EMI and high efficiency.

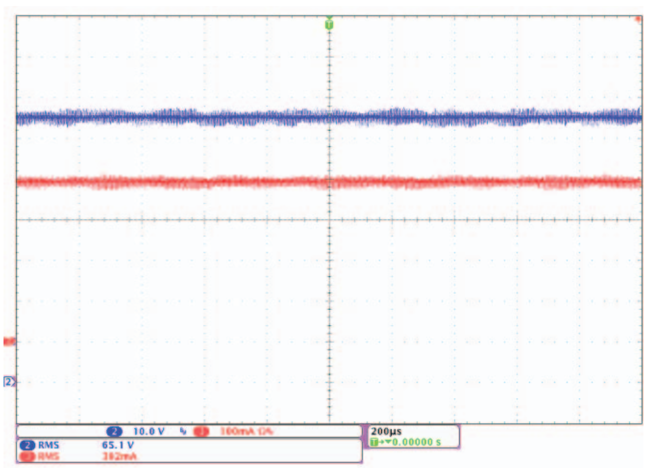

Fig. 14. Top: output voltage V_O. Bottom: output current i_O. 10 V/div, 100 mA/div, 200 µs/div.

A comparison of SC converter topologies have been carried out, showing that the multi-configurable bidirectional resonant SC converter is a very good option for OLED driving. This topology has been tested in an *ad hoc* laboratory prototype, which showed a good potential for this kind of application.

References

[1] Philips Lumiblade. OLED Compendium for Journalists [Online]. Available: http://www.lumiblade.com.

[2] Osram. LED-OLED Lighting. [Online]. Available: http: //www.osram.com/osram_com/tools-and-services/services/faq/ledoled-lighting/index.jsp.

[3] Cheng and P. D. Evans, "Parallel-mode extended period quasiresonant converter," *Proc. Inst. Elect. Eng.*, pt. B, vol. 138, no. 5, pp. 243–251, Sept. 1991.

[4] K. W. E. Cheng and P. D. Evans, "Unified theory of extended-period quasiresonant converters," *IEE Proceedings-Electric Power Applications*, vol. 147, no 2, pp. 119-130, 2000.

[5] O. C. Mak, Y. C. Wong, and A. Ioinovici, "Step-up DC power supply based on a switched-capacitor circuit," *IEEE Trans. Ind. Electron.*, vol. 42, pp. 90–97, Feb. 1995.

[6] J. Liu, Z. Chen, and Z. Du, "A new design of power supplies for pocket computer systems," *IEEE Trans. Ind. Electron.*, vol. 45, pp. 228–235, Apr. 1998.

[7] Bengtsson, "A switch in methods," *New Electronics,* Aug1997, pp. 40-41.

[8] Simon S. Ang and Alejandro R. Oliva, Power-Switching Converters, 2nd ed., 1957, p. 341-371.

[9] K. W. E. Cheng, "New generation of switched capacitor converters," *in Proc. IEEE PESC'98*, pp. 1529-1535.

[10] Y. P. Benny Yeung, K. W. E. Cheng, S. L. Ho, K. K. Law, and Danny Sutanto, "Unified Analysis of Switch Capacitor Resonant Converters," *IEEE Transactions on Industrial Electronics*, vol. 51, no.4, pp. 864-873, Aug. 2004.

[11] Yuanmao Ye, Ka Wai Eric Cheng, Junfeng Liu, and Cuidong Xu, "A Family of Dual-Phase-Combined Zero-Current Switching Switched-Capacitor Converters," *IEEE Transactions on Power Electronics*, vol. 29, no.8, pp. 4209-4218, Aug. 2014.

[12] Alon Cervera, Michael Evzelman, Mor Mordechai Peretz, and Shmuel (Sam) Ben-Yaakov, "A High Efficiency Resonant Switched Capacitor Converter with Continuous Conversion Ratio," University of Negev, Beer-Sheva, Israel, pp. 4969-4976, 2013.

[13] Pedro H. A. Miranda, Edison M.Sá Jr., Antonio V. L. de Oliveira, Esio E. dos Santos F, Fernando L. M. Antunes, "A Switched-Capacitor Driver for Power LEDs," Instituto de Educación federal, Ciencia y Tecnología de Ceará, CE Brasil, pp. 918-923, 2011.

[14] Olegs Tetervenoks, "Sensorless Converter for Low-Power LED Lamp with Improved Power Factor," Instituto de ingeniería Eléctrica y Electrónica Industrial, Universidad Técnica de Riga, Kronvalda Boulevard 1, Riga, Latvia, pp. 285-290, 2014.

[15] Lumiblade OLED Panel. Brite FL300. Product sheet. 2014.

A Systematic Approach to Modeling Complex Magnetic Devices Using SPICE: Application to Variable Inductors

J. Marcos Alonso, *Senior Member, IEEE*, Gilberto Martínez, Marina Perdigão, *Member, IEEE*, Marcelo Rafael Cosetin, and Ricardo N. do Prado, *Member, IEEE*

***Abstract*—In this paper, a methodology to develop SPICE-based models of complex magnetic devices is presented. The proposed methodology is based on a reluctance equivalent circuit, which allows the user to study both the magnetic and electric behavior of the structure under any operating conditions. The different elements required to implement the reluctance model, namely, constant reluctances, variable reluctances, and windings, are implemented using SPICE behavioral modeling. These elements can thus be used to build a complete model for any magnetic device. The modeling process is illustrated with a particular example for a variable inductor. Simulations and experimental results are presented and compared to evaluate the accuracy and usefulness of the proposed modeling procedure.**

***Index Terms*—Magnetic devices, modeling, SPICE behavioral modeling, variable inductor (VI).**

I. Introduction

MODELING magnetic devices, such as inductors and transformers, has been a particularly important topic in power electronics. The great advances achieved in the last decades in the power electronics area in terms of miniaturization, efficiency improvement, and reliability, would have been impossible without new magnetic materials, devices, and modeling techniques. Understanding the real behavior of magnetic devices is a key issue to improve its performance, and that of the whole power electronics converter. Additionally, in today's power electronics applications, more complex magnetic structures are being employed, such as variable inductors (VIs) and transformers, saturable inductors and transformers, integrated magnetics, etc. [1]–[11].

Manuscript received March 10, 2016; accepted May 11, 2016. Date of publication May 24, 2016; date of current version June 24, 2016. This work was supported by the Spain National Government and Asturias Regional Government under research Grants ENE2013-41491-R and GRUPIN14-076, respectively.

J. Marcos Alonso is with the Department of Electrical Engineering, University of Oviedo, Oviedo 33003, Spain.

G. Martínez is with the Department of Electrical Engineering, University of Oviedo, Oviedo 33003, Spain, and also with Continental Automotive R&D; ID HMI Hardware Development Department, 45601-GDL, Jalisco, México .

M. Perdigão is with Instituto de Telecomunicações, University of Coimbra, Coimbra 3000-370, Portugal. He is also with Instituto Superior de Engenharia de Coimbra, Coimbra 3030-199, Portugal.

M. R. Cosetin and R. N. do Prado are with the Group of Intelligence in Lighting, Federal University of Santa Maria, Santa Maria 97105-900, Brazil.

This paper has supplementary downloadable multimedia material available at http://ieeexplore.ieee.org provided by the authors. The material is 48 KB in size.

Color versions of one or more of the figures in this paper are available online at http://ieeexplore.ieee.org.

Digital Object Identifier 10.1109/TPEL.2016.2571845

One of the more accurate and painless ways to study the behavior of magnetic structures is by using computer simulations. Basically, there are two methods to address this task: 1) finite elements analysis (FEA) and 2) SPICE-based behavioral models.

Surely, FEA provides the best accuracy, especially when using three-dimensional (3-D) models. However, it takes a considerable time to develop a 3-D model of a magnetic device. Moreover, the simulation time using FEA results very long; it can take many hours or even days to obtain the final results. Convergence problems may arise, breaking the simulation and wasting many hours of time. Any change or improvement in the model means a new simulation, making the analysis process quite painful and strenuous. On the other hand, computer simulation based on SPICE-like models results much more friendly; simulations can be done in seconds or minutes at the most, and they can easily be used within more complex electrical circuits or power converters. Of course, accuracy is lower than using FEA, nonetheless good enough for many applications.

In this paper, a SPICE-based model for computer simulation of any magnetic structure is presented. The proposed model is inspired on several models previously presented in the literature [12]–[17], which employed a reluctance or permeance equivalent circuit to simulate both the electrical and magnetic behavior of the magnetic structure. Particularly interesting is the methodology used in PSIM simulator [17]. However, the authors have found it too closed to allow the users to attain full benefit from it. This paper explores a similar methodology based on a reluctance model in which the reluctances depend on the magnetic flux level. A variable magnetic permeability, which is derived from the B–$HB - H$ curve of the magnetic material, is used to model the change of the reluctance. In this way, the different elements present in any magnetic structure, such as variable reluctances, air gaps, constant reluctances, and windings, will be modeled separately. Thus, they can be used to build an equivalent circuit of any magnetic structure. The model can be employed under any operating conditions, including dc and ac operation in any winding. In addition, the model will be able to provide electric and magnetic outcomes as voltage, current, magnetic flux, magnetic flux density, inductance, and so forth.

The original motivation to develop this study has been the investigation of the behavior of both saturable and controllable inductors and transformers. These devices have been studied and employed in power electronics applications for many years now with encouraging results [1]–[8], [12]–[26]. Particularly, controllable (variable) inductors are complex magnetic devices

0885-8993 © 2016 IEEE. Personal use is permitted, but republication/redistribution requires IEEE permission.
See http://www.ieee.org/publications_standards/publications/rights/index.html for more information.

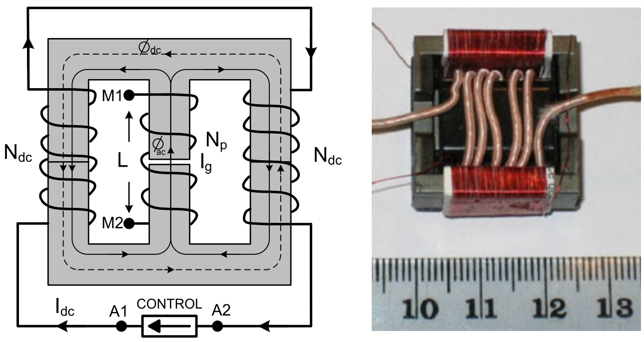

(a) (b)

Fig. 1. Physical structure of a VI implemented in an EE core.

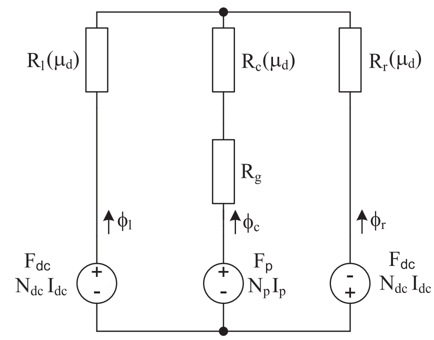

Fig. 2. Reluctance equivalent circuit of the VI shown in Fig. 1.

that deal with several windings under ac and dc superposed operation. In these devices, the reluctance of some sections of the magnetic material experiences a great variation owing to the dc component of the magnetic flux, even though the ac component remains under the saturation level. This makes a conventional analysis of these devices very laborious, while by using computer simulations it can be carried out very easily. Also, computer simulations allow the designer to change core geometry, magnetic properties, number of turns, air gap length, current, and voltage levels, etc., making design and redesign processes extremely straightforward.

In Section II, a review of the VI structure that will be used as a modeling example is carried out. Section III presents the modeling of the different elements of the reluctance equivalent model of a magnetic device. Section IV shows the implementation of the VI SPICE model using the proposed methodology. Section V presents simulation and experimental results. Finally, the conclusions of this study are provided in Section VI. This paper is a revised version of [27], in which several corrections and improvements have been made.

II. Review of the Selected VI Structure

In this paper, the VI structure based on a double E core, as shown in Fig. 1, will be employed as an example to illustrate the use of the proposed modeling technique.

The detailed operation of this device has been presented in previous literature [5] [7] [8]. A summary of its structure and operation can be made as follows. A double-E core with a gapped center arm is used, while no gap is present in the left and right arms. The main coil is wound on the center arm with a given number of turns N_p, which will implement the main inductor. Two auxiliary windings are placed on the left and right arms of the core, with an equal number of turns N_{dc} and with reversed polarity, so that the ac voltages generated across them tend to cancel each other when connected in series. Actually, as demonstrated in [13], a full cancellation is not possible due to the nonlinear behavior of the magnetic material *B–H* curve around the saturation knee. This is one of the aspects that would be very difficult to tackle by an analytical study. However, it is possible to deal with this issue quite straightforwardly by computer simulation.

In the VI structure, a dc current is injected through the auxiliary windings. This generates a dc flux bias that circulates mainly through the outer part of the core, because the center arm is gapped and exhibits a much higher reluctance. On the other hand, the ac flux circulating through the main winding splits into the outer arms, as shown in Fig. 1(a). The dc flux is used to bias the operating point of the magnetic material within the *B–H* curve, thus modifying the reluctances and changing the value of the inductance as seen from the main winding terminals.

This device can be modeled by using the reluctance circuit shown in Fig. 2. In this circuit, $\Re_c$, $\Re_l$, and $\Re_r$ represent the reluctances of the center, left, and right arms, respectively, and, in a general case, their values depend on the dc operating point of the magnetic material, and can therefore be expressed as a function of the material magnetic permeability. $\Re_g$ represents the air gap reluctance and can be assumed as a constant.

The other components in the circuit are the voltage sources F_{dc} and F_p, which represent the magnetomotive forces (MMF) created by the auxiliary and main windings, respectively, which are given by the turns by current product. Next section will present how the different elements of the reluctance model can be implemented following the methodology presented in this study.

III. Basic Elements of the Reluctance Equivalent Circuit

The basic elements of a reluctance equivalent circuit are three: 1) constant reluctances, which model an air gap or any other nonferromagnetic material used in the core structure; 2) variable reluctances, used to model the nonlinear behavior of the magnetic material of the core; and 3) windings, which model the interaction between the electric and magnetic quantities involved in the behavior of any magnetic device. Once these elements are independently modeled for computer simulation, they can be used to implement any magnetic structure model, disregarding its complexity.

A. Constant Reluctance Model

A constant reluctance is used to model the behavior of a nonferromagnetic section of the magnetic device. In the reluctance equivalent circuit, a constant reluctance is modeled by a resistor, whose value is defined as

$$\Re_0 = \frac{l_0}{\mu_0 \ A_0 \nu} \tag{1}$$

where l_0, and A_0 are the length and section of the constant reluctance element, respectively, $\mu_0 = 4\pi 10^{-7}$ H/m is the permeability of free space, and ν is the fringing coefficient, which is equal to 1 when the fringing effect is disregarded. However, a value slightly higher than 1 will usually render a better accuracy. Note that reluctance units are H^{-1}.

B. Variable Reluctance Model

A variable reluctance models the nonlinear behavior of the magnetic material employed in the device. It can be expressed as

$$\Re_m (B) = \frac{l_m}{\mu_d (B) A_m} \tag{2}$$

where l_m, and A_m are the length and section of the variable reluctance element, respectively, and $\mu_d(B)$ is the absolute differential permeability of the material, expressed as a function of the magnetic flux density B.

As can be seen in (2), in this type of element, the reluctance is a function of the magnetic permeability of the material, which in turn depends on the dc operating point within the material *B–H* curve. Therefore, at this point, it is necessary to find a model for the *B–H* characteristic of the magnetic material, from which the permeability can be obtained.

In this study, after testing other possibilities, Brauer's model of the *B–H* curve has been selected [28]–[29]. This model defines the relationship between the magnetic field intensity H and the magnetic flux density B, by expressing H as a function of B as

$$H(B) = \left(k_1 e^{k_2 B^2} + k_3\right) B \tag{3}$$

where k_1, k_2, and k_3 are the Brauer's model constants for each magnetic material.

For the sake of simplicity, the hysteresis effect is being neglected in this study, as it is usually done in most FEA software. From (3), it is very simple to obtain the differential permeability of the magnetic material by differentiation. The result is given in a closed form in (4). Also, note that (4) is valid for positive and negative values of B, because the $\mu_d(B)$ curve is symmetrical with respect to the vertical axis

$$\mu_d (B) = \frac{dB}{dH} = \left[k_1 \left(1 + 2k_2 B^2\right) e^{k_2 B^2} + k_3\right]^{-1}. \tag{4}$$

As an example, which will also be used to test the proposed model against experimental measurements, the N87 material from TDK-EPCOS has been modeled [30]. Brauer's model coefficients were derived from the graphical information given by the manufacturer's datasheet [30], obtaining the *B–H* curve data points and using a mathematical software for curve-fitting. The resulting values are shown in Table I. Fig. 3 shows a comparison between manufacturer's datasheet information and Brauer's model, both for N87 material at 25°C. With this approximation, the maximum relative error was obtained at $B = 0.3$ T and was calculated as 26%.

TABLE I
BRAUER'S COEFFICIENTS FOR N87 MATERIAL AT 25°C

Parameter	Value
k_1	$0.062\ \mathrm{Am^{-1}T^{-1}}$
k_2	$42.995\ \mathrm{T^{-2}}$
k_3	$302.904\ \mathrm{Am^{-1}T^{-1}}$

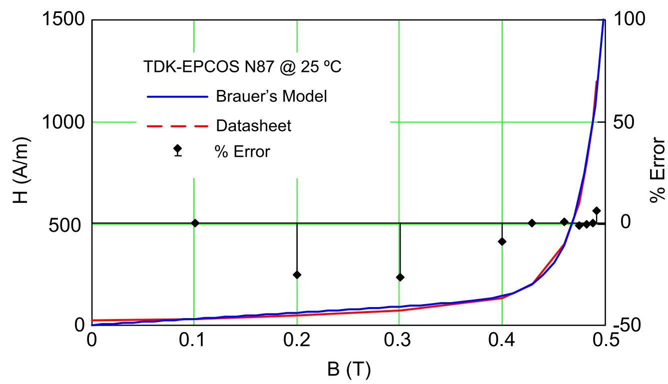

Fig. 3. *B–H* curve of N87 material at 25°C. Comparison between datasheet information and Brauer's model.

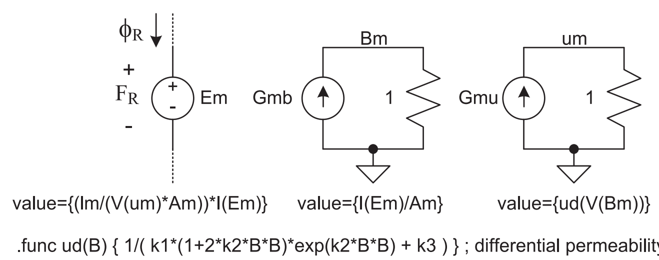

Fig. 4. Implementation of a variable reluctance in LTspice.

Fig. 4 shows the implementation of the variable reluctance component in SPICE, particularly in LTspice, which is the software that has been selected in this study [31]. As can be seen in Fig. 4, a behavioral voltage source E_m is used to implement a resistive behavior that models the variable reluctance. The behavioral current source G_{mb} generates a current equal to the flux density in the magnetic element, which is transformed into a voltage at node B_m. The behavioral current source G_{mu} generates a current equal to the actual differential permeability of the magnetic material by implementing (4). Finally, the voltage at node u_m is used in the expression of E_m to define the component reluctance by using (2).

C. Winding Model

A winding model must represent the electrical and magnetic interaction within the magnetic device structure. Neglecting losses, the winding model can be expressed as follows:

$$\mathcal{F}_w (t) = N_w \cdot i_w (t) \tag{5}$$

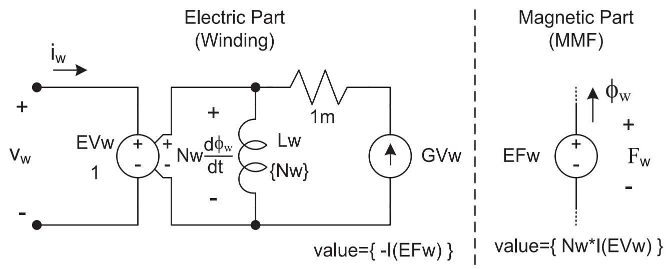

Fig. 5. Winding model implemented in LTspice.

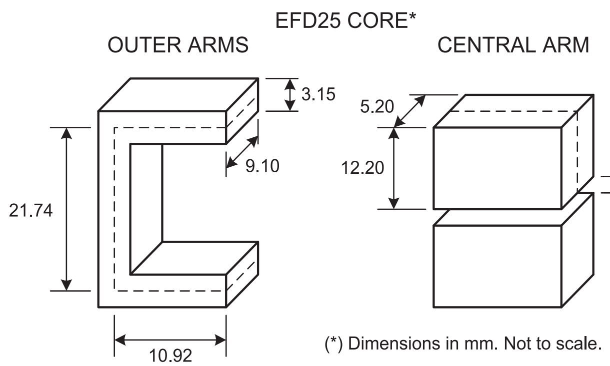

Fig. 6. EFD25 core dimensions [30].

$$v_w\ (t) = N_w\ \cdot \frac{d\emptyset_w\ (t)}{dt} = N_w\ A_w \frac{dB_w\ (t)}{dt} \tag{6}$$

where $\mathcal{F}_w$ is the MMF created by the winding inside the magnetic core, N_w is the winding number of turns, v_w and i_w are the winding voltage and current, $\emptyset_w$ and B_w are the magnetic flux and magnetic flux density in the core, respectively, and A_w is the area of the core.

Fig. 5 shows the SPICE implementation of the winding model. A voltage-dependent voltage source EV_w is used to implement the relationship between voltage and flux as given by (6). The behavioral voltage source EF_w is employed in the magnetic part of the model to generate the corresponding MMF according to (5). The behavioral current source GV_w generates a current equal to the magnetic flux, which is differentiated with respect to time by using the inductance L_w with a value equal to the number of turns of the winding (N_w) so that (6) can be implemented. The 1-mΩ resistance placed in series with GV_w is used to avoid convergence issues during simulation.

IV. Implementation of the VI Model

By using the three basic elements presented in the previous section, the reluctance equivalent circuit of any magnetic structure can be implemented for SPICE simulation. In this section, a model developed for the VI shown in Fig. 1 will be presented. This particular VI has been used in a previous work for the controlling of the output voltage in dc–dc resonant converters [20].

Fig. 6 illustrates the geometric diagram of the EFD25 core, which is used to calculate the average lengths and sections of the magnetic paths. Table II gathers the values of all the parameters related to the VI under study.

TABLE II
VI Data

Core material	N87 TDK-EPCOS	**Air gap length**	0.6 mm
Core type	EFD25	**Estimated fringing factor** (ν)	1.06
Expected inductance range	$1.2 - 4.5\mu\text{H}$	**Central arm average length** (lc)	24.4 mm
Main winding turns (N_p)	6	**Central arm section** (A_c)	59.3 mm^2
Intended operation regime	Sinusoidal, 500 kHz	**Outer arms average length** (l_1)	43.6 mm
Main winding peak current	6.0 A	**Outer arms section** (A_1)	28.7 mm^2
Bias windings turns (N_{dc})	65		

Fig. 7 illustrates the complete electrical diagram of the VI implemented in LTspice. As can be seen, it is divided into two main parts: magnetic part and electric part.

The magnetic part includes the reluctance model, where the variable reluctances $\Re_l,\ \Re_c$, and $\Re_r$ of Fig. 2 are implemented through the voltage sources E_5, E_3, and E_4, respectively. The magnetic flux density and permeability on each arm are calculated by current sources $G_5,\ G_3$ (central arm), $G_8,\ G_6$ (right arm), and $G_{11},\ G_9$ (left arm). Reluctances $R_{sl},\ R_{sc}$, and R_{sr} shown in Fig. 7 are used to measure the flux on each arm and to avoid voltage-loop issues during simulation. Their value of 1 H^{-1} is very small compared to the other series reluctances and therefore have no effect on the structure. Voltage source E_1 implements the magnetic part of the main winding of the VI, while voltage sources E_7 and E_6 implement the magnetic part of the left and right auxiliary windings, respectively.

The electric part of the model includes the implementation of the electric part of the three windings of the VI. Thus, sources E_2, G_1, and L_1 implement the behavior of the main winding, $E_8,\ G_{12}$, and L_2 correspond to the right auxiliary winding and $E_9,\ G_{13}$, and L_3 to the left auxiliary winding. Note that some additional small value resistors $(R_3,\ R_6,\ R_7,\ R_8,\ R_{13})$ are required to avoid voltage-loop and convergence issues.

The circuit shown in Fig. 7 can be employed to perform a dc transient simulation. Thus, the main winding is supplied with a 1-V dc voltage source with a 10-Ω series resistance. Auxiliary windings are supplied by using a dc current source with an output impedance of 100 kΩ. An important point that must be highlighted is that the auxiliary windings must be supplied with a dc source with a high output impedance, just as it is done in a real application. In this way, any interaction of the auxiliary source on the VI will be avoided.

The behavioral current source G_2 is used to calculate the inductance of the main winding by multiplying the flux of the main winding by its number of turns and dividing by its current.

The dc operating point simulation (.dc directive in SPICE) of the circuit shown in Fig. 7 will provide the steady-state values of all magnetic and electric variables of the VI, including the inductance value, given as a voltage at node L_SPICE.

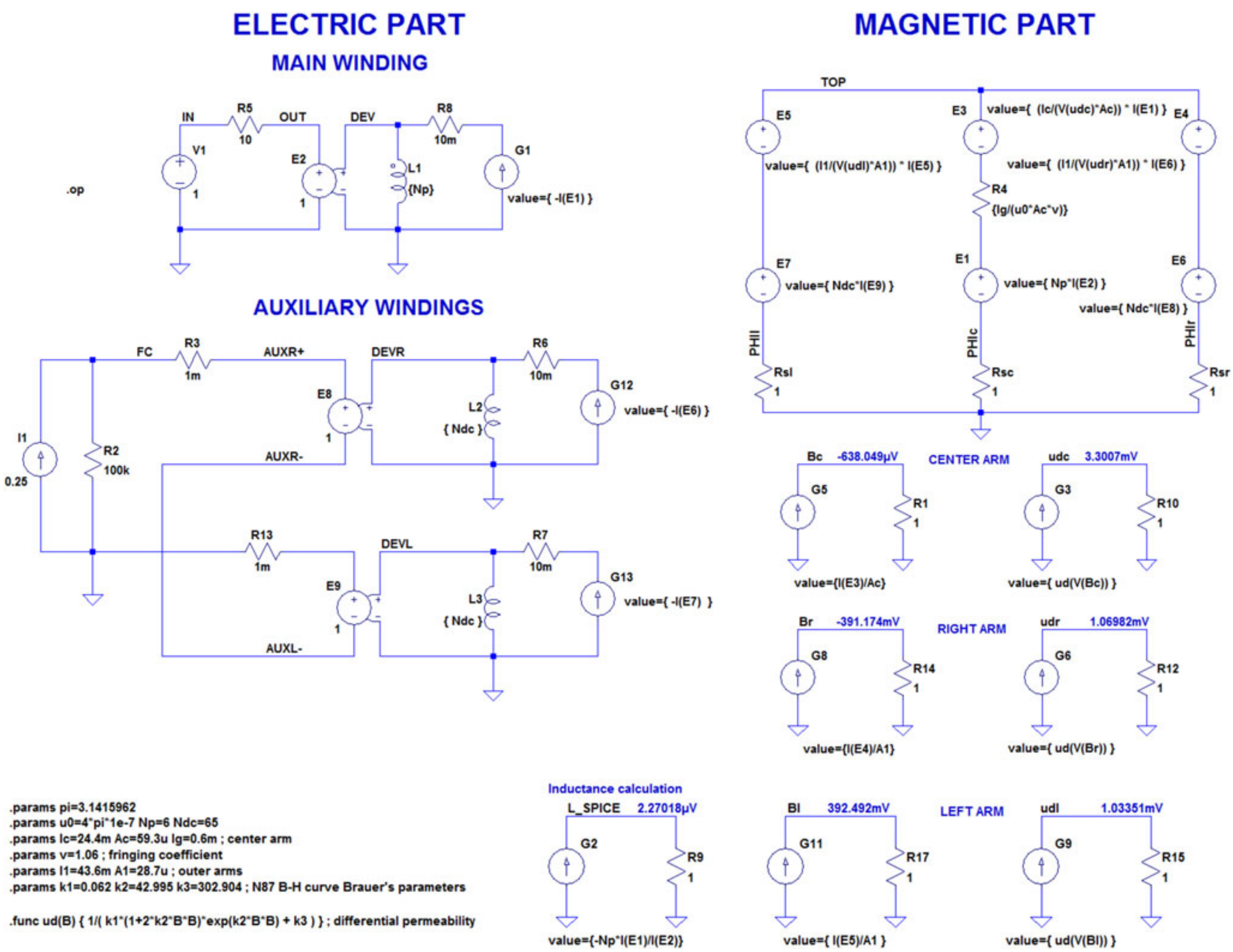

Fig. 7. Complete electrical model of the VI implemented in LTspice.

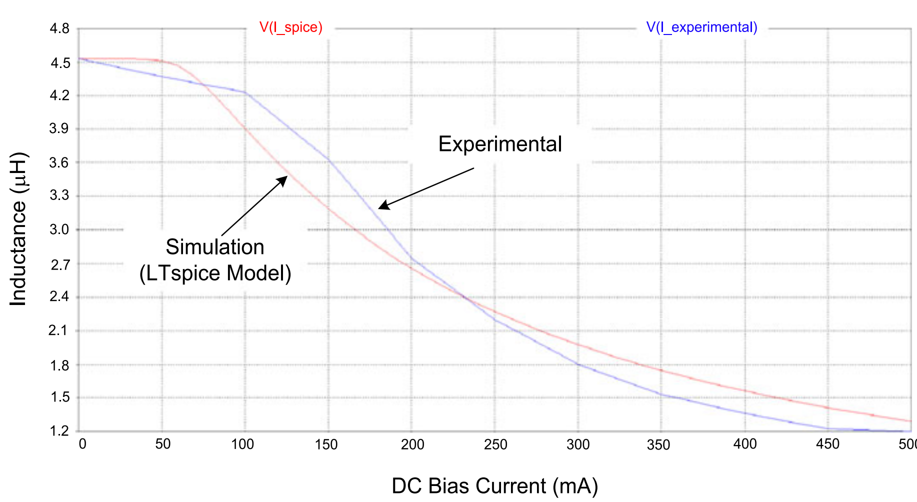

Fig. 8. Small-signal inductance of the VI. Comparison between simulation and experimental results.

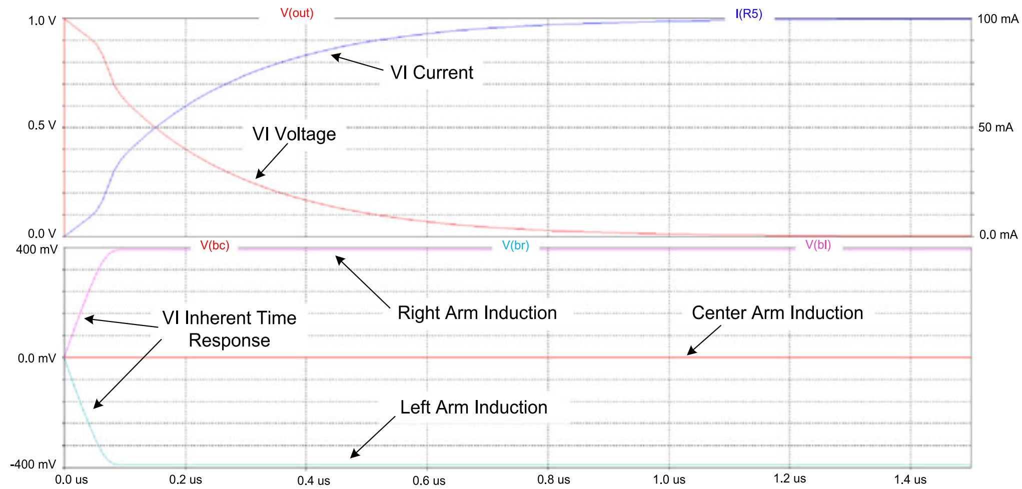

Fig. 9. Simulations results of the VI model under a dc start-up transient.

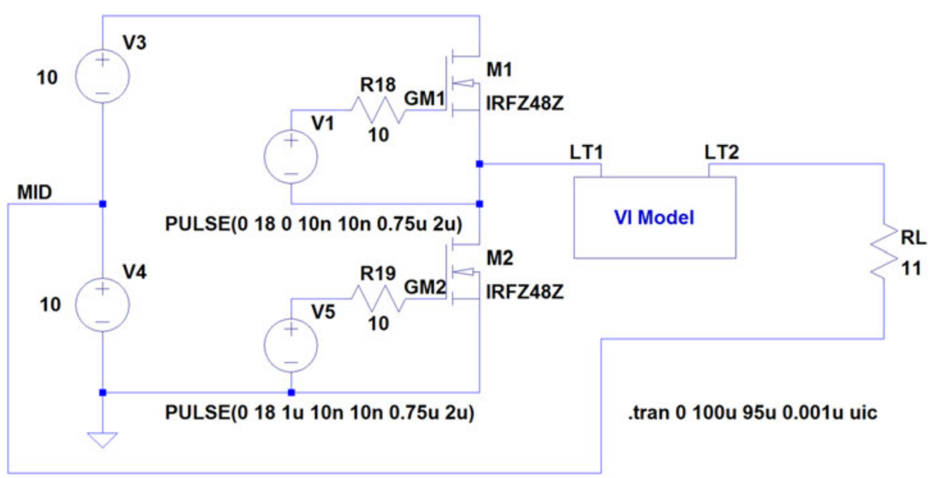

Fig. 10. Electric diagram for the simulation of an *L–R* inverter with VI. The VI is placed across terminals LT1 and LT2 according to the schematic shown in Fig. 7. Readers can refer to the active content for further details.

V. Simulation and Experimental Results

The first simulation carried out was a dc operating point (.dc) using the circuit shown in Fig. 7, in which a small current of 0.1 A is injected to the main winding to reach steady state, while the auxiliary windings carry a dc current of 0.25 A. Fig. 7 itself shows the simulation results by means of the voltage labels on each relevant node. As can be seen, the resulting inductance value is 2.27μH (voltage at node L_SPICE). The magnetic flux density at central, right, and left arms are obtained as voltage at nodes B_c, B_r, and B_l, giving –638.05 μ T, –391.17 mT, and 392.49 mT, respectively. Therefore, the central arm is operating with almost zero flux density (origin of the *B–H* curve), while the right and left arms are operated at a given dc flux density level owing to their biasing by the auxiliary windings, and in opposite direction. The small difference of flux density between left and right arms is due to the small flux level (0.638 mT) generated through the main winding, which adds to the left arm flux density, while subtracts from the right arm's.

The magnetic permeability of central, right, and left arms is obtained as voltages at nodes u_c, u_r, and u_l, respectively. The resulting values are 3.30, 1.070, and 1.033 mH/m, for central, right, and left arms, respectively. As expected, the permeability of the central arm is higher because of the lower flux density; the material of the central arm is operated around the origin of the *B–H* curve. On the other hand, the permeability of right and left arms is lower, because they operate at a much higher flux density level, within the knee of the *B–H* curve.

The above-presented simulation under dc operation can also be used to obtain the small-signal value of the VI inductance with very fast simulations. This can be done by performing a dc sweep analysis over the dc bias current source, shown as I_1 in Fig. 7. Following this procedure, Fig. 8 shows the simulation results in comparison with the experimental results obtained at the laboratory by using an impedance analyzer under small signal measurement of the inductance at a frequency of 1 kHz. Experimental results were added into the simulation for the sake of comparison by using a voltage-controlled source with a

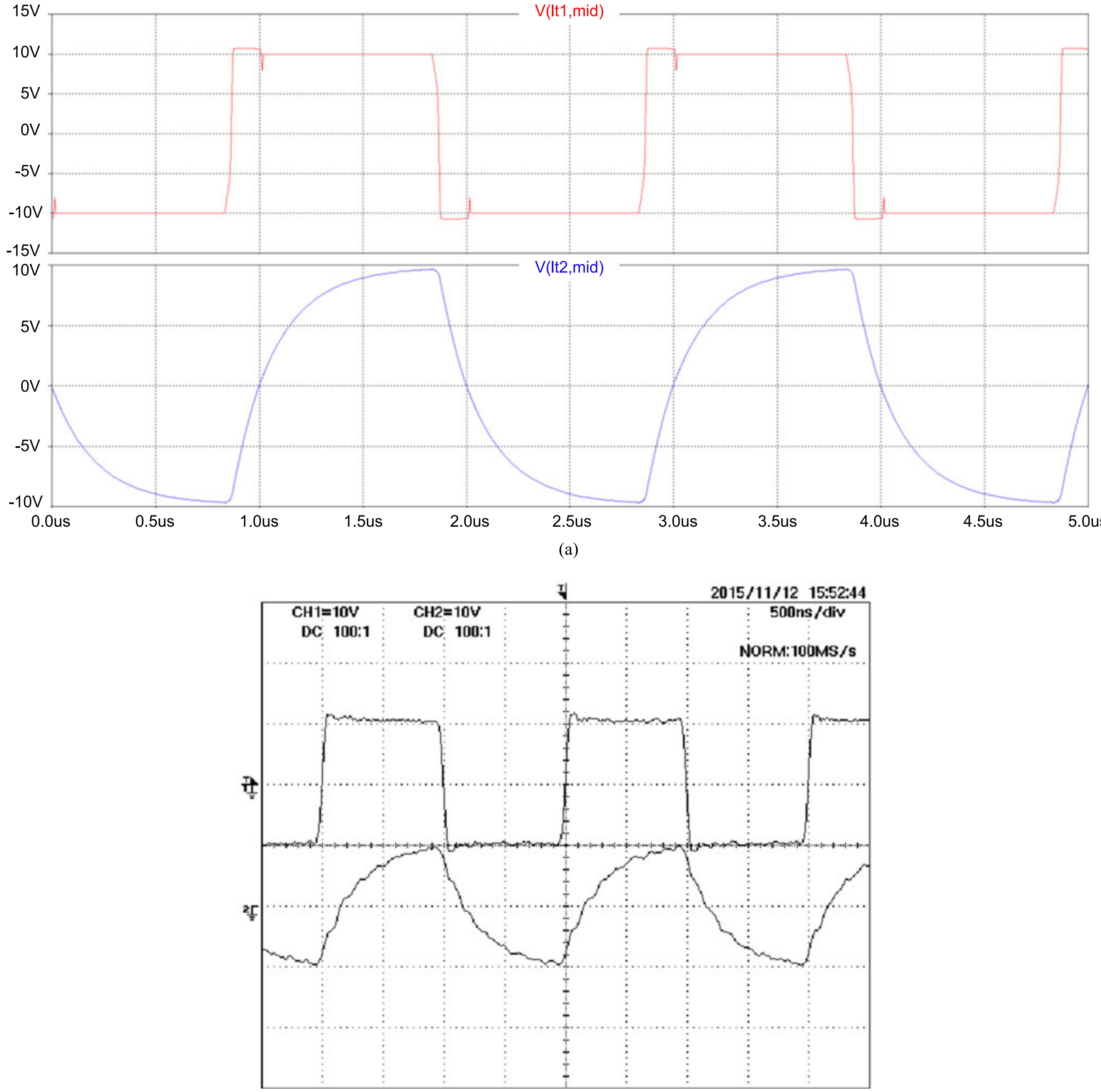

(a)

(b)

Fig. 11. Square voltage (top) and output voltage (bottom) of the circuit shown in Fig. 10: (a) simulation and (b) experimental. VI bias current 0.25 A.

look-up table (not shown in Fig. 7). Relative errors of –11% at 0.125-A bias current and +25% at 0.45-A bias current can be measured.

The difference between simulation and experimental results can be justified by three causes: 1) tolerances during the magnetic material fabrication, producing that the actual material *B–H* curve is not exactly the same as that given in the manufacturer's datasheet, 2) the error in the approximation of the *B–H* curve by the selected equation, in this case Brauer's model, 3) the effect of the leakage flux; the inclusion of a parallel reluctance to model, the leakage flux can render more approximated results. This effect will also be explored in future works [32] [33].

As an example, Fig. 9 shows the waveforms obtained from the same circuit shown in Fig. 7 when a transient simulation is performed. The inductor voltage and current, and the flux density inside the three arms of the structure are shown in this figure. As can be seen, it takes some time to the flux densities in right and left arms to reach their steady-state values, 50 ns approximately. This time is related to the dynamic response of the VI model. In the proposed model, this time is influenced by the output resistance of the current source that supplies the auxiliary

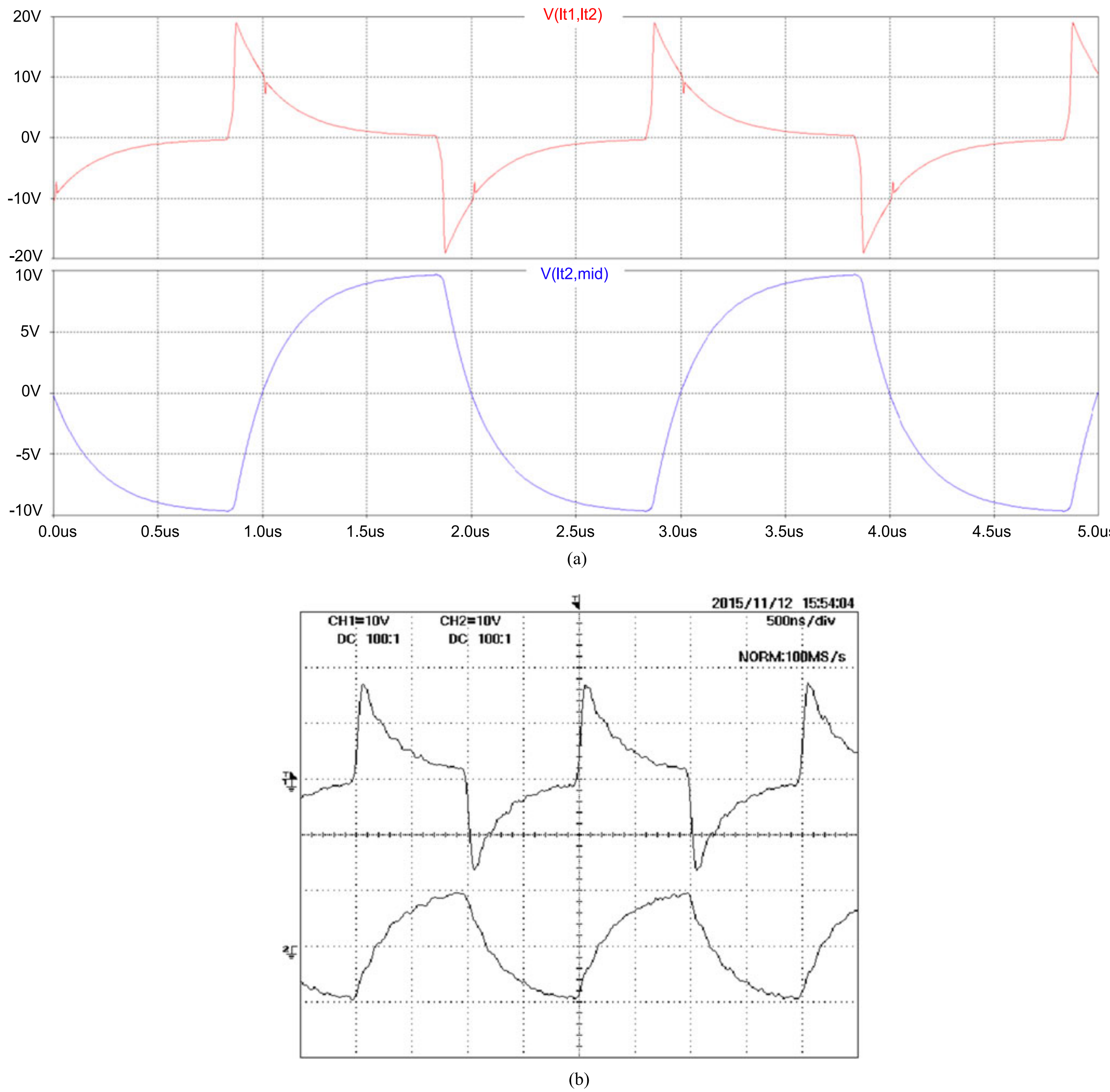

Fig. 12. VI voltage (top) and output voltage (bottom) of the circuit shown in Fig. 10: (a) simulation and (b) experimental. VI bias current 0.25 A.

winding and the equivalent inductance seen from the auxiliary winding. In the example under study, an output resistance of 100 kΩ has been selected in order to have a dynamic response fast enough so that it can be used up to frequencies of several hundreds of kilohertz. Nevertheless, this is a point that requires further investigation. In order to get more accurate results, the VI and its driving circuit should be dynamically modeled, theoretically or experimentally, and the time constant should be adjusted according to the obtained results. These issues will be addressed in future works [32] [33].

Fig. 10 illustrates the electrical diagram used for the simulation of a dc–ac converter with VI control. The converter has an input voltage of 20 V, applying a 10-V peak voltage square waveform to the L–$RL - R$ circuit. The switches are operated at 500 kHz with 200-ns dead time. The load resistance is 11Ω. In the following, simulation and experimental results corresponding to this circuit are presented.

Fig. 11 shows the simulation and experimental results corresponding to the square wave voltage and the output voltage across the load resistance for a VI bias current of 0.25 A. Fig. 12 illustrates the voltage across the VI and the output voltage for the same value of the VI bias current. As can be seen, simulation and experimental results match well.

Fig. 13 shows the simulation and experimental results corresponding to the VI bias windings. As can be seen, bias windings reflect voltages with peak values around 100 V. As expected, a

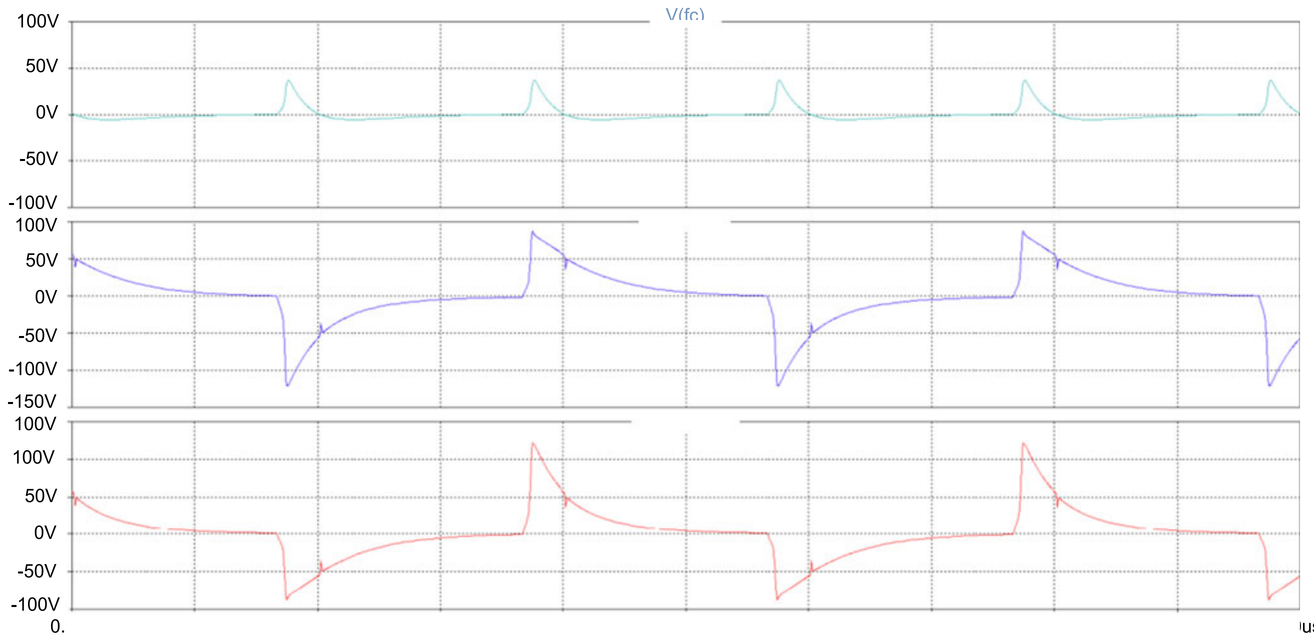

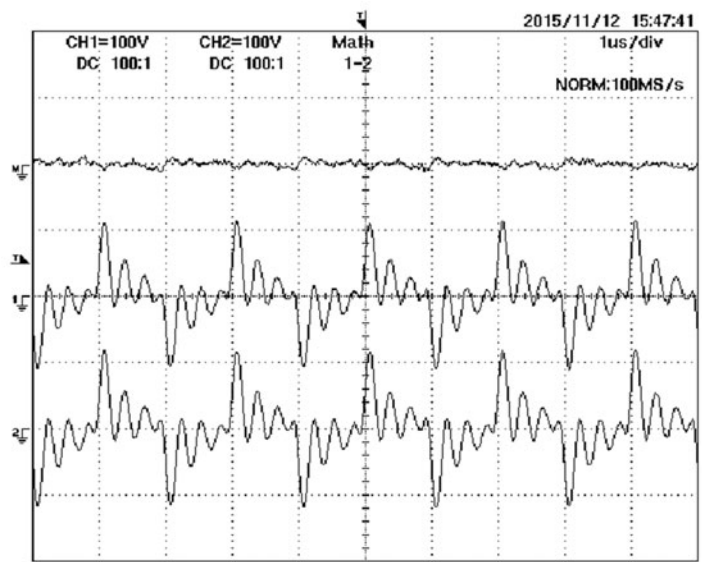

(b)

Fig. 13. Top: total voltage across VI bias windings. Middle: voltage across left bias winding. Bottom: voltage across right bias winding. All of them corresponding to the circuit shown in Fig. 10. (a) simulation and (b) experimental. VI bias current 0.25 A.

small difference can be seen comparing the voltages of left and right bias windings. As commented before, this difference is due to the nonlinear behavior of the magnetic material around the knee of the *B–H* curve [13]. However, the difference is higher in the simulation than in the experiments. This disagreement could be due to the response of the oscilloscope probe, which could not be able to follow so high *dv/dt*. Also, the high-voltage ripple superposed to the experimental waveform does not appear in the simulation. This ripple could also appear due to the effect of the oscilloscope voltage probe or other parasitic elements not considered by the model. The voltage probe used in these measurements was a differential voltage probe model 700924 from Yokowaga with 1:100 attenuation selected.

Fig. 14 shows the simulation results from the circuit in Fig. 10 corresponding to the instantaneous flux density in left, right, and center arms of the structure, and also to the instantaneous inductance of the VI. All of them are obtained from the corresponding nodes in the model. The VI bias current is 0.25 A. Experimental results are not available for these variables due to the difficulty of measuring dc levels of flux density inside a magnetic material. Nevertheless, the simulation results are in accordance with the expected ones.

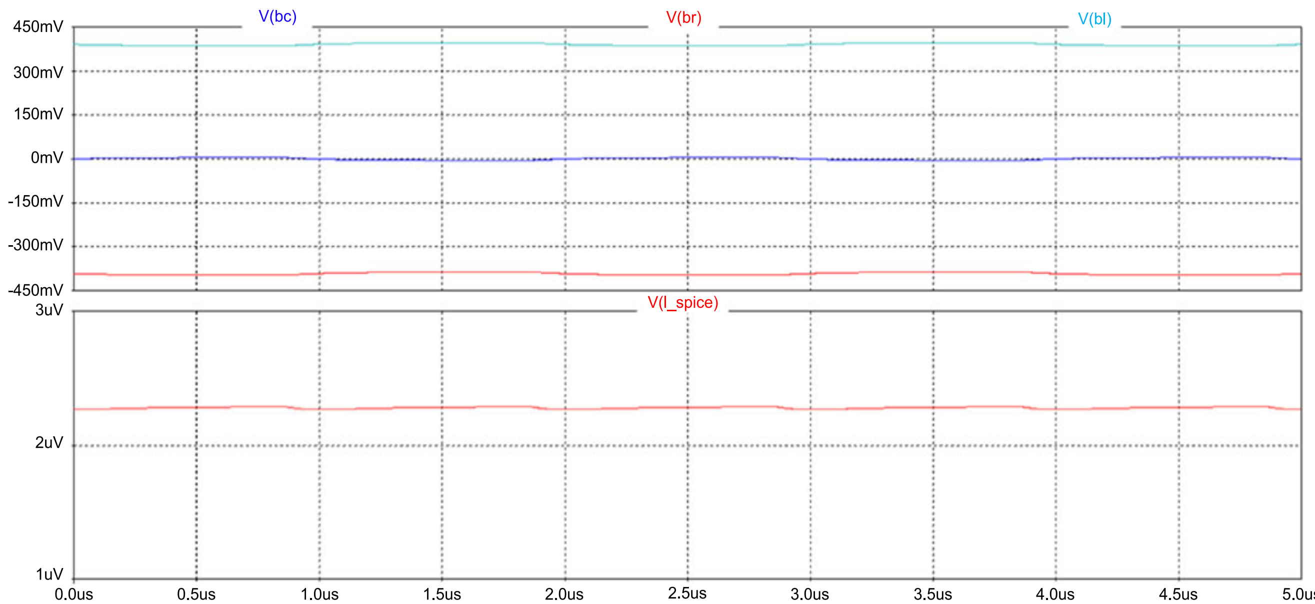

Fig. 14. Simulation results of the circuit in Fig. 10 with the VI bias current of 0.25 A. Top: flux density in each VI arm. Right arm (top), center arm (middle), and left arm (bot.). Scales: 200 mT/div. 500 ns/div. Bottom: inductance of the VI as obtained from the model. Scales: 1 μH/div, 500 ns/div.

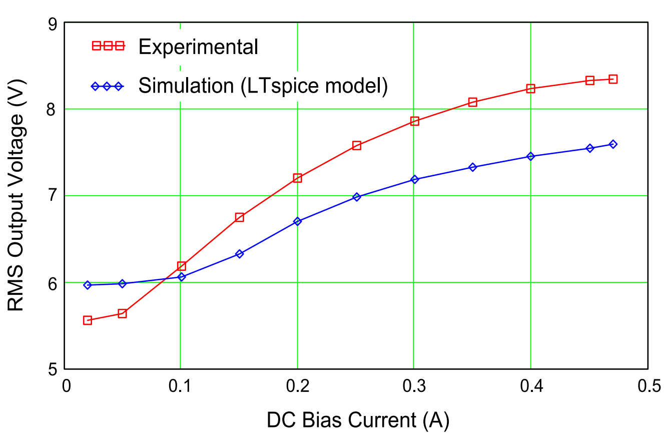

Fig. 15. Comparison between experimental and simulation results. RMS output voltage as a function of the VI dc bias current for the converter shown in Fig. 10.

Finally, in order to test the possibility of controlling the output voltage by means of the bias current on the VI, Fig. 15 presents the simulation and experimental results of the rms voltage in the load resistance of the circuit in Fig. 10 when varying the dc bias current of the VI. As can be seen, simulation and experimental results exhibit a similar curve. Again, the difference between simulation and experiments can be justified by the error in the modeling of the magnetic material *B*–*H* curve.

VI. Conclusion

This paper has presented a modeling technique for magnetic devices based on SPICE behavioral modeling. The three basic elements required for developing a reluctance-based equivalent circuit have been implemented in SPICE. These elements can easily be integrated in a SPICE library in order to simplify its use in circuit simulation [33]. It has been explained how by using these three elements any magnetic structure can be modeled and simulated providing magnetic, electric, and inductance results. Besides, the proposed modeling technique can be used under any operating conditions with good accuracy, because the nonlinear behavior of the magnetic material is taken into consideration. A modeling example of a VI with an EE structure has been presented and simulated, showing good approximation with experimental results. Simulation and experimental results for a VI-controlled dc–ac inverter have also been presented. The comparison between simulated and experimental results rendered good expectancies for the proposed modeling methodology.

Finally, it must be pointed out that the proposed methodology can also be implemented by using mathematical software packages, which could be used to solve the corresponding set of equations. The advantage of using a SPICE model resides in the fact that the model can easily be used to perform complete simulations including the power converter or other any electric or electronic circuit in which the VI is intended to operate.

References

[1] A. S. Kislovski, “Quasi-linear controllable inductor,” *Proc. IEEE*, vol. 75, no. 2, pp. 267–269, Feb. 1987.

[2] A. S. Kislovski, “Linear variable inductor in dc current sensors utilized in telecom solar battery chargers,” in *Proc. Int. Telecommun. Energy Conf.*, 1989, pp. 1–3.

[3] A. S. Kislovski, “Linear variable inductor (LVI) in single-phase off-line telecom rectifiers,” in *Proc. IEEE Int. Telecommun. Energy Conf.*, 1995, pp. 93–98.

[4] D. L. Birx and L. L. Reginato, “Saturable inductor and transformer structures for magnetic pulse compression,” U.S. Patent 4 928 020, 1990.

[5] D. Medini and S. Ben-Yaakov, “A current-controlled variable-inductor for high frequency resonant power circuits,” in *Proc. Appl. Power Electron. Conf. Expo.*, Feb. 1994, vol. 1, pp. 219–225.

[6] W. H. Wölfle and W. G. Hurley, “Quasi-active power factor correction with a variable inductive filter: Theory, design and practice,” *IEEE Trans. Power Electron.*, vol. 18, no. 1 pp. 248–255, Jan. 2003.

[7] J. M. Alonso, M. A. Dalla Costa, J. Cardesín, and J. Garcia, "Magnetic dimming of electronic ballasts," *Electron. Lett.*, vol. 41, no. 12, pp. 718–719, Jun. 2005.

[8] M. S. Perdigão, J. M. Alonso, D.G. Vaquero, and E. S. Saraiva, "Magnetically controlled electronic ballasts with isolated output: The variable transformer solution," *IEEE Trans. Ind. Electron.*, vol. 58, no. 9, pp. 4117–4129, Sep. 2011.

[9] M. Pahlevani, S. Eren, A. Bakhshai, and P. Jain, "A series–parallel current-driven full-bridge DC/DC converter," *IEEE Trans. Power Electron.*, vol. 31, no. 2, pp. 1275–1293, Feb. 2016.

[10] G. Gohil, L. Bede, R. Teodorescu, T. Kerekes, and F. Blaabjerg, "An integrated inductor for parallel interleaved three-phase voltage source converters," *IEEE Trans. Power Electron.*, vol. 31, no. 5, pp. 3400–3414, May 2016.

[11] H. Zhu, D. Zhang, Q. Liu, and Z. Zhou, "Three-Port DC/DC Converter with all ports current ripple cancellation using integrated magnetic technique," *IEEE Trans. Power Electron.*, vol. 31, no. 3, pp. 2174–2186, Mar. 2016.

[12] D. C. Hamill, "Gyrator-capacitor modeling: A better way of understanding magnetic components," in *Proc. Appl. Power Electron. Conf. Expo.*, 1994, vol. 1, pp. 326–332.

[13] E. Rozanov and S. Ben-Yaakov, "Analysis of current-controlled inductors by new SPICE behavioral model," *HAIT J. Sci. Eng. B*, vol. 2, no. 3–4, pp. 558–570, 2005.

[14] K. D. T. Ngo, "Subcircuit modeling of magnetic cores with hysteresis in PSpice," *IEEE Trans. Aerosp. Electron. Syst.*, vol. 38, no. 4, pp. 1425–1434, Oct. 2002.

[15] M. S. Perdigao, J. M. Alonso, M. A. Dalla Costa, and E. S. Saraiva, "A variable inductor MATLAB/Simulink behavioral model for application in magnetically-controlled electronic ballasts," in *Proc. Int. Symp. Power Electron. Electr. Drives, Autom. Motion*, Jun. 11–13, 2008, pp. 349–354.

[16] M. S. Perdigao, "Research and development on new control techniques for electronic ballasts based on magnetic regulators," Ph.D. dissertation, Univ. Coimbra, Coimbra, Portugal. (2011). [Online] Available: https://powersimtech.com/support/resources/tutorials/define-saturable-core/

[17] "Tutorial on how to define the saturable core element," *PSIM Software, Powersim Inc.*, Rockville, MD, USA, July 2006.

[18] J. M. Alonso, M. A. Dalla Costa, M. Rico-Secades, J. Cardesín, and J. Garcia, "Investigation of a new control strategy for electronic ballasts based on variable inductor," *IEEE Trans. Ind. Electron.*, vol. 55, no. 1, pp. 3–10, Jan. 2008.

[19] J. M. Alonso, M. S. Perdigao, D. Gacio, L. Campa, and E. S. Saraiva, "Magnetic control of DC-DC resonant converters provides constant frequency operation," *Electron. Lett.*, vol. 46, no. 6, pp. 440–442, 2010.

[20] J. M. Alonso, M. S. Perdigão, D. G. Vaquero, A. J. Calleja, and E. S. Saraiva, "Analysis, design, and experimentation on constant-frequency dc-dc resonant converters with magnetic control," *IEEE Trans. Power Electron.*, vol. 27, no. 3, pp. 1369–1382, Mar. 2012.

[21] M. S. Perdigao, J. M. Alonso, M. A. Dalla Costa, and E. S. Saraiva, "Comparative analysis and experiments of resonant tanks for magnetically controlled electronic ballasts," *IEEE Trans. Ind. Electron.*, vol. 55, no. 9, pp. 3201–3211, Sep. 2008.

[22] M. S. Perdigao, J. P. F. Trovao, J. M. Alonso, and E. S. Saraiva, "Large-signal characterization of power inductors in EV bidirectional DC–DC converters focused on core size optimization," *IEEE Trans. Ind. Electron.*, vol. 62, no. 5, pp. 3042–3051, May 2015.

[23] M. S. Perdigao, J. M. Alonso, and E. S. Saraiva, "Magnetically-controlled dimming technique with isolated output," *Electron. Lett.*, vol. 45, no. 14, pp. 756–758, Jul. 2009.

[24] M. S. Perdigao, J. M. Alonso, M. A. Dalla Costa, and E. S. Saraiva, "Using magnetic regulators for the optimization of universal ballasts," *IEEE Trans. Power Electron.*, vol. 23, no. 6, pp. 3126–3134, Nov. 2008.

[25] M. S. Perdigao, M. Menke, A. R. Seidel, R. A. Pinto, and J. M. Alonso, "A review on variable inductors and variable transformers: Applications to lighting drivers," *IEEE Trans. Ind. Appl.*, vol. 52, no. 1, pp. 531–547, Sep. 2015.

[26] R. A. Alonso, J. M. Perdigao M. S. Pinto, M. F. da Silva, and R. N. do Prado, "A new technique to equalize branch currents in multiarray LED lamps based on variable inductor," in *Proc. IEEE Ind. Appl. Soc.*, Oct. 5–9, 2014, pp. 1–9.

[27] J. M. Alonso, G. Martínez, M. Perdigão, M. Cosetin, and R. N. do Prado, "Modeling magnetic devices using spice: application to variable inductors," in *Proc. IEEE Appl. Power Electron. Conf.*, Long Beach, CA, USA, Mar. 2016, pp. 20–24.

[28] J. R. Brauer, "Simple equations for the magnetization and reluctivity curves of steel," *IEEE Trans. Magn.*, vol. 11, no. 1, p. 81, Jan 1975.

[29] T. Hülsmann, "Nonlinear material curve modeling and sensitivity analysis for MQS-problems," M.S. thesis, Faculty Elect., Inf. Media Eng., Bergische Universitat Wuppertal, Wuppertal, Germany, 2012.

[30] Ferrite Cores and Accessories Datasheet, *EPCOS*, Munich, Germany, Sep. 2006.

[31] LTspice IV. Getting Started Guide, Linear Technology Corp., Milpitas, CA, USA, 2011.

[32] J. M. Alonso, M. Perdigão, M. A. Dalla Costa, G. Martínez, and R. Osorio, "Analysis and design of a novel variable-inductor-based LED driver for DC lighting Grids," to be published in *Proc. IEEE Ind. Appl. Soc. Annu. Meeting*, Portland, OR, USA, 2016.

[33] J. M. Alonso, M. Perdigão, G. Z. Abdelmessih, and M. A. Dalla Costa, "SPICE-aided design of a variable inductor in LED driver applications," to be published in *Proc. IEEE Ind. Appl. Soc. Annu. Meeting*, Portland, OR, USA, 2016.

J. Marcos Alonso (S'94–M'98–SM'03) received the M.Sc. and Ph.D. degrees in electrical engineering from the University of Oviedo, Oviedo, Spain, in 1990 and 1994, respectively.

Since 2007, he has been a Full Professor at the Electrical Engineering Department, the University of Oviedo. He is the coauthor of more than 350 journal and conference publications, including 85 publications in highly referenced journals. His research interests include electronic ballasts, light-emitting diode power supplies, power factor correction, dc–dc converters, soft-switching converters, resonant inverters, and high-frequency switching converters in general. He was a supervisor of nine Ph.D. thesis and he is the holder of seven Spanish patents. He has participated in more than 50 research projects and contracts with companies. He has been a Visiting Researcher at the Federal University of Santa Maria, Santa Maria, Brazil, in 2011 and 2014, and at the Center for Power Electronics Systems, Virginia Tech., Blacksburg, USA, in 2013.

Dr. Alonso received the Early Career Award of the IEEE Industrial Electronics Society in 2006, and the University of Oviedo Electrical Engineering Doctorate Award, and five IEEE paper awards. He also received the National Funding for Intensification of Research Activity 2008–2012. He is a member of the Power Electronics Technical Committee of the IEEE Industrial Electronics Society. He is also a member of the European Power Electronics Association and he belongs to the International Steering Committee of the European Conference on Power Electronics and Applications. He serves as an Associate Editor of the IEEE TRANSACTIONS ON POWER ELECTRONICS and IEEE JOURNAL ON EMERGING AND SELECTED TOPICS ON POWER ELECTRONICS. He has been Coguest Editor of three special issues on lighting applications published in IEEE journals and has co-organized many IEEE Conference Special Sessions. He was Secretary of the IEEE IAS Industrial Lighting and Display Committee for the term 2013–2014, where he currently serves as Vice-Chair. He has been elected as a Member-at-Large of the IEEE IAS Executive Board for the term 2013–2016, where he collaborates in the Education department and is the Editor of the monthly IAS Newsletter.

Gilberto Martínez received the B.Sc. and M.Sc. degrees in electronic engineering from the Technology Institute of Celaya, Guanajuato, Mexico, in 2007 and 2010, respectively. Since September 2014, he has been working toward the Ph.D. degree in electrical and electronics engineering at the University of Oviedo, Oviedo, Spain.

He was with Philips Lighting as a Design Engineer of fluorescent, LED, and high-intensity discharge Lamp Drivers from December 2010 to April 2014. In July 2014, he joined R&D Continental Automotive as SMPS and LED Drivers Modules Development Engineer. His research interests include electronic ballast, dc–dc power converters, dc–dc switched capacitor converters, power converter modeling, and lighting in general.

Marina S. Perdigão (S'06–M'12) was born in Coimbra, Portugal, in 1978. She received the M.Sc. and Ph.D. degrees in electrical engineering from the University of Coimbra, Coimbra, Portugal, in 2004 and 2012, respectively. She received the Ph.D. degree from the University of Coimbra, in 2012, in cooperation with the University of Oviedo, Spain.

Since 2002, she has been with the Polytechnic Institute of Coimbra, Coimbra Institute of Engineering, Coimbra, first as a Teaching Assistant, and since 2012 as an Assistant Professor. Since 2001, she has also been a researcher at the Instituto de Telecomunicações, Coimbra. Her research interests include high-frequency electronic ballasts, discharge lamp modeling, high-frequency switching converters, resonant converters, dc–dc converters, power electronics for renewable energies, IPT and computer simulation applications. She collaborates as a transactions paper reviewer.

Dr. Perdigão received the Best Paper Award of the 2009 IEEE International Symposium on Industrial Electronics.

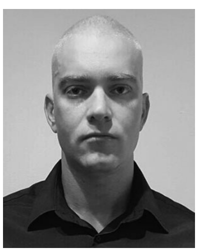

Marcelo Rafael Cosetin was born in Horizontina, Brazil, in 1985. He received the B.S. (Hons.) degree and the master's degree in electrical engineering from Federal University of Santa Maria (UFSM), Santa Maria, Brazil, in 2011 and 2013, respectively, where he is currently working toward the Ph.D. degree at Programa de Pós-Graduação em Engenharia Elétrica, concept six Capes.

In the first semester of 2011, he held Supervised Internship at Fraunhofer Institute for Reliability and Microintegration, Berlin, Germany. Since 2007, he has been a Researcher of Electronic Ballast Research Group, (UFSM. He is also a student/researcher for one year at University of Oviedo, Oviedo, Spain, at the research group Conversión Eficiente de Energía, Electrónica Industrial e Iluminación CE3I2, Gijón, supported by Science Without Boarding Brazilian Mobility Program, Capes/Cnpq. His main areas of interest includes intelligent lighting, electronics ballast, dc/dc converters, power factor correction stages, dimming systems, light-emitting-diode as lighting source, resonant ballast, and variable inductor.

Ricardo N. do Prado (M'00) received the B.Sc. degree in electrical engineering from the Federal University of Santa Maria, Santa Maria, Brazil, in 1984, and the M.Sc. and Ph.D. degrees in electrical engineering from the Federal University of Santa Catarina, Florianopolis, Brazil, in 1987 and 1993, respectively.

From 1987 to 1992, he was with the Federal University of Minas Gerais, Belo Horizonte, Brazil. Since 1993, he has been with the Federal University of Santa Maria, where he is currently a Full Professor with the Department of Electrical Energy Processing. From 2005 to 2006, he was a Postdoctoral Research Scholar with the Fraunhofer Institute, Munich, Germany. He is the author of more than 250 technical papers published in conference proceedings and magazines. He was a Co-Guest Editor of the Special Issue on Power Electronics Applications to Lighting Systems published in the *Power Electronics Brazilian Journal* (2012/2013), and he has co-organized several conference special sessions. His research interests include high frequency, fluorescent, and high-pressure lamps, dimming systems, luminous efficiency, electronic ballast, light emitting diode as a source light, and power-factor correction.

Dr. Prado is a founding member of the Brazilian Power Electronics Society and a member of the Brazilian Automatic Control Society and several IEEE societies. He is a Reviewer for the Brazilian Power Electronics Society, Brazilian Automatic Control Society, and several IEEE Societies. He received one IEEE paper awards.

Modeling Magnetic Devices using SPICE: Application to Variable Inductors

J. Marcos Alonso[1], Gilberto Martínez[1, 2], Marina Perdigão[3, 4], Marcelo Cosetin[5], Ricardo N. do Prado[5]

(1) University of Oviedo, Electrical Eng. Dept., Campus de Viesques, Gijón, Asturias, Spain.
(2) Continental Automotive R&D; ID HMI Hardware Development Dept., Jalisco, México.
(3) Instituto de Telecomunicações, University of Coimbra, DEEC, Coimbra.
(4) IPC, Instituto Superior de Engenharia de Coimbra, ISEC, DEE, Portugal.
(5) Federal University of Santa Maria, Group of Intelligence in Lighting (GEDRE), Brazil.

marcos@uniovi.es; gilbertomar9@hotmail.com; perdigao@isec.pt; mcosetin@gedre.ufsm.br; ricardo@gedre.ufsm.br

***Abstract*—In this paper a methodology to develop SPICE-based models of complex magnetic devices is presented. The proposed methodology is based on a reluctance equivalent circuit (REC), which allows the user to study both the magnetic and electric behavior of the structure under any operating conditions. The different elements required to implement the reluctance model, namely, constant reluctances, variable reluctances and windings, are implemented using SPICE behavioral modeling. These elements can thus be used to build a complete model for any magnetic device. The modeling process is illustrated with a particular example for a variable inductor. Simulations and experimental results are presented and compared to evaluate the accuracy and usefulness of the proposed modeling procedure.**

I. INTRODUCTION

Modeling magnetic devices, such as inductors and transformers, has been a particularly important topic in power electronics. The great advances achieved in the last decades in the power electronics area in terms of miniaturization, efficiency improvement and reliability, would have been impossible without new magnetic materials, devices and modeling techniques. Understanding the real behavior of magnetic devices is a key issue to improve its performance, and that of the whole power electronics converter. Additionally, in today's power electronics applications, more complex magnetic structures are being employed, such as variable inductors (VI) and transformers (VT), saturable inductors (SI) and transformers (ST), etc. [1]-[8].

One of the more accurate and painless ways to study the behavior of magnetic structures is by using computer simulations. Basically, there are two methods to address this task: (i) Finite Elements Analysis (FEA) and (ii) SPICE-based behavioral models.

This work has been supported by Spain national government and Asturias regional government under research grants ENE2013-41491-R and GRUPIN14-076, respectively.

Surely, FEA provides the best accuracy, especially when using 3-D models, but it takes considerable time to develop a 3-D model of a magnetic device. Moreover, the simulation time using FEA is very long; it can take many hours or even days to obtain the final results. Convergence problems may arise, breaking the simulation and wasting many hours of time. Any change or improvement in the model means a new simulation, making the analysis process quite painful and strenuous. On the other hand, computer simulation based on SPICE-like models results much more friendly; simulations can be done in seconds, or minutes at the most. Of course, accuracy is lower than using FEA, nonetheless good enough for many applications.

In this paper, a SPICE-based model for computer simulation of any magnetic structure is presented. The proposed model is inspired in several models previously presented in the literature [9]-[14], which employed a reluctance or permeance equivalent circuit to simulate both the electrical and magnetic behavior of the magnetic structure. Particularly interesting is the methodology used in PSIM simulator [14]. However, the authors have found it too closed to allow the users to attain full benefit of it. This paper explores a similar methodology based on a reluctance model in which the reluctances depend on the magnetic flux level. A variable magnetic permeability, which is derived from the $B-H$ curve of the magnetic material, is used to model the change of the reluctance. In this way, the different elements present in any magnetic structure, such as variable reluctances, air gaps, constant reluctances and windings, will be modelled separately. Thus, they can be used to build an equivalent circuit of any magnetic structure. The model can be employed under any operating conditions, including dc and ac operation in any winding. In addition, the model will be able to provide electric and magnetic outcomes as voltage, current, magnetic flux, magnetic flux density, inductance, and so forth.

The original motivation to develop this work has been the investigation of the behavior of both saturable and controllable inductors and transformers. These devices have been studied and employed in power electronics applications for many years now with encouraging results [1]-[23]. Particularly, controllable (variable) inductors are complex magnetic devices that deal with several windings under ac and dc superposed operation. In these devices, the reluctance of some sections of the magnetic material experiences a great variation owing to the dc component of the magnetic flux, even though the ac component remains under the saturation level. This makes a conventional analysis of these devices very laborious, while by using computer simulations it can be carried out very easily. Also, computer simulations allow the designer to change core geometry, magnetic properties, number of turns, air gap length, current and voltage levels, etc., making design and redesign processes extremely straightforward.

In Section II a review of the variable inductor structure that will be used as a modeling example is carried out. Section III presents the modeling of the different elements of the reluctance equivalent model of a magnetic device. Section IV shows the implementation of the variable inductor SPICE model using the proposed methodology. Section V presents simulation and experimental results. Finally, the conclusions of the paper are provided in Section VI.

II. REVIEW OF THE SELECTED VARIABLE INDUCTOR STRUCTURE

In this paper, the variable inductor (VI) structure based on a double E core, as shown in Fig. 1, will be employed as an example to illustrate the use of the proposed modeling technique.

The detailed operation of this device has been presented in previous literature [5][7][8]. A summary of its structure and operation is as follows. A double-E core with a gapped center arm is used, while there is no gap in the left and right arms. The main coil is wound on the center arm with a given number of turns (N_p), which will implement the main inductor. Two auxiliary windings are placed on the left and right arms of the core, with an equal number of turns (N_{dc}) and with reversed polarity, so that the ac voltages generated across them tend to cancel each other when connected in series. Actually, as demonstrated in [10], a full cancellation is not possible due to the non-linear behavior of the magnetic material $B-H$ curve around the saturation knee. This is one of the aspects that would be very difficult to tackle by an analytical study. However, it is possible to deal with this issue quite straightforwardly by computer simulation.

In the VI structure, a dc current is injected through the auxiliary windings. This generates a dc flux bias that circulates mainly through the outer part of the core, because the center arm is gapped and exhibits a much higher reluctance. On the other hand, the ac flux circulating through the main winding splits into the outer arms, as shown in Fig. 1a. The dc flux is used to bias the operating point of the magnetic material within the $B-H$ curve, thus modifying the reluctances and changing the value of the inductance seen from the main winding terminals.

This device can be modelled by using the reluctance circuit shown in Fig. 2. In this circuit, $\Re_c, \Re_l$ and $\Re_r$ represent the reluctances of the center, left and right arms respectively and, in a general case, their value depend on the dc operating point of the magnetic material, and can therefore be expressed as a function of the magnetic permeability of the material. $\Re_g$ represents the air gap reluctance and can be assumed as a constant.

The other components in the circuit are the voltage sources F_{dc} and F_p, which represent the magnetomotive forces (MMF) created by the auxiliary and main windings respectively, which are given by the turns by current product. Next section will present how the different elements of the reluctance model can be implemented following the methodology presented in this work.

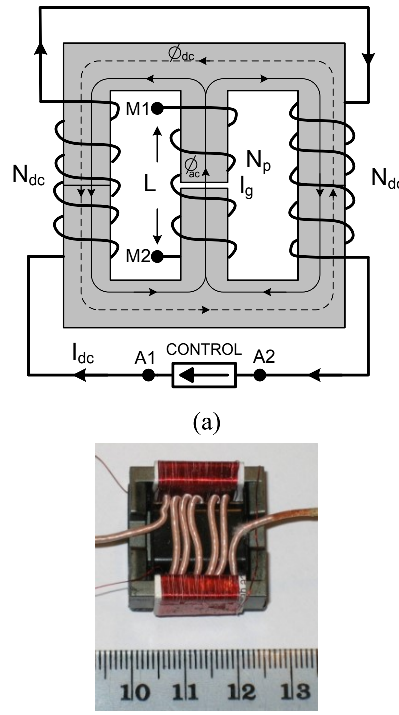

(a)

(b)

Fig. 1. Physical structure of a VI implemented in an EE core.

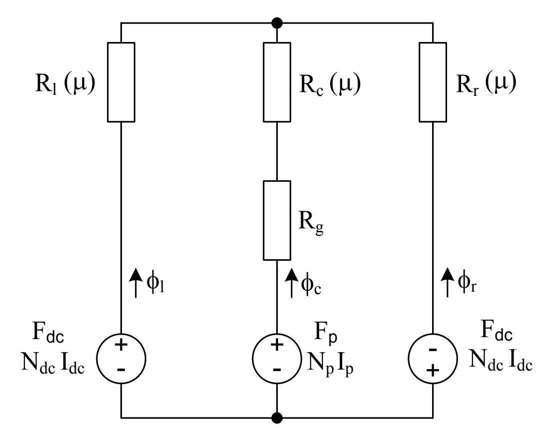

Fig. 2. Reluctance equivalent circuit of the VI shown in Fig. 1.

III. Basic Elements of the Reluctance Equivalent Circuit

The basic elements of a reluctance equivalent circuit are three: (i) constant reluctances, which model an air gap or any other non-ferromagnetic material used in the core structure; (ii) variable reluctances, used to model the non-linear behavior of the magnetic material of the core, and (iii) windings, which model the interaction between the electric and magnetic quantities involved in the behavior of any magnetic device. Once these elements are independently modelled for computer simulation, they can be used to implement any magnetic structure model, disregarding its complexity.

A. *Constant Reluctance Model*

A constant reluctance is used to model the behavior of a non-ferromagnetic section of the magnetic device. In the reluctance equivalent circuit, a constant reluctance is modelled by a resistor, whose value is defined as shown in (1).

$$\Re_0 = \frac{l_0}{\mu_0 \, A_0 \nu}, \qquad (1)$$

where l_0, A_0 are the length and section of the constant reluctance element, $\mu_0 = 4\pi 10^{-7}\, H/m$ is the permeability of free space, and ν is the fringing coefficient, which is equal to 1 when the fringing effect is disregarded. However, a value slightly higher than 1 will usually render a better accuracy. Note that reluctance units are H^{-1}.

B. *Variable Reluctance Model*

A variable reluctance models the non-linear behavior of the magnetic material employed in the device. It can be expressed as shown in (2):

$$\Re_m(\mu) = \frac{l_m}{\mu(B) A_m}, \qquad (2)$$

where l_m, A_m are the length and section of the variable reluctance element, and $\mu(B)$ is the absolute magnetic permeability of the material, expressed as a function of the magnetic flux density B.

As can be seen in (2), in this type of element the reluctance is a function of the magnetic permeability of the material, which in turn depends on the dc operating point within the material $B-H$ curve. Therefore, at this point it is necessary to find a model for the $B-H$ characteristic of the magnetic material, from which the permeability can be obtained.

In this work, after testing other possibilities, the Brauer's model of the $B-H$ curve has been selected [24][25]. This model defines the relationship between the magnetic field intensity H and the magnetic flux density B, by expressing H as a function of B as shown in (3).

$$H(B) = \left(k_1 e^{k_2 B^2} + k_3\right) B, \qquad (3)$$

where k_1, k_2 and k_3 are the Brauer's model constants for each magnetic material.

For the sake of simplicity, in this first work the hysteresis effect is being neglected. Also, it must be noted that (3) gives the $B-H$ relationship only in the first quadrant. It must be extended to the third quadrant taking into account that the curve is symmetrical with respect to the origin of coordinates. This is very easily done in SPICE using the built-in function "*if*".

From (3) it is very simple to obtain by differentiation the differential permeability of the magnetic material. The result is given in a closed form by (4). Also, note that (4) is valid for positive and negative values of B, because the $B-\mu$ curve is symmetrical with respect to the vertical axis.

$$\mu(B) = \left[k_1 (1 + 2k_2 B^2) e^{k_2 B^2} + k_3\right]^{-1}. \qquad (4)$$

As an example, which will also be used to test the proposed model against experimental measurements, the N87 material from TDK-EPCOS has been modelled [26]. The Brauer's model coefficients were derived from the graphical information given by the manurfacturer's datasheet [26], obtaining the $B-H$ curve data points and using a mathematical software for curve-fitting. The resulting values are shown in Table I. Fig. 3 shows a comparison between manufacturer's datasheet information and Brauer's model, both for N87 material at 25 ºC. With this approximation, the maximum error was obtained at $B = 0.3\, T$ and was calculated as 26%.

TABLE I. Brauer's Coefficients for N87 Material at 25ºC

Parameter	Value
k_1	$0.062\ Am^{-1}T^{-1}$
k_2	$42.995\ T^{-2}$
k_3	$302.904\ Am^{-1}T^{-1}$

Fig. 4 shows the implementation of the variable reluctance component in SPICE, particularly in LTspice, which is the software that has been selected in this work [27]. As can be seen in Fig. 4, a behavioral voltage source E_m is used to implement a resistive behavior that models the variable reluctance. The behavioral current source G_{mb} generates a current equal to the flux density in the magnetic element, which is transformed into a voltage at node B_m. The behavioral current source G_{mu} generates a current equal to the actual permeability of the magnetic material by implementing (4). Finally, the voltage at node u_m is used in the expression of E_m to define the component reluctance by using (2).

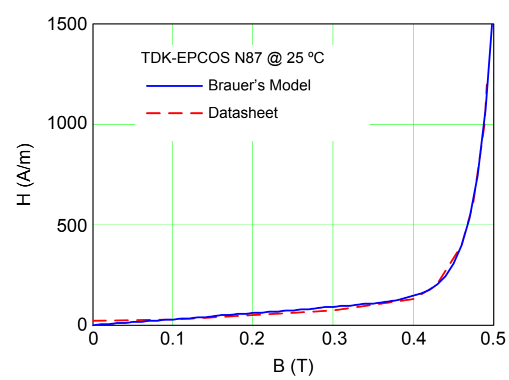

Fig. 3. B-H curve of N87 material at 25 ºC. Comparison between datasheet information and Brauer's model.

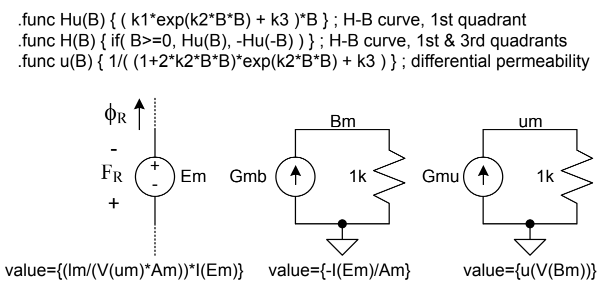

Fig. 4. Implementation of a variable reluctance in LTspice.

C. Winding Model

A winding model must represent the electrical and magnetic interaction within the magnetic device structure. Neglecting losses, the winding model can be expressed by (5) and (6):

$$\mathcal{F}_w(t) = N_w \cdot i_w(t), \tag{5}$$

$$v_w(t) = N_w \cdot \frac{d\emptyset_w(t)}{dt} = N_w A_w \frac{dB_w(t)}{dt}, \tag{6}$$

where $\mathcal{F}_w$ is the magnetomotive force (MMF) created by the winding inside the magnetic core, N_w is the winding number of turns, v_w and i_w are the winding voltage and current, $\emptyset_w$ and B_w are the magnetic flux and magnetic flux density in the core respectively, and A_w is the area of the core.

Fig. 5 shows the SPICE implementation of the winding model. A voltage dependent voltage source EV_w is used to implement the relationship between voltage and flux as given by (6). The behavioral voltage source EF_w is employed in the magnetic part of the model to generate the corresponding MMF according to (5). The behavioral current source GV_w generates a current equal to the magnetic flux, which is time derived using the inductance L_w with a value equal to the number of turns of the winding (N_w) so that (6) can be implemented. The 1 mΩ resistance placed in series with GV_w is used to avoid convergence issues during simulation.

IV. Implementation of the Variable Inductor Model

By using the three basic elements presented in previous section, the reluctance equivalent circuit of any magnetic structure can be implemented for SPICE simulation. In this section, a model developed for the VI shown in Fig. 1 will be presented. This particular VI has been used in a previous work for the controlling of the output voltage in dc-dc resonant converters [17].

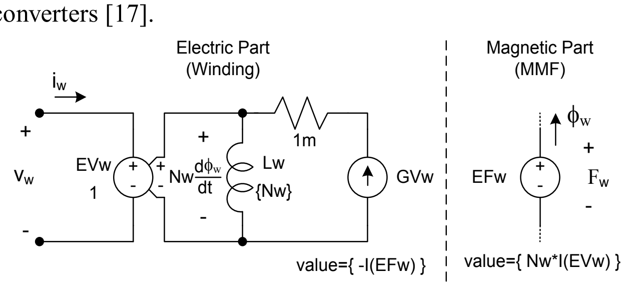

Fig. 5. A winding model implemented in LTspice.

Fig. 6 illustrates the dimensions of the EFD25 core used to calculate average lengths and sections of the magnetic paths. Table I gathers the values of all the parameters related to the VI under study.

Fig. 7 illustrates the complete electrical diagram of the VI implemented in LTspice. As can be seen, it is divided in two main parts: magnetic and electric.

The magnetic part includes the reluctance model, where the variable reluctances R_l, R_c and R_r of Fig. 2 are implemented through the voltage sources E_5, E_3 and E_4 respectively. The magnetic flux density and permeability on each arm are calculated by current sources G_5, G_3 (central arm), G_8, G_6 (right arm) and G_{11}, G_9 (left arm). Reluctances R_{sl}, R_{sc} and R_{sr} are used to measure the flux on each arm and avoid voltage-loop issues during simulation. Their value of 1 H^{-1} is very small compared to the other series reluctances and therefore have no effect on the structure. Voltage source E_1 implements the magnetic part of the main winding of the VI, while voltage sources E_7 and E_6 implement the magnetic part of the left and right auxiliary windings respectively.

The electric part of the model includes the implementation of the electric part of the three windings of the VI. Thus, sources E_2, G_1 and L_1 implement the behavior of the main winding, E_8, G_{12} and L_2 correspond to the right auxiliary winding and E_9, G_{13} and L_3 to the left auxiliary winding. Note that some additional small value resistors $(R_3, R_6, R_7, R_8, R_{13})$ are required to avoid voltage-loop and convergence issues.

The circuit shown in Fig. 7 can be employed to perform a dc transient simulation. Thus, the main winding is supplied with a 1 V dc voltage source with a 10 Ω series resistance. Auxiliary windings are supplied by using a dc current source with an output impedance of 100 kΩ. An important point that must be highlighted is that the auxiliary windings must be supplied with a dc source with a high output impedance, just as it is done in a real application. In this way, any interaction of the auxiliary source on the VI will be avoided.

The behavioral current source G_2 is used to calculate the inductance of the main winding by multiplying the flux of the main winding by its number of turns and dividing by its current.

The dc operating point simulation (.dc directive in SPICE) of the circuit shown in Fig. 7 will provide the steady state values of all magnetic and electric variables of the VI, including the inductance value, given as a voltage at node L_SPICE.

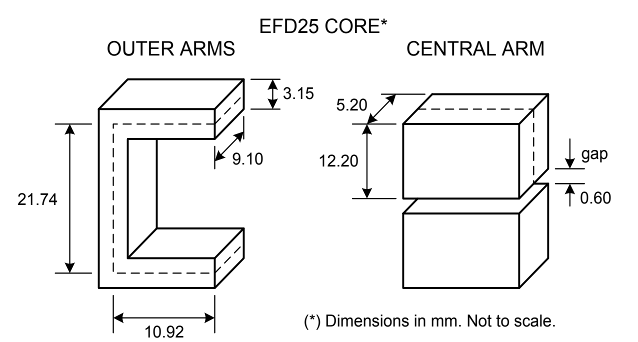

Fig. 6. EFD25 core dimensions.

TABLE II. VARIABLE INDUCTOR DATA

Core material	N87 TDK-EPCOS	**Air gap length**	0.6 mm
Core type	EFD25	**Estimated fringing factor (ν)**	1.06
Expected inductance range	1.2 µH – 4.5 µH	**Central arm average length (lc)**	24.4 mm
Main winding turns (N_p)	6	**Central arm section (A_c)**	59.3 mm^2
Intended operation regime	Sinusoidal, 500 kHz	**Outer arms average length (l_1)**	43.6 mm
Main winding peak current	6.0 A	**Outer arms section (A_1)**	28.7 mm^2
Bias windings turns (N_{dc})	65		

V. SIMULATION AND EXPERIMENTAL RESULTS

The first simulation carried out was a dc operating point using the circuit shown in Fig. 7, in which a small current of 0.1 A is injected to the main winding in steady state, while the auxiliary windings carry a dc current of 0.3 A. Fig. 7 itself shows the simulation results by means of the voltage labels on each relevant node. As can be seen, the resulting inductance value is 2.04 µH (voltage at node L_SPICE). The magnetic flux density at central, right and left arms is obtained as voltage at nodes B_c, B_r and B_l, giving 572.7 µT, 327.8 mT and -328.9 mT, respectively. Therefore, the central arm is operating with almost zero flux density (origin of the $B-H$ curve), while the right and left arms are operated at a given dc flux density level owing to their biasing by the auxiliary windings. The small difference of flux density between them is due to the small flux level (0.57 mT) generated by the main winding, which adds to the left arm, while subtracts to the right arm.

The magnetic permeability of central, right and left arms is obtained as voltages at nodes u_c, u_r and u_l, respectively. The resulting values are 3.29 mH/m, 745.8 µH/m and 723.0 µH/m, for central, right and left arms respectively. As expected, the permeability of the central arm is higher because of the lower flux density; the material of the central arm is operated around the origin of the $B-H$ curve. On the other hand, the permeability of right and left arms is much lower, because they operate at a much higher flux density level, around the knee of the $B-H$ curve.

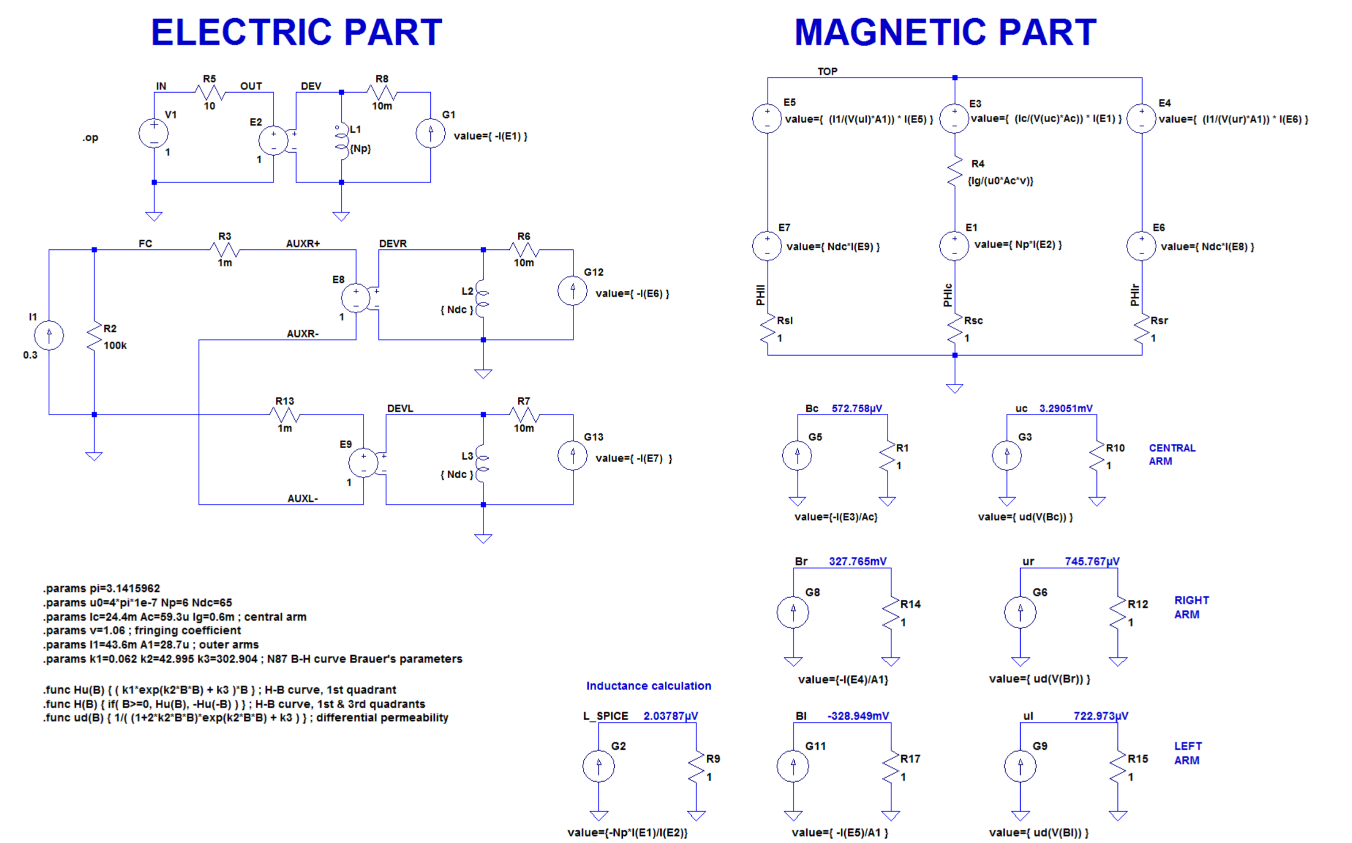

Fig. 7. Complete electrical model of the VI implemented in LTspice.

The above-presented simulation under dc operation is also intended to obtain the small-signal value of the VI inductance with very fast simulations. This can be done by performing a dc sweep analysis over the dc bias current source, shown as I_1 in Fig. 7. Thus, Fig. 8 shows the simulation results in comparison with the experimental results obtained at the laboratory by using an impedance analyzer under small signal measurement of the inductance at a frequency of 1 kHz. Experimental results were added into the simulation for the sake of comparison by using a voltage controlled source with a look-up table (not shown in Fig. 7). Relative errors of -11% at 0.125 A bias current and +25% at 0.45 A bias current can be measured.

The difference between simulation and experimental results can be justified by two causes: (i) tolerances during the magnetic material fabrication, producing that the actual material $B-H$ curve is not exactly the same as that given in the manufacturer's datasheet, and (ii) the error in the approximation of the $B-H$ curve by the selected equation, in this case the Brauer's model.

As an example, Fig. 9 shows the waveforms obtained from the same circuit shown in Fig. 7 when a transient simulation is performed. The inductor voltage and current, and the induction inside the 3 arms of the structure are shown in this figure. As can be seen, it takes some time to the induction in right and left arms to reach their steady-state values, $50\,ns$ approximately. This time is related to the dynamic response of the VI model. In the proposed model this time is affected by the output resistance of the current source that supplies the auxiliary winding. In the example under study, an output resistance of $100\,k\Omega$ has been selected in order to have a dynamic response fast enough so that it can be used up to frequencies of several hundred of kHz. Nevertheless, this is a point that requires further investigation. The VI should be dynamically modelled, theoretically or experimentally, and the time constant should be adjusted according to the obtained results.

Fig. 10 illustrates the electrical diagram used for the simulation of a dc-ac converter with VI control. The converter has an input voltage of 20 V, applying a 10 V peak voltage square waveform to the $L-R$ circuit. The switches are operated at 500 kHz with 200 ns dead time. The load resistance is 11 Ω. In the following, simulation and experimental results corresponding to this circuit are presented.

Fig. 11 shows the simulation and experimental results corresponding to the square wave voltage and the output voltage across the load resistance for a VI bias current of 0.25 A. Fig. 12 illustrates the voltage across the VI and the output voltage for the same value of the VI bias current. As can be seen, simulation and experimental results match well.

Fig. 13 shows the simulation and experimental results corresponding to the VI bias windings. As can be seen, bias windings reflect voltages with peak values around 100 V. Also, a small difference can be seen comparing the voltages of left and right bias windings. As commented before, this difference is due to the non-linear behavior of the magnetic material around the knee of the $B-H$ curve. However, the difference is higher in the simulation than in the experiments. This disagreement could be due to the response of the oscilloscope probe, which could not be able to follow so high a dv/dt. Also, the high voltage ripple superposed to the experimental waveform does not appear in the simulation. This ripple could also appear due to the effect of the oscilloscope voltage probe or other parasitic elements not considered by the model. The voltage probe used in these measurements was a differential voltage probe model 700924 from Yokowaga with 1:100 attenuation selected.

Fig. 14 shows the simulation results from the circuit in Fig. 10 corresponding to the instantaneous flux density in left, right and center arms of the structure, and also to the instantaneous inductance of the VI. All of them obtained from the corresponding nodes in the model. VI bias current is 0.25 A. Experimental results are not available for this variables due to the difficulty of measuring dc levels of flux density inside a magnetic material. Nevertheless, the simulation results are in accordance with the expected ones.

Finally, in order to test the possibility of controlling the output voltage by means of the bias current on the VI, Fig. 15 presents the simulation and experimental results of the rms voltage in the load resistance of the circuit in Fig. 10 when varying the dc bias current of the VI. As can be seen, simulation and experimental results exhibit a similar curve. Again, the difference between simulation and experiments can be justified by the error in the modeling of the magnetic material $B-H$ curve.

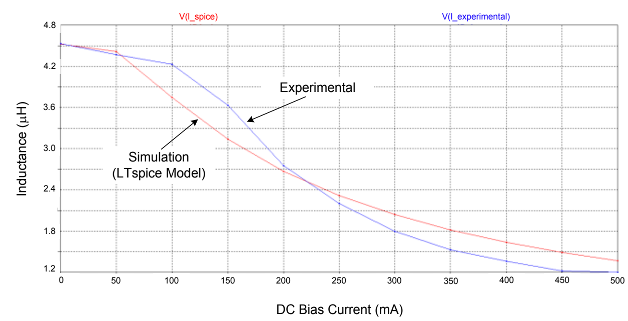

Fig. 8. Small-signal inductance of the VI. Comparison between simulation and experimental results.

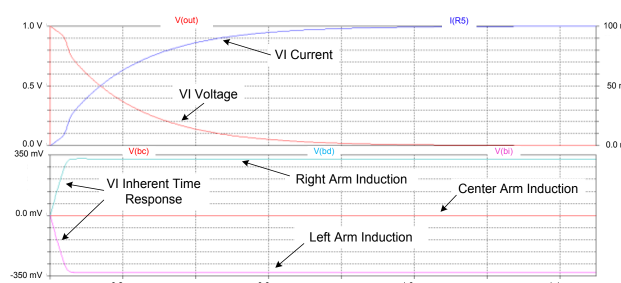

Fig. 9. Simulations results of the VI model under a dc start-up transient.

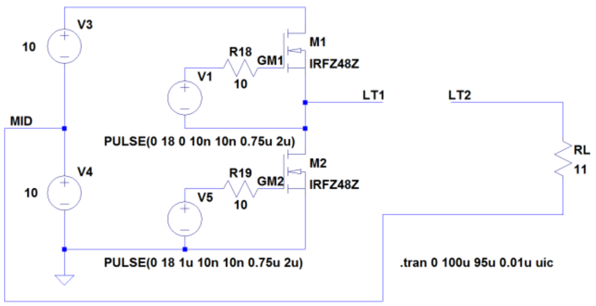

Fig. 10. Electric diagram for the simulation of an L-R inverter with variable inductor. The variable inductor is placed across terminals LT1 and LT2 according to the schematic shown in Fig. 7.

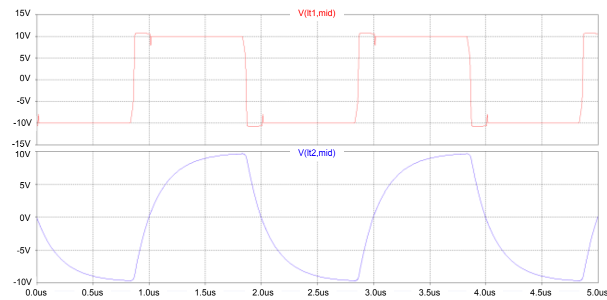

(a)

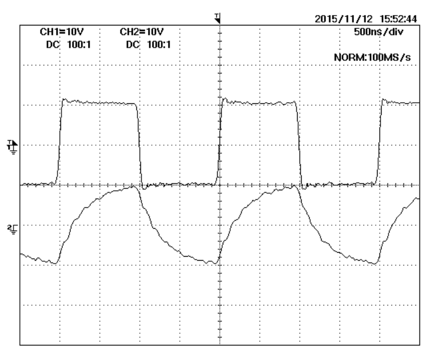

(b) 10 V/div, 500 ns/div

Fig. 11. Square voltage (top) and output voltage (bottom) of the circuit shown in Fig. 10: (a) simulation, (b) experimental. VI bias current 0.25 A.

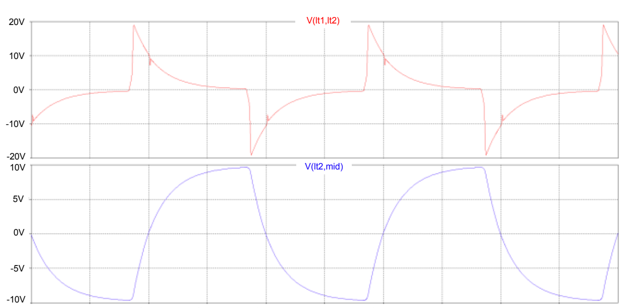

(a)

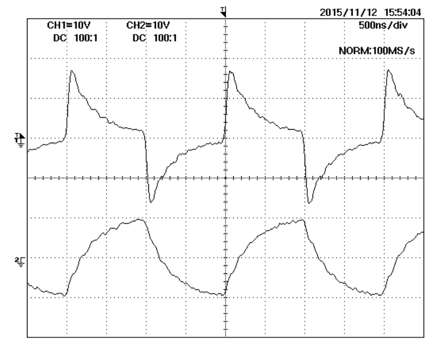

(b) 10 V/div, 500 ns/div

Fig. 12. VI voltage (top) and output voltage (bottom) of the circuit shown in Fig. 10: (a) simulation, (b) experimental. VI bias current 0.25 A.

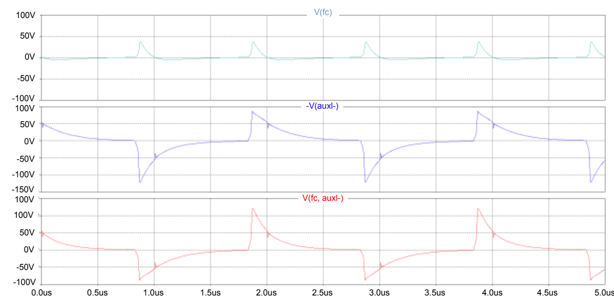

(a)

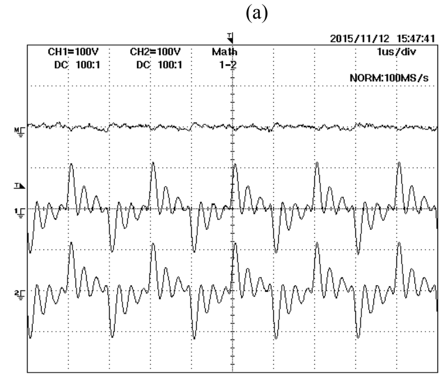

(b) 100 V/div, 500 ns/div

Fig. 13. Top: total voltage across VI bias windings. Middle: voltage across left bias winding. Bottom: voltage across right bias winding. All of them corresponding to the circuit shown in Fig. 10. (a) simulation, (b) experimental. VI bias current 0.25 A.

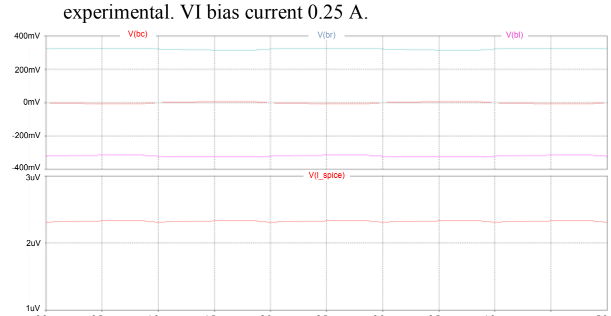

Fig. 14. Simulation results of the circuit in Fig. 10 with VI bias current of 0.25 A. Top: flux density in each VI arm. Right arm (top), center arm (middle) and left arm (bot.). Scales: 200 mT/div. 500 ns/div. Bottom: inductance of the VI as obtained from the model. Scales: 1 µH/div, 500 ns/div.

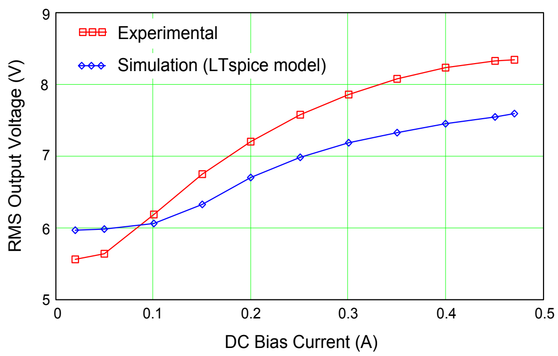

Fig. 15. Comparison between experimental and simulation results. RMS output voltage as a function of VI dc bias current for the converter shown in Fig. 10.

VI. CONCLUSIONS

This paper has presented a modeling technique for magnetic devices based on SPICE behavioral modeling. The three basic elements required for developing a reluctance-based equivalent circuit have been implemented in SPICE. These elements can easily be integrated in a SPICE library in order to simplify its use in circuit simulation. It has been explained how by using these three elements any magnetic structure can be modeled and simulated providing magnetic, electric and inductance results. Besides, the proposed modeling technique can be used under any operating conditions with good accuracy, because the non-linear behavior of the magnetic material is taken into consideration. A modeling example of a VI with an EE structure has been presented and simulated, showing good approximation with experimental results. Simulation and experimental results for a VI-controlled dc-ac inverter have also been presented. The comparison between simulated and experimental results rendered good expectancies for the proposed modeling methodology.

APPENDIX I

LTspice models presented in this work are available to interested readers at the web site indicated below. See resources section. www.unioviedo.net/ate/marcosaa/

REFERENCES

[1] Kislovski, A. S.; "Quasi-linear controllable inductor," Proc. of the IEEE, Vol. 75, No. 2, Feb. 1987, pp. 267-269.

[2] Kislovski, A. S.; "Linear variable inductor in dc current sensors utilized in telecom solar battery chargers," Proc. on International Telecom. Energy Conf., 1989, pp. 1-3.

[3] Kislovski, A. S.; "Linear variable inductor (LVI) in single-phase off-line telecom rectifiers," Proc. of IEEE Int. Telecom. Energ. Conf. (INTELEC), 1995, pp. 93-98.

[4] Birx, Daniel L., and Louis L. Reginato; "Saturable inductor and transformer structures for magnetic pulse compression." U.S. Patent No. 4,928,020. 22 May 1990.

[5] Medini, D., Ben-Yaakov S.; "A current-controlled variable-inductor for high frequency resonant power circuits," Applied Power Electronics Conference and Exposition, pp. 219-225, vol. 1, 13-17 Feb. 1994.

[6] Wölfle, Werner Hugo, and William Gerard Hurley; "Quasi-active power factor correction with a variable inductive filter: theory, design and practice." Power Electronics, IEEE Transactions on 18.1 (2003): 248-255.

[7] Alonso, J. M.; Dalla Costa, M. A.; Cardesín, J.; Garcia, J.; "Magnetic dimming of electronic ballasts", Electronic Letters, vol. 41, nº 12, June 2005.

[8] Perdigão, M. S.; Alonso, J. M.; Vaquero, D.G.; Saraiva, E. S.; "Magnetically Controlled Electronic Ballasts With Isolated Output: The Variable Transformer Solution," Industrial Electronics, IEEE Transactions on , vol. 58, no. 9, pp. 4117-4129, Sept. 2011.

[9] Hamill, D.C.; "Gyrator-capacitor modeling: a better way of understanding magnetic components," Applied Power Electronics Conference and Exposition, vol. 1, pp.326-332, 1994.

[10] Rozanov, E.; Ben-Yaakov, S.; "Analysis of current-controlled inductors by new SPICE behavioral model," HAIT Journal of Sc. and Eng. B, Vol. 2, Iss. 3-4, pp. 558-570, 2005.

[11] Ngo, K.D.T.; "Subcircuit modeling of magnetic cores with hysteresis in PSpice," Aerospace and Electronic Systems, IEEE Transactions on , vol. 38, no. 4, pp. 1425-1434, Oct. 2002.

[12] Perdigao, M.S.; Alonso, J.M.; Dalla Costa, M.A.; Saraiva, E.S.; "A variable inductor MATLAB/Simulink behavioral model for application in magnetically-controlled electronic ballasts," Power Electronics, Electrical Drives, Automation and Motion, International Symposium on, pp. 349-354, 11-13 June 2008.

[13] Perdigao, M. S.; "Research and Development on New Control Techniques for Electronic Ballasts based on Magnetic Regulators," Ph. D. dissertation, University of Coimbra, 2011.

[14] "Tutorial on How to Define the Saturable Core Element." PSIM Software. Powersim Inc. July 2006.

[15] Alonso, J. M.; Dalla Costa, M. A.; Rico-Secades, M.; Cardesín, J.; Garcia, J.; "Investigation of a New Control Strategy for Electronic Ballasts Based on Variable Inductor", IEEE Trans. on Industrial Electronics, Vol. 55, Nº 1, pp. 3-10, January 2008.

[16] Alonso, J. M.; Perdigao, M. S.; Gacio, D.; Campa, L.; Saraiva, E.S.; "Magnetic control of DC-DC resonant converters provides constant frequency operation," Electronics Letters , vol. 46, no. 6, pp. 440-442, March 18, 2010.

[17] Alonso, J.M.; Perdigão, M.S.; Vaquero, D.G.; Calleja, A.J.; Saraiva, E.S.; "Analysis, Design, and Experimentation on Constant-Frequency DC-DC Resonant Converters With Magnetic Control," Power Electronics, IEEE Transactions on , vol. 27, no. 3, pp. 1369-1382, March 2012.

[18] Perdigao, M.S.; Alonso, J.M.; Dalla Costa, M.A.; Saraiva, E.S.; "Comparative Analysis and Experiments of Resonant Tanks for Magnetically Controlled Electronic Ballasts," Industrial Electronics, IEEE Transactions on, vol.55, no.9, pp. 3201-3211, Sept. 2008.

[19] Perdigao, M.S.; Trovao, J.P.F.; Alonso, J.M.; Saraiva, E.S.; "Large-Signal Characterization of Power Inductors in EV Bidirectional DC–DC Converters Focused on Core Size Optimization," Industrial Electronics, IEEE Transactions on , vol.62, no.5, pp.3042-3051, May 2015.

[20] Perdigao, M.S.; Alonso, J.M.; Saraiva, E.S.; "Magnetically-controlled dimming technique with isolated output," Electronics Letters, vol. 45, no. 14, pp. 756-758, July 2009.

[21] Perdigao, M.S.; Alonso, J.M.; Dalla Costa, M.A.; Saraiva, E.S.; "Using Magnetic Regulators for the Optimization of Universal Ballasts," Power Electronics, IEEE Transactions on , vol.23, no.6, pp. 3126-3134, Nov. 2008.

[22] Perdigao, M.S.; Menke, M.; Seidel, A.R.; Pinto, R.A.; Alonso, J.M.; "A review on variable inductors and variable transformers: Applications to lighting drivers," IEEE Trans. on Industry Applications, Jan. 2016.

[23] Pinto, R.A.; Alonso, J.M.; Perdigao, M.S.; da Silva, M.F.; do Prado, R.N., "A new technique to equalize branch currents in multiarray LED lamps based on variable inductor," Industry Applications Society Annual Meeting, IEEE , pp. 1-9, 5-9 Oct. 2014.

[24] Brauer, John R.; "Simple equations for the magnetization and reluctivity curves of steel," Magnetics, IEEE Transactions on, vol.11, no.1, pp.81,81, Jan 1975.

[25] Hülsmann, T.; "Nonlinear Material Curve Modeling and Sensitivity Analysis for MQS-Problems," Master Thesis, Faculty of Electrical, Information and Media Engineering, Bergische Universitat Wuppertal, 2012.

[26] "Ferrite Cores and Accessories", Datasheet, EPCOS, September 2006.

[27] "LTspice IV. Getting Started Guide," Linear Technology, 2011.

Analysis and Experiments on a Single-Inductor Half-Bridge LED Driver With Magnetic Control

José Marcos Alonso, *Senior Member, IEEE*, Marina S. Perdigão, *Member, IEEE*, Marco A. Dalla Costa, *Member, IEEE*, Gilberto Martínez, and René Osorio

***Abstract*—This paper presents the analysis and experiments of a variable inductor (VI) based LED driver for dc grid lighting applications. The proposed driver requires only a series inductor and a transformer as major components to drive the LED lamp from a half-bridge inverter. By introducing a VI as the series inductor, the LED current can be controlled independently from any other parameter, which makes it possible to drive and regulate several LED branches from the same half-bridge output. Other advantages of the proposed converter include inherent open-circuit and short-circuit protections, zero-voltage switching for the bridge transistor and zero-current switching for the output rectifier diodes, simple dynamics, possibility of analog and pulse width modulation dimming, constant switching frequency operation, and high efficiency. The converter is thoroughly analyzed and modeled for both steady-state and dynamic operation. As another novelty of this paper, the dynamic response of the VI has been studied and taken into account to obtain the complete transfer function of the VI-controlled system. In addition, some housekeeping issues that usually arise when dealing with VI, e.g., how to drive the VI bias winding, are solved in this work. Experimental results provided from a 50 W laboratory prototype demonstrate the correctness of the performed analysis and the good possibilities of the proposed converter.**

***Index Terms*—Closed-loop operation, dc grid, dynamic response, LED driver, single inductor converter, variable inductor (VI).**

I. Introduction

WITH the exponential increase of electronic equipment in homes, offices, and buildings, dc power distribution is gaining more and more attention in the present time. The use of a dc grid makes it possible to simplify the power converters used to supply equipment such as computers, TVs, cameras, cell phone battery chargers, and many others, whose number is rapidly increasing, especially under the new Internet of Things trend [1]–[3]. Besides, dc power distribution allows the converters to get rid of the ac–dc conversion stage and also of the electrolytic capacitors required to cope with the ac–dc power unbalance. Therefore, efficiency and reliability are simultaneously improved. These advantages are especially significant in lighting systems and particularly with today's highly efficient highly reliable LED-based lighting technology. In this context, the search for new LED driver topologies specifically developed for dc applications is a relevant field of research.

Most of the works available in the literature agree that the future dc grid for homes, offices, and building applications will be deployed on two voltage levels: 1) a high-voltage level of 380 V, with a 360–400 V range to allow for system regulation, which will be used for high power loads such as main lighting, heating, air conditioning, washing machines, dishwashers, etc.; and 2) a safer low-voltage level of 48 V, to supply low power equipment that operate closer to the end user, such as cell phone battery chargers, side table lights, personal computers and tablets, etc.

In the literature, it is possible to find many works dealing with ac–dc LED drivers, providing power factor correction (PFC), avoiding the use of electrolytic capacitors, improving dimming characteristics, etc. [4]–[16]. However, few proposals can be found related to dc-operated LED drivers aiming for the new dc power distribution. Some of the works that can be found are intended to be used as second or third stage after PFC and conditioning stages [17]–[24].

The goal of this work is to propose a topology for LED driving specifically developed for the future dc grid deployment. The topology will be investigated in order to obtain its static and dynamic behavior, which can be used not only to design the closed loop operation of the converter, but also to investigate its interaction within the dc grid. While the former is of great importance for the operation of the LED driver itself, the latter is essential for the design of the dc bus control strategy [3].

This paper is an improved version of the conference paper presented in [31], which includes several corrections and additional information. In Section II, the proposed LED driver topology is introduced, highlighting its most relevant features and characteristics. Section III presents the static analysis of the converter, which can be used in the design of the LED driver. Section IV deals with the dynamic analysis of the converter, in which the most relevant transfer function for closed loop operation and dc

Manuscript received September 28, 2016; revised November 29, 2016; accepted January 3, 2017. Date of publication January 16, 2017; date of current version August 2, 2017. This work was supported by the Spain National Government and the Asturias Regional Government under Grants ENE2013-41491-R and GRUPIN14-076, respectively. Recommended for publication by Associate Editor M. Ponce-Silva.

J. M. Alonso and G. Martínez are with the Electrical Engineering Department, University of Oviedo, Gijón 33204, Spain (e-mail: marcos@uniovi.es; gilbertomar9@hotmail.com).

M. S. Perdigão is with the Instituto de Telecomunicações, Department of Electrical and Computer Engineering, University of Coimbra, Coimbra 3000-370, Portugal, and also with IPC, Department of Electrical Engineering, Instituto Superior de Engenharia de Coimbra, Coimbra 3030-199, Portugal (e-mail: perdigao@isec.pt).

M. A. Dalla Costa is with the Federal University of Santa Maria, Group of Intelligence in Lighting, Santa Maria 97105-900, Brazil (e-mail: marcodc@gedre.ufsm.br).

R. Osorio is with the Computer Science and Engineering Department, University of Guadalajara, Ameca 46600, México (e-mail: reneosorios@yahoo.com).

Color versions of one or more of the figures in this paper are available online at http://ieeexplore.ieee.org.

Digital Object Identifier 10.1109/TPEL.2017.2651955

0885-8993 © 2017 IEEE. Personal use is permitted, but republication/redistribution requires IEEE permission.
See http://www.ieee.org/publications_standards/publications/rights/index.html for more information.

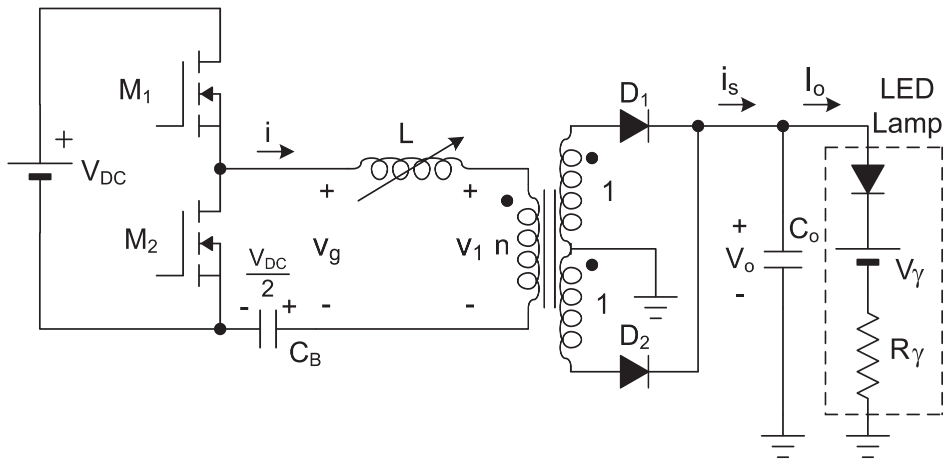

Fig. 1. Proposed LED driver for application in dc grids.

grid interaction will be derived. Section V illustrates a design example for a 50-W 380-V operated LED driver, which can be applied in multi-array lamps. Section VI presents experimental results from the laboratory prototype. Finally, Section VII summarizes the conclusions of the work.

II. Proposed DC-Grid LED Driver

Fig. 1 shows the electric diagram of the proposed LED driver for dc grid applications. A half-bridge inverter followed by a dc blocking capacitor (C_B) is used to generate a symmetrical square voltage waveform (v_g) with an amplitude of $V_{\rm dc}/2$ and a frequency f_s, where $V_{\rm dc}$ is the dc grid voltage and f_s is the switching frequency of the half-bridge transistors. A series inductance L is used to limit the current through the LED lamp. The latter is supplied through an isolating transformer, a full wave rectifier, and a filter capacitor C_o, so that the current through the lamp is continuous, with a small superposed ripple at $2f_s$. In order to provide output current regulation against input and load changes, a variable inductance (VI) is proposed to control the power delivered to the load [25]–[26].

One of the advantages of the proposed driver is that it can be used to supply several LED lamp arrays with an independent regulation of the current through each LED lamp, as illustrated in Fig. 2, where VI L_i controls the current through LED lamp $\#i$. As shown in Fig. 2, it is preferred to connect the second arrangement on the top side of the half-bridge inverter, instead of in parallel with the first arrangement. In this way, the current supplied from the dc bus will not present a dead time, thus requiring a smaller electromagnetic interference (EMI) filter. The structure can be replicated to accommodate any number of LED arrays.

The advantages of the proposed LED driver can be summarized as follows:

1) Ability to supply multiple LED arrays with independent current control to provide current equalization.
2) Ability to include galvanic isolation. However, the transformer could be avoided if galvanic isolation is not required. In this case, the transformer and rectifier can be replaced by a 4-diode full bridge rectifier.
3) Low switching losses owing to zero-voltage switching (ZVS) operation in the half-bridge switches. With proper dead time selection the switching losses can be kept to a minimum.
4) Zero-current switching (ZCS) of the output rectifier diodes, thus providing negligible turn-OFF losses.
5) Constant switching frequency operation provided by inductance variation control. This feature allows for an easy EMI filter design and minimization.
6) Simple first-order dynamics, allowing for an easy closed loop operation and dc grid interaction.
7) Inherent low LED current compensation against LED operating junction temperature.
8) Inherent short-circuit protection. In the case of an output short-circuit the series inductance limits the half-bridge current to a triangular waveform with a maximum peak value.

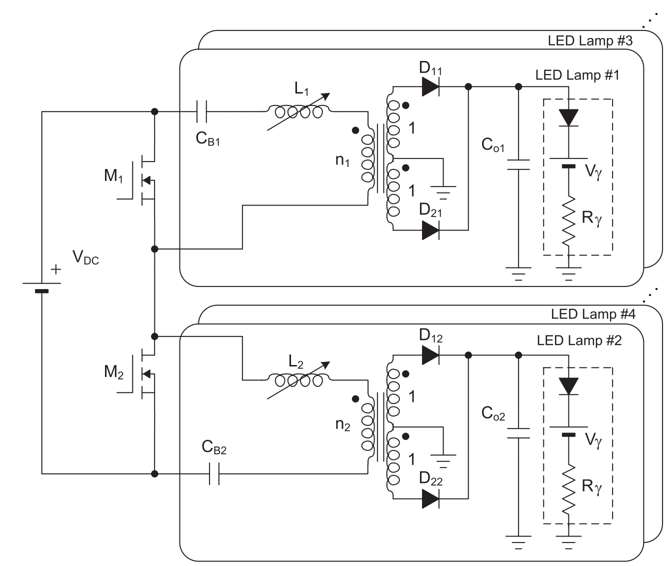

Fig. 2. Proposed driver used to supply several LED arrays.

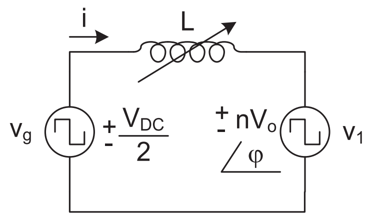

Fig. 3. Equivalent circuit of the proposed LED driver.

9) Inherent open-circuit protection. In an open-circuit situation the current through the series inductor tends to zero.
10) Easy implementation of pulse width modulation (PWM) dimming. This is a consequence of previous features. Since the output can safely be short-circuited or open-circuited, several possibilities are available to implement PWM dimming.
11) Modularity. If the half-bridge inverter is properly designed for high power, which is very easy and low cost goal to achieve, it can be used to supply a large number of modules. Each module could even be independently dimmed or switched ON/OFF by wireless communication and dedicated ICs in high-end smart-lighting applications.

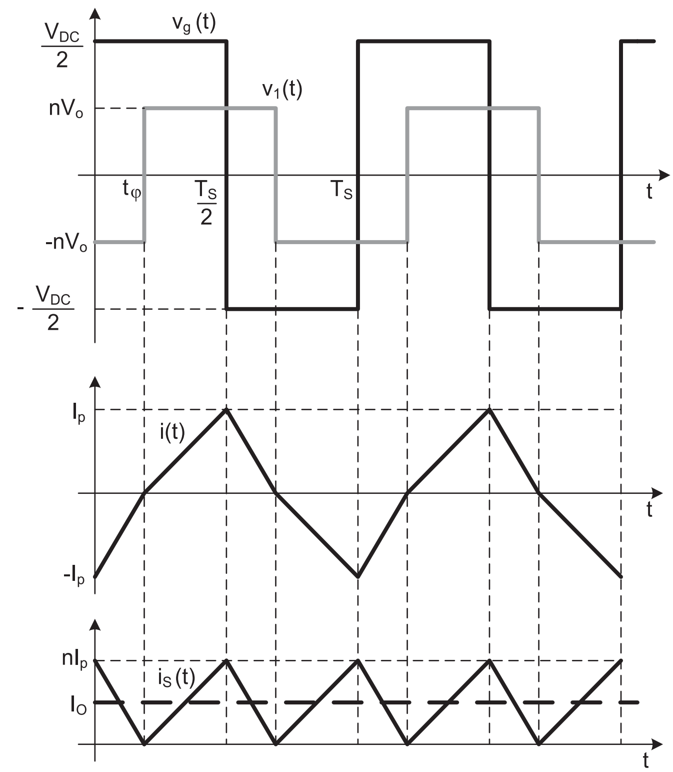

Fig. 4. Main operating waveforms of the proposed LED driver.

III. Static Analysis of the Proposed Converter

A. Basic Analysis of the Converter

Fig. 3 illustrates the equivalent circuit of the proposed LED driver, which can be used to analyze its behavior. The voltage source v_g represents the voltage generated by the half-bridge after removing its dc level by capacitor C_B. The voltage source v_1 represents the voltage at the primary of the transformer, whose amplitude is equal to the dc output voltage V_o times the transformer turns ratio n.

Fig. 4 illustrates the main waveforms of the converter. Because of the effect of the series inductance, the voltage v_1 will lag the input voltage by a phase angle φ, equivalent to a time interval $t_\varphi = \varphi/\omega_s$, where $\omega_s = 2\pi f_s$ is the angular switching frequency. Thus, the inductor current will be delayed by the same angle φ, providing ZVS operation of the bridge transistors, which is an important feature of the proposed converter.

Analyzing the circuit shown in Fig. 3, the evolution of the inductor current during the two time intervals can be expressed as

$$i(t) = -I_p + \frac{0.5V_{\mathrm{dc}} + nV_o}{L}t \qquad t \in [0, t_\varphi], \tag{1}$$

$$i(t) = \frac{0.5V_{\mathrm{dc}} - nV_o}{L}(t - t_\varphi) \qquad t \in [t_\varphi,\, T_s/2] \tag{2}$$

where T_s denotes the switching period ($T_s = 1/f_s$).

In steady-state operation, the following condition must be reached:

$$i(T_s/2) = -i(0). \tag{3}$$

By using condition (3) in (1) and (2), the values of the peak current I_p and time delay t_φ are obtained, respectively, as

$$I_p = \frac{V_{\mathrm{dc}}^2 - 4n^2V_o^2}{8V_{\mathrm{dc}}Lf_s}, \tag{4}$$

$$t_\varphi = \frac{0.5V_{\mathrm{dc}} - nV_o}{2V_{\mathrm{dc}}f_s}. \tag{5}$$

The average current through the LED lamp I_o can be calculated as the average value of the rectified inductor current transformed to the secondary side, this is

$$I_o = \frac{2}{T_s}\int_0^{T_s/2} n \cdot |i(t)|\, dt = \frac{nI_p}{2} \tag{6}$$

$$I_o = \frac{nV_{\mathrm{dc}}^2 - 4n^3V_o^2}{16V_{\mathrm{dc}}Lf_s}. \tag{7}$$

Now, taking into account the following relationship between voltage and current in the LED:

$$V_o = V_\gamma + R_\gamma I_o \tag{8}$$

where V_γ and R_γ are the threshold voltage and dynamic resistance of the LED array, respectively, using (8) in (7) and solving for the LED current, the following expression can be obtained:

$$I_o = -\frac{V_\gamma}{R_\gamma} - \frac{2V_{\mathrm{dc}}Lf_s}{n^3R_\gamma^2} + \frac{1}{2} \times \sqrt{\left(\frac{4V_{\mathrm{dc}}Lf_s}{n^3R_\gamma^2}\right)^2 + \frac{16V_\gamma V_{\mathrm{dc}}Lf_s}{n^3R_\gamma^3} + \frac{V_{\mathrm{dc}}^2}{n^2R_\gamma^2}}. \tag{9}$$

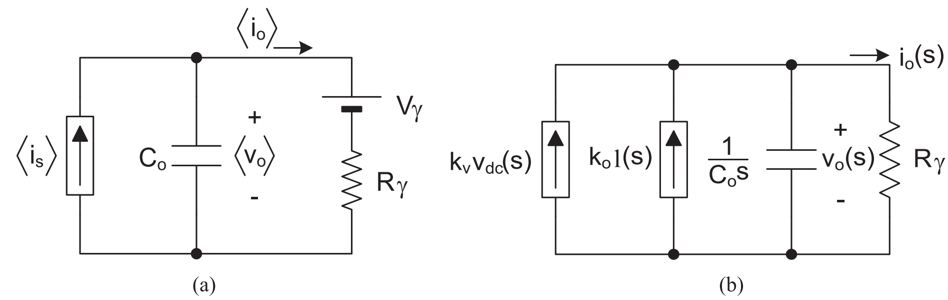

Fig. 5. Equivalent circuits of the proposed LED driver at output terminals: (a) averaged time domain and (b) Laplace domain.

As can be seen, expression (9) is a closed form for the average LED current as a function of all the parameters of the circuit: input voltage, inductance, switching frequency, transformer turn ratio, and LED array parameters. By using this expression, it is possible to design the converter and analyze its operation under different conditions. A design example will be illustrated later.

B. Analysis of Lamp Current Perturbations

At this point, since the LED lamp threshold voltage has a great dependence on the operating junction temperature [27], it is interesting to evaluate how the threshold voltage V_γ will affect the average output current. This can be done by taking a partial derivative in (9)

$$k_\gamma = \frac{\partial I_o}{\partial V_\gamma} = -\frac{1}{R_\gamma} + \frac{4V_{\rm dc}Lf_s}{n^3R_\gamma^3\sqrt{\left(\frac{4V_{\rm dc}Lf_s}{n^3R_\gamma^2}\right)^2 + \frac{16V_\gamma V_{\rm dc}Lf_s}{n^3R_\gamma^3} + \frac{V_{\rm dc}^2}{n^2R_\gamma^2}}} \quad (10)$$

where k_γ is the per-unit change of the output current against LED threshold voltage. Referring to (1) and (2) and Fig. 4, it is easy to understand that when the LED voltage increases, the positive slope of the inductor current will decrease, while its negative slope will increase, thus leading to a lower LED average current and lower power, and reversely. Therefore, the LED power is inherently compensated against changes in LED voltage, which means that small values of k_γ should be expected.

Similarly, the variation of the LED current against perturbations of the dc voltage can be obtained by taking a partial derivative of (7), as follows:

$$k_v = \frac{\partial I_o}{\partial V_{\rm dc}} = \frac{n}{16Lf_s} + \frac{4n^3V_o^2}{16V_{\rm dc}^2Lf_s} \quad (11)$$

where k_v is the per-unit variation of the output current against dc input voltage. As per (11), the changes in the input voltage $V_{\rm dc}$ have the contrary effect on the LED current compared to the LED voltage. This means that the value of k_v will be high, and changes in LED current should be compensated by closed loop operation, which measures the LED current and adjusts the inductance value accordingly.

C. Analysis of Open-Circuit and Short-Circuit Operation

In an open-circuit situation, the current injected to the output capacitance will be equal to zero in steady state. Considering ideal behavior (no losses), the output capacitance C_o will be charged to a voltage level equal to $V_{\rm dc}/2n$; the voltage across the transformer primary $v_1(t)$ will be a square voltage with an amplitude equal to $V_{\rm dc}/2$ and in phase with $v_g(t)$. Thus, no current will circulate through the inductor. The only precaution would be to select an output capacitor with a voltage rating higher than $V_{\rm dc}/2n$.

During a short-circuit on the output, the current through the series inductor will be inherently limited, and so will be the current through the bridge switches. The current through the inductor will be a symmetrical triangular waveform, with a peak value $I_{\rm pcc}$ that, assuming ideal behavior, can be calculated by making null the output voltage in (4), this is

$$I_{\rm pcc} = \frac{V_{\rm dc}}{8Lf_s}\,. \quad (12)$$

IV. Dynamic Analysis of the Proposed Converter

A. Modeling of the Power Stage

The proposed driver can be modeled by the averaged circuit shown in Fig. 5(a). The converter is modeled by a current source, which injects the averaged rectified current i_s into the *RC* network given by the output capacitor and the equivalent circuit of the LED lamp. The equivalent series resistance (ESR) of the output capacitor has been neglected in this case, because usually film capacitors with very low series resistance are employed in LED drivers. Thus, the dynamic effect of the capacitor ESR will be beyond the frequency range of interest.

Using a similar methodology as that presented in [28], the circuit in Fig. 5(a) can be perturbed and represented in the Laplace domain as shown in Fig. 5(b). By analyzing this circuit, the following relationship can be obtained:

$$R_\gamma C_o s\, i_o(s) + i_o(s) = k_v\, v_{\rm dc}(s) + k_{\rm ol}\, l(s) \quad (13)$$

where $l(s)$ and $v_{\rm dc}(s)$ represent the perturbations in the VI inductance and dc bus voltage, respectively, k_v is defined as in (11), and the factor $k_{\rm ol}$ can be calculated by the partial derivative of (7), as follows:

$$k_{\rm ol} = \frac{\partial i_s}{\partial L} = -\frac{I_o}{L}\,. \quad (14)$$

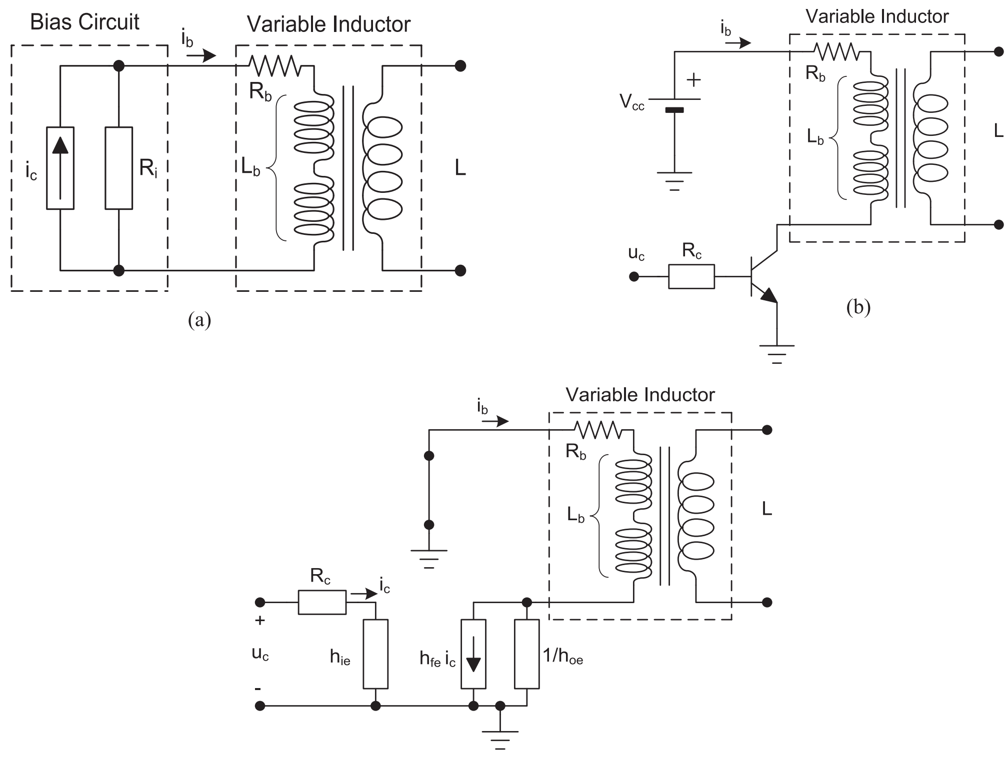

Fig. 6. (a) VI bias circuit, (b) implementation using a bipolar transistor and a low-voltage source, and (c) equivalent circuit for small-signal perturbations.

The corresponding transfer functions can now easily be obtained from (13)

$$G_{\rm ol}(s) = \frac{i_o(s)}{l(s)} = \frac{k_{\rm ol}}{1 + sR_\gamma C_o}, \tag{15}$$

$$G_v(s) = \frac{i_o(s)}{v_{\rm dc}(s)} = \frac{k_v}{1 + sR_\gamma C_o}. \tag{16}$$

B. Modeling of the Variable Inductor

Fig. 6(a) shows the circuit used to provide the bias level to the VI. A current source I_i generates the dc current for the auxiliary windings. R_i represents the output resistance of the current source, R_b is the series resistance of the auxiliary windings, and L_b is the total inductance seen from the auxiliary windings in series connection.

In a VI, the magnitude that modifies the main winding inductance is the dc level of the magnetic flux density introduced by the auxiliary winding inside the magnetic material, namely B_b. A change in B_b will produce a change in the VI inductance. As it will be shown in the following, the auxiliary windings total inductance L_b and resistances R_i and R_b introduce a major time constant in the VI response. Therefore, it is possible to consider an instant response between B_b and VI main inductance, in other words, to neglect the dynamic of the magnetic material itself by assuming that it is much faster than that due to the auxiliary winding components. Following this reasoning, it is easy to analyze the circuit in Fig. 6(a) to obtain the following transfer function between the dc bias current and the VI main inductance:

$$G_{\rm lb}(s) = \frac{l(s)}{i_c(s)} \approx k_l \frac{B_b(s)}{i_c(s)} = k_l \frac{L_b}{N_b A_b} \frac{i_b(s)}{i_c(s)} = \frac{k_{\rm lb}}{1 + s\tau_i}, \tag{17}$$

$$k_{\rm lb} = k_l \frac{R_i}{R_i + R_b} \frac{L_b}{N_b A_b}; \ \tau_i = \frac{L_b}{R_i + R_b} \tag{18}$$

where i_c is the control current of the dc bias circuit, A_b is the effective area of the dc bias magnetic path, and k_l is the dc gain that relates the VI main inductance and the dc magnetic flux density. This gain can be obtained by calculating the slope of the characteristic VI main inductance versus dc magnetic flux density at a given operating point.

Fig. 6(b) shows the implementation of the dc bias circuit proposed in this work. The bias circuit is supplied with a dc voltage $V_{\rm cc}$ obtained from an auxiliary winding in the transformer. The current source is implemented using a bipolar transistor operating in the linear region with low collector–emitter voltage to minimize losses.

The voltage level $V_{\rm cc}$ should be low enough to assure low losses, but high enough to allow the bipolar transistor to control the bias current i_b from the control voltage u_c applied to the transistor base circuit. Fig. 6(c) shows the small-signal equivalent circuit of the bias circuit shown in Fig. 6(b).

The circuit can easily be analyzed to obtain the remaining transfer functions necessary to model the complete system. The transfer function relating dc bias current and control voltage is

TABLE I
CHARACTERISTICS OF THE BXRA-C4500 LED ARRAY

Junction Temperature (°C)	Threshold Voltage, V_γ (V)	LED Array Total Voltage, V_o (V)
–25	25.53	28.74
25	22.33	25.40
70	19.25	22.46

$R_\gamma = 1.53\ \Omega$; $I_o = 2.1$ A

obtained as follows:

$$G_{\mathrm{bc}}(s) = \frac{i_b(s)}{u_c(s)} = \frac{h_{\mathrm{fe}}}{R_c + h_{\mathrm{ie}}} \cdot \frac{1}{1 + h_{\mathrm{oe}} R_b} \cdot \frac{1}{1 + s \frac{L_b}{h_{\mathrm{oe}}^{-1} + R_b}} \tag{19}$$

where h_{ie}, h_{fe}, and h_{oe} are the bipolar transistor input impedance, forward current gain, and output admittance, respectively, which are the common hybrid parameters used for small-signal modeling of bipolar transistors.

The global transfer function of the converter can be obtained as

$$\begin{aligned} G_{\mathrm{oc}}(s) &= \frac{i_o(s)}{u_c(s)} = \frac{i_o(s)}{l(s)} \cdot \frac{l(s)}{u_c(s)} = \frac{i_o(s)}{l(s)} k_l \frac{L_b}{N_b A_b} \frac{i_b(s)}{u_c(s)} \\ &= G_{\mathrm{ol}}(s) k_l \frac{L_b}{N_b A_b} G_{\mathrm{bc}}(s). \end{aligned} \tag{20}$$

Finally, by using (15) and (19) in (21), the final expression can be obtained as

$$G_{\mathrm{oc}}(s) = \frac{k_o}{(1 + s\tau_o)(1 + s\tau_b)}, \tag{21}$$

$$\begin{aligned} k_o &= k_{\mathrm{ol}}\, k_l \frac{L_b}{N_b A_b} \cdot \frac{h_{\mathrm{fe}}}{R_c + h_{\mathrm{ie}}} \cdot \frac{1}{1 + R_b h_{\mathrm{oe}}}\ ;\ \tau_o \\ &= R_\gamma C_o\ ;\ \tau_b = \frac{L_b}{h_{\mathrm{oe}}^{-1} + R_b}. \end{aligned} \tag{22}$$

The most important conclusion that can be extracted from this analysis is that there are two main time constants influencing the dynamic behavior of the proposed converter:

1) τ_o, which is given by the LED dynamic resistance and the output filter capacitance and it is independent of the operating point.
2) τ_b, which is given by the output resistance of the auxiliary power supply plus the series resistance of the auxiliary windings together with the auxiliary windings inductance. This inductance changes with the bias level and therefore it changes with the converter operating point. This can be a difficulty when designing the compensator for closed loop operation.

Therefore, in order to increase the response of a VI-controlled converter, it will be necessary to attain high output impedance of the bias circuit, low series resistance of the bias windings, and low inductance of the bias winding. To decrease the inductance of the bias windings it is necessary to use less turns, but this means that a higher bias current will be necessary to achieve the same dc magnetic flux density, which will decrease efficiency. Thus, there is a design trade-off between fast dynamic response and bias circuit efficiency. Time constants τ_o and τ_b can easily be calculated from the converter components. The dc gain k_o in (21) cannot be calculated so easily because it is necessary to know the dc gain k_l, which as stated previously relates the VI main inductance and dc bias magnetic flux density in steady state. However, a good possibility is to obtain experimentally the converter dc characteristic of output current versus control voltage. Then, from it is possible to obtain the global dc gain k_o by calculating the characteristic slope at the desired operating point. This process will be illustrated in Section VI. Additional information on VI design and SPICE modeling can be found in [32].

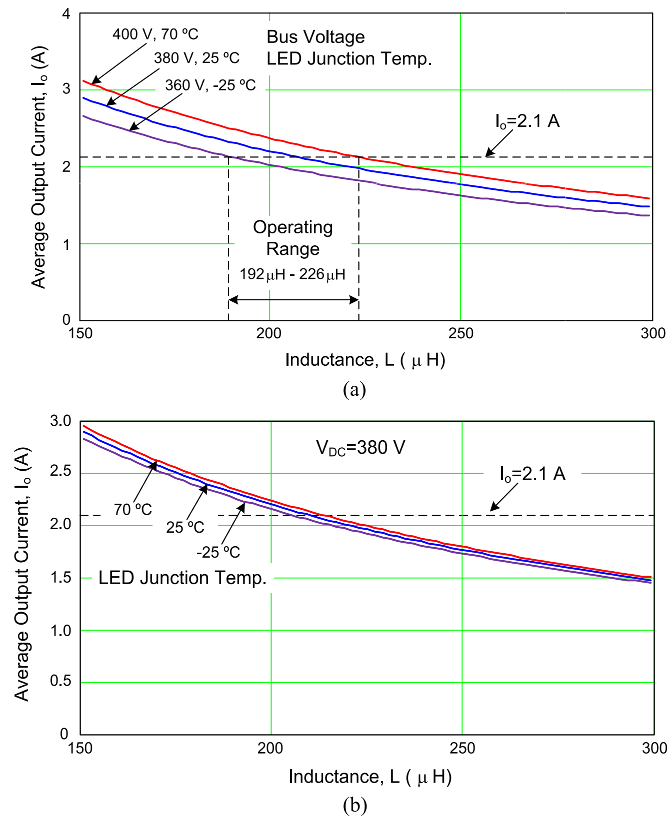

Fig. 7. Output current as a function of series inductance, (a) for the limiting values of the dc grid voltage (360–400 V) and LED junction temperature and (b) for the nominal dc grid voltage (380 V) and limiting values of the LED junction temperature.

V. DESIGN EXAMPLE

A design example for a BXRA-C4500 LED array from Bridgelux will be presented in this section. This LED array has a nominal voltage and current of 25.4 V and 2.1 A. From the datasheet characteristic, taking into account the manufacturing tolerance and the temperature coefficient given by the datasheet, the parameters shown in Table I can be calculated. The LED array series resistance is assumed to be temperature independent. The driver is designed to operate from a dc grid of 380 V nominal voltage, with a variable range from 360 to 400 V. The switching frequency has been selected to be 100 kHz as a compromise between size and efficiency. However, the

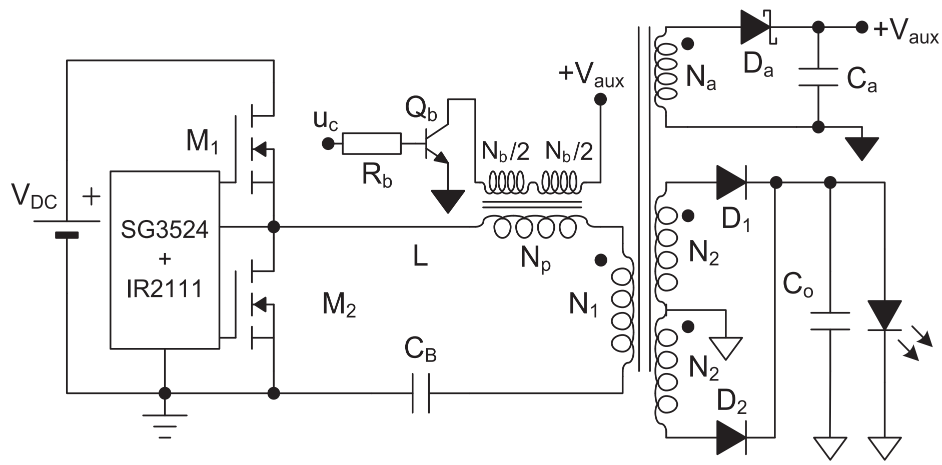

Fig. 8. Electric diagram of the laboratory prototype.

TABLE II
LABORATORY PROTOTYPE MATERIALS

Component	Values
Transistors M_1, M_2	STP28NM50N
Diodes $D_1 - D_2$, D_a	DSSK28-01A, 11DQ10
Capacitors C_b, C_o, C_a	2 μF/400 V, 10 μF/100 V, 220 μF/63 V
Bias circuit Q_b, R_B	BD139, 330 Ω
Transformer	$N_1 = 15$, 66 × 0.08 mm (litz) $N_2 = 8$, 66 × 0.08 mm (litz) $N_a = 1$, 1 × 0.2 mm EFD25/13/9, N87
Variable Inductor	$N_p = 66$, 66 × 0.08 mm (litz) $N_b/2 = 65$, 1 × 0.2 mm Gap 1.6 mm ETD29/16/10, N87

switching frequency can be increased if necessary because of the good soft-switching features of the proposed converter.

The design starts by calculating the nominal value of the series inductance, which can be obtained from (7) as follows:

$$L = \frac{nV_{\rm dc}^2 - 4n^3 V_o^2}{16 V_{\rm dc} I_o f_s}\ . \tag{23}$$

The first step is to select a suitable value of the transformer turn ratio, n. As per (6), for a given output current I_o, n will affect the peak value of the VI current as follows:

$$I_p = \frac{2I_o}{n}\ . \tag{24}$$

Since the VI current is a continuous triangular waveform, the rms current through the VI will be $I_p/\sqrt{3}$. Therefore, the higher the transformer turn ratio, the lower the VI rms current and the lower the VI losses. However, there is a limit for the turn ratio, because for $n = V_{\rm dc}/2V_o$, the phase angle, the primary current, and the output current would be zero, as per (4), (5), and (7), and there will be no energy transfer. In the present design, this limiting value is 7.48. On the other hand, a higher value of the turn ratio will require more turns in the transformer primary, increasing the losses of the transformer. Also, a minimum value of the peak current I_p is necessary to assure proper soft-switching of the bridge transistors. Therefore, in this example a value $n = 2$ has been selected. Using this value in (23), along with the rest of the converter parameters a value of $L = 210\ \mu$H is obtained. The corresponding time delay is $t_\varphi = 1.83\ \mu$s, which gives a current phase angle of 65.9°.

The next step is to evaluate the operating range of the LED driver. For this, using (9) it is possible to plot the output current as a function of the series inductance, as illustrated in Fig. 7. Since the output current increases with increasing values of $V_{\rm dc}$ and with decreasing values of V_γ, the nominal and limiting curves have been plotted in Fig. 7(a). The inductance range required to maintain nominal current of 2.1 A is 192–226 μH.

Fig. 7(b) illustrates the output current as a function of the series inductance for the nominal dc grid voltage of 380 V and the different junction temperatures. As can be seen, the LED voltage influence on the output current is very small, as expected. In any case, closed loop operation is required because dc grid voltage changes must be compensated to maintain a given LED current and lighting level. The use of the inductance as control parameter makes it possible to control each LED array independently.

VI. EXPERIMENTAL RESULTS

A laboratory prototype has been developed following the design example presented in previous section. Fig. 8 illustrates the electric diagram of the laboratory prototype. As can be seen, an auxiliary secondary winding in the transformer is used to generate dc voltage level for the inductor bias winding. The current through the bias winding is controlled by using a bipolar transistor in active region. Thus, the voltage u_c applied to the base resistance can be used to control the inductance and consequently the LED average current. Table II gathers the complete list of materials.

As illustrated in Fig. 8, the bias circuit is supplied from an auxiliary winding in the transformer. The auxiliary voltage $V_{\rm aux}$ is around 2.3 V. For a maximum bias current of 0.67 A, the total bias winding losses are 1.53 W approximately. The bias winding

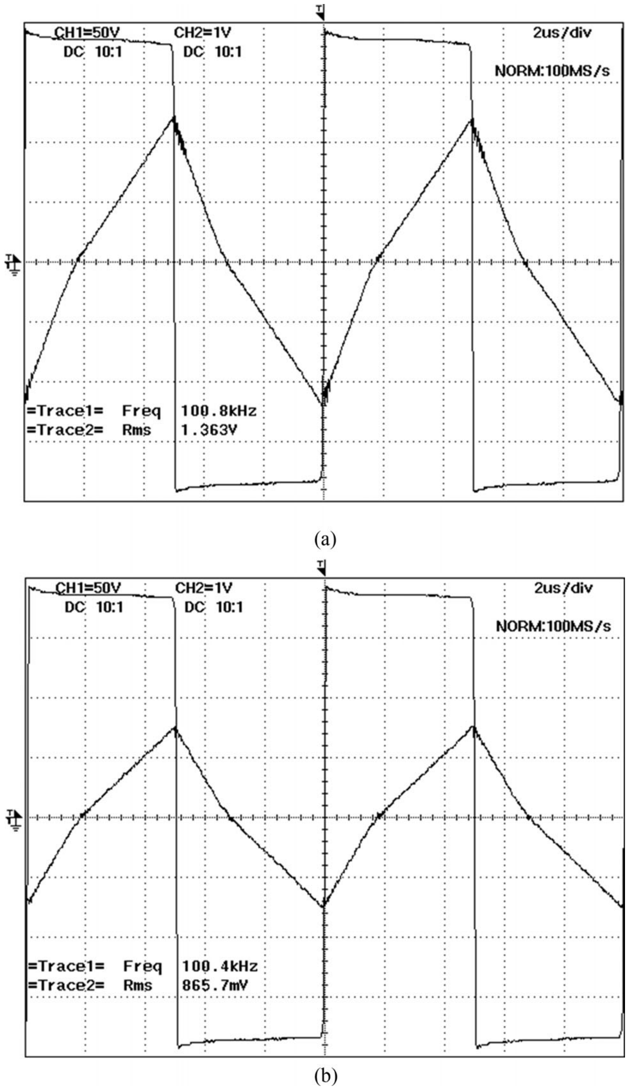

Fig. 9. Inverter voltage and inductor current at (a) nominal output power and (b) reduced output power. 50 V/div, 1 A/div, 2 μs/div. (a) $V_o = 25.5$ V, $I_o = 2.1$ A, $P_o = 53.6$ W and (b) $V_o = 24.3$ V, $I_o = 1.36$ A, $P_o = 33$ W.

voltage is 1.82 V and collector–emitter voltage in transistor Q_b is 0.46 V.

Fig. 9(a) shows the inverter voltage and the inductor current at nominal power (53.6 W). As can be seen, the inductor peak current and phase angle match the theoretical analysis. To illustrate the possibility of analog dimming with the VI technique, Fig. 9(b) shows the operating waveforms at a reduced power level of 33 W.

Fig. 10 presents a detail of the switching waveforms in the half-bridge low transistor. Drain-to-source voltage and drain current are shown. It can be seen how ZVS operation is attained.

Fig. 11 shows the current and voltage waveform in one of the output rectifier diodes. As can be seen, ZCS operation is achieved for the output rectifier diodes, thus minimizing turn-OFF recovery losses.

Fig. 12 shows the dc characteristic of the converter, which represents the output current through the LED I_o as a function of the control voltage u_c applied to the VI bias circuit. As

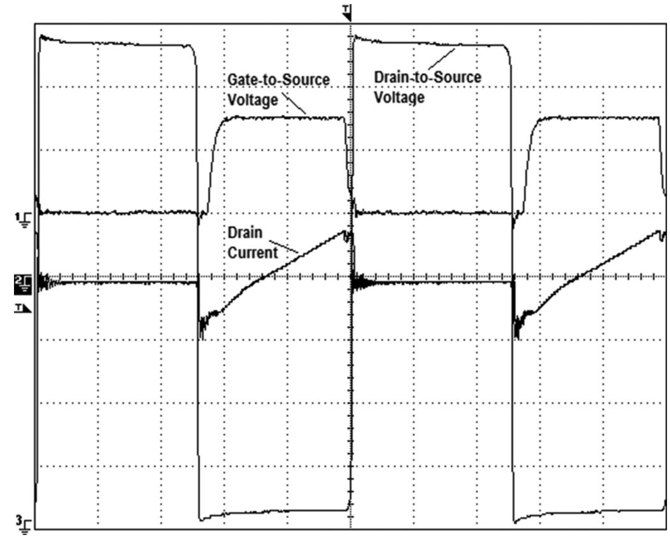

Fig. 10. Detail of the switching waveforms in the bridge low transistor: gate-to-source voltage (CH1: 10 V/div), drain current (CH2: 5 A/div), and drain-to-source voltage (CH3: 50 V/div). Horiz. scale: 1 μs/div.

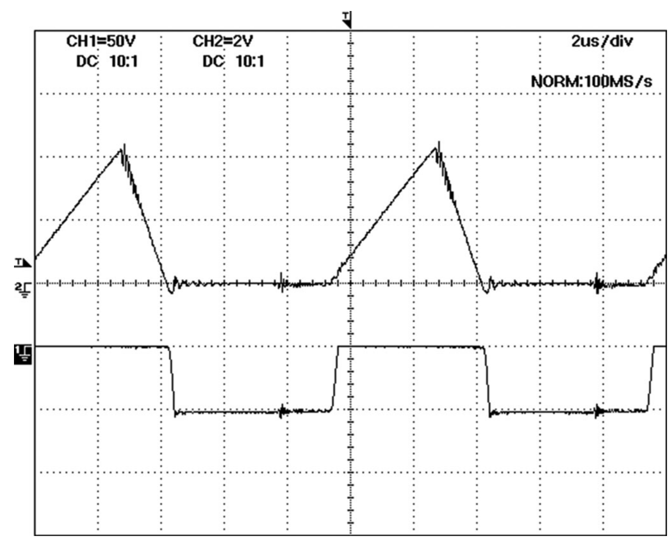

Fig. 11. Output rectifier diode voltage (bottom) and current (top). 50 V/div, 2 A/div, and 2 μs/div.

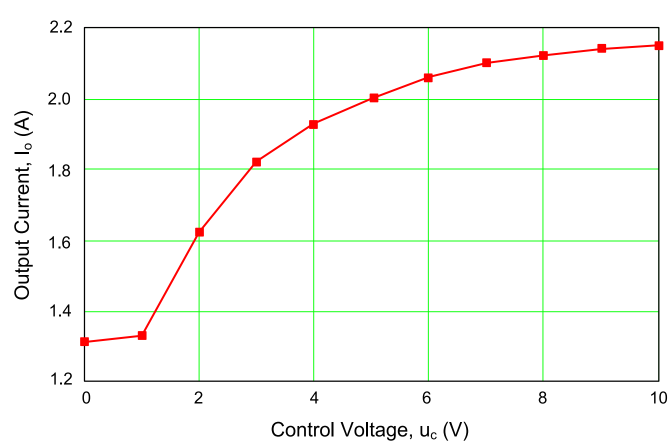

Fig. 12. Experimental result. LED current as a function of the control voltage u_c measured from the laboratory prototype. Grid voltage 380 V.

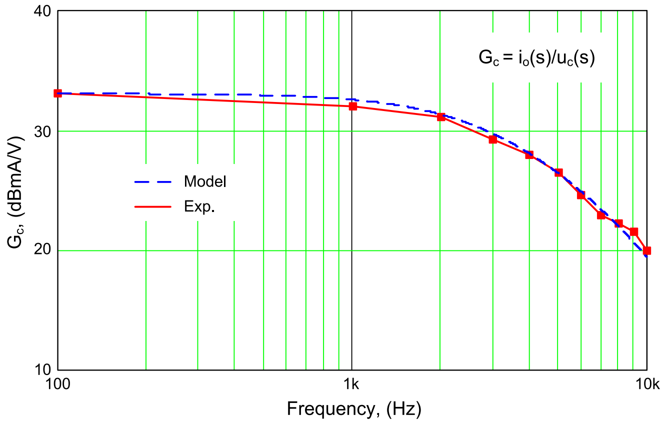

Fig. 13. Control transfer function output current (i_o) to control voltage (u_c) obtained experimentally from the laboratory prototype.

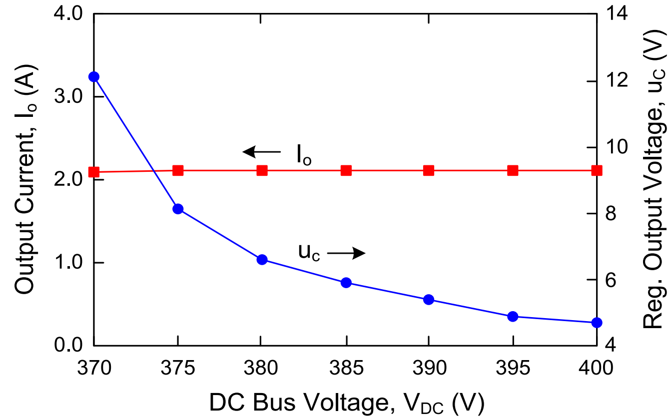

Fig. 15. Closed-loop operation experimental results. LED output current and compensator output voltage as a function of the dc bus voltage.

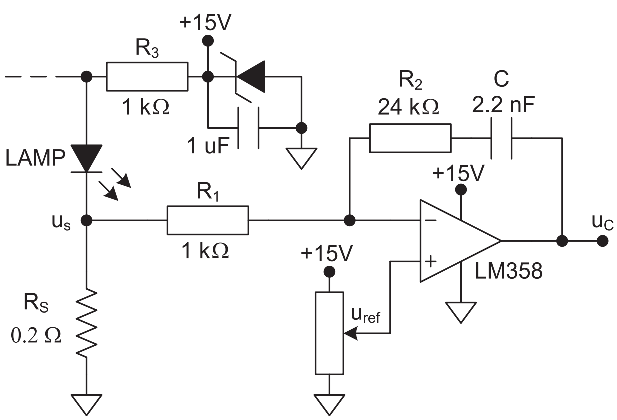

Fig. 14. Implemented PI regulator for closed-loop operation.

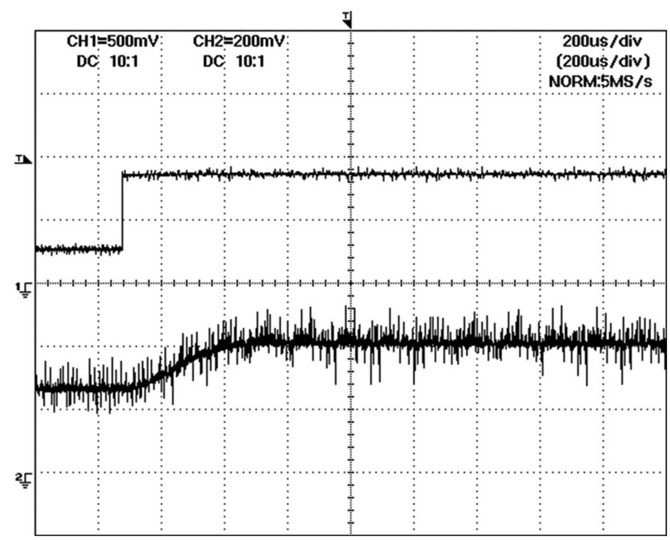

Fig. 16. Output current response for a step-up on the closed-loop reference voltage. Top: closed-loop reference voltage. Bot.: LED output current measured on a 0.2 Ω resistance. (500 mV/div, 1 A/div, and 200 μs/div).

commented previously, from this characteristic it is possible to obtain the dc gain of the converter transfer function k_o by calculating the slope of the curve at a given operating point. For example, at the nominal point, with output current equal to 2.1 A, $k_o \approx 45$ mA/V is obtained, which represents a dB gain of 33 dBmA/V for the transfer function.

Regarding the dynamic behavior, the values of the output filter capacitor and LED dynamic resistance give a cut-off frequency of 1.04 kHz, while the cut-off frequency due to the VI bias circuit is calculated to be around 3 kHz. With this information, and using (21), it is possible to theoretically determine the dynamic behavior of the converter, and design an adequate compensator for closed-loop operation.

The dynamic response of the converter has been verified experimentally by injecting a sinusoidal wave to the control signal u_c. Fig. 13 shows the Bode diagram of the open-loop control transfer function obtained experimentally and its comparison with the theoretical function. As can be seen, a good approximation is obtained with the proposed model.

Using the dynamic response of the system, a PI compensator has been designed for the output current regulation. Fig. 14 illustrates the circuit used for closed-loop operation. A 0.2 Ω series resistance is placed to sense the LED current. The reference

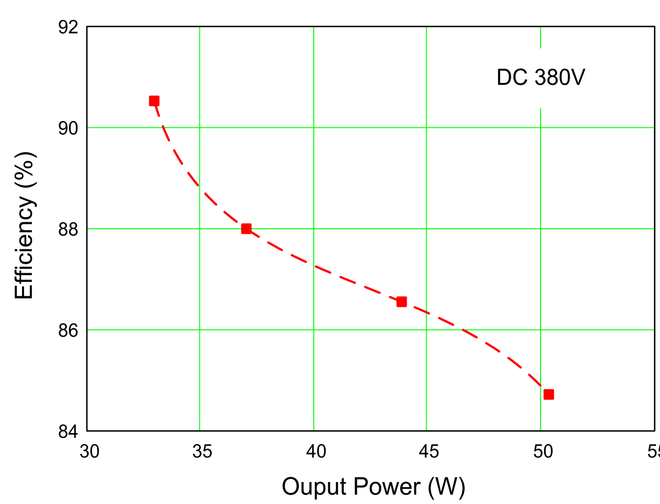

Fig. 17. Experimental results. Efficiency as a function of the output power for a dc input voltage of 380 V.

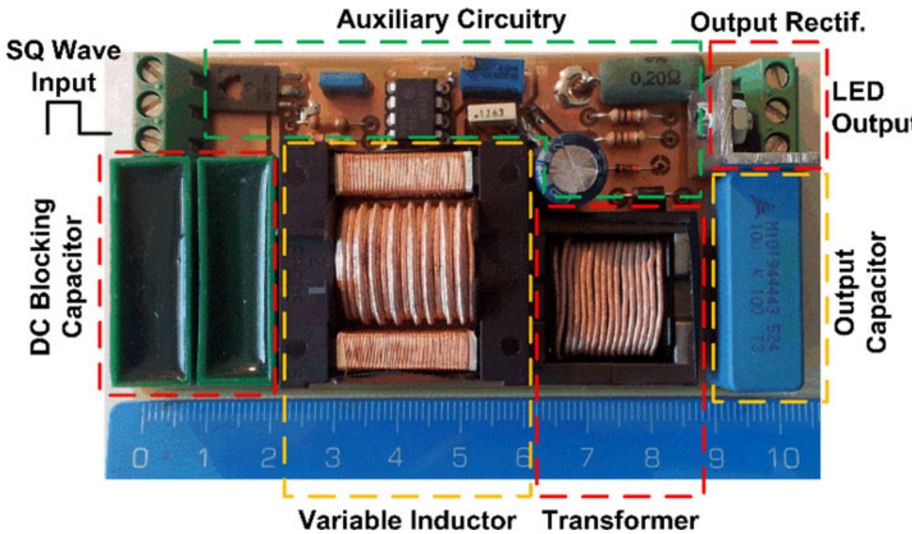

Fig. 18. Photograph of one of the 50 W LED modules.

voltage u_{ref} ranges from 0 to 10 V to control the current through the LED lamp. The PI compensator is built using an LM358 operational amplifier. The implemented transfer function is as follows:

$$C(s) = \frac{u_c(s)}{u_s(s)} = k_c \frac{1 + s/2\pi f_z}{s}. \tag{25}$$

The compensator components were designed using conventional techniques to provide a phase margin of 90°. The following values were attained: $k_c = 450 \cdot 10^3,\ f_z = 3$ kHz.

Fig. 15 shows the output current through the LED in closed-loop operation for different values of the dc bus voltage. As can be seen, the LED current is well regulated since it is maintained almost constant in the range 370–400 V. Fig. 15 also illustrates the controller action by showing its output voltage. As shown, as the input voltage increases the controller decreases its output voltage so that the VI inductance increases and the LED current is regulated. The shape of the control output voltage curve is in accordance to the open loop response characteristic shown in Fig. 12.

Fig. 16 shows the experimental dynamic response of the system for a step-up voltage in the closed-loop reference voltage (u_{ref} in Fig. 14). The first-order response of the output current with a settling time of around 400 μs is in good agreement with the theoretical design.

Fig. 17 shows the measured efficiency as a function of the output power. The maximum efficiency is 90.5% for an output power of 33 W.

Fig. 18 shows a photograph of one of the 50 W LED modules. Each of these modules is intended to be connected at the output of the half-bridge inverter and operated independently. In this way, the proposed LED driver can be used in a modular fashion, connecting the required number of modules for each application. The half-bridge inverter is used only to generate the square wave at the input of each module. The remaining tasks, driving, dimming, and regulation are carried out by each module independently.

VII. Conclusion

This paper has presented and investigated a converter for LED driving for dc grid applications. The converter is based on a half-bridge inverter, a single inductor, a transformer, and a rectifier. This structure can be replicated to supply several LED arrays from the same half-bridge inverter. By using a VI on each branch, it is possible to provide an independent control parameter for each branch, without requiring any additional downstream converter. The converter has thoroughly been studied for both steady-state and dynamic operation. A novelty of this paper is the dynamic modeling of the VI, which makes it possible to obtain the dynamic behavior of the complete system. Both static and dynamic analyses have been verified experimentally by using a 50 W laboratory prototype supplied from a 380–400 V dc grid voltage. The procedure for dynamic modeling of the VI developed in this paper allows for a better understanding of its behavior and opens a new field of research and application of VI-based converters, where the complete static and dynamic behavior of the system can be taken into consideration.

Of course, there are many other possibilities for dc grid LED drivers, especially operating at lower inherently safe voltages. However, the use of 48 V input is suitable only for low power applications, such as those in desks, night tables, side tables, and so on, due to the high currents involved. The presented converter is intended for high power applications, such as those used in ceiling lightings.

The proposed converter presents many favorable features, such as inherent short-circuit and open-circuit protection, which enables it to easily implement PWM dimming. This is a great advantage compared with other popular topologies such as the flyback converter. Besides, the converter operates with ZVS and constant frequency, making it possible to increase the switching frequency to decrease size and volume if required. The simple first-order dynamics is another advantage when compared to other converters because it makes easier the stabilization of the system in closed-loop operation.

Another advantage of the proposed converter resides in its modularity, so that if the half-bridge inverter is properly designed for high power, which is very easy and low cost goal to achieve, it can be used to supply a large number of modules, with a total power in the kW range. Each module could even be independently dimmed or switched ON/OFF by wireless communication and dedicated ICs in high-end smart-lighting applications.

REFERENCES

[1] M. Wright, "Lighting industry progresses on dc-power grids that pair well with LEDs," *LEDs Mag.*, Apr. 2013. Available: http://www.ledsmagazine.com/articles/print/volume-10/issue-6/features/lighting-industry-progresses-on-dc-power-grids-that-pair-well-with-leds-magazine.html

[2] EMerge Alliance, "Public overview of the EMerge alliance occupied space standard," Version 1.1, 2015.

[3] D. Boroyevich, I. Cvetkovic, D. Dong, R. Burgos, F. Wang, and F. C. Lee, "Future electronic power distribution systems a contemplative view," in *Proc. 12th Int. Conf. Optim. Electr. Electron. Equip.*, May 2010, pp. 1369–1380.

[4] D. Gacio, J. M. Alonso, J. Garcia, D. Garcia-Llera, and J. Cardesin, "Optimization of a front-end DCM buck PFP for an HPF integrated single-stage LED driver," *IEEE J. Emerg. Sel. Topics Power Electron.*, vol. 3, no. 3, pp. 666–678, Sep. 2015.

[5] Y. Wang, J. Huang, W. Wang, and D. Xu, "A single-stage single-switch LED driver based on integrated buck-boost circuit and class E converter," in *Proc. IEEE Ind. Appl. Soc. Meeting, Conf. Rec.*, Oct. 2015, pp. 1–5.

[6] P. S. Almeida, H. A. C. Braga, M. A. Dalla Costa, and J. M. Alonso, "Offline soft-switched LED driver based on an integrated bridgeless boost—Asymmetrical half-bridge converter," *IEEE Trans. Ind. Appl.*, vol. 51, no. 1, pp. 761–769, Jan./Feb. 2015.

[7] E. S. Lee, B. H. Choi, J. P. Cheon, G. C. Lim, B. C. Kim, and C. T. Rim, "Temperature-robust LC3 passive LED drivers with low THD, high efficiency and PF, and long life," *IEEE J. Emerg. Sel. Topics Power Electron.*, vol. 3, no. 3, pp. 829–840, Sep. 2015.

[8] P. Fang, Y.-F. Liu, and P. C. Sen, "A flicker-free single-stage offline LED driver with high power factor," *IEEE J. Emerg. Sel. Topics Power Electron.*, vol. 3, no. 3, pp. 654–665, Sep. 2015.

[9] P. S. Almeida, D. Camponogara, M. A. Dalla Costa, H. Braga, and J. M. Alonso, "Matching LED and driver life spans: A review of different techniques," *IEEE Ind. Electron. Mag.*, vol. 9, no. 2, pp. 36–47, Jun. 2015.

[10] D. Camponogara, D. R. Vargas, M. A. Dalla Costa, J. M. Alonso, J. Garcia, and T. Marchesan, "Capacitance reduction with an optimized converter connection applied to LED drivers," *IEEE Trans. Ind. Electron.*, vol. 62, no. 1, pp. 184–192, Jan. 2015.

[11] Y. Qiu, L. Wang, H. Wang, Y.-F. Liu, and P. C. Sen, "Bipolar ripple cancellation method to achieve single-stage electrolytic-capacitor-less high-power LED driver," *J. Emerg. Sel. Topics Power Electron.*, vol. 3, no. 3, pp. 698–713, Sep. 2015.

[12] Y. Wang, Y. Guan, K. Ren, W. Wang, and D. Xu, "A single-stage LED driver based on BCM boost circuit and LLC converter for street lighting system," *IEEE Trans. Ind. Electron.*, vol. 62, no. 9, pp. 5446–5457, Sep. 2015.

[13] J. I. Baek, J. K. Kim, J. B. Lee, H. S. Youn, and G. W. Moon, "Integrated asymmetrical half-bridge zeta (AHBZ) converter for dc/dc stage of LED driver with wide output voltage range and low output current," *IEEE Trans. Ind. Electron.*, vol. 62, no. 12, pp. 7489–7498, Dec. 2015.

[14] Y. C. Li, "A novel control scheme of quasi-resonant valley-switching for high-power-factor ac-to-dc LED drivers," *IEEE Trans. Ind. Electron.*, vol. 62, no. 8, pp. 4787–4794, Aug. 2015.

[15] S. Moon, G. B. Koo, and G. W. Moon, "Dimming-feedback control method for TRIAC dimmable LED drivers," *IEEE Trans. Ind. Electron.*, vol. 62, no. 2, pp. 960–965, Feb. 2015.

[16] S. Buso, G. Spiazzi, and F. Sichirollo, "Study of the asymmetrical half-bridge flyback converter as an effective line-fed solid-state lamp driver," *IEEE Trans. Ind. Electron.*, vol. 61, no. 12, pp. 6730–6738, Dec. 2014.

[17] X. Chen, D. Huang, Q. Li, and F. C. Lee, "Multichannel LED driver with CLL resonant converter," *J. Emerg. Sel. Topics Power Electron.*, vol. 3, no. 3, pp. 589–598, Sep. 2015.

[18] Y. Zhang, C. Hu, and X. Wu, "Analysis and design of LLCC resonant four-channel dc–dc LED driver with current sharing transformer," in *Proc. IEEE Appl. Power Electron. Conf.*, Mar. 2013, pp. 3295–3300.

[19] R. A. Pinto, J. M. Alonso, M. S. Perdigao, M. F. da Silva, and R. N. do Prado, "A new technique to equalize branch currents in multiarray LED lamps based on variable inductors," *IEEE Trans. Ind. Appl.*, vol. 52, no. 1, pp. 521–530, Jan. 2016.

[20] A. T. L. Lee, J. K. O. Sin, and P. C. H. Chan, "Scalability of quasi-hysteretic FSM-based digitally controlled single-inductor dual-string buck LED driver to multiple strings," *IEEE Trans. Power Electron.*, vol. 29, no. 1, pp. 501–513, Jan. 2014.

[21] J. Vollin, F. D. Tan, and S. M. Cuk, "Magnetic regulator modeling," in *Proc. IEEE Appl. Power Electron. Conf. Expo.*, Mar. 1993, pp. 604–611.

[22] J. Vollin, "Resonant Power Processing at a Fixed Frequency using a Controllable Inductance," Ph.D. dissertation, California Inst. Technol., Pasadena, CA, USA, 1994.

[23] D. Medini and S. Ben-Yaakov, "A current-controlled variable-inductor for high frequency resonant power circuits," in *Proc. IEEE Appl. Power Electron. Conf. Expo.*, vol. 1, Feb. 1994, pp. 219–225.

[24] M. Martins, M. S. Perdigão, A. S. Mendes, R. A. Pinto, and J. M. Alonso, "Dimmable LED driver with variable inductor based on a resonant switched-capacitor topology," in *Proc. IEEE Energy Convers. Congr.*, Sep. 2015, pp. 5329–5336.

[25] M. S. Perdigao, M. Menke, A. R. Seidel, R. A. Pinto, and J. M. Alonso, "A review on variable inductors and variable transformers: Applications to lighting drivers," *IEEE Trans. Ind. Appl.*, vol. 52, no. 1, pp. 531–547, Jan. 2016.

[26] J. M. Alonso, M. S. Perdigaão, D. G. Vaquero, A. J. Calleja, and E. S. Saraiva, "Analysis, design, and experimentation on constant-frequency dc-dc resonant converters with magnetic control," *IEEE Trans. Power Electron.*, vol. 27, no. 3, pp. 1369–1382, Mar. 2012.

[27] Electrical Drive Considerations for Bridgelux Vero Series LED Array, *Bridgelux Application Note AN32*, Jun. 2013.

[28] J. M. Alonso, D. Gacio, F. Sichirollo, A. R. Seidel, and M. A. Dalla Costa, "A straightforward methodology to modeling high power factor ac–dc converters," *IEEE Trans. Power Electron.*, vol. 28, no. 10, pp. 4723–4731, Oct. 2013.

[29] Bridgelux RS Array Series, *Product datasheet DS15*, Jan. 2010.

[30] J. M. Alonso, G. Martínez, M. Perdigão, M. Cosetin, and R. N. do Prado, "A systematic approach to modelling complex magnetic devices using SPICE: Application to variable inductors," *IEEE Trans. Power Electron.*, vol. 31, no. 11, pp. 1–12, Nov. 2016.

[31] J. M. Alonso, M. Perdigão, M. A. Dalla Costa, G. Martínez, and R. Osorio, "Analysis and design of a novel variable-inductor-based LED driver for dc lighting grids," in *Proc. IEEE Ind. Appl. Soc. Annu. Meeting Conf. Rec.*, Oct. 2016, pp. 1–8.

[32] J. M. Alonso, M. Perdigão, G. Z. Abdelmessih, M. A. D. Costa, and Y. Wang, "SPICE modeling of variable inductors and its application to single inductor LED driver design," *IEEE Trans. Ind. Electron.*, 2017, to be published, doi: 10.1109/TIE.2016.2638803.

José Marcos Alonso (S'94–M'98–SM'03) received the M.Sc. and Ph.D. degrees both in electrical engineering from the University of Oviedo, Gijón, Spain, in 1990 and 1994, respectively.

Since 2007, he has been a Full Professor in the Electrical Engineering Department, University of Oviedo. He is a Co-author of more than 370 journal and conference publications, including 90 publications in highly referenced journals. He is the holder of seven Spanish patents. His research interests include electronic lighting, dc–dc converters, power factor correction, resonant inverters, and power electronics in general.

Dr. Alonso received seven IEEE awards. He serves as an Associate Editor for the IEEE TRANSACTIONS ON POWER ELECTRONICS and the IEEE JOURNAL ON EMERGING AND SELECTED TOPICS ON POWER ELECTRONICS. He is currently the Chair of the IEEE IAS Industrial Lighting and Displays Committee. He is also serving as the Chair of the IEEE IAS Awards Department.

Marina S. Perdigão (S'06–M'12) was born in Coimbra, Portugal, in 1978. She received the M.Sc. and Ph.D. degrees both in electrical engineering from the University of Coimbra, Coimbra, Portugal, in 2004 and 2012, respectively.

She has been working in the Polytechnic Institute of Coimbra, Coimbra, Portugal, since 2002, first as a Teaching Assistant and since 2012 as an Assistant Professor. She is also a Researcher in the Instituto de Telecomunicações, Coimbra, Portugal. From 2006 to 2012, she conducted her Ph.D. work in the University of Coimbra in co-operation with the University of Oviedo, Gijón, Spain. She is a Co-author of more than 50 journal and conference publications, including 13 publications in IEEE journals.

Dr. Perdigão has received the best paper award of the 2009 IEEE ISIE conference and was awarded by the IAS Industrial Lighting and Display Committee a First Prize paper. She also collaborates as a Transactions Paper Reviewer.

Marco A. Dalla Costa (S'03–M'09) was born in Santa Maria, Brazil, in 1978. He received the B.S. and M.Sc. degrees from the Federal University of Santa Maria, Santa Maria, Brazil, in 2002 and 2004, respectively, and the Ph.D. degree (with Hons.) from the University of Oviedo, Gijón, Spain, in 2008, all in electrical engineering.

From 2008 to 2009, he was an Associate Professor with the Universidade de Caxias do Sul, Caxias do Sul, Brazil. Since 2009, he has been an Associate Professor with the Federal University of Santa Maria. He is a Co-author of more than 50 journal papers and more than 100 international conference papers, and is holder of 2 Spanish patents. His research interests include dc/dc converters, power factor correction, lighting systems, high-frequency electronic ballasts, discharge-lamp modeling, light-emitting-diode systems, renewable energy systems, and solid state transformers.

Dr. Dalla Costa serves as a Reviewer for several IEEE Journal and Conferences in the field of power electronics.

Gilberto Martinez received the B.Sc. and M.Sc. degrees in electronic engineering from the Technology Institute of Celaya, Guanajuato, Mexico, in 2007 and 2010, respectively. He has been working toward the Ph.D. degree in electrical and electronics engineering at the University of Oviedo, Gijón, Spain, since September 2014.

He worked in Philips Lighting as a Design Engineer of fluorescent, LED, and HID lamp drivers from December 2010 to April 2014, and then in R&D Continental Automotive as an SMPS and LED drivers modules Development Engineer from July 2014 to April 2016. Currently, he is working for D&D Hella Automotive Exterior Lighting as a Senior Hardware Design Engineer of rear combination lamps, head lamps, and small lamps. His research interests include electronic ballast, dc–dc power converters, dc–dc switched capacitor converters, power converter modeling, and lighting in general.

René Osorio was born in Veracruz City, México, in 1977. He received the Ph.D. degree in engineering science from the National Center of Research and Technological Development, Cuernavaca, México, in 2007.

He is currently a Teacher and a Researcher with the University of Guadalajara, Ameca, Mexico. His research interests include lighting systems, the application of control strategies to power converters, and the design of mechatronic devices.

Analysis and Design of a Novel Variable-Inductor-Based LED Driver for DC Lighting Grids

J. Marcos Alonso[1], Marina Perdigão[2, 3], Marco A. Dalla Costa[4], Gilberto Martínez[1], René Osorio[5]

(1) University of Oviedo, Electrical Eng. Dept., Campus de Viesques, Gijón, Asturias, Spain.
(2) Instituto de Telecomunicações, University of Coimbra, DEEC, Coimbra.
(3) IPC, Instituto Superior de Engenharia de Coimbra, ISEC, DEE, Portugal.
(4) Federal University of Santa Maria, Group of Intelligence in Lighting (GEDRE), Brazil.
(5) University of Guadalajara, Guadalajara, Jalisco, México.

marcos@uniovi.es; perdigao@isec.pt; marcodc@gedre.ufsm.br; gilbertomar9@hotmail.com; reneosorios@yahoo.com;

***Abstract*— This paper presents a novel variable inductor (VI) based LED driver for DC grid lighting applications. The proposed driver requires only a series inductor and a transformer as major components to drive the LED lamp from a half-bridge inverter. By introducing a VI as the series inductor, the LED current can be controlled independently from any other parameter, which makes it possible to drive and regulate several LED branches from the same half-bridge output. Other advantages of the proposed converter include inherent open circuit and short circuit protections, ZVS for the bridge transistor and ZCS for the output rectifier diodes, simple dynamics, possibility of analog and PWM dimming, constant switching frequency operation and high efficiency. The converter is thoroughly analyzed and modelled for both steady-state and dynamic operation. As another novelty of this paper, the dynamic response of the VI has been studied and taken into account to obtain the complete transfer function of the VI-controlled system. In addition, some housekeeping issues that usually arise when dealing with VI, e.g. how to drive the VI bias winding, are solved in this work. Experimental results provided from a 50 W laboratory prototype demonstrate the correctness of the performed analysis and the good possibilities of the proposed converter.**

***Keywords*—LED driver, DC grid, single inductor converter, variable inductor, variable inductor dynamic response, closed-loop operation.**

I. Introduction

With the exponential increase of electronic equipment in homes, offices and buildings, dc power distribution is gaining more and more attention in the present time. The use of a dc grid makes it possible to simplify the power converters used to supply equipment such as computers, TVs, cameras, cell phone battery chargers, and many others, whose number is rapidly increasing, especially under the new Internet of Things (IoT) trend [1]-[3]. Besides, dc power distribution allows the converters to get rid of the ac-dc conversion stage and also of the electrolytic capacitors required to cope with the ac-dc power unbalance. Therefore, efficiency and reliability are simultaneously improved. These advantages are especially significant in lighting systems and particularly with today's highly-efficient highly-reliable LED-based lighting technology. In this context, the search for new LED driver topologies, specifically developed for dc applications is a relevant field of research.

Most of the works available in the literature agree that the future dc grid for homes, offices and building applications will be deployed on two voltage levels: (i) a high-voltage level of 380 V, with a 360-400 V range to allow for system regulation, which will be used for high power loads like main lighting, heating, air conditioning, washing machines, dishwashers, etc, and (ii) a safer low-voltage level of 48 V, to supply low power equipment that operate closer to the end user, like cell phone battery chargers, side table lights, personal computers and tablets, etc.

In the literature it is possible to find many works dealing with ac-dc LED drivers, providing power factor correction (PFC), avoiding the use of electrolytic capacitors, improving dimming characteristics, etc. [4]-[15]. However, few proposals can be found related to dc operated LED drivers aiming for the new dc power distribution. Some of the works that can be found are intended to be used as second or third stage after PFC and conditioning stages [16]-[20].

The goal of this work is to propose a novel topology for LED driving specifically developed for the future dc grid deployment. The topology will be investigated in order to obtain its static and dynamic behavior, which can be used not only to design the closed loop operation of the converter, but also to investigate its interaction within the dc grid. While the former is of great importance for the operation of the LED driver itself, the latter is essential for the design of the dc bus control strategy [3].

In Section II the proposed LED driver topology is introduced, highlighting its most relevant features and characteristics. Section III presents the static analysis of the converter, which can be used in the design of the LED driver. Section IV deals with the dynamic analysis of the converter, in which the most relevant transfer function for closed loop operation and dc grid interaction will be derived. Section V illustrates a design example for a 50-W 380-V operated LED driver, which can be applied in multi-array lamps. Section VI presents experimental results from the laboratory prototype. Finally, Section VII summarizes the conclusions of the work.

This work has been supported by Spain national government and Asturias regional government under research grants ENE2013-41491-R and GRUPIN14-076, respectively.

II. Proposed DC-Grid LED Driver

Fig. 1 shows the electric diagram of the proposed LED driver for dc grid applications. A half bridge inverter followed by a dc blocking capacitor (C_B) is used to generate a symmetrical square voltage waveform (v_g) with an amplitude of $V_{DC}/2$ and a frequency f_s, where V_{DC} is the dc grid voltage and f_s is the switching frequency of the half bridge transistors. A series inductance L is used to limit the current through the LED lamp. The latter is supplied through an isolating transformer, a full wave rectifier and a filter capacitor C_o, so that the current through the lamp is continuous, with a small superposed ripple at $2f_s$. In order to provide output current regulation against input and load changes, a variable inductance (VI) is proposed to control the power delivered to the load [21][22].

One of the advantages of the proposed driver is that it can be used to supply several LED lamp arrays with an independent regulation of the current through each LED lamp, as illustrated in Fig. 2, where VI L_i controls the current through LED lam $\#i$. As shown in Fig. 2, it is preferred to connect the second arrangement on the top side of the half bridge inverter, instead of in parallel with the first arrangement. In this way, the current supplied from the dc bus will not present a dead time, thus requiring a smaller EMI filter. The structure can be replicated to accommodate any number of LED arrays.

The advantages of the proposed LED driver can be summarized as follows:

- Ability to supply multiple LED arrays with independent current control to provide current equalization.
- Ability to include galvanic isolation. However, the transformer could be avoided if galvanic isolation is not required.
- Low switching losses owing to zero-voltage-switching (ZVS) operation in the half-bridge switches. With proper dead time selection the switching losses can be kept to a minimum.
- Zero current switching (ZCS) of the output rectifier diodes, thus providing negligible turn-off losses.
- Constant switching frequency operation provided by inductance variation control. This feature allows for an easy EMI filter design and minimization.
- Simple first-order dynamics, allowing for an easy closed loop operation and dc grid interaction.
- Inherent low LED current compensation against LED operating junction temperature.
- Inherent short-circuit protection. In the case of an output short-circuit the series inductance limits the half-bridge current to a triangular waveform with a maximum peak value.
- Inherent open-circuit protection. In an open-circuit situation the current through the series inductor tends to zero.
- Easy implementation of PWM dimming. This is a consequence of previous features. Since the output can safely be short-circuited or open-circuited, several possibilities are available to implement PWM dimming.

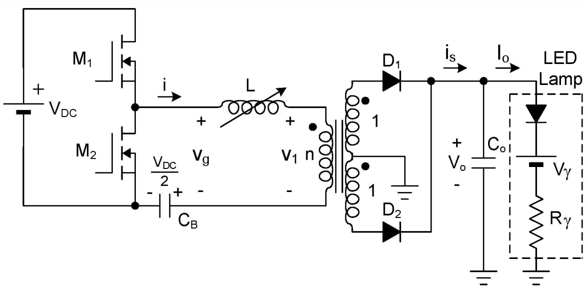

Fig. 1. Proposed LED driver for application in DC grids.

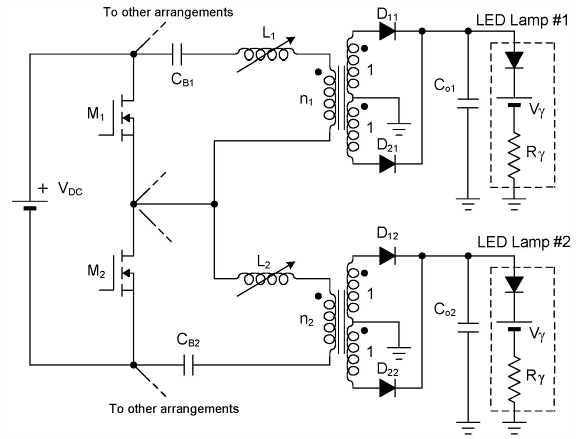

Fig. 2. Proposed driver used to supply two LED arrays.

III. Static Analysis of the Proposed Converter

A.- Basic Analysis of the Converter

Fig. 3 illustrates the equivalent circuit of the proposed LED driver, which can be used to analyze its behavior. The voltage source v_g represents the voltage generated by the half bridge after removing its dc level by capacitor C_B. The voltage source v_1 represents the voltage at the primary of the transformer, whose amplitude is equal to the dc output voltage V_o times the transformer turns ratio n.

Fig. 4 illustrates the main waveforms of the converter. Because of the effect of the series inductance, the voltage v_1 will lag the input voltage by a phase angle φ, equivalent to a time interval $t_\varphi = \varphi/\omega_s$, where $\omega_s = 2\pi f_s$ is the angular switching frequency. Thus, the inductor current will be delayed by the same angle φ, providing ZVS operation of the bridge transistors, which is an important feature of the proposed converter.

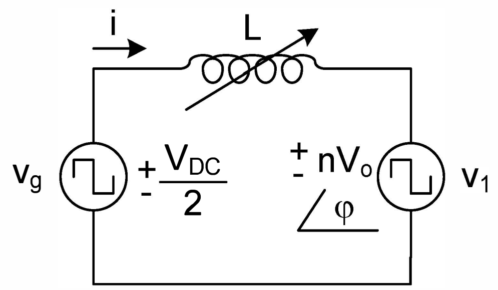

Fig. 3. Equivalent circuit of the proposed LED driver.

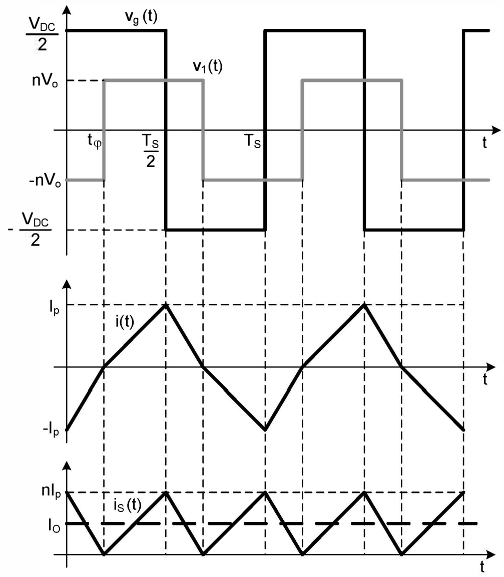

Fig. 4. Main operating waveforms of the proposed LED driver.

Analyzing the circuit shown in Fig. 3 the evolution of the inductor current during the two time intervals can be expressed as in (1) and (2), where T_s denotes the switching period ($T_s = 1/f_s$).

$$i(t) = -I_p + \frac{0.5V_{DC} + nV_o}{L}t \quad t \in [0, t_\varphi], \tag{1}$$

$$i(t) = \frac{0.5V_{DC} - nV_o}{L}(t - t_\varphi) \quad t \in [t_\varphi, T_s/2]. \tag{2}$$

In steady state operation the following condition must be reached:

$$i(T_s/2) = -i(0). \tag{3}$$

By using condition (3) in (1) and (2), the values of the peak current I_p and time delay t_φ are obtained as given in (4) and (5) respectively.

$$I_p = \frac{V_{DC}^2 - 4n^2V_O^2}{8V_{DC}Lf_s}, \tag{4}$$

$$t_\varphi = \frac{0.5V_{DC} - nV_o}{2V_{DC}f_s}. \tag{5}$$

The average current through the LED lamp I_o can be calculated as the average value of the rectified inductor current transformed to the secondary side, this is:

$$I_o = \frac{2}{T_s}\int_0^{T_s/2} n \cdot |i(t)|\, dt = \frac{nI_p}{2}, \tag{6}$$

then:

$$I_o = \frac{nV_{DC}^2 - 4n^3V_O^2}{16V_{DC}Lf_s}. \tag{7}$$

Now, taking into account the following relationship between voltage and current in the LED:

$$V_o = V_\gamma + R_\gamma I_o\,, \tag{8}$$

where V_γ and R_γ are the threshold voltage and dynamic resistance of the LED array respectively, using (8) in (7) and solving for the LED current, the following expression can be obtained:

$$I_o = -\frac{V_\gamma}{R_\gamma} - \frac{2V_{DC}Lf_s}{n^3R_\gamma^2} + \frac{1}{2}\sqrt{\left(\frac{4V_{DC}Lf_s}{n^3R_\gamma^2}\right)^2 + \frac{16V_\gamma V_{DC}Lf_s}{n^3R_\gamma^3} + \frac{V_{DC}^2}{n^2R_\gamma^2}} \tag{9}$$

As can be seen, expression (9) is a closed form for the average LED current as a function of all the parameters of the circuit: input voltage, inductance, switching frequency, transformer turn ratio and LED array parameters. By using this expression it is possible to design the converter and analyze its operation under different conditions. A design example will be illustrated later.

B.- Analysis of Lamp Current Perturbations

At this point, since the LED lamp threshold voltage has a great dependence on the operating junction temperature [23], it is interesting to evaluate how the threshold voltage V_γ will affect the average output current. This can be done by taking a partial derivative in (9):

$$k_\gamma = \frac{\partial I_o}{\partial V_\gamma} = -\frac{1}{R_\gamma} + \frac{4V_{DC}Lf_s}{n^3R_\gamma^3\sqrt{\left(\frac{4V_{DC}Lf_s}{n^3R_\gamma^2}\right)^2 + \frac{16V_\gamma V_{DC}Lf_s}{n^3R_\gamma^3} + \frac{V_{DC}^2}{n^2R_\gamma^2}}} \tag{10}$$

where k_γ is the per-unit change of the output current against LED threshold voltage. Referring to (1) and (2) and Fig. 4 it is easy to understand that when the LED voltage increases, the positive slope of the inductor current will decrease, while its negative slope will increase, thus leading to a lower LED average current and lower power, and reversely. Therefore, the LED current is inherently compensated against changes in LED voltage, which means that small values of k_γ should be expected.

Similarly, the variation of the LED current against perturbations of the dc voltage can be obtained by taking a partial derivative of (7), as follows:

$$k_v = \frac{\partial I_o}{\partial V_{DC}} = \frac{n}{16Lf_s} + \frac{4n^3V_o^2}{16V_{DC}^2Lf_s}, \tag{11}$$

where k_v is the per-unit variation of the output current against dc input voltage. As per (11), the changes in the input voltage V_{DC} have the contrary effect on the LED current compared to the LED voltage. This means that the value of k_v will be high, and changes in LED current should be compensated by closed loop operation, which measures the LED current and adjusts the inductance value accordingly.

C.- Analysis of Open-Circuit and Short-Circuit Operation

In an open circuit situation the current injected to the output capacitance will be equal to zero in steady state. Considering ideal behavior (no losses), the output capacitance C_o will be charged to a voltage level equal to $V_{DC}/2n$; the voltage across the transformer primary $v_1(t)$ will be a square voltage with an amplitude equal to $V_{DC}/2$ and in phase with $v_g(t)$. Thus, no current will either circulate through the inductor. The only precaution would be to select an output capacitor with a voltage rating higher than $V_{DC}/2n$.

During a short-circuit on the output, the current through the series inductor will be inherently limited, and so will be the current through the bridge switches. The current through the inductor will be a symmetrical triangular waveform, with a peak value I_{pcc} that, assuming ideal behavior, can be calculated by making null the output voltage in (4), this is:

$$I_{pcc} = \frac{V_{DC}}{8Lf_s}. \tag{12}$$

IV. Dynamic Analysis of the Proposed Converter

A.- Modelling of the Power Stage

The proposed driver can be modelled by the averaged circuit shown in Fig. 5a. The converter is modelled by a current source, which injects the averaged rectified current $\langle i_s \rangle$ into the RC network given by the output capacitor and the equivalent circuit of the LED lamp. The ESR resistance of the output capacitor has been neglected in this case, because usually film capacitors with very low series resistance are employed in LED drivers. Thus, the dynamic effect of the capacitor ESR will be beyond the frequency range of interest.

Using a similar methodology as that presented in [24], the circuit in Fig. 5a can be perturbed and represented in the Laplace domain as shown in Fig. 5b. By analyzing this circuit the following relationship can be obtained:

$$R_\gamma C_o s\, i_o(s) + i_o(s) = k_v\, v_{dc}(s) + k_{ol}\, l(s), \tag{13}$$

where $l(s)$ and $v_{dc}(s)$ represent the perturbations in the inductance and dc bus voltage respectively, k_v is defined as in (11) and the factor k_{ol} can be calculated by the partial derivative of (7), as follows:

$$k_{ol} = \frac{\partial \langle i_s \rangle}{\partial L} = -\frac{I_o}{L} \tag{14}$$

The corresponding transfer functions can now easily be obtained from (13):

$$G_{ol}(s) = \frac{i_o(s)}{l(s)} = \frac{k_{ol}}{1 + sR_\gamma C_o} \tag{15}$$

$$G_v(s) = \frac{i_o(s)}{v_{dc}(s)} = \frac{k_v}{1 + sR_\gamma C_o} \tag{16}$$

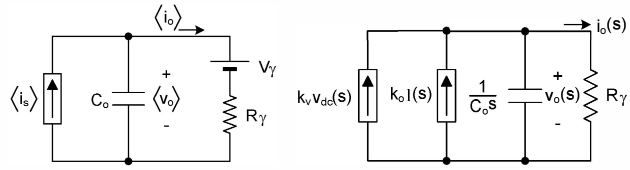

(a) (b)

Fig. 5. Equivalent circuits of the proposed LED driver at output terminals: (a) averaged time domain, (b) Laplace domain.

B.- Modelling of the Variable Inductor

Fig. 6a shows the circuit used to provide the bias level to the VI. A current source I_i generates the dc current for the auxiliary windings. R_i represents the output resistance of the current source, R_b is the series resistance of the auxiliary windings and L_b is the total inductance seen from the auxiliary windings in series connection.

In a VI the magnitude that modifies the main winding inductance is the dc level of the magnetic flux density introduced by the auxiliary winding inside the magnetic material, namely B_b. A change in B_b will produce a change in the VI inductance. As it will be shown in the following, the auxiliary windings total inductance L_b and resistances R_i and R_b introduce a major time constant in the VI response. Therefore, it is possible to consider an instant response between B_b and VI inductance, in other words, to neglect the dynamic of the magnetic material itself by assuming that it is much faster than that due to the auxiliary winding components. Following this reasoning, it is easy to analyze the circuit in Fig. 6a to obtain the following transfer function between the dc bias current and the dc magnetic flux density:

$$G_{lb}(s) = \frac{l(s)}{i_b(s)} \approx k_l \frac{B_b(s)}{i_b(s)} = \frac{k_l\, k_{lb}}{1 + s\dfrac{L_b}{R_i + R_b}} \tag{17}$$

$$k_{lb} = \frac{R_i}{R_i + R_b} \frac{L_b}{N_b A_b} \tag{18}$$

where A_b is the effective area of the dc bias magnetic path and k_l is the dc gain that relates the VI inductance and the dc magnetic flux density. As shown later, this gain can be obtained by calculating the slope of the characteristic VI inductance versus dc magnetic flux density at a given operating point.

Fig. 6b shows the implementation of the dc bias circuit proposed in this work. The bias circuit is supplied with a dc voltage V_{cc} obtained from an auxiliary winding in the transformer.

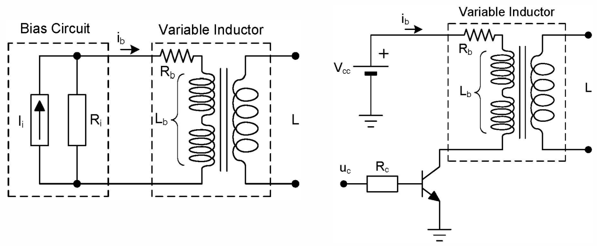

(a) (b)

Fig. 6. (a) VI bias circuit, (b) implementation using a bipolar transistor and a low-voltage source.

The voltage level V_{cc} should be low enough to assure low losses, but high enough to allow the bipolar transistor to control the bias current i_b from the control voltage u_c applied to the transistor base circuit. The complete circuit can easily be analyzed to obtain the remaining transfer functions necessary to model the complete system:

$$G_{bc}(s) = \frac{i_b(s)}{u_c(s)} = \frac{h_{fe}}{R_c + h_{ie}} \tag{19}$$

where h_{ie} and h_{fe} are the bipolar transistor input impedance and forward current gain. The output resistance of the bias circuit is given by the output admittance of the bipolar transistor h_{oe} as follows:

$$R_i = \frac{1}{h_{oe}} \tag{20}$$

Finally, by using (15), (17) and (19) it is possible to obtain the following global transfer function for the output current i_o versus control voltage u_c:

$$G_{oc}(s) = \frac{i_o(s)}{u_c(s)} = \frac{k_o}{(1+s\tau_o)(1+s\tau_b)} \tag{21}$$

$$k_o = \frac{k_{ol}k_l k_{lb} h_{fe}}{R_c + h_{ie}}\ ;\ \tau_o = R_\gamma C_o\ ;\ \tau_b = \frac{L_b}{h_{oe}^{-1} + R_b} \tag{22}$$

The most important conclusion that can be extracted from this analysis is that there are two main time constants influencing the dynamic behavior of the proposed converter:

- τ_o, which is given by the LED dynamic resistance and the output filter capacitance and it is quite independent of the operating point.
- τ_b, which is given by the output resistance of the auxiliary power supply plus the series resistance of the auxiliary windings together with the auxiliary windings inductance. This inductance changes with the bias level and therefore it changes with the converter operating point.

Therefore, in order to increase the response of a VI controlled converter it will be necessary to attain high output impedance of the bias circuit, low series resistance of the bias windings and low inductance of the bias winding. To decrease the inductance of the bias windings it is necessary to use less turns, but then higher bias current will be necessary to achieve the same dc magnetic flux density, which will decrease efficiency. Thus, there is a design trade-off between fast dynamic response and bias circuit efficiency.

Time constants τ_o and τ_b can easily be calculated from the converter components. The dc gain k_o in (21) cannot be calculated so easily because it is necessary to know the dc gain k_l, which as stated previously relates inductance and bias magnetic flux density in steady state. However, a good possibility is to obtain experimentally the converter dc characteristic of output current versus control voltage. Then, from it is possible to obtain the global dc gain k_o by calculating the characteristic slope at the desired operating point. This process will be illustrated in the experimental results section.

V. Design Example

A design example for a BXRA-C4500 LED array from Bridgelux [25] will be presented in this section. This LED array has a nominal voltage and current of 25.4 V and 2.1 A. From the datasheet characteristic, taking into account the manufacturing tolerance and the temperature coefficient given by the datasheet, the parameters shown in Table I can be calculated. The LED array series resistance is assumed to be temperature independent. The driver is designed to operate from a dc grid of 380 V nominal voltage, with a variable range from 360 V to 400 V. The selected switching frequency is 100 kHz.

TABLE I. Characteristics of the BXRA-C4500 LED Array

Junction Temperature (ºC)	Threshold Voltage, V_γ (V)	LED Array Total Voltage, V_o (V)
-25ºC	25.53	28.74
25ºC	22.33	25.40
70ºC	19.25	22.46
$R_\gamma = 1.53\,\Omega\,;\, I_o = 2.1\,A$		

The design starts by calculating the nominal value of the series inductance, which can be obtained from (7) as follows:

$$L = \frac{nV_{DC}^2 - 4n^3V_O^2}{16V_{DC}I_of_s}. \tag{23}$$

The first step is to select an adequate value of the transformer turn ratio, n. According to (5), n will impact the current phase angle given by the time interval t_φ, as shown in Fig. 4. The higher the turn ratio n, the lower the current phase angle and the lower rms current through the inductor. However, n cannot be made very high. In fact, for $n = V_{DC}/2Vo$ the phase angle, the primary current and the output current would be zero, as per (4), (5) and (7), and there will be no energy transfer. In the present design this limiting value is around 3.8.

In order to increase efficiency, it is convenient to have a moderate rms current through the inductor. Thus, in this example a value $n = 2$ has been selected. Using this value in (21), along with the rest of the converter parameters a value of $L = 210\ \mu H$ is obtained. The corresponding time delay is $t_\varphi = 1.83\ \mu s$, which gives a current phase angle of 65.9º.

The next step is to evaluate the operating range of the LED driver. For this, using (9) it is possible to plot the output current as a function of the series inductance, as illustrated in Fig. 7. Since the output current increases with increasing values of V_{DC} and with decreasing values of V_γ, the nominal and limiting curves have been plotted in Fig. 7a. The inductance range required to maintain nominal current of 2.1 A is 192-226 µH.

Fig. 7b illustrates the output current as a function of the series inductance for the nominal dc grid voltage of 380 V and the different junction temperatures. As can be seen, the LED voltage influence on the output current is very small, as expected. In any case, closed loop operation is required because dc grid voltage changes must be compensated to maintain a given LED current and lighting level. The use of the inductance as control parameter makes it possible to control each LED array independently. A detailed SPICE modelling of both VI and LED driver can be found in [26].

VI. EXPERIMENTAL RESULTS

Fig. 8 illustrates the electric diagram of the laboratory prototype. As can be seen, an auxiliary secondary winding in the transformer is used to generate dc voltage level for the inductor bias winding. The current through the bias winding is controlled by using a bipolar transistor in active region. Thus, the voltage u_c applied to the base resistance can be used to control the inductance and consequently the LED average current. Table II gathers the complete list of materials.

As illustrated in Fig. 8, the bias circuit is supplied from an auxiliary winding in the transformer. The auxiliary voltage V_{aux} is around 2.3 V. For a maximum bias current of 0.67 A, the total bias winding losses are 1.53 W approximately. The bias winding voltage is 1.82 V and collector-emitter voltage in transistor Q_b is 0.46 V.

Fig. 9a shows the inverter voltage and the inductor current at nominal power (53.6 W). As can be seen, the inductor peak current and phase angle match the theoretical analysis. To illustrate the possibility of analog dimming with the VI technique, Fig. 9b shows the operating waveforms at a reduced power level of 33W.

Fig. 10 presents a detail of the switching waveforms in the half-bridge low transistor. Drain-to-source voltage and drain current are shown. It can be seen how ZVS operation is attained.

Fig. 11 shows the current and voltage waveform in one of the output rectifier diodes. As can be seen, ZCS operation is achieved for the output rectifier diodes, thus minimizing turn-off recovery losses.

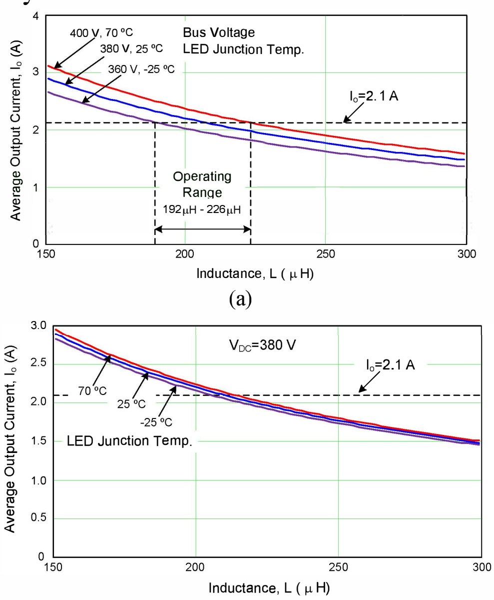

(a)

(b)

Fig. 7. Output current as a function of series inductance, (a) for the limiting values of the dc grid voltage (360-400V) and LED junction temperature, (b) for the nominal dc grid voltage (380V) and limiting values of the LED junction temperature.

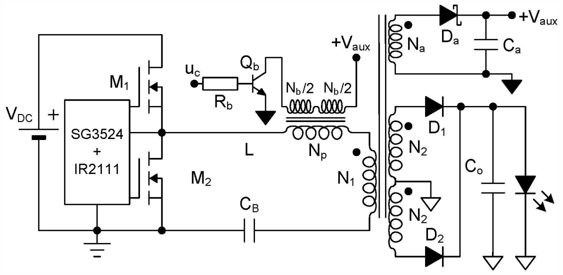

Fig. 8. Electric diagram of the laboratory prototype.

TABLE II. LABORATORY PROTOTYPE MATERIALS

Component	Values
Transistors M_1, M_2	STP28NM50N
Diodes D_1-D_2, D_a	DSSK28-01A, 11DQ10
Capacitors C_B, C_o, C_a	2 μF/400V, 10μF/100V, 220 μF/63V
Bias circuit Q_b, R_b	BD139, 330 Ω
Transformer	N_1=15, 66x0.08 mm (litz) N_2=8, 66x0.08 mm (litz) N_a=1, 1x0.2 mm EFD25/13/9, N87
Variable Inductor	N_p=66, 66x0.08 mm (litz) N_b/2=65, 1x0.2 mm Gap 1.6 mm ETD29/16/10, N87

Fig. 12 shows the dc characteristic of the converter, which represents the output current through the LED I_o as a function of the control voltage u_c applied to the VI bias circuit. As commented previously, from this characteristic it is possible to obtain the dc gain of the converter transfer function k_o by calculating the slope of the curve at a given operating point. For example, at the nominal point, with output current equal to 2.1 A, $k_o \approx 45\ mA/V$ is obtained, which represents a dB gain of 33 dBmA/V for the transfer function.

Regarding the dynamic behavior, the values of the output filter capacitor and LED dynamic resistance give a cut-off frequency of 1.04 kHz, while the cut-off frequency due to the VI bias circuit is calculated to be around 3 kHz. With this information, and using (21) it is possible to theoretically determine the dynamic behavior of the converter, and design an adequate compensator for closed-loop operation.

The dynamic response of the converter has been verified experimentally by injecting a sinusoidal wave to the control signal u_c. Fig. 13 shows the Bode diagram of the open-loop control transfer function obtained experimentally and its comparison with the theoretical function. As can be seen, a good approximation is obtained with the proposed model.

Using the dynamic response of the system, a PI compensator has been designed for the output current regulation. Fig. 14 illustrates the circuit used for closed-loop operation. A 0.2 Ω series resistance is placed to sense the LED current. The PI compensator is built using a LM358 operational amplifier. The implemented transfer function is as follows:

$$C(s) = \frac{u_c(s)}{u_s(s)} = k_c \frac{1 + s/2\pi f_z}{s} \qquad (24)$$

The compensator components were designed using conventional techniques to provide a phase margin of 90º. The following values were attained: $k_c = 450 \cdot 10^3, f_z = 3\ kHz.$

Fig. 15 shows the output current through the LED in closed-loop operation for different values of the DC bus voltage. As can be seen, the LED current is well regulated since it is maintained almost constant in the range 370V-400V. Fig. 15 also illustrates the controller action by showing its output voltage. As shown, as the input voltage increases the controller decreases its output voltage so that the VI inductance increases and the LED current is regulated. The shape of the control output voltage curve is in accordance to the open loop response characteristic shown in Fig. 12.

Fig. 16 shows the experimental dynamic response of the system for a step-up voltage in the closed-loop reference voltage (u_{ref} in Fig. 14). The first-order response of the output current with a settling time of around 400 µs is in good agreement with the theoretical design.

Finally, the maximum efficiency of the converter was 90% for an output power of 32 W.

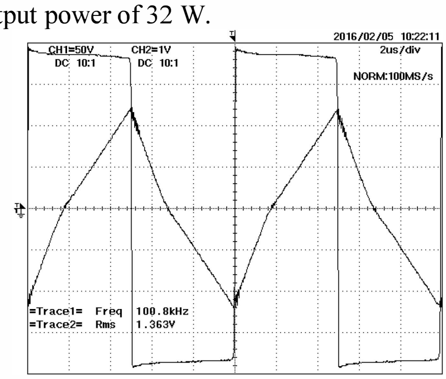

(a) $V_o = 25.5\ V, I_o = 2.1\ A, P_o = 53.6\ W$

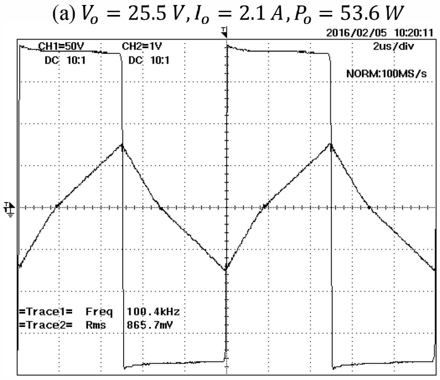

(b) $V_o = 24.3\ V, I_o = 1.36\ A, P_o = 33\ W$

Fig. 9. Inverter voltage and inductor current at (a) nominal output power, (b) reduced output power. 50 V/div, 1 A/div, 2 µs/div.

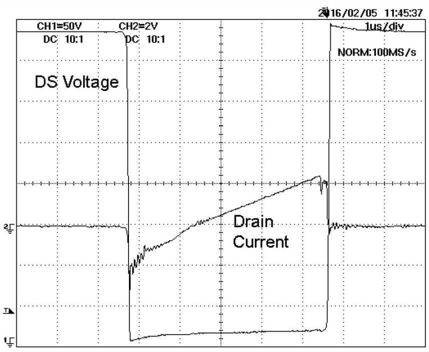

Fig. 10. Detail of the switching waveforms in the bridge low transistor: drain-to-source voltage and drain current. 50 V/div, 1 A/div, 1 µs/div.

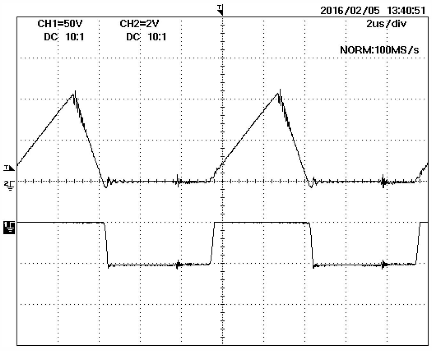

Fig. 11. Output rectifier diode voltage (bottom) and current (top). 50 V/div, 2 A/div, 2 µs/div.

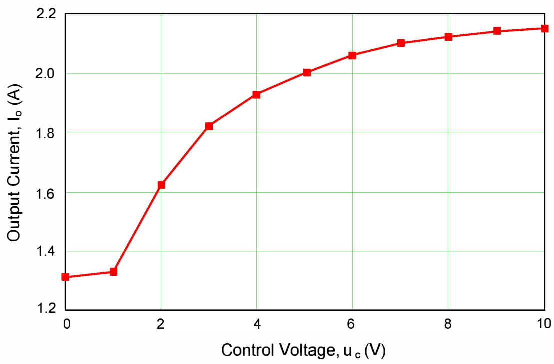

Fig. 12. Experimental result. LED current as a function of the control voltage u_c measured from the laboratory prototype.

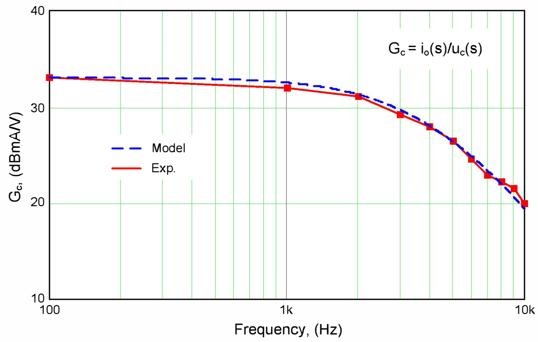

Fig. 13. Control transfer function output current (i_o) to control voltage (u_c) obtained experimentally from the laboratory prototype.

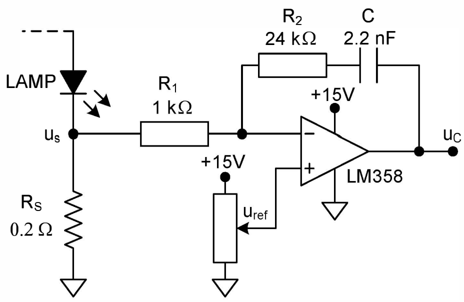

Fig. 14. Implemented PI regulator for closed-loop operation.

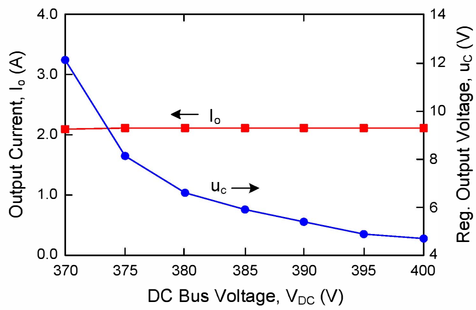

Fig. 15. Closed-loop operation experimental results. LED output current and compensator output voltage as a function of the DC bus voltage.

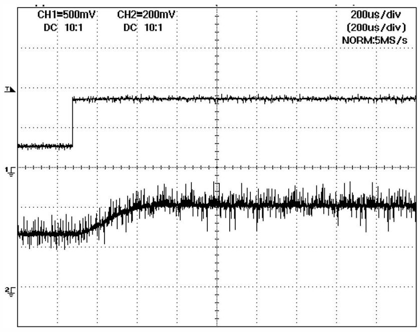

Fig. 16. Output current response for a step-up on the closed-loop reference voltage. Top: closed-loop reference voltage. Bot.: LED output current measured on a 0.2 Ω resistance. (500 mV/div, 1 A/div, 200 µs/div).

VII. Conclusions

This paper has presented and investigated a novel converter for LED driving for DC grid applications. The converter is based on a half bridge inverter, a single inductor, a transformer and a rectifier. This structure can be replicated to supply several LED arrays from the same half-bridge inverter. By using a VI on each branch it is possible to provide an independent control parameter for each branch, without requiring any additional downstream converter. The converter has thoroughly been studied for both steady state and dynamic operation. A novelty of this paper is the dynamic modelling of the VI, which makes it possible to obtain the dynamic behavior of the complete system. Both static and dynamic analysis have been verified experimentally by using a 50 W laboratory prototype supplied from a 380-400 V dc grid voltage. The procedure for dynamic modelling of the VI developed in this paper allows for a better understanding of its behavior and opens a new field of research and application of VI-based converters, where the complete static and dynamic behavior of the system can be taken into consideration.

References

[1] Wright, M.; "Lighting industry progresses on DC-power grids that pair well with LEDs," LEDs Magazine, April 2013.

[2] EMerge Alliance; "Public Overview of the EMerge Alliance Occupied Space Standard," Version 1.1, 2015.

[3] Boroyevich, D.; Cvetkovic, I.; Dong Dong; Burgos, R.; Fei Wang; Lee, F., "Future electronic power distribution systems a contemplative view," in Opt. of Electr. and Electro. Equip. (OPTIM), 2010 12th Int. Conf. on, pp.1369-1380, 20-22 May 2010.

[4] Gacio, D.; Alonso, J.M.; Garcia, J.; Garcia-Llera, D.; Cardesin, J., "Optimization of a Front-End DCM Buck PFP for an HPF Integrated Single-Stage LED Driver," in Em. and Sel. Topics in Power Electr., IEEE J. of , vol.3, no.3, pp. 666-678, Sept. 2015.

[5] Wang, Y; Huang, J.; Wang, W.; Xu, D; "A Single-stage Single-switch LED Driver Based on Integrated Buck-boost Circuit and Class E Converter," IEEE Ind. Appl. Soc. Meeting, Conf. Record, 2015.

[6] Almeida, P.S.; Braga, H.A.C.; Dalla Costa, M.A.; Alonso, J.M., "Offline Soft-Switched LED Driver Based on an Integrated Bridgeless Boost–Asymmetrical Half-Bridge Converter," in Ind. App., IEEE Tran. on , vol.51, no.1, pp.761-769, Jan.-Feb. 2015.

[7] Lee, E.S.; Choi, B.H.; Cheon, J.P.; Lim, G.C.; Kim, B.C.; Rim, C.T., "Temperature-Robust LC3 Passive LED Drivers With Low THD, High Efficiency and PF, and Long Life," in Em. and Sel. Topics in Power Electr., IEEE Journal of , vol.3, no.3, pp.829-840, Sept. 2015.

[8] Peng Fang; Yan-Fei Liu; Sen, P.C., "A Flicker-Free Single-Stage Offline LED Driver With High Power Factor," in Em. and Sel. Topics in Power Electr., IEEE Journal of , vol.3, no.3, pp.654-665, Sept. 2015.

[9] Santos Almeida, P.; Camponogara, D.; Dalla Costa, M.; Braga, H.; Alonso, J.M., "Matching LED and Driver Life Spans: A Review of Different Techniques," in Ind. Electr. Mag., IEEE , vol.9, no.2, pp.36-47, June 2015.

[10] Camponogara, D.; Ribeiro Vargas, D.; Dalla Costa, M.A.; Alonso, J.M.; Garcia, J.; Marchesan, T., "Capacitance Reduction With An Optimized Converter Connection Applied to LED Drivers," in Ind. Electr., IEEE Tran. on , vol.62, no.1, pp.184-192, Jan. 2015.

[11] Yajie Qiu; Laili Wang; Hongliang Wang; Yan-Fei Liu; Sen, P.C., "Bipolar Ripple Cancellation Method to Achieve Single-Stage Electrolytic-Capacitor-Less High-Power LED Driver," in Em. and Sel. Top. in Power Electr., IEEE Journal of , vol.3, no.3, pp.698-713, Sept. 2015.

[12] Y. Wang, Y. Guan, K. Ren, W. Wang and D. Xu, "A Single-Stage LED Driver Based on BCM Boost Circuit and LLC Converter for Street Lighting System," in IEEE Tran. on Ind. Electr., vol. 62, no. 9, pp. 5446-5457, Sept. 2015.

[13] J. I. Baek, J. K. Kim, J. B. Lee, H. S. Youn and G. W. Moon, "Integrated Asymmetrical Half-Bridge Zeta (AHBZ) Converter for DC/DC Stage of LED Driver With Wide Output Voltage Range and Low Output Current," in IEEE Tran. on Ind. Electr., vol. 62, no. 12, pp. 7489-7498, Dec. 2015.

[14] Y. C. Li, "A Novel Control Scheme of Quasi-Resonant Valley-Switching for High-Power-Factor AC-to-DC LED Drivers," in IEEE Tran. on Ind. Electr., vol. 62, no. 8, pp. 4787-4794, Aug. 2015.

[15] S. Moon, G. B. Koo and G. W. Moon, "Dimming-Feedback Control Method for TRIAC Dimmable LED Drivers," in IEEE Tran. on Ind. Electr., vol. 62, no. 2, pp. 960-965, Feb. 2015.

[16] Xuebing Chen; Daocheng Huang; Qiang Li; Lee, F.C., "Multichannel LED Driver With CLL Resonant Converter," in Em. and Sel. Topics in Power Electr., IEEE Journal of , vol.3, no.3, pp.589-598, Sept. 2015.

[17] Yuanjun Zhang; Chen Hu; Xinke Wu, "Analysis and design of LLCC resonant four-channel DC-DC LED driver with current sharing transformer," in App. Power Electr. Conf. (APEC), pp.3295-3300, 17-21 March 2013.

[18] Pinto, R.A.; Alonso, J.; Perdigao, M.S.; da Silva, M.F.; do Prado, R.N., "A New Technique to Equalize Branch Currents in Multiarray LED Lamps Based on Variable Inductors," in Ind. App., IEEE Tran. on, vol. 52, pp. 521-530, Jan. 2016.

[19] Lee, A.T.L.; Sin, J.K.O.; Chan, P.C.H., "Scalability of Quasi-Hysteretic FSM-Based Digitally Controlled Single-Inductor Dual-String Buck LED Driver to Multiple Strings," in Power Electr., IEEE Tran. on , vol.29, no.1, pp.501-513, Jan. 2014.

[20] Martins, M.; Perdigao, M.S.; Mendes, A.S.; Pinto, R.A.; Alonso, J.M., "Dimmable LED driver with variable inductor based on a resonant switched-capacitor topology," in Energy Conv. Cong. (ECCE), 2015 IEEE, pp. 5329-5336, 20-24 Sept. 2015.

[21] Perdigao, M.S.; Menke, M.; Seidel, A.R.; Pinto, R.A.; Alonso, J.M.; "A review on variable inductors and variable transformers: Applications to lighting drivers," IEEE Trans. on Ind. App., vol. 52, pp. 531-547, Jan. 2016.

[22] Alonso, J.M.; Perdigão, M.S.; Vaquero, D.G.; Calleja, A.J.; Saraiva, E.S.; "Analysis, Design, and Experimentation on Constant-Frequency DC-DC Resonant Converters With Magnetic Control," Power Electr., IEEE Trans. on , vol. 27, no. 3, pp. 1369-1382, March 2012.

[23] Electrical Drive Considerations for Bridgelux Vero Series LED Array. Bridgelux Application Note AN32. June 3, 2013.

[24] Alonso, J.M.; Gacio, D.; Sichirollo, F.; Seidel, A.R.; Dalla Costa, M.A., "A Straightforward Methodology to Modeling High Power Factor AC–DC Converters," in Power Electr., IEEE Tran. on , vol. 28, no. 10, pp. 4723-4731, Oct. 2013.

[25] Bridgelux RS Array Series. Product datasheet DS15. Jan. 2010.

[26] J. M. Alonso, M. Perdigão, G. Z. Abdelmessih, M. A. Dalla Costa, Y. Wang; "SPICE-Aided Design of a Variable Inductor in LED Driver Applications," IEEE Ind. Appl Soc. Ann. Meeting, Conf. Rec., Oct. 2016.

978-1-4799-8397-1/16/$31.00 © 2016 IEEE

INTERNATIONAL JOURNAL OF CIRCUIT THEORY AND APPLICATIONS
Int. J. Circ. Theor. Appl. (2017)
Published online in Wiley Online Library (wileyonlinelibrary.com). DOI: 10.1002/cta.2355

Simplified electrical modelling of power LEDs for DC–DC converter analysis and simulation

R. Osorio[1,*,†], J.M. Alonso[2], S.E. Pinto[3], G. Martínez[4], N. Vázquez[5], M. Ponce-Silva[6] and A.J. Martínez[7]

[1] *Department of Computer Science and Engineering, University of Guadalajara, Guadalajara-Ameca Highway Km. 45.5, Ameca, Jalisco ZC 46600, Mexico*
[2] *Electrical and Electronics Engineering Department, University of Oviedo, ZC 33204 Gijón, Spain*
[3] *Electronic Engineering Department, University of Panama, Octavio Méndez Pereira Avenue, Panama City, Republic of Panama*
[4] *R&D ID HMI Hardware Development Department, Continental Automotive, South peripheral ring, ZC 45601 Guadalajara, Jalisco, Mexico*
[5] *Electronic Department, Technological Institute of Celaya, Antonio García Cubas Street, number 600, ZC 38010 Celaya, Guanajuato, Mexico*
[6] *Electronic Engineering Department, National Center of Research and Technological Development, Cuernavaca ZC 62490, Mexico*
[7] *Metal Mechanics Department, Technological Institute of Zacatepec, Tecnológico Street, number 27, ZC 62780 Zacatepec, Morelos, Mexico*

SUMMARY

This paper presents a model of power light emitting diodes (LEDs) based on electrical variables and considering the concept of LED 'equivalent resistance', which has previously been used in discharge lamp modelling and is suitable to achieve fast simulations of LED converter systems. The model can be obtained with only some simple electrical measurements, thus making its implementation quite straightforward. The proposed model is oriented to the electronic engineering area, and it has special application for the simulation of the electrical behaviour of LEDs and dc–dc converter systems by using software like Simulink. In addition, the proposed model can also be employed for the theoretical analysis and design of LED drivers. Experimental and simulation results are obtained proving the feasibility of the proposed model.
Copyright © 2017 John Wiley & Sons, Ltd.

Received 12 October 2016; Revised 18 January 2017; Accepted 21 March 2017

KEY WORDS: power LED; modelling; simulation; LED driver

1. INTRODUCTION

Nowadays, power light emitting diodes (LEDs) are a good alternative for many lighting applications, because they have a high luminous efficiency and a long useful life. Therefore, several dc–dc converters have recently been proposed to feed power LEDs [1–6]. The simulations of these systems must be carried out with a reliable LED model so that the complete system behaviour can be investigated [7–14]. For that reason, an LED model that represents the electrical behaviour of the power LED with acceptable accuracy and with a simple parameter estimation process will be an excellent tool for electronic engineers, in order to perform a suitable analysis and simulation of power LED–dc–dc converter systems.

*Correspondence to: R. Osorio, Department of Computer Science and Engineering, University of Guadalajara, Guadalajara-Ameca Highway Km. 45.5, Ameca, Jalisco ZC 46600, Mexico.
†E-mail: reneosorios@yahoo.com

Copyright © 2017 John Wiley & Sons, Ltd.

LED modelling commonly requires advanced physics knowledge (electronic structure, optical and thermal properties) to develop a suitable model [7–10]. Also, the parameter estimation in some complex models is complicated due to the fact that in certain cases it requires complex laboratory tests [7–11], while some of these tests require sophisticated equipment, as for example an integrating sphere with an spectrometer [7–9]. Therefore, a simplified electrical model of power LEDs is proposed in this paper, in order to obtain acceptable simulation results of LED–dc–dc converter system simulations with a feasible parameter extraction process. The LED parameters are evaluated by means of straightforward measurements of current and voltage with the help of conventional instruments like multimeter and oscilloscope, which are available in a conventional electronic laboratory. Presently, there are some models proposed in the literature [7–18], but they are difficult to use, because they have several optical and thermal parameters to be extracted like for example the LED junction temperature.

In this paper, a simplified electrical nonlinear dynamic model to simulate LED–converter systems, prior to their physical implementation, is proposed. The model is suitable to minimize simulation time of LED converter systems due to its simplicity. Also, this model property is more useful if the designer requires to make some complex simulations (e.g. Monte Carlo). The model is obtained with only some simple electrical measurements. Therefore, the present model is a simple and alternative tool for LED driver designers. The model was extrapolated from the model of a discharge lamp presented in [19, 20], where the equivalent resistance and the constant time of the lamp were considered.

The proposed model only considers electrical variables. The optical variables are not considered here because they are used mainly to achieve a suitable illumination level in rooms. In other words, optical variables practically do not have any effects in the electric performance of the LED. On the other hand, the temperature variable is indirectly considered in the power of the LEDs because this power is affected by the temperature in a similar form than a discharge lamp [19, 20].

This paper is structured as follows: the power LED behaviour and modelling are presented in Section 2. The evaluation of the LED parameters is presented in Section 3. In Section 4, the simulation and experimental results are presented, and finally Section 5 furnishes the conclusions of this work.

2. POWER LIGHT EMITTING DIODE BEHAVIOUR AND MODELLING

2.1. Stationary-state behaviour

Power LEDs present a steady-state voltage–current characteristic, where each point of the curve is measured when the voltage and the current in the LED have reached steady state, in a similar form to a conventional diode characteristic. However, the forward voltage of power LEDs is higher than that of a regular diode used for signal rectification (e.g. 1N4001), as can be observed in Figure 1.

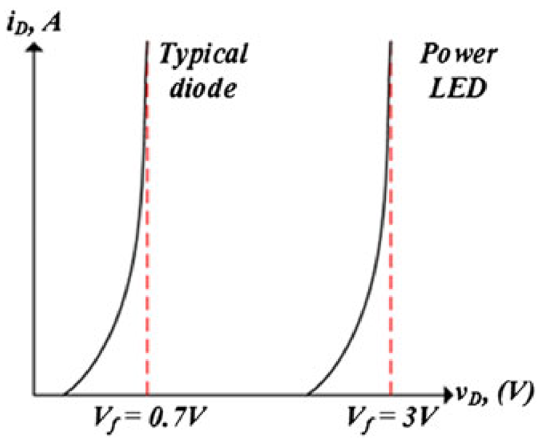

Figure 1. iD vs. vD, under steady-state conditions. [Colour figure can be viewed at wileyonlinelibrary.com]

Copyright © 2017 John Wiley & Sons, Ltd.

DOI: 10.1002/cta

The Shockley equation (1) is commonly used to model diode behaviour, and it can also be used to model the power LED behaviour [7–9].

$$i_D = I_s\left(e^{\frac{qv_D}{nkT_j}} - 1\right) \tag{1}$$

Equation (1) states that the diode current i_D is a function of the junction temperature T_j and the LED voltage v_D.

The junction temperature T_j is a function of the LED power p_D, as it is presented in equation (2). Also, LED voltage v_D is a function of the LED power p_D and the 'equivalent resistance' of the LED R_D, which is shown in equation (3). Similarly, the diode current i_D can be expressed as function of the LED power p_D and the 'equivalent resistance' of the LED, R_D, which is shown in equation (4).

$$T_j = f_2(p_D) \tag{2}$$

$$v_D = f_3(p_D, R_D) = \sqrt{p_D R_D} \tag{3}$$

$$i_D = f_4(p_D) = \sqrt{\frac{p_D}{R_D}} \tag{4}$$

On the other hand, power LEDs have different values of the 'equivalent resistance' R_D at different operating points. This resistance is a function of the LED voltage and current. Therefore, R_D is also a function of p_D, which is shown in equation (5). This equation has a typical representation as shown in Figure 2.

$$R_D = f_4(p_D) \tag{5}$$

Combining equations (1), (2), (3) and (4), an expression for equation (5) could be developed. However, equation (1) is a transcendental equation (exponential), and because of that, it is practically impossible to solve these equations for R_D as function of P_D in a closed form. Therefore, it is necessary to explore other ideas to solve the problem, which can be based on proposing a mathematical expression for equation (5). In this paper, the expression given by equation (6), previously presented in [20], is proposed because the graph of the 'equivalent resistance' of the discharge lamps modelled in that prior work has a similar form to the graph of the power LED 'equivalent resistance'.

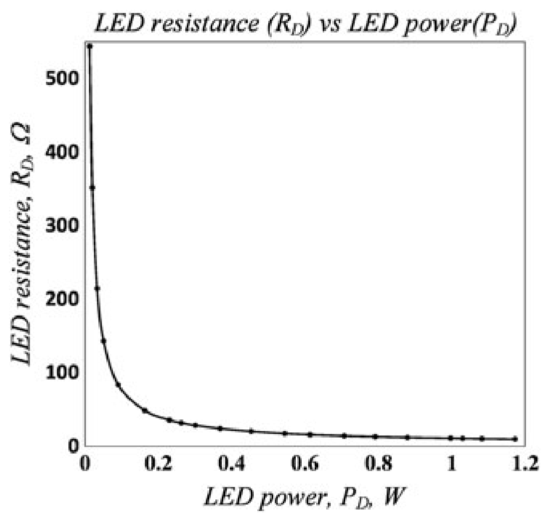

Figure 2. Typical form of the characteristic RD vs. pD of a power LED under steady-state conditions.

Copyright © 2017 John Wiley & Sons, Ltd.

DOI: 10.1002/cta

$$R_D = f_4(p_D) = B_1 {p_D}^{B_2} + B_3 \tag{6}$$

2.2. Dynamic behaviour

The time constant of LEDs has the same meaning as the time constant of discharge lamps, whose electric dynamical model was presented in [19, 20]. This time constant is related to the dynamic behaviour of the power LED, and it shows how fast is the dynamic response of the LED when the current has time-dependent behaviour. This time constant depends on the speed response of the LED voltage, and it can be measured from the LED voltage when a step current test is applied to the LED [19, 20]. It has been observed that power LEDs have a very fast dynamic response, with a very small time constant (in the order of nano seconds). This behaviour is demonstrated in Figure 3 (a) and (b), where current steps are applied to the LED by using the test circuit shown in Figure 4. However, the rise time of the current steps applied to the LED is not short enough to observe the constant time in the LED voltage with a proper precision. Therefore, only an approximation of the time constant can be measured with this test.

Therefore, the time constant of power LEDs is very difficult to measure with a simple electronic circuit with common devices (transistors and resistors with poor dynamical properties and with

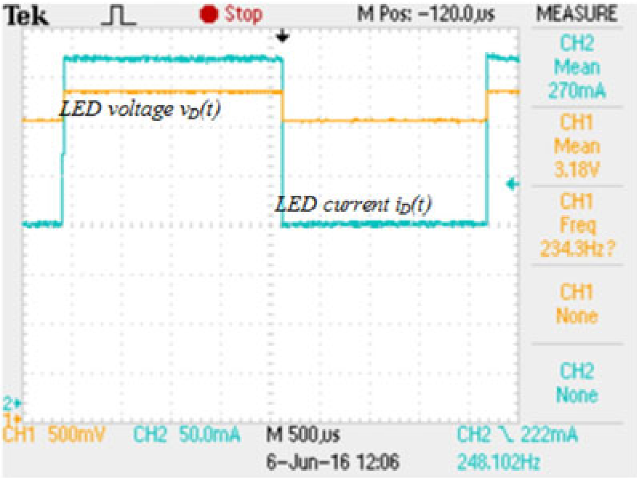

(a)

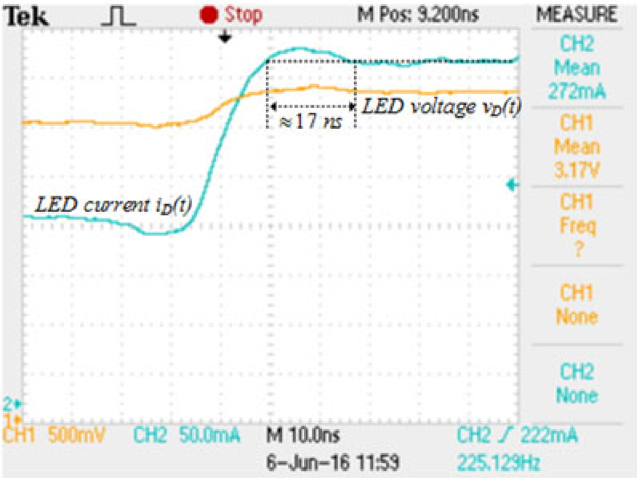

(b)

Figure 3. (a) Current steps applied to one LED of the panel (LMT-P12Y-77-N LED panel from Siled Company), CH2: 0.875A per division; (b) zoom of the current step test. [Colour figure can be viewed at wileyonlinelibrary.com]

Copyright © 2017 John Wiley & Sons, Ltd.

DOI: 10.1002/cta

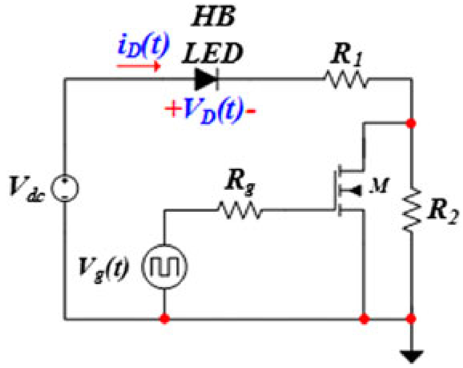

Figure 4. Test circuit #. [Colour figure can be viewed at wileyonlinelibrary.com]

considerable parasitic inductance) and using conventional equipment of an electronic laboratory, because with a small time constant the parasitic elements and the Printed Circuit Board (PCB) layout will affect the measurements. Thus, taking into account this fact, a fast mosfet transistor with low on resistance (PSMN1R2-25YL from NXP company) and Surface Mount Device (SMD) technology has been used to get an approximation of the time constant. For one of the LEDs on the Panel LMT-P12Y-77-N from Siled Company, an approximated measure of the time constant (17 ns) of the LED is shown in the Figure 3(b). The time constant was calculated as the time needed to reach 100% voltage from the point of 100% current.

2.3. *Light emitting diode modelling*

Based on [19, 20], the 'equivalent resistance' of the LED R_D can be expressed as function of its power p_D. Therefore, equation (7) is expressed as a function of time, which is shown in equation (8).

$$R_D(t) = f(p_{Dx}(t)) = B_1 p_{Dx}(t)^{B_2} + B_3 \tag{7}$$

where: p_{dx} is a variable related to the LED power, which can be observed in Figure 5.

The time constant of the LED is modelled by using an *RC* network, which is shown in Figure 5.

3. EVALUATION OF THE LIGHT EMITTING DIODE PARAMETERS

The schematic diagram of the test circuit used to extract the steady-state LED parameters is shown in Figure 6.

A test under steady-state conditions was carried out to obtain the parameters needed in equation (8). The characterization methodology is shown in Table I.

The experimental results for one LED of the panel (*LMT-P12Y-77-N from Siled Company*) are shown in Table II and plotted in Figure 7.

At stationary state, equation (7) is transformed into equation (9):

$$R_D = f(p_{Dx}) = B_1 p_{Dx}{}^{B_2} + B_3 \tag{8}$$

Using a curve fitting method (nonlinear least squares) and the data in Table II, B_1, B_2 and B_3 values of the equation (8) are obtained as 7.986, −0.9607 and 2.828, respectively. The curve fitting process was realized with the help of the curve fitting toolbox of MATLAB software. Equation (8) is plotted in Figure 7(a) along with experimental results. Both curves (theoretical and experimental) match very well, showing a relative error of only 1.13%. The range of value for the LED power are (0.0123 W, 1.1725 W), and for the LED resistance (9.57 Ω, 544.12 Ω). Figure 7(b) shows the VI curve of the LED under test, which is obtained by using equation (8). This figure shows how the equation also reproduces the voltage threshold of the LED, which is achieved by means of the exponential term, P_{Dx}^{B2}. The minimum current in the VI curve was 1 μA.

Copyright © 2017 John Wiley & Sons, Ltd.

DOI: 10.1002/cta

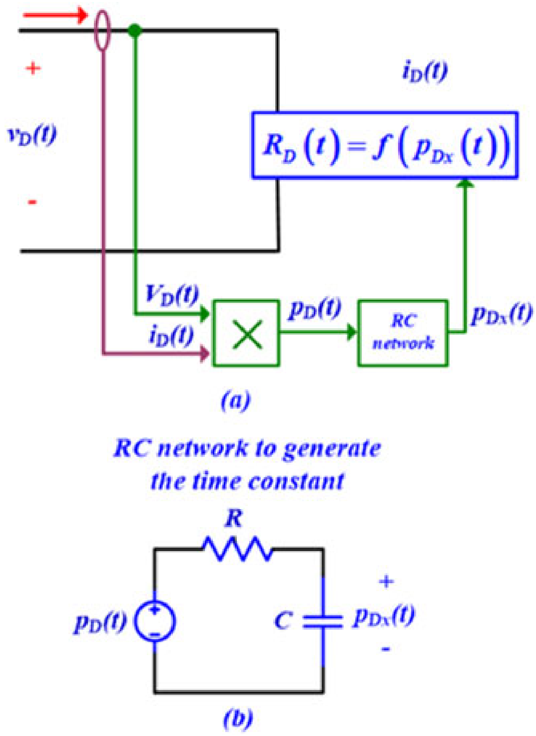

Figure 5. Diagrams of the proposed model: (a) block diagram; (b) schematic diagram of the RC network. [Colour figure can be viewed at wileyonlinelibrary.com]

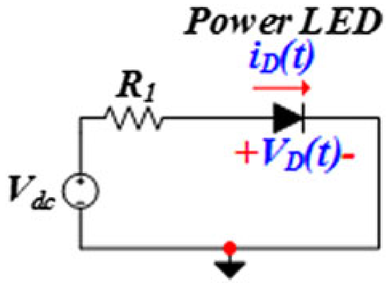

Figure 6. Test circuit #2. [Colour figure can be viewed at wileyonlinelibrary.com]

Table I. LED characterization methodology under steady-state conditions.

a. Operation conditions
a.1. The LED resistance R_D and the LED power p_D are obtained for different operation points.
a.2. About ≅20 values are taken between maximum and minimum values, which allow for an appropriate characterization of the LED resistance.
b. Measurement procedure
b.1. Turn on the LED,
b.2. Adjust the LED current to the required level,
b.3. Measure the LED current and voltage.
c. Obtained data and graphs
c.1. LED current i_D and LED voltage v_D.
c.2. LED resistance vs. LED power: R_D vs. p_D.

In order to implement the time constant of 17 ns, the following values were employed for the R_i and C_i components: $R_i = 1\ \Omega$ and $C_i = 17$ nF.

Copyright © 2017 John Wiley & Sons, Ltd.

DOI: 10.1002/cta

Table II. Experimental data for one LED from the LED panel (*LMT-P12Y-77-N from Siled Company*) for different power levels, at steady state and at approximately 27 °C.

Number of samples	v_D (V)	i_D (A)	p_D *or* p_{Dx} (W)	R_D (Ω)
1	3.35	0.35	1.1725	9.57
2	3.31	0.327	1.0824	10.12
3	3.29	0.313	1.0298	10.51
4	3.28	0.304	0.9971	10.79
5	3.22	0.273	0.8791	11.79
6	3.19	0.248	0.7911	12.86
7	3.14	0.225	0.7065	13.96
8	3.1	0.198	0.6138	15.66
9	3.06	0.178	0.5447	17.19
10	3.02	0.15	0.4530	20.13
11	2.97	0.124	0.3683	23.95
12	2.92	0.103	0.3008	28.35
13	2.88	0.0911	0.2624	31.61
14	2.86	0.0804	0.2299	35.57
15	2.81	0.0578	0.1624	48.62
16	2.74	0.0328	0.0899	83.54
17	2.69	0.0188	0.0506	143.09
18	2.66	0.0124	0.0330	214.52
19	2.64	0.00751	0.0198	351.53
20	2.59	0.00476	0.0123	544.12

The proposed model was implemented in Simulink, which is a tool included in Matlab software. The schematic diagram of the Simulink circuit is shown in Figure 8(a). This diagram was implemented with the same technique used in references [19, 20], where voltage controlled voltage sources were used to implement, in electronic simulation software like Simulink, Pspice, Psim, etc., an electronic component with a nonlinear behaviour. In this case, a variable resistance expressed by a nonlinear function. This is the case of discharge lamps and power LEDs proposed in this work.

where:

VD(t)1 and pD(t)1 are voltage controlled voltage sources,

vD(t) and vD(t)2 are voltage sensors,

iD(t) is a current sensor,

pD(t) and iD(t)*RD(t) are multipliers,

Resistance limiter is a limiter or saturation block.

RD(t) is a function block,

Ri is a resistor,

Ci is a capacitor.

The resistance limiter is a saturation block (0.1 to 10 kΩ), and its purpose is to avoid the simulation of unmodelled operation points with the proposed model.

The source VD(t)1 is used to implement the LED voltage behaviour, and it is used to connect the model to dc–dc converters. The source pD(t)1 and the multiplier pD(t) are used to generate the LED power. The sensors iD(t) and vD(t) are used to sense the LED current and voltage, respectively. The block RD(t) represents the LED resistance, and the multiplier iD(t)*RD(t) is used to generate the LED voltage, which controls the source vD(t)1. The sensor vD(t)2 is used to measure the variable $p_{Dx}(t)$ presented in equation (8). As previously commented, Ri and Ci components implement the LED time constant.

4. EXPERIMENTAL AND SIMULATION RESULTS

4.1. Model validation

In order to validate the proposed model, experimental and simulation results were compared. The test circuit is the same as that previously presented in Figure 4, which is implemented with the following specifications: nominal LED power $p_D = 1$ W, input voltage $V_{dc} \cong 8.55$ *Vdc*, LED voltage $v_D = 3.3$

Copyright © 2017 John Wiley & Sons, Ltd.

DOI: 10.1002/cta

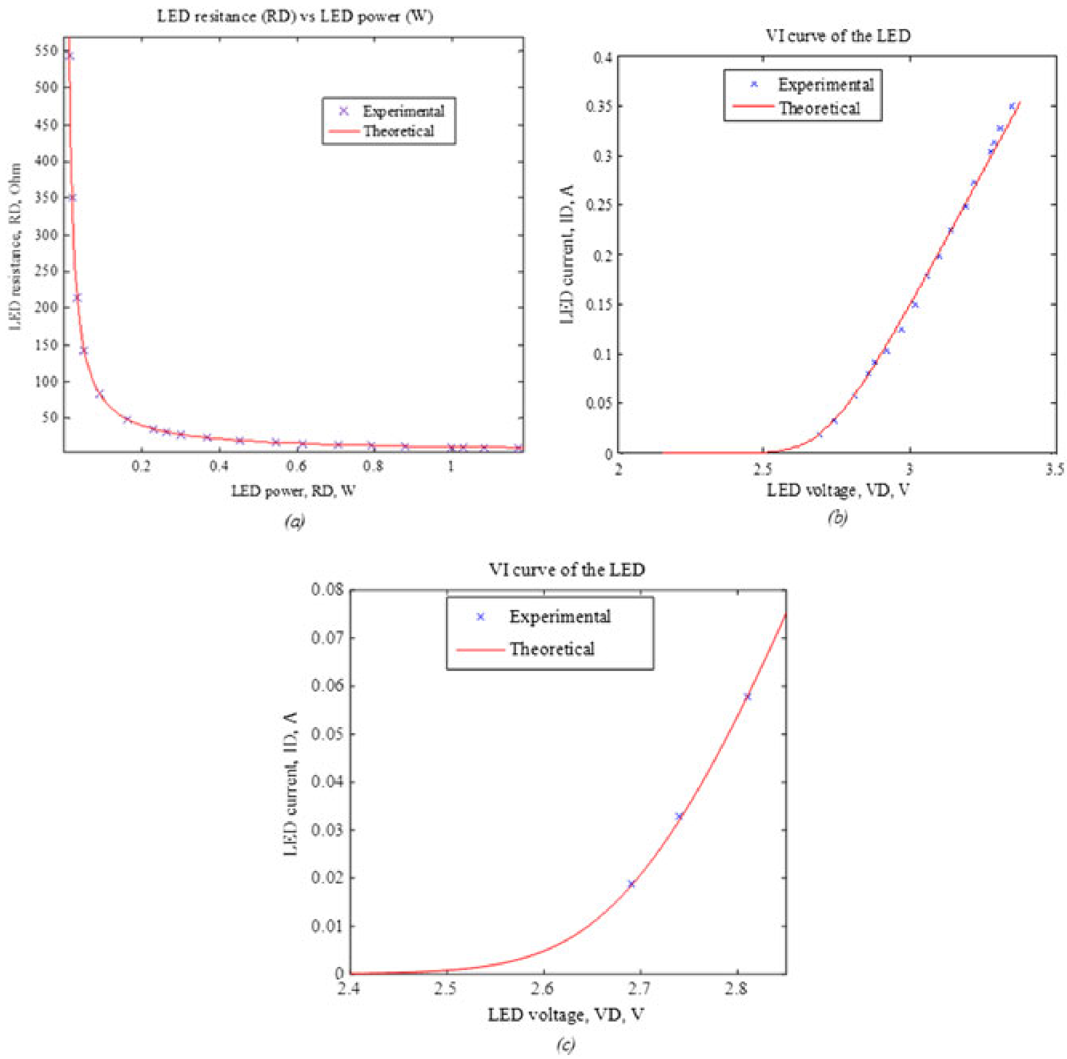

Figure 7. Curves of the LED: (a) RD vs. pD, experimental results vs. modelling results under steady-state conditions; (b) VI curve; (c) zoom in of the curve VI. [Colour figure can be viewed at wileyonlinelibrary.com]

Vdc, LED current $i_D = 0.350$ A, $R_1 = R_2 \cong 15\ \Omega$, Q = PSMN1R2-25YL, one LED of the LED panel (*LMT-P12Y-77-N from Siled Company*).

The experimental data obtained for the LED current are introduced in the model in order to test the LED voltage behaviour. This process was carried out in Simulink using the model shown in Figure 8 (b).

Figure 9 shows a dynamic test based on pulses applied to transistor Q of Figure 4. As can be seen in the figure, the model reproduces appropriately the real behaviour of the LED voltage. Also, oscilloscope waveforms are the same as that previously presented in Figure 3.

4.2. *Simulation example with a dc–dc converter*

In order to verify the correct operation of the proposed LED model working with a dc–dc converter, a laboratory prototype of Buck converter without output capacitor was built so that experimental results and model simulation results can be compared. A Buck converter without output capacitor was selected because it can be used to apply a large current ripple to the LED panel with the purpose of testing the complete range of operation. Also, this test is useful to evaluate the accuracy of the

Copyright © 2017 John Wiley & Sons, Ltd.

DOI: 10.1002/cta

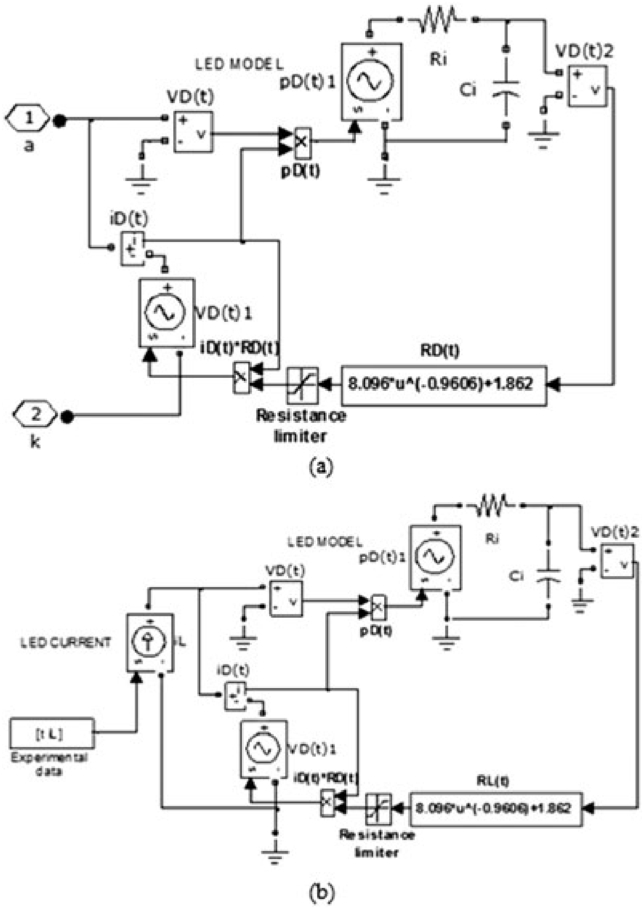

Figure 8. (a) Proposed model implemented in Simulink; (b) test circuit for the model validation implemented in Simulink.

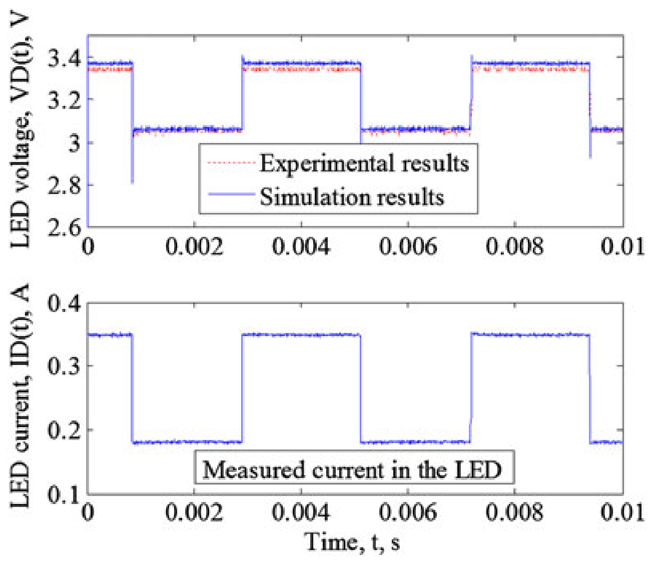

Figure 9. Simulation results vs. experimental results under dynamic operation conditions. [Colour figure can be viewed at wileyonlinelibrary.com]

Copyright © 2017 John Wiley & Sons, Ltd.

DOI: 10.1002/cta

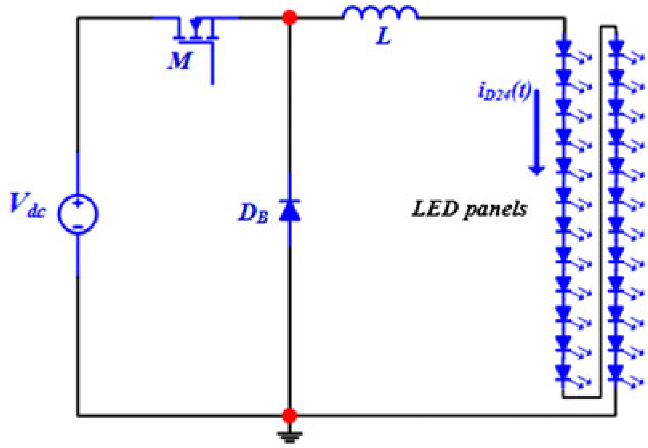

Figure 10. Buck converter without output capacitor. [Colour figure can be viewed at wileyonlinelibrary.com]

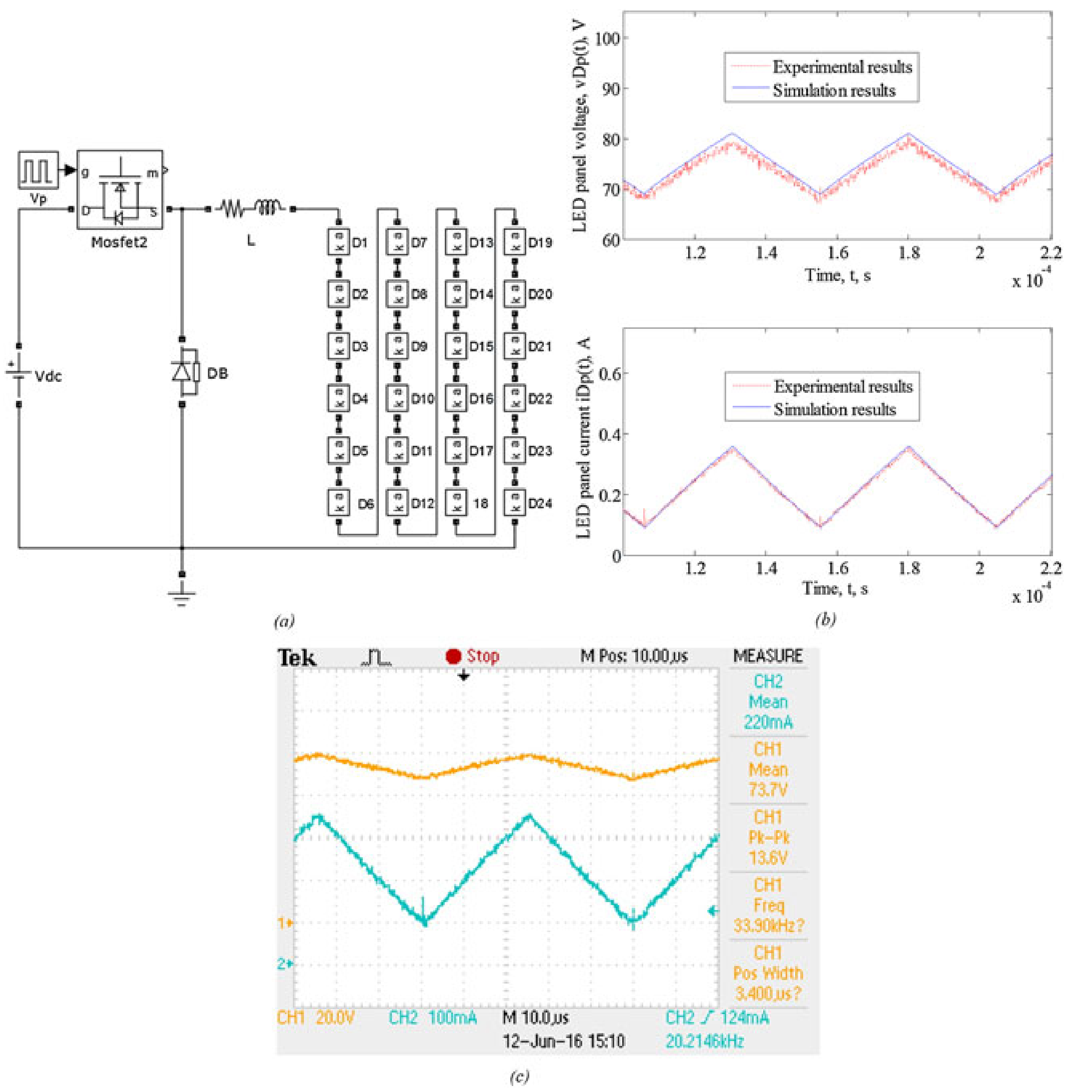

Figure 11. Results of the buck converter: (a) Simulink diagram; (b) simulation and experimental results; (c) oscilloscope waveforms. [Colour figure can be viewed at wileyonlinelibrary.com]

Copyright © 2017 John Wiley & Sons, Ltd.

DOI: 10.1002/cta

model when is used to simulate several LEDs connected in series. In this case, two panel LMT-P12Y-77-N from Siled Company with 12 LEDs in series (in total 24 LEDs were used) was connected to the Buck converter. A comparison between experimental and simulation results was carried out.

The schematic diagram of the Buck converter is shown in Figure 10, which has the following specifications: nominal power of the panel p_{D24} = 24 W, input voltage V_{dc} = 154 *Vdc*, panel voltage v_{D24} = *79.2 Vdc*, panel current i_{D9} = 0.350 A, L = 7.126 mH, f = 20 kHz, LED panel *LMT-P12Y-77-N from Siled Company*. The circuit was also simulated in Simulink, as illustrated in Figure 11(a). Each LED of the panel was simulated using the model shown in Figure 8.

Figure 11(b) shows the experimental and simulation results of the LED–Buck converter system. As can be seen, the obtained results are very satisfactory, because the plots have similar waveforms. Also, this test proves that the model can be connected in series to simulate the behaviour of an LED panel composed with several power LEDs. The mean square error was 2.82 V (3.76%), which can be attributed to the tolerances among the different LEDs that made up the string. Also, oscilloscope waveforms are shown in Figure 11(c).

The models presented in [7–15] have parameters that are difficult to measure, as the junction temperature for instance, because this variable needs to be measured inside the LEDs, which is difficult to access. The model presented in [16, 17] also incorporates optic concepts that are not essentials to simulate the electric behaviour of the LEDs. In [18], a review of LED models is presented; some of them are good alternatives to simulate the electrical behaviour of LEDs. There are linear models with a simple extraction parameter process and nonlinear model with a more complex parameter extraction process. The proposed model is a simplified nonlinear model with a simple parameter extraction process based on a different concept, which is the 'equivalent resistance' of the LED. This makes it a good alternative to perform LED simulations of its electrical behaviour.

The equipment used in the test were power supply model DLM300-2 (Sorensen), one bench supply GPS-3303 (GW Instek), one oscilloscope TDS2002B (Tektronix), one voltage differential probe N2791A (Keysight Technologies) and one current probe TCP2020 (Tektronix).

5. CONCLUSIONS

In this paper, a simplified electrical model for power LEDs has been proposed where the concept of 'LED equivalent resistance' is used. This model is based on electrical variables like the voltage, current, resistance and power in the LEDs. The time constant of the LEDs is also considered in the model, which is related to the dynamical behaviour of the LEDs. This modelling method was satisfactorily used in the modelling of discharge lamps, and it was extrapolated to the modelling of the power LEDs. The model can be implemented in simulation programs like Simulink and PSIM. The parameters of the proposed model are obtained from experimental measurements of current and voltage in the LED. The model was implemented in 'Simulink' and 'PSIM'. The simulation and experimental results were compared, and the obtained results were satisfactory. The proposed model is recommended to simulate lighting systems based on power LEDs and dc–dc converters. A future work about this kind of model for power LEDs contemplates a more complex LED model version with the incorporation of temperature effects for application where the operating temperature is a critical parameter, for example to perform a proper selection of the LED heatsink. Also, it is necessary to find other methods to obtain a better measurement of the time constant of the LEDs, which will be investigated and presented in the future.

ACKNOWLEDGEMENTS

This work was supported by the National Council of Science and Technology (CONACYT), the Professional Development Program for Teachers (PRODEP) and The University of Guadalajara (UDG).

Copyright © 2017 John Wiley & Sons, Ltd.

DOI: 10.1002/cta

NOMENCLATURE

B_1, B_2 and B_3	are constants.
$i_D(t)$	is the LED current, Ampere (A).
i_D	is the steady-state value of $i_D(t)$, Ampere (A).
$p_D(t)$	is the LED power, Watt (W).
p_D	is the steady-state value of $p_D(t)$, Watt (W).
R_1 and R_2	are constant resistances, Ohm (Ω).
$R_D(t) = v_D(t)/i_D(t)$	is the 'equivalent resistance' of the LED, Ohm (Ω).
R_D	is the steady-state value of the 'equivalent resistance' of the LED, Ohm (Ω).
$v_D(t)$	is the LED voltage, Volt (V).
v_D	is the steady-state value of $v_D(t)$, Volt (V).
$T_j(t)$	is the junction temperature of the LED, Kelvin (K).
T_j	is the steady-state value of $T_j(t)$, Kelvin (K).
I_S	is the reverse bias saturation current, Ampere (A).
k	is the Boltzmann constant.
q	is the magnitude of charge of an electron, Coulomb (C).
T_j	is the absolute temperature of the p-n junction, Kelvin (K).
n	is the emission coefficient.

REFERENCES

1. Lin Y-L, Leng C-M, Wang J-M. A simple LED driver with low dimming switch stress. *International Journal of Circuit Theory and Applications* 2016; **44**(3):683–692.
2. Ma H, Zheng C, Yu W, Lai J-S(J). A single-stage integrated bridgeless AC/DC converter for electrolytic capacitor-less LED lighting applications. *International Journal of Circuit Theory and Applications* 2015; **43**(6):742–755.
3. Chiu H-J, Cheng S-J. Design considerations of an SEPIC PFC converter for driving multiple lighting LED lamps. *International Journal of Circuit Theory and Applications* 2009; **37**(8):928–940.
4. Chiu H-J, Huang H-M, Yang H-T, Cheng S-J. An improved single-stage Flyback PFC converter for high-luminance lighting LED lamps. *International Journal of Circuit Theory and Applications* 2008; **36**(2):205–210.
5. Zhang T, Qian Q, Xu S, Lu S, Sun W. An electrolytic capacitor-less LED driver with interleaving flyback topology. *International Journal of Circuit Theory and Applications* 2015; **43**(12):2025–2038.
6. Ma H, Lai J-S(J), Feng Q, Yu W, Zheng C. A universal-input high-power-factor power supply without electrolytic capacitor for multiple lighting LED lamps. *International Journal of Circuit Theory and Applications* 2013; **41**(5):514–534.
7. Park J, Lee CC. An electrical model with junction temperature for light-emitting diodes and the impact on conversion efficiency. *IEEE Electron Device Letters* 2005; **26**(5):308–310.
8. Baureis P. Compact modeling of electrical, thermal and optical LED behavior. IEEE Solid-State Device Research Conference, ESSDERC 2005; 145–148.
9. Marcuse D, Kaminow I. Computer model of a superluminescent LED with lateral confinement. *IEEE Journal of Quantum Electronics* 1981; **17**(7):1234–1244.
10. Gacio D, Alonso JM, Garcia J, Perdigao MS, Saraiva E, Bisogno FE. Effects of the junction temperature on the dynamic resistance of white LEDs. *IEEE Transactions on Industry Applications* 2013; **49**(2):750–760.
11. Farkas G, Vader QV, Poppe A, Bognar G. Thermal investigation of high power Optical Devices by transient testing. *IEEE Transactions on Components and Packaging Technologies* 2005; **28**(1):45–50.
12. Poppe A, Lasance CJM. On the standardization of thermal characterization of LEDs. *25th Annual IEEE Semiconductor Thermal Measurement and Management Symposium (SEMI-THERM)*, San Jose, CA, 2009; 151–158.
13. Poppe A. Multi-domain compact modeling of LEDs: an overview of models and experimental data. *Microelectronics Journal* 2015; **46**(12, Part A):1138–1151.
14. Lasance CJM, Poppe A. Challenges in LED thermal characterisation. *10th International Conference on Thermal, Mechanical and Multi-Physics simulation and Experiments in Microelectronics and Microsystems (EuroSimE)*, Delft, 2009; 1–11.
15. Górecki K. Modelling mutual thermal interactions between power LEDs in SPICE. *Microelectronics Reliability* 2015; **55**(2):389–395.
16. Almeida PS, Bender VC, Braga HAC, Dalla Costa MA, Marchesan TB, Alonso JM. Static and dynamic photoelectrothermal modeling of LED lamps including low-frequency current ripple effects. *IEEE Transactions on Power Electronics* 2015; **30**(7):3841–3851.

Copyright © 2017 John Wiley & Sons, Ltd.

17. Lin R-L, Tsai J-Y, Alonso JM, Gacio D. Four-parameter Taylor series based light-emitting-diode model. *IEEE Industry Application Society Annual Meeting*, Vancouver, BC, Canada, 2014; 1–6.
18. Bender VC, Marchesan TB, Alonso JM. Solid-state lighting: a concise review of the state of the art on LED and OLED modeling. *IEEE Industrial Electronics Magazine* 2015; **9**(2):6–16.
19. Osorio R, Pinto S, Vázquez N, Martínez G, Ponce M, Padilla A, Prado J. Stationary state error reduction on the electrical modelling of high pressure sodium lamps. *IET Electric Power Applications* 2011; **5**(4):350–358
20. Osorio R, Vázquez N, Hernández C, Rodríguez E, Pinto SE, Juárez M. Electric dynamic modeling of HID lamps for electronic ballast design. *IEEE Transactions on Industrial Electronics* 2010; **57**(5):1655–1662.

Copyright © 2017 John Wiley & Sons, Ltd.

DOI: 10.1002/cta

Design calculation:

Input parameters:

Switching frequency (Hz):	$f_s := 100 \cdot 10^3$
Maximum inductance (H):	$L_r := 18.52 \cdot 10^{-6}$
Permeability of the free space (Wb/A):	$\mu 0 := 4 \cdot \pi \cdot 10^{-7}$
Permeability of the material:	$\mu r := 2200 \quad -8$
Copper resistivity (Ohm.m):	$\rho_{Cu} := 1.72 \cdot 10$
RMS inductor current (A):	$I_{rms} := 1.55$
Winding length (m):	$G_w := 16.4 \cdot 10^{-3}$
Maximum current (A):	$I_{max} := 3.3$
Magnetic flux density (T):	$B_{ac} := 0.095$
DC winding current (A):	$I_{dc} := 0.5$

EFD25/13/9 N87 TDK EPCOS Core parameters:

Effective area (m): $Ae := 58.61 \cdot 10^{-6}$

Effective length (m): $le := 57 \cdot 10^{-3}$

Bobbin window area (m): $A_{wb} := 40.7 \cdot 10^{-6}$

Core window area (m): $A_{wc} := 69.86 \cdot 10^{-6}$

Effective volume (m): $Ve := 3310 \cdot 10^{-9}$

Average length per turn (m): $l_N := 50 \cdot 10^{-3}$

External path length (m): $l_{ext} := 100 \cdot 10^{-3}$

AC main winding calculation:

Number of turns: $N_{ac} := \dfrac{L_r \cdot I_{max}}{B_{ac} \cdot Ae}$ $\qquad N_{ac} = 10.9764$

Air gap length (m): $lg := \mu 0 \cdot Ae \cdot \left(\dfrac{{N_{ac}}^2}{L_r} - \dfrac{le}{\mu 0 \cdot \mu r \cdot Ae} \right)$ $\qquad lg = 4.5323 \times 10^{-4}$

Fringing flux factor: $F_f := \left(1 + \frac{lg}{\sqrt{Ae}} \cdot \ln\left(\frac{2 \cdot G_w}{lg}\right)\right)$ $F_f = 1.2535$

Air gap available (m): $lg_1 := 0.57 \cdot 10^{-3}$

Recalculating fringing flux factor:

New winding length for 11 turns (m): $G_{w1} := 9.57 \cdot 10^{-3}$

Fringing flux factor: $F_{f1} := \left(1 + \frac{lg_1}{\sqrt{Ae}} \cdot \ln\left(\frac{2 \cdot G_{w1}}{lg_1}\right)\right)$ $F_{f1} = 1.2616$

Recalculating inductance Lr:

New Inductance (H):

$$L_{r1} := \frac{\left(\mu 0 \cdot N_{ac}^{2} \cdot Ae \cdot F_{f1}\right)}{lg_1 + \frac{le}{\mu r}} = 1.8787 \times 10^{-5}$$

Recalculating magnetic flux density:

New magnetic flux density (T):

$$B_{ac1} := \frac{\left(N_{ac} \cdot \mu 0 \cdot F_{f1}\right)}{\frac{le}{\mu r} + lg_1} \cdot I_{max} = 0.0964$$

AC winding wire maximum diameter:

Skin depth: $\delta_{sk} := \sqrt{\frac{\rho_{Cu}}{\pi \cdot f_s \cdot \mu 0}}$ $\delta_{sk} = 2.0873 \times 10^{-4}$

Maximum wire diameter (m): $D_{max} := 2 \cdot \delta_{sk}$ $D_{max} = 4.1746 \times 10^{-4}$

Selected wire diameter (m): $D_{ac} := 0.08 \cdot 10^{-3}$

Number of wires: $N_{wac} := \frac{4 \cdot 0.3 \cdot A_{wb}}{N_{ac} \cdot \pi \cdot D_{ac}{}^2}$ $N_{wac} = 221.3024$

Number of wires selected: $N_{ws} := 66$

DC auxiliary windings calculation:

Magnetic flux density (T): $B_{dc} := B_{ac1} \cdot 4.5 = 0.4337$

Number of turns: $N_{dc} := \dfrac{B_{dc} \cdot l_{ext}}{0.5 \cdot \mu r \cdot \mu 0 \cdot I_{dc}} = 62.7442$

Selected wire diameter (m): $D_{dc} := 0.35 \cdot 10^{-3}$

Number of wires: $N_{wdc} := \dfrac{4 \cdot 0.3 \cdot A_{wb}}{N_{dc} \cdot \pi \cdot D_{dc}{}^{2}}$ $N_{wdc} = 2.0226$

Number of wires selected: $N_{ws1} := 1$

Total window utilization factor:

$$A_{wtotal} := N_{wac} \cdot N_{ac} \cdot \frac{\left(\pi \cdot D_{ac}{}^{2}\right)}{4} + N_{wdc} \cdot N_{dc} \cdot \frac{\left(\pi \cdot D_{dc}{}^{2}\right)}{4} = 2.442 \times 10^{-5}$$

$$A_{wavg} := \frac{\left(A_{wc} + A_{wb}\right)}{2} = 5.528 \times 10^{-5}$$

$$K_{u} := \frac{A_{wtotal}}{A_{wavg}} = 0.4418$$